STINFO Copy

Mixing Dynamics of Supercritical Droplets and Jets

D.G. Talley
R.K. Cohn
E.B. Coy

AFRL/PRSA
10 E. Saturn Blvd.
Edwards AFB CA 93524-7680

B. Chehroudi
D.W. Davis

ERC, Inc.
10 E. Saturn Blvd.
Edwards AFB, CA 93524-7680

Revised August 2006 to Include Appendices
April 2005
Final Report

AIR FORCE RESEARCH LABORATORY
AIR FORCE MATERIEL COMMAND
EDWARDS AIR FORCE BASE CA 93524-7048

REPORT DOCUMENTATION PAGE

Form Approved
OMB No. 0704-0188

1. REPORT DATE *(DD-MM-YYYY)*	**2. REPORT TYPE**	**3. DATES COVERED** *(From - To)*
17-03-2005	Final In-House Report	01 Oct 1992 – 31 Dec 2004

4. TITLE AND SUBTITLE

Mixing Dynamics of Supercritical Droplets and Jets (Revised To Include Appendices)

5a. CONTRACT NUMBER

5b. GRANT NUMBER

5c. PROGRAM ELEMENT NUMBER
61102F

6. AUTHOR(S)

D.G. Talley; B. Chehroudi; D.W. Davis; R.K. Cohn; E.B. Coy

5d. PROJECT NUMBER
2308

5e. TASK NUMBER
M13C

5f. WORK UNIT NUMBER
346057

7. PERFORMING ORGANIZATION NAME(S) AND ADDRESS(ES)

AFRL/PRSA
10 E. Saturn Blvd.
Edwards AFB CA 93524-7680

ERC, Inc.
10 E. Saturn Blvd.
Edwards AFB CA 93524-7680

8. PERFORMING ORGANIZATION REPORT NO.

9. SPONSORING / MONITORING AGENCY NAME(S) AND ADDRESS(ES)

Air Force Research Laboratory (AFMC)
AFRL/PRS
5 Pollux Drive
Edwards AFB CA 93524-7048

10. SPONSOR/MONITOR'S ACRONYM(S)

XC

11. SPONSOR/MONITOR'S REPORT NUMBER(S)

AFRL-PR-ED-TR-2005-0023

12. DISTRIBUTION / AVAILABILITY STATEMENT

Approved for public release; distribution unlimited. Public Affairs No. AFRL-ERS-PAS-06-283.

13. SUPPLEMENTARY NOTES

14. ABSTRACT

This report summarizes a research program to understand the mixing dynamics of supercritical droplets and jets. The research was motivated by the recognition that pressures in modern liquid rocket engine combustion chambers tend to be higher than the critical pressure of one or more of the propellants. Prior to the beginning of this research, combustion processes were largely modeled using low pressure, subcritical spray combustion concepts. At supercritical pressures, however, a distinct difference between "gaseous" and "liquid" phases no longer exists, surface tension and the enthalpy of vaporization vanish, and "gas" phase density can approach that of the "liquid" with correspondingly significantly enhanced aerodynamic forces relative to the "liquid." These and other effects are discussed in detail in the references contained in the report. Under such conditions, questions such as whether droplets can even exist or what "spray combustion" would look like lacked even qualitative answers at the beginning. As a result of the research conducted under this program, most of the qualitative questions have now been answered, and significant progress has been made in determining quantitative mechanisms.

15. SUBJECT TERMS
liquid rocket engine; combustion chamber; supercritical droplets; jets; spray combustion

16. SECURITY CLASSIFICATION OF:			**17. LIMITATION OF ABSTRACT**	**18. NUMBER OF PAGES**	**19a. NAME OF RESPONSIBLE PERSON**
a. REPORT	**b. ABSTRACT**	**c. THIS PAGE**			Douglas G. Talley
Unclassified	**Unclassified**	**Unclassified**	A	375	**19b. TELEPHONE NO** *(include area code)* (661) 275-6174

Standard Form 298 (Rev. 8-98)
Prescribed by ANSI Std. 239.18

STINFO COPY
NOTICE AND SIGNATURE PAGE

Using Government drawings, specifications, or other data included in this document for any purpose other than Government procurement does not in any way obligate the U.S. Government. The fact that the Government formulated or supplied the drawings, specifications, or other data does not license the holder or any other person or corporation; or convey any rights or permission to manufacture, use, or sell any patented invention that may relate to them.

This report was cleared for public release by the Air Force Research Laboratory [AFRL/ PROI, Edwards AFB CA] Public Affairs Office and is available to the general public, including foreign nationals. Copies may be obtained from the Defense Technical Information Center (DTIC) (http://www.dtic.mil).

AFRL-PR-ED-TR-2005-0023 HAS BEEN REVIEWED AND IS APPROVED FOR PUBLICATION IN ACCORDANCE WITH ASSIGNED DISTRIBUTION STATEMENT.

FOR THE DIRECTOR:

//signed//
DOUGLAS G. TALLEY
Project Manager

//signed//
INGRID J. WYSONG
Chief, Aerophysics Branch

//signed//
PHILIP A. KESSEL
Technical Advisor
Space & Missile Propulsion Division

This report is published in the interest of scientific and technical information exchange, and its publication does not constitute the Government's approval or disapproval of its ideas or findings.

*Disseminated copies will show "//signature//" stamped or typed above the signature blocks.

This Page Intentionally Left Blank

TABLE OF CONTENTS

EXECUTIVE SUMMARY

This report summarizes a research program to understand the mixing dynamics of supercritical droplets and jets. The research was motivated by the recognition that pressures in modern liquid rocket engine combustion chambers tend to be higher than the critical pressure of one or more of the propellants. Prior to the beginning of this research, combustion processes were largely modeled using low pressure, subcritical spray combustion concepts. At supercritical pressures, however, a distinct difference between "gaseous" and "liquid" phases no longer exists. Surface tension and the enthalpy of vaporization vanish, and "gas" phase density can approach that of the "liquid," with corresponding significantly enhanced aerodynamic forces relative to the "liquid." These and other effects are discussed in detail in the references listed below. Under such conditions, questions such as whether droplets can even exist or what "spray combustion" would look like lacked even qualitative answers at the beginning. As a result of the research conducted under this program, most of the qualitative questions have now been answered, and significant progress has been made in determining quantitative mechanisms.

Early work consisted of studying cryogenic liquid oxygen (LOX) droplet behavior at subcritical and supercritical pressures [1-11]. This included a considerable effort to learn how to produce droplets at supercritical pressures. Shadowgraph and spontaneous Raman scattering measurements showed that the classical low-pressure sequence of primary atomization, secondary breakup, and vaporization is not accurate at supercritical pressures. Due to the lack of surface tension, droplets at supercritical pressures instead continuously deform while simultaneously vaporizing.

Initial work on single jets (as opposed to droplets) at various pressures also took place during this initial period. Visualizations of nearly laminar liquid nitrogen (LN2) jets clearly demonstrated that surface tension becomes vanishingly small as the critical pressure is approached, even while density gradients remain large enough to make the LN2/ambient gas interface look smooth and glassy [6]. This work also showed that adding helium to the ambient gas could cause surface tension to clearly reappear even at pressures above the critical pressure of N2, due to mixture effects.

Research then turned to the behavior of simple, round, turbulent jets at various pressures ranging from subcritical to supercritical [12-23]. It was found that at subcritical pressures, the jets had a classical spray appearance, but that as pressure was increased past the critical pressure, the jets assumed an appearance of gaseous jets with no evidence of droplets. The initial divergence angle indicating the growth rate of the jet was measured using shadowgraphy at the jet exit. These values were then compared with those measured from a large number of other mixing layer flows, including atomized liquid sprays, turbulent incompressible gaseous jets, supersonic jets, and incompressible but variable density jets covering over four orders of magnitude of the gas-to-liquid density ratio. This was the first time such a plot had been reported for such a large range of density ratios. At and above the critical pressure, it was found that the growth rate measurements agreed well with both theory and measurements for incompressible, variable density, gaseous mixing layers. At subcritical pressures, the growth rate measurements were consistent with those reported for classical sprays. A physics-based mechanism was postulated and used to correlate the data over the entire four-decade range of density ratios. Spreading rate measurements of the supercritical jets were also made using spontaneous

Raman scattering. Raman measurements of subcritical jets were found not to be useful due to broadband emissions caused by focusing of the laser illumination by the jets. The Raman measurements were found to be consistent with the shadowgraph measurements if twice the full-width-half-maximum normalized intensity measurements were used. Finally, measurements of the fractal dimension of the shadowgraph images were performed. These provided further evidence of the gas-like behavior of the supercritical jets. The fractal dimension of the supercritical jets was consistent with the fractal dimension reported by others for gaseous jets; while the fractal dimension of the subcritical jets was consistent with the fractal dimension reported by others for classical sprays. Some of these results could be compared with similar work being reported out of Germany. The results of the two independent laboratories were found to corroborate each other [23-24].

Steady-state studies of simple round jets were followed by studies of acoustically driven round jets [25-26]. The jets were driven transversely by acoustic drivers specially designed for operation at high pressures. In all cases, the jets tended to flatten in the mean, with the long dimension perpendicular to the direction of the acoustic waves. This could be explained by the lower pressures around the shoulders of the jet caused by the higher velocities there through the Bernoulli effect. The magnitude of the effect, however, was found to depend strongly on the pressure. The magnitude of the effect was strong at subcritical pressures, strongest near the critical pressure, but weak at supercritical pressures. The implications of these results regarding liquid rocket combustion instabilities were considered. It was concluded that coupling mechanisms for supercritical jets were likely to be very different from those for subcritical jets, and that insufficient attention had been paid to supercritical effects in past studies of liquid rocket combustion instabilities.

Simple round jet results were then extended to coaxial jets, where the central condensed jet is surrounded by a co-annular gaseous flow [27-28]. Care was taken to maintain traceability to previous simple round jet results in the limit as the annular flow went to zero. Facility capabilities limited early results to low gas-to-liquid velocity ratios not representative of liquid rocket injectors. Preliminary results after facility modifications at high velocity ratios indicated that the effect of acoustic waves is to impose sinusoidal structures onto the jet, but the effect seemed to depend in a complex way on pressure, velocity ratio, and on internal heat transfer inside the coaxial passages. Because density depends strongly on temperature in the vicinity of the critical pressure, it was determined that very accurate initial temperature measurements were required. Preparations to measure these temperatures to within 1 K were underway at the conclusion of this project. These measurements are planned to be performed in a follow-on project.

A small portion of this project was devoted to a separate effort to investigate detonations of subcritical liquid oxygen sprays in gaseous hydrogen [29-31]. The motivation was potential application in a pulsed detonation upper stage rocket engine. An experiment was conducted to understand the effect of gas-to-liquid oxygen ratio on wave speeds and post-detonation pressures. An analytical model of the constant volume limit of pulsed propulsion was also developed during the course of this research [29]. In the process of conducting the experiment, a great deal was also learned about instrumentation, ignition, and control approaches that could simultaneously survive cryogenic temperatures and withstand detonations. Reference detonations with room temperature gase-

ous hydrogen and gaseous oxygen produced classical Chapman-Jouget (CJ) detonations. Detonations with identical mass loadings of hydrogen and oxygen but with oxygen in a liquid phase produced significantly larger wave speeds and post-pressures than predicted by CJ theory. Computations were performed to show that the reason could be attributed to radial stratifications of oxygen concentrations caused by the coaxial injector used in the experiment.

REFERENCES

1. Woodward, R.D., Talley, D.G., Anderson, T.J, and Winter, M., "Shadography of Transcritical Cryogenic Fluids," 6th Annual Penn State PERC Symposium, NASA Lewis Research Center, Cleveland, Ohio, 13 September 1994.

2. Woodward, R.D., Bates, R., and Talley, D.G., "Transcritical Propellant Injection Experiments," 32nd JANNAF Combustion Meeting / 7th Annual Penn State PERC Symposium, NASA Marshal Space Flight Center, 23-27 Oct 1995. **[Appendix A]**

3. Anderson, T., Woodward, R.D., and Winter, M., "Oxygen Concentration Measurements in a High Pressure Helium Environment Using Raman Imaging," 33rd Aerospace Sciences Meeting & Exhibit, paper AIAA 95-0140, January 1995. **[Appendix B]**

4. Woodward, R.D., and Talley, D.G., "Progress in Transcritical Injection Experiments at the Phillips Laboratory," 8th Annual Penn State PERC Symposium, The Pennsylvania State University, 30-31 October, 1996.

5. Mitts, C., Talley, D.G., and Poulikakos, D., "A Fundamental Study of Supercritical Droplet Deformation and Breakup Through a Miscible Fluid Analog," 32nd AIAA/ASME/SAE/ASEE Joint Propulsion Conference, paper AIAA 96-2858, 1-3 July (1996). **[Appendix C]**

6. Woodward, R.D., and Talley, D.G., "Raman Imaging of Transcritical Cryogenic Propellants," 34th Aerospace Sciences Meeting and Exhibit, paper AIAA 96-0468, Jan 15-18, 1996. **[Appendix D]**

7. Mitts, C., Poulikakos, D., and Talley, D.G., "The Characterization of Supercritical Droplet Deformation and Breakup Through a Miscible Fluid Analog," Ninth Annual Conference on Liquid Atomization and Spray Systems, San Francisco, CA, 19-22 May 1996.

8. Woodward, R.D., and Talley, D.G., "Transcritical LOX Droplet Gasification," 9th Annual Penn State PERC Symposium, NASA Lewis Research Center, Cleveland, Ohio, 1-2 October 1997.

9. Talley, D.G., and Woodward, R.D., "Experimental Studies of Transcritical Cryogenic Droplets and Jets," invited paper presented at the 13th Annual Conference on Liquid Atomization and Spray Systems, Florence, Italy, July 1997. **[Appendix E]**

10. Mayer, W.O.H., Schik, A.H.A., Vieille, B., Chauveau, C., Gokalp, I., Talley, D.G., and Woodward, R.D., "Experimental Investigations of Atomization and Breakup of Cryogenic Propellants Under High-Pressure Subcritical and Supercritical Conditions," Journal of Propulsion and Power, vol. 14, no. 5, 835-842 (Sept 1998). **[Appendix F]**

11. Talley, D.G., Woodward, R.D, Kaltz, T.L., Long, L.N., and Micci, M.M., "Experimental and Numerical Studies of Transcritical LOX Droplets," invited paper presented at the 14th Annual Conference on Liquid Atomization and Spray Systems, Manchester, England, 6-8 July 1998, ADA409836.

12. Chehroudi, B., Talley, D.G., and Coy, E.B., "Behavior of a Round Cryogenic Jet at Below and Above the Critical Pressure," 10th Annual Penn State PERC Symposium, NASA Marshal Space Flight Center, Huntsville, Alabama, October 26-27, 1998, ADA386244.

13. Chehroudi, B., Talley, D.G., and Coy, E., "Fractal Geometry and Growth Rate Changes of Cryogenic Jets Near the Critical Point," 35th AIAA/ASME/SAE/ASEE Joint Propulsion Conference and Exhibit, paper AIAA 99-2489, Los Angeles, CA, 20-24 June, 1999, ADA410388. **[Appendix G]**

14. Chehroudi, B., Talley, D.G., and Coy, E.B., "Initial Growth Rate and Visual Characteristics of a Round Jet into a Sub- to Supercritical Environment of Relevance to Rocket, Gas Turbine, and Diesel Engines," 37th Aerospace Sciences Meeting and Exhibit, paper AIAA 99-0206, Reno, NV, January 1999, ADA409800. **[Appendix H]**

15. Chehroudi, B., Talley, D.G., and Coy, E.B., "Anatomical Changes of a Cryogenic Jet in Transition to the Thermodynamic Supercritical Condition," invited paper presented at the 15th Annual Conference on Liquid Atomization and Spray Systems, Toulouse, France, 5-7 July 1999, ADA410389.

16. Chehroudi, B., Talley, D.G., and Coy, E.B., "Atomization Under Sub- and Supercritical Condition with Applications to Cryogenic Rocket Engines," 12th Annual Conference on Liquid Atomization and Spray Systems, Indianapolis, IN, 16-19 May 1999.

17. Chehroudi, B., Cohn, R. and Talley, D.G., "Spray/Gas Behavior of Cryogenic Fluids under Sub- and Supercritical Conditions," Eighth International Conference on Liquid Atomization and Spray Systems, Pasadena, CA (16-20 July, 2000). **[Appendix I]**

18. Chehroudi, B., Cohn, R., Talley, D., and Bakakhshan, A., "Raman Scattering Measurements in the Initial Region of Sub- and Supercritical Jets," 36th AIAA/ASME/SAE/ASEE Joint Propulsion Conference, paper AIAA-2000-3392, 17-19 July, 2000, ADA409828. **[Appendix J]**

19. Chehroudi, B., Cohn, R., and Talley, D.G., "The Behavior of Cryogenic Shear Layers under Supercritical Conditions," 2nd International Symposium on Turbulence and Shear Flow Phenomena, Stockholm, Sweden (27-29 June 2001), ADA409825.

20. Chehroudi, B., and Talley, D., "The Fractal Geometry of Round Turbulent Cryogenic Nitrogen Jets at Subcritical and Supercritical Pressures," Atomization and Sprays, vol. 14, no. 1, pp 81-91, Jan-Feb 2004, ADA410951. **[Appendix K]**

21. Chehroudi, B., Coy, E., and Talley, D.G., "Visual Characteristics and Initial Growth Rates of Round Cryogenic Jets at Subcritical and Supercritical Pressures," Physics of Fluids, vol. 14, no. 2, pp.850-861 (2002), ADA409837. **[Appendix L]**

22. Chehroudi, B., Cohn, R., and Talley, D.G., "Cryogenic Shear Layers: Experiments and Phenomenological Modeling of the Initial Growth Rate Under Subcritical and

Supercritical Conditions," International Journal of Heat and Fluid Flow, vol. 23, pp. 554-563 (2002), ADA409838. **[Appendix M]**

23. Chehroudi, B., Talley, D., Mayer, W., Branam, R., Smith, J.J., Schik, A., and Oschwald, M, "Understanding Injection Into High Pressure Supercritical Environments," Fifth International Symposium on Liquid Space Propulsion, Chattanooga, TN, 27-30 October 2003, ADA417985.

24. Oschwald, M., Smith, J.J., Branam, R., Hussong, J., Schik, A., Chehroudi, B., and Talley, D., "Injection of Fluids into Supercritical Environments," invited paper submitted to *Combustion Science and Technology* (2004), ADA426295. **[Appendix N]**

25. Chehroudi, B., and Talley, D.G., "Interaction of Acoustic Waves with a Cryogenic Nitrogen Jet at Sub- and Supercritical Pressures," 40th AIAA Aerospace Sciences Meeting and Exhibit, paper AIAA 2002-0342, Reno, NV, 14-17 January, 2002, ADA410897. **[Appendix O]**

26. Chehroudi, B., and Talley, D., "Preliminary Visualizations of Acoustic Waves Interacting With Subcritical and Supercritical Cryogenic Jets," 15th Annual Conference on Liquid Atomization and Spray Systems, Madison, WI, 14-17 May 2002, ADA410959.

27. Chehroudi, B., Davis, D., and Talley, D., "Initial Results From A Cryogenic Coaxial Injector In An Acoustic Field," 41th AIAA Aerospace Sciences Meeting and Exhibit, paper AIAA 2003-1339, Reno, NV, 6-9 January 2003, ADA410882. **[Appendix P]**

28. Davis, D., and Chehroudi, B., "The Effects of Pressure and Acoustic Field on a Cryogenic Coaxial Jet," 42st AIAA Aerospace Sciences Meeting and Exhibit," paper AIAA 2004-1330, Reno, NV, 5-8 January 2004, ADA419454. **[Appendix Q]**

29. Talley, D.G., and Coy, E.B., "The Constant Volume Limit of Pulsed Propulsion for a Constant γ Ideal Gas," *Journal of Propulsion and Power*, vol. 18, no. 2, pp 400-406, March-April 2002. **[Appendix R]**

30. Coy, E.B., Watts, J.M., and Palaniswamy, S. "Cryogenic, Multiphase, Hydrogen-Oxygen Detonations," 43rd AIAA Aerospace Sciences Meeting and Exhibit," paper AIAA 2005-1462, Reno, NV, 10-13 January 2005. **[Appendix S]**

31. Coy, E.B, and Watts, J.M., and Palaniswamy, S., "Cryogenic, Multiphase, Hydrogen-Oxygen Detonations," submitted to the Journal of Propulsion and Power (2005). **[Appendix T]**

This Page Intentionally Left Blank

APPENDIX A

“Transcritical Propellant Injection Experiments”

This Page Intentionally Left Blank

TRANSCRITICAL PROPELLANT INJECTION EXPERIMENTS

R. D. Woodward, R. Bates, and D. G. Talley
USAF Phillips Laboratory
Edwards AFB, CA

ABSTRACT

The objective of this research is to explore the transcritical atomization and vaporization behavior of cryogenic droplets, jets, and sprays. By this is meant the behavior of propellant injected at supercritical pressures but initially at a subcritical temperature, which then undergoes a transition to a supercritical state as it is heated in a hot environment. The experimental approach has been to first investigate transcritical droplets using a free droplet technique, whereby monodisperse droplets are studied as they fall freely in a pressure chamber. The goal is to measure velocity fields and temperature and species concentration profiles, measurements that have not previously been available for these conditions. Lessons learned from preliminary experiments related to transcritical cryogenic droplet generation, vaporization behavior at high pressures for different propellant/simulant compositions, and the application of laser diagnostics, i.e., Raman imaging, to this system have been incorporated into the design of a new high-pressure chamber that emphasizes integration of the cryogenic droplet generator with a tailored internal flow field to accomplish truly transcritical droplet conditions. The new chamber is also optimized for maximum optical access.

While awaiting fabrication of the optimized transcritical droplet pressure vessel, shadowgraph and Raman imaging experiments of transcritical nitrogen jets have been conducted. Shadowgraph imaging of liquid nitrogen jets injected into nitrogen and nitrogen/helium at pressures below, at, and well above the critical pressure of nitrogen demonstrate the profound effect that transcritical vaporization has on jet structure, atomization, and mixing. Also, demonstrated is the profound opposite effect that mixture properties can have on the would-be transcritical interface. Raman imaging diagnostics look promising for use with transcritical jets. The diagnostic was able to distinguish the structural differences between transcritical nitrogen jets injected into helium or nitrogen. The results indicate that Raman imaging will be useful to evaluate vaporization and mixing rates of jets at various conditions.

INTRODUCTION

Reducing the cost of future Air Force rocket propulsion systems requires an improved understanding of combustion fundamentals. It is necessary to better understand and predict mechanisms tied to combustion performance, chamber wall and injector faceplate heat transfer, and combustion instabilities. This is particularly true in high pressure systems which exceed the critical pressure of the propellants. In many cases the fuel or oxidant (liquid oxygen in rocket propulsion systems) is injected at supercritical pressures but initially at a subcritical temperature. The propellant then undergoes a transition to a supercritical state as it is heated and burned in the combustion chamber, the so-called transcritical process. Compared with the analogous subcritical case, transcritical and supercritical injection and combustion remains relatively poorly understood.

Droplets remain the simplest and most easily studied of spray systems, and despite the added complexities of full fledged sprays many of the interfacial transport and breakup mechanisms applicable to them can be understood from single droplets. The goal of this work is to better understand these applicable mechanisms for transcritical spray injection, through a better understanding of droplet processes. There are a number of differences from the subcritical case that need to be addressed. Gas/liquid density ratios are of the same order, so the quasi steady gas phase assumption commonly employed in subcritical studies is no longer valid. The equilibrium “wet bulb” condition may also not exist. Thus transcritical droplet vaporization/combustion is a fully unsteady phenomenon. The computation of properties becomes significantly more complicated in that properties such as diffusion coefficients become functions of pressure as well as temperature, and the solubility of the gas phase in the

Approved for public release; distribution is unlimited.

liquid phase increases significantly. The latter effect can mean that the effective critical pressure of the soluble mixture can be several times the critical pressure of the pure phase. Other property anomalies can lead to singular behavior near the critical condition. For instance, the burning rate has been observed to reach a maximum near the critical pressure, and the potential to couple with combustion instabilities may be increased. The surface tension also vanishes, potentially leading to significantly different jet and droplet deformation and breakup mechanisms. These latter mechanisms can be particularly important because they have a direct effect on mixing.

Past experimental studies of transcritical droplet processes have been mostly limited to global measurements such as the variation of droplet lifetimes and burning times as a function of pressure.[1-4] While useful, these provide an incomplete picture of the transport and breakup mechanisms that can contribute to mixing and the potential to couple with combustion instabilities. On the other hand, the theoretical understanding of transcritical droplet vaporization, combustion, and breakup has advanced significantly in recent years due to the introduction of new models.[5-7] However, these remain unverified experimentally. The objective of this work is to provide detailed measurements of transcritical droplet flow fields and temperature and composition profiles that can be used to validate these models, as well as to develop semi-empirical correlations for direct use in comprehensive engine design and performance codes. These measurements will be performed both in quiescent environments and in the presence of acoustic disturbances representative of combustion instabilities. Additionally, an effort has been initiated to study the transcritical behavior, breakup, and atomization of jets/sprays.

TRANSCRITICAL DROPLET MEASUREMENTS

Detailed measurements of droplet flow fields and temperature and composition profiles are believed to be feasible through a combination of 1) precise control of the droplet generation process to achieve repeatable, monosized droplets, and 2) incorporation of laser-based droplet diagnostic techniques that have recently been developed.

Since the primary application at the Phillips Laboratory is rocket propulsion where the transcritical fluid is liquid oxygen, a piezo-electric droplet generator has been developed which is capable of producing a monodisperse stream of cryogenic droplets at high pressures. The droplet generator is pictured in Fig. 1. To date, the generator has successfully produced monodisperse streams of liquid nitrogen (LN_2) and liquid oxygen (LOX) droplets in an acoustically excited Rayleigh breakup mode at pressures somewhat beyond 70 atm (> 1000 psig). Extension to even higher pressures is in progress and in fact is necessary to fully investigate transcritical phenomena in the system of interest. The generator has also successfully operated in a drop-on-demand mode for hydrocarbon and water droplets at atmospheric pressure, but the severe heat transfer environment coupled with decreased surface tension as transcritical conditions are approached has so far precluded operating in this mode with cryogenic fluids. These issues have been addressed and the methodology for achieving these objectives is described in a following section.

Innovative laser-diagnostic techniques have been applied to droplet experiments for a number of years; however, these have been limited almost exclusively to subcritical droplets. Application of such techniques to the transcritical problem is currently being evaluated in a collaborative effort with the United Technologies Research Center. At present, Raman imaging appears attractive at high pressures due to the high molecular number density enhancement to the typically weak signal. Raman diagnostics can potentially provide both species and temperature measurements, and there should be no physical barrier to its application to the trans- or supercritical regime. Anderson et al.[8] demonstrated the feasibility of Raman imaging diagnostics for concentration field determination around cryogenic liquid droplets vaporizing in a high pressure environment. Streams of LOX droplets in the size range of 100-300 μm were injected into a helium environment at pressures to approximately 70 atm. Quantitative measurements of instantaneous (single 10-ns laser shot) O_2 concentration resulting from droplet vaporization demonstrated measurement sensitivity of at least 10 kg-mole/m^3 (4% mole fraction in helium at 69 atm). Vaporized oxygen distributions from Raman imaging of LOX droplet streams into high pressure helium clearly exhibited unsteady, asymmetric vaporization and strong droplet/wake interactions at those conditions.

In a transcritical phenomenology study, Woodward et al.[9] provided preliminary shadowgraph visualizations of transcritical cryogenic droplet flows and discussed the strong effect of mixture properties on the effective critical point for the propellant simulant combinations. A series of experiments were conducted with liquid nitrogen injected into gaseous or supercritical nitrogen, starting with a droplet stream flow at subcritical conditions

and then increasing the pressure while approximately maintaining the same low flow rate. At and above the critical pressure of this uni-molecular system, no liquid-like structures were observed. Transition from subcritical behavior appeared to begin at about 60-80% of the critical pressure (enhanced aerodynamic drag effects also played a role here), with dramatic changes to liquid structures exhibited within a few percent of critical pressure. The addition of helium into the slightly supercritical nitrogen system caused liquid nitrogen structures to re-appear due to local composition and temperature conditions. Likewise, it had been observed that LOX droplets could maintain their surface tension and hence a well-defined structure in a supercritical helium environment at a pressure of at least 1.7 times the critical pressure of pure oxygen due to the solubility of the helium into the LOX. Therefore, even higher pressures need to be obtained to study transcritical effects in the LOX/He (thus presumably LOX/H_2) system.

These studies[8,9] were conducted in simple cylindrical pressure vessels with the Phillips Laboratory high pressure, cryogenic droplet generator adapted to mount on and operate with these chambers. There are two major deficiencies with the pressure vessels used for these experiments. One is the poor optical access which limits the field of view for imaging and limits the solid angle of light collection, a quantity that must be maximized for low signal-to-noise diagnostics such as Raman imaging. In the above experiments, the pressure vessel windows limited the f/# of the optical system to f/4. The other major deficiency is the un-optimized integration of the cryogenic droplet generator to the pressure vessel, resulting in less than ideal droplet production due to heat transfer problems and an inability to tailor the flow field surrounding the droplet. Also, the need for higher operating pressures to fully investigate transcritical phenomena dictated designing a new windowed chamber.

OPTIMIZED EXPERIMENTAL CHAMBER

A custom pressure vessel has been designed specifically for future transcritical vaporization experiments. Valuable lessons learned have been incorporated from the above works[8,9] in terms of transcritical cryogenic droplet generation, expected vaporization and breakup behavior at high pressures for different propellant/simulant compositions, and the application of laser diagnostics, especially Raman imaging, to this system. This chamber, optimized for such experiments, was designed with the following important features:

- operating pressure capability to 137 atm (2,000 psig)
- operating temperature to 473K (with potential steep temperature gradients from 77-473K)
- excellent optical access for imaging and signal collection with two opposed 133.4 mm (5.25”) diameter windows (clear aperture of 120.7 mm (4.75”) diameter) and non-axisymmetric shape to minimize the distance from the droplets to the windows
- laser beam and sheet access (in and out) to the injection axis through two oblong windows, perpendicular to the large round viewing windows
- highly integrated and modular interface between the droplet generator and the windowed pressure vessel to provide a controlled environment for drop production and injection into the viewing area
- droplet generator height adjustment capability without the necessity for removal of any components
- provisions for mounting high-intensity acoustic drivers
- easy and abundant access to the inside of the pressure vessel through the large windows without removal of any fasteners
- built-in provisions for heating elements
- optic mounting provisions in the floor of the chamber

A front view of the transcritical cryogenic droplet pressure vessel assembly is shown in Fig. 2(a). At the heart of this view are the large round windows (one on front and one on back). These 133.4 mm (5.25”) diameter windows are only 25.4 mm (1”) thick because they are made from sapphire (Hemlite) which has excellent strength. These windows are interchangeable with an experimental chamber already on-line at the Phillips Laboratory with the same operating pressure range. Considerable effort was made to design and prove these windows for the other vessel, and so significant time was saved to incorporate this design directly. A threaded flange holds the window and screws directly into the chamber housing, allowing internal chamber access without the need to remove several

bolts. The 120.7 mm (4.75”) diameter aperture of these windows is sufficiently large to view the entire cryogenic droplet history even at low pressures. Also, these windows, because of their size and proximity to the injection axis, offer a large signal collection angle such that the system f/# becomes limited now by the collection optics rather than the vessel windows. The size of these windows enable the use of wide variety of diagnostic techniques that might require bringing in laser beams or viewing with multiple detectors at a variety of angles.

A side view of the pressure vessel assembly is shown in Fig. 2(b). In this view, one is looking into the oblong laser input/output windows that provide a clear aperture of 120.7 mm x 12.7 mm (4.75” x 0.50”). These windows are made from UV-grade quartz. They offer slightly less light absorption than the sapphire windows and are relatively less expensive. This is important since they are operationally more susceptible to laser damage. They were designed to be oblong to keep the chamber as thin as possible while still providing laser access to the injection axis for the entire vertical height of the viewing windows.

Perhaps the most significant feature of the transcritical droplet experimental chamber is in the integration of the droplet generator with the pressure vessel. The droplet generator interface housing internal flow field is shown schematically in Fig. 3. The design is optimized for LN_2 or LOX cryogenic droplet production at high pressures using either piezoelectric or a hybrid piezoelectric/aerodynamic droplet generation scheme for the production of freely falling droplets. In our experience, the production of freely falling, truly monodisperse, and truly transcritical droplets is severely limited if heat transfer to the droplet generator tip is not carefully controlled because reduction of the surface tension as the critical condition is approached prevents distinct droplets from forming. In the present design, this problem is solved by producing the droplets in a coflowing stream of helium prechilled to the same temperature as the droplets, where the large difference in molecular weight helps ensure the presence of an interface. The droplet/helium stream then impinges on a counterflowing stream of the warmer test gas. Bleed ports at four locations on the periphery of the impingement plane are plumbed to vent the impinging gas mixture from the chamber. These four vents have independent control to properly balance the flows so that the droplet stream is not perturbed from the centerline. The counterflow configuration creates a relatively sharp transition to the temperature and composition desired for testing. It is hoped that this design will allow high-pressure, cryogenic droplet-on-demand operation by stabilizing the droplet generation in an environment where surface tension forces have been predicted to exist even at the full operating pressure of the vessel. This is a critical feature to the operation of the droplet generator for production of transcritical droplets. Without sufficient surface tension, distinct droplets cannot be formed. Once the droplet crosses the relatively sharp temperature and composition transition at the entrance into the windowed region of the main chamber, transcritical vaporization of the droplet may begin to occur.

Considering the importance of combustion stability to liquid rocket engine design, the transcritical droplet chamber, although not optimized for this application, has been designed to accommodate high-intensity acoustic drivers to investigate transcritical droplet/acoustic wave interactions. In this mode, the oblong laser-input windows are replaced at one or both ends by an acoustically tailored coupler that attaches existing high-intensity sound sources. The high-pressure, high-temperature acoustic drivers are in the final stages of development as part of a Phillips Laboratory Small Business Innovative Research (SBIR) Phase II contract. Initial tests of the prototype acoustic drivers have indicated the capability to generate rms acoustic pressures greater than 100 psi at an ambient pressure of 1000 psig at 3 kHz. These drivers will be used to investigate the effect of acoustic disturbances on the breakup and vaporization of transcritical cryogenic droplets. This is a subject for which there is intense interest because of its relevance to high pressure rocket engine stability but one for which little has been accomplished experimentally. Anderson et al.[10] of United Technologies Research Center have attempted a similar study of LOX droplet interaction with weak shock waves but have yet to achieve true transcritical conditions.

Due to the stringent requirements and complexity of the transcritical cryogenic droplet experimental vessel, considerable time has been invested in its design and construction. The chamber fabrication should be complete as of the date of this meeting. Installation will occur shortly, and experimentation will begin before the end of calendar year 1995.

PRELIMINARY RESULTS IN NON-OPTIMIZED VESSEL: TRANSCRITICAL JETS

Transcritical droplets are important to study for the reasons stated initially in this paper; however, the investigation of droplets constitutes only a first step in attacking the transcritical propellant atomization and vaporization problem. Thus, the authors have recently proposed to extend the AFOSR-funded effort to include the investigation of transcritical jets/sprays. The remainder of this paper will describe the results of some preliminary experiments conducted to know what kind of behavior to expect from transcritical jets and to demonstrate the feasibility of using Raman imaging diagnostics with transcritical jets.

While designing and awaiting construction of the optimized transcritical experimental chamber, an existing cylindrical pressure vessel similar to that used by Anderson et al.[8] and Woodward et al.[9] was modified to accommodate the LN_2-cooled cryogenic droplet generator. For this paper, however, the piezoelectric element and 127 μm diameter droplet-generating orifice were removed, and a straight capillary tube with inner diameter (injector diameter) of 0.25 mm (0.010") and length-to-diameter ratio (L/D) of approximately 300 were installed. Liquid nitrogen was used as the LOX simulant in the following experiments. High-pressure gaseous nitrogen was condensed within the injector approach tube which runs through the droplet generator's double-pass, low pressure LN_2 cooling jacket. Condensed liquid nitrogen was injected into helium, nitrogen, and mixtures of helium and nitrogen at various chamber pressures. Chamber temperatures varied from 280-310K, always well above the critical temperature of nitrogen (126K). LN_2 injectant temperatures, measured on the outside of the injector tube, varied from 88-115K (typically 90K or less).

Back-lit videography (shadowgraphy) and Raman imaging of nitrogen were the two techniques used to investigate the transcritical nitrogen jets. The experimental set-up is depicted schematically in Fig. 4.

SHADOWGRAPHY

The shadowgraphs were taken with an unintensified RS-170 CCD camera through a long-distance microscope to provide good spatial resolution to discern fine structures in the relatively small jet. A strobe was used to illuminate the shadowgraphs with a sufficiently short pulse (~10 μs) to freeze the motion of the jet. Similar transcritical injection experiments were conducted previously by Woodward et al.[9] The major difference here is that the injectant mass flow rate is an order of magnitude greater for these jet flows compared to the droplet generation flow rate used then.

A matrix of shadowgraph images is depicted in Fig. 5. A series of images of LN_2 injection into nitrogen is given for three different pressures, corresponding to subcritical (Fig. 5(a), 28 atm, $P/P_{crit} = 0.83$), approximately critical (Fig. 5(b), 35 atm, $P/P_{crit} = 1.03$), and supercritical (Fig. 5(c), 69 atm, $P/P_{crit} = 2.03$) conditions. Additionally, in Fig. 5(d), a LN_2 jet is injected into a mixture of nitrogen and helium. The jet mass flow rate for all images was constant at 0.068 g/s (3.5 SLPM). Flow is downward from the injector exit in position (1) at 0-1.9 mm to position (2) at 7.4-9.5 mm then to position (3) at 15-17.1 mm and finally to position (4) at 22.6-24.7 mm near the bottom of the viewing window. The vertical field of view in each image is approximately 2.1 mm (8.3 injector diameters) with approximately a 5.5 mm gap between images.

The subcritical jet in Fig. 5(a)(1-4) has a sharp gas/liquid interface throughout. The relatively low speed jet does not exhibit much breakup although disturbances are evident on the surface of the jet. Beginning at position (2), the jet would intermittently breakup into large liquid globs that were never really spherical. Also, intermittently the subcritical jet would be nearly free of disturbances, being smooth and straight past the bottom of the viewing window. Most frequently, the jet would appear as in Fig. 5(a)(1-4), with both symmetric and anti-symmetric disturbances exhibited. The symmetric disturbances generally dominated closer to the injector and helical instabilities dominated further downstream.

The LN_2 jet issuing into the approximately critical pressure environment in Fig. 5(b)(1-4) behaves much differently than the subcritical case as one might expect. In Fig. 5(b)(1), the injected nitrogen appears as a liquid presumably because of the steep gradient between the subcritical temperature of the jet and the supercritical temperature of the ambient. Thus a steep density gradient exists as well, providing a distinct surface. However, the

jet is initially very smooth due to insufficient surface tension to promote the growth of capillary instabilities. The jet remains very smooth until aerodynamic disturbances shear the surface and cause unstable wave growth. It is interesting to note the sheet-like fan of liquid originating presumably from an imperfection in the injector orifice (since the location of the fan was apparent at a variety of conditions and consistently in that location). The jet fluid has insufficient surface tension to bring the fan back to the jet, and we see the fan begin to disintegrate due to aerodynamic interactions downstream in Fig. 5(b)(2). Examining Fig. 5(b)(2) and beyond, apparently no droplet-like structures are actually being formed. Instead stringy, fluid structures that exhibit some interfacial behavior are created. These fluid structures seem to readily vaporize and mix.

The supercritical jet at 69 atm in Fig. 5(c) is very similar to the slightly supercritical jet at 35 atm in Fig. 5(b) except that the onset of aerodynamic instabilities occurs much sooner and more vigorously as expected in the higher density ambient. Jet spreading is quite rapid, and by Fig. 5(c)(4) there is no evidence of any liquid-like structures with distinct interfaces. Note that in Figs. 5(b)(1) and 5(c)(1), ambient nitrogen condensation and subsequent vaporization is occurring around the cooled injector tip, creating steep density gradients that obscure light in the near injector region.

The LN_2 jet in Fig. 5(d) was created by starting from the 69 atm jet in Fig. 5(c) and introducing a small flow of helium into the chamber while venting at the bottom of the chamber to maintain constant pressure. The initial helium mass flow rate was 0.0097 g/s. After a few minutes, the supercritical nitrogen jet appeared to be more coherent, but not drastically. Thus, the helium flow rate was gradually increased to 0.0174 g/s, where after a few minutes the jet appeared as it does in Fig. 5(d). With steady N_2 and He mass flows in and steady outflow to maintain chamber pressure, we assume that for Fig. 5(d), the ambient mass ratio is 3.9 parts N_2 to one part He. (For simulating a LOX/H_2 system this corresponds to a slightly fuel rich mixture ratio.) Obviously, the addition of the helium had a profound effect on the jet structure. The nitrogen jet in Fig. 5(d), although at 69 atm, is that of a subcritical jet with a distinct interface and re-newed surface tension. This jet most closely resembles the LN_2 jet of Fig. 5(a) except that breakup occurs more readily at the elevated chamber pressure. Perhaps the irregular, sometimes jellyfish-like, sometimes rock-like liquid blobs in the second half of the depicted flow are beginning to undergo transcritical vaporization as they heat up, vaporize, and locally increase the nitrogen concentration. By comparing Figs. 5(c)(4) and 5(d)(4), there is no doubt that the mixing efficiency is vastly different for the two nitrogen jets at 69 atm.

RAMAN IMAGING

With a similar set-up, Anderson et al.[8] demonstrated the feasibility of using Raman imaging to measure vaporized oxygen concentrations in the vicinity of LOX droplets falling in a helium environment. Here, transcritical nitrogen jets injected into either nitrogen or helium are imaged using the Raman Stokes scattering from nitrogen at 607 nm (532 nm excitation). A frequency-doubled, pulsed (~6 ns, 10 Hz) Nd:YAG laser was used to generate the Raman scattering. Results were obtained at an average pulse energy of 225 mJ. The laser beam was focused into a constant dimension (25 mm high by 1 mm thick) sheet using two pairs of cylindrical lenses before being passed into the pressure vessel. Raman scattering was imaged perpendicular to the laser sheet. Discrimination of the Raman signal from the laser was accomplished with 6 mm of Schott OG570 filter glass, which attenuates the laser wavelength by over 50 orders of magnitude while decreasing the Raman signal from the nitrogen by less than 2%. Raman images were recorded on a Princeton Instruments 576x384 CCD detector with a fiber-coupled intensifier. The intensifier was gated for a 200 ns exposure to minimize ambient light detection.

Two cases were considered for demonstrating the use of Raman imaging diagnostics for transcritical jet vaporization and mixing studies. Similar to Figs. 6(c) and 6(d), they are 1) LN_2 injected into nitrogen at 69 atm and 2) LN_2 injected into helium at 69 atm. In both cases, the nitrogen mass flow rate was maintained, as before in this study, at 0.068 g/s so that all the images can be consistently compared.

The injection of LN_2 into nitrogen is depicted in Raman images in Fig. 6. Figure 6(a) is a raw, single laser shot image of the Raman scattering from nitrogen in the path of the laser sheet. Note that this also includes a signal in the shape of the light sheet from the ambient supercritical nitrogen in the vessel. The top of the laser sheet hits the jet at about 5 diameters downstream of the injector. The field of view in the vertical direction is approximately 13

mm (about 6 times that for the shadowgraph images in the previous section). The single shot Raman signal from the nitrogen jet is weak but easily seen above the signal from the ambient nitrogen. The Raman image of the jet contour looks "fuzzy," as it should because the LN2 is undergoing supercritical vaporization, as we saw in Fig. 5(c), after about 5 to 10 diameters downstream of injection. Due to a lack of spatial resolution and signal-to-noise, it is difficult to make a strong statement about the condition of the jet, but in conjunction with the shadowgraph images, the Raman image is obviously consistent with what we would expect to see.

To improve the signal-to-noise ratio, a four-laser-shot ensemble average was recorded under the same conditions and is depicted in Fig. 6(b). This image is much cleaner, and would lend itself better to quantification of the Raman signal. Note, however, that there are a few bright spots on the leading edge of the upper part of the jet. The laser sheet is incident on this side and is being locally focused by the distinct surfaces (steep index of refraction gradients) that exist in this part of the jet. This can cause several problems: 1) local bright spots can use up the dynamic range available; 2) laser-induced breakdown can occur, causing a very bright, broadband flash of light that will overwhelm the Raman signal and saturate the detector; 3) it may induce stimulated Raman scattering which is difficult to quantify; or 4) alter the laser sheet profile across the jet due to extinction and thus introduce an apparent asymmetry in the concentration profile. Note that in Figs. 7(a) and (b), there is a black band coming from the left middle side that goes transversely through the jet. This no-light band is caused by an imperfection in the laser input window. Also note that the band gets washed out after going through the jet due to local random scattering of the sheet from the jets fine scale, density fluctuations that cause index of refraction gradients.

Now consider the other jet case. A single shot Raman image of a LN_2 jet into helium at 69 atm is shown in Fig. 7. The first thing to note is that there is no Raman signal from the laser sheet going through the ambient helium since it is Raman inactive. This helps to distinguish the jet from the background. The Raman signal from the nitrogen jet tracks the jet profile fairly well. It is obvious from this image that, as we saw before, the LN_2 jet in helium is much more coherent and undergoes significantly slower vaporization. Distinct surfaces are suggested by the "beaded" structure seen in the image even though the edges of the Raman contours are somewhat fuzzy. This could be due to noise, or it could be a real effect caused by vaporization of nitrogen or helium solubility into the nitrogen. Also, local bright spots can be seen in this image as in Fig. 6(b), but here they are further downstream, indicating again the presence of liquid-like interfaces.

Such Raman images can easily be made quantitative by ratioing to a calibrated response image of Raman scattering from the laser sheet going through a known concentration of nitrogen. Thus, the species concentration distribution of nitrogen in the jet, near the jet, and in the far-ambient can simultaneously be determined. Note that for the case of a nitrogen jet into nitrogen, variations in Raman scattering intensity can directly be interpreted as temperature distributions since there is only one molecular species. As stated above, complications enter when stimulated Raman scattering occurs, which is likely in the liquid-like jet. Coherent structures with a sharp interface will tend to focus the laser light, inducing stimulated Raman and nonlinear effects. Although difficult to quantify, this effect when seen could help determine the presence of liquid-like structures.

SUMMARY AND CONCLUSIONS

Incorporating lessons learned from preliminary experiments and building on the development of a unique high-pressure cryogenic droplet generator, a promising new transcritical droplet experimental chamber has been designed and fabricated. With a highly integrated scheme to produce truly transcritical droplets in a pressure vessel optimized for optical access, we look forward to some first ever experimental results on the vaporization behavior of transcritical nitrogen and oxygen droplets in high-pressure helium and other mixed environments. Detailed measurements of temperature and concentration fields will be made using Raman and other laser diagnostic techniques, as well as conventional shadowgraph and Schlieren visualizations. Also, results are anticipated on the vaporization and atomization response of transcritical droplets to the presence of strong acoustic excitation.

Shadowgraph imaging of liquid nitrogen jets injected into nitrogen and nitrogen/helium at pressures below, at, and well above the critical pressure of nitrogen re-iterate the profound effect that transcritical vaporization has on jet structure, atomization, and mixing. Also, re-iterated is the profound opposite effect that mixture properties and steep composition and density gradients can have on the would-be transcritical interface. The real effect of these phenomena in an actual rocket engine has yet to be determined. Due to the transient nature of propellant injection,

atomization, vaporization, and combustion, the practical problem is determined by transitory local conditions within the engine. Vastly different behavior could occur at different locations, and the behavior at certain locations could be oscillating through a critical transition depending on the changing local composition of propellants and combustion products and temperature. Obviously this is a complex problem. Progress can be made step-wise by mapping critical transitions versus pressure, temperature, and relevant composition for simple systems such as the droplets and low speed jets that were discussed here. The next step would be to scale up the jet flow and then move into combusting systems of small then increasing scale.

Raman imaging diagnostics look promising for use with transcritical jets. In this preliminary study, Raman imaging was able to distinguish the structural differences between liquid nitrogen jets injected into helium or nitrogen. Simultaneously the technique can be used to quantify the ambient concentration of the species of interest (nitrogen or oxygen) as well as the vaporizing concentration field of the transcritical jet, or if higher order scattering causes problems, give a qualitative indication of the structure of the jet. The results indicate that Raman imaging will be useful to evaluate vaporization and mixing rates of jets at various conditions. With the need to reach higher pressures to fully investigate the transcritical behavior of the LN_2/helium (or LOX/hydrogen) system, the prospects for Raman diagnostics actually improve thanks to the increase in signal strength with pressure (molecular number density).

ACKNOWLEDGMENTS

The authors gratefully acknowledge the support and encouragement for this work from the Air Force Office of Scientific Research and contract monitor Dr. Mitat Birkan under task 2308AP. The efforts of Mr. Bruce Petrites of General Physics Corporation to enhance and complete the detailed design of the transcritical droplet pressure vessel are recognized and appreciated. The authors thank Dr. James F. Verdieck for his assistance with the Raman imaging experiments. Dr. John C. Pan is acknowledged for his early development work on the high-pressure cryogenic droplet generator.

REFERENCES

[1]Faeth, G.M. Dominicis, D.P. Tulpinsky, J.F., and Olson, D.R., “Supercritical Bipropellant Droplet Combustion,” *Twelfth Symposium (International) on Combustion*, The Combustion Institute, pp. 9–18 (1969).

[2]Sato, J., Tsue, M., and Kono, M., “Effects of Natural Convection on High Pressure Droplet Combustion,” *Comb. Fl.* 82: 142–150 (1990).

[3]Natarajan, R., and Brzustowski, T.A., “Some New Observations on the Combustion of Hydrocarbon Droplets at Elevated Pressures,” *Comb. Sci. and Tech.* 2: 259–269 (1970).

[4]Sowles, R.E., “An Experimental Study of Carbon Dioxide Droplets Falling Through Inert High Pressure High Temperature Environments,” Ph.D. Thesis, Dept. of Mech. Eng., University of Wisconsin (1973).

[5]Shuen, J.S., Yang, V., and Hsiao, G.C., “Combustion of Liquid-Fuel Droplets at Supercritical Conditions,” *Comb. Fl.* 89: 299–319 (1992).

[6]Yang, V., Lin, N. N., and Shuen, J. S., “Vaporization of Liquid Oxygen (LOX) Droplets in Supercritical Hydrogen Environments,” *Comb. Sci. and Tech.* 97: 247 (1994).

[7]Delplanque, J.-P., and Sirignano, W.A., “Numerical Study of the Transient Vaporization of an Oxygen Droplet at Sub- and Supercritical Conditions,” *Int. J. Heat Mass Transfer* 36: 303–314 (1993).

[8]Anderson, T.J., Woodward, R.D., Winter, M., “Oxygen Concentration Measurements in a High Pressure Environment Using Raman Imaging,” 33rd AIAA Aerospace Sciences Meeting & Exhibit, Reno, NV, paper 95–0140 (1995).

[9]Woodward, R.D., Talley, D.G., Anderson, T.J., and Winter, M., "Shadowgraphy of Transcritical Cryogenic Fluids," 6th Annual Penn State PERC Symposium, NASA Lewis Research Center, Cleveland, OH (1994).

[10]Anderson, T.J., Winter, M., and Haas, M., “Observation of Droplet/Shock Interactions in a Supercritical Environment,” 32nd AIAA Aerospace Sciences Meeting, Reno, NV, paper 94-0557, (1994).

APPENDIX B

"Oxygen Concentration Measurements in a High Pressure Helium Environment Using Raman Imaging"

AIAA 95-0140

Oxygen Concentration Measurements in a High Pressure Environment Using Raman Imaging

Torger J. Anderson
United Technologies Research Center
East Hartford, Connecticut 06108

Roger D. Woodward
Phillips Laboratory
Edwards AFB, California 93524

Michael Winter
United Technologies Research Center
East Hartford, Connecticut 06108

33rd Aerospace Sciences Meeting and Exhibit
January 9-12, 1995 / Reno, NV

Oxygen Concentration Measurements in a High Pressure Environment Using Raman Imaging

by

Torger J. Anderson
United Technologies Research Center
East Hartford, Connecticut 06108

Roger D. Woodward
Phillips Laboratory
Edwards AFB, California 93524

Michael Winter
United Technologies Research Center
East Hartford, Connecticut 06108

Abstract

This paper describes the development of Raman imaging as a diagnostic for concentration measurements in high pressure and supercritical environments. The objective is to study liquid oxygen droplet breakup under supercritical conditions simulating a liquid-fueled rocket engine combustor. While future measurements will involve droplet interaction with a strong acoustic field, the initial measurements described here show the applicability of the Raman diagnostic to the measurement environment.

Introduction

The enhancement of droplet breakup and vaporization by acoustic pulses leading to combustion instabilities in liquid-fueled rocket engines may be affected by thermodynamic conditions within the combustor. Models have been developed[1-2] and experiments conducted[3-4] to quantify the acoustic field enhancement to droplet vaporization which may lead to these combustion instabilities. While the initial experiments were limited to low pressures and temperatures, actual conditions within the combustor are quite different from this. These differences may lead to significantly different modes and rates of droplet breakup than expected and, therefore, have not been modeled in previous studies. In particular, the fact that the combustor temperatures and pressures are typically well above the critical levels for the injected fluids could significantly alter the mode of droplet breakup or dispersion in the surrounding fluid.[5] Since surface tension becomes negligible in a supercritical fluid, droplets (or "masslets") will not necessarily be perturbed in the same manner typically observed in low pressure laboratory environments (where surface tension plays a significant role). Understanding the critical transition of subcritical droplets injected into a supercritical environment is necessary for understanding of the mixing processes which occur in liquid-fueled rocket engines.

In a typical rocket combustor environment cryogenic oxidizer sprays are injected into hot fluids at supercritical temperatures and pressures. Heat transfer to a droplet elevates the temperature to supercritical conditions, but this is a transient process which, in the absence of a strong convective field, occurs along a radially inward path as

This paper is work funded by the U.S. Government and is not subject to copyright protection in the United States.

heat is absorbed. The effect of an acoustic pulse and the associated velocity field in enhancing heat transfer and breaking up a droplet undergoing such a transition is not fully understood. Models of this process have been developed and scaled experiments have been performed to investigate this behavior.[6]

A pulse tube facility has been built to study the breakup of supercritical droplets under realistic pressure and acoustic conditions.[7] It has been used to observe this process with liquid O_2 (LOX) droplets using schlieren photography, but only limited qualitative data has been acquired. A diagnostic is necessary which is capable of providing temporally-resolved O_2 concentration measurements in the region surrounding a droplet as it is interacting with an acoustic pulse. One possible technique is Raman imaging. This technique has been developed for this application and evaluated by UTRC and the Air Force Phillips Laboratory under an Air Force program.

Discussion

Raman scattering measurements have been applied to a wide range of processes ever since the laser became a practical laboratory tool.[8] With this technique, a signal is generated which is spectrally shifted from an incident laser beam providing a means of separating it from scattered laser light. The spectral shape and intensity of the signal identifies temperature and species concentrations of complex molecules (diatoms or larger) in the measurement volume. The limitation of the use of Raman scattering has been the relative weakness of the signal in comparison to strong background interferences in most combustion applications.

Despite these limitations, the technique has potential in the type of experiments described above. The high molecular number density at O_2 supercritical pressures and room temperature is sufficient to generate a measurable Raman signal from a typical pulsed frequency-doubled Nd:YAG laser beam (a green beam at 532 nm). Simple spectral filtering requirements and the lack of combustion make it possible to eliminate background interferences to make such measurements. This paper describes the initial experiments and indicates the potential capabilities of Raman imaging as a measurement tool for LOX droplet measurements.

Experiment

Raman measurements were made in a cylindrical pressure bomb (102 mm dia. x 305 mm) with optical access through four 25 mm dia. windows allowing the laser beam to be projected through a stream of LOX droplets and out of the bomb with 90 deg. optical access for imaging of the Raman signal. The bomb was capable of withstanding pressures well in excess of the O_2 critical condition (T=155K, P=49.8 atm) and tests were run with pressures as high as 68 atm. The temperature was nominally below room temperature; injection of the LOX and conduction from the attached droplet generator suppressing the temperature below that of the surrounding ambient. Gas temperature in the bomb was continually monitored and registered between 250 and 273 K during the measurements.

Droplets were injected with a cryogenic droplet generator developed and fabricated at the Phillips Laboratory. A schematic drawing is shown in figure 1 and the injector is discussed in more detail in Ref. 9. The device uses liquid N_2 (LN2) to condense a small amount of high pressure O_2 flowing from a gas cylinder through a 7 μm filter and into a chamber

Transcritical droplets are important to study for the reasons stated initially in this paper; however, the investigation of droplets constitutes only a first step in attacking the transcritical propellant atomization and vaporization problem. Thus, the authors have recently proposed to extend the AFOSR-funded effort to include the investigation of transcritical jets/sprays. The remainder of this paper will describe the results of some preliminary experiments conducted to know what kind of behavior to expect from transcritical jets and to demonstrate the feasibility of using Raman imaging diagnostics with transcritical jets.

While designing and awaiting construction of the optimized transcritical experimental chamber, an existing cylindrical pressure vessel similar to that used by Anderson et al.[8] and Woodward et al.[9] was modified to accommodate the LN_2-cooled cryogenic droplet generator. For this paper, however, the piezoelectric element and 127 μm diameter droplet-generating orifice were removed, and a straight capillary tube with inner diameter (injector diameter) of 0.25 mm (0.010") and length-to-diameter ratio (L/D) of approximately 300 were installed. Liquid nitrogen was used as the LOX simulant in the following experiments. High-pressure gaseous nitrogen was condensed within the injector approach tube which runs through the droplet generator's double-pass, low pressure LN_2 cooling jacket. Condensed liquid nitrogen was injected into helium, nitrogen, and mixtures of helium and nitrogen at various chamber pressures. Chamber temperatures varied from 280-310K, always well above the critical temperature of nitrogen (126K). LN_2 injectant temperatures, measured on the outside of the injector tube, varied from 88-115K (typically 90K or less).

Back-lit videography (shadowgraphy) and Raman imaging of nitrogen were the two techniques used to investigate the transcritical nitrogen jets. The experimental set-up is depicted schematically in Fig. 4.

SHADOWGRAPHY

The shadowgraphs were taken with an unintensified RS-170 CCD camera through a long-distance microscope to provide good spatial resolution to discern fine structures in the relatively small jet. A strobe was used to illuminate the shadowgraphs with a sufficiently short pulse (~10 μs) to freeze the motion of the jet. Similar transcritical injection experiments were conducted previously by Woodward et al.[9] The major difference here is that the injectant mass flow rate is an order of magnitude greater for these jet flows compared to the droplet generation flow rate used then.

A matrix of shadowgraph images is depicted in Fig. 5. A series of images of LN_2 injection into nitrogen is given for three different pressures, corresponding to subcritical (Fig. 5(a), 28 atm, $P/P_{crit} = 0.83$), approximately critical (Fig. 5(b), 35 atm, $P/P_{crit} = 1.03$), and supercritical (Fig. 5(c), 69 atm, $P/P_{crit} = 2.03$) conditions. Additionally, in Fig. 5(d), a LN_2 jet is injected into a mixture of nitrogen and helium. The jet mass flow rate for all images was constant at 0.068 g/s (3.5 SLPM). Flow is downward from the injector exit in position (1) at 0-1.9 mm to position (2) at 7.4-9.5 mm then to position (3) at 15-17.1 mm and finally to position (4) at 22.6-24.7 mm near the bottom of the viewing window. The vertical field of view in each image is approximately 2.1 mm (8.3 injector diameters) with approximately a 5.5 mm gap between images.

The subcritical jet in Fig. 5(a)(1-4) has a sharp gas/liquid interface throughout. The relatively low speed jet does not exhibit much breakup although disturbances are evident on the surface of the jet. Beginning at position (2), the jet would intermittently breakup into large liquid globs that were never really spherical. Also, intermittently the subcritical jet would be nearly free of disturbances, being smooth and straight past the bottom of the viewing window. Most frequently, the jet would appear as in Fig. 5(a)(1-4), with both symmetric and anti-symmetric disturbances exhibited. The symmetric disturbances generally dominated closer to the injector and helical instabilities dominated further downstream.

The LN_2 jet issuing into the approximately critical pressure environment in Fig. 5(b)(1-4) behaves much differently than the subcritical case as one might expect. In Fig. 5(b)(1), the injected nitrogen appears as a liquid presumably because of the steep gradient between the subcritical temperature of the jet and the supercritical temperature of the ambient. Thus a steep density gradient exists as well, providing a distinct surface. However, the jet is initially very smooth due to insufficient surface tension to promote the growth of capillary instabilities. The jet

Research intensified CCD camera and a 75 mm f/1.3 lens. The camera was located 200 mm from the droplet stream and the aperture was effectively limited by the bomb window diameter to f/4.0. The intensifier was gated to time the laser pulse during a 50 μsec camera exposure, but longer gates could have been used since background interferences were very small.

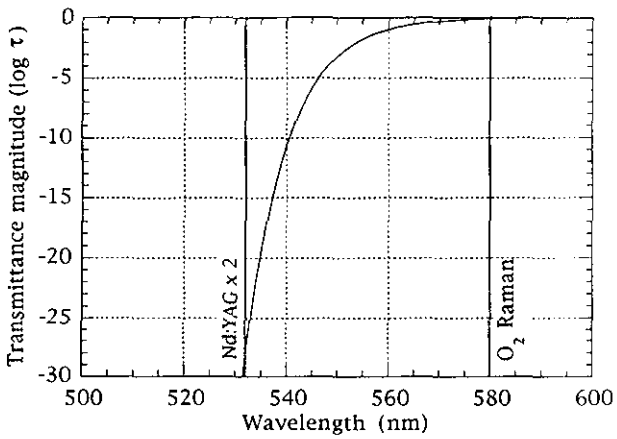

Fig. 2. The O_2 Raman signal is separated from the 532 nm laser beam with 3 mm of OG570 glass. This attenuates the laser beam by over 25 orders of magnitude while reducing the Raman signal by only 2%.

Separation of the Raman signal from the laser was accomplished with 3 mm of Schott OG570 filter glass. As can be seen from figure 2, this glass alone provides over 25 orders of magnitude of discrimination between the signal and laser while attenuating the signal intensity by no more than 2% (excluding surface losses). Care was taken to minimize background contributions from weak window fluorescence and emissions occurring due to laser beam reflections from bomb internal walls. A background signal would eventually build up as LOX droplets evaporated and O_2 became a significant constituent of the buffer gas. To reduce this effect, a small vent was installed in the bottom of the bomb below the droplet stream and gas was vented while He buffer gas was introduced to maintain constant bomb pressure and buffer gas consistency. A small funnel was located above the vent to capture any un-evaporated LOX and to increase the O_2 concentration of the vented gas. This allowed operation of the system at high pressure for sufficient time to adjust the droplet stream and acquire data.

Results

Difficulties were continuously encountered with optical breakdown of O_2 molecules in the droplets caused by focusing of the high power laser beam into the interior. The generation of this plasma produced a bright broadband flash which would overwhelm the Raman signal and could potentially damage the intensified camera. A considerable effort was made to overcome this problem by compromising laser intensity for Raman signal strength in various ways. Initially, the laser sheet was expanded in the sheet plane to further separate the planar and transverse focuses, reducing the energy concentration within the droplets. This was insufficient to eliminate the problem, however. The laser sheet focus was moved axially along the beam path to reduce the intensity at the droplet stream (sheet thickness at the droplet stream became approximately 500 μm). This configuration was necessary to acquire data through the remainder of the testing. The most successful method of reducing breakdown was the introduction of a loop in the laser beam path (figure 3) which spread the 10 nsec. pulse temporally, lowering the peak power and increasing the pulse energy necessary to reach the breakdown threshold.

Figure 4 shows the effect of the beam splitting loops on the pulse shape and length. The peak intensity is reduced by more than 60% (excluding mirror losses) and the pulse has been expanded by over 100%. The pulse

energy was reduced with this technique to 250 mJ, but the breakdown threshold was increased from about 150 mJ/pulse without the loop to about 210 mJ/pulse after its installation.

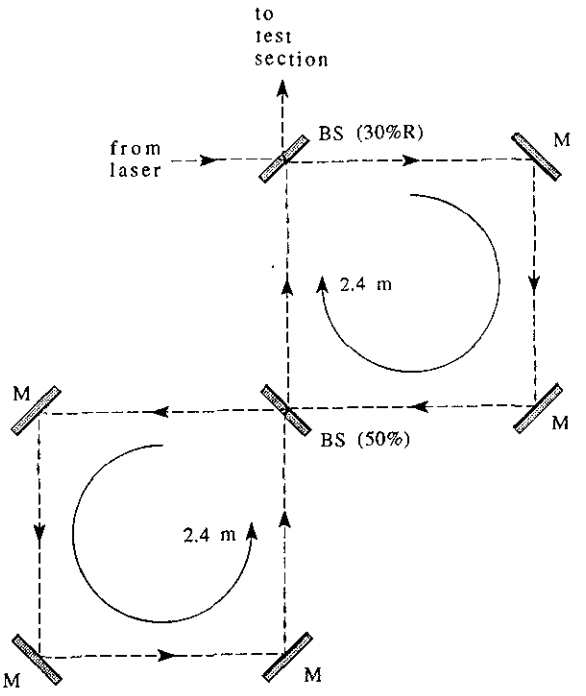

Fig. 3. Beam splitting optical circuit used to lower the laser pulse peak power.

Predictions of Raman signal intensity using ref. 8 and 11 were based on the optical geometry, conditions in the bomb, pulse energy and camera sensitivity. They indicated that measurements of O_2 could be made at 68 atm (supercritical pressure for pure O_2) with a sensitivity of about 3.4 kg mol./m^3 (1% mole fraction). To provide a means of quantifying O_2 concentration and to verify the sensitivity analysis, calibration images were acquired using room temperature O_2 at several pressures. The measured sensitivity of the technique was limited by the noise level of the camera to approximately 10 mol./m^3 (4% mole fraction at 68 atm). The difference from the calculated value rests primarily in camera- and optics-related losses and background noise not considered in the analysis.

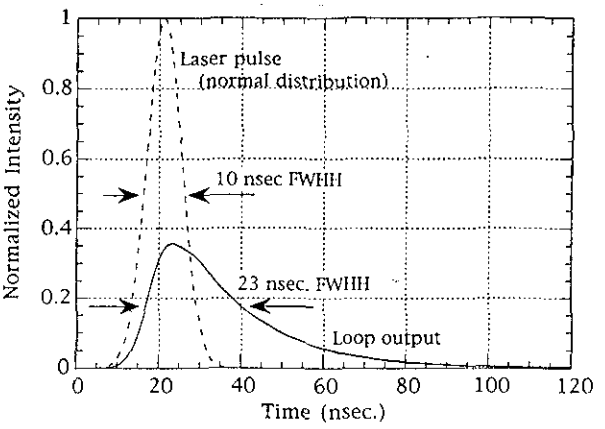

Fig. 4. Analytical comparison of a 10 nsec laser pulse with the output of the beam splitting loop in figure 3.

Figure 5 is a sample backlit image of the droplet stream at 68 atm. Figure 6 contains Raman images of several comparable droplet streams. The wake of supercritical O_2 can be clearly seen in the Raman images and, despite the low signal strength, concentration contours can be drawn as shown in figure 7. The raggedness of the 340 kg/m^3 contour indicates that the system has reached the minimum level of sensitivity (signal/noise). These images do not show a clearly defined orientation of the wake which one would expect as a result of the downward velocity of the droplet stream. Several factors may account for this. The wake region contains accumulated O_2 from many droplets in the stream and convection is occurring due to the continual purging of the buffer gas. Also the "evaporation" (to supercritical fluid) is occurring at a very high rate and may generate a flow field much stronger than that produced by the droplet stream.

An unexpected result of these tests was the discovery of a strong signal generated at a low pulse energy, when the laser was run un-Q switched. Under this condition, the laser pulse was approximately 100 µsec in length

with an energy of 0.5 mJ; insufficient to generate a detectable spontaneous Raman signal. The signal was not spectrally characterized except through visual observation. Droplets appeared to be distinctly orange - in the spectral region of the O_2 Raman signal. A likely possibility is that a morphology dependent resonance (MDR)[10] based on a stimulated Raman signal[12] constrained to the interior of the LOX droplets. The existence of such a signal suggests that there is a clearly defined liquid/vapor interface and that, in fact, the critical condition for O_2 in He has not yet been reached. Alternatively, the refractive index gradient of a transcritical fluid is great enough to minimize losses at the interface and produce the MDR's (consistent with the analysis of S. Hill[14]).

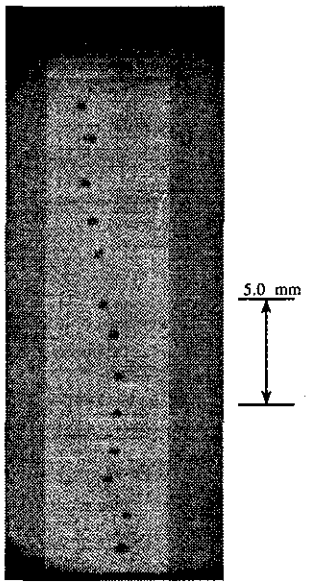

Fig. 5. LOX droplet stream in a high pressure He environment (68 atm, room temp.). Droplet size is approximately 300 μm. The stream is being deflected by convection currents and droplet/wake interactions.

Conclusions

The measurements acquired thus far indicate that spontaneous Raman imaging has potential as a diagnostic in the supercritical mixing experiments to be conducted. While the signal has been less than desired for accurate measurements, some paths to improving the signal strength are apparent. Lower f/# optical axis is desirable and will be available as the experiment moves from the bomb to the pulse tube. The breakdown limitation to laser pulse power was found to be dependent on laser pulse length. However, it appears that significant increases over the 10 nsec. pulse length are necessary to have much of an effect.

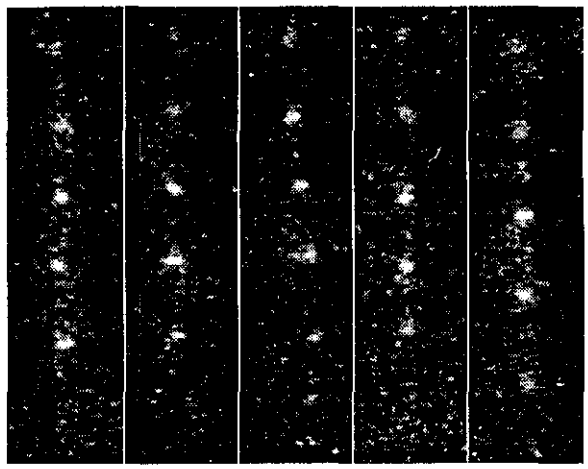

Fig. 6. Five Raman images of LOX droplet stream at 68 atm. and room temp. (supercritical condition for pure O_2) The image is the central portion of the stream illuminated by the laser sheet.

The observation of what is believed to be stimulated Raman MDR's deserves further investigation. An understanding of this phenomenon through spectral analysis could provide information on the process that is occurring at the critical interface of liquid structures in a supercritical environment.

Future Work

A continuation of this program will address several important areas. The existence of the MDR's may provide important information about the fluid

within the LOX droplets under supercritical and subcritical conditions. However, it will be necessary to examine these signals spectrally. A high resolution Raman spectrometer will be used to make these measurements in the bomb.

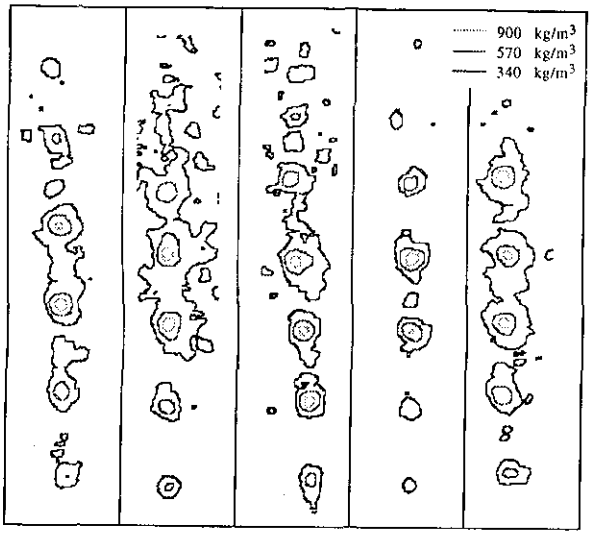

Fig. 7. O_2 concentration contours derived from intensities in the images of figure 6 after correcting for background and response. Three concentration levels are shown with different contours.

Accurate Raman concentration measurements will require more laser pulse energy, currently restricted by LOX breakdown in the droplets. The use of an ultraviolet laser (either the fourth harmonic of the Nd:YAG or an excimer laser) was considered for this application since the Raman signal is enhanced due to the shorter wavelength (λ) by a factor of λ^{-4}. (In the case of the Nd:YAG laser, the signal would be improved by a factor of 16 at fixed laser intensity.) However, the enhancement of the signal strength is more than overcome by losses in filtering to separate the laser scattering at those wavelengths and by the increased background due to a variety of laser-induced fluorescence.

The ability to raise the breakdown threshold by lowering the peak laser power suggests the use of a long pulse laser to continue the program. At UTRC, a high power dye laser (Candela model UV-8000) capable of generating 45 J in a 6 μsec pulse will be used in the continuation of this work. Although it is operated at a different wavelength, spectral filtering can be accomplished in a similar manner using a different filter glass.

A variable pulse Nd:YAG laser (800 mJ/pulse at 532 nm) with the ability to extend the pulse length to more than 200 nsec will be used in similar efforts at the Air Force Phillips Lab.

Acknowledgments

This work was completed under contract number DAAH04-94-G-0020 from the U.S. Army Research Office and the Air Force Phillips Laboratory. The authors would like to acknowledge the guidance provided by many useful discussions with J. Levine and D. G. Talley of the Air Force Phillips Laboratory. The authors would also like to acknowledge the contributions of A. C. Eckbreth who suggested the technique for extending the laser pulse length.

References

1. Tong, A. Y. and W. A. Sirignano, "Oscillatory Vaporization of Fuel Droplets in an Unstable Combustor," *AIAA Journal of Propulsion*, Vol. 5, pp. 257-261, May-June 1989.

2. Tong, A. Y. and W. A. Sirignano, "Multicomponent Transient Droplet Vaporization: Integral Equation Formulation and Approximate Solution," *Numerical Heat Transfer*, Vol. 10, pp. 253-278, 1986.

3. Anderson, T. J. and M. Winter, "Measurements of the Effect of Acoustic Disturbances on Droplet Vaporization Rates," presented at the JANNAF Combustion Meeting, October 19-23, 1992 at NASA Langley, Hampton, VA.

4. Eastes, T. W. and G. S. Samuelsen, "Secondary Atomization by High Amplitude Pressure Waves," AIAA paper number 92-3120 presented at the 28th Joint Propulsion Conference, July 6-8, 1992, Nashville, TN.

5. Yang, Y., N. N. Lin and J.-S. Shuen, "Vaporization of Liquid Oxygen (LOX) Droplets in Supercritical Hydrogen Environments," *Combus-tion Science and Technology*, Vol. 97, pp. 247-270, 1994.

6. Wu, P.-K., L.-P. Hsiang and G. M. Faeth, "Aerodynamic Effects on Primary and Secondary Spray Breakup," presented at the First International Symposium on Liquid Rocket Combustion Instability, January, 1993, Pennsylvania State University, University Park, PA.

7. Anderson, T. J., M. Winter and M. Haas, "Observation of Droplet/Shock Interactions in a Supercritical Environment," presented at the AIAA 32nd Aerospace Sciences Meeting, January 10-13, 1994 at Reno, NV.

8. Gardiner, D. J. and P. R. Graves (editors), Practical Raman Spectroscopy, Springer-Verlag, New York, 1989.

9. Woodward, R. D., D. G. Talley, T. J. Anderson and M. Winter, "Shadowgraphy of Transcritical Cryogenic Fluids," presented at the 6th Annual Symposium of the Pennsylvania State University Propulsion Engineering Research Center, NASA LeRC, Cleveland, OH, September, 1994.

10. Faeth, G. M., D. P. Dominicis, J. F. Tulpinsky and D. R. Olson, "Supercritical Bipropellant Droplet Combustion," *Twelfth Symposium (International) on Combustion*, The Combustion Institute, pp. 9-18, 1969.

11. Inaba, H. and T. Kobayasi, "Laser-Raman Radar - Laser-Raman Scattering Methods for Remote Detection and Analysis of Atmospheric Pollution," *Opto-electronics*, Vol. 4, pp. 101-123, 1972.

12. Tzeng, H.-M., K. F. Wall, M. B. Long and R. K. Chang, "Laser Droplets: Highlighting the Liquid-Air Interface by Laser Emission," Science, Vol. 231, pp. 486-488, Jan. 1986.

13. Walmsley, I. A., "The Stimulated Raman Effect, An Introduction," The Institute of Optics, University of Rochester, Rochester, NY, 1989.

14. Chowdhury, D. Q., S. C. Hill and P. W. Barber, "Morphology-dependent Resonances in Radially Inhomogeneous Spheres," *Journal of the Optical Society* of America, Vol. 8, pp. 1702-1705, 1991.

APPENDIX C

"A Fundamental Study of Supercritical Droplet Deformation and Breakup Through a Miscible Fluid Analog"

AIAA Meeting Papers on Disc, July 1996
A9637062, AF-AFOSR-96-0831, AIAA Paper 96-2858

A fundamental study of supercritical droplet deformation and breakup through a miscible fluid analog

Chad Mitts
Illinois Univ., Chicago

Douglas Talley
USAF, Phillips Lab., Edwards AFB, CA

Dimos Poulikakos
Swiss Federal Inst. of Technology, Zurich, Switzerland

AIAA, ASME, SAE, and ASEE, Joint Propulsion Conference and Exhibit, 32nd, Lake Buena Vista, FL, July 1-3, 1996

In the current study, the deformation and breakup of a zero-surface tension particle was examined through the use of miscible fluids as an analogy to transcritical droplet dynamics. The following four primary breakup regimes were identified as a function of the viscosity ratio and the Reynolds number: viscous globule, viscous bag, multimode, and shear-driven vortex. The distance and time to the onset of primary particle breakup decreased with the viscosity ratio. Furthermore, the expansion of the particles' major axis at the onset of primary breakup in the shear-driven vortex regime also decreased with the viscosity ratio. In addition to the viscous and inertial forces, dynamic interfacial tension was recognized as a contributing force in the evolution of a zero-surface tension particle, and convective mixing of the particle and ambient fluids was observed to be significant. Finally, the qualitative experimental results of the current study agreed well with the previous numerical investigation of the deformation of a supercritical droplet that was conducted by Lee et al. (1990). (Author)

A FUNDAMENTAL STUDY OF SUPERCRITICAL DROPLET DEFORMATION AND BREAKUP THROUGH A MISCIBLE FLUID ANALOG

Chad Mitts
Department of Mechanical Engineering
The University of Illinois at Chicago
Chicago, IL 60607

Douglas Talley
Phillips Laboratory
Edwards AFB, CA 93524

Dimos Poulikakos
Institute of Energy Technology
Swiss Federal Institute of Technology
CH-8092 Zurich, Switzerland

Abstract

In the current study, the deformation and breakup of a zero-surface tension particle was examined through the use of miscible fluids as an analogy to transcritical droplet dynamics. The following four primary breakup regimes were identified as a function of the viscosity ratio and the Reynolds number: viscous globule, viscous bag, multi-mode, and shear-driven vortex. The distance and time to the onset of primary particle breakup decreased with the viscosity ratio. Furthermore, the expansion of the particles' major axis at the onset of primary breakup in the shear-driven vortex regime also decreased with the viscosity ratio. In addition to the viscous and inertial forces, dynamic interfacial tension was recognized as a contributing force in the evolution of a zero-surface tension particle, and convective mixing of the particle and ambient fluids was observed to be significant. Finally, the qualitative experimental results of the current study agreed well with the previous numerical investigation of the deformation of a supercritical droplet that was conducted by Lee, Fernandez-Pello, Corcos, and Oppenheim.[2]

Introduction

One of the most important criteria for the effective design and analysis of combustion devices such as liquid propellant rocket engines, diesel engines, and multi-stage gas turbines is a thorough understanding of the atomization mechanisms that distribute fuel within the combustor. As a result, the atomization fundamentals of sprays and droplets have been the focus of intensive research for many years. However, the majority of the studies conducted thus far have considered only the thermodynamically subcritical regime of fluid atomization. As the operating temperatures and pressures of contemporary engines increase beyond the critical point of the fuels in an attempt to satisfy stringent emission, efficiency, and power requirements, a detailed understanding of supercritical spray and droplet dynamics is necessary to produce a design that satisfies the cost and reliability constraints.

In relevant rocket engine applications, the fuel is initially at a subcritical temperature and a supercritical pressure, and it is injected into an environment of both a supercritical temperature and pressure. The droplet is then heated to a supercritical state by the hot ambient gas. This process, termed transcritical injection, has many thermodynamic and transport complexities that are distinctly different from the traditional subcritical analysis. First, a substance above its thermodynamic critical pressure consists of only one phase[1], thus, the distinction between the gas and liquid states that has traditionally defined the spray and droplet boundaries becomes obscured.

Second, surface tension approaches zero, therefore, particle deformations become significant.[2] Next, thermodynamic property correlations are not well established, and there exists singularities at the critical point such as the infinite compressibility and specific heat[1], as well as the vanishing enthalpy of vaporization[3]. In addition, the solubility of the gas phase into the subcritical liquid phase is greatly increased at near critical and transcritical conditions.[4] As a result, all of the fluid properties, including the critical point itself, become a function of the composition of a multi-component mixture. Furthermore, properties such as the density of a transcritical droplet and the supercritical ambient environment approach similar orders of magnitude. The noted characteristics of transcritical atomization processes establish a problem that is fundamentally different from the subcritical case, therefore, the distinctions severely limit the applicability of the abundant research data available for the subcritical case to the supercritical scenario. Consequently, there exits a significant need to study transcritical atomization.

Over the past 35 years, there have been a number of studies, both experimental[4-8] and theoretical,[2-3,9-11] into the vaporization and combustion of fuel droplets in supercritical conditions. However, with a few exceptions,[2,12] the majority of the previous studies have neglected the large droplet deformations that are prevalent in the convective conditions within actual combustion chambers. Both the mixing of the ambient gas into the droplet and heat and mass transfer to and from the droplet will be enhanced by particle deformations. The altered mixing and diffusion processes will have a significant impact on the occurrence of the critical point and the value of various thermodynamic and transport properties that are affected by composition. One of the most comprehensive models of supercritical droplet deformation by Lee et al. resolved the particle deformation and mixing dynamics at the expense of the thermodynamic complexities. Their model assumed a priori that the droplet was at a supercritical state, and they neglected the property variations that are significant in transcritical dynamics. Nonetheless, this was the first comprehensive study of the deformation of a supercritical droplet, and it provided insight into an area of transcritical droplets that had previously been neglected. The results indicated that vorticity generated within the droplet from aerodynamic interactions with the ambient environment produced significant deformations of the initially spherical, quiescent droplet. The resulting particle was a flattened disc, with the periphery of the disc rolling up under the action of the vorticity in a manner similar to the production of a vortex ring. Finally, due to the difficulty inherent in generating a free droplet in a reduced surface tension, supercritical environment, there exists very little experimental data on the deformations of transcritical particles to compare with the numerical results.

The Miscible Fluid Analog

One novel method of studying aspects of the deformation and breakup of a transcritical droplet is through a miscible fluid analog. The analog consists of introducing a single particle into a quiescent fluid with which it is miscible. This simple idea bears a great deal of similarity to the actual transcritical case. First, since surface tension is caused by an asymmetry of molecular forces at the interface of two fluids,[13] it will rapidly vanish as the two miscible fluids begin to dissolve into each other and consequently destroy the discontinuous fluid interface. Furthermore, density and viscosity ratios of the transcritical case can be achieved within an order of magnitude by carefully selecting the proper miscible fluid pairs. In addition, the high solubility of the two miscible fluids approximates the enhanced solubility associated with the transcritical case. While the analog does not replicate the thermodynamic property singularities or the thermal transport phenomenon inherent to transcritical droplets, it could replicate aspects of the kinematic nature of particle deformation and breakup, and thus provide insight into the real case.

Characterizing the deformation and breakup of a zero-surface tension particle requires a new approach due to the absence of surface tension. Traditional dimensionless parameters relevant in subcritical particle deformation and breakup such as the Weber number (We) and Ohnesorge number (Oh) both approach infinity as surface tension tends to zero; therefore, they become uninformative. However, the two primary forces that are significant in the absence of surface

tension are the viscous forces which tend to resist breakup, and the inertial forces which tend to enhance deformation. The interaction of the inertial and viscous forces can be described in terms of the Reynolds number (Re) and the viscosity ratio (VR), which are given in equations (1) and (2) respectively. Furthermore, the density ratio is also an important parameter, and it is given in equation (3).

$$Re = \frac{u\, d_p}{\nu_{amb}} \tag{1}$$

$$VR = \frac{\mu_p}{\mu_{amb}} \tag{2}$$

$$DR = \frac{\rho_p}{\rho_{amb}} \tag{3}$$

In equations (1) through (3), the parameters u, d, μ, ρ, and ν are the relative velocity between the droplet and the ambient, the particle diameter, the absolute viscosity, the density, and the kinematic viscosity respectively. The subscript "p" refers to the particle fluid and the subscript "amb" refers to the ambient fluid. As defined in equation (1), the Reynolds number represents the interaction of the inertial and viscous forces in the ambient fluid. The viscosity ratio is an indication of in which medium, the ambient fluid or the particle fluid, the transfer of momentum will be more significant. In the current work, the influence of the density ratio was not examined, and all of the fluid pairs had a DR between unity and 1.6. Therefore, the characteristics of zero-surface tension particle deformation and breakup should be describable solely in terms of the Reynolds number and the viscosity ratio for a DR near unity. This idea was first proposed by Talley et al.[14]

Currently, there does not exist an experimentally validated model of transcritical droplet evolution that incorporates both the large deformations and the thermodynamic complexities inherent in the complete physics of the problem. While there has been significant experimental work performed in regards to understanding the thermodynamics, the particle kinematics has received very little attention. Therefore, it is the primary goal of this work to characterize the deformation and breakup regimes of a zero-surface tension particle through the use of the miscible fluid analog as a means of gaining an understanding of the relevant mechanisms associated with transcritical particle dynamics.

Experimental Setup and Procedure

Overview of the Experiments

An experimental apparatus was established that permitted the evolution of a droplet to be observed as it free fell through a quiescent ambient fluid with which it was miscible. As a means of examining the widest range of dimensionless parameters, seven different fluids were utilized in the current study: water, glycerin, propylene glycol, 1-octanol, 2-propanol, heptane, and pentane. The seven individual fluids were combined into the following eight pairs: glycerol in water and a 30% by weight mixture of water and 2-propanol, propylene glycol in water and 2-propanol, 1-octanol in heptane, pentane and 2-propanol, and water in 2-propanol. In addition to describing the qualitative breakup regimes of the droplets, the images obtained from the visualization experiments were also used to quantify various characteristics such as the distance, time, velocity, and dimensions of the particle at the onset of primary breakup.

Test Section and Droplet Injection System

The experimental test section and heat exchanger assembly are shown in Figure 1. The main body of the test section had a square cross-section with a width of 9.84 cm and a height of 57.9 cm. All four walls were constructed of 0.953 cm thick mar-resistant Lexan™ (polycarbonate) sheets joined with a clear epoxy. The main body was mounted onto a 38.1 cm long, 25.4 cm wide base plate that was also constructed of a 0.953 cm thick Lexan sheet. A 1.27 cm thick Plexiglass top plate was mounted to the main body with eight #10-20 socket head screws, and a silicone rubber gasket was used to seal the interface. A 3.81 cm high Plexiglass cylinder with a radius of 1.75 cm was secured with epoxy in the center of the top plate. A 1.59 cm hole was bored through the center of the cylinder and through the top plate. A 2.2 cm counterbore was machined 0.3 cm deep at

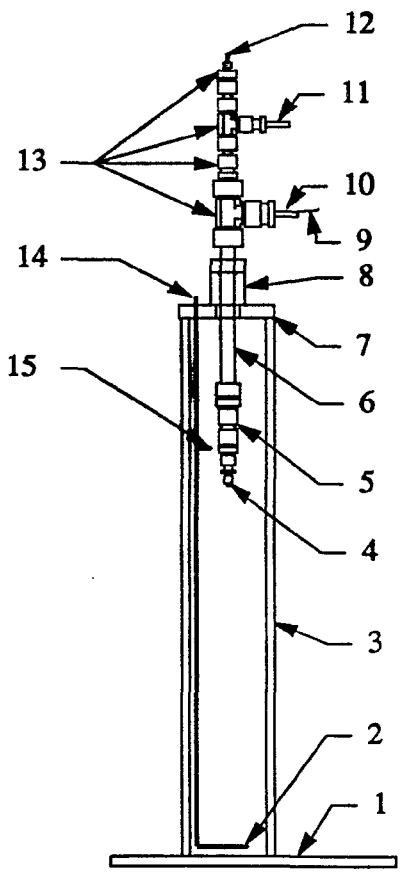

Fig. 1. Experimental test section and heat exchanger assembly. The components are: (1) base plate, (2) amb. fluid thermocouple, (3) test section wall, (4) injector tip and thermocouple, (5) coupling assembly, (6) H. E. outer tube, (7) top plate, (8) H. E. mounting assembly, (9) injector tip thermocouple lead, (10) H. E. fluid outlet, (11) H. E. fluid inlet, (12) particle fluid inlet, (13) coupling and tee assembly, (14) ambient gas and liquid thermocouple leads, and (15) ambient gas thermocouple.

the top of the cylinder to allow for the placement of an O-ring. An additional Plexiglass cylinder with a radius of 1.75 cm, a height of 1.27 cm, and a hole of 1.59 cm bored through was secured on top of the initial cylinder with three #8-20 socket cap screws spaced 120° apart on a radius of 1.27 cm. The upper cylinder served as an O-ring clamp. In addition, a threaded hole was also machined into the top plate to allow the test section to be connected to a nitrogen gas cylinder.

The droplet injection system consisted of a concentric tube heat exchanger that allowed the particle fluid temperature to be varied between 0°C and 100°C. The outer tube of the heat exchanger was a 1.59 cm OD copper tube. As indicated in Figure 1, the outer tube was mounted through the top plate of the test section, and it was held in place by clamping an O-ring around it. When the O-ring clamp was loosened, the height of the injector assembly could easily be adjusted. The lower end of the outer tube terminated in a series of Swagelok™ reducing couplings, and the upper end terminated in a 1.59 cm coupling tee. A 1.59 cm to 0.953 cm reducer was mounted onto the upper branch of the 1.59 cm tee, and it was bored through to permit a 0.953 cm OD tube to be concentrically inserted into the 1.59 cm tube. The 0.953 cm tube was mounted such that its lower end terminated slightly above the lower end of the 1.59 cm tube, thus creating an opening for the flow of the heat exchanger fluid. A 0.953 cm coupling tee was mounted on the upper end of the 0.953 cm tube. The upper branch of the 0.953 cm tee was mounted to a 0.953 cm to 0.016 cm reducing coupling that was also bored through. A 0.016 cm stainless steel tube was inserted through the upper reducer, down the entire length of the heat exchanger assembly, and through the lower terminal coupling. The 0.016 cm tube was completely sealed from the heat exchanger fluid, and it was used to transport the particle fluid. The particle fluid tube was extended 0.5 cm beyond the end of the reducer, and a K type thermocouple was mounted to it to allow the particle fluid temperature to be monitored. Furthermore, two type K thermocouples were mounted in the test section: one to monitor the ambient liquid temperature and one to monitor the ambient gas temperature. The output from both of the ambient fluid thermocouples and from the thermocouple mounted on the injector tip were monitored via a Hewlett-Packard 3467A logging digital multi meter.

Water was used as the heat exchanger fluid. The water entered the device through the middle branch of the 0.953 cm coupling tee. It then traveled the entire length of heat exchanger, through the opening between the 0.953 cm and 1.59 cm tube, and back up the length of the heat exchanger where it exited through the middle branch of the 1.59 cm tee. A Neslab model RTE-110 circulating bath served as the distribution and temperature control unit for the water.

The particle fluid was fed to the heat

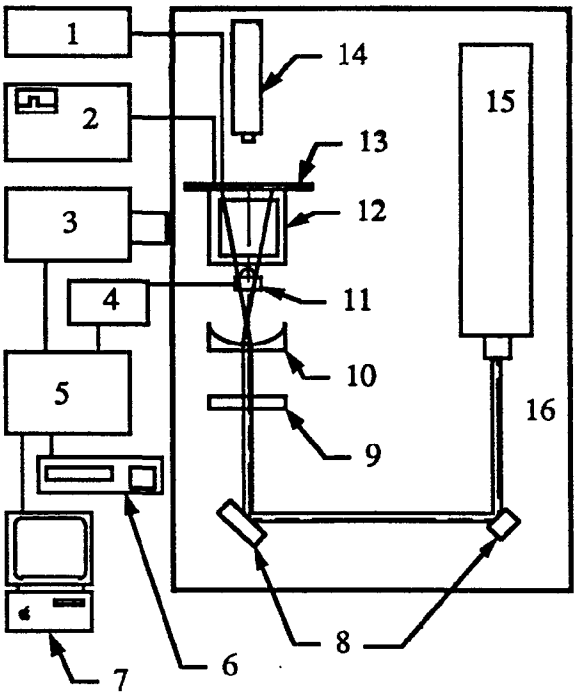

Fig. 2. Schematic of the droplet evolution imaging experimental setup. The components are: (1) Neslab RTE-110 circ. bath, (2) HP 3467A digital multimeter, (3) Kodak Ektapro model 1000 HRC CCD camera, (4) TTL pulse generator, (5) Kodak Ektapro model 1000 HRC processing unit, (6) Panasonic S-VHS VCR, (7) Macintosh Iix with Data Translation Frame Grabber Board, (8) mirrors, (9) clyindrical lens, (10) concave lens, (11) infrared sensor, (12) test section, (13) reflective plate, (14) Metrologic He-Ne laser, (15) Lexel model 95 Argon ion laser, and (16) optical table.

exchanger via two methods. The first method consisted of a manually operated syringe that was used to feed the particle fluid directly to the heat exchanger through a connection of 0.016 cm Teflon tubing. The second method utilized a positive displacement pump that was capable of delivering the small volumes of particle fluid required. The pump consisted of a 3.18 mm piston that was actuated by a 6.35 mm diameter lead screw. A Kollmorgen SM39V2 stepper motor and SMC-401-PS programmable control unit rotated the lead screw. Both methods were used, and the experimental results were observed to be independent of the method used.

Droplet Evolution Imaging Setup

The most important apparatus in the imaging system was the Kodak Model 1000 HRC Ektapro Motion Analyzer shown in Figure 2. The motion analyzer consisted of two parts, the imager and the processor. The imager was a monochrome camera with a 512 by 384 pixel CCD sensor. The processor was capable of acquiring 1,364 images from the imager at acquisition rates of 250, 500, and 1000 images per second. A Panasonic AG-1970 S-VHS video cassette recorder was interfaced with the motion analyzer directly through a S-VHS video port on the processor, and all experimental data were downloaded onto S-VHS tapes. An optical drive was available, but the large number of experimental runs conducted favored the S-VHS tapes as the data storage media. Due to the limited number of frames available on the motion analyzer, the image acquisition rate was normally set to 250 images per second with an exposure time of 4 ms. Furthermore, to optimize the use of the available memory, the camera recording sequence was triggered by a TTL pulse generator that was interfaced with an infrared sensor. A Metrologic 20 mW He-Ne laser was mounted on a vertical traverse, and the beam was leveled with the free surface of the ambient fluid such that it terminated on the infrared sensor. At the moment a passing droplet blocked the beam, the TTL pulse generator delivered a signal to the motion analyzer, and thus triggered the recording sequence. The time lag between the start of the recording sequence and the impact of the droplet with the free surface was accounted for by examining the recordings and the average value was five ms.

Droplet illumination was achieved through a laser induced fluorescence technique. To create the luminescent droplets, Fluorescein sodium salt was added to the particle fluid at a 0.05 % by weight mixture ratio. Peck and Sigurdson[15] utilized a similar ratio of Fluorescein to illuminate water droplets and found that the dye altered the fluid properties less than 1 %. A Lexel Model 95 argon ion laser operating in single line mode at 514.5 nm was used to excite the dyed particles. The beam was reflected at a 90° angle twice after exiting the laser, as indicated in Figure 2. The beam was then expanded both vertically into a sheet by a 3.18 mm radius half cylindrical lens and horizontally by a 42.0 mm diameter, 100.0 mm focal length concave lens. The test section and droplet injection system were placed in the path of

the beam such that the laser sheet was centered with the entire droplet trajectory. The laser sheet had a width of approximately 30 mm and a height of 500 mm once it reached the test section. A reflective aluminum sheet was placed on the exterior of the test section and on the opposite side of the laser entrance to create an evenly illuminated droplet. Without the reflective sheet, the laser sheet would be partially extinguished before it passed through the entire droplet.

To calibrate the imaging system, a reticule consisting of eight solid black dots with known center distances was placed in the plane of the droplet parallel to the laser beam centerline, and it was illuminated with an incandescent light. A digital image of the reticule was then downloaded to a Macintosh IIx personal computer via a Data Translation Frame Grabber board. Image Analyst, an image processing package from Automatix Inc., was used to determine a mm to pixel ratio from the image of the dots. The calibration sequence was a standard feature of Image Analyst and it is a thorough algorithm that takes into account any halos around the dots due the reticule being slightly out of the focal plane. The imaging system was re-calibrated on a regular basis.

Results

General Classification of the Breakup Regimes

As discussed earlier, the characterization of zero-surface tension droplets with a density ratio of near unity can be described solely in terms of the viscosity ratio and the Reynolds number. To this end, Figure 3 is a plot of the viscosity ratio versus the Reynolds number for the conditions and fluids examined in the current work. The plot has been subdivided into four rather robust breakup regimes: viscous globule, viscous bag, multi-mode, and shear-driven vortex. The viscous globule and multi-mode regimes were further subdivided into two sub-regimes that were distinct from each other in subtle ways, yet still similar enough to remain in their more general parent regime. Each of the four general breakup regimes and the corresponding sub-regimes will be discussed in the following sections.

Viscous Globule Regime

The viscous globule mode is a general category in which the droplets deformed slowly and uniformly into an oblate disc under the action of the inertial forces. This was the dominant mode for viscosity ratios of approximately 140 and greater and Reynolds numbers below 500, with the exception of the range of Reynolds numbers of 300 and greater with corresponding viscosity ratios between 140 and 300. Once the flattened droplet thinned significantly, the viscous forces were no longer capable of maintaining a coherent particle and it consequently broke up. The manner in which the deformed particle broke up varied with the Re. For Reynolds numbers less than 300, the flattened particles tended to collapse inward towards the low pressure suction region aft of the particles. For Reynolds numbers above 300, the particles formed a parachute shape with a thin membrane connecting a circumferential ring where the majority of the particle mass was concentrated. Once the parachute shape began to form, the particle would rapidly expand; thus, the ring would become unstable and the membrane would rupture. Due to the distinct difference between the manner in which the viscous disc broke up, two sub-regimes were identified as the viscous globule collapse regime and the viscous globule membrane rupture regime.

Figure 4 illustrates the evolution of a highly viscous, zero-surface tension particle in the viscous globule collapse regime with a Re of 250 and a VR of 1,050. From the time of impact to approximately 2.9 seconds after impact, the globule mass was redistributed into a homogeneous, oblate disc as a result of the aerodynamic pressure exerted on the forward side of the particle. Neither the shear stresses acting on the particle boundaries nor the low pressure suction region aft of the particle influenced the shape significantly up to this point. However, at approximately 2.9 seconds, the internal viscous forces of the particle were no longer capable of withstanding the influence of the shear and pressure induced stresses, thus, the particle rapidly collapsed. After collapsing, the globule accelerated briefly due to the reduced drag forces. Shortly after the acceleration of the particle, at a time of approximately four seconds after free surface impact (not shown in Figure 4), the collapsed particle disintegrated into an asymmetric collection of smaller globules interconnected by

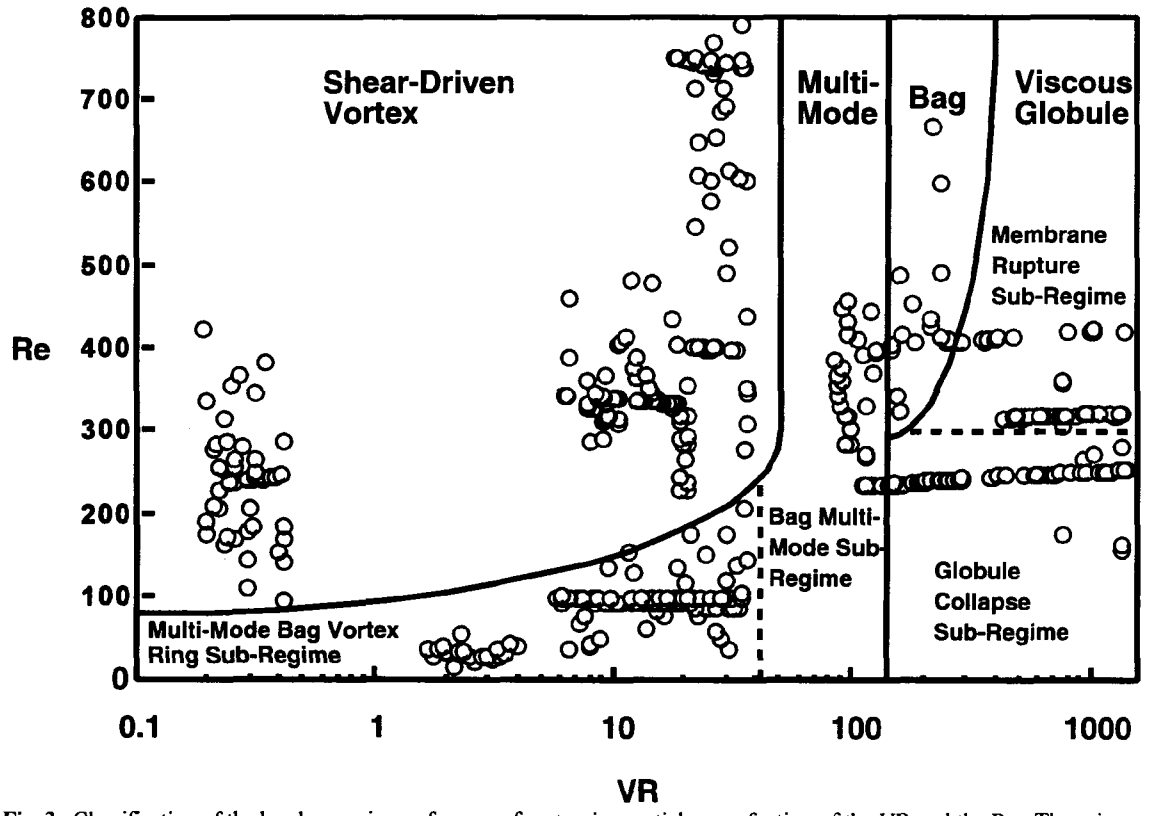

Fig. 3. Classification of the breakup regimes of zero-surface tension particles as a fuction of the VR and the Re. The primary breakup regimes are separated by the solid lines, and the sub-regimes are divided by the dashed lines.

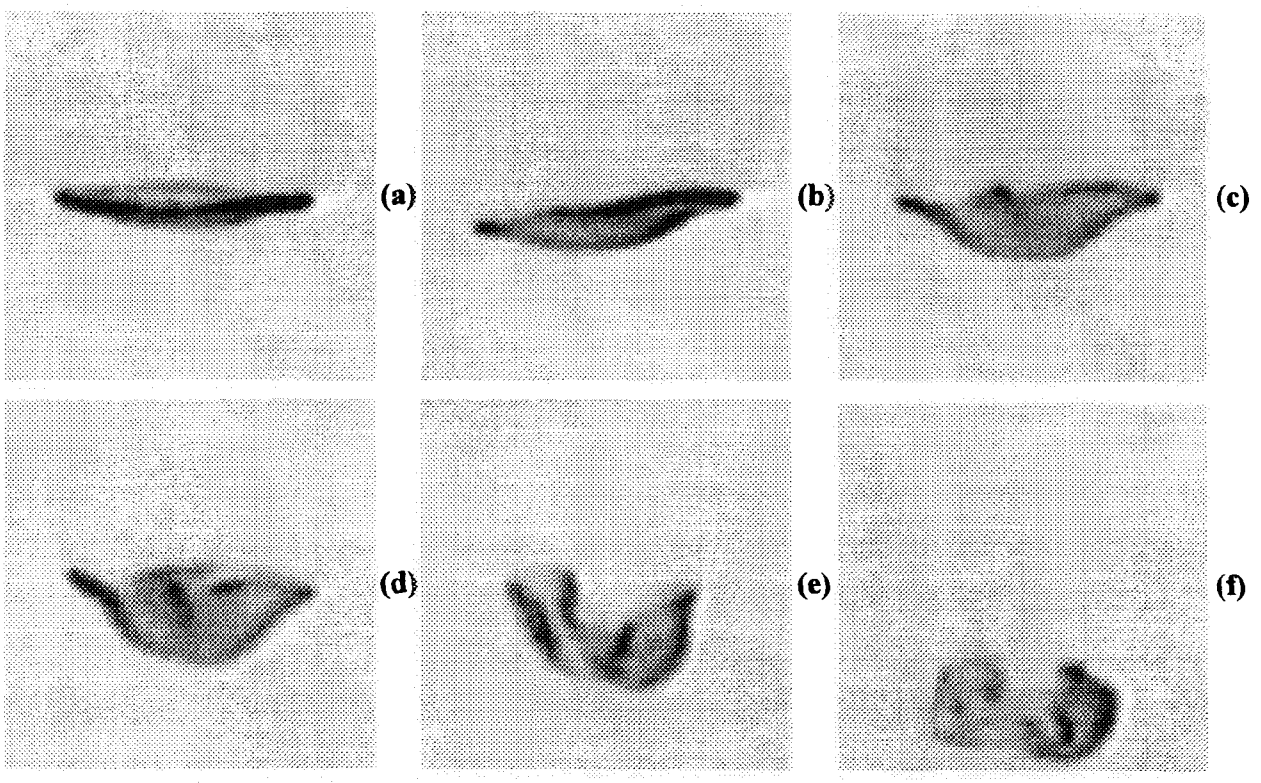

Fig. 4. Evolution of a zero-surface tension particle illustrating the globule collapse sub-regime of the viscous globule breakup mode with initial conditions of VR=1,050 and Re=250. The corresponding times are (a) 2.892, (b) 3.088, (c) 3.280, (d) 3.364, (e) 3.476, and (f) 3.548 seconds after free surface impact.

thin ligaments of the highly viscous fluid. The collection of smaller particles then slowed to almost a complete stop and they diffused into the dilute ambient fluid.

The qualitative nature of the viscous globule collapse sub-regime was virtually identical over the entire range of viscosity ratios from 1100 to 140. However, the quantitative aspects of the droplet breakup were altered greatly. Figure 5 is a plot of the distance at which the onset of primary breakup began to occur, x_b, normalized by the initial particle diameter, d_o. In addition, the normalized time corresponding to the onset of primary breakup is also plotted as a function of the viscosity ratio in Figure 5. Both the distance and the time at which the particles began to breakup increased steadily with the viscosity ratio as a result of the greater resistance to deformation from the internal particle viscous forces.

For the globule membrane rupture sub-regime, which was the dominant mode in the viscous globule category for Re greater than 300, the viscous disc would form a parachute structure instead of collapsing. Figure 6 typifies the evolution of a viscous particle evolving in the membrane rupture sub-regime with an initial VR of 773 and an initial Re of 320. The deformation of the particle was virtually identical to the viscous globule collapse case up to a time of approximately two seconds after the impact with the free surface. At this point, the center of the disc was pushed upwards relative to the particle periphery, as opposed to the collapse regime where the periphery was pushed upwards relative to the center. Simultaneously, the mass of the particle had become almost entirely distributed in a ring around the periphery of the droplet. The concentration of mass in the circumferential ring retained more momentum than the thin membrane center, thus, the ring traveled faster than the center, stretching the membrane as it did so. The membrane rapidly thinned to the point where it was no longer able to resist the pressure differences between the forward and aft sides of the particle; therefore it began to rupture at approximately 2.6 seconds. The membrane served as a stabilizing mechanism for the ring; thus, after the membrane ruptured, the ring rapidly became unstable and bent into two symmetric halves as shown in Figures 6(e) and 6(f). Immediately after the ring folded, it slowed down and the particle

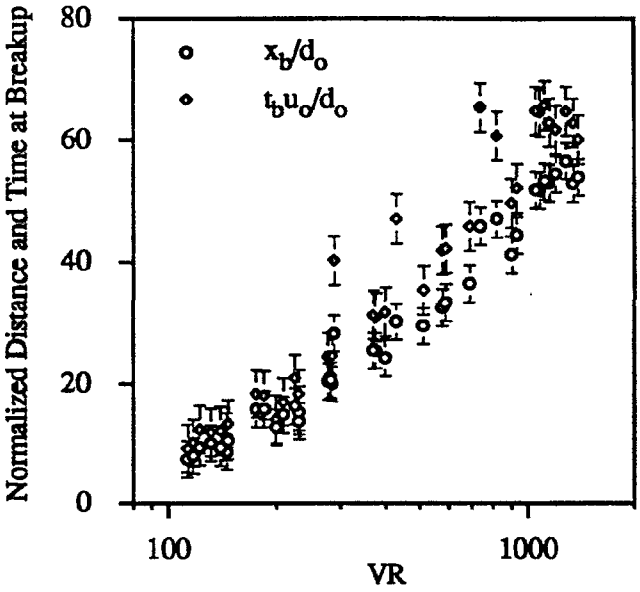

Fig. 5. Normalized distance and time to the onset of primary breakup as a function of the viscosity ratio for the viscous globule collapse sub-regime.

mass dissipated via diffusion into the surrounding dilute ambient solution.

The membrane rupture sub-regime exhibited varying secondary breakup characteristics as the viscous forces were reduced. Figure 7 is representative of the droplet evolution for the lower VR particles of the membrane rupture mode. At a time of approximately 800 ms after free surface impact, the shape of the particle in Figure 7 was very similar to that of Figure 6 at 2.3 seconds. However, due to the increased effect of the inertial forces, the membrane ruptured much more violently and the resulting ring was less stable. This lead to an asymmetric ring that was destroyed and dispersed primarily by shear forces as opposed to the diffusion controlled dispersion of the disintegrated ring of Figure 6.

Despite the variety of the breakup characteristics within the viscous globule regime, the initial particle deformation was virtually identical. In all cases the globule flattened into a circular disc before it broke up. This distinguishes the viscous globule mode from the other primary breakup regimes that will be discussed in the following sections.

Viscous Bag Regime

As the viscous forces were reduced and

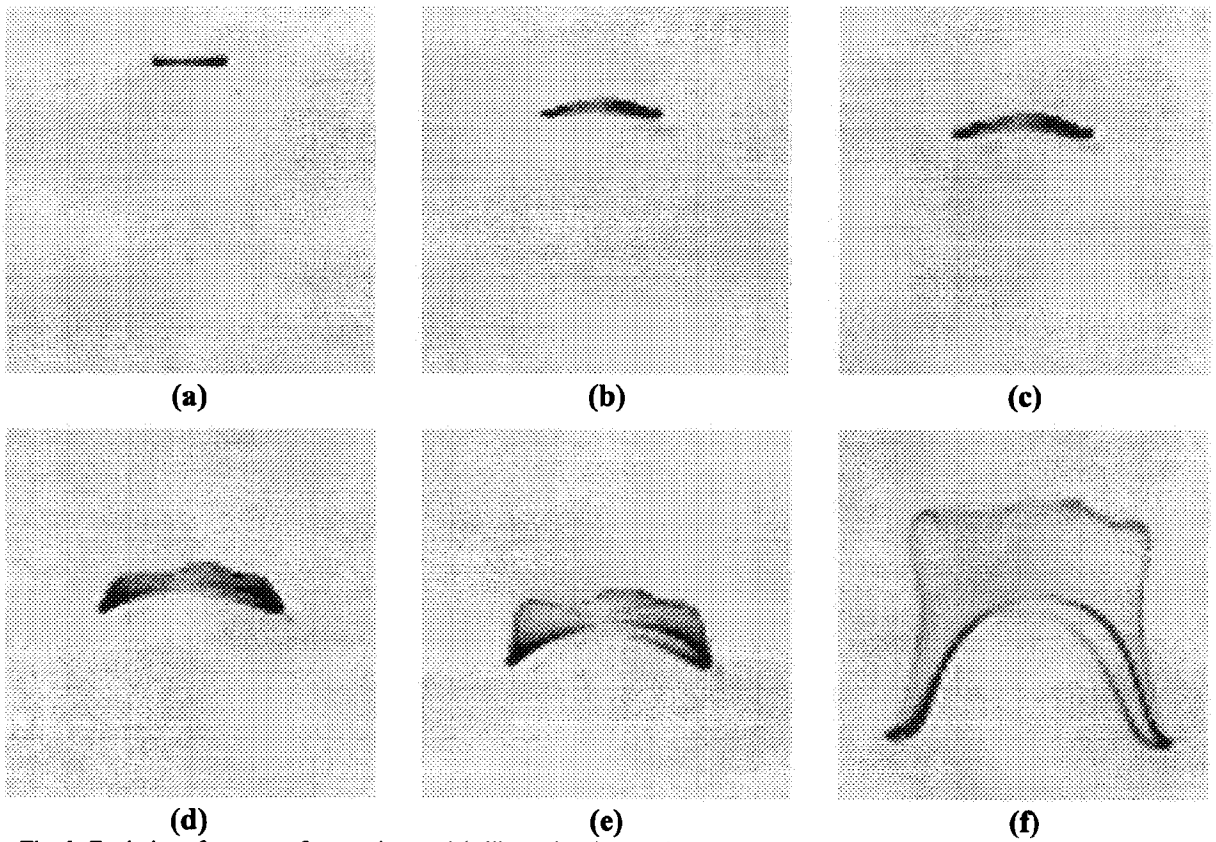

Fig. 6. Evolution of a zero-surface tension particle illustrating the membrane rupture sub-regime of the viscous globule breakup mode with initial conditions of VR=770 and Re=320. The corresponding times are (a)1.74, (b) 2.216, (c) 2.316, (d) 2.536, (e) 2.692, and (f) 3.316 seconds after free surface impact.

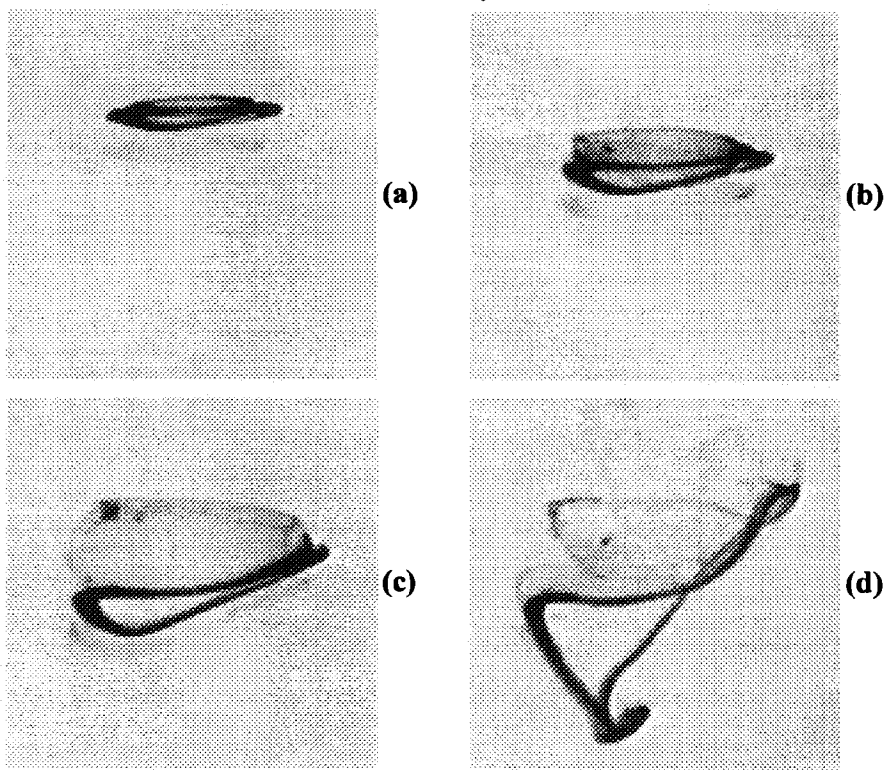

Fig. 7. Evolution of a zero-surface tension particle illustrating the membrane rupture sub-regime of the viscous globule breakup mode with initial conditions of VR=370 and Re=410. The corresponding times are (a) 0.82, (b) 0.988, (c) 1.208, and (d) 1.7 seconds after free surface impact.

the inertial forces increased, the initial particle deformation and breakup transitioned into the viscous bag regime. This regime was observed for Reynolds numbers greater than 300 with viscosity ratios between 140 and 300. In this regime, the particle mass on the leading edge boundary of the initially spherical droplet was pulled upwards by shear forces; thus, it formed the distinct bag shape that has also been observed for droplets in which surface tension is a factor.[16] Figure 8 is an illustrative example of particle deformation in the viscous bag regime. At a time of 300 ms after free surface impact, the particle already had deformed greatly, with a significant portion of the particle mass distributed into the bag rim. The shear stresses that caused the bag shape were due to the initially discontinuous velocities at the boundary of the particle and ambient fluids. However, the internal viscous forces of the particle were still significant enough to prevent the sheared fluid from being completely stripped away. Furthermore, once the sheared fluid reached the bag rim, the magnitude of the shear forces were reduced locally as a result of it being aft of the leading edge of the droplet; thus, the velocity of the fluid at the bag rim was reduced relative to the center of the droplet. As the bag rim velocity slowed, the shear induced circulation of the fluid at the leading edge also slowed as a result of internal particle viscous forces. This reduction in the particle fluid velocity relative to the drop centroid resulted in an increase in the particle fluid velocity relative to the ambient fluid. Therefore, the magnitude of the shear stresses at the leading edge also necessarily increased again, giving rise to an additional shear flow of particle fluid that was distinct from, but nearly identical in appearance to the first. This second wave of sheared fluid can clearly be seen in Figure 8(b). Once the second wave of sheared fluid reached the bag rim, the main body of the bag was thinned to such a degree that the internal particle viscous forces were no longer capable of maintaining the bag shape. As a result, the remaining particle fluid that comprised the bag body was completely destroyed and stripped upwards, leaving the majority of the original particle fluid in a circumferential ring as seen in Figure 8(d). The ring then behaved in a similar manner to the ring that resulted from the viscous membrane rupture regime described and shown in Figure 7. The existence of the true viscous bag regime as defined above occurred over a rather small range of viscosity ratios and Reynolds numbers; however, the general nature of the shear-induced flow of particle fluid at the interface giving rise to a crude bag like structure was dominant in the multi-mode regime to be discussed in the next section.

Multi-Mode Regime

Beyond the viscous globule and bag regimes, a significant quantity of the data fell into the multi-mode regime. In this rather broad category, neither the viscous nor the inertial forces dominated, and the resulting deformation varied greatly with the VR and the Re. The sub-regimes are noted in Figure 3. For viscosity ratios greater than 40, the viscous bag multi-mode sub-regime was prevalent. Initially, this mode was very similar in appearance to the pure viscous bag deformation described earlier. However, as Figure 9 illustrates, the key difference was that the particle fluid that was initially sheared at the interface established a macro-scale (relative to the droplet) circulation region instead of being held at the bag rim by the internal viscous forces of the particle. Once the circulating fluid entered the low pressure region aft of the particle, there was little resistance to its momentum. Thus, the recirculating fluid would impact the fluid that was now at the particle leading edge, as shown in Figure 9(c). The hyperboloid shape of Figure 9(d) resulting from the impact of the recirculating mass with the leading edge mass was inherently unstable, and the high relative velocity between the particle mass and the ambient fluid resulted in droplet breakup in less than 200 ms after the recirculating mass impacted. After the initial breakup of the droplet, the resulting globules' Reynolds number was significantly reduced, and they proceeded to diffuse into the dilute ambient solution.

The remainder of the multi-mode regime, as shown in Figure 3, was characterized by the bag-vortex ring sub-regime. Again, this sub-regime was remarkably similar to both the pure bag regime and the multi-mode viscous bag sub-regime; however, in the bag-vortex ring mode, the recirculation region developed into a distinct ring located at the bag periphery. As illustrated in Figure 10, the recirculation region was created at

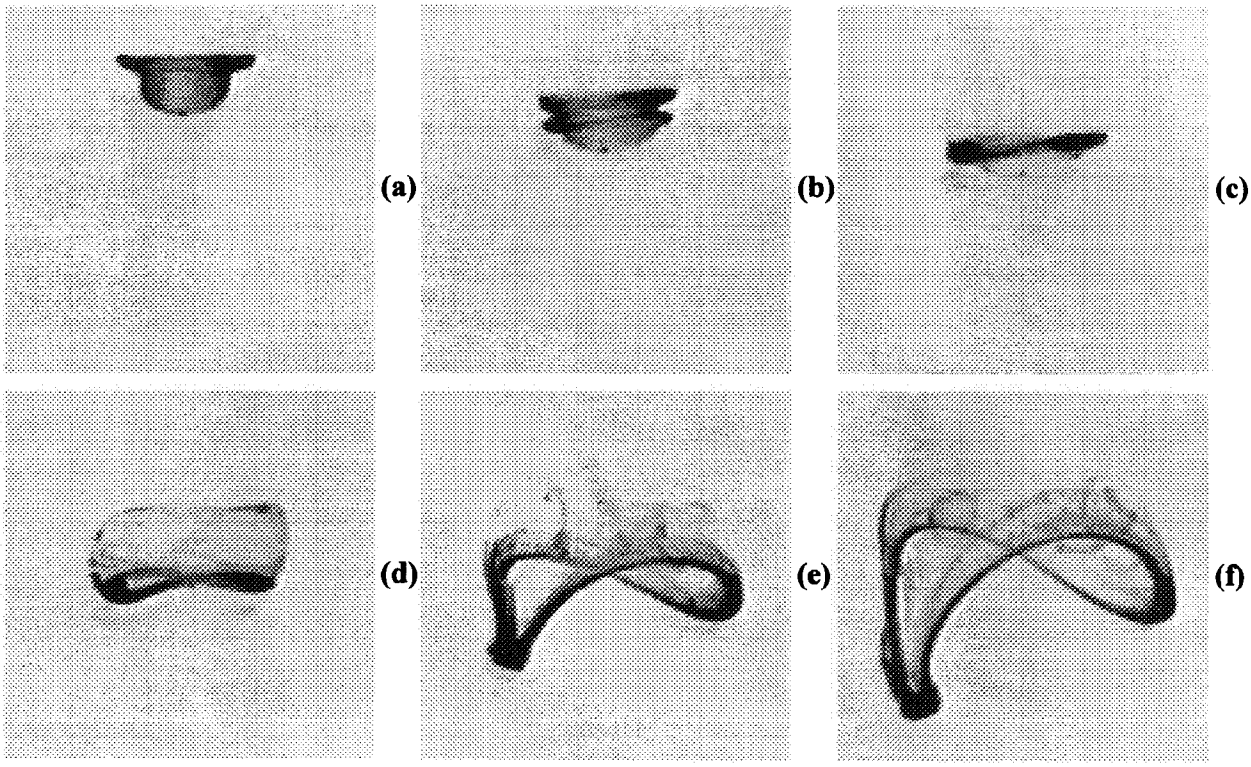

Fig. 8. Evolution of a zero-surface tension particle illustrating the viscous bag breakup regime with initial conditions of VR=250 and Re=410. The corresponding times are (a) 0.3, (b) 0.444, (c) 0.536, (d) 0.719, (e) 1.152, and (f) 1.332 seconds after free surface impact.

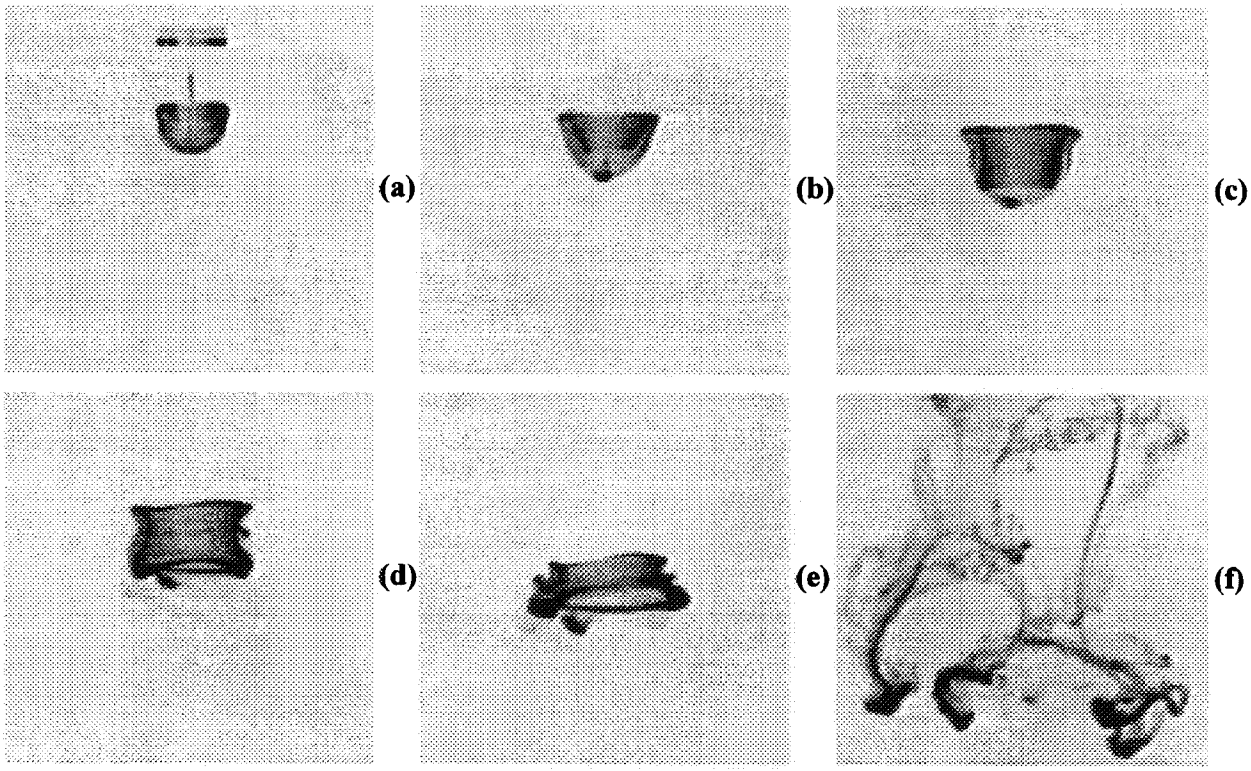

Fig. 9. Evolution of a zero-surface tension particle illustrating the viscous bag multi-mode sub-regime with initial conditions of VR=110 and Re=330. The corresponding times are (a) 0.056, (b) 0.168, (c) 0.312, (d) 0.4, (e) 0.484, and (f) 1.604 seconds after free surface impact.

the moment of impact in response to the step change in shear stresses at the particle boundary. After only 50 ms, the recirculation region was stable and freely rotating. As more fluid was sheared from the leading edge of the droplet and deposited into the recirculation region, the bag shaped body of the droplet rapidly thinned. However, before the bag structure was completely destroyed, the vortex ring at the periphery of the particle became unstable and began to divide into four symmetric quadrants. Each of these four sections of the original vortex ring would then proceed to form another vortex ring as shown in Figure 10(e). The four new vortex structures were still connected to one another through ligaments comprised of the original vortex ring. They were very unstable and they began to split in manner identical to the original vortex ring. The result of this cascading effect was a collection of small scale vortice structures interconnected by a network of ligaments that were comprised of the parent vortex rings' mass. Figure 10(f) is a typical example of the final shape of the particle mass for this mode. The axial view of particle evolution in the bag-vortex ring sub-regime, as shown in Figure 11, clearly illustrates the degree of symmetry by which the vortex structures cascade. This suggests that perhaps the nature of the instabilities could be identified through a linear stability analysis. Furthermore, the particle in Figure 11 shows the existence of a distinct second recirculation ring that occurred for VR less than 20.

Shear-Driven Vortex Regime

The final primary deformation and breakup mode identified was the shear-driven vortex regime. This regime was characterized by the generation of a vortex ring upon impact with the free surface. There has been a great deal of work done on understanding this phenomenon by Peck and Sigurdson[15,17] and the references contained therein. Generally, the small scale characteristics of the vortex rings change a great deal with both the fluid property values and the oscillation phase of the droplet prior to impact.[17] However, the primary vortex ring that was generated in response to the shear forces at the droplet boundary was always the dominant large scale structure in this regime. It is the large scale structure that is more important in terms of droplet deformation and breakup for fuel combustion because the majority of the particle mass is contained within the large scale elements. Therefore, the fine details of the vortex rings such as the separate hairpin vortices generated at impact[15] will merely be noted, and they will not be discussed in any great depth.

A typical example of a stable vortex ring is given in Figure 12 for a particle with a VR of 35 and a Re of 1,100. This is from data that is not included in Figure 3, however, the shear-driven vortex mode can be extrapolated to increased Reynolds numbers up to a value of 1,200 (the maximum Re investigated in the current study). At the moment the particle impacted the free surface, the majority of the vorticity created was concentrated in a torroidal region oriented perpendicular to the droplet's axis of travel. This vortex ring was seen to be laminar for the first 100 ms of the particle life time, with the transition occurring at approximately 150 ms. At a time of approximately 400 ms, the vortex ring restabilized as seen in Figure 12(f). The vortex remained stable until a time of one second, at which point it again became turbulent. The turbulent ring would then continue to convect through the ambient fluid for times as great as three seconds before completely dissipating.

Figure 13 illustrates the evolution of a particle with a Re of 390 and a VR of 10 from an axial view. The resulting vortex was laminar up to 500 ms after free surface impact, at which point the transition to turbulence began. However, the turbulent vortex ring was still well defined at a time of 1.3 seconds and beyond. While both of the rings shown in Figures 12 and 13 were initially laminar, the occurrence of initially laminar and initially turbulent vortex rings was quite random . for Reynolds numbers less than 400. This was most likely due to the influence of the droplet oscillation phase prior to impact, as this was noted by Peck and Sigurdson[17] to have a significant effect on the characteristics of the vortex. The oscillation phase of the droplet is very sensitive to the fluid properties and the height of the droplet free fall through the air. Since the fluid properties of the droplets were constantly altered to achieve different VR and Re values, the droplet shape at impact necessarily passed from vertically oblate to vertically prolate and every shape in between

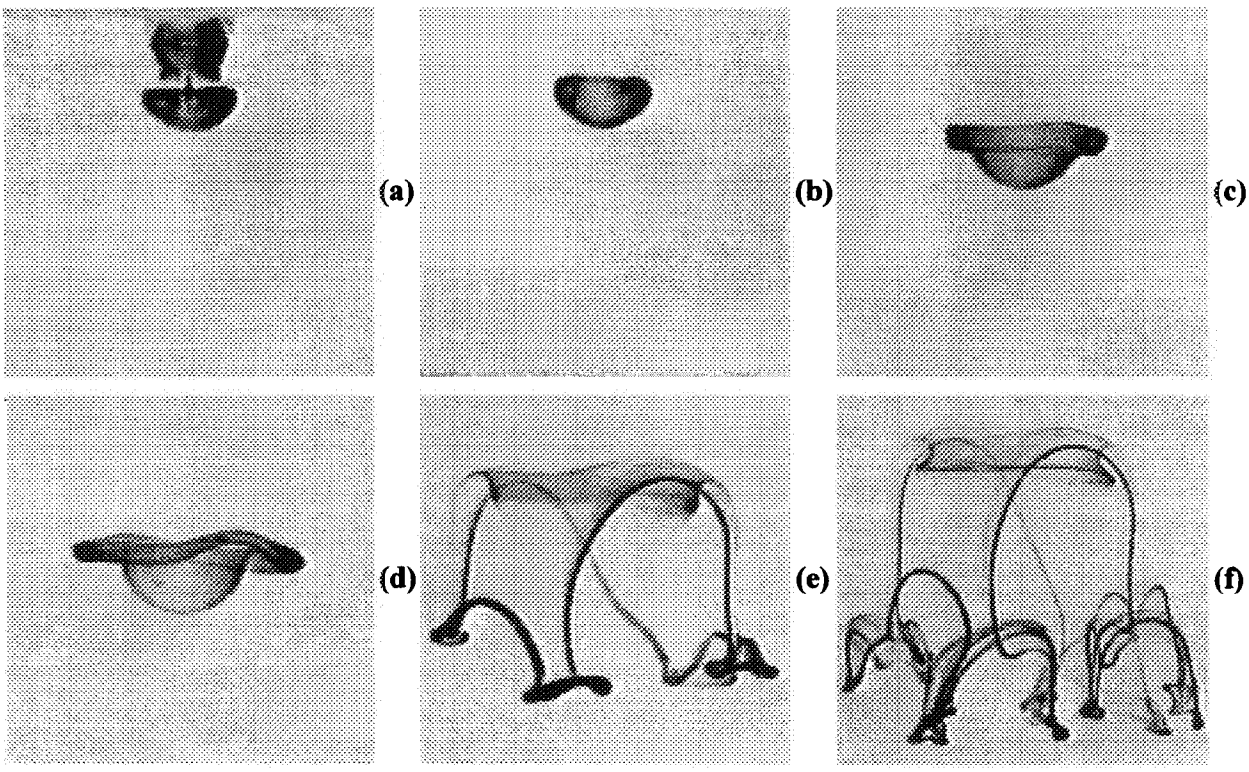

Fig. 10. Evolution of a zero-surface tension particle illustrating the bag-vortex ring sub-regime of the multi-mode breakup category with initial conditions of VR=34 and Re=140. The corresponding times are (a) 0.018, (b) 0.052, (c) 0.152, (d) 0.274, (e) 0.858, and (f) 1.534 seconds after free surface impact.

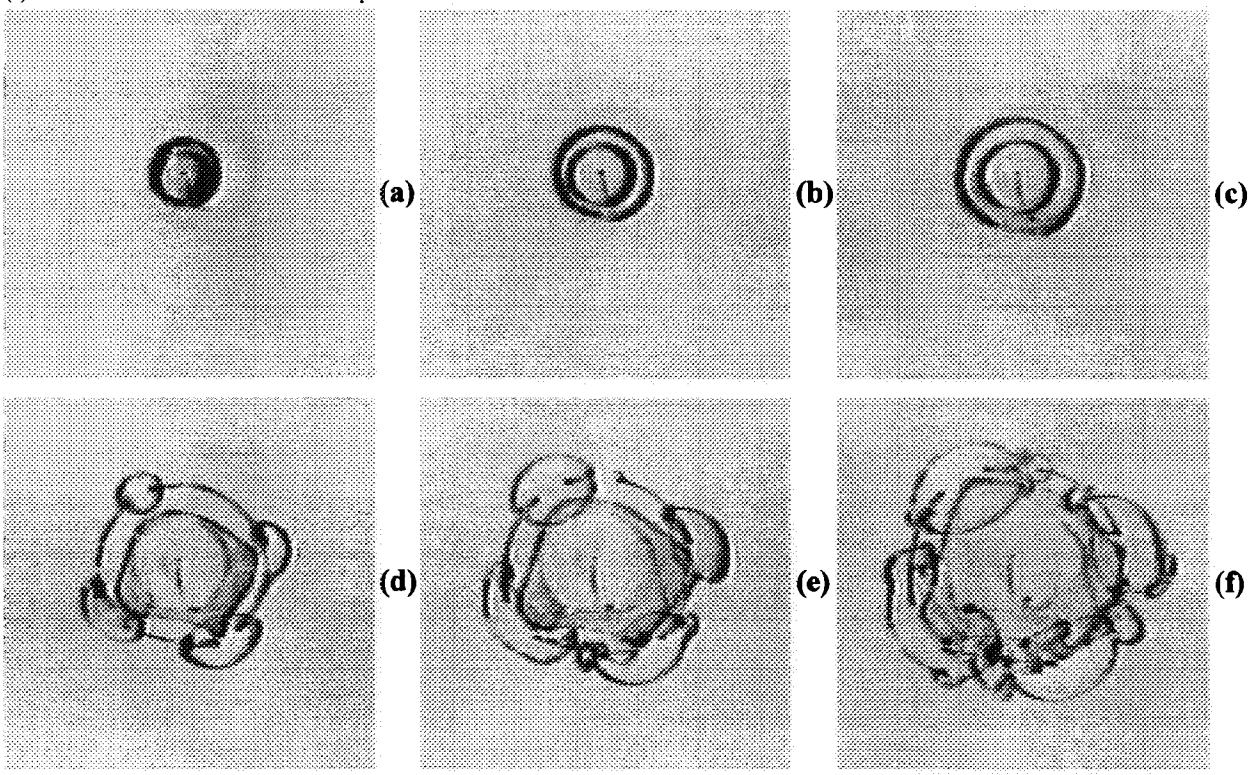

Fig. 11. Evolution of a zero-surface tension particle illustrating the bag-vortex ring sub-regime of the multi-mode breakup category with initial conditions of VR=15 and Re=100. The corresponding times are (a) 0.174, (b) 0.278, (c) 0.446, (d) 0.906, (e) 1.182, and (f) 1.630 seconds after free surface impact.

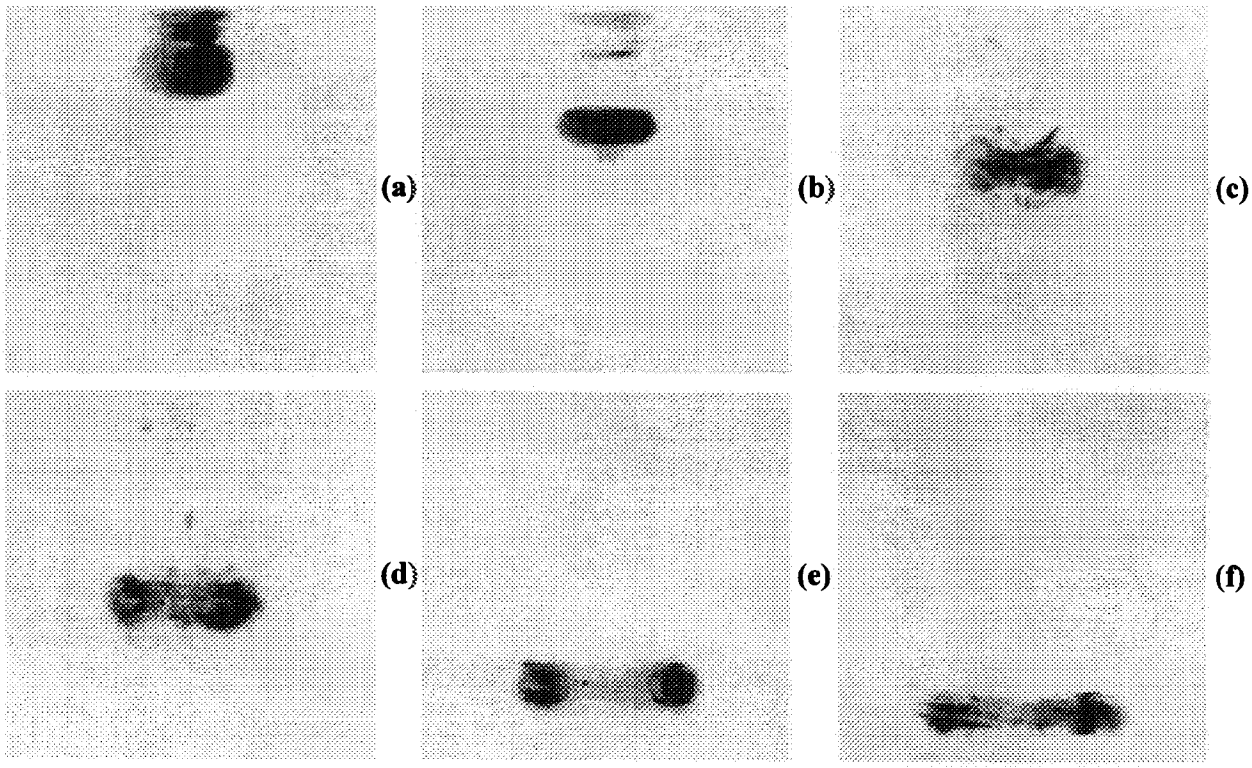

Fig. 12. Evolution of a zero-surface tension particle illustrating the shear-driven vortex breakup regime with initial conditions of VR=35 and Re=1,100. The corresponding times are (a) 0.02, (b) 0.036, (c) 0.176, (d) 0.348, (e) 0.544, and (f) 1.064 seconds after free surface impact.

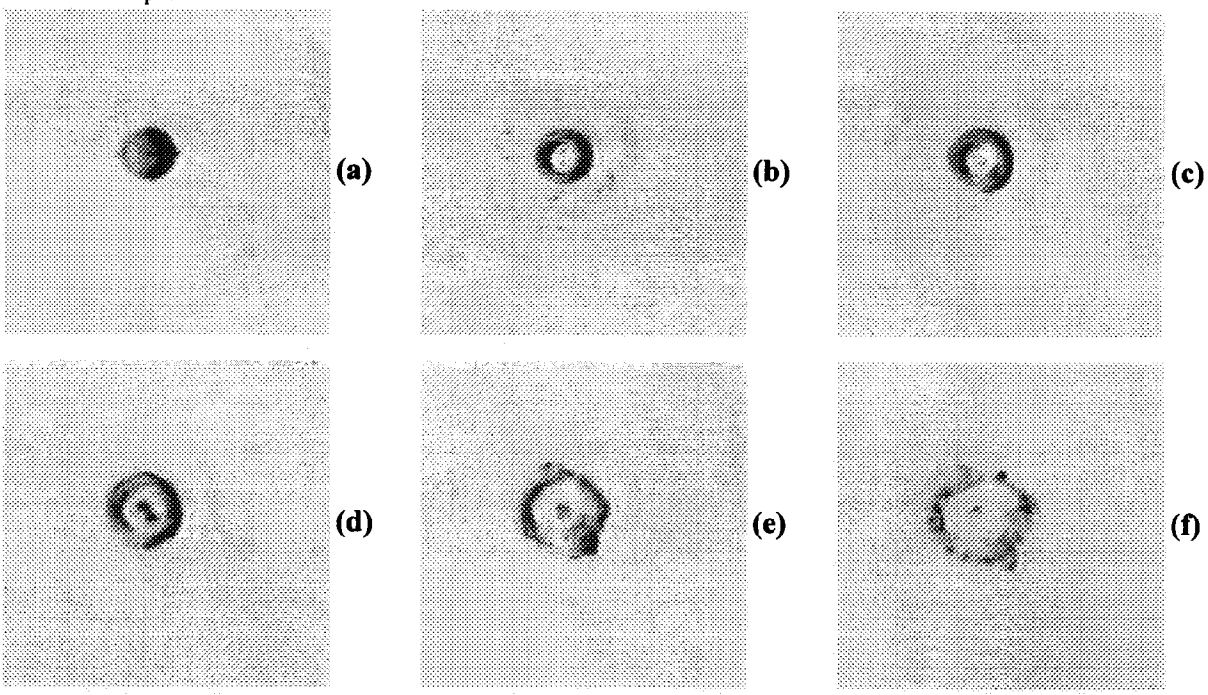

Fig. 13. Axial view of the evolution of a zero-surface tension particle illustrating the shear-driven vortex breakup regime with initial conditions of VR=10 and Re=390. The corresponding times are (a) 0.01, (b) 0.246, (c) 0.37, (d) 0.51, (e) 0.75 and (f) 0.986 seconds after free surface impact.

during course of the experiments. However, because the laminar vortex rings eventually became turbulent as the vortex major axis expanded, the final distribution of mass was very similar in both the laminar and turbulent cases.

One aspect of the experiments that appeared to be a limiting factor in the applicability of the results to other droplets with similar VR's and Re's was the effect of the free surface recoil dynamics. However, for the case of a 1-octanol droplet falling in a pentane ambient fluid for a VR of 20 to 40 and Re from 700 to 800, an interesting free surface anomaly occurred that provided an opportunity to observe the vortex generation process without the influence of the free surface impact crater. This anomaly is shown in Figure 14. When the droplet impacted the free surface, the buffer layer of air between the droplet and the ambient fluid remained in the crater without being displaced by the droplet. As the droplet passed through the free surface, the impact crater would pinch off and trap the buffer layer of air with the 1-octanol droplet. Because surface tension exists between the air layer and the pentane, and the air layer and the 1-octanol droplet, the air was pulled into a sphere with the 1-octanol forming a sphere inside of the air bubble, as shown in Figure 14(b). The 1-octanol droplet, enclosed in the air bubble, would then travel through the ambient fluid to a distance 30 to 40 droplet diameters beyond the free surface in a spherical state. At this location, the buoyancy forces would overcome the surface tension forces holding the air bubble around the 1-octanol droplet, thus, the bubble would burst and travel back up the test section. As shown in Figure 14(c), there was a rapid expansion of the 1-octanol droplet's boundary as it came into contact with the pentane. At this point there was a sudden jump in the shear stresses at the particle boundary due to the discontinuous velocity induced by suddenly being introduced into the pentane with a net downward velocity. As a result, the fluid at the interface was pulled upwards and the particle momentarily developed the bag shape shown in Figure 14(f). At a time approximately 32 ms after the bubble released from the 1-octanol droplet (Figure 14(g)), a developing recirculation region was clearly visible at the droplet leading edge. This recirculation region developed into a stable, laminar ring of azimuthally aligned vorticity similar in nature to those produced directly through impact with the free surface. Thus, it is most likely the step change in shear stresses at the particle interface that is the dominant factor in generating the vortex rings, and not the recoil dynamics of the free surface.

As the viscosity ratio was reduced below a value of unity, the resulting vortex structures were completely turbulent and the secondary vortice structures were much more distinct. Figure 15 illustrates the typical evolution of a particle with a VR of 0.38 and a Re of 250. At 16 ms after free surface impact, there were two distinct regions of vorticity evolving in the particle. One of the regions was located at the particle leading edge, and one was situated slightly aft of the leading edge. The cause of the two distinct regions is most likely a result of the magnitude of the vorticity generated. The greatest amount of shear at the particle interface will initially occur at the point of surface curvature that has a unit vector normal to the direction of the flow. Due to the low VR, the amount of energy transferred to vorticity within the droplet will be much larger than the previous cases examined. This causes the high vorticity particle fluid aft of the leading edge to "pinch" off from the lower vorticity region of the stagnation point fluid. At 76 ms, the aft recirculation region begins to overtake the lower recirculation region. By 200 ms, the two zones have combined to form one primary torus of highly turbulent, high vorticity fluid. In addition, Figure 15 lends strong support to the vortex skeletal structure proposed by Sigurdson and Peck,[15] and it suggests that the structure is more general than the limited cases they have investigated.

Figure 16 provides an axial view of the same vortex structure as that of Figure 15. There was remarkable similarity between the manner in which the unstable, turbulent vortex ring of Figure 15 and 16 broke up in comparison with the multi-mode bag-vortex ring particle of Figures 10 and 11. Furthermore, the large, faint ring that appears to encompass the droplet in the axial view of Figure 16 was actually a pair of rotating vortex rings located at the free surface. These structures complete the validation of the vortex skeletal structure that Peck and Sigurdson[15] have so carefully described.

Figure 17 is a plot of the normalized distance to the onset of primary breakup versus the

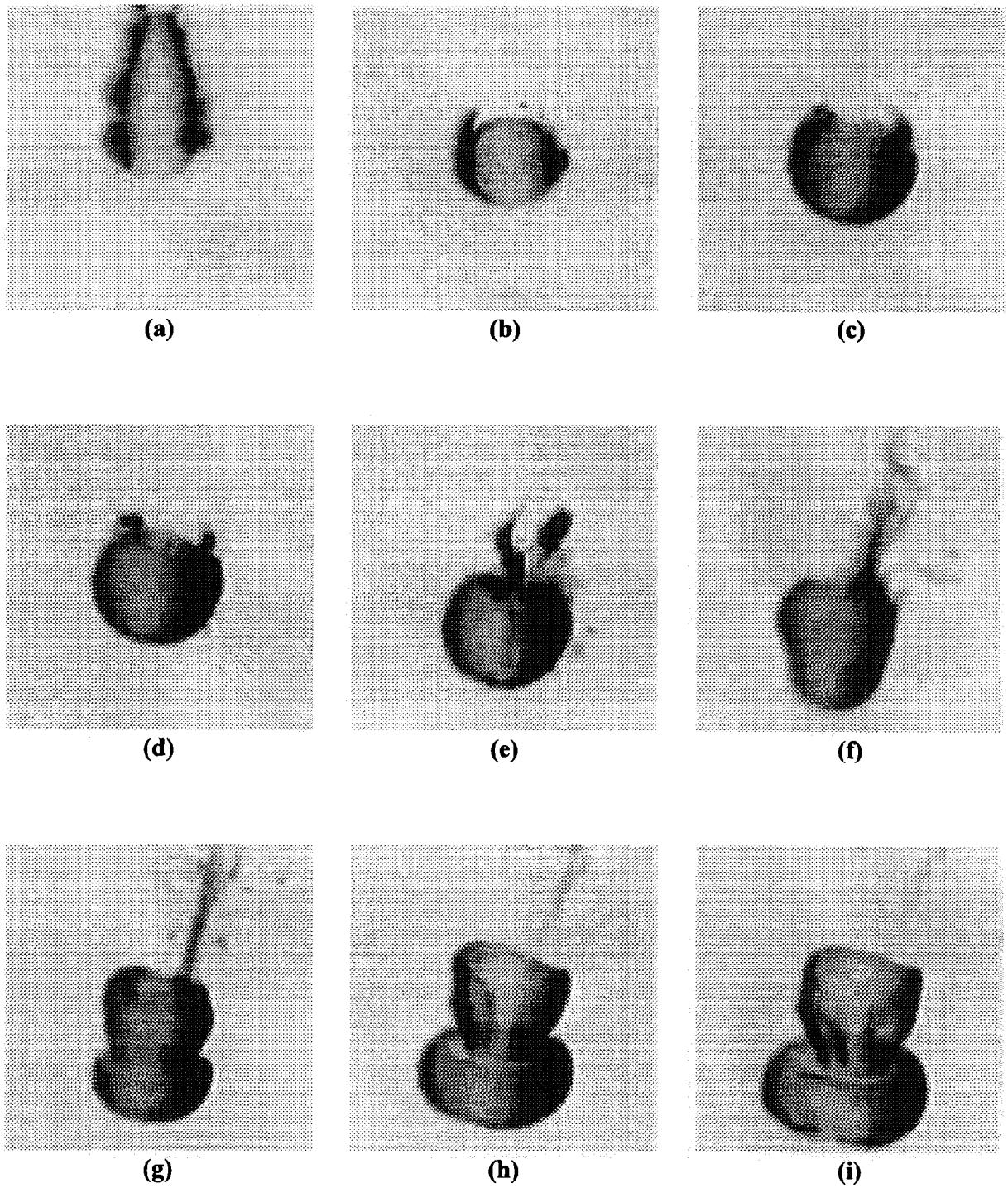

Fig. 14. Evolution of a zero-surface tension particle with initial conditions of VR=20 and Re=750. It illustrates the bubble encapsulation phenomenon leading to a shear-driven vortex ring. The corresponding times of the images relative to the moment of droplet impact with the free surface are (a) 5 ms, (b) 219 ms, (c) 272 ms, (d) 273 ms, (e) 278 ms, (f) 294 ms, (g) 310 ms, (h) 336 ms, and (i) 346 ms.

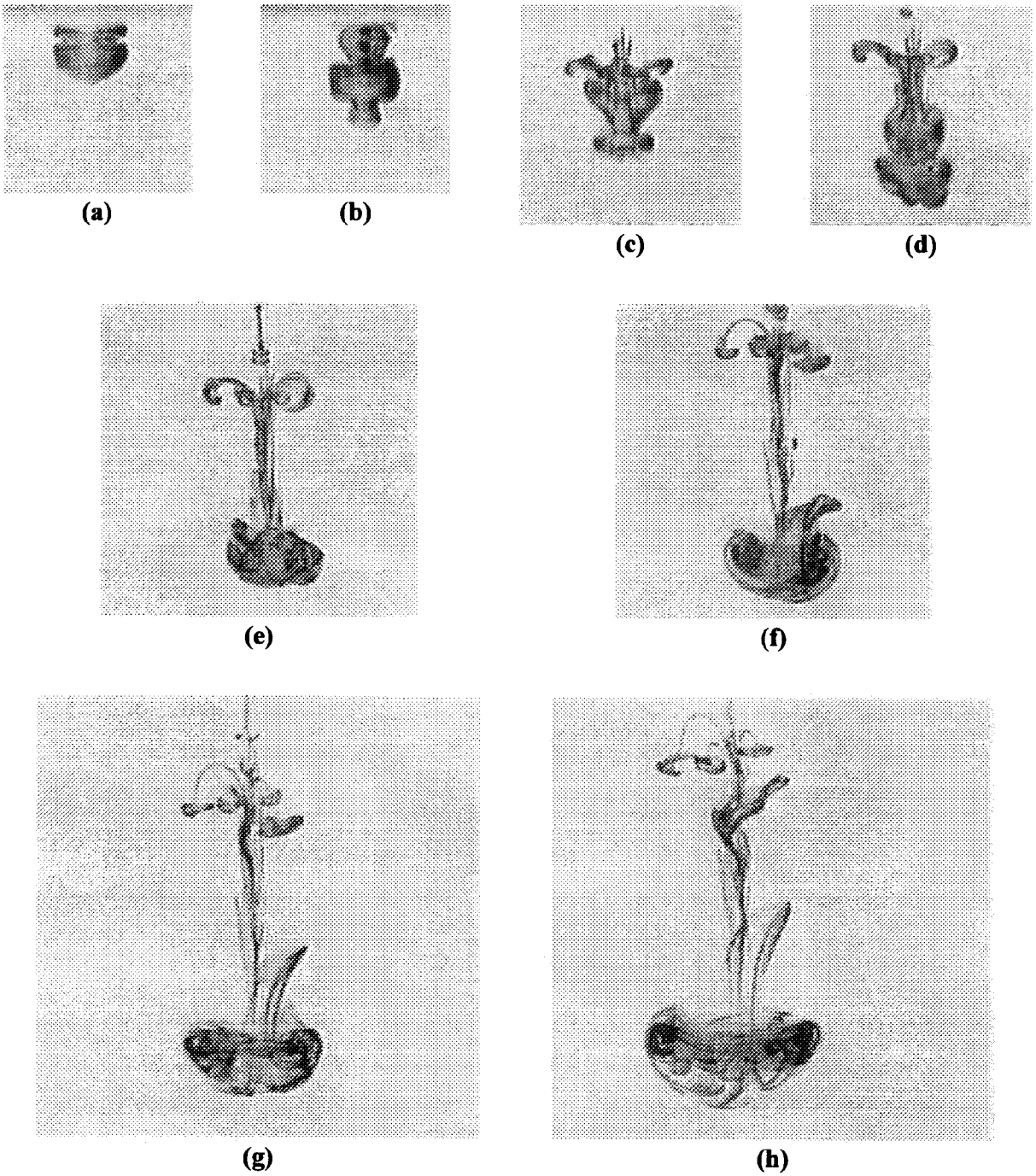

Fig. 15. The evolution of a zero-surface tension particle with initial conditions of VR=0.38 and Re=250. It illustrates the shear-driven vortex regime. The corresponding times are (a) 0.008, (b) 0.016, (c) 0.044, (d) 0.076, (e) 0.12, (f) 0.208, (g) 0.268, and (h) 0.48 seconds after free surface impact.

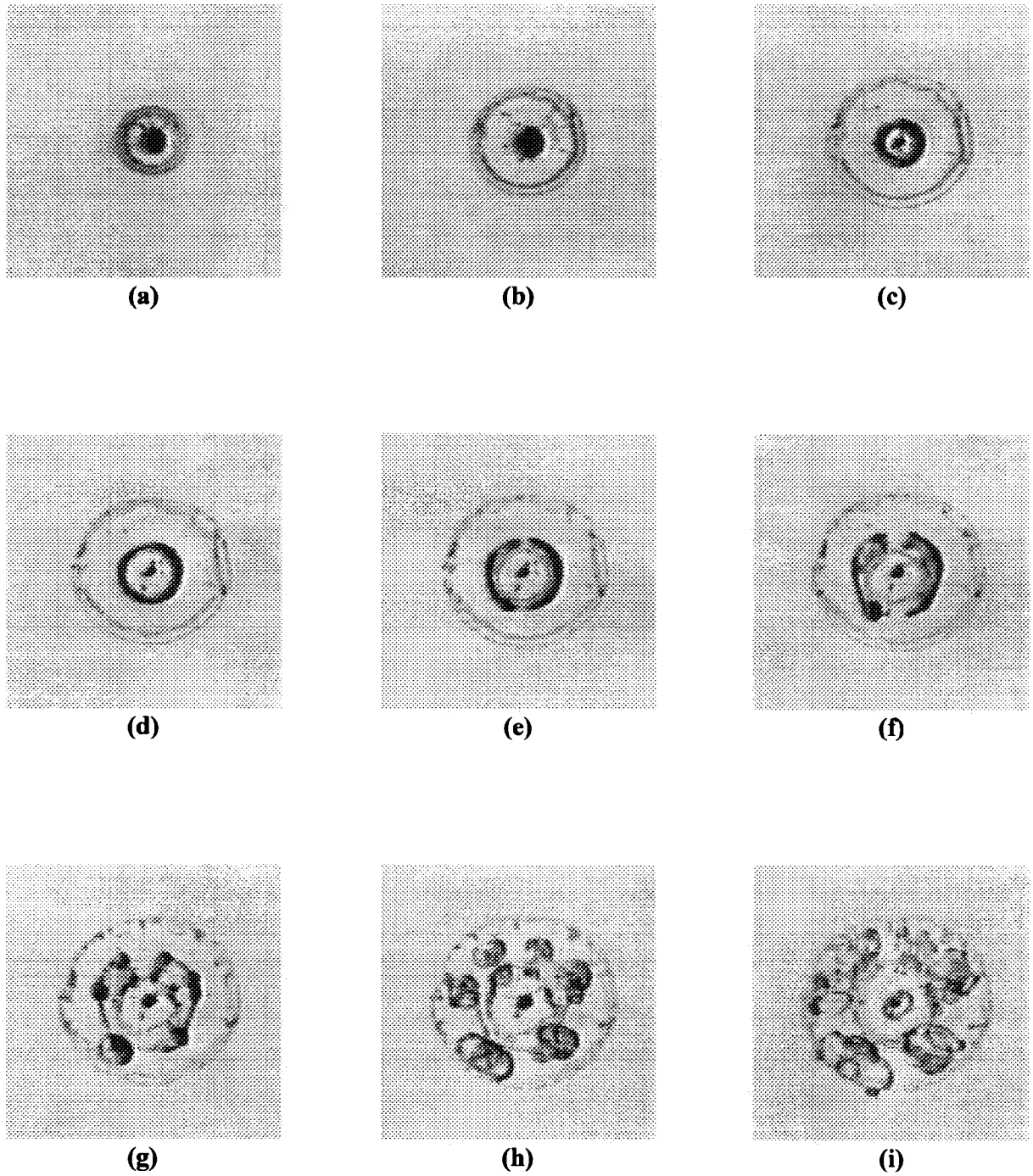

Fig. 16. Axial view of the evolution of a zero-surface tension particle with initial conditions of VR=0.4 and Re=250. The corresponding times are (a) 0.056, (b) 0.096, (c) 0.18, (d) 0.272, (e) 0.34, (f) 0.424, (g) 0.56, (h) 0.79, and (i) 0.952 seconds after free surface impact.

viscosity ratio for the shear-driven vortex regime. As in the case of the viscous globule data, the distance to primary breakup decreases with the viscosity ratio. As the viscosity ratio is reduced, the vorticity induced within the droplet by the shear stresses at the boundary is intensified as a result of the lower internal particle viscous forces. Thus, the resulting vortex becomes unstable more quickly as the viscosity ratio is reduced, and it therefore breaks up at a shorter distance from the free surface. Consequently, the vortex ring has less time to expand and the major axis (the axis normal to the direction of travel) at the time of breakup was steadily reduced with the viscosity ratio. This is reflected in Figure 18, which is a plot of the major axis normalized by the initial particle diameter versus the viscosity ratio.

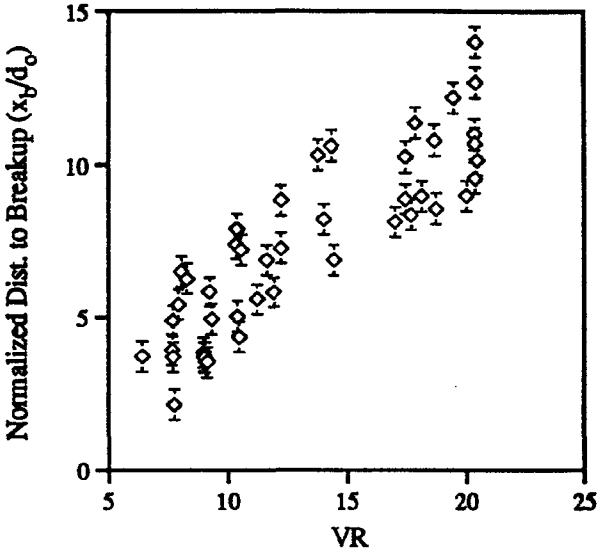

Fig. 17. Normalized distance to the onset of primary breakup as a function of the viscosity ratio for the shear-driven vortex regime.

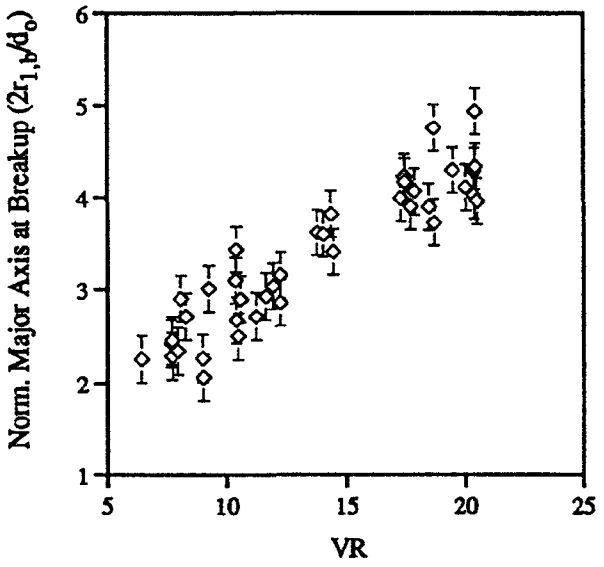

Fig. 18. Normalized major particle axis at the onset of primary breakup as a function of the viscosity ratio for the shear-driven vortex regime.

Discussion

Comparison of Results

As stated earlier, virtually no experimental data detailing the deformation and breakup of a transcritical droplet is available to compare the current results with. However, a numerical study conducted by Lee et al.[2] on the deformation of a supercritical droplet does provide a basis for comparison. The model used in the numerical study assumed that the droplet was heated to a supercritical temperature prior to injection into the ambient environment. Furthermore, a Schmidt number of unity and constant property assumptions were incorporated into the analysis to as simplifying assumptions. In the numerical study, Reynolds numbers of 50 and 200 were examined. The particle deformations observed from the numerical model for the Re of 200 case were nearly identical to the bag multi-mode sub-regime represented in Figure 9, which has a Re of 330. Other cases in the sub-regime represented by Figure 9 with Reynolds numbers of approximately 200 were compared with the results and again the similarities were striking. Within the regime that similarity was observed, experimental Reynolds numbers of 50 were not available for comparison. However, based on the observed trends in the bag multi-mode regime, it is likely that at a reduced Re of 50, the miscible fluid analog would again be comparable with the numerical model of Lee et al.[2]

The Effect of Dynamic Interfacial Tension

While it was reasonable to categorize the primary breakup modes of a zero-surface tension particle in terms of the viscous and inertial forces, an additional force, the dynamic interfacial tension, does have an impact on the particle

characteristics. Interfacial tension is a result of the discontinuous chemical potentials between two initially separate and different fluid components that are brought into contact with each other.[18] This force exists even between two miscible fluids; however, it is transient and it decreases with time as the fluids dissolve into each other along the interface. This parameter has been measured between two miscible fluids and it was observed to decrease rapidly even in the absence of convective mixing.[18] Furthermore, the magnitude of the interfacial tension is approximately 20 to 100 times smaller than typical surface tension values encountered when the constituent fluids are present in air. Despite the relatively small magnitude of the interfacial tension, Kojima et al.[19] found that the spreading rates of a viscous drop could only be accurately represented numerically by including the interfacial tension in the governing equations. In the current work, the existence of the spanning membrane in both the membrane rupture mode and the bag-vortex ring sub-regime suggests that interfacial tension does play a role in the characteristics of the evolving particles. Due to the limited interfacial tension data available, it was not incorporated into the classification of the breakup regimes. However, the magnitude of the decrease of the interfacial tension with time will depend on the mutual diffusion coefficient of the two fluids. The behavior of the diffusion coefficient with temperature is analogous to the behavior of the viscosity ratio; thus, the relative effect of the interfacial tension is indirectly represented by the viscosity ratio.

Summary and Conclusions

The miscible fluid analog is a promising tool in the investigation of zero-surface tension droplet deformation and breakup. The utility of the analog is evident when compared with the results from the numerical study of supercritical droplet deformation that was performed by Lee, Fernandez-Pello, Corcos, and Oppenheim.[2] The particle dynamics observed from the analog were similar to the results from the numerical model in regards to the qualitative nature of particle deformation.

Thus, the breakup regimes of the miscible fluid analog were categorized over a wide range of Reynolds numbers and viscosity ratios. The following four primary breakup regimes were identified as a function of the viscosity ratio and the Reynolds number: viscous globule, viscous bag, multi-mode, and shear-driven vortex. The distance and time to the onset of primary particle breakup decreased with the viscosity ratio. Furthermore, the expansion of the particles' major axis at the onset of primary breakup in the shear-driven vortex regime also decreased with the viscosity ratio. In addition to the viscous and inertial forces, dynamic interfacial tension was recognized as a contributing force in the evolution of a zero-surface tension particle.

As a result of the large particle deformations observed in the miscible fluid analog, convective mixing of the ambient fluid into the particle fluid will be significant. In earlier transcritical droplet studies, the dissolution of ambient gasses into the droplet from diffusion was observed to have a tremendous impact on the particle vaporization and combustion.[3-5,11] Thus, the enhanced mixing that could occur due to the convective effects that are typical in realistic combustion chambers could be a crucial addition to the study of transcritical droplets. Further study of the miscible fluid analog will be extremely valuable as means of determining the extend of ambient fluid mixing in the particle.

Acknowledgments

This work was conducted under Research and Development Laboratory's Summer Faculty Extension Grant No. 96-0831 from the Air Force Office of Scientific Research.

References

1. Stanley, H.E., *Introduction to Phase Transitions and Critical Phenomena*, Oxford University Press, Oxford, 1971.

2. Lee, H.S., Fernandez-Pello, A.C., Corcos, G.M., and Oppenheim, A.K., "A Mixing and Deformation Mechanism for a Supercritical Fuel Droplet," *Combust. and Flame*, Vol. 81, pp. 50-58, 1990.

3. Hsieh, K.C., Shuen, J.S., and Yang, V., "Droplet Vaporization In High Pressure Environments I: Near Critical Conditions," *Combust. Sci. and Tech.*, Vol. 76, pp. 111-132, 1991.

4. Canada, G.S. and Faeth, G.M., "Fuel Droplet Burning Rates At High Pressures," *Fourteenth Symposium*

(International) on Combustion, The Combustion Institute, pp. 1345-54, 1973.

5. Faeth, G.M., Dominicis, D.P., Tulpinsky, J.F., and Olson, D.R., "Supercritical Bipropellant Droplet Combustion," *Twelth Symposium (International) on Combustion*, The Combustion Institute, pp. 9-18, 1969.

6. Kadota, T. and Hiroyasu, H., "Combustion of a Fuel Droplet in Supercritical Gaseous Environments," Eighteenth Symposium (International) on Combustion, The Combustion Institute, pp. 275-82, 1981.

7. Nakanishi, R., Kobayashi, H., Kato, S., and Niioka, T., "Ignition Experiment of a Fuel Droplet in High-Pressure High Temperature Ambient," *Twenty-Fifth Symposium (International) on Combustion*, The Combustion Institute, pp. 447-53, 1994.

8. Anderson, T.J., Woodward, R.D., and Winter, M., "Oxygen Concentration Measurements in a High Pressure Environment Using Raman Imaging," AIAA Paper 95-0140, 1995.

9. Spalding, D.B., "Theory of Particle Combustion at High Pressures," *ARS Journal*, Vol. 28, pp. 828-835, 1959.

10. Bruzustowski, T.A., "Chemical and Physical Limits on Vapor-Phase Diffusion Flames of Droplets," The Canadian Journal of Chemical Engineering, Vol. 43, pp. 30-35, 1965.

11. Shuen, J.S., Yang, V., and Hsiao, C.C., "Combustion of Liquid-Fuel Droplets In Supercritical Conditions," *Combustion and Flame*, Vol. 89, pp. 299-319, 1992.

12. Deng, Z.T., Litchford, R., and Jeng, S.M., "Two-Dimensional Simulations of Droplet Evaporization and Deformation at High Pressures," AIAA Paper 92-3122, 1992.

13. Probstein, R.F., *Physiochemical Hydrodynamics*, Butterworths, London, 1989.

14. Talley, D.G., Woodward, R.D., and Pan, J.C., "Supercritical Droplet Behavior," AFOSR Task 2308AP, 1995.

15. Peck, B., and Sigurdson, L., "The Vortex Ring Velocity Resulting From an Impacting Water Drop," *Experiments in Fluids*, Vol. 18, pp. 351-357, 1995.

16. Hsiang, L.P., and Faeth, G.M., "Near Limit Drop Deformation and Secondary Breakup," *International Journal of Multiphase Flow*, Vol. 5, pp. 721-35, 1993.

17. Peck, B., and Sigurdson, L., "The Three-Dimensional Vortex Structure of an Impacting Water Drop," *Physics of Fluids*, Vol. 6, pp. 564-76, 1994.

18. Smith, P.G., M. Van de Ven, T.G., and Mason, S.G., "The Transient Interfacial Tension Between Two Miscible Fluids," *Journal of Colloid and Interface Science*, Vol. 80, pp. 302-3, 1981.

19. Kojima, M., Hinch, E.J., and Acrivos, A., "The Formation and Expansion of a Toroidal Drop Moving in a Viscous Fluid," *Physics of Fluids*, Vol. 27, pp. 19-32, 1984.

This Page Intentionally Left Blank

APPENDIX D

“Raman Imaging of Transcritical Cryogenic Propellants”

AIAA Meeting Papers on Disc, January 1996
A9618429, AF Task 2308AP, AIAA Paper 96-0468

Raman imaging of transcritical cryogenic propellants

Roger D. Woodward
USAF, Phillips Lab., Edwards AFB, CA

Douglas G. Talley
USAF, Phillips Lab., Edwards AFB, CA

AIAA 34th Aerospace Sciences Meeting and Exhibit, Reno, NV Jan 15-18, 1996

The objective of this research is to explore the atomization and vaporization behavior of cryogenic droplets, jets, and sprays that are injected at a supercritical pressure but subcritical temperature into an environment that is at supercritical pressure and temperature. Shadowgraph imaging of liquid nitrogen jets injected into nitrogen and nitrogen/helium mixtures at pressures below, at, and well above the critical pressure of nitrogen demonstrates the profound effect that transcritical vaporization has on jet structure, atomization, and mixing. Also demonstrated is the profound effect that mixture properties can have on the would-be transcritical interface. Raman imaging diagnostics were evaluated and look promising for use with transcritical jets. The diagnostic was able to distinguish the structural differences between transcritical nitrogen jets injected into helium or nitrogen. The results indicate that Raman imaging will be useful for evaluating vaporization and mixing rates of jets at various conditions. (Author)

RAMAN IMAGING OF TRANSCRITICAL CRYOGENIC PROPELLANTS

R. D. Woodward* and D. G. Talley†
USAF Phillips Laboratory
Edwards AFB, CA

ABSTRACT

The objective of this research is to explore the atomization and vaporization behavior of cryogenic droplets, jets, and sprays that are injected at a supercritical pressure but subcritical temperature into an environment that is at supercritical pressure and temperature. Lessons learned from developmental experiments have been incorporated into the design of a new high-pressure chamber that is optimized for this study. In preliminary efforts, using an existing pressure vessel not optimized for this purpose, shadowgraph and Raman imaging experiments of transcritical nitrogen jets have been conducted. Shadowgraph imaging of liquid nitrogen jets injected into nitrogen and nitrogen/helium mixtures at pressures below, at, and well above the critical pressure of nitrogen demonstrate the profound effect that transcritical vaporization has on jet structure, atomization, and mixing. Also demonstrated is the profound effect that mixture properties can have on the would-be transcritical interface. Raman imaging diagnostics were evaluated and look promising for use with transcritical jets. The diagnostic was able to distinguish the structural differences between transcritical nitrogen jets injected into helium or nitrogen. The results indicate that Raman imaging will be useful to evaluate vaporization and mixing rates of jets at various conditions.

INTRODUCTION

With the current down-sizing trend in the global aerospace industry, funds for new propulsion systems have to be spent wisely and efficiently. Thus, systems must be designed using as accurate performance predictions as possible to eliminate costly "trial-and-error" testing. This requires a good understanding of the fundamental processes to enable inexpensive and accurate predictions of system behavior. For chemical propulsion, much research benefit can be obtained by studying the significant unknowns associated with propellant injection and combustion. The unknowns are particularly large in high pressure systems which exceed the critical pressure of the propellants. In many cases, such as in high pressure rocket engines, the fuel or oxidant is injected at supercritical pressure but initially at a subcritical temperature. The propellant then undergoes a transition to a supercritical state as it is heated and burned in the combustion chamber, the so-called transcritical process. Compared with the analogous subcritical case, transcritical and supercritical injection and combustion remain poorly understood.

The authors have undertaken a program to investigate the transcritical injection, breakup, vaporization/gasification, and mixing of liquid rocket propellants. The propellants of primary interest are liquid oxygen (LOX) and hydrogen. In the following, we discuss our efforts to study transcritical droplet and jet flows of LOX (or liquid nitrogen (LN_2)) under non-reacting conditions, using helium as a hydrogen simulant.

Transcritical Droplet Research

Droplets are the simplest and most easily studied of spray systems, and hence, a great deal of research has been conducted and a number of reviews have been published in the area of droplet breakup, vaporization, and combustion.[1-3] Although neglecting the complexities of real sprays, many of the interfacial transport and breakup mechanisms applicable to them can be understood from single droplets. Despite the voluminous work carried out to understand droplet combustion processes, transcritical droplet processes remain a mystery due to poor understanding of thermodynamic and transport properties of mixtures under those conditions and the significant difficulties in conducting experiments at such conditions. It is well known that there are a number of differences from the subcritical case that need to be addressed. Near the critical point, gas/liquid density ratios are of the same order, so the quasi steady gas phase assumption commonly employed in subcritical studies is no longer valid. The equilibrium "wet bulb" condition may also not exist. Thus, transcritical droplet vaporization/combustion is a fully unsteady phenomenon. The computation of properties becomes significantly more

*Mechanical Engineer, Propulsion Sciences Division, Member AIAA
†Research Physical Scientist, Propulsion Sciences Division, Member AIAA

complicated due to departures from ideal behavior and property anomalies that are known to exist near the critical point. Also, properties such as diffusion coefficients become functions of pressure as well as temperature, and the solubility of the gas phase in the liquid phase increases significantly at high pressures. The latter effect can mean that the effective critical pressure of the soluble mixture can be several times the critical pressure of the pure phase. As the critical condition is approached, the surface tension vanishes, blurring the distinction between gas and liquid and potentially leading to significantly different droplet deformation and breakup mechanisms which will in turn have a significant effect on subsequent mixing processes.

Past experimental studies of transcritical droplet processes have been mostly limited to global measurements such as the variation of droplet lifetimes and burning times as a function of pressure.[4-7] While useful, these provide an incomplete picture of the transport and breakup mechanisms that can contribute to mixing and the potential to couple with combustion instabilities. On the other hand, the theoretical understanding of transcritical droplet vaporization, combustion, and breakup has advanced significantly in recent years due to the introduction of new models.[8-10] These models focus on obtaining accurate predictions of the thermodynamic and transport properties of mixtures of fluids at high pressures and tracking the critical mixing temperature surface in a fully transient analysis. However, these models remain unverified experimentally. One objective of the research is to provide detailed measurements of transcritical droplet flow fields, including temperature and composition profiles, that can be used to validate these models, as well as to develop semi-empirical correlations for direct use in comprehensive engine design and performance codes.

In a transcritical phenomenology study, Woodward et al.[11] provided preliminary shadowgraph visualizations of transcritical cryogenic droplet flows and discussed the strong effect of mixture properties on the effective critical point for the propellant simulant combinations. A series of experiments were conducted with liquid nitrogen injected into gaseous or supercritical nitrogen, starting with a droplet stream flow at subcritical conditions and then increasing the pressure while approximately maintaining the same low flow rate. At and above the critical pressure of this uni-molecular system, no liquid-like structures were observed. Transition from subcritical behavior appeared to begin at about 60-80% of the critical pressure (enhanced aerodynamic drag effects also played a role here), with dramatic changes to liquid structures exhibited within a few percent of critical pressure. The addition of helium into the slightly supercritical nitrogen system caused liquid nitrogen structures to re-appear due to local composition and temperature conditions. Likewise, it had been observed that LOX droplets could maintain their surface tension and hence a well-defined structure in a supercritical helium environment at a pressure of at least 1.7 times the critical pressure of pure oxygen due to the solubility of the helium into the LOX. Therefore, even higher pressures need to be obtained to study transcritical effects in the LOX/He system.

Transcritical Jets/Sprays

In the far subcritical regime where distinct interfaces between gas and liquid phases exist, injection produces atomizing sprays. Consideration is then given to various primary atomization regimes, secondary breakup regimes, droplet vaporization, group combustion, and droplet/turbulence interactions. Alternately, in the far supercritical regime where distinct phases are not possible, injection is probably more like that of classical turbulent jets. Concern is then given to self-similarity issues, coherent structures, compressibility and Mach number effects, and single phase mixing.

Transcritical atomization probably involves aspects of both kinds of injection. The vanishing of surface tension above the critical pressure could imply jet-like behavior, although large initial temperature and density ratios complicate the classical concept of turbulent jets. Moreover, the critical pressure itself depends on local mixture ratios, and can be several times higher than the critical pressure of the pure constituents. Thus, the critical pressure becomes a dynamic variable, dependent on the mixing. This suggests that "interfaces" might come and go in unexpected ways. Additionally, for local mixtures near the critical point, thermal, mass, and momentum transfer become affected by very singular fluid properties.

Due to experimental difficulties associated with operating at pressure and temperature extremes and simultaneously obtaining optical access, transcritical jets/sprays have been investigated to a very narrow extent. Newman and Brzustowski[12] made one of the earliest attempts to investigate the transcritical injection process using shadowgraph visualizations of small diameter (0.66 mm) CO_2 jets into mixtures of CO_2 and N_2. They varied environment pressure, temperature, and composition and noted occurrences of both spray-like and single-phase-jet-like behavior at near critical

conditions. More recently, Birk et al.[13] have used flash x-ray radiography to investigate, mostly qualitatively, the transcritical breakup and combustion of liquid jets for liquid propellant gun applications. They report that jet core penetration decreases with increasing ambient pressure until a minimum is reached at the critical pressure of the liquid; further increase in pressure results in increased core penetration. Of greatest relevance to rockets, Mayer and Tamura[14] made shadowgraph and Schlieren visualizations of the near injector region of a windowed, subscale rocket engine, which employed a single coaxial injector (LOX jet surrounded by an annular, high-speed, supercritical H_2 flow). Their transcritical injection results at pressures to about two times the critical pressure of O_2 suggest an absence of any spherical droplets in the chamber. Instead, large, fuzzy, globular structures as well as small, thread-like O_2 structures were observed at supercritical chamber pressures. However, some uncertainty existed due to significant optical distortions caused by severe refractive index gradients between the LOX jet and the windows.

High Pressure Diagnostics for Transcritical Processes

As was indicated, most investigations[4-7,11-14] of transcritical propellant processes have involved qualitative visualizations using long-standing conventional techniques. Laser-based diagnostics[15] have long since been developed to measure flow field velocities, temperatures, and species concentrations, but, for the most part, have yet to be proven in high-pressure, multi-phase environments. Most optical diagnostics are developed at ambient laboratory conditions. Thus many difficulties arise that may render a given technique ineffective when an attempt is made to apply it to practical situations. Problems such as unwanted elastic scattering especially from particulates or surfaces, excessive absorption, refractive index gradients, interfering spectral components, collisional quenching of signal, or the inability to gain sufficient optical access often combine to thwart an elegant optical measurement technique. Laser-induced fluorescence (LIF) is a good example of a widely used reacting flow measurement technique that is difficult to quantify at high pressures. The main problem for LIF to overcome is enhanced collisional quenching of the fluorescence signal at elevated pressures, making quantification difficult. Practical measurements with LIF has yet been limited to pressures of about 10 atm.[16] A few laser-based techniques have demonstrated at least a strong potential for success in high-pressure (> 100 atm) environments. Examples of such techniques include, coherent anti-Stokes Raman spectroscopy (CARS),[17] spontaneous Raman scattering,[18] degenerate four wave mixing (DFWM),[19] and Rayleigh-Brillouin spectroscopy.[20]

Of the listed high-pressure diagnostics, Raman scattering is by far the simplest to apply although signal levels are generally weak. Spontaneous Raman scattering refers to the inelastic scattering of light due to photon release from vibrational/rotational transitions in a molecular species. The observed Raman shift is species dependent while being independent of the excitation wavelength. The intensity of spontaneous Raman scattering is linearly dependent on the number density of the species of interest. Hence, signal levels are naturally enhanced as pressure is increased. Raman scattering diagnostics can be applied in point, line, and imaging techniques using simple optical filtering. Spectroscopic detection can be used to simultaneously monitor a number of species. Temperature measurements can be obtained by comparing observed Raman spectra to calculated or calibrated spectra at known temperatures, or in systems at sufficient temperature to yield a measurable anti-Stokes signal (scattered light shifted to higher frequency than excitation), by Stokes/anti-Stokes ratioing. There is no fundamental barrier to the application of Raman scattering diagnostics to the trans- or supercritical regime. By filtering out the stronger elastic scattering, Raman diagnostics can be applied successfully to multi-phase systems.

Application of novel optical diagnostic techniques to the transcritical problem has been evaluated in a collaborative effort with the United Technologies Research Center. As part of this effort, Anderson et al.[21] demonstrated the feasibility of Raman imaging diagnostics for concentration field determination around cryogenic liquid droplets vaporizing in a high pressure environment. Streams of LOX droplets in the size range of 100-300 μm were injected into a helium environment at pressures to approximately 70 atm. The experiment used a piezo-electric droplet generator, developed at the Phillips Lab, which is capable of producing a monodisperse stream of cryogenic droplets at high pressures. The droplet generator is pictured in Fig. 1. To date, the generator has successfully produced monodisperse streams of LN_2 and LOX droplets in an acoustically excited Rayleigh breakup mode at pressures somewhat beyond 70 atm (> 1000 psig). Quantitative measurements of instantaneous (single 10-ns laser shot) O_2 concentration resulting from droplet vaporization demonstrated measurement sensitivity of at least 10 kg-mole/m^3 (4% mole fraction in helium at 69 atm). Vaporized oxygen distributions from Raman imaging of LOX droplet streams into high pressure helium clearly exhibited unsteady, asymmetric

vaporization and strong droplet/wake interactions at those conditions.

The previous studies[11,21] were conducted in simple cylindrical pressure vessels with the Phillips Laboratory high pressure, cryogenic droplet generator adapted to mount on and operate with these chambers. There are two major deficiencies with the pressure vessels used for these experiments. One is the poor optical access which limits the field of view for imaging and limits the solid angle of light collection, a quantity that must be maximized for low signal-to-noise diagnostics such as Raman imaging. In the above experiments, the pressure vessel windows limited the f/# of the optical system to f/4. The other major deficiency is the non-optimized integration of the cryogenic droplet generator to the pressure vessel, resulting in less than ideal droplet production due to heat transfer problems and an inability to tailor the flow field surrounding the droplet. Also, the need for higher operating pressures to fully investigate transcritical phenomena dictated designing a new windowed chamber.

OPTIMIZED EXPERIMENTAL CHAMBER

A custom pressure vessel has been designed specifically for future transcritical vaporization experiments. Valuable lessons learned have been incorporated from the above works[11,21] in terms of transcritical cryogenic droplet generation, expected vaporization and breakup behavior at high pressures for different propellant/simulant compositions, and the application of laser diagnostics, especially Raman imaging, to this system. This chamber, optimized for such experiments, was designed with the following important features:

- operating pressure capability to 137 atm (2,000 psig)
- operating temperature to 473K (with potential steep temperature gradients from 77-473K)
- excellent optical access for imaging and signal collection with two opposed 133.4 mm (5.25") diameter windows (clear aperture of 120.7 mm (4.75") diameter)
- laser beam and sheet access (in and out) to the injection axis through two oblong windows, perpendicular to the large round viewing windows
- narrow-block shape to minimize distance from injection axis to viewing windows and hence minimize distorting effect of refractive index gradients
- highly integrated and modular interface between the droplet generator and the windowed pressure vessel to provide a controlled environment for drop production and injection into the viewing area
- droplet generator height adjustment capability without the necessity for removal of any components
- provisions for mounting high-intensity acoustic drivers
- easy and abundant access to the inside of the pressure vessel through the large windows without removal of any fasteners

A front view of the transcritical cryogenic droplet pressure vessel assembly is shown in Fig. 2(a). At the heart of this view are the large round windows (one on front and one on back). These 133.4 mm (5.25") diameter windows are only 25.4 mm (1") thick because they are made from sapphire (Hemlite) which has excellent strength. A threaded flange holds the window and screws directly into the chamber housing, allowing internal chamber access without the need to remove several bolts. The 120.7 mm (4.75") diameter aperture of these windows is sufficiently large to view the entire cryogenic droplet history even at low pressures. Also, these windows, because of their size and proximity to the injection axis, offer a large signal collection angle such that the system f/# becomes limited now by the collection optics rather than the vessel windows. The size of these windows enable the use of a wide variety of diagnostic techniques that might require bringing in laser beams or viewing with multiple detectors at a variety of angles.

A side view of the pressure vessel assembly is shown in Fig. 2(b). In this view, one is looking into the oblong laser input/output windows that provide a clear aperture of 120.7 mm x 12.7 mm (4.75" x 0.50"). These windows are made from UV-grade quartz. They offer slightly less light absorption than the sapphire windows and are substantially less expensive. This is important since they are operationally more susceptible to laser damage. They are oblong to minimize the distance from the round windows to the droplet stream while still providing laser access to the injection axis for the entire vertical height of the viewing windows.

Perhaps the most significant feature of the transcritical droplet experimental chamber is in the integration of the droplet generator with the pressure vessel. The droplet generator interface housing internal flow field is shown schematically in Fig. 3. The design is optimized for LN_2 or LOX cryogenic droplet production at high pressures using either piezoelectric or a hybrid piezoelectric/aerodynamic droplet generation scheme for the production of freely falling droplets. In our experience, the production of freely falling, truly monodisperse, and truly transcritical droplets is severely limited if heat transfer to the droplet generator tip is not carefully controlled because reduction of the surface tension as the critical condition is approached prevents

distinct droplets from forming. In the present design, this problem is solved by producing the droplets in a coflowing stream of helium prechilled to the same temperature as the droplets, where the large difference in molecular weight helps ensure the presence of an interface. The droplet/helium stream then impinges on a counterflowing stream of the warmer test gas. Bleed ports at four locations on the periphery of the impingement plane are plumbed to vent the impinging gas mixture from the chamber. These four vents have independent control to properly balance the flows so that the droplet stream is not perturbed from the centerline. The counterflow configuration creates a relatively sharp transition to the temperature and composition desired for testing. It is hoped that this design will allow high-pressure, cryogenic droplet-on-demand operation by stabilizing the droplet generation in an environment where surface tension forces have been predicted to exist even at the full operating pressure of the vessel. Once the droplet crosses the relatively sharp temperature and composition transition at the entrance into the windowed region of the main chamber, transcritical vaporization of the droplet may begin to occur.

Due to the stringent requirements and complexity of the transcritical cryogenic droplet experimental vessel, considerable time has been invested in its design and construction. The chamber fabrication should be complete as of the date of this meeting. Installation will occur shortly, and experimentation will begin in early 1996.

PRELIMINARY RESULTS IN NON-OPTIMIZED VESSEL: TRANSCRITICAL JETS

Transcritical droplets are important to study for the reasons stated initially in this paper; however, the investigation of droplets constitutes only a first step in attacking the transcritical propellant atomization and vaporization problem. The remainder of this paper will describe the results of some preliminary experiments conducted to know what kind of behavior to expect from transcritical jets and to demonstrate the feasibility of using Raman imaging diagnostics with transcritical jets.

While designing and awaiting construction of the optimized transcritical experimental chamber, an existing cylindrical pressure vessel similar to that used by Woodward et al.[11] and Anderson et al.[21] was modified to accommodate the LN_2-cooled cryogenic droplet generator. For this paper, however, the piezoelectric element and 127 μm diameter droplet-generating orifice were removed, and a straight capillary tube with inner diameter (injector diameter) of 0.25 mm (0.010") and length-to-diameter ratio (L/D) of approximately 300 were installed. Liquid nitrogen was used as the LOX simulant in the following experiments. High-pressure gaseous nitrogen was condensed within the injector approach tube which runs through the droplet generator's double-pass, low pressure LN_2 cooling jacket. Condensed liquid nitrogen was injected into helium, nitrogen, and mixtures of helium and nitrogen at various chamber pressures. Chamber temperatures varied from 280-310K, always well above the critical temperature of nitrogen (126K). LN_2 injectant temperatures, measured on the outside of the injector tube, varied from 88-115K (typically 90K or less).

Back-lit videography (shadowgraphy) and Raman imaging of nitrogen were the two techniques used to investigate the transcritical nitrogen jets. The experimental set-up is depicted schematically in Fig. 4.

Shadowgraphy

The shadowgraphs were taken with an unintensified RS-170 CCD camera through a long-distance microscope to provide good spatial resolution to discern fine structures in the relatively small jet. A strobe was used to illuminate the shadowgraphs with a sufficiently short pulse (~10 μs) to freeze the motion of the jet. Similar transcritical injection experiments were conducted previously by Woodward et al.[11] The major difference here is that the injectant mass flow rate is an order of magnitude greater for these jet flows compared to the droplet generation flow rate used then.

A matrix of shadowgraph images is depicted in Fig. 5. A series of images of LN_2 injection into nitrogen is given for three different pressures, corresponding to subcritical (Fig. 5(a), 28 atm, P/P_{crit} = 0.83), approximately critical (Fig. 5(b), 35 atm, P/P_{crit} = 1.03), and supercritical (Fig. 5(c), 69 atm, P/P_{crit} = 2.03) conditions. Additionally, in Fig. 5(d), a LN_2 jet is injected into a mixture of nitrogen and helium. The jet mass flow rate for all images was constant at 0.068 g/s (3.5 SLPM). Liquid jet Reynolds numbers based on injection velocity and injector diameter were 4090 (a) , 4010 (b), and 3350 (c,d). To calculate the Reynolds numbers, the density and viscosity of nitrogen at the appropriate conditions were obtained using the extended corresponding states property computation scheme of Oefelein and Yang[22] which accounts for thermodynamic non-idealities and transport anomalies over a wide range of pressures and temperatures.

Flow is downward from the injector exit in position (1) at 0-1.9 mm to position (2) at 7.4-9.5 mm then to position (3) at 15-17.1 mm and finally to

position (4) at 22.6-24.7 mm near the bottom of the viewing window. The vertical field of view in each image is approximately 2.1 mm (8.3 injector diameters) with approximately a 5.5 mm gap between images.

The subcritical jet in Fig. 5(a)(1-4) has a sharp gas/liquid interface throughout. The relatively low speed jet does not exhibit much breakup although disturbances are evident on the surface of the jet. Beginning at position (2), the jet would intermittently breakup into large liquid globs that were never really spherical. Also, intermittently the subcritical jet would be nearly free of disturbances, being smooth and straight past the bottom of the viewing window. Most frequently, the jet would appear as in Fig. 5(a)(1-4), with both symmetric and anti-symmetric disturbances exhibited. The symmetric disturbances generally dominated closer to the injector and helical instabilities dominated further downstream.

The LN_2 jet issuing into the approximately critical pressure environment in Fig. 5(b)(1-4) behaves much differently than the subcritical case as one might expect. In Fig. 5(b)(1), the injected nitrogen appears as a liquid presumably because of the steep gradient between the subcritical temperature of the jet and the supercritical temperature of the ambient. The temperature gradient and thus density gradient are steep enough to give the appearance of a well defined surface, but at supercritical pressure, the property profiles are continuous and thus the gradients do not approach infinity as in the subcritical case. The jet is initially very smooth due to insufficient surface tension to promote the growth of capillary instabilities. The jet remains very smooth until aerodynamic disturbances shear the surface and cause unstable wave growth. It is interesting to note the sheet-like fan of liquid originating presumably from an imperfection in the injector orifice (since the location of the fan was apparent intermittently at a variety of conditions but consistently in that location). Compared to the subcritical jet in Fig. 5(a)(1), the jet fluid in Fig. 5(b)(1) has insufficient surface tension to bring the fan back to the jet, and we see the fan begin to disintegrate due to aerodynamic interactions downstream in Fig. 5(b)(2). Examining Fig. 5(b)(2) and beyond, apparently no droplet-like structures are actually being formed. Instead stringy, fluid structures that exhibit some interfacial behavior are created. These fluid structures seem to readily vaporize and mix. This apparent absence of droplet formation from a transcritical jet is in agreement with the findings of Mayer and Tamura.[14]

The supercritical jet at 69 atm in Fig. 5(c) is very similar to the slightly supercritical jet at 35 atm in Fig. 5(b) except that the onset of aerodynamic instabilities occurs much sooner and more vigorously as expected in the higher density ambient. Jet spreading is quite rapid, and by Fig. 5(c)(4) there is no evidence of any liquid-like structures with distinct interfaces. Note that in Figs. 5(b)(1) and 5(c)(1), ambient nitrogen condensation and subsequent vaporization is occurring around the cooled injector tip, creating steep density gradients that obscure light in the near injector region.

The LN_2 jet in Fig. 5(d) was created by starting from the 69 atm jet in Fig. 5(c) and introducing a small flow of helium into the chamber while venting at the bottom of the chamber to maintain constant pressure. The initial helium mass flow rate was 0.0097 g/s. After a few minutes, the supercritical nitrogen jet appeared to be more coherent, but not drastically. Thus, the helium flow rate was gradually increased to 0.0174 g/s, where after a few minutes the jet appeared as it does in Fig. 5(d). With steady N_2 and He mass flows in and steady outflow to maintain chamber pressure, we calculate that the ambient mass ratio is 3.9 parts N_2 to one part He in Fig. 5(d). (For simulating a LOX/H_2 system this corresponds to a slightly fuel rich mixture ratio.) Obviously, the addition of the helium had a profound effect on the jet structure. The nitrogen jet in Fig. 5(d), although at 69 atm, has a structure like that of a subcritical jet with a distinct interface and evidence of surface tension. This jet most closely resembles the LN_2 jet of Fig. 5(a) except that breakup occurs more readily at the elevated chamber pressure. Perhaps the irregular, sometimes jellyfish-like, sometimes rock-like liquid blobs in the second half of the depicted flow are beginning to undergo transcritical vaporization as they heat up, vaporize, and locally increase the nitrogen concentration. By comparing Figs. 5(c)(4) and 5(d)(4), there is no doubt that the mixing efficiency is vastly different for the two nitrogen jets at 69 atm.

Raman Imaging

With a similar set-up to that of Fig. 4, Anderson et al.[21] demonstrated the feasibility of using Raman imaging to measure vaporized oxygen concentrations in the vicinity of LOX droplets falling in a helium environment. Here, transcritical nitrogen jets injected into either nitrogen or helium are imaged using the Raman Stokes scattering from nitrogen at 607 nm (532 nm excitation). A frequency-doubled, pulsed (~6 ns, 10 Hz) Nd:YAG laser was used to generate the Raman scattering. Results were obtained at an average pulse energy of 225 mJ. The laser beam was focused into a constant dimension (25 mm high by <1 mm thick) sheet using two pairs of cylindrical lenses before being passed into the pressure vessel. Raman scattering was imaged perpendicular to the laser sheet. Discrimination of the Raman signal from the laser was accomplished with 6 mm of Schott OG570 filter glass, which

attenuates the laser wavelength by over 50 orders of magnitude while decreasing the Raman signal from the nitrogen by less than 2%. Raman images were recorded on a Princeton Instruments 576x384 CCD detector with a fiber-coupled intensifier. The intensifier was gated for a 200 ns exposure to minimize ambient light detection.

Two cases were considered for demonstrating the use of Raman imaging diagnostics for transcritical jet vaporization and mixing studies. Similar to Figs. 5(c) and 5(d), they are 1) LN_2 injected into nitrogen at 69 atm and 2) LN_2 injected into helium at 69 atm. In both cases, the nitrogen mass flow rate was maintained, as before in this study, at 0.068 g/s so that all the images can be consistently compared.

The injection of LN_2 into nitrogen is depicted in Raman images in Fig. 6. Figure 6(a) is a raw, single laser shot image of the Raman scattering from nitrogen in the path of the laser sheet. Note that this also includes a signal in the shape of the light sheet from the ambient supercritical nitrogen in the vessel. The top of the laser sheet hits the jet at about 5 diameters downstream of the injector. (The upper boundary of the laser sheet is pointed out in Fig. 6(a).) The field of view in the vertical direction is approximately 13 mm (about 6 times that for the shadowgraph images in the previous section). The single shot Raman signal from the nitrogen jet is weak but easily seen above the signal from the ambient nitrogen. The Raman image of the jet contour looks "fuzzy," as it should because the LN_2 is undergoing supercritical vaporization and mixing, as we saw in Fig. 5(c), after about 5 to 10 diameters downstream of injection. Due to a lack of spatial resolution and signal-to-noise compared to the shadowgraphs, it is difficult to make a strong statement about the condition of the jet, but in conjunction with the shadowgraph images, the Raman image is obviously consistent with what we would expect to see.

To improve the signal-to-noise ratio, a four-laser-shot ensemble average was recorded under the same conditions and is depicted in Fig. 6(b). This image is much cleaner, and would lend itself better to quantification of the Raman signal. Note, however, that there are a few bright spots on the leading edge of the upper part of the jet. The laser sheet is incident on this side and is being locally focused by the distinct surfaces (steep index of refraction gradients) that exist in this part of the jet. This can cause several problems: 1) local bright spots can use up the dynamic range available; 2) laser-induced breakdown can occur, causing a very bright, broadband flash of light that will overwhelm the Raman signal and saturate the detector; 3) it may induce stimulated Raman scattering, a nonlinear process, which is difficult to quantify; or 4) alter the laser sheet profile across the jet due to extinction and thus introduce an apparent asymmetry in the concentration profile. Note that in Figs. 6(a) and (b), there is a black band coming from the left middle side that goes transversely through the jet. This no-light band is caused by a small surface defect in the laser input window. Also note that the band gets washed out after going through the jet due to local random scattering of the sheet from the jets fine scale, density fluctuations that cause index of refraction gradients.

Now consider the other jet case. A single shot Raman image of a LN_2 jet into helium at 69 atm is shown in Fig. 7. The first thing to note is that there is no Raman signal from the laser sheet going through the ambient helium since it is Raman inactive. This helps to distinguish the jet from the background. The Raman signal from the nitrogen jet tracks the jet profile fairly well. It is obvious from this image that, as we saw before, the LN_2 jet in helium is much more coherent and undergoes significantly slower mixing with ambient fluid. Distinct surfaces are suggested by the "beaded" structure seen in the image even though the edges of the Raman contours are somewhat fuzzy. This could be due to noise, or it could be a real effect caused by vaporization of nitrogen or helium solubility into the nitrogen. Also, local bright spots can be seen in this image as in Fig. 6(b), but here they are further downstream, indicating again the presence of liquid-like interfaces.

The technique for making the Raman images quantitative in terms of species concentration is straightforward. The process involves subtracting off the appropriate background and then ratioing to a calibrated response image of Raman scattering from the laser sheet passing through a known concentration of nitrogen. Thus, the species concentration distribution of nitrogen in the jet, near the jet, and in the far-ambient can simultaneously be determined. Note that for the case of a nitrogen jet into nitrogen, variations in Raman scattering intensity represent a density distribution since there is only one molecular species and therefore can be interpreted as a temperature distribution. As stated previously, complications enter when stimulated Raman scattering occurs, which is likely in the liquid-like jet. Coherent structures with a sharp interface will tend to focus the laser light, potentially inducing stimulated Raman and nonlinear effects. In the local regions where this occurs, intensity measurements will not be directly indicative of the species concentration, but outside of the affected regions, accurate quantification of species concentration should still be possible. Although difficult to quantify, the nonlinear effect, when observed, can help determine the presence of liquid-like structures.

Although the Raman imaging results are encouraging, several challenges obviously were encountered in this study (and also in Ref. 21). The characteristically low Raman signal-to-noise ratio lead to difficulties with insufficient light collection. Light focusing due to steep refractive index gradients (especially due to highly curved liquid surfaces) caused laser-induced-breakdown (LIB), stimulated Raman scattering, or altered the laser sheet profile. The new chamber design described earlier in this paper was created to alleviate most of the above issues. The large round viewing windows will allow significantly greater signal collection, and the shape of the chamber represents an attempt to minimize the path length affected by refractive index gradients. Also, the chamber is designed for twice the pressure used to obtain the present results. Thus, Raman signal levels will be greatly increased over those depicted in this paper. The enhanced signal should enable the use of higher magnification detection optics to obtain spatial resolution similar to that of the shadowgraphs of Fig. 5. Finally, to alleviate the LIB problem, a new Nd:YAG laser with a variable pulse option has been procured. This laser has twice the rated power (800 mJ/pulse @ 532 nm) of the laser used for the present results, but can deliver its energy in an elongated pulse on the order 100 ns, so that peak powers will be reduced to avoid LIB while providing more energy for a stronger Raman signal.

SUMMARY AND CONCLUSIONS

Incorporating lessons learned from preliminary experiments and building on the development of a unique high-pressure cryogenic droplet generator, a promising new transcritical droplet experimental chamber has been designed and fabricated.

Shadowgraph imaging of liquid nitrogen jets injected into nitrogen and nitrogen/helium mixtures at pressures below, at, and well above the critical pressure of nitrogen emphasize the profound influence that transcritical effects have on jet structure, atomization, and mixing. Also emphasized is the profound effect that mixture properties and steep composition and density gradients can have on the would-be transcritical interface. Results indicate that even at subcritical temperature, droplets may not be formed from jet breakup at supercritical pressure. However, it was also demonstrated that small quantities of helium mixed directly with LN_2 could be enough to cause classical subcritical liquid jet breakup with the participation of surface tension driven mechanisms and resulting in the formation of irregularly-shaped, droplet-like structures with discernible interfaces. From these preliminary results, it is unwise to make generalizations; further work with various ambient mixtures including simulated combustion products (e.g., H_2O) is required.

Raman imaging diagnostics look promising for use with transcritical jets. In this preliminary study, Raman imaging was able to distinguish the structural differences between liquid nitrogen jets injected into helium or nitrogen. The technique can be used to quantify simultaneously the ambient concentration of the species of interest (nitrogen or oxygen) as well as the vaporizing concentration field of the transcritical jet With the need to reach higher pressures to fully investigate the transcritical behavior of the LN_2/helium (or LOX/hydrogen) system, the prospects for Raman diagnostics actually improve thanks to the increase in signal strength with pressure (molecular number density).

ACKNOWLEDGMENTS

The authors gratefully acknowledge the support and encouragement for this work from the Air Force Office of Scientific Research and contract monitor Dr. Mitat Birkan under task 2308AP. The efforts of Mr. Bruce Petrites of General Physics Corporation to enhance and complete the detailed design of the transcritical droplet pressure vessel are recognized and appreciated. The authors thank Dr. James F. Verdieck and Mr. Ron Bates for their assistance with the Raman imaging experiments. Thanks to Mr. Joseph Oefelein and Professor Vigor Yang at The Pennsylvania State University for giving us their high pressure fluid property calculation code and to Mr. Michael McKee of the Phillips Lab for running the code.

REFERENCES

[1]Faeth, G.M., "Current Status of Droplet and Liquid Combustion," *Prog. Energy Combust. Sci.*, Vol. 3, pp. 191-224 (1977).

[2]Law, C.K., "Recent Advances in Droplet Vaporization and Combustion," *Prog. Energy Combust. Sci.*, Vol. 8, pp. 171-201 (1982).

[3]Sirignano, W.A., "Fuel Droplet Vaporization and Spray Combustion Theory," *Prog. Energy Combust. Sci.*, Vol. 9, pp. 291-322 (1983).

[4]Faeth, G.M. Dominicis, D.P. Tulpinsky, J.F., and Olson, D.R., "Supercritical Bipropellant Droplet Combustion," *Twelfth Symposium (International) on Combustion*, The Combustion Institute, pp. 9–18 (1969).

[5]Sato, J., Tsue, M., and Kono, M., "Effects of Natural Convection on High Pressure Droplet Combustion," *Comb. Fl.* 82: 142–150 (1990).

[6]Natarajan, R., and Brzustowski, T.A., "Some New Observations on the Combustion of Hydrocarbon Droplets at Elevated Pressures," *Comb. Sci. and Tech.* 2: 259–269 (1970).

[7]Sowles, R.E., "An Experimental Study of Carbon Dioxide Droplets Falling Through Inert High Pressure High Temperature Environments," Ph.D. Thesis, Dept. of Mech. Eng., University of Wisconsin (1973).

[8]Shuen, J.S., Yang, V., and Hsiao, G.C., "Combustion of Liquid-Fuel Droplets at Supercritical Conditions," *Comb. Fl.* 89: 299–319 (1992).

[9]Yang, V., Lin, N. N., and Shuen, J. S., "Vaporization of Liquid Oxygen (LOX) Droplets in Supercritical Hydrogen Environments," *Comb. Sci. and Tech.* 97: 247 (1994).

[10]Delplanque, J.-P., and Sirignano, W.A., "Numerical Study of the Transient Vaporization of an Oxygen Droplet at Sub- and Supercritical Conditions," *Int. J. Heat Mass Transfer* 36: 303–314 (1993).

[11]Woodward, R.D., Talley, D.G., Anderson, T.J., and Winter, M., "Shadowgraphy of Transcritical Cryogenic Fluids," 6th Annual Penn State PERC Symposium, NASA Lewis Research Center, Cleveland, OH (1994).

[12]Newman, J.A. and Brzustowski, T.A., "Behavior of a Liquid Jet Near the Thermodynamic Critical Region," *AIAA Journal*, Vol. 9, No. 8, pp.. 1595-1602 (1971).

[13]Birk, A., McQuaid, M., and Gross, M, "Liquid Core Structure of Evaporating Sprays at High Pressures - Flash X-Ray Studies," Army Research Lab Report, ARL-TR-901 (1995).

[14]Mayer, W. and Tamura, H., "Flow Visualization of Supercritical Propellant Injection in a Firing LOX/GH2 Rocket Engine," 31st AIAA/ASME/SAE/ASEE Joint Propulsion Conference & Exhibit, San Diego, CA, paper 95–2433 (1995).

[15]Eckbreth, A.C., *Laser Diagnostics for Combustion Temperature and Species*, Energy and Engineering Science Series, Vol. 7, Gupta, A.K. and Lilley, D.G., Eds., Abacus Press (1988).

[16]Allen, M.G., McManus, K.R., and Sonnenfroh, D.M., "PLIF Imaging in Spray Flame Combustors at Elevated Pressure," 33rd AIAA Aerospace Sciences Meeting & Exhibit, Reno, NV, paper 95–0172 (1995).

[17]Dreier, T., Ridder, M., Schiff, G., Saur, A., and Suvernev, A.A., "Determination of Temperature from N2 and O2 CARS Spectra at Very High Pressure," *Twenty-Fifth Symposium (International) on Combustion*, The Combustion Institute, pp. 1727-1734 (1994).

[18]Shirley, J.A., "Fiber Optic Raman Thermometer for Space Shuttle Main Engine Preburner Profiling," NASA Conference Publication 2436: 107-123 (1986).

[19]Cummings, E.B., Hornung, H.G., Brown, M.S., and DeBarber, P.A., "Measurement of Gas-Phase Sound Speed and Thermal Diffusivity Over a Broad Pressure Range Using LITA," submitted to *Optics Letters* (1995).

[20]Seasholtz, R.G., "Rayleigh-Brillouin Scattering for High-Pressure Gas Temperature Measurements," NASA Conference Publication 10064: 21-27 (1991).

[21]Anderson, T.J., Woodward, R.D., Winter, M., "Oxygen Concentration Measurements in a High Pressure Environment Using Raman Imaging," 33rd AIAA Aerospace Sciences Meeting & Exhibit, Reno, NV, paper 95–0140 (1995).

[22]Oefelein, J.C. and Yang, V. "High Pressure Spray Field Dynamics in Turbulent Mixing Layers," 31st AIAA/ASME/SAE/ASEE Joint Propulsion Conference & Exhibit, San Diego, CA, paper 95–2434 (1995).

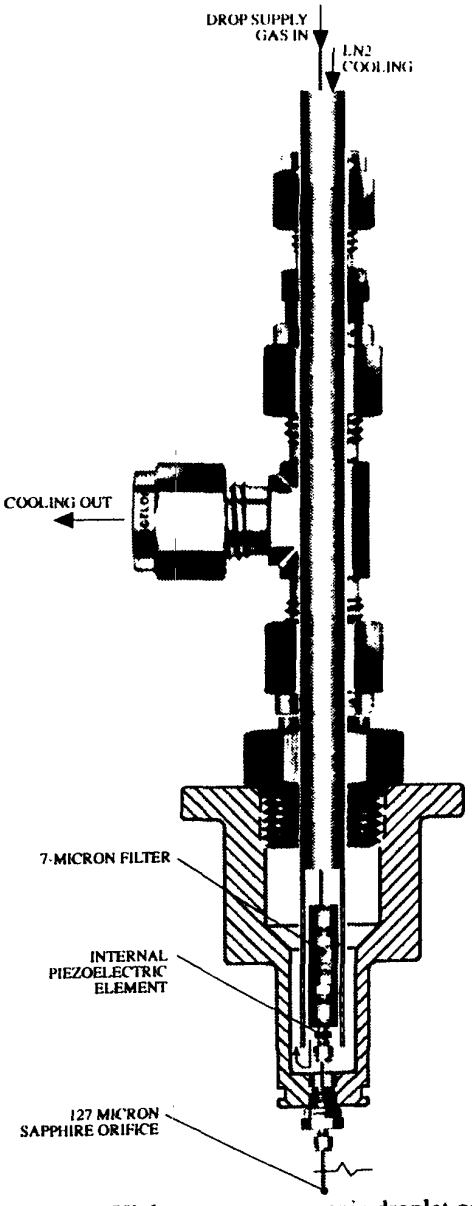

Fig. 1. High-pressure cryogenic droplet generator

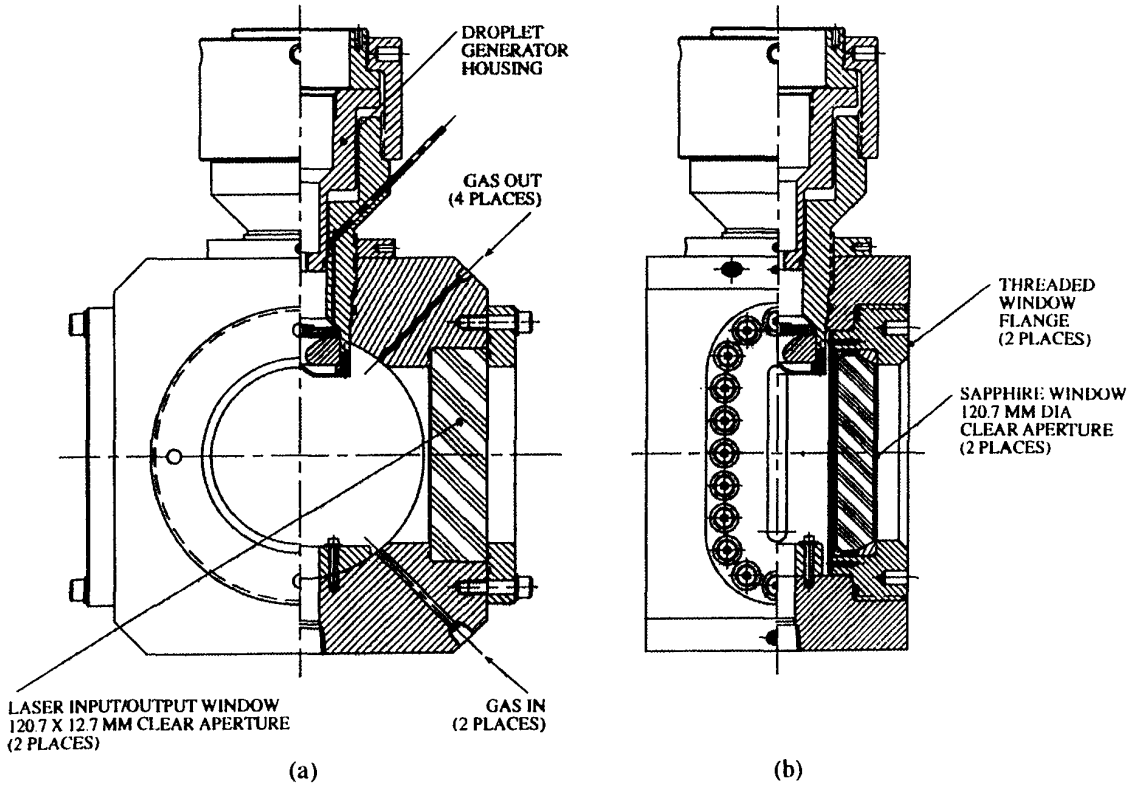

Fig. 2. Transcritical droplet pressure vessel
(a) front view
(b) side view

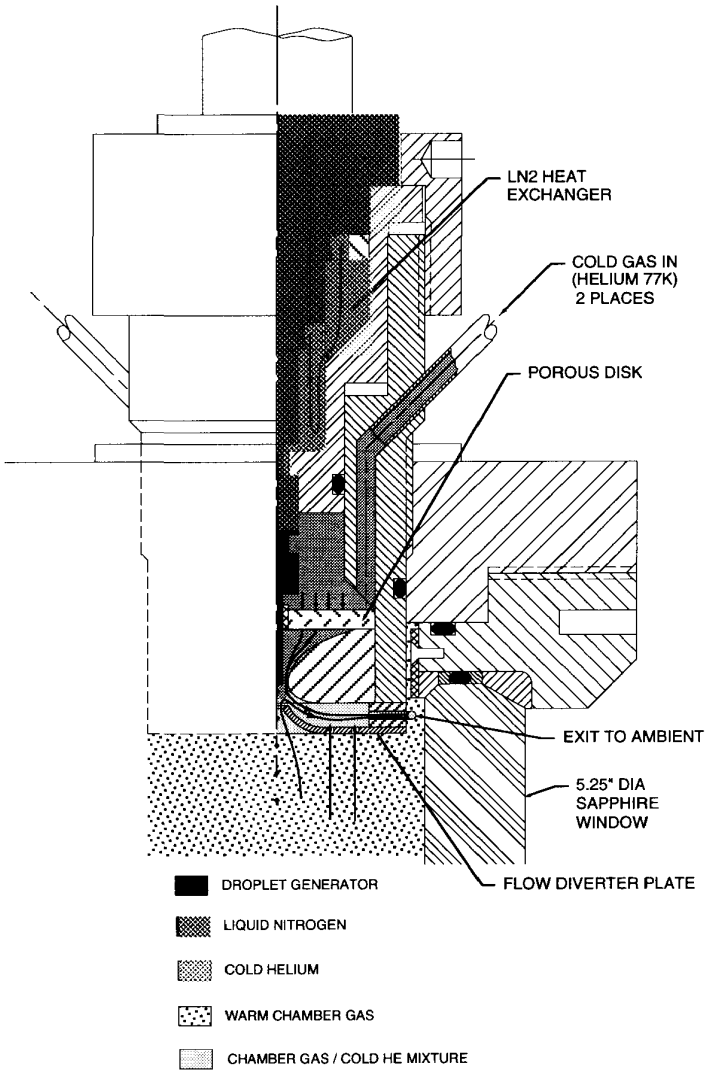

Fig. 3. Pressure vessel/droplet generator interface

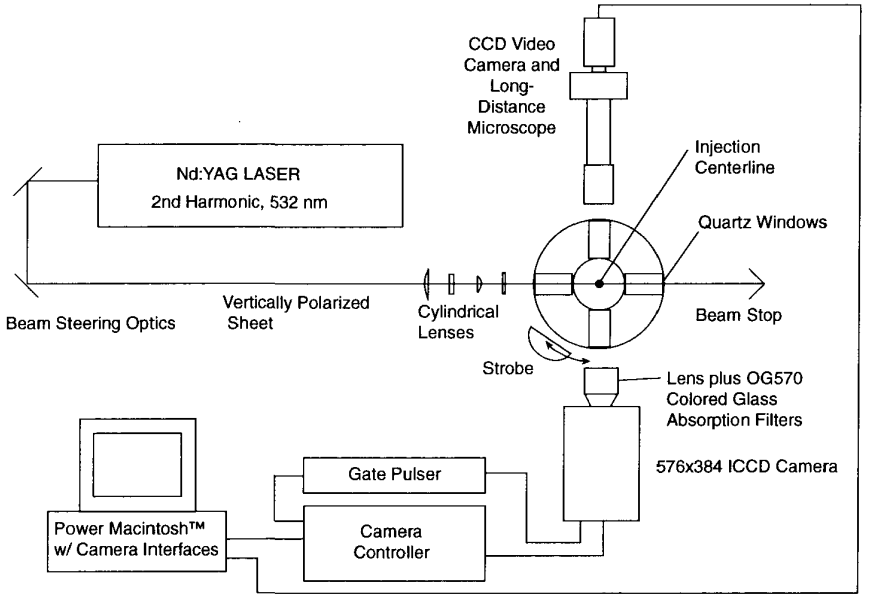

Fig. 4. Experimental set-up

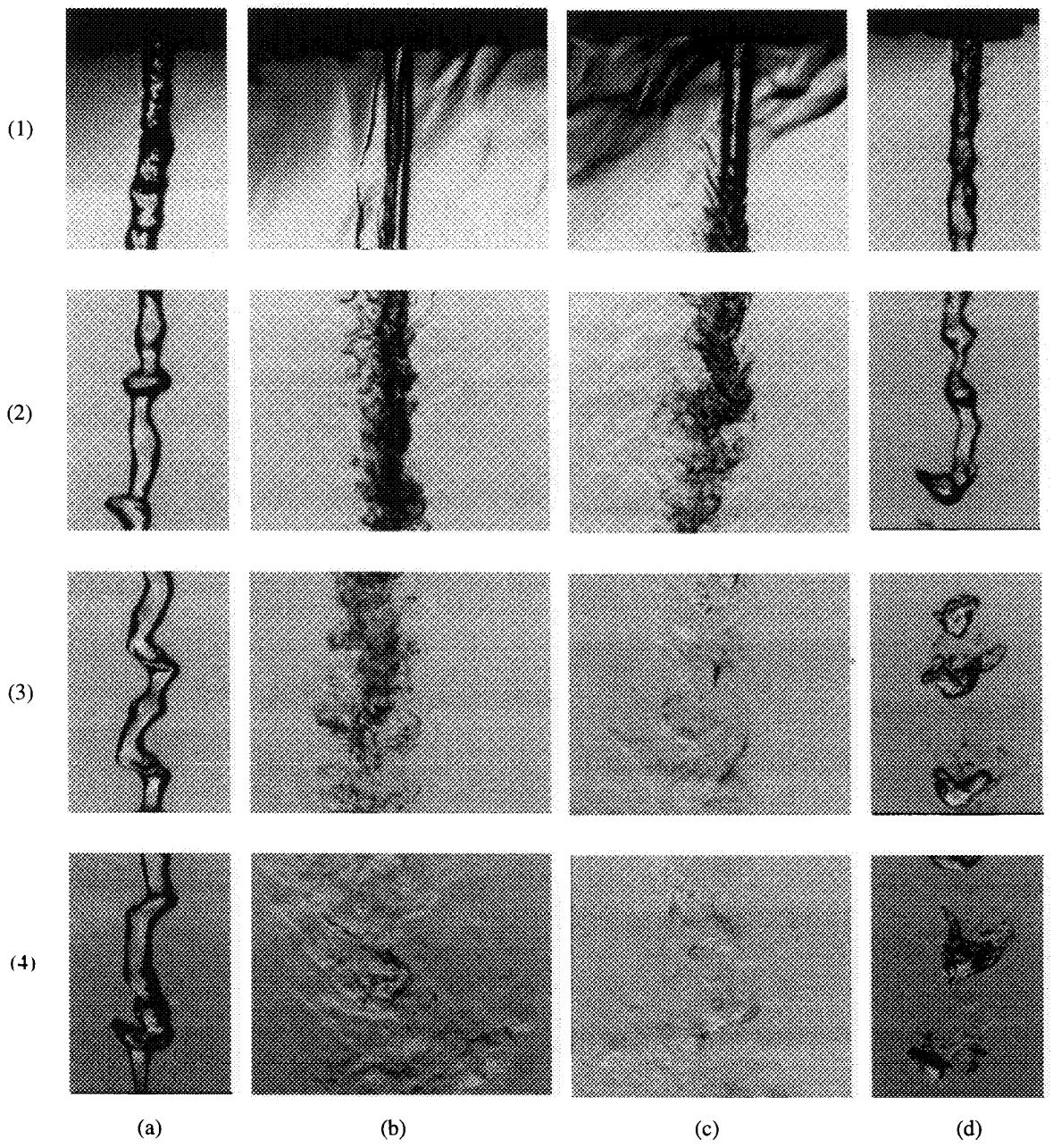

Fig. 5. Shadowgraph images of liquid nitrogen jets issuing into a pressurized chamber. Injection diameter is 0.25 mm (0.010").

(a) into subcritical nitrogen: 28 atm, P/Pcrit = 0.83
(b) into near-critical nitrogen: 35 atm, P/Pcrit = 1.03
(c) into supercritical nitrogen: 69 atm, P/Pcrit = 2.03
(d) into a mixture of nitrogen and helium at 69 atm, mixture ratio (N2/He) of 3.9

Images recorded at the following locations downstream of the injector exit:
(1) 0.0 to 1.9 mm, (2) 7.4 to 9.5 mm, (3) 15.0 to 17.1 mm, (4) 22.6 to 24.7 mm

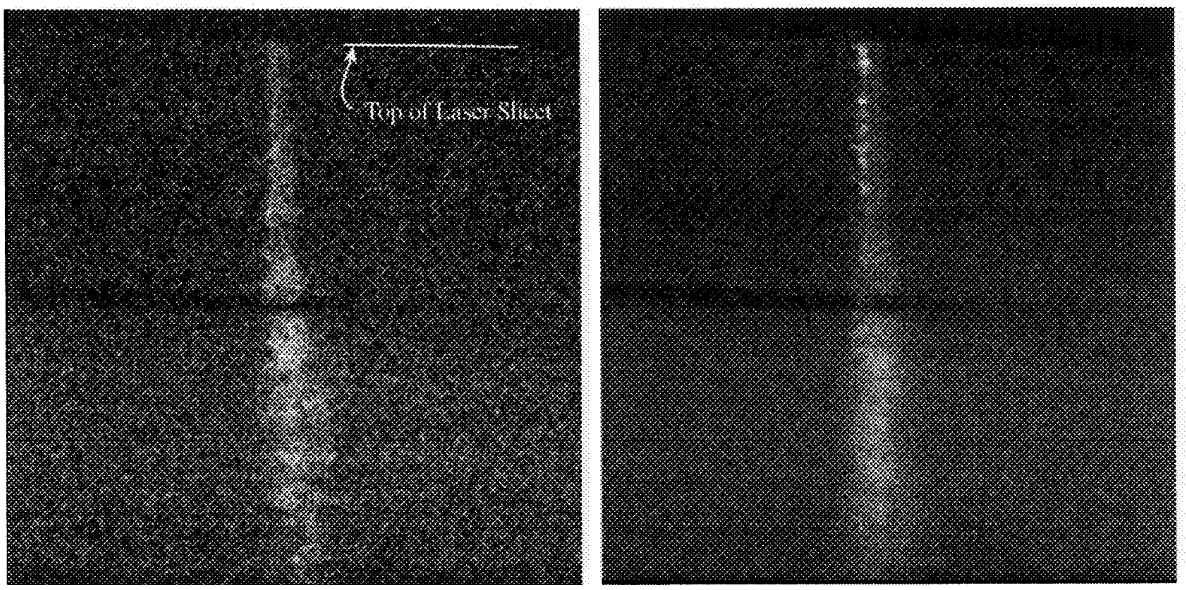

(a) (b)

Fig. 6. Raman images of liquid nitrogen jet into supercritical nitrogen (69 atm, P/Pcrit = 2.03)
(a) single laser shot exposure
(b) four laser shot exposure

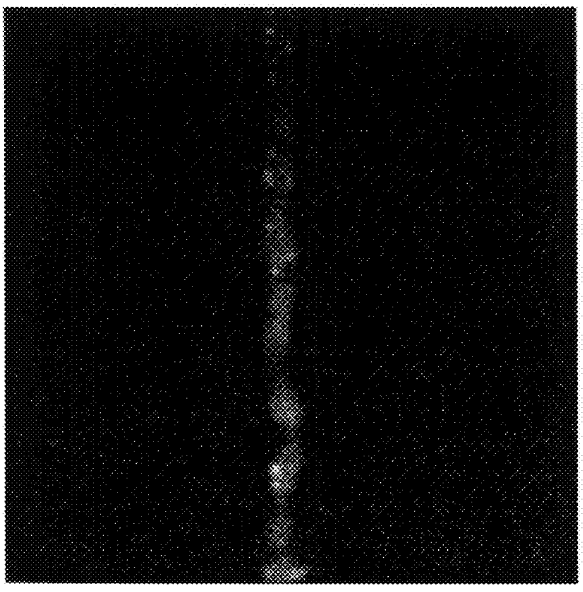

Fig. 7. Raman image of liquid nitrogen jet into helium at 69 atm

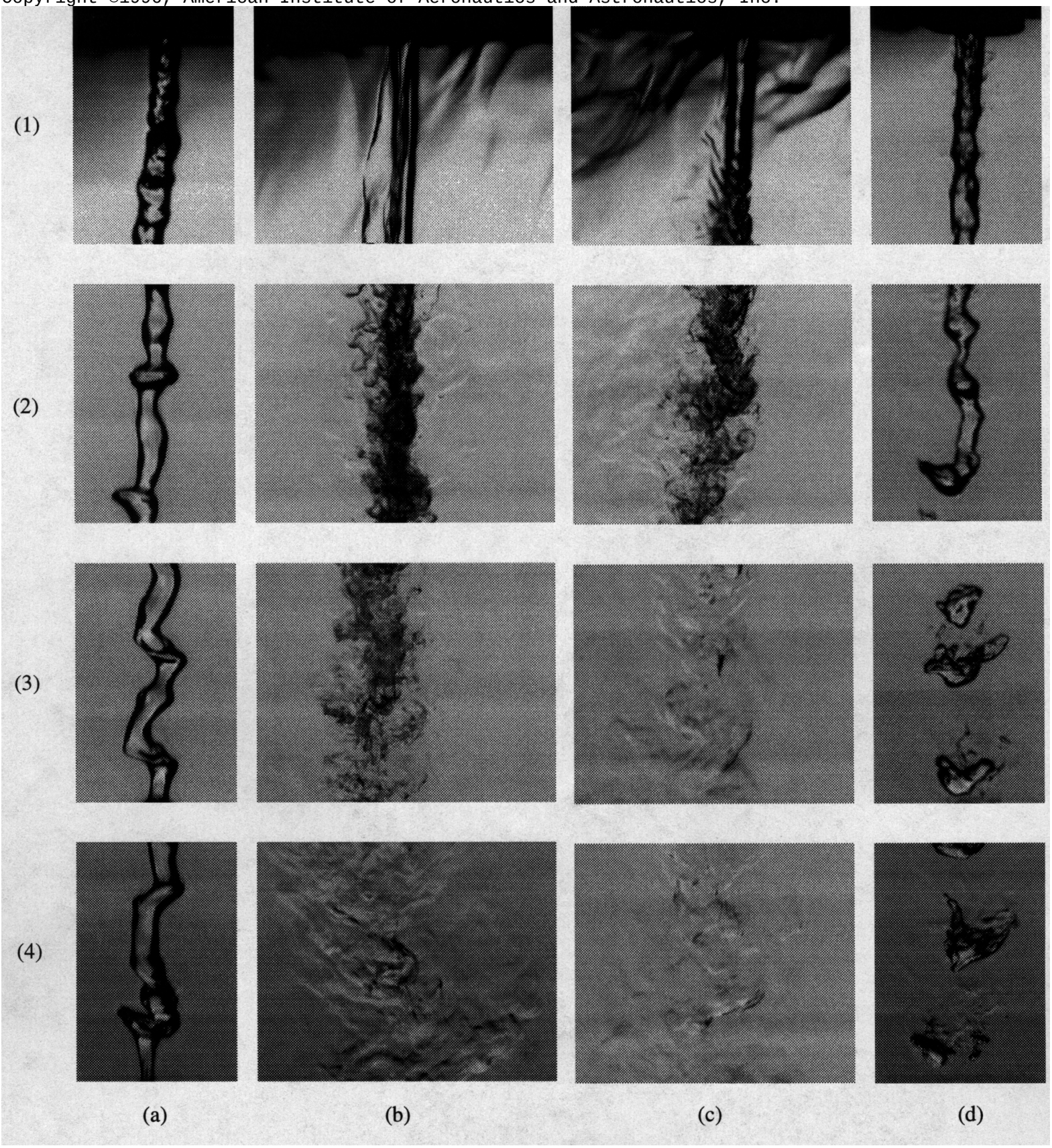

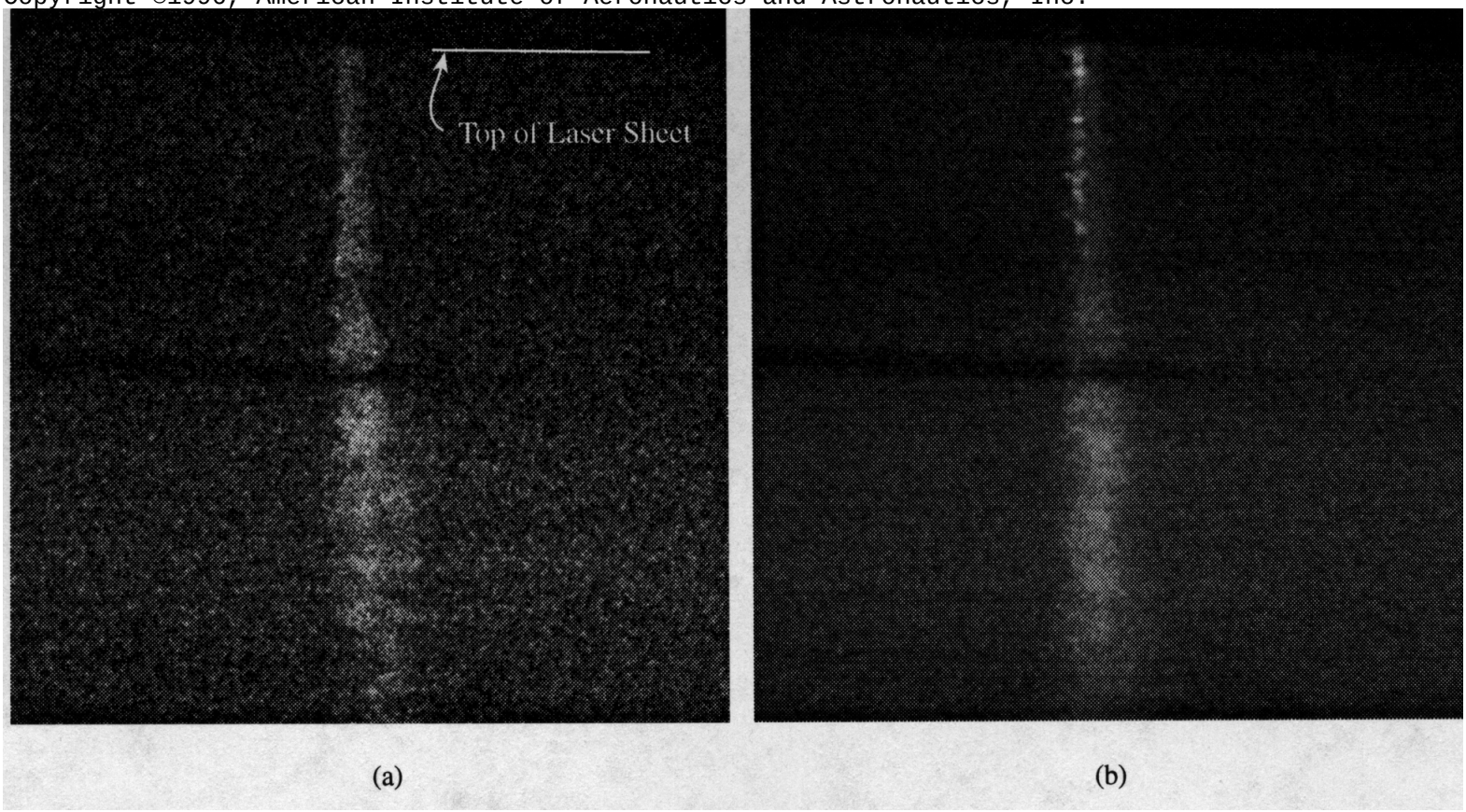

Fig. 7

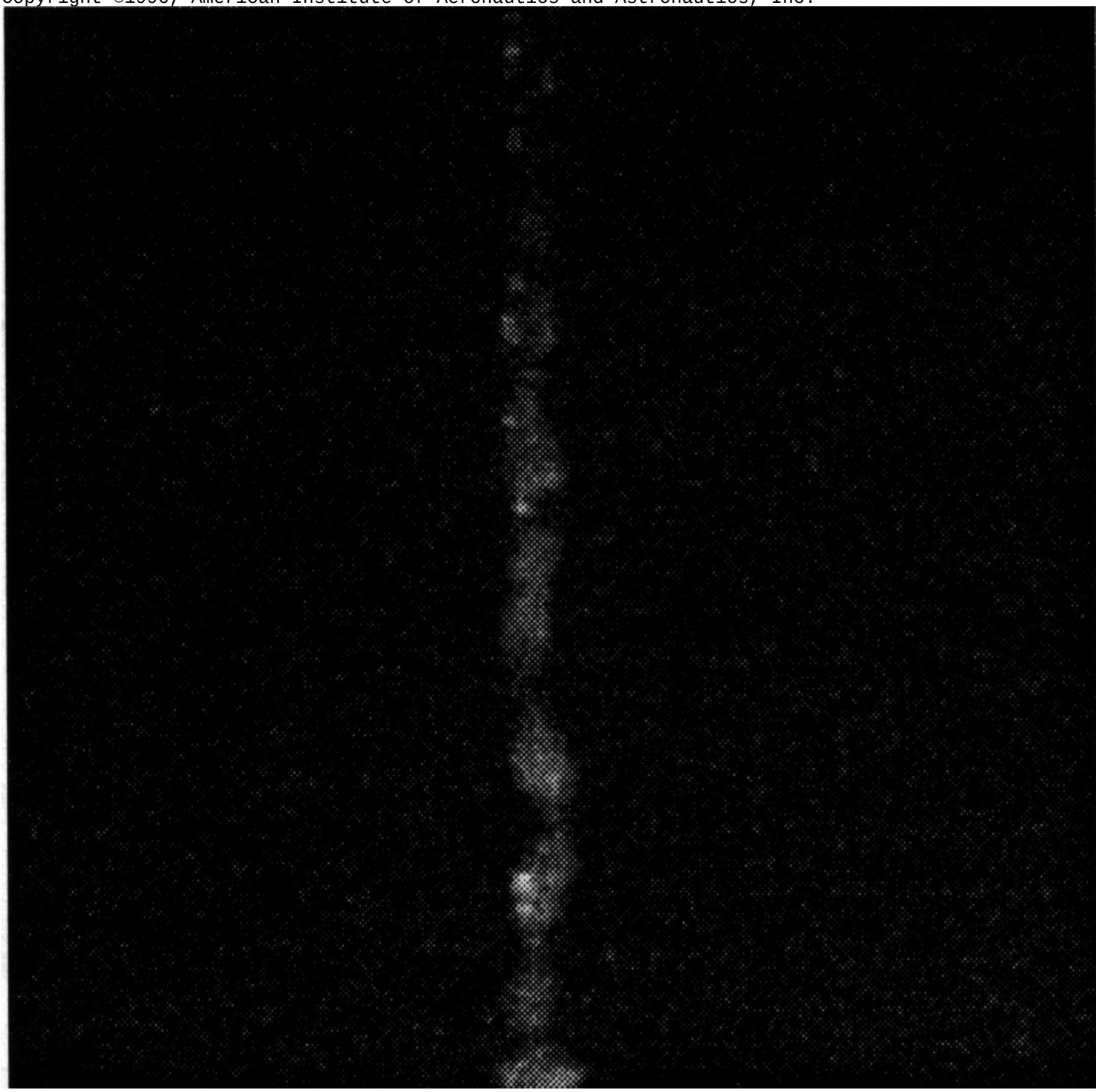

APPENDIX E:

"Experimental Studies of Transcritical Cryogenic Droplets and Jets"

This Page Intentionally Left Blank

13th Annual Conference on Liquid Atomization Spray Systems - Europe
Florence, Italy, 9-11 July 1997

Experimental Studies of Transcritical Cryogenic Droplets and Jets

Douglas G. Talley and Roger D. Woodward
Phillips Laboratory, OLAC PL/RKS
10 East Saturn Blvd,
Edwards AFB, CA 93524-7660, USA

Introduction

In high pressure liquid rocket engines, liquid oxygen can be injected at an initially subcritical temperature into an environment exceeding the critical temperature and pressure of the oxygen. The term "transcritical" is used here to denote this process. There are several reasons why transcritical atomization should be quite different than what is conventionally understood to occur under low pressure, subcritical conditions [1-3]. These include the disappearance of surface tension, vanishing enthalpy of vaporization and other property singularities near the critical point, and enhanced solubility of the dispersed phase in the condensed phase. The latter creates mixture effects whereby the critical pressure of the mixture can reach several times the critical pressure of the pure phase. This in turn implies that the critical point is not fixed but varies dynamically with mixing. Thus it is possible that gas/liquid interfaces could come and go in unexpected ways. The objective of this work is ultimately to understand and predict how transcritical phenomena affect rocket engine performance and the onset of combustion instabilities.

Experiment

Numerous practical difficulties must be overcome in order to scientifically study transcritical cryogenic flows. Optical access into high pressure environments is not easily achieved. Diagnostics can be problematic if windows are too small, and visualization tends to be obscured by index of refraction gradients which become accentuated at high pressures. Many optical diagnostic techniques are difficult to implement or fail to yield quantitative measurements at the pressures required. For droplet studies, the use of supporting structures such as fibers or thermocouples is unsuitable because these obscure how the lack of surface tension affects deformation and breakup. On the other hand, free droplet experiments are also a challenge because of various factors which tend to interfere with drop formation, such as enhanced aerodynamic interactions, heat transfer to the drop generator tip, and the lack of surface tension for forming droplets in the first place. Finally, the study of acoustic interactions is impeded because conventional speakers and sirens tend to be designed for atmospheric use and cannot produce the required amplitudes at elevated pressures.

To address these difficulties, a 137 atm pressure vessel with highly integrated drop generator has been developed for the study of transcritical liquid oxygen and liquid nitrogen droplets and jets, as illustrated in Fig. 1. Optical access is provided by two 133.4 mm opposed sapphire windows, and advantage is taken of the small droplet size to locate the windows as close as is structurally possible to the droplet stream, thus minimizing the optical path and reducing the impact of index of refraction gradients. The large window size and close spacing dictated a rectangular shape for the pressure vessel, with the result that the f-number is limited by the collection optics, not the window size. Additional oblong fused silica windows perpendicular to the sapphire windows allow introduction of a laser sheet which can be viewed through the sapphire windows. The diagnostics of choice are shadowgraph visualization and 2D visualization of spontaneous Raman scattering from a frequency-doubled (532 nm) or -tripled (355 nm) Nd-YAG laser. The Raman diagnostic was selected due to its species selectivity and enhanced signal strength at high pressures.

The highly integrated monodisperse droplet generator for producing freely falling droplets is illustrated in Fig. 2. High pressure gaseous oxygen or nitrogen is condensed in a central tube by a 1 atm liquid nitrogen bath. A piezoelectric crystal inside the tube provides acoustic excitation for forming the droplets. The droplets are formed in a flow of gaseous helium also chilled to liquid nitrogen temperatures. The molecular weight difference between the helium and the condensed fluid provides a surface for forming the droplets, and the chilled temperature reduces heat transfer to the generator tip. The helium flows through a converging-diverging section with the drop generator located near the throat. This provides an aerodynamic stripping action which has also been demonstrated to produce monodisperse droplet streams. The availability of both piezoelectric excitation and aerodynamic stripping thus provide for maximum control of the droplets. Test gas having controlled composition and temperature up to 473K flows upward to meet the downward flowing droplet and helium flows. These meet in a stagnation plane designed to provide the droplets with an abrupt transition into the desired test conditions. The colliding gases are stripped away around the periphery of the stagnation plane, while the droplets fall through the plane.

Finally, acoustic drivers capable of producing intense sound at elevated pressures have been developed under a separate effort. Advantage of small droplet sizes will again be taken by focusing the acoustic waves to achieve intensities characteristic of rocket instabilities. Acoustic horns for accomplishing this will be mounted onto fittings currently used for mounting the oblong fused silica windows. These horns are currently under fabrication.

Results

To date, monodisperse streams of liquid oxygen droplets (Pcr = 49.05 atm) in helium have been successfully produced at pressures up to 83 atm, but transcritical effects have not yet been observed due to the mixture effects noted above. Round liquid nitrogen jets (Pcr = 33.06 atm) have been produced in He/N2 mixtures at pressures where supercritical behavior has been observed, as shown in Figs. 3-5 and discussed further below. Raman imaging has been successfully demonstrated for both droplets and jets [5,6], but the near field resolution has so far been only marginal. The far field Raman data is used to characterize the ambient mixture with a 5% molar concentration sensitivity detection limit of N2 at 69 atm and 300K.

Strobe-lit shadowgraphs have provided considerable insight into atomization and breakup behavior at transcritical conditions. Example round jet results are shown in Fig. 3. Vertical positions (1)-(4) correspond to different axial locations in this figure, while horizontal locations (a)-(d) correspond to different experimental conditions. Images of liquid nitrogen jets into pure gaseous nitrogen is shown in (a)-(c), for subcritical (a), near critical (b), and supercritical (c) pressures. The effect of pressure on mixing is quite drastic, with jets in (b) and (c) exhibiting a laminar liquid-like appearance near the orifice and a turbulent gas-like appearance further downstream. A small sheet of fluid can be seen emanating from the side of the jet in (b)(1) and (c)(1) due to a small imperfection in the orifice, but the sheet is not present in (a)(1). Surface tension is evidently large enough to prevent the formation of this sheet at the subcritical pressures in (a)(1), while it is not sufficient to do so at the near- and supercritical pressures of (b)(1) and (c)(1). This is despite the fact that density gradients at the interface in (b)(1) and (c)(1) are large enough to cause a liquid-like appearance. Evidently they are not steep enough to result in appreciable surface tension. For series (d), the pressure was kept at twice the critical pressure of pure nitrogen, as in (c), but a small amount of helium was added to the ambient in (d). Liquid-like structures exhibiting evidence of surface tension are shown to be recovered due to the mixture effects involved in adding helium. See [6] for a more in depth analysis of these images.

Figure 4 depicts another series of shadowgraph images of LN_2 jets injected this time into gaseous helium at chamber pressures of 33 atm, 55 atm, 69 atm, and 83 atm. The injected nitrogen temperature is 83K and the average ambient temperature in the chamber is 292K. Thus, the ambient temperature is always well above the critical temperature of nitrogen, which is 126K. The jet mass flow rate is constant at 0.068 g/s in each case, yielding a jet velocity of 1.7 m/s and a jet Reynolds number of approximately 3000, which differs slightly between cases due to property changes.

In Fig. 4(a)(1), Rayleigh-type breakup has already disintegrated the jet flow into a non-uniform droplet stream. At positions (2) to (4) in Fig. 4(a), it can be seen from the shadowgraphs that significant vaporization is occurring at the elevated chamber pressure of 33 atm. Although the ambient temperature is more than twice the critical temperature for pure nitrogen and the pressure is very near the critical value for pure nitrogen, we see coherent droplet structures with smooth and distinct surfaces, though often with a high degree of asphericity. In contrast, at approximately the same pressure and temperature for LN_2 injection into nitrogen, Fig. 3(b), the absence of surface tension in breakup behavior was clearly evident.

In Fig. 4(b), capillary forces apparently are still dominating the jet breakup dynamics. Jet breakup length in this particular case is longer than seen in Fig. 4(a)(1) possibly because surface tension is relatively weaker for the higher pressure case, resulting in decreased capillary forces and hence delayed Rayleigh breakup, regardless of the fact that aerodynamic forces are enhanced at this significantly higher pressure. Of course, the breakup regime is beginning to change to aerodynamically dominated modes as Weber number and Ohnesorge number are increased with increasing pressure and decreasing surface tension. Although it is difficult to obtain an accurate value for surface tension under these conditions, estimates for these parameters would put the breakup mode somewhere in the wind-induced regime, according to Tseng *et al.* [7]. After initial jet breakup, no spherical structures are formed, and it is evident that secondary breakup is significantly different and more vigorous than in Fig. 4(a). Many surface perturbations are apparent on the globular structures that are created, indicating that the globules possess insufficient surface tension to smooth the surface. Unsteady aerodynamic forces cause many irregular shapes as interfacial tension is too weak to reshape the fluid into a minimized-surface-area structure. As this happens, the "droplets" become more susceptible to aerodynamic breakup and more unstable. Also as ambient nitrogen concentration and LN_2 temperature increase with downstream distance, locally supercritical conditions may begin to occur for these irregularly-shaped nitrogen structures. All of these conditions can cause significant changes in propellant breakup, vaporization, and mixing.

Figure 4(c) reveals a marked change in the nature of the jet structure from the previous case in Fig. 4(b). Although what appear to be interfacial features continue to be observed, any remnants of surface tension playing a role in the jet disintegration appear to have vanished. Injection under these latter conditions is seemingly more characteristic of a turbulent, viscous gas jet. Jet structure is characterized by wispy structures barely, if at all, retained by interfacial forces. Thin threads of fluid, remaining undisturbed by capillary forces, are able to connect larger blobs

until aerodynamic forces perturb them. Consistently, no structures suggestive of surface discontinuities are observed downstream of position (3), indicating an advanced state of mixing (though not necessarily complete) by about 90 injector diameters. Index of refraction (density) gradients caused by temperature and composition gradients are easily observed.

Figure 4(d) depicts turbulent gas-like jet behavior similar to that in Fig. 4(c) except that aerodynamic effects are stronger at this higher pressure, and thus jet disintegration occurs sooner. Underlying the fine scale perturbations on the apparent jet surface are large scale structural disturbances that hint at helical instabilities. This is also somewhat discernible in the previous lower pressure supercritical jet case. In Fig. 4(d), no structures consistent with surface discontinuities are evident beyond 55 injector diameters.

From Fig. 4, surface tension apparently ceases to be important in the jet disintegration process somewhere between 55 and 69 atm (1.6 to 2.1 times the critical pressure of pure nitrogen), for the particular conditions of this nitrogen/helium system, as witnessed in the upper part of the jet. Figure 5 depicts a liquid nitrogen jet injected into helium at the low pressure end of this transition range, 55 atm. Jet and ambient conditions are the same as in Fig. 4(b). In this sequence of ten images recorded over the course of approximately one second at identical injection conditions, we see an oscillation between gas-like and liquid-like jet behavior. This illustrates that under certain conditions, the nature of the jet breakup process can be extremely sensitive to small perturbations in pressure, temperature, local mixture concentrations, and initial jet conditions. In application, the oscillation in the jet breakup behavior could lead to local propellant mixture ratio oscillations and conceivably unstable combustion behavior.

Conclusions

As pressure is increased, transcritical jets eventually reach a point where breakup and mixing behavior is no longer affected by surface tension. Subsequently, the jets behave more like viscous turbulent jets, but perhaps at density ratios and viscosity ratios that have not been well explored. The pressure at which the transition occurs is a strong function of the ambient composition and initial jet conditions, and cannot be deduced from the critical pressure of the pure species alone. The jets are in all cases highly transient, but at pressures where the transition occurs, these can lead to oscillations between jet-like and liquid-like behavior. Additional conclusions await more complete mapping of breakup and "vaporization" regimes currently underway.

References

1. Yang, V., Lin, N.N.,and Shuen, J.S., "Vaporization of Liquid Oxygen (LOX) Droplets in Supercritical Hydrogen Environments," *CST* 93-01-06 (1993).
2. Delplanque, J.-P., and Sirignano, W.A., "Numerical Study of the Transient Vaporization of an Oxygen Droplet at Sub- and Supercritical Conditions," *Int. J. Heat Mass Transfer* 36: 303–314 (1993).
3. Oefelein, J.C. and Yang, V., "Simulation and Analysis of Supercritical Multiphase Combustion Processes," AIAA Paper 96-2880, 32nd AIAA/ASME/SAE/ASEE Joint Propulsion Conference, Lake Buena Vista, FL, Jul. 1996.
4. Woodward, R.D., Talley, D.G., Anderson, T.J., and Winter, M., "Shadowgraphy of Transcritical Cryogenic Fluids," 6th Annual Penn State PERC Symposium, NASA Lewis Research Center, Cleveland, OH, Sept. 94.
5. Anderson, T.J., Woodward, R.D., and Winter, M., "Oxygen Concentration Measurements in a High Pressure Environment Using Raman Imaging," AIAA Paper 95-0140, 33rd AIAA Aerospace Sciences Meeting & Exhibit, Reno, NV, Jan. 1995.
6. Woodward, R.D. and Talley, D.G., "Raman Imaging of Transcritical Cryogenic Propellants," AIAA Paper 96-0468, 34th AIAA Aerospace Sciences Meeting & Exhibit, Reno, NV, Jan. 1996.
7. Tseng, L.-K., Ruff, G.A., Wu, P.-K., and Faeth, G.M., "Continuous- and Dispersed-Phase Structure of Pressure-Atomized Sprays," Recent Advances in Spray Combustion, AIAA Progress Series, Vol. 171, K.K. Kuo (ed.), 1996.

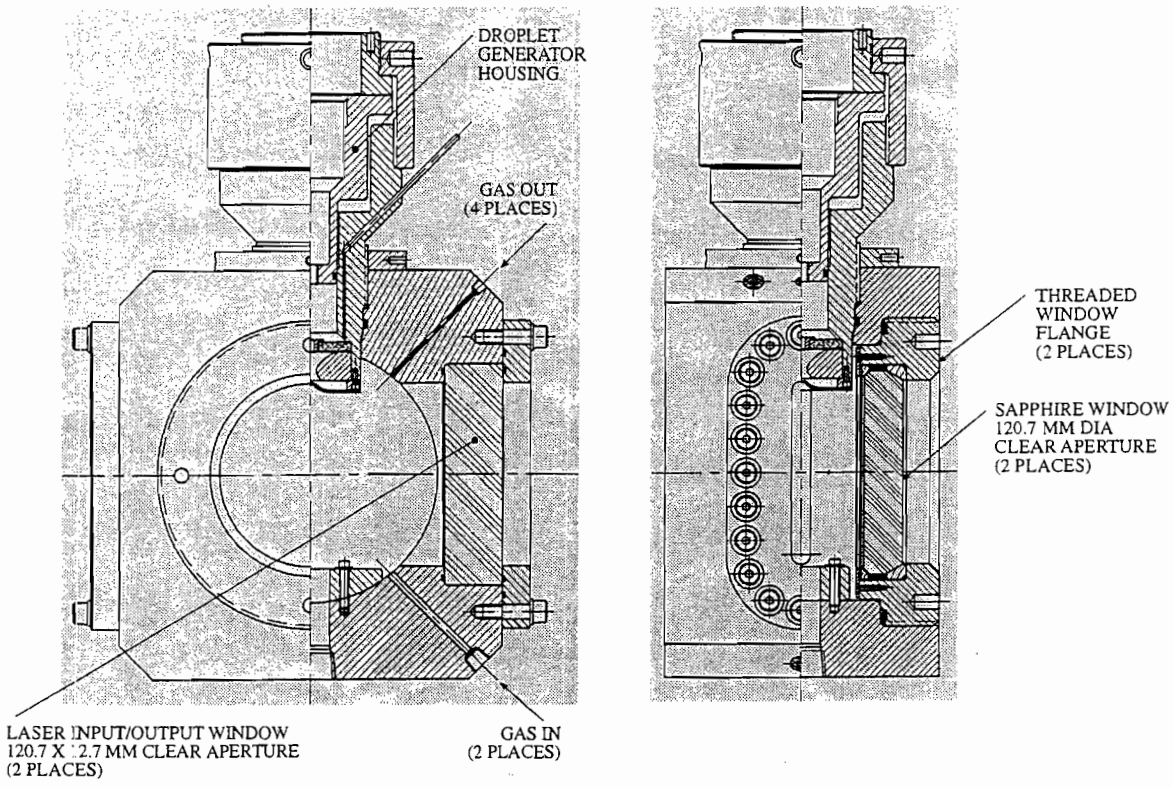

(a) front view (b) side view

Fig. 1. Transcritical experimental pressure vessel

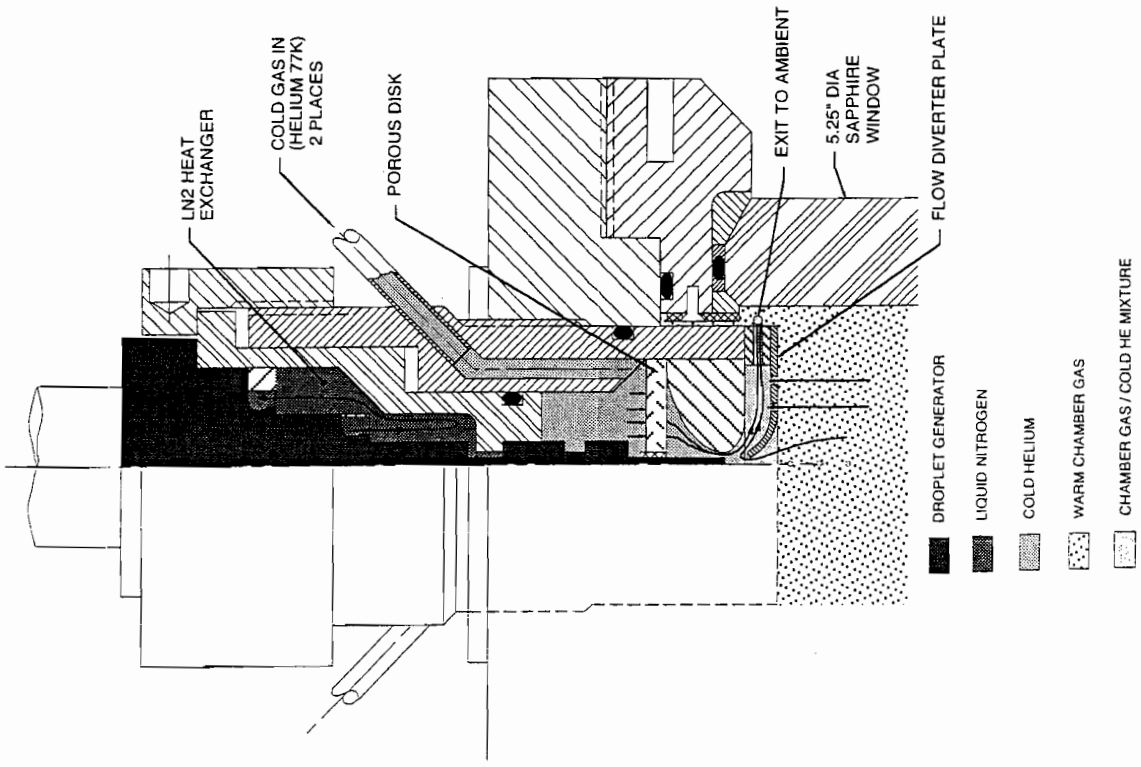

Fig. 2. Pressure vessel/droplet generator interface

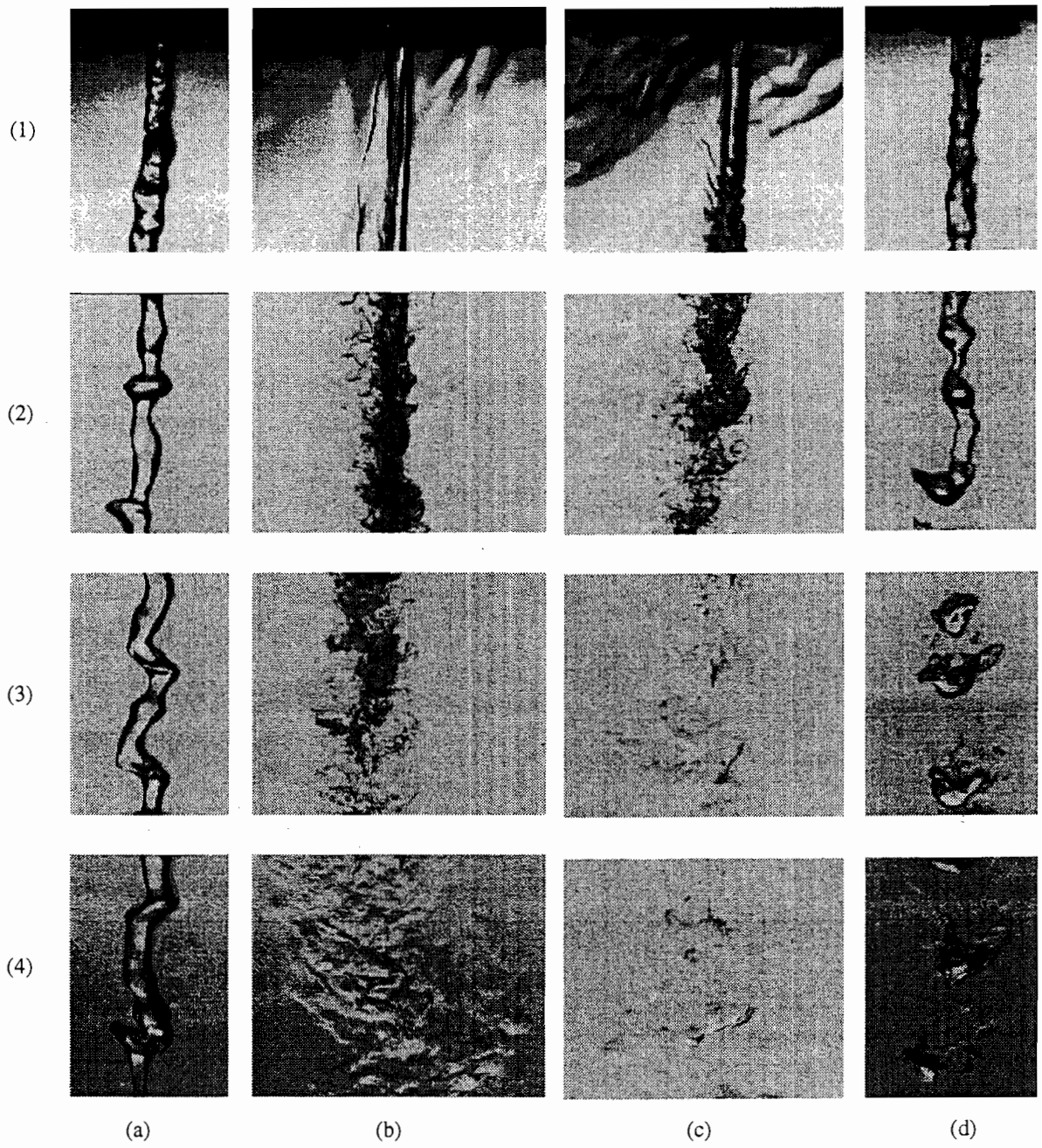

Fig. 3. Shadowgraph images of liquid nitrogen jets issuing into a pressurized chamber. Injection diameter is 0.25 mm (0.010").

(a) into subcritical nitrogen: 28 atm, P/Pcrit = 0.83
(b) into near-critical nitrogen: 35 atm, P/Pcrit = 1.03
(c) into supercritical nitrogen: 69 atm, P/Pcrit = 2.03
(d) into a mixture of nitrogen and helium at 69 atm, mixture ratio (N2/He) of 3.9

Images recorded at the following locations downstream of the injector exit:
(1) 0.0 to 1.9 mm, (2) 7.4 to 9.5 mm, (3) 15.0 to 17.1 mm, (4) 22.6 to 24.7 mm

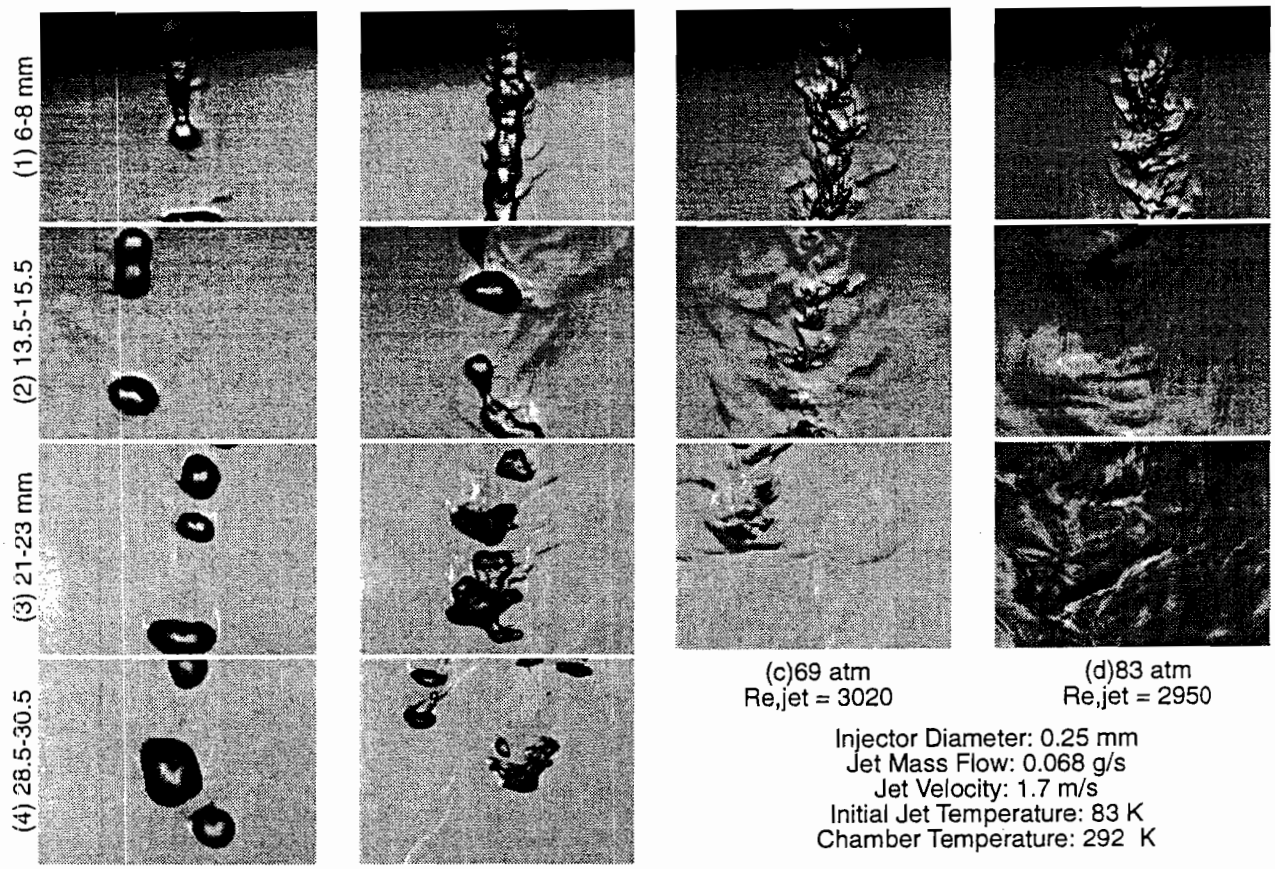

Figure 4. Liquid nitrogen jets injected into helium at elevated chamber pressures.

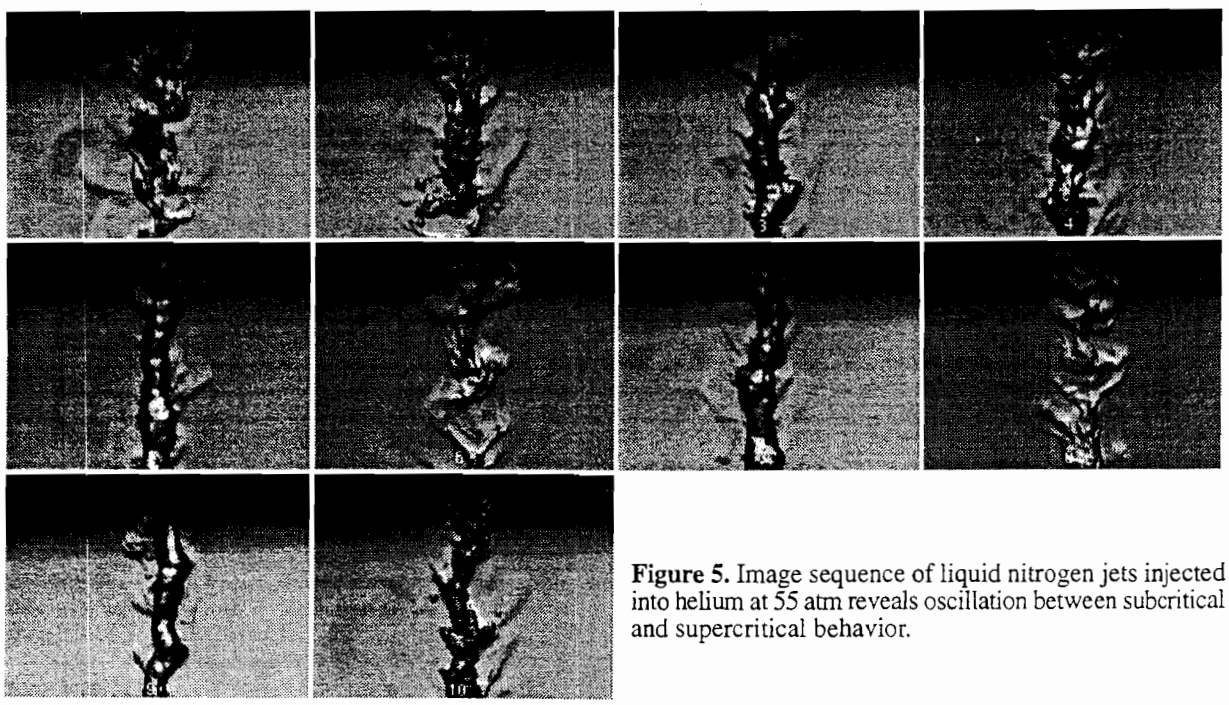

Figure 5. Image sequence of liquid nitrogen jets injected into helium at 55 atm reveals oscillation between subcritical and supercritical behavior.

APPENDIX F

"Experimental Investigations of Atomization and Breakup of Cryogenic Propellants Under High-Pressure Subcritical and Supercritical Conditions"

This Page Intentionally Left Blank

JOURNAL OF PROPULSION AND POWER
Vol. 14, No. 5, September–October 1998

Atomization and Breakup of Cryogenic Propellants Under High-Pressure Subcritical and Supercritical Conditions

Wolfgang O. H. Mayer* and Axel H. A. Schik†
DLR, German Aerospace Center, Lampoldshausen, 74239 Hardthausen, Germany
Bruno Vielle,‡ Christian Chauveau,§ and Iskender Gökalp¶
Centre National de la Recherche Scientifique, 45071 Orleans Cedex 2, France
and
Douglas G. Talley** and Rodger D. Woodward††
U.S. Air Force Research Laboratory, Edwards Air Force Base, California 93524-7660

Recent results on the atomization and breakup of cryogenic propellants under high-pressure subcritical and supercritical conditions are surveyed. Cryogenic fluids were injected into various gases under both cold-flow and hot-fire conditions, and the results were visualized using flashlight photography and high-speed cinematography. In some cases, simulation fluids were used to study atomization and breakup behavior. In others, hot-fire tests with liquid oxygen and gaseous hydrogen demonstrated flow phenomena under realistic cryogenic rocket engine conditions. The visualizations reveal a remarkable difference between subcritical spray formation and evaporation and supercritical injection and mixing. As chamber pressure approaches the critical pressure, injection can no longer be regarded as simple "spray" formation, but rather as a fluid/fluid mixing process that can be extremely sensitive to small perturbations in pressure, temperature, local mixture concentrations, and initial injection conditions.

Introduction

CRYOGENIC rocket engines have evolved over the past 30 years and have been used in a number of operational launch vehicles wordwide. The thrust chamber is the core of any liquid rocket engine and consists of an array of injectors, a combustion chamber, and a nozzle. High performance and reusability are the most challenging requirements for future thrust chamber development, and will require large technical advancements for most of the engine components.[1]

Recent research into the injection, mixing, and combustion behavior of liquid oxygen/gaseous hydrogen (LOX/GH_2) propellants has provided an improved understanding of combustion processes in cryogenic rocket engine thrust chambers.[2–4] Despite this, many basic phenomena such as turbulent mixing still cannot be quantitatively predicted. The problem becomes increasingly severe at elevated chamber pressures. At pressures exceeding the critical points of the propellants, even qualitative understanding has often not been available.

In high-pressure liquid rocket engines, LOX can be injected at an initially subcritical temperature into an environment that exceeds the critical temperature and pressure of the oxygen. The LOX then undergoes a transition to a supercritical state as it is heated and burned. There are several reasons why such a process should be expected to be quite different than what is conventionally understood to occur under low-pressure, subcritical conditions.[5–8] These include the disappearance of surface tension, vanishing enthalpy of vaporization and other property singularities near the critical point, and enhanced solubility of the dispersed phase in the condensed phase. The latter reason creates mixture effects whereby the critical pressure of the mixture can reach several times the critical pressure of the pure component, depending on the environmental temperature. This in turn implies that instead of being fixed, the critical point can vary dynamically depending on the mixing, potentially causing the appearance or disappearance of gas/liquid interfaces. In addition, significantly reduced liquid/gas density ratios compared with conventional subcritical experience should cause comparatively stronger aerodynamic interactions, the magnitude of which should be even further enhanced as surface tension at the liquid interface is weakened.[9–11] Thus, turbulence interactions could play a more dominant role. The sum of all of these factors should affect the entire gamut of injection phenomena, from primary atomization, to secondary deformation and breakup, to "gasification," mixing, and combustion. For the sake of brevity, the term "transcritical" has often been used to refer to injection processes under conditions where the propellants can transform from a subcritical to a supercritical state, or vice versa, as a result of temperature, pressure, or mixture variations.

To better understand high-pressure subcritical and transcritical injection phenomena, several studies have been initiated by the authors. Recent progress is summarized later in this paper. The discussion begins with a hot-fire investigation of LOX/GH_2 injection under subcritical and supercritical conditions in a windowed combustion chamber. Cold-flow studies of jets where high-pressure subcritical and transcritical phenomena can be observed without the complications of chemical reactions are presented next. Finally, recent progress in studying the deformation and breakup of high-pressure subcritical and transcritical droplets is presented. The critical properties of relevant fluids are provided in Table 1.

Received Sept. 2, 1997; revision received May 11, 1998; accepted for publication May 18, 1998.

*Head of Propellant Injection Research, Rocket Propulsion. E-mail: wolfgang.mayer@dlr.de. Member AIAA.
†Research Engineer and Ph.D. Student, Rocket Propulsion.
‡Research Engineer and Ph.D. Student, Laboratoire de Combustion et Systèmes Réactifs.
§Scientist, Laboratoire de Combustion et Systèmes Réactifs.
¶Director of Research, Laboratoire de Combustion et Systèmes Réactifs.
**Group Leader, Rocket Combustion Devices, Propulsion Sciences and Advanced Concepts Division, 10 East Saturn Boulevard. Member AIAA.
††Scientist, 10 East Saturn Boulevard; currently Associate Director, Propulsion Engineering Research Center, Pennsylvania State University, University Park, 16802. Member AIAA.

Hot-Fire Jet Studies

Test Facility and Experimental Setup

An experimental rocket combustion chamber equipped with two flat windows for optical access was used to study injection and mixing under hot-fire subcritical and supercritical conditions.[3] The test rig consisted of an injector head with a single shear coaxial element, a circular, uncooled combustion chamber with a length and diameter of 400 and 40 mm, respectively, and a variable (exchangeable) nozzle (Fig. 1). The windowed section was cooled by a layer of GH_2, which was injected in the direction of the nozzle. Metal dummy windows with thermocouples were used to develop the startup and shutdown sequence and a suitable window-cooling technique. LOX was supplied to the test section from a helium- (He-) pressurized, vacuum-jacketed 90-m^3 storage tank. GH_2 to the injector and the window purge ports was supplied from a 20.0-MPa bottle depot. To cool the cryogenic supply line, a liquid nitrogen (LN_2) cooling jacket was installed between the LOX tank and the LOX dome. Chilling of the LOX line made it possible to reach steady-state firing conditions in less than 1 s. A small LOX/GH_2 pilot flame was used as the ignition source. The igniter was mounted on the lower part of the chamber wall. The typical duration of a firing was 5 s, including startup transients of approximately 0.1 s. A nontapered shear coaxial injector without recess was evaluated. The injector baseline dimensions were as follows: The outer diameter was 3.9 mm, the LOX post i.d. was 1 mm, and the LOX post tip-wall thickness was 0.3 mm. Further details may be found in Mayer and Tamura.[3]

Table 1 Critical properties of various fluids

	He	H_2	O_2	N_2	C_2H_6O
P_{cr}, MPa	0.231	1.307	5.081	3.42	6.38
T_{cr}, K	5.25	33.25	154.58	126.05	516

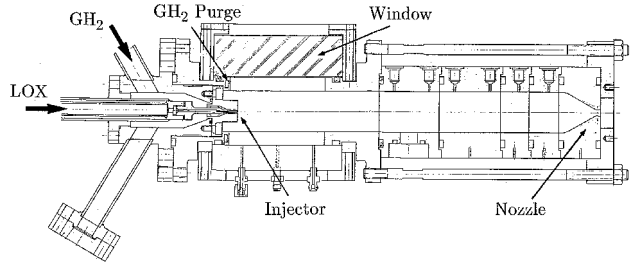

Fig. 1 Experimental LOX/GH_2 rocket combustion chamber with optical windows.

At low chamber pressures (2.0 MPa or less), flow-visualization studies were conducted with a standard camera and a flashlight in a shadowgraph and Schlieren setup. The typical shutter time was 1/60 s. A spark flashlight was used that had a typical pulse duration of less than 50 ns. The optical setup and filters were carefully selected and tested to determine the optimum between filtering propellant flame radiation and flashlight intensity losses.

The flame radiance increased dramatically at high chamber pressures. This required a special shadowgraph setup that included the need for a high-speed rotating disk shutter to be developed. The shutter speed was less than 1/1000 s. To filter the radiance of the flame an aperture was set between the combustion chamber and the camera lens. The light of the flash lamp was focused down to the aperture of the lens and was therefore not parallel. Thus, density gradients were visible when using this technique.

Test Conditions

The firing test conditions covered in this study were as follows: A chamber pressure of 1.0–10.0 MPa, an oxygen (O_2) injection velocity of 10–30 m/s, an O_2 injection temperature of 100 K, an H_2 injection velocity of 300 m/s, and an H_2 hydrogen injection temperature of 150–300 K.

Hot-fire tests with a nonrecessed coaxial injector at chamber pressures P_c of 1.5, 4.5, 6.0, and 10.0 MPa were conducted as described by test cases 1–4 in Table 2. The corresponding O_2 and H_2 velocities (u_{LOX}, u_{GH_2}) were 30 and 300 m/s, respectively, except for test case 1, where the LOX velocity was reduced to 10 m/s. This velocity reduction was necessary because the atomization and mixing efficiency at a chamber pressure of 1.5 MPa was so low that otherwise a large part of the LOX jet and ligaments would leave the chamber unburned and could not be visualized. The LOX temperature T_{LOX} was 100 K and the H_2 temperature T_{GH_2} was 300 K.

Results

Figure 2 shows shadowgraphs of the LOX jet taken at a subcritical pressure of 1.5 MPa (test case 1). At chamber pressures much less than the critical pressure of O_2, the LOX jet was atomized into a conventional spray. Following an initially

Table 2 Test case conditions

Test case	p_c, MPa	u_{LOX}, m/s	u_{GH_2}, m/s	T_{LOX}, K	T_{GH_2}, K
1	1.5	10	300	100	300
2	4.5	30	300	100	300
3	6.0	30	300	100	300
4	10.0	30	300	100	300

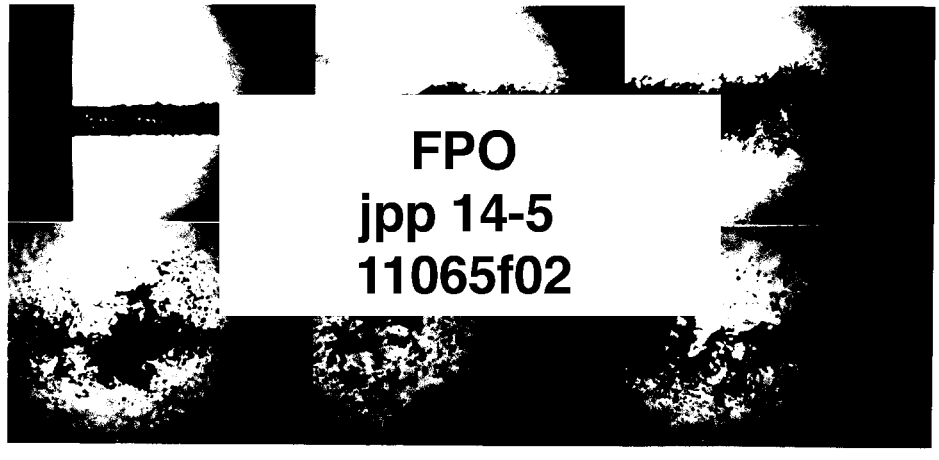

Fig. 2 Burning LOX jet at a subcritical pressure of 1.5 MPa (test case 1). Axial positions are x = 0 (faceplate), 12, 24, 36, 48, and 60 mm, from left to right and top to bottom.[3]

very smooth appearance of the jet surface close to the injector, ligaments formed and detached from the jet surface. These broke down into mostly nonspherical droplets that eventually evaporated. Secondary droplet breakup was also observed of the vibrational and bag types.

Figure 3 shows a comparison between cold-flow and hot-fire results that demonstrates the effect of the flame on the spray. The chamber pressure was the same as in Fig. 2: 1.5 MPa in both cases. Fine oxidizer ligaments and droplets were visible in the cold-flow, but not in hot-fire. The presence of the flame evidently vaporized such structures rapidly, leading to a significantly lower droplet number density. In fact, no droplets can be observed at all in the hot-fire visualization of Fig. 3. The smoothness of the round jet that can be seen in hot-fire can be attributed in part to rapid vaporization of the surface wave structures, but also to a considerable reduction in aerodynamic forces between the LOX jet and the H_2, because of the reduction in the density of all the gases in the 3500 K hot reaction zone.

Upon approaching and exceeding the critical pressure, distortion of the optical field by the surrounding coaxial flame increased. Careful interpretation of the results was required. Sample results are shown in Fig. 4 for a supercritical pressure of 6.0 MPa (test case 3). Despite the distortion, little evidence could be found that any droplets existed. Instead, stringy or thread-like structures developed and grew; they did not detach but rapidly dissolved and faded away. The LOX core broke up several tens of jet diameters downstream into large lumps that dissolved in the same manner. The average jet breakup length decreased with increasing chamber pressure. It may be noted that mixing and combustion was not yet complete at the farthest axial distance visualized in Fig. 4.

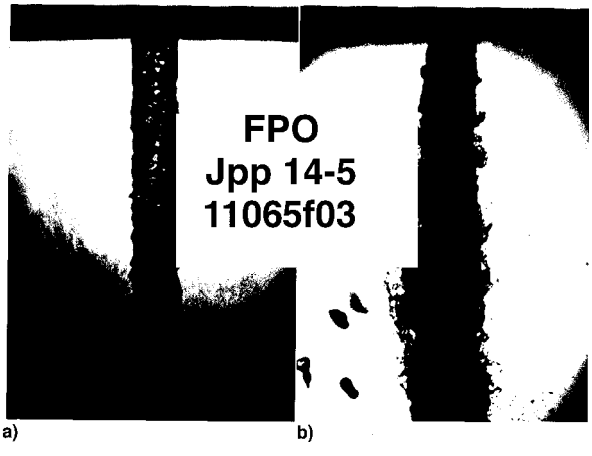

Fig. 3 Comparison of cold-flow and hot-fire visualizations at 1.5 MPa (test case 1): a) Burning after ignition and b) cold-flow before ignition.[3]

A very important result of this study was the observation of a LOX post wake flame and its interaction with the H_2/O_2 shear layer. This is illustrated in Fig. 5 for test case 2 (4.5 MPa). The photograph in Fig. 5a was taken with a standard shadowgraph setup and allows visualization of the LOX/hydrogen flame. To filter out the flame radiation, the photograph in Fig. 5b was taken by focusing the flash lamp through the lens aperture as described earlier, creating nonparallel rays allowing density gradients to be visible. The flame always attached instantaneously to the LOX post after ignition. A bright flame spot observed close to the LOX post tip suggests that a well-mixed flame with strong radiation was anchored in an intensive recirculation zone. This could be observed over the entire range of test conditions, for injectors with and without recess, and for a LOX post tip thickness of only 0.3 mm. The well-mixed flame then functioned as a flameholder for the rest of the flame. The LOX post wake could be tracked at least 15 LOX jet diameters downstream and significantly influenced the layer of reacting gases.

The influence of H_2 injection temperature on mixing performance near the injector was also studied over the temperature range of 150–300 K. Two chamber pressures of 6.0 and 10.0 MPa were selected for comparison, with O_2 and H_2 injection velocities kept constant at 30 and 300 m/s, respectively. Because of the marginal, though not exactly known, value of the surface tension, the Weber number did not seem to be an appropriate parameter to characterize the mixing process. Assuming mixing is controlled by the momentum ratio, and assuming this was controlled by the fuel stagnation pressure because the LOX momentum was almost constant in this study, it was expected that a decreased H_2 injection temperature would lead to an increased H_2 density that would intensify the mixing process. However, varying H_2 temperature affected mixing to a smaller extent than the overall chamber pressure. Increasing the chamber pressure also increases the H_2 density, and this turned out to have a larger effect on mixing than the H_2 temperature. Futher details of this study may be found in Mayer and Tamura.[3]

Cold-Flow Jet Studies

Although lacking the realism of combustion, cold-flow studies provide the opportunity to visualize atomization and breakup processes without the optical distortions that combustion introduces. Cold-flow studies have been performed at full scale,[4] where injector sizes and flow rates are similar to those in actual applications, and also using smaller, subscale elements and flows.[5] Recent results are summarized next.

Fig. 4 Burning LOX jet at a supercritical pressure of 6.0 MPa (test case 3). Axial positions are x = 0 (faceplate), 12, 24, 36, 48, and 60 mm, from left to right and top to bottom.[3]

Full-Scale Studies

LN_2 and GH_2 or gaseous helium (GHe) were used as simulants in cold-flow studies using the test apparatus illustrated in Fig. 6.[4] The pressure was kept constant (up to 6.0 MPa), independent of the injected mass flow. The temperatures of the injected fluids were measured close to the injector exit. The LN_2 injection temperatures reached as low as 90 K, whereas the GHe and GH_2 temperatures ranged between 100 and 370 K. The study covered a range of injection conditions and injector geometries. Quantitative measurements of time and length scales were obtained using flashlight photography and high-speed cinematography (30 kHz), and qualitative measurements of species distributions were obtained using Raman spectroscopy. Flow regimes were expressed in terms of appropriate dimensionless numbers such as the Weber number ($We = u_{rel}^2 \rho_g D_{jet}/\sigma$), and liquid and gas Reynolds numbers.

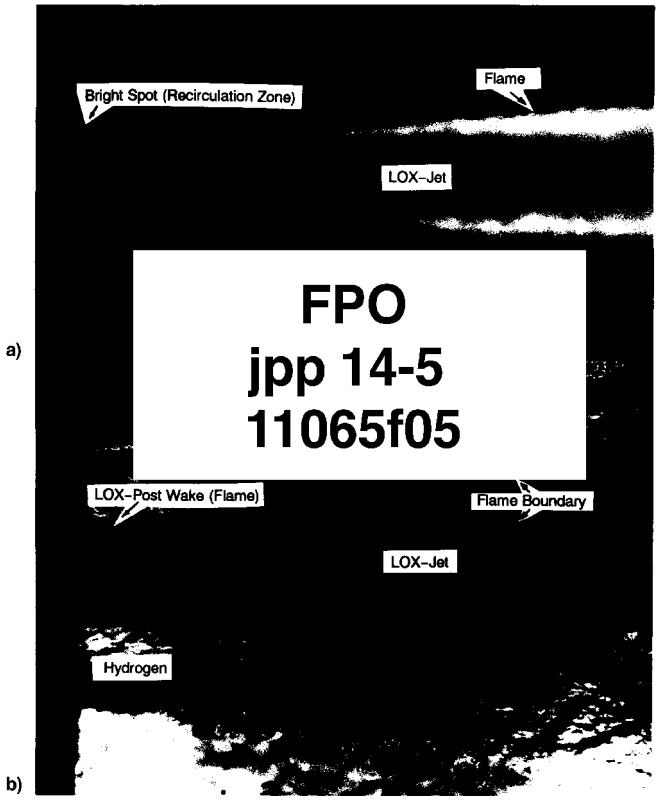

Fig. 5 Near injector region for a supercritical pressure of 4.5 MPa (test case 2): a) Flame and b) corresponding flowfield.[3]

Figure 7 shows the injection of LN_2 at 97 K with coaxially flowing helium (He) at 280 K into GHe at 300 K, at backpressures of 1.0 and 6.0 MPa. In this figure, the LN_2 injection velocity was 10 m/s, the GHe velocity was 100 m/s, the initial LN_2 diameter was 1.9 mm, and the GHe annular gap thickness was 0.2 mm. The formation of ligaments and the detachment of droplets from them can be seen at 1.0 MPa, but not at 6.0 MPa. Mixing in the latter case is more like that between a dense and a light fluid in a turbulent shear layer. At Reynolds numbers exceeding 1×10^4 and for pressures higher than 70% of the critical pressure, the structure of the interface was dominated by turbulence at reduced surface tension, and did not depend on whether the pressure was supercritical or subcritical.

Figure 8 shows injection behavior in a pure N_2 system in the absence of He, where mixture effects on the critical properties are absent. LN_2 was injected at 105 K and a velocity of 1 m/s into warm N_2 at 300 K at chamber pressures of 2.0, 3.0, and 4.0 MPa. The injector diameter was 1.9 mm. At the subcritical pressure of 2.0 MPa, the jet surface is smooth and clearly identified with large-scale disturbances. At 3.0 MPa, which is 0.4 MPa below the critical pressure, the jet looks quite different. Because of the reduced surface tension, small-scale turbulent structures are able to disturb the interface and even leave the jet in the form of droplets. At the supercritical pressure of 4.0 MPa, the surface changes into a streaky interface. The cross section of the jet increases with the downstream distance like a gaseous jet. The state of the injected N_2 changes from a liquid to a dense fluid with rising pressure. The atomization mechanism seems to change considerably in the absence of surface tension. As ambient pressure is increased with surface tension present, the length scales of breakup (ligament and droplet diameters) decrease. As surface tension drops further below a certain limit, the atomization mechanism changes to one of a shear-layer instability. Observable length scales become larger.

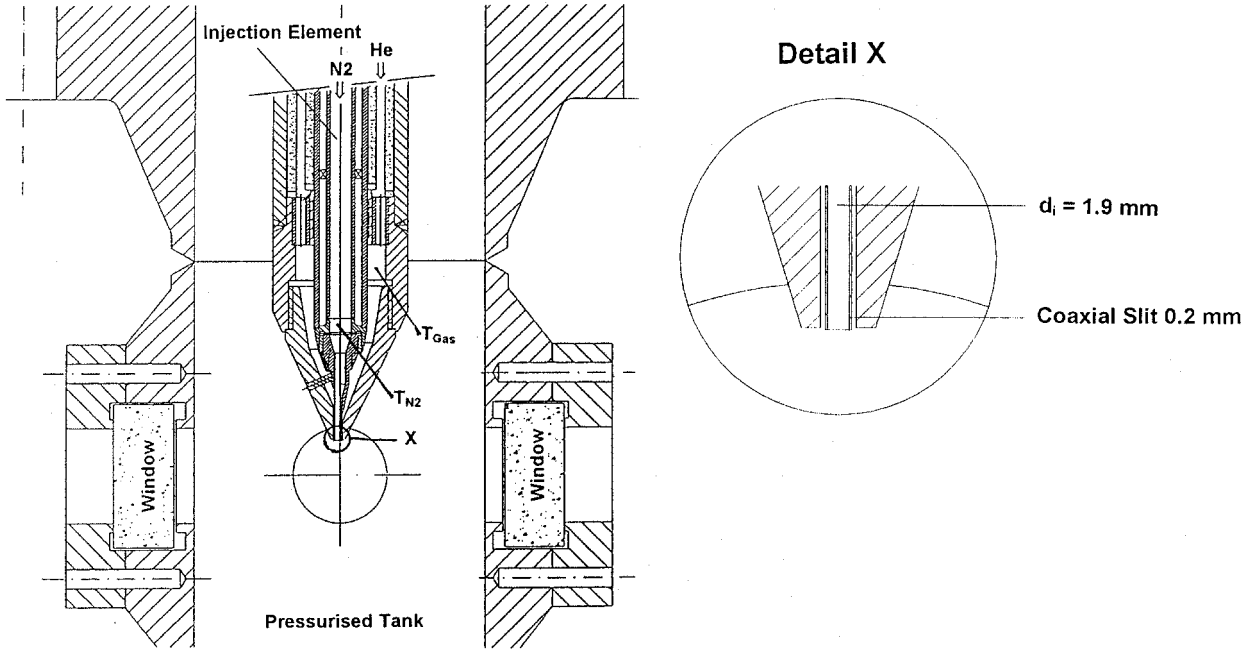

Fig. 6 Test chamber for full-scale cold-flow studies.

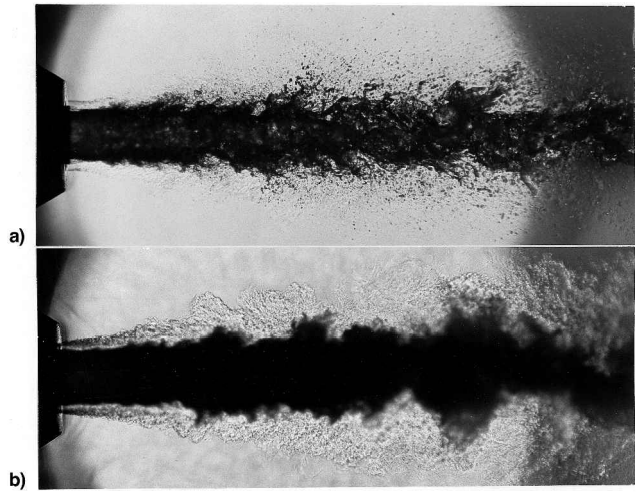

Fig. 7 Coaxial LN_2/GHe injection at a) 1.0 and b) 6.0 MPa.

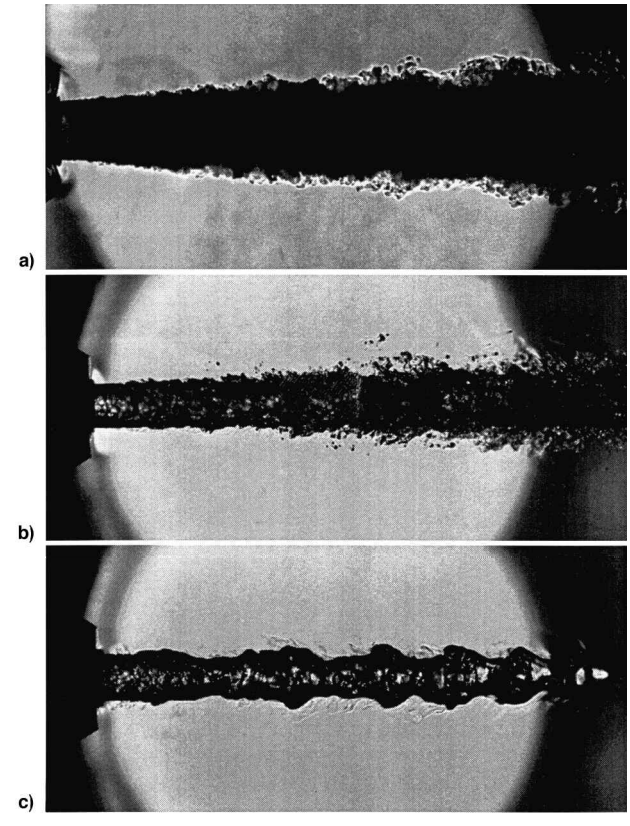

Fig. 8 LN_2 injection into GN_2 at a) 4.0, b) 3.0, and c) 2.0 MPa.

Subscale Studies

Subscale cold-flow studies with smaller injector dimensions than in actual applications have been performed to further reduce optical distortions and better resolve the details of the fluid interfaces.[5] Experimental results for subscale round LN_2 jets injected into GHe/GN_2 mixtures are shown in Fig. 9 at various pressures for an injector diameter of 0.25 mm, a LN_2 temperature of 90 K, a chamber temperature of 250 K, and an injection velocity of 1.3 m/s. In Fig. 9 the horizontal rows (1)–(3) correspond to different axial locations in this figure, whereas the vertical columns (9a–9d) correspond to different experimental conditions. Shadowgraph images of LN_2 jets into pure GN_2 are shown in Figs. 9a–c, for subcritical (Fig. 9a), near critical (Fig. 9b), and supercritical (Fig. 9c) pressures. The effect of pressure (and thus fluid state) on mixing is quite drastic, with jets in Figs. 9b and 9c exhibiting a laminar liquid-like appearance near the orifice and a turbulent gas-like appearance farther downstream. A small sheet of fluid can be seen emanating from the side of the jet in Fig. 9b (row 1) and 9c (row 1) as a result of a small imperfection in the orifice, but the sheet is not present in Fig. 9a (row 1). Surface tension is evidently large enough to prevent the formation of this sheet at the subcritical pressures in Fig. 9a (row 1), whereas it is not sufficient to do so at the near- and supercritical pressures Figs. 9b (row 1) and 9c (row 1). This is despite the fact that density gradients at the interface in Fig. 9b (row 1) and Fig. 9c (row 1) remain large enough to cause a liquid-like appearance. For Fig. 9d, the pressure was kept at twice the critical pressure of pure N_2, as in Fig. 9c, but He was added to the ambient in 9d to a GN_2/GHe ratio of 3.9 by mass. Liquid-like structures exhibiting evidence of surface tension are shown to be recovered because of the mixture effects involved in adding He.

Figure 10 depicts another series of shadowgraph images of LN_2 jets injected this time into GHe at chamber pressures of 5.5, 6.9, and 8.3 MPa. The jet velocity was 1.7 m/s, the LN_2 temperature was 83 K, and the chamber temperature was 292 K. In Fig. 10b, surface tension apparently still dominates the jet breakup dynamics. After initial jet breakup, no spherical structures are formed. Unsteady aerodynamic forces cause many irregular shapes as interfacial tension is too weak to reshape the fluid into spheres. Figure 10c reveals a marked change in the nature of the jet structure. Although what appear to be interfacial features continue to be observed, any remnants of surface tension playing a role in the jet disintegration appear to have vanished. Injection under these latter conditions is seemingly more characteristic of a turbulent, viscous gas jet. Jet structure is characterized by wispy structures barely, if at all, retained by interfacial forces. Thin threads of fluid, undisturbed by surface tension forces, are able to connect larger blobs until aerodynamic forces perturb them. Consistently, no structures suggestive of surface discontinuities are observed downstream of position 2, indicating an advanced state of mixing, though not necessarily complete. Surface tension apparently ceases to be important in the jet disintegration process somewhere between 5.5 and 6.9 MPa (1.6–2.1 times the critical pressure of pure N_2), for the particular conditions of this N_2/He system, as witnessed in the upper part of the jet. However, one might question why the LN_2 jet in Fig. 9d, injected into the N_2/He mixture at 6.9 MPa, exhibits jet behavior indicative of a subcritical liquid state, whereas the jet in Fig. 10b in pure He at the same pressure exhibits behavior indicative of a supercritical state. The answer is probably related to the relatively small differences in jet and ambient temperatures and jet velocities. Figure 11 depicts a LN_2 jet injected into He at the low-pressure end of this transition range, 5.5 MPa. Jet and ambient conditions are the same as in Fig. 10b. In this sequence of images recorded at identical injection conditions, an oscillation between gas-like and liquid-like jet behavior can be seen. These examples illustrate that under certain conditions the nature of the jet breakup process can be extremely sensitive to small perturbations in pressure, temperature, local mixture concentrations, and initial jet conditions. In application, the oscillation in the jet breakup behavior could lead to local propellant mixture ratio oscillations and conceivably unstable combustion behavior.

Single Droplet Studies

Single droplet processes provide even more opportunity to clearly visualize simple flows and are themselves important processes in combustion. Studies of single cryogenic droplets at high pressures have been undertaken under both subcritical[9,10] and transcritical conditions. The transcritical results are reported herein for the first time.

High-Pressure Subcritical Droplet Studies

Breakup regimes of subcritical cryogenic LOX droplets subject to aerodynamic shear forces were investigated for various

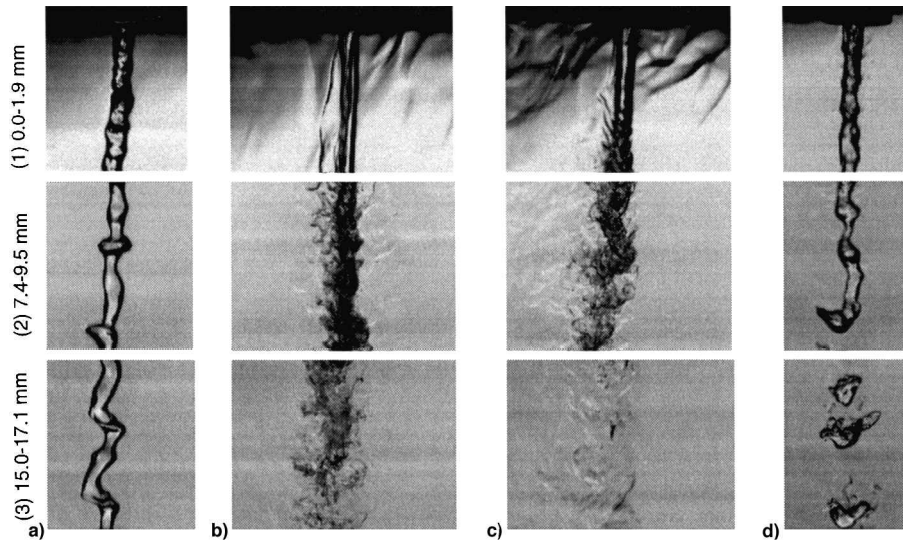

Fig. 9 Subscale LN_2 injection into a pressurized chamber. Horizontal rows correspond to distance from the injector tip. Vertical columns correspond to different experimental conditions as follows: a) Into subcritical N_2 at 2.8 MPa, $p/p_{crit} = 0.83$; b) into near critical N_2 at 3.5 MPa, $p/p_{crit} = 1.03$; c) into supercritical N_2 at 6.9 MPa, $p/p_{crit} = 2.03$; and d) into a $N_2/O_2 = 3.9$ mixture at 6.9 MPa, $p/p_{crit} = 2.03$.

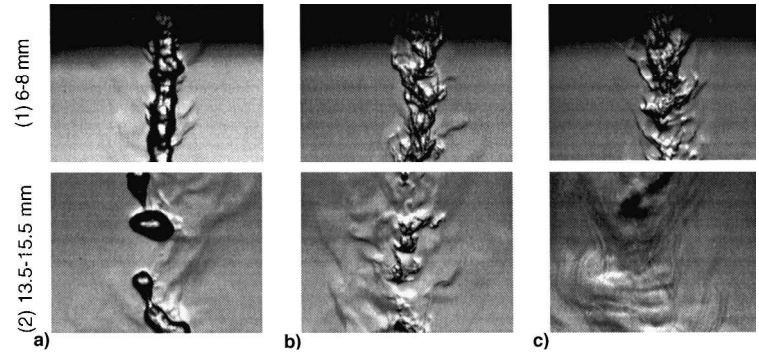

Fig. 10 LN_2 jets injected into He at elevated pressures.

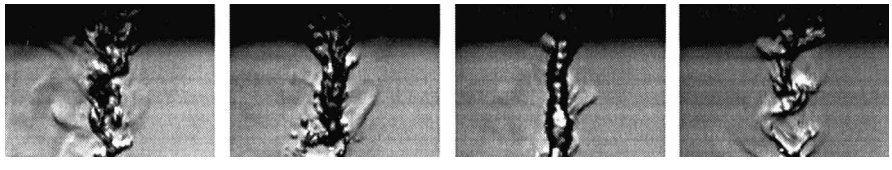

Fig. 11 Image sequence of LN_2 jets injected into He at 5.5 MPa reveals oscillation between liquid-like and gas-like behavior.

droplet Reynolds numbers, Weber numbers, and liquid-to-gas density ratios.[9] Single droplets were vertically injected into the potential core region of a horizontal 300-K dry airjet in a pressure vessel capable of sustaining pressures up to 12.0 MPa. This allowed for the investigation of droplet behavior at lower density ratios than has previously ever been examined. Flow and turbulence characteristics of the jet were determined by two-component laser Doppler anemometry, and the droplets were visualized using rapid video imaging and numerical image analysis.

LOX droplets with diameters between 600 μm and 1.0 mm were studied over a pressure range of 0.1–4.0 MPa for jet velocities ranging from 0.4 to 86 m/s. The corresponding maximum values of the droplet Weber number ($We = u_{rel}^2 \rho_g D/\sigma$), Reynolds number ($Re = \rho_g u_{rel} D/\mu_g$), and Ohnesorge number [$Oh = \mu_g/(\rho_g D\sigma)^{1/2}$] were 800, 7500, and 0.01, respectively. The liquid-to-gas density ratio varied between 20 and 1040. The surface tension changed significantly over this pressure range, decreasing from 13.6×10^{-3} N/m at 0.1 MPa to 4.97×10^{-3} N/m at 3.0 MPa. The enthalpy of vaporization also decreased significantly as pressure increased, which reduced global gasification times. Four droplet-jet interaction regimes are illustrated in Fig. 12 corresponding to deformation, bag, transitional, and shear breakup regimes.

To better isolate the effects of vaporization and reduced surface tension from the effect of changing density ratio, ethanol droplets were also studied (see Table 1). The ethanol droplets vaporized much more slowly than the LOX droplets, and the surface tension changed by only about 10%, from 22.8×10^{-3} at 0.1 MPa to 20.0×10^{-3} at 3.0 MPa. In the ethanol experiments, the pressure was varied from 0.1 to 5.0 MPa, and the corresponding liquid-to-gas density ratio varied between 16 and 800. The maximum droplet Weber number was 90, and the maximum droplet Reynolds number was 1.6×10^4. The droplet Ohnesorge number was less than 0.02 for all cases. The diameters of ethanol droplets were kept at 600 μm.

A comparison between the results obtained for the ethanol and LOX experiments is presented in Fig. 13 for a pressure of 3.0 MPa. Transition droplet Reynolds numbers are observed to be much higher for the ethanol droplets. For example, the shear breakup regime was attained at a droplet Reynolds number of 4×10^3 for LOX droplets but at a droplet Reynolds number of 1.2×10^4 for the ethanol droplets. Because of the reduced surface tension of the LOX, the same droplet Reyn-

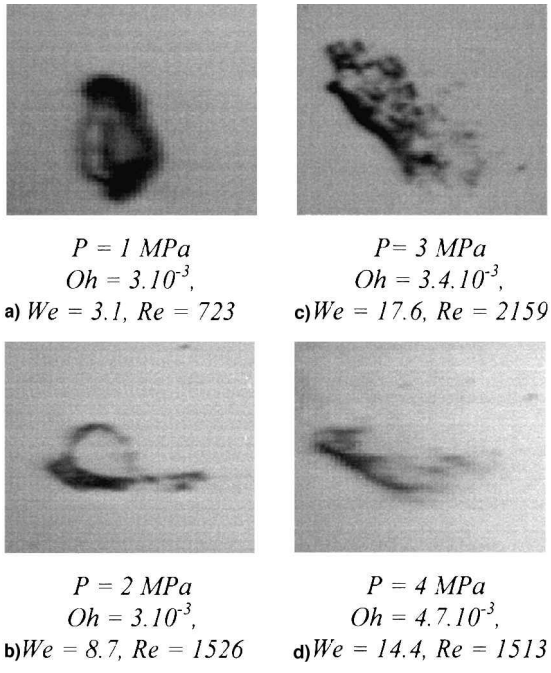

Fig. 12 Droplet breakup regimes for LOX droplets: a) Deformation, b) bag, c) transitional, and d) shear.

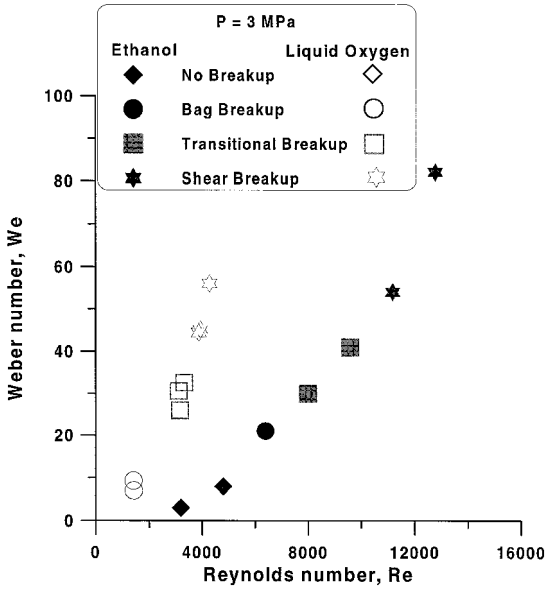

Fig. 13 Comparison of the deformation and breakup regimes between ethanol and LOX droplets.

olds numbers produce higher droplet Weber numbers than the ethanol droplets. As a result, higher breakup regimes are attained with smaller aerodynamic forces. It is important to note that the variations in droplet Reynolds numbers in Fig. 13 were obtained entirely by varying the airjet velocity. All other physical parameters remained constant, including densities, droplet diameter, and dynamic viscosity.

Breakup initiation times were another important feature that was determined for LOX droplets at various pressures. Experimental initiation and total breakup times, normalized by $(D/V)(\rho_l/\rho_g)^{1/2}$, are shown in Fig. 14 for LOX droplets at 4.0 MPa. The breakup initiation time was defined as the time delay between the exposure of the droplet to the aerodynamic shear forces and the first clear observation of the corresponding breakup regime (bag, transitional, or shear). The total breakup time was defined as the time delay from the entry of the droplet into the airjet to the end of the deformation and breakup processes undergone by all of the droplets.[10] As shown in Fig. 14, total breakup times increased with Weber number, but initiation times decreased. These opposite trends mean that drop deformation and breakup occur sooner but last longer as the Weber number is increased.

Transcritical Droplet Studies

A unique droplet generator for producing transcritical LOX and LN_2 droplets was constructed. The generator was mounted in a 13.7-MPa pressure vessel having two 133.4-mm sapphire windows for observation. High-pressure gaseous O_2 or N_2 was condensed in a central tube by an atmospheric pressure LN_2 bath. A piezoelectric crystal inside the tube provides acoustic excitation for forming the droplets. The droplets are created in a flow of GHe chilled to the same temperature as the droplets. The He provides a molecular weight difference to provide a surface for forming the droplets. The helium flows through a converging–diverging section with the drop generator located near the throat. This allows aerodynamic stripping to also be used to produce droplets. In the pressure vessel, He forms a buoyant layer and the droplets fall into warm test gas of interest, for example, N_2/He mixtures.

A representative shadowgraph of the results is given in Fig. 15. LOX droplets having an initial temperature of 177 K were produced in a chilled helium coflow of about the same temperature and fell into a pure GN_2 gas at a pressure of 6.6 MPa and a temperature of 290 K. N_2 gas was used in the pressure vessel instead of O_2 gas for safety reasons and because N_2 has very little effect on the critical properties of O_2. The increasing panel numbers in Fig. 15 correspond to increasing distances downstream. The 0.254-mm wire visible in panel 1 was in-

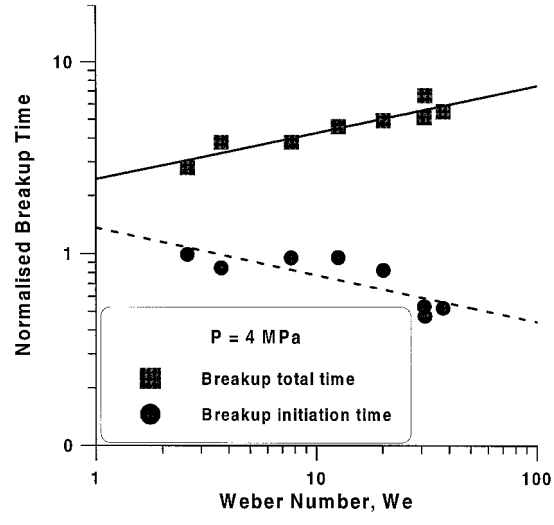

Fig. 14 Comparison between breakup initiation and total breakup times at 4.0 MPa for LOX droplets.

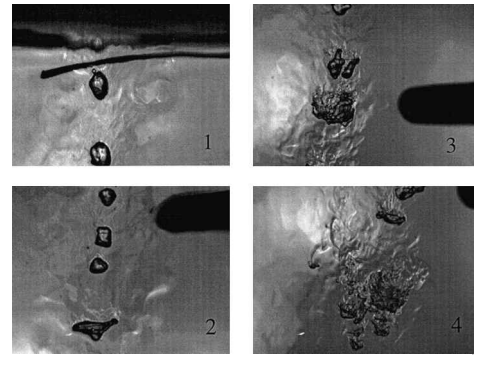

Fig. 15 Transcritical LOX droplets falling into GN_2. Increasing panel numbers correspond to increasing distances downstream.

serted behind the droplet stream as a size reference and also to provide an indication of the degree of optical distortion. Panel 1, which exhibited very low distortion, provides a good indication of the shape of the reference wire, which was not straight. The dark shadows visible in the images are 1.6-mm thermocouples. A buoyant He layer was formed at the top of the pressure vessel that extends just below the bottom of panel 1. The fluids seen in panels 2–4 are largely N_2 and O_2. A slow N_2 "wind" is flowing from right to left in these images. Thus, the smooth gray areas to the right of the panels are N_2 and the lighter-colored turbulent areas to the left are in the droplets' wake and are N_2/O_2 mixtures.

Quantitative results have not yet been obtained, but qualitatively it was observed that the droplets exhibited no resistance to deformation and, therefore, no evidence of surface tension once they dropped below the He layer. An inverse bag shape can be seen in panel 2, and in panel 4 such shapes are seen to be joined by "tails" in a mushroom shape that are often observed. Various-sized globs of fluid break off at unpredictable times and spread, contributing to the mixing. Cellular structures can be observed in panel 3, but it is unclear whether this is because of an instability or simply a response to turbulence. Further efforts are underway to quantify these effects as a function of various parameters.

Summary and Conclusions

Recent results on the atomization and breakup of cryogenic propellants under high-pressure subcritical and supercritical conditions have been reviewed. The work ranged from studies of the principal character of coaxial flow to detailed investigations of ligament and drop breakup and mixing.

All of the experiments show that as pressure is increased, fluids eventually reach a transcritical regime where breakup and mixing are no longer influenced by surface tension. Subsequently, the fluids behave more like viscous miscible fluids. The pressure at which the transition occurs is a strong function of the ambient composition and initial conditions, and cannot be deduced from the critical pressure of the pure species alone. Strong convection effects may make precise identification of the transition pressure impossible.

The hot-fire tests revealed that a flame was always attached to the LOX post, and the interface between the propellants is separated by a layer of hot reacting gas. At very low pressures, the LOX jet exhibits a smooth surface and breaks up into a small number of nonspherical droplets that evaporate rapidly. At transcritical pressures the LOX jet develops stringy fluid structures that rapidly dissolve. Further downstream the jet develops nonaxisymmetric snake-like oscillations of growing amplitude until it breaks up. Large lumps of O_2 were visualized several tens of jet diameters downstream. This "heavy mixing zone" is characterized by large-scale turbulence, maximum amplitudes of O_2 jet oscillations, a slight widening of the O_2 jet and of the flame, dispersion of the O_2 ligaments, and the strongest combustion radiation.

Studies of LOX droplet breakup under high-pressure subcritical conditions near the critical pressure show that breakup initiation times decrease but that the total breakup time increases as the droplet Weber number increases. A comparison between the LOX droplets and ethanol droplets under similar conditions, where the LOX droplets had lower surface tension than the ethanol droplets, showed that transition to higher breakup regimes occur at larger droplet Reynolds numbers for the enthanol droplets. As pressures increase into a transcritical regime, no indication of surface tension was found and the droplets were incapable of resisting deformation. Random clumps of fluid broke off at unpredictable times, which may enhance the mixing.

Acknowledgments

The work done at DLR Lampoldshausen was supported by Deutsche Agentur für Raumfahrtangelegenheiten; the work at the U.S. Air Force Research Laboratory was supported by the U.S. Air Force Office of Scientific Research; and the work at Laboratoire de Combustion et Systèmes Réactifs, Orleans, France was supported by the joint CNRS/CNES/SEP program on Combustion in Cryogenic Rocket Motors.

References

[1]Immich, H., and Mayer, W., "Cryogenic Liquid Rocket Engine Technology Developments Within the German National Technology Programme," AIAA Paper 97-2822, July 1997.

[2]Mayer, W., "Coaxial Atomization of a Round Liquid Jet in a High-Speed Gas Stream: a Phenomenological Study," *Journal of Experiments in Fluids*, Vol. 16, No. 6, 1994, pp. 401–410.

[3]Mayer, W., and Tamura, H., "Propellant Injection in a Liquid Oxygen/Gaseous Hydrogen Rocket Engine," *Journal of Propulsion and Power*, Vol. 12, No. 6, 1996, pp. 1137–1147.

[4]Mayer, W., Schik, A., Schweitzer, C., and Schäffler, M., "Injection and Mixing Processes in High-Pressure LOX/GH2 Rocket Combustors," AIAA Paper 96-2620, 1996.

[5]Woodward, R. D., and Talley, D. G., "Raman Imaging of Transcritical Cryogenic Propellants," AIAA Paper 96-0468, 1996.

[6]Yang, V., Lin, N. N., and Shuen, J. S., "Vaporization of Liquid Oxygen (LOX) Droplets in Supercritical Hydrogen Environments," *Combustion Science and Technology*, Vol. 97, 1994, pp. 247–270.

[7]Delplanque, J.-P., and Sirignano, W. A., "Numerical Study of the Transient Vaporization of an Oxygen Droplet at Sub- and Supercritical Conditions," *International Journal of Heat and Mass Transfer*, Vol. 36, 1993, pp. 303–314.

[8]Oefelein, J. C., and Yang, V., "Simulation and Analysis of Supercritical Multiphase Combustion Processes," AIAA Paper 96-2880, 1996.

[9]Chesneau, X., Chauveau, C., and Gökalp, I., "Experiments on High-Pressure Vaporization of Liquid Oxygen Droplets," AIAA Paper 94-0688, 1994.

[10]Vieille, B., Chauveau, C., and Gökalp, I., "Droplet Breakup Regimes Under High-pressure Conditions," *Proceedings of the 13th Annual Conference on Liquid Atomization and Spray Systems* (Florence, Italy), 1997, pp. 195–201.

[11]Vieille, B., Chauveau, C., and Gökalp, I., "Droplet Break-Up Regimes of LOX Droplets Under High-pressure Conditions," AIAA Paper 98-0715, Jan. 1998.

[12]Anderson, T., Woodward, R. D., and Winter, M., "Oxygen Concentration Measurements in a High-pressure Helium Environment Using Raman Imaging," AIAA Paper 95-0140, Jan. 1995.

Color reproductions courtesy of DLR, German Aerospace Research Center.

APPENDIX G

"Fractal Geometry and Growth Rate Changes of Cryogenic Jets Near the Critical Point"

A99-31260

AIAA 99-2489

Fractal Geometry and Growth Rate Changes of Cryogenic Jets Near the Critical Point

B. Chehroudi[*], *D. Talley, and E. Coy*

Air Force Research Laboratory
Propulsion Directorate
10 E. Saturn Boulevard
Edwards AFB, CA 93524-7680

35th AIAA/ASME/SAE/ASEE Joint Propulsion Conference and Exhibit
20–24 June 1999
Los Angeles, California

AIAA 99-2489

Fractal Geometry and Growth Rate Changes of Cryogenic Jets Near the Critical Point

B. Chehroudi[*], *D. Talley, and E. Coy*

Air Force Research Laboratory; AFRL/PRSA
10 E. Saturn Boulevard
Edwards AFB, CA 93524-7680

Abstract

A high pressure chamber with a variety of ambient fluids is used into which pure N_2 , He, and O_2 fluids are injected. The effects of chamber pressure (density) ranging from the thermodynamic subcritical to supercritical values at a supercritical chamber temperature are observed by acquisition of shadow images from the injector exit region using a CCD camera illuminated by short-duration light pulses. At sufficiently low subcritical chamber pressures, the jet interface disturbances amplify and eventually break up downstream into irregularly-shaped small entities. Increasing the chamber pressure causes the formation of many small ligaments and droplets on the surface of the jet only within a narrow regime below the thermodynamic critical pressure of the injected fluid, resembling a second wind-induced liquid jet breakup. At even higher chamber pressures, near but below the critical pressure of the injectant, the expected transition into a full atomization regime to produce a liquid spray is inhibited due to sufficient reduction of both the surface tension and the heat of vaporization. The jet appearance changes abruptly at this pressure and resembles a turbulent gas jet injection for all higher chamber pressures. The jet initial growth rate is plotted together with available data on liquid fuel injection in diesel engine environments, and turbulent incompressible, supersonic, and variable-density jets and mixing layers. The resulting plot is unique on its own right. At near- and super-critical pressures, the present measurements agree well with theoretical growth rate equations proposed *by Brown [1]/Papamoschou and Roshko [2]* and *Dimotakis [3]* for incompressible but variable-density turbulent mixing layers. This constitutes the first quantitative evidence in support of qualitative observations that the jet appears to evolve into a gas-like behavior. The geometry of the jet interface has also been examined for the first time by fractal analysis. The results clearly indicate a transition from a Euclidean to a fractal interface, with a fractal dimension close to values measured for gaseous turbulent jets. This provides additional quantitative evidence for the hypothesis that the jet evolves into a gas-like behavior. Finally, an "intuitive/smart" equation is proposed that agrees well with the experimental growth rate data, based on a proposed physical mechanism and characteristic gasification times and interfacial bulge formation/separation times.

Introduction

In designs of chemical rocket engines, liquid fuel and oxidizer are often injected as round jets, for instance coaxial or impinging types, into the hot and elevated-pressure environment of the thrust chamber. Higher specific impulse is a major motivation for operating rocket thrust chambers at progressively higher pressures. Conditions therefore exist in which the injected liquid finds itself near or even above the thermodynamic critical condition. Examples are Space Shuttle main engine and Vulcain (Ariane 5) with liquid H_2/liquid O_2. More information is needed on liquid jets injected into supercritical condition. This was the motivation for establishing an organized and systematic experimental investigation on liquid jet injection under such conditions.

Major changes occur in some important properties of a pure substance as it approaches the thermodynamic critical point. For example, under thermodynamic equilibrium, the distinction between the liquid and gas phases disappears at and above the critical point and it is referred to as a "fluid". Also, large changes of density occurs near the critical point. The constant-pressure specific heat becomes very large and surface tension vanishes at and beyond the critical point. As ambient pressure is raised, the importance of the solubility of ambient gases into the injected liquid phase increases and one should consider multicomponent phase equilibrium information. For mixtures, the determination of the critical conditions, called the "critical mixing temperature or pressure", is complex, see *Bruno and Ely [4]* and *Lazar and Faeth [5]*. For example, when a pure liquid hudrocarbon fuel drop is introduced into nitrogen, a thin layer on its surface is a mixture of nitrogen and the fuel that spreads spatially in time, see *Umemura [6]*. In what follows, unless otherwise made clear, the terms subcritical and supercritical, and reduced pressure and temperature, are referenced with respect to the critical condition of the

pure substance used in drops or jets and not the environment nor the mixture therein.

There are a few works on liquid jet injection into a supercritical condition, notably *Newman and Brzustowski [7]* and *Mayer et al.[8], [9], Chen and Sui [19], and Birk and McQuaid [11]* at high Reynolds numbers and *Woodward and Talley [12]* at low Reynolds numbers. The major outcome of these works, summarized in *Chehroudi et al. [13],* is the realization of the visual and qualitative structural changes of the jet under supercritical condition as contrasted with the subcritical one. No experimentally-confirmed quantitative results addressing this issue has been offered.

In the following, the experimental arrangement is described, followed by presentation of results and discussion. The paper concludes with summary and conclusion section.

Experimental Setup

The stainless steel chamber in Fig. 1 can withstand pressures and temperatures of up to 137 atm (2000 psi) and 473 K, respectively, and has two facing circular sapphire windows and two UV-grade side-mounted slot-shaped quartz windows for optical diagnostics and laser illumination of the chamber. Transport of the liquid through the lines and the injector is achieved as shown in Figure 1. The liquid N_2 from a dewar is used to cool and/or liquefy the injectant passing through the cryogenic cooler prior to injection. In addition to N_2, a branch is connected for possibly introducing other gases or mixtures of gases as a chamber medium. The mass flow rate of the injectant is regulated and also measured via a mass flowmeter, and a precision micrometer valve. For more details refer to *Woodward and Talley [12]* and *Chehroudi et al. [13].* The injection in this study is through a sharp-edged 50 mm long stainless steel tube with a 1.59 mm (1/16") diameter and a 254 micron (0.010") inner hole (length-to-diameter ratio of 200). With the Reynolds number ranging from 25,000 to 70,000, the entrance length of 50 to 100 is needed for fully-developed turbulent flow, see *Schlichting [14].* The length is therefore long enough to ensure fully-developed turbulent pipe flow at the exit. The rig is fully instrumented with thermocouples, pressure gages, transducers, and mass flowmeters at the locations indicated in Fig. 1. Back-illumination and visualization using a model K2 Infinity long-distance microscope is used with a TM-745E high resolution (768(H) x 493(V) pixels in 8.8(H)x6.6(V) mm actual sensing area) interlaced CCD camera by PULNix to form images of the injected jets. For more details refer to *Chehroudi et al. [13].*

General Appearance of the Jet

At a constant mass flow rate, the exit N_2 temperature is measured to vary from 99 K to 110 K as reduced (chamber) pressure (P_r) changes from 0.23 to 2.74. This is due to changes in injected N_2 specific heat and density as chamber pressure is varied. This exit temperature is then used for calculations of the other jet property values.

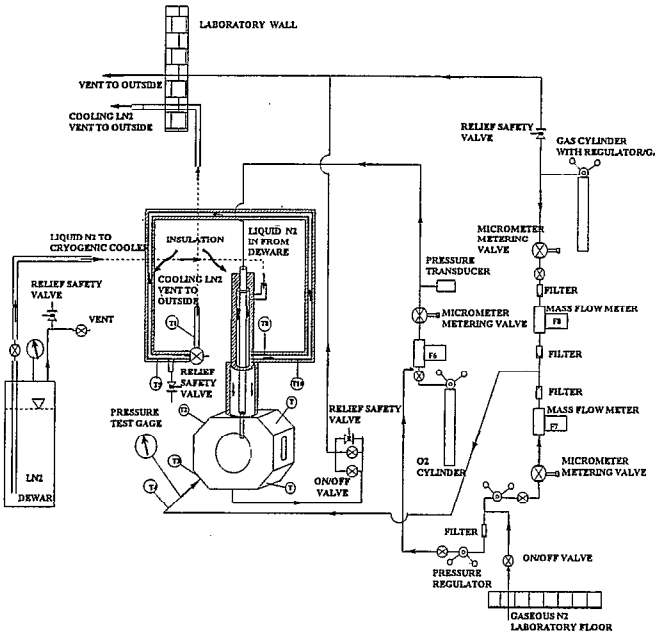

Figure 1. Schematic diagram of experimental setup for sub- to supercritical jet injection

Pictures presented here cover up to about 5.5 mm (axial distance/diameter ratio of 21.6) from the injector and the jet is momentum dominated in this region. It should be noted that in all the experiments where liquid nitrogen was injected into various gases, the initial jet temperature remained largely in the narrow range given above, and the ambient temperature also varied only narrowly around 300 K. Thus the temperature difference remained approximately constant at around 200 K in all the experiments. For more details refer to *Chehroudi et al. [13].*

Figure 2 shows images of the N_2 jet injected into N_2 at a constant supercritical chamber temperature but varying sub- to supercritical pressure. At the lowest subcritical chamber pressure the jet is liquid-like with surface instabilities that grow downstream. At P_r of 0.83 very fine drops are seen ejecting from the jet interface and the jet width grows downstream. At P_r of 1.03 the N_2 jet enters into a supercritical temperature and pressure environment and drastic structural changes are seen. In particular, no drops are detectable under this condition even with the highest magnification. There are thread- or finger-like entities emerging from the jet which are not broken up into droplets but are seemingly dissolved at a spectrum of distances from the jet dark core region. This forms a mixing layer in which phase transition and/or large local density nonuniformities occur. A further increase of chamber pressure decreases the length and the thickness of the internal dark core, see Fig. 2, and images

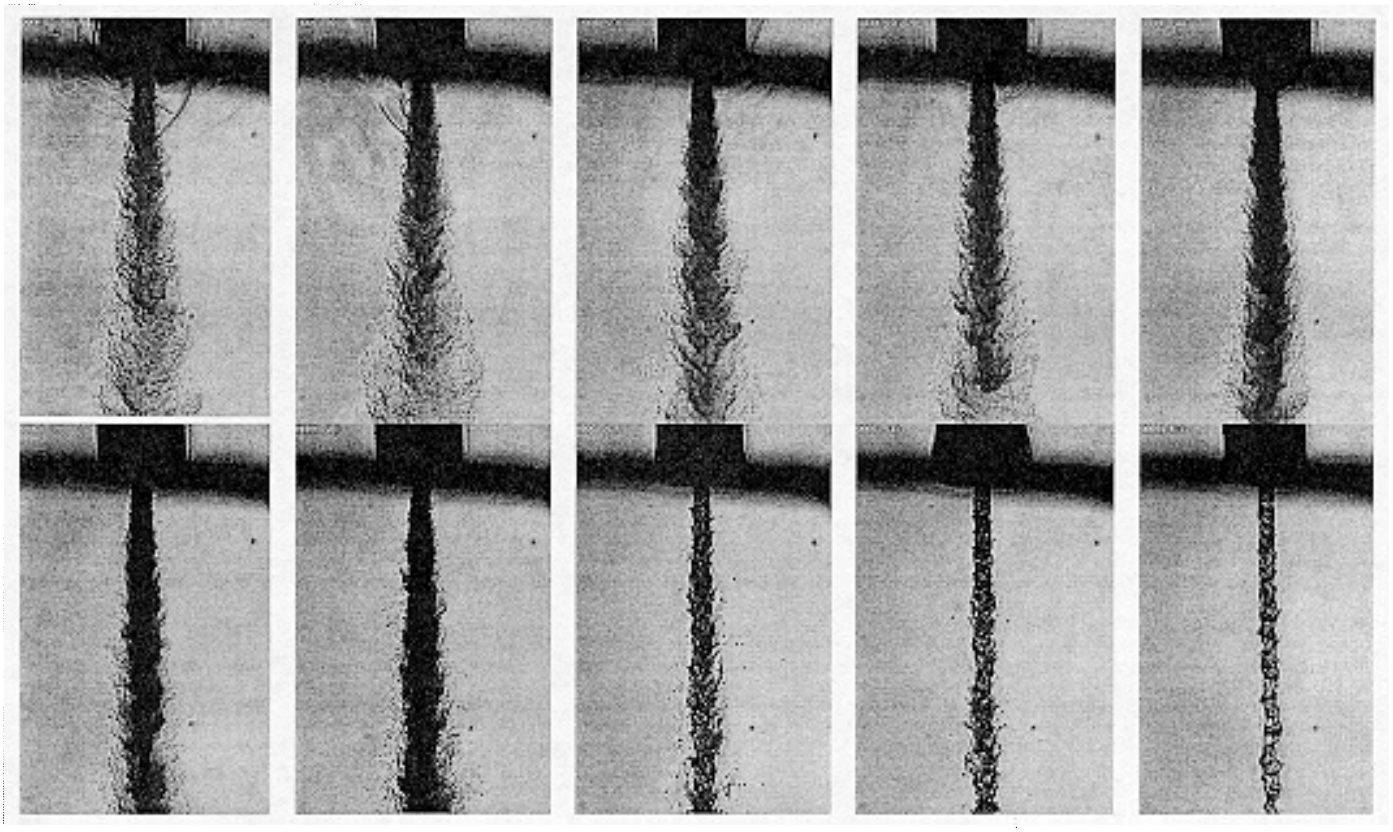

Figure 2. Back-illuminated images of nitrogen injected into nitrogen at a fixed supercritical temperature of 300 K but varying sub- to supercritical pressures ($P_{critical}$ = 3.39 MPa; T_c = 126.2 K). $P_{ch}/P_{critical}$= 2.74, 2.44, 2.03, 1.62, 1.22, 1.03, 0.83, 0.62, 0.43, 0.23; from upper left to lower right. Re= 25,000 to 75,000. Injection velocity: 10-15 m/s. Froud number: 40,000 to 110,000. Injectant temperature: 99 to 110 K.

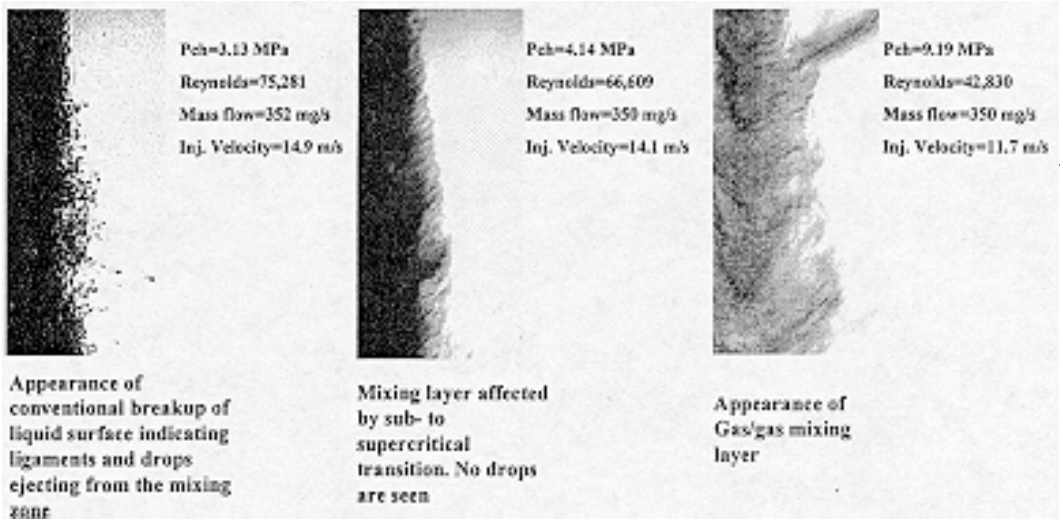

Figure 3. Software magnified images of the jet at its outer boundary showing transition to the gas-jet like-appearance starting at just below the critical pressure of the injectant. Images are at fixed supercritical chamber temperature of 300 K.

resemble injection of a gaseous turbulent jet into a gaseous environment. Figure 3 shows the magnified images of the mixing layer at three subcritical, transitional, and supercritical chamber pressures. A gradual transition from classical liquid-like ligament and drop formations at the interface, seen in the liquid atomization regime, to a comb-like structure near the critical point and finally to where a submerged turbulent gas jet appearance emerges can be observed. Similar observations are made for other injectant/ambient substances that were tested. Observation of the gas-like jet behavior and the lack of any drop formation raises question on relevancy of current injection models and some drop vaporization/combustion results within this regime.

Traditionally, the breakup and atomization regimes of liquid jets within a narrow chamber-to-density ratio range are shown on plots of Ohnesorge number versus Reynolds number (ignoring gas density and nozzle geometrical factors) or by a more refined criterion of *Reitz and Bracco [15]* in which chamber-to-injectant density ratio, nozzle geometrical factor, and Weber and Reynolds numbers are all included. In Fig. 2, as chamber pressure approaches the critical condition, surface tension is reduced to a near-zero value and for the range of Reynolds number calculated here (25,000 to 75,000), the Ohnesorge number sharply swings from a low (estimated to be 2.8×10^{-3}) to a very large (infinity when surface tension is zero) value. The large Ohnesorge number regime and its importance are indicated by *Faeth [16]* and *Tseng et al. [17]*. At the low Ohnesorge number in this work, the second-wind induced liquid jet breakup behavior is observed, similar to what is seen in Fig. 3. Past the second wind-induced behavior, it seems that before the jet has the opportunity for full atomization, the surface tension is sufficiently and rapidly reduced so one achieves a gas-like jet appearance near but before reaching the critical pressure, see Fig. 2. The aforementioned threads or fingers are gasified and drops are no longer detected. Transition into a full atomization regime is therefore inhibited. The investigated jet exhibits liquid-jet like and gas-jet like features depending on the magnitudes of the surface tension and heat of vaporization. Approximate characteristic time estimates made by *Chehroudi et al. [13]* also point towards the inhibition of transition to the atomization regime.

Jet Growth Rate

The spreading angle or growth rate in our work are measured from the information within a 5.5 mm distance close to the injector exit face (distance-to-diameter ratio of up to 21.6). Note that, according to *Abramovich [18]* the length of the potential core in isothermal uniform-density axisymmetric and two-dimensional jets are estimated to be about 6 to 10 injector diameters whereas for nonisothermal cold-into-hot jets it can reach up to about 25 injector diameters depending on jet temperature. Also, according to *Chehroudi et al. [19]* the intact core of the liquid sprays similar to the ones used in diesel engines is $Cd(\rho_l/\rho_g)^{1/2}$ where ρ_l and ρ_g are liquid injectant and chamber gas densities, respectively, d is the effective jet exit diameter and C is a constant between 3.3 to 11. This translates to an intact core length of between 33 to 110 injector diameters for the chamber-to-injectant density ratio of 0.01 and between 16.5 to 55 diameters for the chamber-to-injectant density ratio of 0.04. These results are presented in Fig. 4 for better comparison. Assuming that the jet dark-core seen in images plays the same role as the intact core or potential core, Fig. 4 indicates that our growth rate data is taken from corresponding and appropriate initial region to ensure existence of a classical mixing layer.

The initial jet spreading angle or its growth rate is measured for all acquired images and results along with those of others are presented in Fig. 5. Of importance in this figure are the justification for the selection of the data sets and the nature of their measurements by other

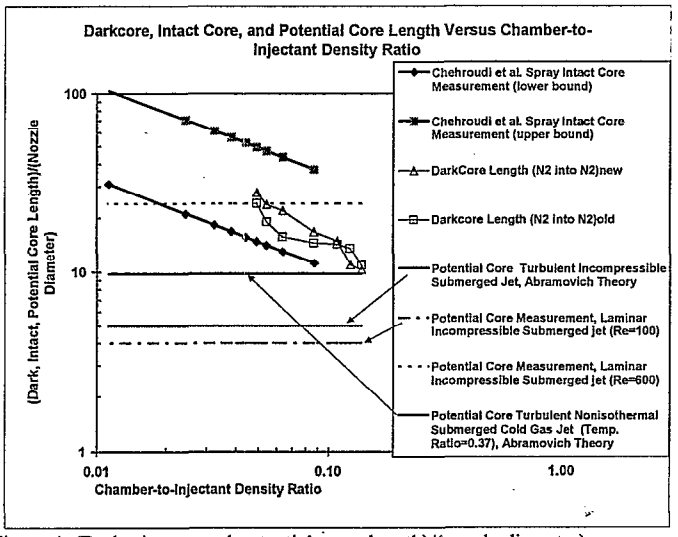

Figure 4. (Dark-, intact- and potential- core length)/(nozzle diameter) as a function of chamber-to-injectant density ratio.

researchers. They are elaborated in sufficient details in our earlier paper to provide a deeper appreciation of Fig. 5 and its uniqueness, see *Chehroudi et al. [13]*.. Therefore, they are only mentioned here in brief as needed. Since the jets investigated here exhibit both liquid-like and gas-like jet appearances, appropriate results for both are presented here. The simplest is the prediction of the linear jet growth or constant spreading angle for the turbulent incompressible submerged using the mixing length concept. Next, following *Abramovich [18]*, is the semi-empirical equation that attempts to incorporate the effects of density variations by introduction of a characteristic velocity, see also *Chehroudi et al. [13]*.

Brown and Roshko [20] measure spreading for a subsonic two-dimensional incompressible turbulent mixing layer in which helium and nitrogen are used. They make distinction between mixing layers in which density

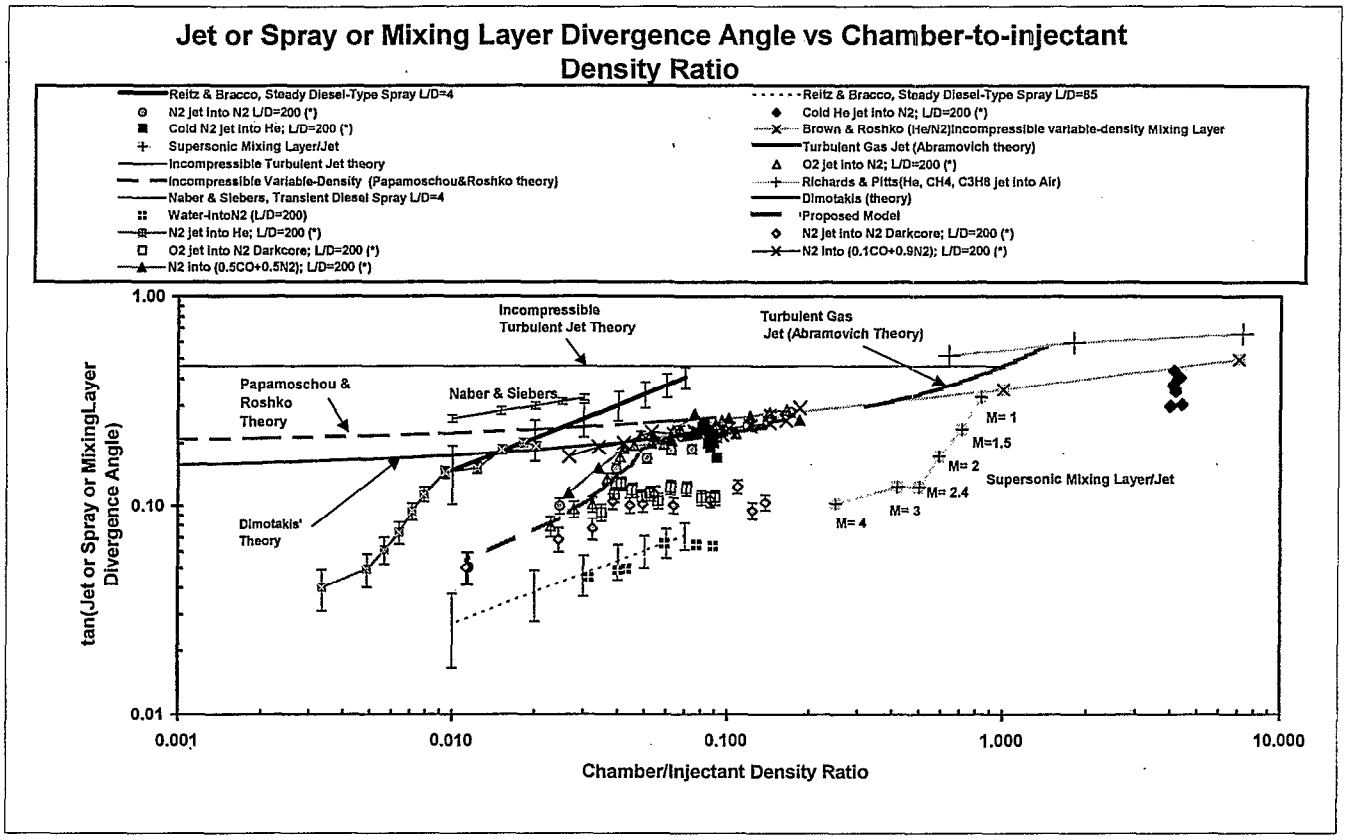

Figure 5. Shows spreading or growth rate as tangent of the visual spreading angle versus the chamber-to-injectant density ratio. (*) refers to data taken at AFRL.

changes are caused by temperature changes, high-speed compressible (high Mach number and supersonic) flows, and differences in molecular weights (i.e. different gases). In the jet investigated here there are both differences in temperature as well as molecular weight except for the N_2-into-N_2 case. Their measurements are shown in Fig. 5. *.Brown [1]* (for temporally growing mixing layer) and *Papamoschou and Roshko [2]* proposed a theoretical equation for the incompressible variable-density mixing layer as shown in Fig. 5. Finally, *Dimotakis [3]* uses the observation that, in general, the entrainment into the mixing layer from each stream is not the same and, in a system moving with a convection velocity, offers a geometrical argument to derive an equation for the two-dimensional incompressible variable-density mixing layer, see Fig. 5. Conversion of the two-dimensional mixing layer data for comparison with our initial growth rate is justified since according to both *Brown and Roshko [20]* and *Abramovich et al. [21]*, two-dimensional mixing layers are found to be fairly well approximated by the initial mixing region of axisymmetric jets. For this reason all angle measurements in our work are made using only the information within the first 5.5 mm distance of the injector exit plane.

Because both liquid-like and gas-like visual jet behaviors are observed, the growth rate for liquid sprays produced from single-hole nozzles typical of the ones used in diesel engines are also shown. Due to profound nozzle geometrical effects, see *Reitz and Bracco [15]* and *Hiroyasu and Arai [23]*, isothermal spray angle theoretical equations proposed by *Reitz and Bracco [15]* at two different nozzle length-to-diameter ratios, along with their corresponding vertical error-bands indicating experimental scatter around them, are shown in Fig. 5. A recent curve-fitted equation to experimental data from transient sprays proposed by *Naber and Siebers [24]* is also shown. Their angle measurement zone extends beyond our initial region and this to some extent contributes to disagreement seen between the two sets of data for liquid sprays at injector length-to-diameter ratio of about 4, see Fig. 5.

Figure 5 covers a density ratio of four orders of magnitude, from liquid sprays to supersonic mixing layers, a unique and new plot on its own right. To some extent, for comparable measured values, disagreements in this figure can be attributed to differences in the definition of the mixing layer thicknesses and their measurement methods. For detailed discussion of this figure see *Chehroudi et al. [13]*. The important point shown in *Chehroudi et al. [13]* is that for a range of density ratios in which our images show gas-jet like appearance, the experimental data agrees well with the proposed theoretical equation by *Dimotakis [3]* and closely follows the trend of Brown/*Papamoschou and Roshko [2], see Fig. 5*. This can be taken as an important quantitative evidence that at ambient supercritical pressure and temperature conditions (based on the pure injectant's

critical data), the injected jets visually behave like a gas. To our knowledge, this is the first time such quantitative evidence has been developed. Above the critical condition, there is a marked disagreement in both magnitude and slope between liquid sprays (at a comparable length-to-diameter ratio of 85) and our data, see Fig. 5, even though the jet investigated here appears to go through initial phases of the liquid atomization process, see Figs. 2. The reason is that although the jet studied here shows second wind-induced breakup features similar to liquid jets, it fails to reach a full atomization state as chamber pressure (actually, density) is raised. This is because the thermodynamic state approaches the critical point and consequently both surface tension and heat of vaporization are reduced to near-zero values. Transition into the full liquid atomization regime is therefore inhibited.

General Background on Fractals

Fractals are intimately connected to the concept of self-similarity and in a sense are geometrical/visual interpretation of the underlying algebraic laws (or power laws) of scales. The notion of a fractal has been given a strong foundation and application by its father *Mandelbrot [25]*. Self-similarity in a common sense is self-explanatory. Multiple photocopy reductions of a given picture at any fixed reduction level look similar but the picture itself is not self-similar. The reduction process generates copies each being similar to the original and is called a similarity transformation. In general, a similarity transformation, using mathematical language, involves one or combination of multiplication by a scale factor, pure translation, and pure rotation. Under such a transformation a geometrical object stays similar to the original or to a preceding stage if repetitively applied. Self-similarity, however, in a strict sense means that if one chooses any point of a geometrical object and locally magnifies, it will look similar to the "whole" object. In a sense infinite number of the scaled-down version of the "whole" are embedded in the "whole." In nature such idealized mathematical objects do not exit. For example, *Peitgen et al [26]* explain that a cauliflower head contains branches or parts, which when removed and compared with the whole are very much the same, only smaller. These can again be decomposed into smaller ones, which again look very similar to the whole as well as to the first generation branches. This self-similarity carries through for about three to four stages, unlike the mathematical fractals. After that the structures are too small for a further dissection. Hence, in natural geometrical constructs self-similarity is confined between two sizes (or scales) referred to as inner (the smallest size) and outer cut-offs (the largest size).

Fractal Dimension

The other important concept related to fractals is the fractal dimension. In Euclidean geometry a line, a plane, and a surface in space have dimension of one, two, and three respectively. In topology, a straight line and any non-self-intersecting curve are equivalent and have the same topological dimension. The creation of the so-called "space-filling" curve has shaken the concept of the dimension in mathematics. That is, given some patch of the plane, there is a space-filling curve which meets every point in that patch. Thus, a curve, which by nature is something one-dimensional, can fill something two-dimensional. This questions the intuitive perception of curves as one-dimensional objects, because they fill the plane, an object which is intuitively perceived as two-dimensional. Looking at a self-similar curve with the notion defined in relation to the cauliflower, there is a power law relation between the number of pieces, P, and the reduction factor, ε, as: $P = (1/\varepsilon)^{D_S}$. In other words, this power-law relationship states that if a self-similar curve is reduced by, say, $\varepsilon = 1/2$ there are 2^{D_S} number of same pieces in the whole. D_S is defined as self-similarity dimension of the curve. Obviously, for a line, a square, and a cube, we have D_S=1, 2, 3, respectively, which happen to be the topological dimensions. For self-similar curves this dimension is determined through an exercise to measure the total length of the curve using different compass settings (or yardstick lengths). The reciprocal compass setting can be thought of the precision of the length measurement. Mechanistically, one selects a fixed compass setting and attempts to find the number of compass settings needed to cover the entire curve. In other words, one measures the total length of the curve using a fixed setting of the compass. This is repeated for different compass settings. Plotting the number of compass lengths required to cover the curve at a given compass setting as a function of the reciprocal compass setting itself traces a line in a log-log plot for a self-similar curve. The slope of this line, d, and the self-similarity dimension, D_S, can be shown related by: $D_S = 1 + d$ (d is positive in magnitude). Usually, however, the number of compass lengths at a given fixed setting is plotted against the compass setting itself (which in this case, $D_S = 1 - d$ as d is negative in magnitude). Motivated by this result for self-similar curves, the fractal (compass) dimension for shapes that are not strictly self-similar curves such as the jet boundary we would like to analyze are defined as: $D_C = 1 + d$. With this, the fractal dimension of the coast of the England that has many wrinkles is 1.36 whereas that of the state border of Utah having smooth straight lines is equal to 1. Note that a non-integer number is attributed to the dimension (fractal). The fractal dimension of any curve is between 1 and 2 and the more wrinkled and space-filling it looks the larger the dimension value becomes. Natural curves, similar to a cauliflower, are self-similar only to within a narrow range of scales. Our objective here is to measure the fractal dimension of the interface of the jets injected into the chamber to see if any pattern is uncovered. To our knowledge, this is the first application of the fractal approach to the liquid jet interface under sub- and supercritical conditions.

Box-counting and Minkowski Dimensions

In the literature there are several methods with variety of names to determine the fractal dimension of a boundary. For example the above-mentioned compass setting method is also called caliper method or arc swinging method. This method is difficult to implement for computer analysis and therefore more computer-compatible and faster algorithms are devised. One such popular method for fractal dimension evaluation is referred to as box-counting or Kolmogorov dimension, for example, see *Russ [27], [28], and Kaye [29].* One overlays the curve on a square grid with mesh size ε and counts the number of grid boxes which contain any part of the curve. This gives a number, say, $N(\varepsilon)$ which depends on the mesh size ε. The slope of the line fitted to the linear section of the log-log plot of $N(\varepsilon)$ as a function of $1/\varepsilon$ is the box-counting dimension, D_B . This is one of the special forms of Mandelbrodt's fractal dimensions. We also consider another approach that leads to what is referred to as Minkowski dimension. In this method the center of a circle with radius ε is swept continuously along the curve. This creates what is called as Minkowski sausage around the curve. The area of the sausage as a function of the radius of the circle is drawn on a log-log plot. The Minkowski dimension is equal to (2 - slope of the linear region). In this paper we use both box-counting and Minkowski methods to calculate fractal dimension. For the latter method the Euclidean Distance Mapping (EDM) algorithm of *Russ [27]* is implemented. Consider a black object in a white background. The fractal dimension of the boundary between the two is desired. EDM is an image processing operation that is applied to a black and white image to produce a gray-scale image in which each black pixel is given a brightness value equal to its distance from the nearest white background point. Therefore, the larger the distance of a pixel from the nearest border the higher its assigned gray-scale intensity value, being linearly proportional to the distance. The same procedure can assign values to the white background pixels based on their distance from the nearest point on the object. Thresholding the distance map for either the object or the background produces uniform erosion and dilation of the boundary to any desired distance from the original boundary, without iteration. EDM method is superior to the classical erosion/dilation method, see *Russ [28].* It is really not necessary to perform the thresholding operations. Counting the pixels as a function of their brightness (distance) values produces a plot that directly provides the Minkowski dimension. Both Box-counting and Minkowski methods are shown to provide reliable results, see *Hall et al [30].* However, the EDM algorithm in determining the fractal dimension is more isotropic, more efficient, and generally more precise than the box-counting method, and easy to implement on a computer, see *Russ and Russ [31].* Both techniques are limited to only self-similar and not self-affine boundaries.

Fractal Analysis on Cryogenic Jets

Before being able to run the fractal analysis program for computation of fractal dimension, images need to be conditioned. In particular, corrections to images are applied knowing the reference background condition. Then smoothing and twice-sharpening filters are applied. Also, an appropriate (described later) pixel intensity threshold level is selected to identify the boundary of the jet injected into the chamber. A 200X200 pixel image of a square boundary within our 432x477 full frame size is used as a test image to evaluate the fractal analysis program. Theoretically, the fractal dimension of the smooth boundary of this square must be equal to one. The analysis, however, provides fractal dimension higher than one by at most 3% for the box-counting and EDM methods. For box-counting dimension two different methods are used to change the mesh size. In one case, the mesh size is increased by the following sequence, 1x1, 2x2, 3x3,..., 32x32 pixels, and in the other by 2x2, 4x4, 6x6, 8x8, ..., 64x64 pixels. In this paper they are referred to as BOX32 and BOX64 respectively.

Looking at the jet images in Fig. 2, in order to define a closed-loop jet boundary for fractal analysis, one needs to manually select a section of the jet image excluding regions covering the image of injector tip and the part of the image near the lower edge of the frames. This in a sense creates two smooth straight lines joining the left and the right boundaries of the jet at the top and the bottom. The effect of addition of these two smooth sections on fractal dimension value is analyzed by several different methods. First, the left and the right boundaries are manually moved close to each other so the length of the upper smooth line is minimized. The minimization is done on the upper section because the jet diverges downward in images. Second, the upper and lower smooth lines are replaced by pieces of the right and/or left boundaries of the jet. The fractal dimension has increased by 2 to 3 % applying such corrections on jet images for various chamber pressures. For ease of analysis, however, we determine the fractal dimension of jet images with two upper and lower smooth lines and uniformly apply a 2.5% increase to all final values as a first-degree correction measure. The selection of the pixel intensity threshold for jet boundary determination is an important factor. For this reason, at each tested chamber pressure the fractal dimensions of the N_2-into-N_2 jets are calculated for a wide range of threshold levels and results are plotted. Maximum excursion is observed at high pressures of up to 10% as threshold is varied. In most cases, one can detect a plateau region in which a threshold value can be selected. If not, a value at the center of the explored threshold range is chosen. As a cross check the boundary generated at the chosen threshold is visually overlaid and inspected to follow the original gray scale image as close as discernable. Figure

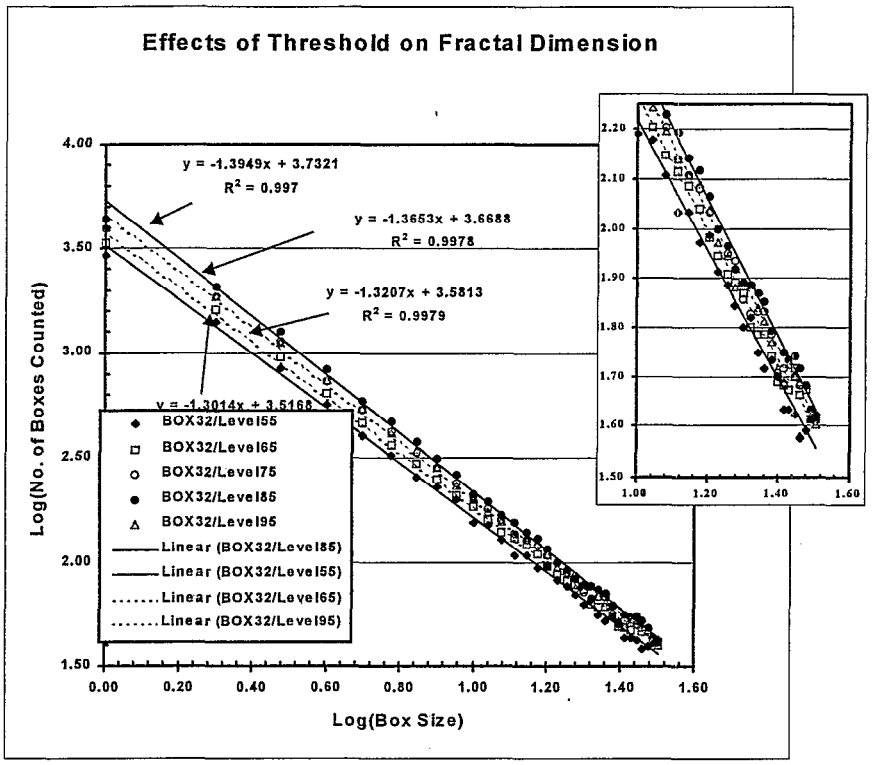

Figure 6. Log-log plot of the number of boxes counted as a function of the box size for four different thresholded binary images of the same original high-chamber-pressure gray-scale jet image indicating effects of the threshold level on the fractal dimension. The slope of the least square fit line is the negative of the box-counting dimension.

6 shows log-log plot of the number of boxes counted versus the box size for a selected jet at high pressure and for five different threshold levels. On the thresholded images one observes many vein-like structures that are not part of the closed-loop jet boundary but attached to it. These are removed by an appropriately selected sequence of erosion/dilation image processing cycles. Special treatment is also required for images at low pressures at and before the second-wind-induced-like appearance zone. The boundary of the jet is determined such that all isolated and single-pixel touching ligaments and drops are excluded. This is achieved by application of series of erosion/dilation approach described in *Russ[27].* The value of fractal dimension at each pressure (density) condition in Fig. 7 is the average of 18 to 20 images.

In the past ten years a number of applications of fractal analysis have been demonstrated in different disciplines. For example, *Sreenivasan and Meneveau [32]* compute the (Box-counting and Minkowski) fractal dimension of the turbulent/non-turbulent (or strictly speaking, smoke/no-smoke) boundary of an incompressible axisymmetric gaseous jet and report a value of 1.33 using two-dimensional slicing by a laser sheet. The laser sheet thickness is to be smaller or comparable to Kolmogorov scale to minimize 'fuzzing' due to the finite thickness of the sheet. *Sreenivasan [33]* also reports values of 1.35, 1.34, and 1.38 for a round gaseous jet, a plane gaseous mixing layer, and a boundary layer flow, respectively, using two-dimensional digital imaging from LIF intersections. It is also interesting to mention that *Mantzaras et al [34]* (who used flames in spark-ignited engine, measured Minkowski dimension) and *North and Santavicca [35]* (who used atmospheric premixed flames and measured Minkowski dimension) report a progressive increase in fractal dimension from 1.05 to 1.36 as turbulence level is increased. This indicates progressive wrinkling and space-filling of the flame front by turbulence. Finally, modeling turbulent flames using fractal concept are discussed in *Gouldin [36]* and *Gouldin et al. [37].*

The first logical attempt here is to compare our fractal dimension measurements with those of round gaseous jets and mixing layers. Figure 7 shows results of fractal dimension calculations using BOX32, BOX64, and EDM methods applied to the N_2-into-N_2 jets as a function of relative chamber pressure. In this figure the fractal dimension measured by other researchers in the gaseous jets, mixing layer, and boundary layers are also shown for comparison purposes. Our analysis of the gaseous jet images by *Dimotakis et al. [38]* is also shown. The interesting part is that the average value measured for our jet reaches very near those of gaseous jets and mixing layers above the critical point of the injectant. This is an additional quantitative data in support of the gaseous jet

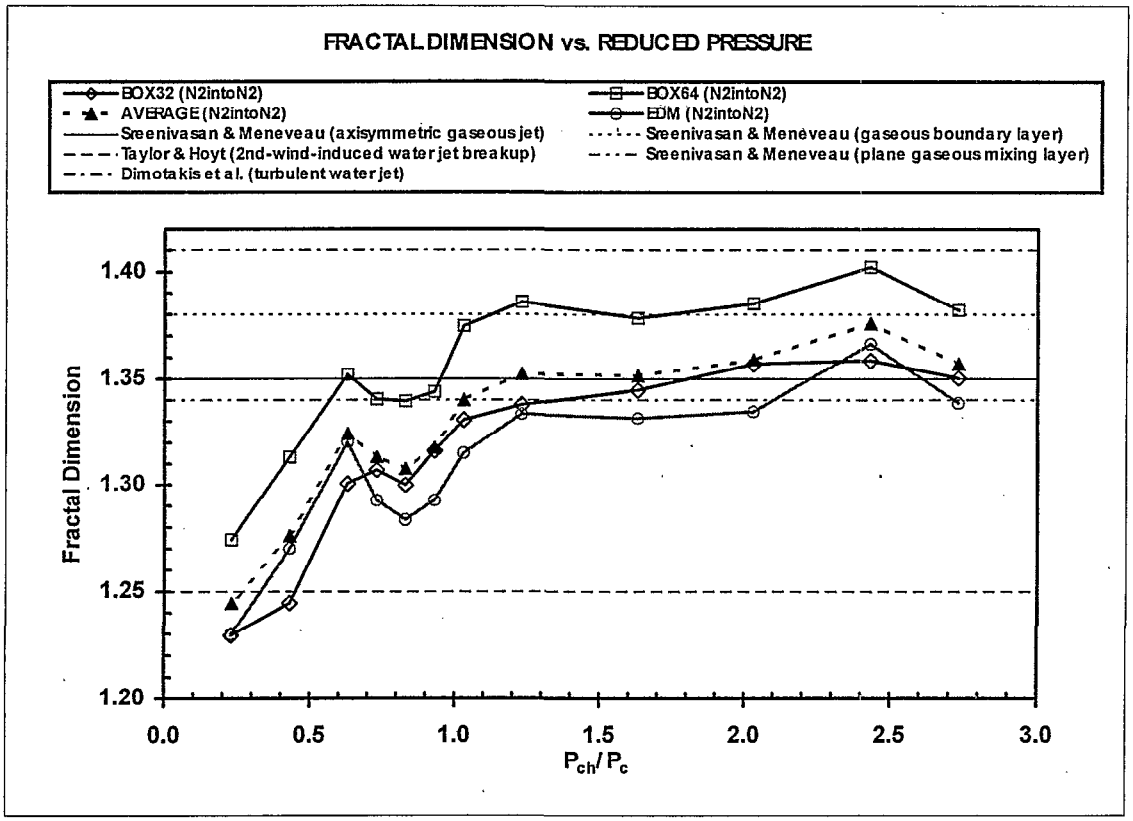

Figure 7. Box-counting and Minkowski (EDM algorithm) fractal dimensions of the visual boundary of the jet as a function of the reduced chamber pressure for N_2-into-N_2 injection.

behavior evidenced through our growth rate measurements in this region and reported first in *Chehroudi et al. [13, 39]*. As pressure (density) is decreased below P_r of about 0.6 the fractal dimension rapidly reduces towards the Euclidean value of 1 for smooth circular cylinder with no surface irregularities. The dip in the profiles shown in Fig. 7 is the reflection of the transitions to the second wind-induced atomization and the gas-jet like appearance. Considering the geometric interpretation of the fractal dimension, the measured values are quite consistent with the visual observations of jet interface changes in our tests. The higher values of the BOX64 is believed to be due to contributions of the data beyond the 32x32 grid size. However, considering better accuracy of the EDM method and its closeness to BOX32 results we tend to favor them in terms of magnitudes of the fractal dimensions calculated here. However, all methods provide the same general trend. It is also worthwhile to indicate that our fractal dimension calculation of the boundary of the water jets shown by *Taylor & Hoyt [40]* which show very similar appearance to the liquid jets in the second wind-induced regime is close to what is measured in our N_2-into-N_2 jets as shown in Fig. 7.

Modeling the Growth Rate

In the absence of a detailed treatment starting from basic principles, the idea is to intelligently search for a form of an equation based on an intuitive and physically reasonable picture that can predict the jet growth rate data presented in Fig. 5. Our approach is to discuss two appropriate characteristic times of the problem, combined with a hypothesis and growth rate equations for isothermal liquid sprays and gaseous mixing layers to propose an "intuitive/smart" equation that is able to closely mimic the experimental growth rate data for the sub- and supercritical conditions presented here.

Imagine a jet that is being injected into a subcritical pressure environment similar to the ones shown in Fig. 2. Clearly there are drops and ligaments, testifying for the existence of surface tension. Also evidences of phase change are seen. Hence, one appropriate characteristic time of the problem (at subcritical pressure, $P_r<1$) is the "bulge" formation/separation time (τ_b) on the interface of the turbulent liquid jet. This time characterizes the formation and separation event of bulges from the liquid jet producing isolated ligaments and drops. *Tseng et al. [17]* suggest that this time is equal to $(\rho_l L^3/\sigma)^{1/2}$ for the primary breakup of turbulent liquid jets where ρ_l, L, and σ are liquid density, characteristic dimension of turbulent eddy, and surface tension, respectively. The second relevant characteristic time (at subcritical pressure) is the gasification time (τ_g). Here, an estimate of this time is calculated through the so-called D-square law for drops to be equal to D^2/K where D and K are drop diameter and vaporization constant, respectively. In addition, we also propose the following hypothesis. If the aforementioned

characteristic times (calculated for appropriate length scales) are nearly equal in magnitude, then the interface bulges are not able to separate as unattached entities from the jet interface to form ligaments and drops because they are gasified as fast as they desire to be detached. Here, this is defined as the onset of the gas-jet like behavior. Later a value is proposed for the relative magnitudes of these time scales.

The next issue to discuss is a form of the growth rate equation. To intelligently propose this form, it is important to notice that the jets investigated here exhibit both liquid-like and gas-like behaviors and that the growth rate of the latter agrees well with those of incompressible variable-density gaseous mixing layers. It is therefore instructive and natural to inspect the forms of the growth rate equations for the liquid sprays as well as incompressible variable-density gaseous jets. For liquid sprays, *Reitz and Bracco [15]* using linear instability theoretical analysis propose the following equation for the isothermal liquid spray growth rate:

$$\theta_S \cong 0.27\,[0 + (\rho_g/\rho_l)^{0.5}],$$

where θ is spray full-cone angle. Also, from Brown/Papamoschou/Rashko's theory for an incompressible variable-density gaseous mixing layer one can show that :

$$\theta_{B/P/R} \cong 0.212\,[1 + (\rho_g/\rho_l)^{0.5}],$$

where here θ is the visual jet full-cone angle. Finally, based on a somewhat different theoretical treatment by Dimotakis for incompressible variable-density gaseous mixing layers, an equation of the following form can be derived for the growth rate:

$$\theta_D \cong 0.265\,[0.59 + (\rho_g/\rho_l)^{0.5}].$$

The similarity of these equations is remarkable despite their different theoretical treatments in deriving them. In particular, the absence of a constant (i.e. zero value) in the bracket for the isothermal liquid spray and presence of one for the gaseous cases prompted the following proposed "intuitive/smart" form of an equation describing the growth rate for both sub- and supercritical jets:

$$\theta_{Ch} \cong 0.27\,[(\tau_b/(\tau_b+\tau_g)) + (\rho_g/\rho_l)^{0.5}].$$

In a sense a physical meaning is attributed to the first term in the bracket and it is linked to the physical picture hypothesized earlier. Note that, in the limit, this equation collapses to the isothermal liquid spray case when $\tau_g >> \tau_b$ and $\tau_g \to \infty$. Because the solubility of the ambient gas into the injectant substance is not an issue for the special case of N_2-into-N_2 injection the $\tau_b/(\tau_b+\tau_g)$ ratio can be calculated with good accuracy. The calculations for the N_2-into-N_2 starts from the lowest subcritical condition, where the above equations for τ_b and τ_g are valid and the jet divergence can be measured, by computing the parameter $\tau_b/(\tau_b+\tau_g)$ until it reaches a value close to 0.5 (i.e. $\tau_b \cong \tau_g$; onset of the gas-jet like behavior) as chamber pressure is raised towards the critical value. After that,

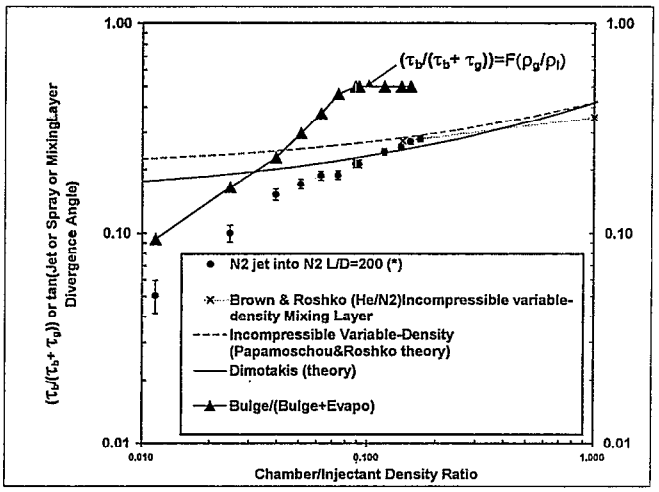

Figure 8. calculated $(\tau_b/(\tau_b+\tau_g))$ along with corresponding measured growth rate as a function of the density ratio for the N2-into-N2 jet.

this term is maintained at a constant value of 0.5 for the ambient conditions producing gas-jet like appearance. In a sense the transition point from sub- (liquid-jet like) to supercritical (gas-jet like) behavior is proposed to be when the ratio $\tau_b/(\tau_b+\tau_g) \cong 0.5$. Figure 8 shows the actual values of $\tau_b/(\tau_b+\tau_g)$ calculated for the N_2-into-N_2 case. The magnitudes for the two characteristic times are calculated assuming D and L values of 65 and 50 microns respectively. The initial approximate values for these characteristic dimensions are based on the observations of many magnified images and then they are fine tuned to produce the best agreement with the N_2-into-N_2 experimental data. Also, $\tau_b/(\tau_b+\tau_g)$ for the N_2-into-N_2 jet does not appear to be a strong function of the aforementioned characteristic lengths if their ratio is maintained the same, a positive feature of the proposed model. Also plotted in Fig. 8 is the spreading rate data for N_2-into-N_2 and the theoretical expressions for the gas/gas regime. The figure shows the ratio $\tau_b/(\tau_b+\tau_g)$ is equal to 0.5 at the density ratio where the experimental data begins to agree with gas/gas theory. At density ratios above this value, the ratio $\tau_b/(\tau_b+\tau_g)$ is kept fixed at 0.5.

Figure 9 shows comparison of the proposed model equation with the characteristic time ratio calculated for the N_2-into-N_2 Case. Good agreement is observed. For cases other than the N_2-into-N_2, such as N_2-into-He or N_2-into-Ar, similar calculations for the characteristic time ratio are not readily possible. This is because the extent of the solubility of the chamber gases into the condensed-phase injectant substance and its effects on thermodynamic properties, and in particular the surface tension, are not well established. To model these cases, it is here proposed that the characteristic time ratio $\tau_b/(\tau_b+\tau_g)$ is a dominant function of the density ratio only. Mathematically speaking, it means that $\tau_b/(\tau_b+\tau_g) = F(\rho_g/\rho_l)$ as shown in Fig. 8. This is reasonable to expect

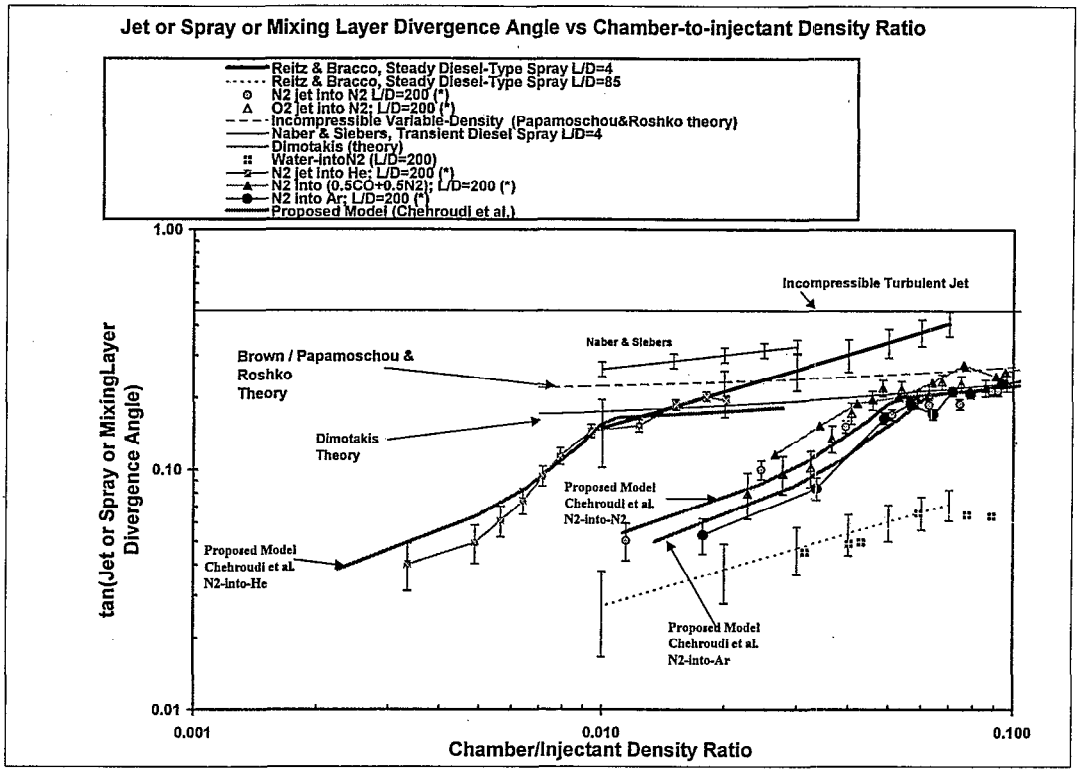

Figure 9. Comparison of the proposed growth rate model with the experimental data for the sub- to supercritical jet. (*) refers to data taken at AFRL.

as *Brown and Roshko [20]* indicate that at low Mach number squared values there is no distinction between mixing layers made of two streams with differences in molecular weights, differences in temperature, and high speed compressibility effects, see also *Chehroudi et al. [13]*. Also, *Siebers [41]* shows for the growth rate of the liquid sprays in diesel environment that effects of vaporization at high ambient temperature can be represented by an addition of a term involving density ratio. Thus it was found that the same function $F(\rho_g/\rho_l)$ calculated through measurements for the N_2-into-N_2 case could be made to work for other cases provided a case-dependant shift is made to the density ratio at which F is evaluated. Specifically,

$$\theta_{Ch} \cong 0.27\,[\,G(\rho_g/\rho_l) + (\rho_g/\rho_l)^{0.5}]$$

where

$$G(\rho_R) = F(\rho_R'); \quad \rho_R = (\rho_g/\rho_l)$$

$$\rho_R' = \rho_R - (1-X)\rho_R = X\rho_R$$

and where

X=1.0 for N_2-into-N_2
X=0.2 for N_2-into-He
X=1.2 for N_2-into-Ar.

In other words, the same functional form of the characteristic time ratio, $\tau_b/(\tau_b+\tau_g)=F(\rho_g/\rho_l)$, for the N_2-into-N_2 case is used but with a density-ratio coordinate transformation of $\rho_R'=X\rho_R$. The quality of the agreement with experimental data is demonstrated in Fig. 9. Hence there are no major changes in the form of the proposed model equation even for as extreme of an arrangement as injection of N_2 into He. However, an observation is made here. The factor X=0.2 in the N_2-into-He case is comparable to the molecular weight ratio of He to N_2 of 0.14, while the factor X=1.2 in the N_2-into-Ar case is comparable to the molecular weight ratio of 1.42. This also suggests the dominant effect of the density ratio parameter between the cases.

Summary and conclusions

Through injection of several pure fluids into a chamber with different ambient gases under supercritical temperature but sub- to supercritical pressure based on the injectant thermodynamic critical properties the following is shown. The jet exhibits classical liquid-like jet second wind-induced type breakup until chamber pressure reaches near the critical point of the jet substance, beyond which a gas-like visual behavior is observed and no drops are found. For the first time, these qualitative observations are supported quantitatively by the agreement between the experimental growth rate of the jets reported here and those developed theoretically by *Brown[1]/Papamoschou and Roshko[2]* and *Dimotakis[3]* for the incompressible variable-density mixing layers. Further quantitative support is obtained for the first time by fractal analysis of the outer contour of the jet. The geometry of the jet interface shows a transition from Euclidean to a fractal interface with a fractal dimension near the values measured and reported

by others for gaseous turbulent jets. Finally, based on a physical hypothesis implying that at the point where gas-like behavior appears, the value of the jet interface bulge separation/formation characteristic time should be near that of gasification time, an "intuitive/smart" equation is proposed for the growth rate that agrees well with the presented experimental data for a wide range of density ratios.

Acknowledgements

The authors would like to thank Mr. Mike Griggs for machine-shop work and assisting in setup modifications. Mr. Earl Thomas is thanked for his valuable support in this project. We appreciate Mr. Theodore Miles's effort in searching copies of many requested publications. In particular, Mr. Paul Loftsgard is thanked for his assistance in part of the data acquisition/processing and most of the fractal analysis work. This work is sponsored by the Air Force Office of Scientific Research under Mr. Mitant Birkan, program manager.

References

1. Brown G., "The entrainment and large structure in turbulent mixing layers," 5th Australasian Conf. on Hydraulics and Fluid Mech., 1974, pp. 352-359.

2. Papamoschou, D. and Roshko, A. "The compressible turbulent shear layer: an experimental study," J. Fluid Mech., vol. 197, 1988, pp. 453-477.

3. Dimotakis, P. E. "Two-dimensional shear-layer entrainment," AIAA Journal, 21, No. 11, 1986, pp. 1791-1796.

4. Bruno, T. J. and Ely, J. F. *Supercritical fluid technology: review in modern theory and applications*, CRC Press, 1991.

5. Lazar R. S. and Faeth, G. M. "Bipropellant droplet combustion in the vicinity of the critical point", Thirteen Symposium (International) on Combustion, The Combustion Institute, P. 801, 1971.

6. Umemura, A. "Supercritical droplet gasification combustion," IUTAM Symposium on theories combustion on droplets and sprays, Taiwan, December 1994.

7. Newman, J. A. and Brzustowski. "Behavior of a liquid jet near the thermodynamic critical region," AIAA Journal, vol. 9, no. 8, pp. 1595-1602, 1971.

8. Mayer, W., Schik, A., Schweitzer, C., and Schaffler, M. "Injection and mixing processes in high pressure LOX/GH2 rocket combustors," AIAA Paper no. 96-2620, 32nd AIAA/ASME/SAE/ASEE Joint Propulsion Conference & Exhibit, Lake Buena Vista, Florida, 1996.

9. Mayer, W., Ivancic, A., Schik, A., and Hornung, U. "Propellant atomization in LOX/GH2 rocket combustors," AIAA Paper no. 98-3685, 34 the AIAA/ASME/SAE/ASEE Joint Propulsion Conference & Exhibit, Cleveland, Ohio, ; July 13-15, 1998.

10. Chen, L.-D. and Sui, P.-C. "Atomization during the injection of supercritical fluid into high pressure environment," in *Mechanics and Combustion of Droplets in Sprays* by Chiu and Chigier.

11. Birk A. and McQuaid, M. "Delibrations on dynamics and core structure of reacting sprays at elevated pressures," *Recent Advances in Spray Combustion: Spray Atomization and Drop Burning Phenomena*, Vol. 1, Edited Kuo, K. K. , pp. 309-325, 1996

12. Woodward , R. D. and Talley, D. G. "Raman imaging of transcritical cryogenic propellants," AIAA Paper 96-0468, 34 the AIAA Aerospace Sciences Meeting and Exhibit, Reno, Nevada, January 1996.

13. Chehroudi, B., Talley, D., and Coy, E. Initial Growth Rate and Visual Characteristics of a Round Jet into a Sub- to Supercritical Environment of Relevance to Rocket, Gas turbine, and Diesel Engines. 37th AIAA Aerospace Science Meeting and Exhibit, AIAA 99-0206, Reno, NV, January 11-14, 1999.

14. Schlichting, H. *Boundary Layer Theory*, MacGraw-Hill Book Company, seventh edition, 1979.

15. Reitz, R. D. and Bracco, F. V. "On the dependence of spray angle and other spray parameters on nozzle design and operating condition," SAE international Congress and Exposition, SAE Paper no. 790494, Detroit, Michigan, February 26-March 2, 1979.

16. Faeth, G. M., "Structure and atomization properties of dense turbulent sprays," Twenty-third Symposium (International) on Combustion, The Combustion Institute, P.1345, 1990.

17. Tseng, L.,-K., Ruff, G. A., P.-K., Wu, Faeth, G. M., "Continuous- and dispursed-phase structure of pressure-atomized sprays," Progress in Astronautics and Aeronatics: Recent Advances in Spray Combustion, February, 1995.

18. Abramovich, G. N. *The theory of turbulent jets*, M.I.T. Press, 1963.

19. Chehroudi, B., Chen, S. H., Bracco, F. V., and Onuma, Y. "On the Intact Core of Full-Cone Sprays," Society of Automotive Engineers, 1985 Congress and Exposition, SAE Transaction Paper 850126, February 25-March 1, 1995.

20. Brown, G. and Roshko, A. "On density effects and large structure in turbulent mixing layers," J. Fluid Mech., vol. 64, 1974, part 4, pp. 775-816.

21. Abramovich, G. N., Yakovlevsky, O. V., Smirnova, I. P., Secundov, A. N., and Krasheninnkov, S., Yu. "An Investigation of turbulent jets of different gases in a general stream," Astronautica Acta, 14, 1969, 229.

22. Richards, C. D. and Pitts, W. M. "Global density effects on the self-preservation behavior of turbulent free jets," J. Fluid Mech., vol. 254, 1993, pp. 417-435.

23. Hiroyasu, H. and Arai, M. "Fuel spray penetration and spray angle in diesel engines," Trans. JSAE, Vol. 21, 1980, pp. 5-11.

24. Naber, J. D. and Siebers, D. L. "Effects of gas density and vaporization on penetration and dispersion of diesel sprays," SAE international Congress and Exposition, SAE Paper no. 960034, Detroit, Michigan, February 26-29, 1996.

25. Mandelbrot, B. B. "The Fractal Geometry of Nature," W. H. Freeman and Company, San Francisco, 1983.

26. Peitgen, H-O, Hartmut, J., Dietmar, S. "Fractals for the Classroom, Part one Introduction to Fractals and Chaos," Springer-Verlag New York Inc., New York, 1992.

27. Russ, J. C. "The image processing handbook: 2nd edition," Boca Raton, FL, CRC Press, Inc., P. 674, 1995.

28. Russ, J. C. "Fractal Surfaces," New York: Plenum Press, 1998.

29. Kaye, B H. "Image analysis techniques characterizing fractal structures from the fractal approach to heterogeneous chemistry," (D. Avnir, editor). John Wiley & Sons , 1989.

30. Hall, M. J., Dai, W., and Matthews, R. D. "Fractal analysis of turbulent premixed flame images from SI engines," International Fuel and Lubricants Meeting and Exposition, San Francisco, California, SAE Technical paper 922242, October 19-22, 1992.

31. Russ J. C. and Russ, J. C. "Uses of Euclidean Distance Map for the measurement of features in images," Journal of computer assisted microscopy, Vol.1, no. 4, pp. 343-375, 1989.

32. Sreenivasan, K. R. and Meneveau, C. "The fractal facets of turbulence," J. Fluid Mech. Vol. 173, pp. 357-386, 1986.

33. Sreenivasan, K. R. "Fractals and multifractals in fluid turbulence," Annu. Rev. Fluid Mech, Vol. 23 pp. 539-600, 1991.

34. Mantzaras, J., Felton, P. G., and Bracco, F. V. "Fractals and turbulent premixed engine flames," Combustion and Flames, vol. 77, pp. 295-310, 1989.

35. North, G. L. and Santavicca, D. A. "The fractal nature of premixed turbulent flames," Combust. Sci. and Tech., vol. 72, pp. 215-232, 1990.

36. Gouldin, F. C. "An application of fractals to modeling premixed turbulent flames," Combustion and Flames, vol. 68, pp. 249-266, 1987.

37. Gouldin F. C., Hilton, S. M., and Lamb, T. "Experimental evaluation of the fractal geometry of flamelets," Twenty-second Symposium (International) on Combustion/ The combustion Institute, pp. 541-550, 1988.

38. Dimotakis, P. E., Miake-Lye, W. G., and Papantoniou, D. A., Phy. Fluids, 26, p. 3185.

39. Chehroudi, B., Talley, D., and Coy, E. Behavior of a round cryogenic jet at below and above the critical pressure. The Tenth Annual Propulsion Symposium, Propulsion Engineering Research Center (PERC) at Penn State, NASA Marshall Space Flight Center, Huntsville, Alabama, October 26-27, 1999.

40. Taylor, J. J. and Hoyt, J. W., Water Jet Photography-Techniques and Methods, Exp. Fluids, Vol. 1, pp. 113-120, 1983.

41. Siebers D. L. Scaling liquid-phase fuel penetration in diesel sprays based on mixing-limited vaporization. Society of Automotive Engineers, 1999 Congress and Exposition, SAE Transaction Paper 1999-01-0528, March 1-4, 1999.

Nomenclature

- d : Injector tube diameter
- D : Drop diameter for gasification characteristic time computation
- F_r : Froud number
- K : Vaporization constant in D-square law for a drop
- L : Characteristic dimension of turbulent eddy
- P_c : Critical pressure of the injectant
- P_{ch} : Chamber pressure
- P_r : Reduced pressure, P/P_c
- R_e : Reynolds number
- T_r : T/T_c
- T_c : Critical temperature of the injectant
- T_{ch} : Chamber temperature
- ρ_l : Liquid density
- ρ_g : Gas density
- ρ_R : (ρ_g/ρ_l)
- σ : Surface tension
- θ : Jet or spray full cone angle

This Page Intentionally Left Blank

APPENDIX H

"Initial Growth Rate and Visual Characteristics of a Round Jet into a Sub- to Supercritical Environment of Relevance to Rocket, Gas Turbine, and Diesel Engines"

AIAA 99-0206
Initial Growth Rate and Visual Characteristics of a Round Jet into a Sub- to Supercritical Environment of Relevance to Rocket, Gas Turbine, and Diesel Engines

B. Chehroudi*[*], *D. Talley, and E. Coy

Air Force Research Laboratory
10 E. Saturn Boulevard
Edwards AFB, CA 93524-7680

Initial Growth Rate and Visual Characteristics of a Round Jet into a Sub- to Supercritical Environment of Relevance to Rocket, Gas Turbine, and Diesel Engines

B. Chehroudi[*]*, D. Talley, and E. Coy*

Air Force Research Laboratory; AFRL/PRSA
10 E. Saturn Boulevard
Edwards AFB, CA 93524-7680

Abstract

The combustion chamber temperature and pressure in many liquid rocket, gas turbine, and diesel engines are quite high and can reach above the critical point of the injected fuels and/or oxidizers. A high pressure chamber is used to investigate and understand the nature of the interaction between the injected fluid and the environment under such conditions. Pure N_2 , He, and O_2 fluids are injected. Several chamber media are selected including, N_2, He, and mixtures of CO+N_2. The effects of chamber pressure ranging from a subcritical (i.e. relative pressure, $P_r = P/P_{injectant\ critical} < 1$) to a supercritical ($P_r > 1$) values at a supercritical chamber temperature (i.e. relative temperature $T_r = T/T_{injectant\ critical} > 1$) are photographically observed and documented near the injector hole exit region using a CCD camera illuminated by a short-duration back-lit strobe light. At low subcritical chamber pressures, the jets exhibit surface irregularities that amplify downstream, looking intact, shiny, but wavy (sinuous) on the surface which eventually break up into irregularly-shaped small entities. Further increase of chamber pressure causes formation of many small droplets on the surface of the jet ejecting away only within a narrow region below the critical pressure of the injected fluid similar to a second wind-induced liquid jet breakup regime. Raising the chamber pressure, transition into a full atomization regime is inhibited by reaching near, but slightly lower than, the critical pressure of the injectant where both surface tension and heat of vaporization are sufficiently reduced. The jet appearance changes abruptly at this point and remains the same to resemble a turbulent gas jet injection. In this region, and within the imaging resolution limitation, no droplets are seen forming and/or departing from the jet. The jet initial total divergence angle, indicating initial growth or spreading rate, is extracted from a large set of images and plotted along with the available data on liquid fuel injection in diesel engine environment, turbulent incompressible, supersonic, and variable-density jets and mixing layers, creating a unique plot on its own. The jet spreading rate measurements agree well with a theoretical equation proposed by *Papamoschou and Roshko [1]* and closely follow the trend of that of *Dimotakis [2]* for incompressible but variable-density turbulent mixing layers, thus quantitatively strengthening the gas-jet like appearance. Considering this agreement, the inhibition of transition to atomization regime and its confirmation through the examined atomization criteria, and the visual lack of any drop; the relevancy of current injection models and some drop vaporization/combustion results under conditions where gas-jet like appearance is observed should be reexamined.

Introduction

In many power production machines liquid fuel is injected into a high temperature and pressure combustion chamber to react with an oxidizer for release of the fuel's chemical energy. Such relevant examples are rocket, gas turbine, and diesel engines. In the designs of chemical rocket engines liquid fuel and oxidizer are injected through openings to form round jets, coaxial or impinging types, entering into the hot and elevated pressure environment of the combustion chamber. Simple thermodynamic analysis of the rocket thrust chamber (combustion chamber plus the expansion nozzle) shows that, for a given thrust, the rocket size may be decreased as chamber pressure is increased. The extent of this benefit, however, is lowered by other considerations such as higher thrust chamber stresses, heat transfer rates, and pump power and size. As far as the combustion is concerned, effects of increased chamber pressure are to decrease dissociation of the molecules and hence increase the effective heat release. Higher effective heat release, theoretically, delivers higher specific impulse. Hence motivation towards higher chamber pressures are justified. In diesel engines, the higher the compression ratio the higher the thermal efficiency, being the desired trend. In addition, extremely high in-cylinder liquid fuel injection pressures of up to 200 MPa are employed for better air/fuel mixing to reduce soot formation and EPA-regulated exhaust smoke. In gas turbine engines, high compressor pressure ratios (translate into high chamber

[*] *Chief Scientist, Raytheon STX*

pressures) and elevated combustor exit temperatures lead to better thermal efficiencies.

In all of the above examples, due to the high pressure trends and existence of high temperature in the combustor, injected liquid may find itself near or even above the thermodynamic critical condition. For example, the Space Shuttle main engine thrust chamber pressure is about 22.3 MPa. And, the combustion chamber pressure for Vulcain (Ariane 5) with liquid H_2/liquid O_2 can reach up to 10 MPa while a record pressure of nearly 28.2 MPa has been reported. Very little information is available on liquid jets injected into supercritical condition. And this leads to our motivation in initiating an organized and systematic experimental effort investigating liquid jets under sub- and supercritical conditions.

There are drastic changes in some important properties of a pure substance as it approaches the thermodynamic critical point (CP). For example, under thermodynamic equilibrium condition, the distinction between liquid and gas phases disappears at and above the critical point and it is simply referred to as "fluid". This phenomenon was first discovered in 1821 by Baron Charles Cagniard dela Tour, a French scientist, who heard no splashing of the mixture of liquid and gas above a certain temperature. Also, large changes of density occurs near the critical point. Other properties that change widely near the critical point are thermal conductivity, mass diffusivity, and surface tension. Indeed, constant-pressure specific heat becomes very large and surface tension vanishes at the critical point. For these reasons most applications avoid operation near the critical point. In many practical applications liquid fuel is vaporized or burned in an environment consisting of air and/or products of combustion. Also, as ambient pressure is raised the importance of solubility of gases into the liquid phase increases and one should consider multicomponent phase equilibrium information. For mixtures, determination of the critical conditions, called "critical mixing temperature or pressure" (critical lines for a two-component mixture as opposed to a critical point for a pure substance), are complex, see *Bruno and Ely [3]*. For example, for a pure hydrocarbon drop in a nitrogen environment, the amount of nitrogen dissolved on the surface of the liquid drop increases with pressure and, in addition, critical mixing temperature declines, see *Lazar and Faeth [4]*. Therefore, although a pure liquid fuel drop is introduced, a thin layer, due to low liquid mass diffusivity neglecting internal flows, on its surface is a mixture of nitrogen and the fuel that spreads spatially in time, see *Umemura [5]*. In what follows, unless otherwise made clear, the terms subcritical and supercritical, and relative pressure and temperature are referenced with respect to the critical condition of the pure substance used in drops or jets and not the environment.

Prior to introduction to liquid jet injection into sub- to supercritical condition it is informative to briefly review important findings of liquid droplet vaporization and combustion at high pressure conditions in this and the next paragraphs. The justification is that some physical phenomena observed in these studies may be of use for jet injection. After all, the expectation is that upon injection a jet is atomized into droplets that are then exposed to these conditions. There are many experimental and computer modeling works on droplet vaporization and combustion at elevated pressures. In summary, for nonreacting case, when a drop of a pure substance is exposed to an environment of a different pure substance at $T_r > 1$ but at P_r less than some value ($P_r = P_t$; P_t near 2), drop temperature increases up to a pseudo-wet bulb temperature and settles there until full evaporation. At the wet-bulb condition, all of the heat added to the drop is for the latent heat of vaporization and there is no drop heat up. As environment pressure is increased, in a transition region, $P_t < P_r < P_m$, the pseudo-wet bulb temperature approaches the mixture critical temperature, the drop surface temperature reaches the critical mixing temperature sometime during its life time (for example, at P_t it occurs at the end of its lifetime), and the enthalpy of vaporization vanishes. Above the P_m, drop temperature monotonically increases and rapidly reaches the critical mixing temperature before its lifetime. There is no pseudo-wet bulb temperature in this case. Due to the increased solubility at high pressure, the drop (particularly a thin layer near the surface neglecting drop internal flow) reaches the critical mixing temperature, distinction between phases is then lost and, for surface regression rate analysis, the movement of the "front" at critical mixing temperature is tracked in computational efforts. The center of the drop is believed to be in liquid phase until the critical mixing temperature "front" is arrived. Generally, for hydrocarbons in nitrogen environment and at any fixed relative ambient temperature of up to about 2, the drop gasification lifetime increases with ambient pressure and levels off (or starts to decrease mildly) at about (1 to 3)*$P_{critical}$ depending on T_r. Above T_r of 2, gasification lifetime drops sharply with pressure, *see Giveler and Abraham [6]*, to a minimum at about P_r of 5 , *see Umemura [5]*, and rises again due to lowered mass diffusivity at high pressures. Initial decline in gasification time with pressure is primarily due to reduced enthalpy of vaporization but later when it vanishes, low mass diffusivities slow down the gasification process.

For the combustion of drops, the flame envelope creates another source of heat addition after ignition and also acts as a sink for the vaporized and diffused fuel and oxidizer molecules. Pioneering drop combustion experiments by *Faeth et al. [7]* in lowered gravity condition show that at low pressures, pure fuel drop temperature, measured inside of it via a thermocouple bead junction, rises to a plateau at wet-bulb temperature, being near the boiling temperature at pressures below the critical pressure of drop. After the end of this plateau period, also called quasi-steady-state-behavior period, where gasification is completed, the measured temperature rises again until the end of the combustion. This whole picture repeats itself up to about two and a

half the critical pressure of the fuel beyond which no wet-bubble plateau is observed. *Faeth et al. [7]* define this condition as the onset of the supercritical burning. Beyond this ambient pressure, drop temperature increases monotonically until the complete burnout. It is also found that the combustion time (i.e. from ignition to when all fuel is burned) decreases to a local minimum near the fuel's critical pressure and then increases, whereas gasification time (i.e. from when drop is exposed to ambient to when all fuel is gasified) continuously shortens. Computational modeling work by *Shuen et al [8]* reveals detailed information on a liquid drop combustion under sub- and supercritical conditions. According to them, as ambient pressure is raised, ambient-gas solubility in the liquid phase increases causing lowered critical mixing temperature until eventually the time-increasing surface temperature reaches this critical mixing value at which time latent heat of vaporization vanishes. Computed trends of combustion lifetime with ambient pressure for large drops (1000 micron) behave similar to the experimental observations of *Faeth et al. [7]*. Similar results for small drops do not show this trend and combustion time increases monotonically. *Shuen et al. [8]* also show that flame radiation can play an important role for large drops and must be accounted for in modeling efforts. There are two other interesting results. First, time histories of the fuel mass, as opposed to surface regression rate, indicates that gasification is facilitated more at high pressures. Second, flame temperature continuously decreases with ambient pressure for large drops due to importance of lowered mass diffusivity at high pressures and also, for the same conditions, flame temperature is higher for small drops. These two results suggest higher ambient pressures and better liquid fuel atomization for rocket, gas turbine, and diesel engines.

There are a few works on liquid injection into supercritical condition, notably *Newman and Brzustowski [9]* and *Mayer et al.[10], [11]* at high Reynolds numbers and *Woodward and Talley [12]* at low Reynolds numbers. *Newman and Brzustowski [9]* use steady CO_2 jet injected into a chamber of pure N_2 and mixtures of CO_2+N_2at both sub- and supercritical pressures and temperatures. Note that if chamber is at supercritical pressure the injected jet pressure is higher and must also be supercritical. At just above critical pressure of CO_2, injection of CO_2 into mixtures of CO_2+N_2 , varying initial CO_2 concentration to change mixture density, shows thickening and widening of the jet due to changes in chamber-to-injectant density ratio. At a high supercritical pressure, injection of CO_2 into a pure varying sub- to supercritical temperature N_2 causes shortening of both the jet length and its width with chamber temperature. They explain effects of increased chamber temperature on jet appearance to be due to progressive reduction in ambient gas density, lowering in surface tension to zero at critical temperature, and increase in liquid CO_2 evaporation. *Newman and Brzustowski [9]*, in experiments where CO_2 is injected into a mixture of CO_2+N_2 with constant but large initial CO_2 mass fraction (to reduce jet evaporation) at a fixed supercritical temperature but varying sub- to supercritical pressures, propose possibility of gasification and that at supercritical temperatures and pressures the jet can be considered as a variable-density single-phase turbulent submerged gas jet. Finally, assuming self-preserving flow, negligible gravity, zero latent heat of vaporization, ideal gas behavior, and thermal equilibrium between gas and drops, they develop a model for predicting the profile of the outer extent of a supercritical steady jet and its centerline mean axial velocity. Comparison with experiment was poor near the injector. *Mayer et al [11]* use liquid N_2 (LN_2) jet at 105 K into a N_2 environment at 300 K but at varying ambient pressures ranging from sub- to supercritical conditions and observe drastic changes in the jet structure near and above the critical pressure. The jet behaves similar to the classical atomization of liquid fuel with ligaments and drops near the critical pressure. They attribute this behavior to a continual decline of surface tension until it vanishes at and beyond critical point. They also consider He(at 280K) and N_2(at 97K) combination injection, as simulant fluids for H_2 and O_2 combination, through a coaxial injector (N_2 in the center hole, He through the outer annular space) similar to the ones used in the cryogenic rocket engines. Again, changes in the jet structure at high pressures as solubility of He into N_2 increases and surface tension reduces are clear. For example, at each fixed pressure above the critical pressure of oxygen, for a binary mixture of H_2+O_2, surface tension declines with temperature to a zero value at the critical mixing temperature. They also observe jet structural changes in both ignition and combustion phases of the H_2 and O_2 system in a model of a rocket combustion chamber. They report no evidence of droplets at supercritical combustion. For an N_2-into-N_2 cryogenic jet, *Woodward and Talley [12]* showed that the addition of He gas to the supercritical ambient N_2 fluid forced the jet to look like injection into the subcritical ambient condition.

In what follows experimental arrangement is described followed by presentation of results and their discussion under jet structure and jet spreading angle. The paper concludes with summary and conclusion section.

Experimental setup

Figure 1 shows schematic drawing of the experimental set up. It consists of three main sections: high pressure chamber, cryogenic cooler, and plumbing for introduction of different substances as ambient media inside the chamber and for routing of the injectants through the injector. The high pressure chamber is constructed with stainless steel to withstand pressures and temperatures of up to 137 atm (2000 psi) and 473 K, respectively. For optical diagnostics, there are provisions for two facing circular sapphire windows of 133.4 mm (5.25") diameter and two facing UV-grade side-mounted slot-shaped quartz windows of 120.7 mm x 12.7 mm (4.75" x 0.50") for laser in/out of the chamber. Critical pressure and temperature of N_2 are 3.4 MPa and 126.2 K and, under

thermodynamic equilibrium, as long as temperature is below the critical temperature it can be considered as liquid. Since liquid phase N_2 injection into the chamber at above the critical pressure is to be attempted, injectant temperature must always be kept below its critical temperature. Also, transport of the liquid through the

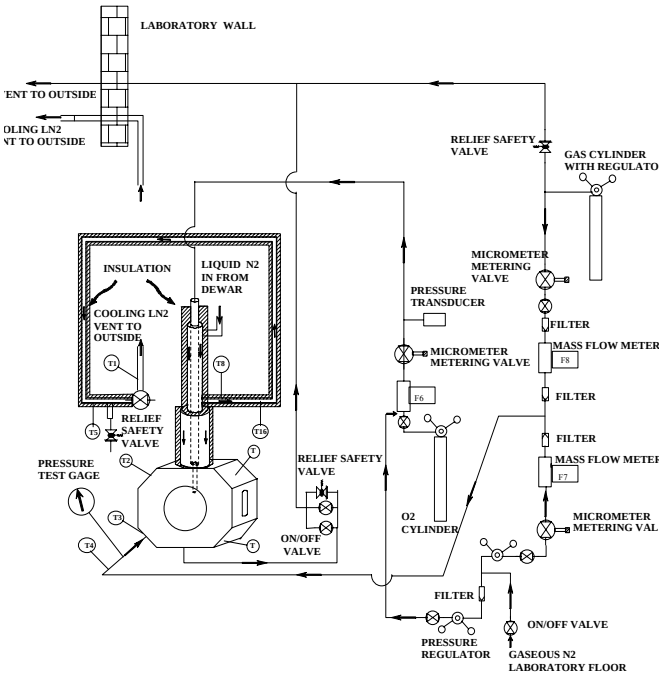

e 1. Schematic diagram of experimental setup for sub- to supercritical jet injecti

lines and the injector can be achieved either via application of high pressure inert gas applied into a high pressure cooled N_2 dewar connected to the chamber as in *Mayer et al.[11],* accepting possibility of dissolved gas; or in our case as shown in Figure 1. The cryogenic cooler uses liquid N_2 from a dewar as the cooling medium. The purpose of this cooler is to cool and/or liquify the injectant passing through it. N_2 from the laboratory is available to be used both as an injectant as well as the chamber medium. Also, a branch is connected for possibility of introduction of other pure or mixture of gases as chamber medium. The mass flow rate of the injectant is regulated and also measured via a mass flowmeter and a precision micrometer valve. For more details refer to *Woodward and Talley [12].* The injector in this study is a sharp-edged 50 mm long stainless steel tube with 1.59 mm (1/16") diameter and a 254 micron (0.010") inner hole (length-to-diameter ratio of 200). Inlet region for the laminar flow in pipes at Reynolds numbers of 5000 to 10,000 is from 150 to 300 pipe diameters and for turbulent flow from 50 to 100, see *Schlichting [13].* The length is therefore long enough to ensure fully-developed turbulent pipe flow at the exit.

The experimental rig is fully instrumented with thermocouples, pressure gages and transducers, and mass flowmeters at the locations indicated in Fig. 1. Figure 2 shows details of the image acquisition logical setup along with the timing diagram. The outputs of all measurement devices are connected to a National Instrument AMUX-64T analog multiplexer with special provision for temperature sensor, which itself is connected to a NB-MIO-16X multifunction I/O board (not shown) for Macintosh NuBus computer. A Macintosh computer with a Labview data acquisition software continuously updates all the measured quantities for live inspection and can all be saved with a click of a mouse button. Back-illuminated arrangement is used for initial visual characterization. A QuadTech Stroboslave with a light diffuser in its front provides externally-triggered choices for flash durations

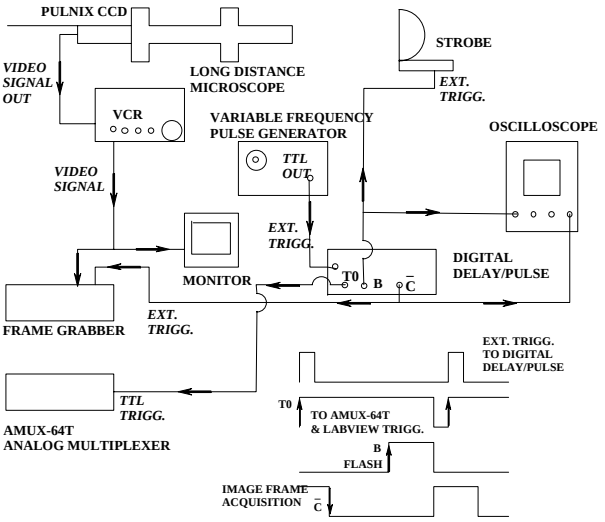

Figure 2. Schematic diagram of the image and data acquisition systems with timing diagram.

of 3, 1.2, and 0.8 microseconds. Almost all the pictures presented in this paper are taken with flash duration of 1.2 microseconds. A model K2 Infinity long-distance microscope with variable focus and manual iris, for illumination and depth of field control, is used to form images of the injected jets presented in this paper. A TM-745E high resolution (768(H) x 493(V) pixels in 8.8(H)x6.6(V) mm actual sensing area) interlaced CCD camera by PULNix with composite video output is used in free run operating mode. The image is captured by a scientific image grabber LG-3 from Scion Corporation installed in another dedicated Macintosh computer and run by the NIH (National Institute of Health) image acquisition and processing software package for Macintosh. Images are analyzed by either ImagePro from Media Cybernatics or NIH image processing softwares. The pulse command to activate the frame grabber is set to 9.11 ms earlier than the flash timing to ensure capture of the illuminated jets in this free run operating mode. This system provides reliable frame rates of up to 20 frames per second.

Jet structure

Prior to systematic acquisition of images at different conditions, a need for initial evaluation of the system is realized. Specifically, effects of injector mass flow rate and chamber pressure on the injector exit N_2 temperature are investigated. Exit N_2 temperature at the tip of the small injector for this study is measured by installation of an identical tube injector with its hole enlarged only for the last 3 to 4 mm of the length at the exit tip to accommodate a small-sized thermocouple bead without severely obstructing the flow of N_2 through the injector. In this region, a hole is made through the tube's side wall to insert a miniature Omega Type-E 304 SS Sheath Chromega-Constantan exposed-junction thermocouple. A second thermocouple exposed junction is attached to the injector outer wall near the tip and held in contact with the wall by a thick Teflon insulating sheath covering the entire injector tube. These two temperatures are measured simultaneously to document their relationship. The information for the wall temperature alone is then used to estimate the actual tip exit N_2 temperature during all tests when unmodified injector tube is used. Tests indicates that both thermocouple readings stabilize to different constant values when the injected mass flow rate is above about 125 mg/s. Wall temperature is about 66 +/- 1 C higher than the tip exit value. At a constant mass flow rate, the exit N_2 temperature varies from 99 K to 120 K as relative (chamber) pressure changes from 0.23 to 2.74. This is due to changes in injected N_2 specific heat and density as chamber pressure is varied. In this work, tip temperature is used for calculations of the other jet property values.

To see if effects of buoyancy forces are important within the distances looked in this study, Froude number values are calculated at each chamber pressure. This number changes from 42,000 to 110,000. *Chen and Rodi [14]* propose that the flow is momentum driven as long as a defined nondimensional buoyancy number is less than 0.53 whereas *Papanicolaou and List [15]* suggest this number being less than 1. Considering the more conservative estimate by *Chen and Rodi [14],* the jet used here is momentum dominated for distances less than 30 to 40 mm from the injector exit. Pictures presented here cover up to about 7 mm (axial distance/diameter ratio of 28) from the injector and hence buoyancy effects can be ignored in favor of the inertia forces.

Figure 3 shows images of the N_2 jet injected into N_2 at a fixed supercritical chamber temperature but varying sub- to supercritical pressure. The iris of the camera and the flash intensity are adjusted to acquire images at the highest contrast possible. A 3.5 mm long real object projects to fill the vertical extent of the images in Fig. 3. Hence, considering 493 pixels in this direction, theoretically, a pixel-to-pixel distance represents 7 micron of real object. On the high resolution prints of the processed images one can recognize objects with real size of about 30 microns and larger. Of course this is an estimate being good by +/- 7 micron band. What we see in these images are demarcation of regions where changes in index of refraction occur due to density variations. At the lowest subcritical chamber pressure in Fig. 3 the jet is liquid-like with surface instabilities that grow downstream where it has twisted appearance. At P_r of 0.43 all instabilities are further amplified until at the next higher pressure where many surface ligaments and drops are seen ejected from the jet. At P_r of 0.83 very fine drops are seen surrounding the jet and its spanwise dimension noticeably grows away from the injector exit plane (i.e. jet diverges). At P_r of 1.03 the N_2 jet enters into a supercritical temperature and pressure environment. There are drastic changes in details of the interface. There are no detectable drops under this condition with the highest software magnification used to view these high resolution images. There are thread- or finger-like entities emerging from the jet which are not broken up into droplets as before but are seemingly dissolved at a spectrum of distance from the dark core. This, in a sense, forms a mixing layer in which phase transition and/or large local density nonuniformities occur. Any further increase of chamber pressure decreases the length and the thickness of the internal dark core and images progressively resemble injection of a gaseous turbulent gas jet into a gaseous environment. Figure 4 is the magnified images of the mixing layer at three subcritical, transitional, and supercritical chamber pressures. Gradual transition from classical liquid-like ligament and drop formations at the interface, seen in liquid atomization regime, to a comb-like structure near the critical point and finally to where submerged turbulent jet appearance emerges can be observed. Inspecting a large set of images at high magnifications, no evidence of drop formation is seen in this gas-like jet regime. These observations are also consistent with images presented by *Mayer et al [11].* As briefed in the introduction section, the gas-like jet appearance was also proposed by *Newman and Brzustowski [9]* although no high magnification near-injector photographs are shown in their paper. In summary, for N_2 into N_2 injection at the supercritical ambient temperature tested here, there appears to be two structural transitions. One is when the intact jet with irregularly-looking surface waves and downstream shiny twisted-shaped column turns into a somewhat diverging jet with ligaments and many small droplets. The other is when the latter structure changes into a gas-like jet appearance near but below the point where the medium pressure changes from sub- to supercritical conditions (based on the injectant critical pressure). The reason for this behavior, particularly for the change into gas-jet behavior, should be sought in progressive reduction of surface tension and heat of vaporization until they both vanish at and above the critical point. Similar observations are made for the O_2-into-N_2 case but with the transition to gas-like jet at near oxygen critical pressure (P_r = 0.85). Observation of the gas-like jet behavior and the lack of any drop formation raises question on relevancy of current injection models and some drop vaporization/combustion results within this regime.

Breakup and atomization regimes of the liquid jet within a narrow chamber-to-density ratio is traditionally shown on a plot of Ohnesorge number versus Reynolds number (Ohnesorge number $=\sqrt{We}/Re$, where We, Weber number, equals to $\rho_l U^2 d/\sigma$, and Reynolds number, Re, is $\rho_l Ud/\mu_l$; ρ_l, σ, and μ_l are the liquid density, surface tension, and viscosity respectively; U is liquid exit velocity , and d is the nozzle diameter). On such a plot, in an application where a single liquid is used and surface tension is constant, one moves from left to right on a horizontal line as Reynolds number is increased by changing the injection velocity. Along such a horizontal line and according to *Reitz and Bracco [16],* one moves from Rayleigh jet breakup to first and second wind-induced breakups and finally to atomization regimes. Rayleigh breakup is caused by the growth of axisymmetric oscillations of the jet surface, induced by surface tension and drop diameters larger than the jet diameter is produced. In the second wind-induced regime, drops are generated by growth of short-wavelength surface waves on the jet surface due to relative motion of the jet and the environment. This unstable growth is opposed by the surface tension, breakup happens at multiple diameter distance, and finally drops with average diameter of less than the jet diameter is produced. In the atomization regime, however, the jet is completely broken up at the nozzle exit and average drop diameter of much less than jet diameter is observed. In Fig. 3, as chamber pressure is increased approaching the critical condition, surface tension is reduced to a near-zero value and for the range of Reynolds number calculated here (25,000 to 75,000) the Ohnesorge number sharply swings from a low (estimated to be $2.8x10^{-3}$) to a very large (infinity when surface tension is zero) value. The large Ohnesorge number regime and its importance are indicated in *Faeth [17]* and *Tseng et al. [18]*. The jet under this condition is named "sable jet" for Ohnesorge number values of above 2 to 3 and they state that heavy fuels have higher Ohnesorge number while it becomes large for all liquids at high ambient pressure approaching the critical point due to lowered surface tension.They acknowledge the need for further study in this region. Looking at the regime boundaries proposed by *Reitz and Bracco [16],* our jet should start in the first and/or second wind-induced zone and quickly pass the atomization regime as chamber pressure is raised from the lowest value shown in Fig. 3. In Fig. 3, one can see first or second wind-induced-like tendencies for the first two lowest chamber pressures, quickly entering into a clear second wind-induced appearance as seen in the next two higher pressure images. However, it seems that before having a chance to show full atomization character, surface tension is sufficiently and rapidly reduced so one achieves gas-like jet appearance near but before reaching the critical pressure value, see Fig. 3. At this condition one sees, in magnified images shown in Fig. 4, that thread-like or finger-like structures are stretched out into the ambient but interestingly appear not broken up into droplets. As surface tension and heat of vaporization approach near zero values in the vicinity of the critical point, the threads or fingers are gasified and no drops are detected. Transition into full atomization regime is therefore inhibited. Note that the Ohnesorge-versus-Weber number transition criteria do not have gas density or nozzle geometrical effects. Our observed transition inhibition event is therefore tested by another criterion of *Reitz and Bracco [16]* in which chamber-to-injectant density ratio, nozzle geometrical factor, and Weber and Reynolds numbers are all included. Within the limitations of this criteria, no full atomization is allowed. In a sense, as it approaches the critical point, the jet investigated here exhibits a dual character depending on the magnitudes of the surface tension and heat of vaporization: liquid-jet like and gas-jet like faces.

Approximate characteristic time estimates also point towards inhibition of the atomization as follows. *Tseng et al. [18]* describe the initial turbulent breakup scenario of the intact jet by formation of a drop from a turbulent eddy with characteristic dimension and cross-stream velocity of "L" and v_L , respectively, in a form of a bulge from the surface of the jet. A characteristic time for the separation of this bulge from the jet to form a drop is proposed to be proportional to $(\rho_l L^3/\sigma)^{1/2}$. On the other hand, vaporization characteristic time of an isolated liquid drop with a diameter of D using the "D-square" law is proportional to D^2/K, where K is the vaporization constant related to the Spalding B-constant by $K=(8k_g/(\rho_l C_{pg}))\ln(B+1)$ and $B=C_{pg}(T_{oo} - T_{boil})/h_{fg}$. Here, k_g , C_{pg} are thermal conductivity and constant-pressure specific heat of the chamber environment gas. The h_{fg} and ρ_l are the density of the liquid drop and latent heat of vaporization at chamber pressure. T_{oo} and T_{boil} are the chamber gas temperature at large distance from the drop and boiling temperature of the liquid substance, respectively. It can be seen that approaching the critical point the σ and h_{fg} decrease to zero and characteristic drop formation becomes very large whereas evaporation time shortens. As indicated in the introduction, the gasification lifetime decreases to a minimum with pressure up to about P_r of 5. Therefore, bulge separation time (to form a drop) is expected to be much larger than the gasification time. Here, the heat up time is neglected as the liquid is near the saturation line. This approximate analysis suggests nonexistence of any drop in the flow field under supercritical condition in an injected liquid jet arrangement. In other words, it will take progressively longer time for the bulges to turn into isolated drops and when/if they do, they are gasified increasingly faster as critical condition is approached. In the limit, although irregularly-shaped jet boundary is formed, they gasify before having the chance to separate into isolated entities.

Jet spreading angle

Looking at images in Fig. 3, one important geometrical parameter that can be quantitatively evaluated is the initial

jet spreading angle or its growth rate. Therefore, this parameter is measured for all acquired images and results along with those of others are presented in Fig. 5. A universal trend can be discovered if nondimensionalized grouping numbers based on appropriate characteristic properties are used to plot the experimental data. As an example see the relevant and excellent work of *Papamoschou and Roshko [1]*. Our initial choice of density ratio in Fig. 5 follows both from liquid spray and gaseous mixing layer works. The angles in our work are measured from the information within a 7 mm distance close to the injector exit face (distance-to-diameter ratio of up to 28). Note that, according to *Abramovich [19]* the length of the potential core in isothermal uniform-density axisymmetric and two-dimensional jets are estimated to be about 16 to 18 injector diameters whereas for nonisothermal cold-into-hot jets it can reach up to about 50 injector diameters. Also, accoring to *Chehroudi et al [20]* the intact core of the liquid sprays similar to the ones used in diesel engines is $C.d(\rho_l/\rho_g)^{1/2}$ where ρ_l and ρ_g are liquid injectant and chamber gas densities, respectively, d is the effective jet exit diameter and C is a constant between 3.3 to 11. This reflects to an intact core length of between 33 to 110 injector diameters for the chamber-to-injectant density ratio of 0.01 and 16.5 to 55 diameters for the chamber-to-injectant density ratio of 0.04. See Fig. 5 for the range of the density ratio. The foregoing information is to justify that data from corresponding and appropriate initial region is used for growth rate estimations to ensure existence of mixing layer region. At each condition 20 images are used to form an averaged image from which angle measurements are made for presentation in Fig. 5. Both the outer limit and the dark inner core angles are determined by inspection on the computer. A typical example is shown in the inset of Fig. 5. Maximum uncertainty band on angle measurements are also shown for O_2 and N_2 data. Alternatively, the angle for each of the 20 images per condition is measured separately and then averaged. No appreciable differences are observed between the two methods.

Of importance in Fig. 5 are the justification for the selection of the data sets and the nature of their measurements by other researchers. They are elaborated in the following. We consider offering adequate description and review of data by others so that a deeper appreciation of Fig. 5 and its uniqueness can be realized and a reasonable degree of self-sufficiency is achieved. After justification of the selected data and its relation to ours we present our data and offer interpretations. Since the jets investigated here exhibit both liquid-like and gas-like jet appearances, appropriate results for both are discussed here. The simplest is the prediction of the linear jet growth or constant spreading angle for the turbulent incompressible submerged jet. This is derived using the mixing length concept as detailed in the Appendix. Here, the parameter "2b", the jet thickness from the velocity profiles, is apparently measured at the 95% roll-off point. Next, following *Abramovich [19],* is the semi-empirical equation that attempts to incorporate the effects of density variations by introduction of a characteristic velocity as shown in the Appendix. See Fig. 5 for the plots of these two cases.

Results of *Brown and Roshko [21]* taken in an experimental setup in which helium and nitrogen are used as the two fluids for their subsonic two-dimensional incompressible turbulent mixing layer studies are important. Note that we also use cooled helium and nitrogen gases in our jet injection study as seen in Fig. 5. They measure mixing layer spreading in a two-dimensional arrangement by both shadowgraphy (called visible jet thickness) as well as through velocity profiles extracted from results of a concentration probe, see *Brown and Rebollo [22]*, along with Pitot tube dynamic pressure measurements within the layer (called vorticity thickness as described in the Appendix). They make distinction between mixing layers in which density changes are caused by temperature changes, high-speed compressible (high Mach number and supersonic) flows, and differences in molecular weights (i.e. different gases). Using forms of the turbulent continuity and momentum equations that are applicable for both the supersonic and incompressible but variable-density cases, they show that if the $\overline{\rho' v'}$ and $\overline{u' v'}$ correlations depend only on density and velocity (and not specifically on temperature or Mach number) then experimental differences between the supersonic and incompressible variable-density mixing layers must be due to differences in other equations to be satisfied for these two cases (i.e. energy equation for the supersonic and mass diffusion equation for the incompressible variable-density cases). Here, the v', u', ρ' are spanwise, streamwise, and density fluctuations with overbar standing for time averaging. The mass diffusion equation leads to $\nabla.\mathbf{U} = 0$, a form of the incompressibility statement, in which $\mathbf{U}$ is the time-averaged two-dimensional velocity vector. The energy equation for the turbulent supersonic case simplifies to a similar equation but with the left hand side of $P[\nabla.\mathbf{U}]$ plus two extra terms. These terms involve the correlation between pressure and transverse velocity fluctuations in one term and pressure gradient across the layer in the other. They state that if these two terms are negligible (i.e. at low Mach number squared values) then there is no distinction between mixing layers made of two streams with differences in molecular weights, differences in temperature, and high speed compressibility effects. This is clear as both equations lead to $\nabla.\mathbf{U} = 0$. In the jet we are investigating here there are both differences in temperature as well as molecular weight except for the N_2-into-N_2 case.

For comparison purposes, the two-dimensional turbulent mixing layer experimental data of the *Brown and Roshko [21] is* used to infer the initial spreading rate for axisymmetric jets. Results are plotted in Fig. 5. This is justified since according to both *Brown and Roshko [21]* and *Abramovich et al. [23],* two-dimensional mixing

layers are found to be fairly well approximated by the initial mixing region of axisymmetric jets. For this reason all angle measurements in our work are made using only the information within the first 7 mm distance of the injector exit plane. We assume a zero value for the ambient velocity (chamber is quiescent in our case) , and for this case, there are only two visual growth rates with their corresponding vorticity growth rates reported by *Brown and Roshko [21]*. All other data including the supersonic mixing layer measurements by other researchers (used by *Brown and Roshko* for comparison) are given as vorticity growth rates. Based on these two data points a conversion factor is calculated between the visual and vorticity growth rates. This factor is also applied to the vorticity growth rate values of other researchers collected by and reported in *Brown and Roshko [21]* for the supersonic jets.

Richards and Pitts [24] use a long sharp-edged round tube injecting momentum-dominated helium, propane, and methane turbulent round jets into air. Rayleigh scattering is used to measure concentrations and through concentration plots they define and present a half-radius jet thickness (the radius at which concentration drops by fifty percent of its maximum centerline value). Their first two reported measurement locations, where data for all gases exists, are at distance/radius ratios of 40 and 60 from the injector and are used to calculate the jet spreading angle. Images in Fig. 3 are up to distance/radius ratio of about 55. For this reason we do not use results taken at higher distances for comparison to our data presented in this paper. Based on their mass fraction plots, we judge the full thickness of the jet to be about 4 times the half-radius jet thickness value. This is taken to be the equivallent of the jet visual thickness. Considering that in jets the concentration profiles are generally wider than the velocity profiles, higher values of spreading is expected as shown in Fig. 5.

Papamoschou and Roshko [1] in a series of experiments on sub- to supersonic plane two-dimensional turbulent mixing layers use schlieren photography and Pitot probe (dynamic pressure) to document the mixing layer spreading characteristics. They see, as others in the past, that at supersonic velocities the spreading angle decreases as compared to those of classical turbulent incompressible cases. Although effects of compressibility is at work here but spreading angle also depends on other important parameters such as velocity and density ratios for the two streams forming the mixing layer. Their spreading rate is determined by a linear least square fit to the "Pitot tube thickness" data at distances above 75 mm from a centerbody divider installed in their flow facility. In this work they also discuss the relationship between the three mixing layer thicknesses, namely, δ_{vis} (visual thickness), δ_{pit} (Pitot tube thickness), and δ_{ω} (vorticity thickness). These are defined in the Appendix. They propose the following relationships between them: $\delta_{\omega} = 0.5\ \delta_{vis}$ and $\delta_{pit} = 1.44\ \delta_{\omega}$, leading to $\delta_{pit} = 0.72\delta_{vis}$. However, based on the data from *Brown and Roshko,* $\delta_{pit} = 0.90\ \delta_{vis}$ although $\delta_{pit} = 0.80\ \delta_{vis}$ was finally used following *Konrad [25]*. We use $\delta_{\omega} = 0.5\ \delta_{vis}$ to convert the supersonic mixing layer results to compare with our visual thickness values.

To separate effects of the compressibility, following *Bogdanoff [26]*, *Papamoschou and Roshko [1]* define a convective velocity (U_c) and a convective Mach number $(M_c = (U - U_c)/a;\ a \text{ is speed of sound})$ to be more appropriate than the individual streams' Mach numbers in the mixing layer due to the coherent structures observed by *Brown and Roshko [20]*. It is shown that in a convective system there is a common stagnation saddle point for both streams (first proposed to be considered by *Dimotakis)*. At this point, by setting the total pressure expressions the same for the two streams and considering near-equal specific heat ratios one has: $U_c = (\sqrt{\rho_1}U_1 + \sqrt{\rho_2}U_2)/(\sqrt{\rho_1} + \sqrt{\rho_2})$. Where ($\rho_1$, U_1) and (ρ_2 , U_2) are density and actual velocity pair of the two streams forming the mixing layer. Note the difference between this equation and the characteristic velocity of equation 5 in the Appendix. For an incompressible variable-density mixing layer, they assume that the main effect of the density ratio is to determine the convective velocity of the structure. And that in a reference frame moving with convection velocity the growth rate is conjectured to be proportional to $\Delta U = U_1 - U_2$. Hence, the density ratio is not in the equation in this moving reference frame and it leads to $\delta_{vis} \sim \Delta U/U_c$. From this, a form of an equation is proposed for the δ'_{vis} (i.e. rate of change of visual thickness in streamwise direction) applicable for incompressible variable-density mixing layers: $\delta'_{vis} = 0.17(\Delta U/U_c) = 0.17(1 - U_2/U_1)[1 + (\rho_2/\rho_1)^{1/2}]/[1 + (U_2/U_1)(\rho_2/\rho_1)^{1/2}]$

The constant 0.17 was obtained experimentally from *Brown and Roshko [21]*. This equation is used to compare with our results and is plotted in Fig. 5 for the U_2/U_1 of zero value. Finally, interesting but not perhaps directly related to our current work, they plot the normalized growth rate of $\delta'_{pit} / \delta'_{pit,0}$ versus the convective Mach number, where $\delta_{pit,0}$ is the Pitot thickness for the incompressible variable-density shear layer having the same density and velocity ratios as the compressible case (i.e. the equation above), and show that all data cluster to form a universal curve. Here, δ_{pit} is the Pitot thickness for the compressible mixing layers at different Mach numbers similar to the ones shown in Fig. 5. Results for different Mach numbers are shown for comparison and completeness only and are not further discussed here. Interested readers should refer to *Papamoschou and Roshko [1]*

Finally, *Dimotakis [2]* uses the observation that, in general, the entrainment into the mixing layer from each stream is not the same and, in a system moving with the

aforementioned convection velocity, offers a geometrical argument to derive an equation for the two-dimensional incompressible variable-density vorticity thickness growth of the form

$$\delta'_{\omega} = \varepsilon\{(1-U_2/U_1)/[1+(\rho_2/\rho_1)^{1/2}(U_2/U_1)]\}\{1+(\rho_2/\rho_1)^{1/2} - [1-(\rho_2/\rho_1)^{1/2}]/[1+2.9(1+U_2/U_1)/(1-U_2/U_1)]\}$$

This growth rate is multiplied by a factor of 2 to convert to visual shear layer thickness growth rate and is plotted in Fig. 5 for ε value of 0.17/2 after adaptation to the axisymmeteric jets. In Fig. 5 this equation intersects the one by *Papamoschou and Roshko [1]* at density ratio of 1 and they gradually depart on either sides.

Since images in Fig. 3 show both liquid-like and gas-like visual jet appearances, it makes sense and is appropriate to also show the spreading angle for liquid sprays produced from single-hole nozzles typical of the ones used in diesel engines. The atomization of liquids is a complex phenomenon that depends on many parameters among them are: injector geometry, ambient density, viscosity and surface tension of the liquid, initial turbulence, cavitation, and liquid supply pressure oscillations. According to *Reitz and Bracco [16]*, visually, in "full" or simply atomization regime the liquid jet diverges at the exit of the injector hole. Also, using aerodynamic surface wave growth mechanism for liquid atomization they show that the spray angle can be determined by combining the radial velocity of the fastest growing unstable surface waves with the axial injection velocity. A form of an equation is then derived for the spray spreading angle that reproduces the experimental trends of square root of the ambient-to-injectant density ratio as well as the viscosity dependencies. They indicate that the incompressible variable-density equation proposed in *Abramovich [19]*, significantly overpredicts the spray spreading angle for all nozzles at low chamber gas densities (this equation is derived by setting the U_r to zero in equation 6 of the Appendix). This can be seen in Fig. 5. The spray angle in the atomization regime is measured using information within the first 5 mm distance from the nozzle exit plane (distance-to-diameter ratio ranging from 20 to 40). Therefore, the measurements are within the comparable spatial region where we measure our spreading rates. For the two cases shown in Fig. 5 the Reynolds number range between 25,000 to 40,000. For any given nozzle with fixed length-to-diameter ratio the spray angle widens appreciably beyond the Reynolds number values of about 25,000. Both *Reitz and Bracco [16]* and *Hiroyasu and Arai [27]* show profound effects of the nozzle design on the spray angle. Therefore, equations proposed by *Reitz and Bracco [16]* for two different length-to-diameter ratios along with their corresponding vertical bar-bands indicating experimental scatter around them are shown in Fig. 5. Experimental data are taken for the isothermal sprays. As a cross check, recent curve-fitted equation to experimental data proposed by *Naber and Siebers [28]* is also shown. They use transient liquid fuel jet into a high pressure chamber for both nonvaporizing and vaporizing sprays. Their angle measurement zone extends beyond our initial region and this to some extent contributes to disagreement seen between the two sets of data for liquid sprays at injector length-to-diameter density ratio of about 4, see Fig. 5. Their vaporizing liquid spray data show 15% reduction in spreading angle at density ratio of 0.01 decreasing to no noticeable reduction at the ratio of 0.04. This is explained to be due to contraction of the jet caused by the entrained ambient gas cooled by the vaporizing liquid as well as the vaporization of the drops at the outer boundary of the spray. This is important and suggests that the vaporizing versions of the isothermal sprays in Fig. 5 are not much different from the ones shown therein.

The choices of the axes in Fig. 5 are affected by the form of the theoretical equations proposed by *Reitz and Bracco [16]* and *Papamoschou and Roshko [1]* as discussed above. This figure covers a density ratio of a 1000 from liquid sprays to supersonic mixing layers, a unique and new plot on its own. Unfortunately, data presented in this figure does not cluster to form a universal curve and as such choices of the normalized axes are incomplete. This is not surprising in light of the proposal by *Papamoschou and Roshko [1]* in relation to their mixing layer data mentioned earlier. Clearly, within the range plotted, the results of constant spreading angle of incompressible turbulent jet overpredicts nearly all others in Fig. 5. There are also increasing disagreement between turbulent gas jet of *Abramovich [19]* and incompressible variable-density model of *Papamoschou and Roshko [1]* as density ratio increases. Within the range shown, axisymmetric jet spreading angle by *Richards and Pitts [24]* is higher in value than all others due to the reason mentioned earlier. Supersonic jet angle narrows as density ratio is decreased (or Mach number increased). To some extent, for measured values, disagreements in this figure can be attributed to different definitions of the mixing layer thicknesses and their measurement methods. In a sense, data in Fig. 5 is visual thicknesses and not always they are measured directly, hence conversion from vorticity and/or Pitot thicknesses are required. We have used the best estimates of this conversion factor based on works of others as described earlier. Even for those cases where visual thicknesses are measured directly, different photographic techniques are employed causing a certain yet-to-be-assessed degree of variability between different researchers.

For the N_2-into-N_2 case tested in this work, an average curve (not drawn) through the data points in Fig. 5 intersects the *Papamoschou and Roshko [1]* curve somewhere at the density ratio of 0.09. This can be closely observed in the inset in Fig. 5. Departure between the two increases below the critical pressure of N_2 where the jet appears liquid-like, going even below the *Dimotakis's* equation, see Fig. 3 and 5. Note that the tendency of our data to approach those of liquid sprays generated by a comparable high length-to-diameter ratio nozzle (i.e. 85) is evident. Data for O_2-into-N_2 case shows a steeper drop in angle near but below its own

critical pressure in Fig. 5. To build confidence and also generate gaseous jet data using the identical arrangement employed by us to acquire the sub- to supercritical jet images, we injected cooled He gas into the N_2 chamber and vice versa. Results are shown in Fig. 5 for a range of chamber pressures from 0.77 to 9.19 MPa. Although there is scatter in the data at various chamber pressures, it is interesting that the narrowing of the angle is seen as injection of the cooled N_2 into He is considered, consistent with the *Brown and Roshko's* data. The shift to lower density ratios seen in our data is because the injectants are cooled. Injection of N_2 into mixtures of N_2+CO is also considered. In general, effects of these mixtures are through the changes they cause in chamber-to-injectant density ratio, surface tension, and diffusion of N_2 into the ambient. In a binary mixture, we speak of critical "mixing" condition. The case of CO is interesting as its critical pressure and temperature (3.494 MPa, 132.82 K) are very close to those of N_2, so critical mixing condition should be near the pure N_2 case, and has the same molecular weight and specific heat values. Hence, addition of any fraction of CO to N_2 should not change the density ratio, critical condition, and thermal properties. The only relevant property expected to change is the surface tension and its effects should be felt in structural transitions discussed earlier. A more comprehensive discussion of these results should await completion of all the scheduled experiments. However, the spreading rate measurements of the N_2 into N_2+CO mixture closely follows the *Papamoschou and Roshko [1]* theoretical curve increasing the confidence level on our measurements.

It is clear that for a range of density ratios in which our images show gas-jet like appearance the experimental data agrees well with the proposed theoretical equation by *Papamoschou and Roshko [1]* and closely follows the trend of *Dimotakis [2]***.** This can be taken as further and quantitative confirmation that at ambient supercritical pressure and temperature conditions (based on the injectant values) the injected jets visually behave like a gas though technically it may be referred to as "fluid". It is interesting that results for the liquid sprays tend to converge to incompressible jet value at high density ratios for the short length-to-diameter nozzle and not the proposed *Papamoschou and Roshko [1]* equation. There is marked disagreement in both magnitude and slope between liquid sprays (at a comparable length-to-diameter ratio of 85) and our data, see Fig. 5, even though the jet investigated here appears to go through initial phases of the liquid atomization process, see Figs. 3. One expects that our jet should follow the liquid spray results but it does not. Also, pure evaporation of the liquid sprays should narrow the spreading angle as shown by *Naber and Siebers [28]* making this disagreement even farther. The reason is that although the jet studied here shows second wind-induced breakup features similar to liquid jets, it fails to reach full atomization state as chamber pressure (really density) is raised. This is because the thermodynamic state approaches the critical point and consequently both surface tension and heat of vaporization are reduced to a near zero value. Transition into the full atomization region is therefore inhibited.

Therefore, all evidences presented here point towards a gas-jet like behavior within the indicated region. They are: (1) lack of droplet visual detection in the acquired images (smallest detectable is about 30 microns) and visual impression of a gaseous jet; (2) inhibition of transition into the full atomization zone due to lowered surface tension tested by the available atomization criteria; (3) rapid gasification due to vanishingly small heat of vaporization; and (4) agreement of the jet spreading rate measurements with those of incompressible but variable-density gas jets theory (5) disagreement of the liquid spray spreading rate data with comparable nozzle geometry. Although strictly speaking droplets less than about 30 microns cannot be definitively judged by the imaging system employed here, all aforementioned evidences tend to strengthen our gas-jet like picture of the investigated jet near and above the critical point of the injectant. A search for a universal curve to cover all the data in Fig. 5 is a challenging one. To date, no appropriate nondimensionalized parameters are found to collapse all spreading rate information on a single curve. Appropriateness of the surface tension for liquid jets and sprays and its irrelevance for gaseous jets are among the issues to be reconciled.

Summary and conclusions

Structural transition and spreading angle (or growth rate) of jets injected into an environment at fixed supercritical temperature but varying pressure from sub- to supercritical are analyzed. N_2, O_2, and He are injected into N_2, He, and mixtures of CO+N_2 at different proportions. Increasing chamber pressure from a low subcritical value, the fluid in the jet appears to go through classical liquid jet breakup stages up to a second wind-induced breakup regime. In this regime one sees a divergent jet with ligaments and many droplets ejecting from the jet. Penetration into the full atomization regime is inhibited near but before the critical pressure of the injectant because of the combined effects of lowered surface tension and heat of vaporization. At this point the jet assumes a gas-jet like appearance that remains up to the highest pressure tested here. Also, a unique and new plot is formed by converting all other types of spreading rates to the visual growth rate using most relevant works of others on variable density incompressible mixing layers, axisymmetric incompressible and compressible gas jets, supersonic jets/mixing layers, and liquid sprays, covering an ambient-to-injectant density ratio range of a 1000. Spreading angle of the jets in our work is measured from a large set of images and compared with all the aforementioned data by others. Results clearly follow a theoretical equation proposed by *Papamoschou and Roshko [1]* for an incompressible but variable density turbulent mixing layers. This agreement for spreading angles starts at a pressure near but below the

thermodynamic critical value of the injectant substance, quantitatively confirming gas-jet like visual appearance observed in images of the jets for the first time. This jet, therefore, exhibits a dual character behavior: a liquid-jet like and gas-jet like faces depending on the values of surface tension and heat of vaporization. Therefore, (1) inability of droplet visual detection in the acquired images and their visual impression of a gaseous jet, (2) inhibition of transition into the full atomization zone due to lowered surface tension tested by the available atomization criteria, (3) rapid gasification due to vanishingly small heat of vaporization, and (4) agreement of the jet spreading rate experimental measurements with those of incompressible but variable density gas mixing layers theory, (5) disagreement with the liquid spray spreading rate data, all tend to strengthen the position that at near and above the critical point of the injectant the jet exhibits gas-jet like behavior. Considering this, relevancy of current injection models and some drop vaporization/combustion results under the conditions where gas-jet like behavior is detected should be reexamined.

Acknowledgement

The authors would like to thank Mr. Mike Griggs for some machining work and assisting in setup modifications. We appreciate Mr. Theodore Miles's effort in searching copies of many requested publications. Also, Mr. Paul Loftsgard is thanked for his assistance in part of the data acquisition and processing.

References

1. Papamoschou, D. and Roshko, A.. "The compressible turbulent shear layer: an experimental study," J. Fluid Mech., vol. 197, 1988, pp. 453-477.

2. Dimotakis, P. E. "Two-dimensional shear-layer entrainment," AIAA Journal, 21, No. 11, 1986, pp. 1791-1796.

3. Bruno, T. J. and Ely, J. F. *Supercritical fluid technology: review in modern theory and applications*, CRC Press, 1991.

4. Lazar R. S. and Faeth, G. M. "Bipropellant droplet combustion in the vicinity of the critical point", Thirteen Symposium (International) on Combustion, The Combustion Institute, P.801, 1971.

5. Umemura, A. "Supercritical droplet gasification combustion," IUTAM Symposium on theories ? combustion on droplets and sprays, December 1994, Taiwan.

6. Givler, S. D. and Abraham, J. "Supercritical droplet vaporization and combustion studies," Prog. Energy Combust. Sci. vol. 22, 1996, pp. 1-28.

7. Faeth, G. F., Dominicis, D. P., Tulpinsky, J. F., and Olson, D. R. Supercritical bipropellant droplet combustion," Twelfth Symposium (International) on Combustion, The Combustion Institute, 1969, P. 9.

8. Shuen, J. S., Yang, V., and Hsiao, C. C. "Combustion of liquid fuel droplets in supercritical conditions," Combustion and Flame, 89, 1992, pp. 299-319.

9. Newman, J. A. and Brzustowski. "Behavior of a liquid jet near the thermodynamic critical region," AIAA Journal, vol. 9, 1971, no. 8, pp. 1595-1602.

10. Mayer, W., Schik, A., Schweitzer, C., and Schaffler, M. "Injection and mixing processes in high pressure LOX/GH2 rocket combustors," AIAA Paper no. 96-2620, 32nd AIAA/ASME/SAE/ASEE Joint Propulsion Conference & Exhibit, Lake Buena Vista, Florida, 1996.

11. Mayer, W., Ivancic, A., Schik, A., and Hornung, U. "Propellant atomization in LOX/GH2 rocket combustors," AIAA Paper no. 98-3685, 34 the AIAA/ASME/SAE/ASEE Joint Propulsion Conference & Exhibit, Cleveland, Ohio, , July 13-15, 1998.

12. Woodward , R. D. and Talley, D. G. "Raman imaging of transcritical cryogenic propellants," AIAA Paper 96-0468, 34 the AIAA Aerospace Sciences Meeting and Exhibit, Reno, Nevada, January 1996.

13. Schlichting, H. *Boundary Layer Theory*, MacGraw-Hill Book Company, seventh edition, 1979.

14. Chen, C. J. and Rodi, W. "Vertical Turbulent Buoyant Jets- A Review of Experimental Data. 1980, Pergamon.

15. Papanicolaou, P. N. and List, E. J. "Investigations of round vertical turbulent buoyant jets," J. Fluid Mech., 195, 1988, pp. 341-391.

16. Reitz, R. D. and Bracco, F. V. "On the dependence of spray angle and other spray parameters on nozzle design and operating condition," SAE international Congress and Exposition, SAE Paper no. 790494, Detroit, Michigan, February 26-March 2, 1979.

17. Faeth, G. M., "Structure and atomization properties of dense turbulent sprays," Twenty-third Symposium (International) on Combustion, The Combustion Institute, P.1345, 1990.

18. Tseng, L.,-K., Ruff, G. A., P.-K., Wu, Faeth, G. M., "Continuous- and dispursed-phase structure of pressure-atomized sprays," Progress in Astronautics and Aeronatics: Recent Advances in Spray Combustion, February, 1995.

19. Abramovich, G. N. *The theory of turbulent jets*, M.I.T. Press, 1963.

20. Chehroudi, B., Chen, S. H., Bracco, F. V., and Onuma, Y. "On the Intact Core of Full-Cone Sprays," Society of Automotive Engineers, 1985 Congress and Exposition, SAE Transaction Paper 850126, February 25-March 1, 1995.

21. Brown, G. and Roshko, A. "On density effects and large structure in turbulent mixing layers," J. Fluid Mech., vol. 64, 1974, part 4, pp. 775-816.

22. Brown G L, and Rebollo, M R, "A small fast-response probe to measure composition of a binary gas mixture," AIAA Journal, 10, 1972, 649.

23. Abramovich, G. N., Yakovlevsky, O. V., Smirnova, I. P., Secundov, A. N., and Krasheninnkov, S., Yu. "An Investigation of turbulent jets of different gases in a general stream," Astronautica Acta, 14, 1969, 229.

24. Richards, C. D. and Pitts, W. M. "Global density effects on the self-preservation behavior of turbulent free jets," J. Fluid Mech., vol. 254, 1993, pp. 417-435.

25. Konard, J. H. "An experimental investigation of mixing in two-dimensional turbulent shear flows with applications to diffusion-limited chemical reactions," PhD thesis, California Institute of Technology, 1976.

26. Bogdanoff, D. W. "Compressibility effects in turbulent shear layers," AIAA Journal, 21, 1983, pp. 926-927.

27. Hiroyasu, H. and Arai, M. "Fuel spray penetration and spray angle in diesel engines," Trans. JSAE, Vol. 21, 1980, pp. 5-11.

28. Naber, J. D. and Siebers, D. L. "Effects of gas density and vaporization on penetration and dispersion of diesel sprays," SAE international Congress and Exposition, SAE Paper no. 960034, Detroit, Michigan, February 26-29, 1996.

Appendix

(a) Growth rate for the incompressible and compressible jets are documented in *Abramovich [19]:*

For an incompressible turbulent submerged jet three special regions are defined: initial, transitional, and main regions. Initial region roughly extends just beyond the end of the potential core and the main region is where strictly self-similarity solution becomes applicable. Using Prandtel's mixing length theory, assuming mixing length being only function of streamwise distance, *Abramovich [19]* indicates that the jet growth rate is controlled by the transverse velocity fluctuations, v':

$$\frac{Db}{Dt} \propto v' \propto -\ell \frac{\partial U}{\partial y} \propto -\ell \frac{U_{cl}}{b} \propto U_{cl} \qquad (1)$$

and since

$$\frac{Db}{Dt} = \frac{db}{dx}\frac{dx}{dt} \propto U_{cl}\frac{db}{dx} \qquad (2)$$

from the above two :

$$\frac{db}{dx} = \text{constant} \Rightarrow b = (\text{constant})x \Rightarrow$$

$$\ell = (\text{constant})\, x \qquad (3)$$

2b is defined as the thickness of the velocity profile, Db/Dt is the total derivative, ℓ is mixing length, v' is the transverse velocity fluctuations, and U_{cl} is the centerline maximum value of the time-averaged streamwise velocity profile.

Abramovich [19] in a semi-empirical theory proposes an equation for the jet spreading considering compressibility as follows:

$$\frac{db}{dx} \propto \frac{U_1 - U_2}{U_{char}}$$; where U_1 and U_2 are streamwise velocities at the boundaries of the mixing zone, U_{char} a characteristic velocity in the zone, and x is in streamwise direction.

$$\text{For incompressible flow}: U_{char} = \frac{U_1 + U_2}{2} \quad (4)$$

$$\text{For compressible flow}: U_{char} = \frac{\rho_1 U_1 + \rho_2 U_2}{\rho_1 + \rho_2} \quad (5)$$

In the main region of the jet :

$$U_r = \frac{U_{ambient}}{U_{cl}};$$

$$\rho_r = \frac{\rho_{ambient}}{\rho_{cl}}; U_{cl} = U_{cl}(x); \rho_{cl} = \rho_{cl}(x)$$

If U_r and ρ_r do not depend on x then from above :

$$\frac{b}{x} = C\frac{1+\rho_r}{2}\frac{1-U_r}{1+\rho_r U_r} \qquad (6).$$

From experiments in the initial region of the submerged jet (i.e. $U_r = 0$) of an incompressible fluid ($\rho_r = 1$) $C = 0.27$

is proposed. However, various experiments in hot jets, high - velocity jets, and supersonic jets under off - design discharge suggest a value of $C = 0.22$.

From above equations for compressible flow :

$$\frac{db}{dx} = C\frac{1+\rho_r}{2}\frac{1-U_r}{1+\rho_r U_r}; \text{ where}$$

$$U_r = \frac{U_2}{U_1} \text{ and } \rho_r = \frac{\rho_2}{\rho_1}.$$

(b) Definition of different mixing layer thicknesses:

Vorticity thickness: δ_ω is defined through measurements of the streamwise time-averaged (U) velocity profile in the mixing layer. It is equal to $(U_1 - U_2)/ (dU/dy)_{max}$ where derivative is taken across the mixing layer and U_1 and U_2 are the free stream velocities for each stream forming the mixing layer. *Brown and Roshko [21]* state that this definition in addition to being convenient is also appropriate. The problem of the growth of the turbulent mixing layer being basically the kinematic problem of the unstable motion induced by the vorticity.

Pitot thickness: δ_{pit} is the width of the Pitot-tube-measured pressure profile from 5% to 95% of the difference of the two free-stream values, see *Papamoschou and Roshko [1].*

Visual thickness: δ_{vis} is the thickness determined via a photographic technique. It is measured by shadowgraphy and schlieren approaches in *Brown and Roshko[21]* and *Papamoschou and Roshko [1],* respectively.

Nomenclature

b :Velocity profile half thickness
C_{pg} :Constant pressure specific heat for the gas
d :Injector tube diameter
D :Drop diameter
F_r :Froud number
h_{fg} :Heat of vaporization
k_g :Thermal conductivity of the gas
ℓ :Prantdel's mixing length
L :Characteristic dimension of turbulent eddies
M_c :Convective Mach number
Oh :Ohnesorge number
P_c :Critical pressure of the injectant
P_{ch} :Chamber pressure
P_r :P/P_c
R_e :Reynolds number
T_r :T/T_c
T_{ch} :Chamber temperature
T_{00} :Environment temperature at a large distance from the surface of the drop
T_{boil} :Boiling point temperature
u' :Streamwise velocity fluctuations
U_1 :Free stream velocity of the high-velocity stream in the mixing layer
U_2 :Free stream velocity of the low-velocity stream in the mixing layer
U_c :Convection velocity
U_{cl} :Jet centerline velocity
U_r :U_2/U_1
v' :Spanwise velocity fluctuations
v_L :Cross stream velocity over a separating bulge from the interface of the liquid jet
W_e :Weber number

ρ_l :Liquid density
ρ_g :Gas density
ρ' :Density fluctuations
ρ_1 :Free stream density of the low-velocity stream in the mixing layer
ρ_2 :Free stream density of the high-velocity stream in the mixing layer
ρ_r : ρ_2/ρ_1
σ :Surface tension
δ_{vis} :Visual mixing layer thickness. See Appendix
δ_{pit} :Pitot-tube mixing layer thickness. See Appendix
δ_ω :Vorticity thickness. See Appendix

δ' :Spatial rate of change of the thickness or spreading rate
$\delta_{pit,0}$:Pitot thickness for the incompressible variable-density shear layer having the same density and velocity ratios as the compressible case

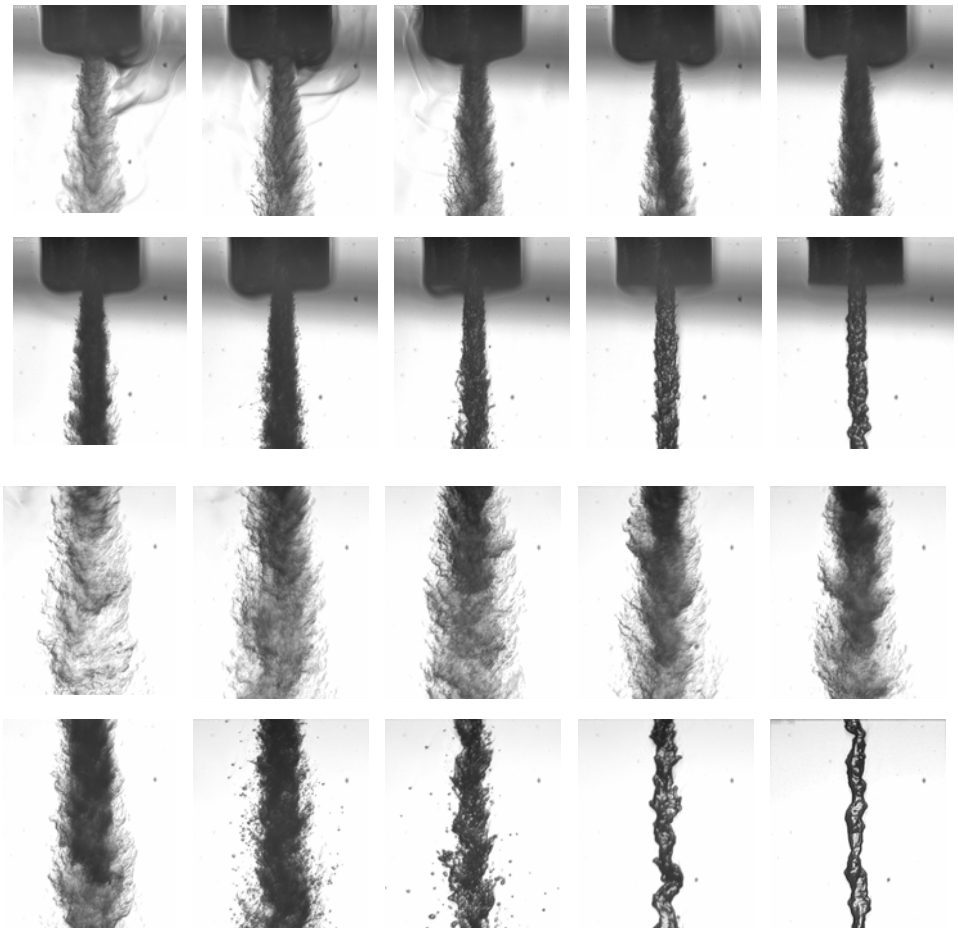

Figure 3. Back-illuminated images of the nitrogen injected into a chamber of nitrogen at a fixed supercritical temperature of 300 K but varying sub- to supercritical pressure. For the first two rows, chamber pressure decreases left to right from upper-left to lower-right corner: P_{ch}/P_c= 2.74, 2.44, 2.03, 1.64, 1.23, 1.03, 0.83, 0.63, 0.43, and 0.23. Lower two row images are corresponding images for the upper ones but further downstream. The axial distance at the bottom of the upper two row images is the same as the top of the ones in the two lower rows. The magnification can be inferred knowing the injector outer diameter of 1.59 mm (1/16"). Re # range: 25,000 to 75,000; injection velocity range: 10 to 15 m/s; Froude # range: 40,000 to 110,000. P_c and T_c are critical pressure and temperature of the injectant and P_{ch} and T_{ch} are chamber pressure and temperature. For N_2: P_c=3.4 MPa, T_c=126.2 K.

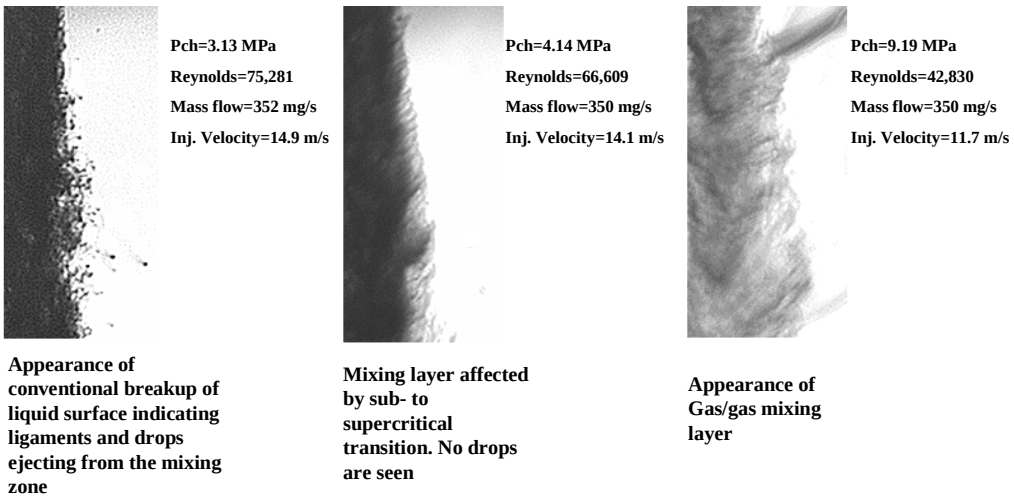

Figure 4. Software magnified images of the jet at its outer boundary showing transition to the gas-jet like appearance starting at just below the critical pressure of the injectant. Images are at fixed supercritical chamber temperature of 300 K.

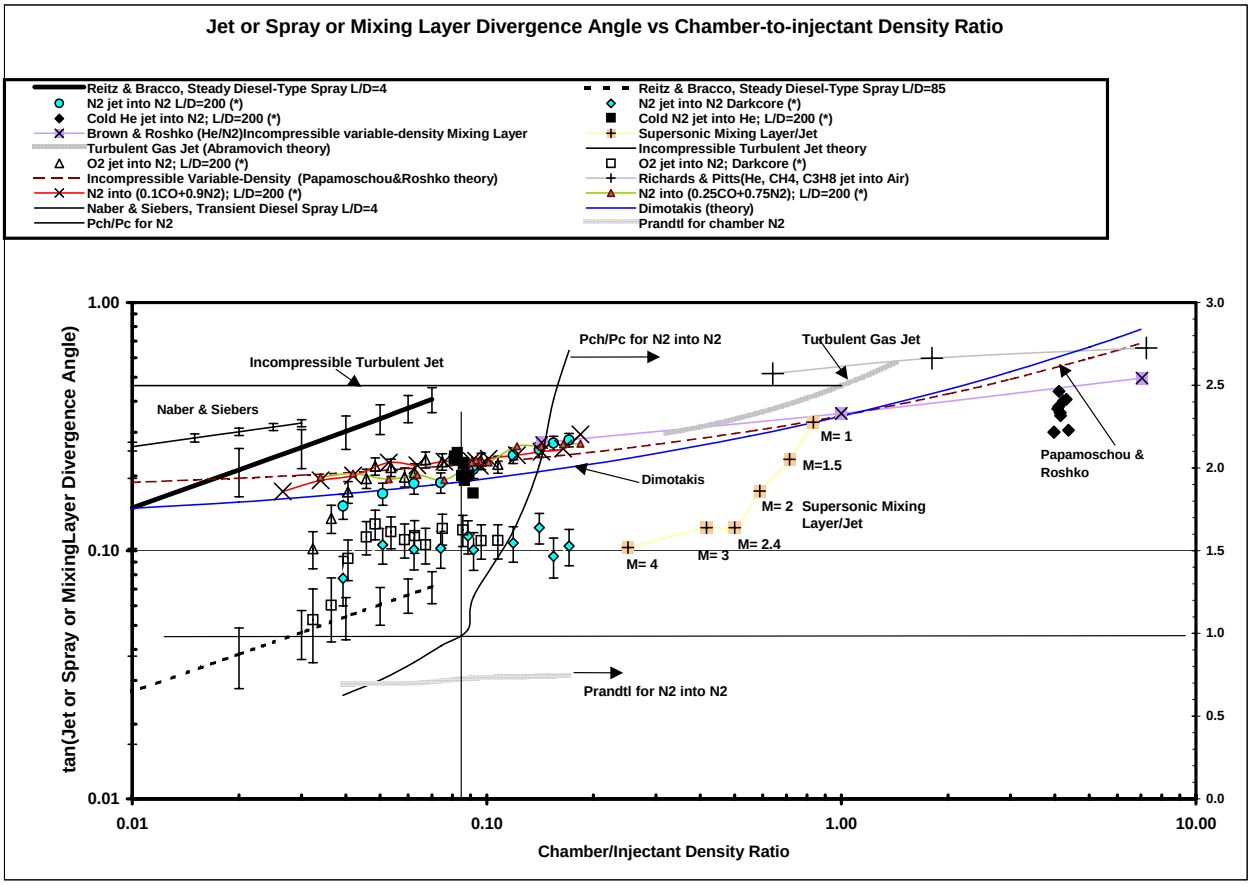

Figure 5. Shows spreading or growth rate as tangent of the visual spreading angle versus the chamber-to-injectant density ratio. (*) refers to data taken at AFRL.

This Page Intentionally Left Blank

APPENDIX I

"Spray/Gas Behavior of Cryogenic Fluids under Sub- and Supercritical Conditions"

This Page Intentionally Left Blank

Spray/Gas Behavior of Cryogenic Fluids under Sub- and Supercritical Conditions

B. Chehroudi*, R. Cohn[1], and D. Talley[1]
ERC, Inc., 10 E. Saturn Blvd., Edwards AFB, CA, USA 93524-7680
[1]Air Force Research Laboratory, AFRL/PRSA, 10 E. Saturn Blvd., Edwards AFB, CA, USA 93524-7660

Abstract

Recent experience gained at AFRL with the injection of cryogenic fluids into high back pressures is summarized. The temperature of cryogenic fluids was initially below the critical temperature of the fluid, while the temperature of the ambient was higher than the critical temperature. Chamber pressures ranged from below the critical pressure to above it. The boundary between the injected fluid and the surrounding medium was found to change from spray-like behavior to gas jet-like behavior as pressure increased, the transition occurring near the critical pressure of the fluid. The initial jet growth rate was plotted against the chamber-to-injectant density ratio, along with available data for other liquid and gaseous jets and mixing layers, producing a unique and informative plot. For supercritical conditions, the measured growth rate agreed well with predictions for incompressible (low Mach number) but variable-density gaseous turbulent mixing layers. Fractal analysis of the jet boundary also showed a quantitative similarity to gas jet-like behavior under supercritical conditions, and to spray-like behavior under subcritical conditions. An equation based on a physical model was proposed for the growth rate that agrees well with the presented experimental data for a wide range of density ratios, including both subcritical (spray) and supercritical (jet) pressures. Preliminary analysis of Raman scattering measurements of the density profiles showed that the spread rate measured at twice the full-width-half-maximum (FWHM) point agreed well with the spread rate measured by shadowgraphy techniques. Radial profiles appeared to show similarity behavior, but not of the classical type observed for turbulent gaseous jets in the far field.

Introduction

As combustion chamber pressures become increasingly higher in order to realize performance and/or efficiency benefits in a wide range of propulsion and energy conversion applications, the injected fluid(s) may experience ambient pressures exceeding the critical pressure(s) of the propellants. For example, in the cryogenic liquid hydrogen/liquid oxygen Space Shuttle Main Engine, the thrust chamber pressure is about 22.3 MPa, while thrust chamber pressures for the Vulcain (Ariane 5) engine have been recorded to reach up to 10 MPa. Both of these pressures exceed the critical pressure of P_{cr} = 5.043 MPa for liquid oxygen. In these applications, the initial temperature of the oxygen can initially be below the critical temperature of the oxygen (T_{cr} = 154.58 K), and then undergo a transition to a supercritical temperature as the oxygen is mixed and burned in the combustion chamber.

For single component fluids, the distinct difference between the gas and liquid phases disappears when the pressure exceeds the critical pressure or the temperature exceeds the critical temperature. Surface tension and the enthalpy of vaporization vanish, and large variations in the density, thermal conductivity, and mass diffusivity occur near the critical point. For multicomponent fluids, the solubility of the gas phase in the liquid phase increases as pressure approaches the critical pressure, and mixture effects need to be taken into account in calculating the critical properties. The critical properties of mixtures are referred to as the "critical mixing temperature" and the "critical mixing pressure" (*Bruno and Ely* [1]). The critical mixing pressure can be many times the critical pressure of the propellant of interest, for instance the fuel in hydrocarbon/air systems or the oxygen in oxygen/hydrogen systems.

Past efforts by other researchers on this subject can be found in, for example, *Newman and Brzustowski* [2], *Mayer, et. al.* [3-4], *Chen and Sui* [5], and *Woodward and Talley* [6]. In summary, these authors all reported a gas jet-like visual appearance at a supercritical chamber temperature and pressure with no evidence of droplets, even when the jet was initially cool enough to be very densified. *Woodward and Talley* [6] showed that adding helium to the ambient nitrogen mixture caused a liquid nitrogen jet to exhibit evidence of surface tension, and hence of subcritical surface conditions, despite the fact that the ambient pressure was nearly twice the critical pressure of pure nitrogen.

Raman scattering was used by *Anderson, et. al.* [7], *Decker, et. al.* [8], *Oschwald and Schik* [9], and *Oschwald, et. al.* [10] to investigate the structure of a cryogenic nitrogen jet under supercritical conditions. In these experiments, *Decker, et. al.* [8] observed a smooth

* Corresponding author

transition from the high-density core of a cryogenic, densified N_2 jet to the more rarefied, warmer N_2 in the ambient outer region. There was no distinct phase interface. The density radial profile was never observed to have a top-hat profile even as close as 2.5 diameters. Based on limited tests, they concluded that the thermodynamic state of an injected supercritical fluid was of prime importance in determining the jet growth, and not the injection velocity or momentum.

The objective of this paper is to concisely present the experimental and modeling experience gained thus far at AFRL on injecting cryogenic fluids at subcritical to supercritical pressures. In what follows, structural features of the jets observed using shadowgraphy will first be described, and growth rate measurements obtained from the shadowgraph images will be explained. Next, a fractal analysis of the images will be briefly summarized. Thirdly, an initial attempt to model the measured growth rate of the jet will be presented. Finally, preliminary results from recent efforts to quantitatively measure density profiles using spontaneous Raman scattering will be described.

Experimental Apparatus

The experimental apparatus has been thoroughly described by *Woodward and Talley* [6] and *Chehroudi, et. al.* [11]. The apparatus was capable of injecting cryogenic fluids into ambient pressures as high as 137 atm (2000 psi). For the results reported herein, fluids were injected through a sharp-edged 50 mm long stainless steel tube having a 1.59 mm (1/16") outer diameter and a 254 micron (0.010") inner diameter, therefore having an inner length-to-diameter ratio of almost 200. The Reynolds numbers in these studies ranged from 25,000 to 70,000. Thus the entrance length well exceeded the 50 to 100 diameters needed to ensure that fully developed turbulent pipe flow existed at the exit (see *Schlichting* [12]). The rig was fully instrumented with thermocouples, pressure gages and transducers, and mass flow meters. Back-illuminated images were acquired using a model K2 Infinity long-distance microscope for magnification with a TM-745E PULNix interlaced CCD camera to form images of the injected jets at a resolution of 768(H) x 493(V) pixels, on a 8.8(H) x 6.6(V) mm actual sensing area.

Changes in the Visual Appearance of LN_2 Jets

Liquid nitrogen (LN_2) jets having a critical pressure of P_{cr} = 3.39 MPa and a critical temperature of T_{cr} = 126.2 K were injected at an initial temperature of 99-110 K into room temperature (300 K) gaseous nitrogen (GN_2) at various chamber pressures. Representative changes in the visual appearance of the jets are shown in Fig. 1. The bottom row of Fig. 1 contains magnified images of the upper row where the Froude number

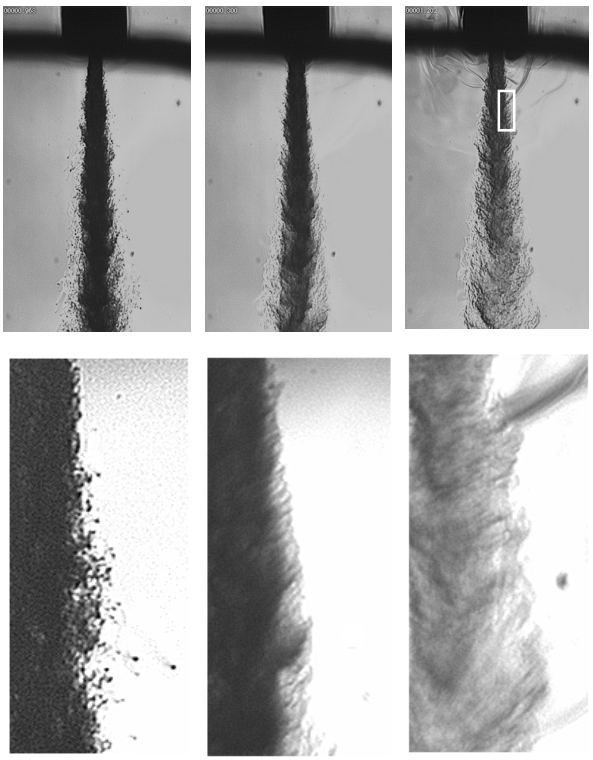

(a) Pr=0.91 Re=75,281 (b) Pr=1.22 Re=66,609 (c) Pr=2.71 Re=42,830

Figure 1. Liquid nitrogen injected into room temperature nitrogen at different pressures. The bottom row contains magnified images of the top row. The approximate location and the amount of magnification is indicated by the white box.

ranged between 40,000 to 110,000; the shear layer structures shown in the bottom row are therefore inertially dominated. The reduced pressure Pr in Fig. 1 is defined to be the ratio of the chamber pressure to the critical pressure. The Reynolds numbers, defined at the jet exit condition, suggests that the initial condition of the jets was fully developed turbulent pipe flow. Large density gradients occurred across the mixing layer in all cases.

In column (a), where the chamber pressure was subcritical, the jet was observed to be liquid-like in the classical sense, with surface instabilities that grew downstream from the injector. Very fine drops were also seen to be ejected from the jet. The Ohnesorge number was estimated to be about 2.8×10^{-3} at this pressure, corresponding to a second wind-induced atomization regime by *Reitz and Baracco* [13].

Major structural and interfacial changes were found to occur at about P_r = 1.03. At this pressure, drops were no longer detected, and somewhat regular finger-like or comb-like entities at the interface were

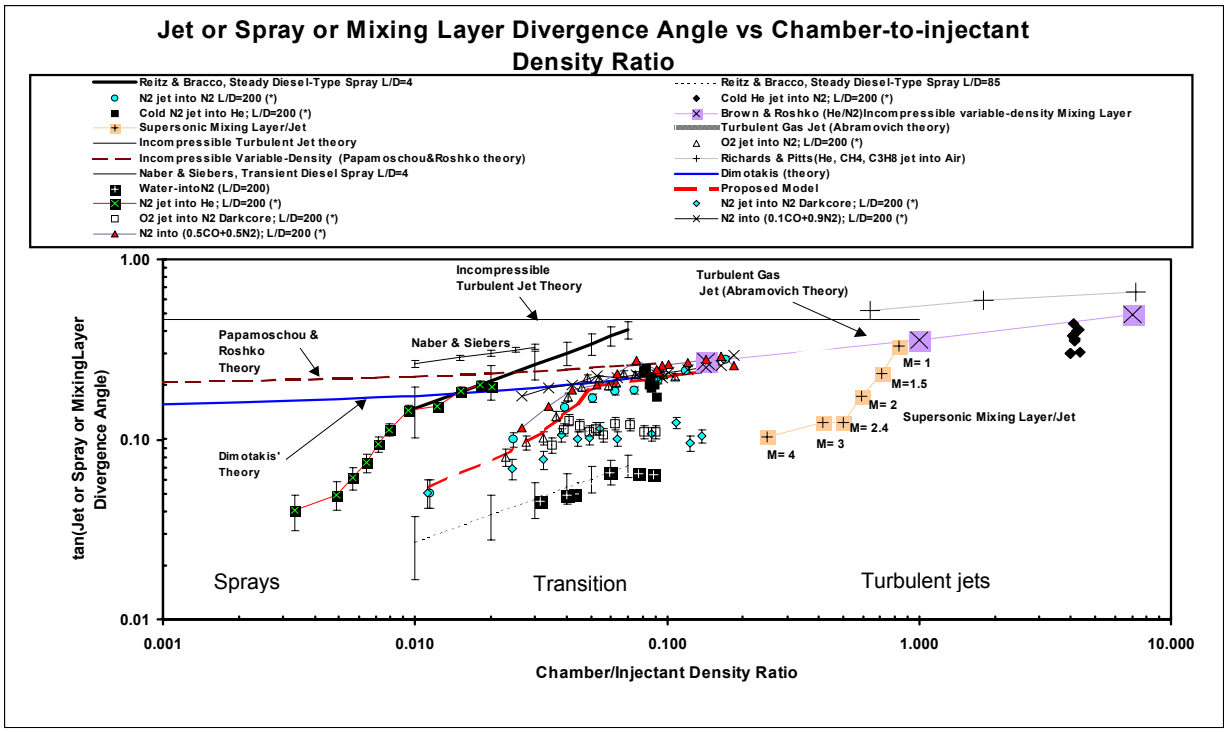

Figure 2. Tangent of the visual spreading angle versus the chamber-to-injectant density ratio. Data shown with an asterisk (*) was taken at AFRL.

observed instead. These were not broken up into droplets, but dissolved instead at different distances from the dense core. These structures are illustrated at a reduced pressure of 1.22 in column (b) of Fig. 1. This change in the morphology of the mixing layer is evidently due to a reduction in the surface tension towards zero (Ohnesorge number approaching infinity) as the critical pressure is exceeded. The enthalpy of vaporization also vanishes because of this transition.

As chamber pressure was further increased, the length and thickness of the dense core decreased, until at high enough chamber pressures, the jet assumed the appearance of a turbulent gaseous jet injected into a gaseous environment, as illustrated in column (c). Any further droplet production and consequently any additional atomization regimes were completely surpressed.

Injecting liquid oxygen (LO_2) into gaseous nitrogen resulted in similar observations to the above, except that transition from liquid-like to gas-like structures occurred near the critical pressure of oxygen.

Jet Growth Rates

The initial growth rate of the jets was measured to within 7 mm from the jet exit (less than 28 diameters). As discussed by *Chehroudi, et. al.* [11], this distance was well within the mixing layer region, so that comparison with classical Cartesian mixing layers was justified (see also *Chehroudi, et. al.* [14] and *Abromovich* [15]). The results were then plotted in Fig. 2 as the tangent of the spreading angle *vs.* the chamber-to-injectant density ratio, along with the results of other researchers. Because the present results spanned both gas-like and liquid-like behavior, comparison with the results of others required plotting the growth rates of both sprays and turbulent jets. The result was a plot that spanned nearly four orders of magnitude in density ratio. This appeared to be the first time that growth rates have been plotted over such a large range in density ratio. It also appeared to be the first time that growth rates for both sprays and turbulent jets have been compared in a single plot. The major features of Fig. 2 are summarized briefly below.

At density ratios large enough to correspond to supercritical chamber pressures, when the jet appearance was found to visually resemble that of a turbulent gas jet as in Fig. 1(c), the data was found to agree well with a theoretical equation proposed by *Dimotakis* [16], and closely follow an independently-derived equation by *Papamoschou and Roshko* [17], both for incompressible variable-density mixing layers. The data was also found to agree with the spreading angle measurements of *Brown and Roshko* [18] for a subsonic Cartesian incompressible turbulent mixing layer between helium and nitrogen gases at atmospheric pressure. All these spreading rates were noted to be less than that predicted by the semi-empirical correlation of *Abramovich* [15].

As the density ratio was decreased, the growth rate was found to also decrease. At a certain density ratio corresponding to chamber pressures near the critical pressure, the rate of decrease in the growth rate became

abruptly much steeper. The jet appearance in this transition region resembled that of Fig. 1(b). The density ratio at which the transition occurs is different for different data sets in Fig. 2 because the data sets correspond to different mixtures having different critical properties.

As the density ratio was further decreased below the transition value, the jet took on the visual appearance of a spray as in Fig. 1(a), and the growth rate approached the growth rate of sprays measured by others. Growth rate results from *Reitz and Bracco* [13] for isothermal steady sprays issuing from a round orifice at the end of a straight tube are plotted in Fig. 2 for two different tube internal length-to-diameter ratios, L/D=4 and L/D=85. The curves in these plots represent the predictions of theory, while the error bars represent the extent of experimental scatter around the theoretical predictions. The plots show the well known result that the initial spreading rates of sprays from plain round orifices are sensitive to the internal L/D. Fully developed pipe turbulence should exist at the orifice exit for L/D=85. This condition most closely corresponds to the exit condition of the authors' data, for which L/D=200. The experimental data can be observed to approach the *Reitz and Bracco* [13] curve for L/D=85 as the density ratio decreases. In other data not plotted in Fig. 2, the data is found to effectively merge with the *Reitz and Bracco* curve at a low enough density ratio. Also shown for comparison in Fig. 2 are the results for pulsed non-isothermal sprays by *Naber and Siebers* [19] for L/D=4. As before, The curve shows model predictions and the error bars represent the scatter in the experimental data around these predictions. The difference between the results of *Reitz and Bracco* and those of *Naber and Siebers*, as well as between other data sets in Fig. 2 in general, can be attributed to various factors, including different downstream distances where the measurements are made, differences in the definition of the mixing layer thicknesses, and differences in measurement techniques. A complete discussion of these and the other plots in Fig. 2 can be found in *Chehroudi, et. al.* [11].

The conclusions to be drawn from the above growth rate measurements compliment and extend those from the visualizations in the previous section. At supercritical pressures, not only do the jets have the visual appearance of a turbulent gas jet, they have quantitatively the same growth rates as incompressible variable-density turbulent jets. At subcritical pressures, not only do the jets have the same appearance as sprays, they have quantitatively the same growth rate as sprays. The transition between the two regimes begins at slightly below the critical pressure. The above conclusions apply at least when fully-developed turbulence exists at the jet exit. Other initial conditions have not yet been examined.

Fractal Analysis

The fractal dimension of jets at various pressures ranging from subcritical to supercritical pressures was also computed and compared to results from other researchers. For example, *Sreenivasan and Meneveau* [20] used a laser sheet to slice an incompressible axisymmetric turbulent gas jet in a quiescent environment. They computed the fractal dimension of the boundary thus revealed and reported a fractal dimension of 1.33. The same authors also reported fractal dimensions of 1.35, 1.34, and 1.38 for a round gaseous jet, a plane gaseous mixing layer, and a boundary layer flow, respectively. In addition, images of a turbulent water jet from *Dimotakis, et. al.* [21] and of second wind-induced atomization from *Hoyt and Tayler* [22] were scanned and the fractal dimension was computed.

The results are shown in Fig. 3. The horizontal lines show the fractal dimensions taken from the references discussed in the above paragraph. The discrete data points were measured from the authors' own images of LN_2 jets being injected into GN_2 at various chamber pressures. The various curves are the result of different methods of measuring the fractal dimension and therefore provide an indication of the uncertainty in determining the fractal dimension. At supercritical chamber pressures, it was found that the fractal dimension approached the range of turbulent jets and mixing layers. The fractal dimension decreased as the chamber pressure decreased, until below a reduced pressure of about 0.8, the fractal dimension was rapidly reduced to that of a spray in second wind-induced atomization. That the fractal dimension of a spray in a second wind-induced regime should be lower than the fractal dimen-

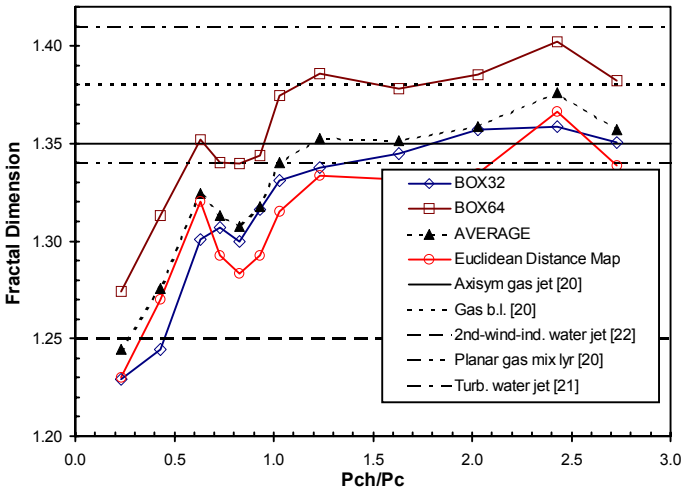

Figure 3. Fractal dimensions of the boundaries of various jets. Discrete points are data from the present effort.

sion of a turbulent jet can be understood by considering the limit of a smooth circular cylinder with no surface irregularities, for which the fractal dimension is the Euclidean value of 1.

For a thorough discussion of the above results, see *Chehroudi, et. al.* [23]. The key observation to be taken here is that the results from the fractal analysis even further compliment and extend the previous results. At supercritical pressures, jets which appear and grow like turbulent gas jets also have a fractal dimension similar to turbulent gas jets. At subcritical pressures, jets which appear and grow like sprays also have a fractal dimension similar to sprays. The transition occurs at about the same pressure as the transition in visual appearance and the transition in the growth rate.

Modeling the Growth Rate

A semi-empirical equation of the growth rate of jets over the entire range of chamber pressures examined was developed. Complete details about the development of this equation are given in *Chehroudi, et. al.* [23]. The physical reasoning motivating the equation is outlined below.

It was noted first that previous expressions for the growth rate of sprays and of turbulent jets had a remarkably similar form. For instance, *Reitz and Bracco* [13] proposed that the growth rate of an isothermal liquid spray could be expressed as

$$\theta \approx 0.27[0 + (\rho_g / \rho_l)^{0.5}],$$

while *Papamoschou and Roshko* [17] suggested the following form for incompressible but variable density turbulent jets:

$$\theta = 0.212[1 + (\rho_g / \rho_l)^{0.5}].$$

This similarity suggested a basic form for the equation.

Next, it was hypothesized that the transition between the liquid-like and gas-like regimes might be governed by the relationship between the time it takes turbulence to eject fluid structures from the jet, and the time it takes structures to dissolve ("vaporize," when subcritical) into the ambient. In the liquid-like regime, turbulence throws droplets off much faster than they can vaporize. In the gas-like regime, they dissolve much faster than they can be thrown off. The transition between the two regimes would then be governed by when these two times are approximately equal. This hypothesis was suggested by comb-like structures in Fig 1(b), for which it appeared that these two times might be equal. If τ_b is the characteristic turbulence or "bulge formation" time, then an estimate of this time is given by *Faeth* [24] and by *Tseng, et. al.*[25] for subcritical pressures to be

$$\tau_b = (\rho_l L^3 / \sigma)^{1/2},$$

where ρ_l is the liquid density, L is the characteristic dimension of a turbulent eddy, and σ is the surface tension. An estimate of the vaporization time τ_g, also for subcritical pressures, is then

$$\tau_g = D^2 / K,$$

where D is the droplet diameter and K is the evaporation constant.

An equation was thus proposed for the N_2/N_2 system as

$$\theta = 0.27[(\tau_b /(\tau_b + \tau_g) + (\rho_g / \rho_l)^{0.5}]$$

Note that, in the limit, this equation collapses to the isothermal liquid spray case when $\tau_g >> \tau_l$ and $\tau_g \to \infty$. This equation was found to apply at subcritical pressures until $\tau_b /(\tau_b + \tau_g) = 0.5$. After that, a constant value of 0.5 wass used to predict the spreading rate for higher pressures, including supercritical pressures.

The characteristic time ratio $\tau_b /(\tau_b + \tau_g)$ was calculated from experimental measurements of bulge and droplet sizes for the N_2/N_2 system and calculations of the relevant properties. For the case of nitrogen injection into gases other than nitrogen, however, a lack of reliable information about the mixture properties at the interface, particularly the surface tension, prevented such a calculation from being performed. To model these cases, it was hypothesized that the characteristic time ratio is a dominant function of the density ratio only, i.e. $\tau_b /(\tau_b + \tau_g) = F(\rho_g / \rho_l)$. As indicated by *Brown and Roshko* [18], this hypothesis is reasonable because at low Mach numbers there is no distinction

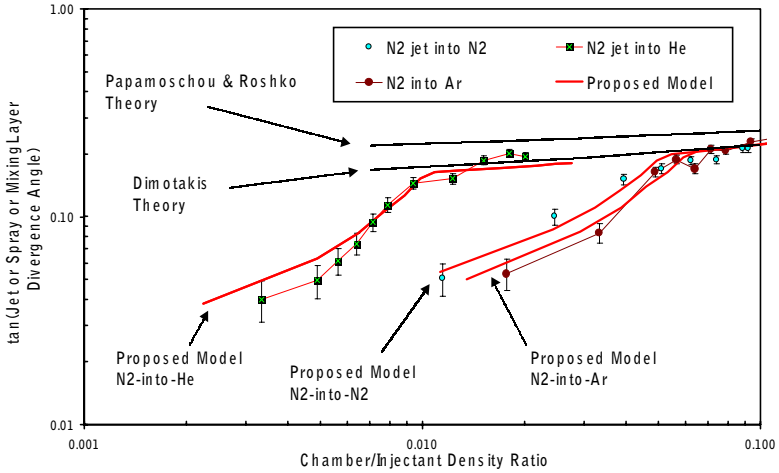

Figure 4. Comparison of the proposed growth rate model with experimental data.

between mixing layers made of two streams with differences in molecular weights, differences in temperatures, or differences in high speed compressibility effects. Measurements of F for the N_2/N_2 system were provided as a plot in ref. [23]. A curve fit of that plot gives

$$F(\rho_g/\rho_l) = 5.325(\rho_g/\rho_l) + 0.0288 \; ; \quad \rho_g/\rho_l < 0.0885$$
$$= 0.5 \qquad\qquad\qquad\qquad ; \quad \rho_g/\rho_l \geq 0.0885$$

It was found that the same function F calculated from measurements of the N_2/N_2 system could be made to work for other cases provided a case-dependant transformation was made to the density ratio at which F is evaluated. The final form of the equation thus arrived at was

$$\theta = 0.27[F(\mathrm{x}(\rho_g/\rho_l)) + (\rho_g/\rho_l)^{0.5}]$$

where

x=1.0 for N_2-into-N_2
x=0.2 for N_2-into-He
x=1.2 for N_2-into-Ar

The quality of the agreement with experimental data is demonstrated in Fig. 4 and is considered to be good.

Spontaneous Raman Scattering Measurements

All the preceding results were obtained from line-of-sight shadowgraph images. In this section, recent efforts to use spontaneous Raman scattering (SRS) to obtain spatially-resolved quantitative measurements of density distributions are described. Preliminary results are summarized briefly below. Complete details may be found in *Chehroudi, et. al.*[26].

A Nd:YAG pulsed laser at 532 nm was used with an optical delay loop to lengthen the pulse duration from 10 ns to about 36 ns. Lengthening the pulse was required to reduce the peak power, in order to reduce the possibility of producing stimulated Raman scattering or broadband breakdown caused by the lensing effect of the jet itself, as reported by *Anderson, et. al.* [7]. The transmitting optics created a controllable laser sheet with precise traversing capabilities in two directions. The Raman scattered light by N_2 at 607 nm was detected by a 256X256 CCD camera equipped with a suitably chosen number of filters which, when combined with a background subtraction technique, maximized the signal-to-noise ratio.

The Raman signal intensity was assumed to be proportional to the N_2 density. This assumption was tested by measuring the intensity of a pure, uniform nitrogen gas in the high pressure chamber at several pressures. The measured intensity ratios at different pressures were found to agree to within 2% with the density ratios calculated for an ideal gas. Figure 5 shows the time-averaged increment in jet intensity over

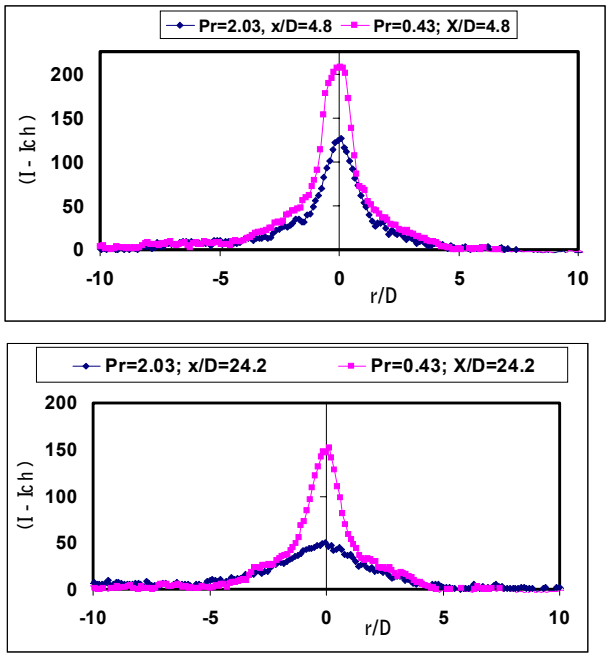

Figure 5. Density increment as a function of radial distances, for a subcritical and a supercritical pure nitrogen system, at two different axial distances.

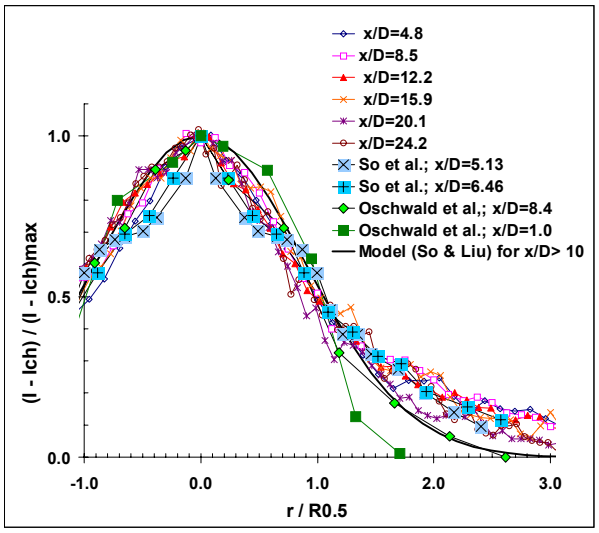

Figure 6. Intensity profiles in similarity coordinates for a pure nitrogen system at Pr = 2.03.

the background intensity in the chamber, $I - I_{ch}$, as a function of the radial distance r, for a pure nitrogen system in which N_2 is injected into N_2, at a subcritical and a supercritical pressure, and for two different axial distances downstream. The peak intensity increment of the subcritical jet was found to be larger than the peak intensity increment for the supercritical jet, consistent with smaller overall density ratios across the supercritical jet. The magnitude of the peak intensity increment was also found to decrease with axial distance for both

the subcritical jet and the supercritical jet, consistent with increased mixing at increasing axial distances. Thus the trends exhibited by the Raman measurements were found to be qualitatively correct.

As discussed in ref. [26], the reflections of the laser light from the shiny gas/liquid interface of the subcritical jet make quantitative interpretation of the Raman measurements difficult for subcritical jets. Thus subcritical results will not be further discussed here. Reflections are not as much of an issue for supercritical jets, however. Raman measurements for the supercritical jet at several axial distances are plotted in similarity coordinates in Fig. 6. The axial distances are in general too close to the jet exit to expect the initial pipe turbulence to have relaxed to fully developed jet turbulence. As indicated previously, measurements were generally made close to the jet exit in order to ensure the Froude numbers were large enough for the jet to be inertially dominated. However, as a reference, a similarity profile for fully developed jet turbulence from a model by *So, et. al.* [27] is also plotted in Fig 6. The experimental measurements are shown to possibly approach a self-similar curve (to within the experimental scatter). However, the curve is not the same curve as the curve of *So, et. al.* for fully developed jet turbulence.

So, et.al. also performed density measurements in gas jets at axial distances too close to the exit for fully developed jet turbulence to exist. These results are also plotted in Fig. 6 and are shown to agree reasonably well to within the experimental uncertainty. Finally, recent results by *Oschwald et al.* [9] are also plotted in Fig. 6. The latter measurements are particularly relevant in that they were also taken in a supercritical pure nitrogen system. The agreement in this case is less satisfactory. However, no conclusions about this have been drawn thus far due to differences in the initial conditions between the two sets of data known to affect spreading rates.

The full width of the radial profiles measured where the intensity increment was half the maximum (Full-Width-Half-Maximum, FWHM) was extracted from the measured Raman data, and the spreading rate thus measured was compared with the spreading rate measured from the shadowgraph visualizations. The results are plotted in Fig. 7. It was found that the spreading rate measured at twice the FWHM values of the Raman data agreed well with the shadowgraph measurements. Thus the correspondence of the two different techniques of measuring the width of the jet was established.

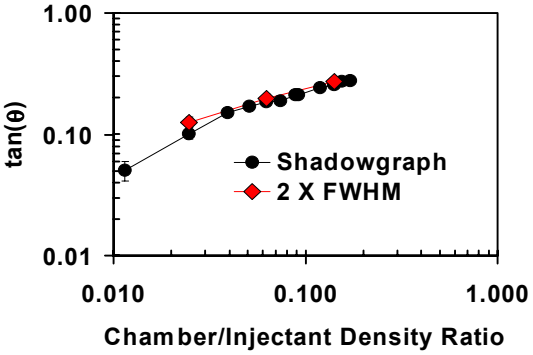

Figure 7. Comparison of the spreading angle of an N2/N2 system measured using shadowgraph and spontaneous Raman techniques.

Summary and Conclusions

The structure and growth rates of cryogenic jets injected initially at a subcritical temperature into an environment at a supercritical temperature over a range of subcritical and supercritical pressures have been studied for several years at AFRL. Results to date were summarized. The growth rates of both turbulent jets and sprays were plotted over a range of density ratios spanning four orders of magnitude, the first time such a plot has evidently ever been constructed. At subcritical pressures, careful comparisons of shadowgraph measurements have shown that the jets have the appearance of conventional liquid sprays, their growth rate quantitatively approaches the growth rates for sprays measured by others, and their fractal dimension approaches quantitatively the same values as for conventional sprays. As pressure is increased beyond a transition pressure near but slightly below the critical pressure of the fluid, the jet structure changes. The jets have the appearance of turbulent gaseous jets, they have quantitatively the same growth rate, and they have the quantitatively the same fractal dimension. An physically based empirical equation was developed based on a mechanism governed by characteristic gasification times and interfacial turbulent bulge formation times to predict the growth rate behavior over the entire range of density ratios studied, including subcritical and supercritical conditions. Most recently, spontaneous Raman scattering measurements of the density profiles of the jets were performed. A preliminary analysis of the results suggests that the near-field density profiles may approach a self-similar shape, but not the same shape as for fully developed jet turbulence. It was found that growth rate measurements taken from the Raman measurements at twice the FWHM distance correspond to the growth rate taken from the shadowgraph measurements.

Acknowledgements

Mr. Mike Griggs and Mr. Earl Thomas are thanked for their valuable support. Mr. Paul Loftsgard is thanked for his assistance in part of the data acquisition/processing and most of the fractal analysis work. Professor A. Badakhsshan, summer faculty visitor, is thanked for his contributions on initial setup and testing

of the Raman measurement system. This work is sponsored by the Air Force Office of Scientific Research under Dr. Mitant Birkan, program manager.

References

1. Bruno, T. J. and Ely, J. F. *Supercritical fluid technology*, CRC Press, 1991.
2. Newman, J. A. and Brzustowski. "Behavior of a liquid jet near the thermodynamic critical region," *AIAA Journal*, vol. 9, 1971, no. 8, pp. 1595-1602.
3. Mayer, et al. "Injection and mixing processes in high pressure LOX/GH2 rocket combustors," AIAA Paper no. 96-2620, Lake Buena Vista, Florida, 1996.
4. Mayer, et al. "Propellant atomization in LOX/GH2 rocket combustors," AIAA Paper no. 98-3685, 1998.
5. Chen, L.-D. and Sui, P.-C. "Atomization during the injection of supercritical fluid into high pressure environment," in *Mechanics and Combustion of Droplets in Sprays* by Chiu and Chigier.[DGT1]
6. Woodward , R. D. and Talley, D. G. "Raman imaging of transcritical cryogenic propellants," AIAA Paper 96-0468, Reno, Nevada, January 1996.
7. Anderson, T.J., Woodward, R.D., and Winter, M. "Oxygen Concentration Measurements in a High Pressure Environment Using Raman Imaging," AIAA Paper 95-0140, 33rd Aerospace Sciences Meeting and Exhibit, January 9-12, Reno, Nevada, 1995.
8. Decker, M C, Schik, A, Meier, U E, Stricker R W. "Quantitative Raman Imaging Investigations of Mixing Phenomena in High Pressure Cryogenic Jets," *Appl Opt* 37:5620-5627, 1998.
9. Oschwald, M. and Schik, A. "Supercritical Nitrogen Free Jet Investigated by Spontaneous Raman Scattering," *Experiments in Fluids*, 27, 497-506, 1999.
10. Oschwald, M, Schik, A, Klar, M, Mayer, W, "Investigation of Coaxial LN2/GH2-Injection at Supercritical Pressure by Spontaneous Raman Scattering," 35th AIAA/ASME/SAE/ASEE Joint Propulsion Conference and Exhibit, Los Angeles, CA, 20-24 June, 1999.
11. Chehroudi, B., Talley, D.G., and Coy, E.B., "Initial Growth Rate and Visual Characteristics of a Round Jet into a Sub- to Supercritical Environment of Relavance to Rocket, Gas Turbine, and Diesel Engines," AIAA paper 99-0206, Reno, Nevada, 1999.
12. Schlichting, H. *Boundary Layer Theory*, MacGraw-Hill Book Company, seventh edition, 1979.
13. Reitz, R. D. and Bracco, F. V. "On the dependence of spray angle and other spray parameters on nozzle design and operating condition," SAE international Congress and Exposition, SAE Paper no. 790494, Detroit, Michigan, February 26-March 2, 1979.
14. Chehroudi, et al. "On the Intact Core of Full-Cone Sprays," Society of Automotive Engineer, SAE Transaction Paper 850126, 1985.
15. Abramovich, G. N. *The theory of turbulent jets*, M.I.T. Press, 1963.
16. Dimotakis, P. E. "Two-dimensional shear-layer entrainment," *AIAA Journal*, 21, No. 11, 1986, pp. 1791-1796.
17. Papamoschou, D. and Roshko, A. "The compressible turbulent shear layer: an experimental study," *J. Fluid Mech.*, vol. 197, 1988, pp. 453-477.
18. Brown, G. and Roshko, A. "On density effects and large structure in turbulent mixing layers," *J. Fluid Mech.*, vol. 64, 1974, part 4, pp. 775-816.
19. Naber, J. D. and Siebers, D. L. "Effects of gas density and vaporization on penetration and dispersion of diesel sprays," Society of Automotive Engineer, Int. Congress & Exposition, Detroit, SAE Paper no. 960034, 1996.
20. Sreenivasan, K. R. and Meneveau, C. "The fractal facets of turbulence," *J. Fluid Mech.,* Vol. 173, pp. 357-386, 1986.
21. Dimotakis, P. E., Miake-Lye, W. G., and Papantoniou, D. A., Phy. Fluids, 26, p. 3185.
22. Taylor, J. J. and Hoyte J. W., "Water jet photography- Technique and methods," Exp. Fluids, vol. 1, 1983, pp. 113-120.
23. Chehroudi, B., Talley, D., and Coy, E. "Fractal geometry and growth rate of cryogenic jets near critical point," AIAA Paper 99-2489, 35th AIAA/ASME/SAE/ASEE Joint Propulsion Conference, Los Angeles, CA, June 20-24, 1999.
24. Faeth, G. M., "Structure and atomization properties of dense turbulent sprays," *Twenty-third Symposium (International) on Combustion*, The Combustion Institute, P.1345, 1990.
25. Tseng, L.,-K., Ruff, G. A., P.-K., Wu, Faeth, G. M., "Continuous- and dispursed-phase structure of pressure-atomized sprays," Progress in Astronautics and Aeronautics: *Recent Advances in Spray Combustion*, February, 1995.
26. Chehroudi, B, Badakhshan, A, Talley, D, and Cohn, R, "Raman Scattering Measurements in the Initial Region of Sub- and Supercritical Jets," AIAA Paper 2000-3392, 36th AIAA/ASME/-SAE/ASEE Joint Propulsion Conference and Exhibit, Huntsville, Alabama 16-19 July 2000.
27. So, R M C, Zhu, J Y, Otugen, M V, and Hwang, B C, "Some Measurements in a Binary Gas Jet," *Experiments in Fluids*, 9, 273-284, 1990.

APPENDIX J

"Raman Scattering Measurements in the Initial Region of Sub- and Supercritical Jets"

A00-36609

AIAA 2000-3392

Raman Scattering Measurements in the Initial Region of Sub- and Supercritical Jets

B. Chehroudi[*], *R. Cohn*[#], *D. Talley*[#], *and A. Badakhshan*[†]

[*]Engineering Research Corporation Inc
10 E. Saturn Boulevard
Edwards AFB, CA 93524-7680

[#]Air Force Research Laboratory
Propulsion Directorate
10 E. Saturn Boulevard
Edwards AFB, CA 93524-7680

[†]Department of Physics
University of Northern Iowa
1620 Birch St.
Cedar Falls, IA 50613

36th AIAA/ASME/SAE/ASEE
Joint Propulsion Conference and Exhibit
17-19 July, 2000
Huntsville, Alabama

AIAA 2000-3392

Raman Scattering Measurements in the Initial Region of Sub- and Supercritical Jets

B. Chehroudi[*], *R. Cohn*[#], *D. Talley*[#], *and A. Badakhshan*[+]

[*]Engineering Research Corporation Inc.
10 E. Saturn Boulevard
Edwards AFB, CA 93524-7680
(Corresponding author)

[#]Air Force Research laboratory
10 E. Saturn Boulevard
Edwards AFB, CA 93524-7680

[+]University of Northern Iowa
1620 Birch St.
Cedar Falls, IA 50613

Abstract

A high-pressure chamber is used to investigate the behavior of liquid N_2 jets having an initial temperature less than the critical temperature of N_2, into ambient N_2 at greater than the critical temperature, at various pressures ranging from less than to greater than the critical pressure. Two-dimensional Raman scattering is used as a diagnostic tool. The injector was a straight tube with a length-to-diameter ratio of 100. The optical setup used a pulsed frequency-doubled Nd:Yag laser at 532 nm as an incident beam. Two-dimensional images were taken near the injector and results were interpreted in terms of density plots. At subcritical ambient pressures, a strong Raman signal was obtained and only a small number of images were needed for averaging. Substantial reduction of this signal was observed at supercritical pressures due to jet radial growth and mixing. The radial profiles of the intensity-surplus exhibited self-similar behavior at all the conditions tested. These profiles were shown to have been broadened by the interaction of the laser sheet and the jet interface. At pressures near and above the critical pressure, the modified profiles tended to assume the self-similarity profile of gaseous turbulent jets. The initial growth rate of the jet as judged by the Raman signature also showed such a tendency towards gaseous turbulent jets. However, the differences in growth rates remained quite distinct, being nearly half the growth rate reported for gaseous jets. The initial growth rate was in reasonably good agreement with our earlier measurements using shadowgraphy if twice the FWHM of the normalized intensity plots was used.

Introduction

It is recognized that there are advantages in operating most power and thrust producing engines at higher combustion chamber pressures and temperatures for enhanced efficiency and/or output thrust levels. In this paper, however, the main interest is in cryogenic liquid-propulsion rockets. Progress in material science and technological achievements in designing vessels to withstand high pressure and temperature conditions bring us close to harnessing the theoretical gains in high pressure and temperature engine operation. However, there are some new issues that arise as a result of the elevated chamber conditions which must be understood for better engine design and performance predictability. One such issue is the realization that in cryogenic rockets, particularly under full throttle or take-off conditions, liquid propellants may be injected into the combustion chamber at a pressure exceeding the critical pressure of the propellants. Our understanding of the injection process under these conditions has been limited until recently, when progress has been made in both experimental and theoretical areas. See for example *Mayer et al. [1,2], Chen and Sui [3], Woodward and Talley [4], Harstad and Bellan [5], Delplanque and Sirignano [6], Oefelein and Yang [7]*, and *Chehroudi et al. [8, 9]*.

In most previous experimental works, the initial attempts were to visualize the drop/jet formation and evolution using a high speed photography technique. Valuable information was gathered and analyzed using such methods and reported in the aforementioned publications. In an attempt to acquire more detailed and quantitative information, several laser diagnostic techniques were evaluated, and the spontaneous Raman scattering was identified to be one of the most suitable candidates, see *Anderson et al. [10]*. Many of the advantages of the Raman effect are indicated in the Appendix of this paper. Raman scattering was also used by *Woodward and Talley [4], Decker et al. [11], Oschwald and Schik [12], and Oschwald et al. [13]* to investigate the structure of nitrogen fluid jets under supercritical pressures.

One of the fundamental difficulties in extracting true density information from the Raman effect has been the uncertainty in the functional dependence of the Raman scattering cross section on temperature under very high density conditions. The Raman scattering cross section in liquids is larger than in gases by a correction factor that depends on the refractive index (n). For liquid nitrogen (LN_2), for example, it is larger by a factor of 1.73 at n=1.2. Not being strictly a liquid under supercritical conditions, a rough estimate of 10% on density measurements was given by *Decker et al [11]* for N_2 at 6 MPa. The other practical problems, enhanced by the lensing effect of the jet itself, are the onset of stimulated Raman scattering (same wavelength as the spontaneous Raman), and broad-band radiation caused by plasma formation. Both of these (broad-band radiation) interfere with the linear intensity-

to-density relationship in spontaneous Raman measurements. *Anderson et al. [10]* attempted to reduce the stimulated Raman problem by designing a passive pulse stretcher in the path of the incident beam. They measured Raman-shifted light from O_2 at 580nm using a 300mJ frequency-doubled Nd:YAG at 532nm. The pulse was stretched from 10ns to 23ns as measured at the so-called full-width half-maximum (FWHM) point of the temporal profile. *Decker et al. [11]* used a double-oscillator Excimer laser to produce two back-to-back lowered-power two-dimensional pulses. They measured the Raman effect from N_2 at 382nm using a 150mJ XeF laser at 351nm. The total pulse width was 40ns.

Oschwald and Schik [12] employed a 1.5W continuous wave Ar^+ laser at 488nm and detected the Raman signal in a N_2 jet at 550.6 nm scattered from within the beam focused volume at supercritical pressures. No special provision was used for the removal of the stimulated Raman effect. In these experiments, *Decker et al [11]* observed a smooth transition from the high-density core of a LN_2 jet injected into N_2 towards the gaseous outer region; that is, there was no distinct phase interface. The density radial profile was never a top-hat even as close as a distance-to-diameter ratio of 2.5. *Oschwald et al. [13]* injected LN_2 into N_2 at supercritical chamber pressures (Pr=1.17 and 1.76) and at three different initial injection temperatures (100, 118, and 140 K). Although scatter can be seen in their data, the centerline density axial profile at Pr=1.17 relaxed to the chamber density faster the higher the injection initial temperature. At the Pr of 1.76, however, the centerline density values were observed to be insensitive to the initial temperature. The corresponding centerline temperature axial profile at Pr of 1.17, calculated through an equation of state, showed a constant-value region near the injector. This temperature was close to the temperature at which the specific heat as a function of temperature reached a maximum (referred to as T_{max}). This was observed only for the cases when the initial injection temperature was less than the T_{max}. Under this condition, the centerline temperature increased downstream from the injector exit plane until it reached T_{max}. Therefore, most of the heat transferred was used to expand the jet (reduce the density) and not to increase the temperature. This general behavior was not maintained with the same degree of contrast when chamber pressure was raised (at Pr = 1.76) away from the critical pressure of N_2. Based on limited tests, they also concluded that the thermodynamic state of an injected supercritical fluid was of prime importance in determining the jet growth, and not the injection velocity or momentum.

Experimental Setup

High Pressure Chamber Facility

The high pressure facility is shown schematically in Fig. 1. The stainless steel chamber could withstand pressures and temperatures of up to 137 atm (2000 psi) and 473 K, respectively. It had two facing circular sapphire windows with two UV-grade side-mounted slot-shaped quartz windows for optical diagnostics and laser illumination of the chamber. The flow of the liquid through the lines and the injector was achieved as shown in Figure 1. Liquid N_2 from a dewar was used to cool and/or liquefy the injectant passing through the cryogenic cooler prior to injection. A branch was connected to allow for the possibility of introducing other gases as the chamber medium. The mass flow rate of the injectant was measured and regulated via a mass flowmeter, and a precision micrometer valve. For more details the reader is invited to refer to *Chehroudi et al. [8, 9]*.

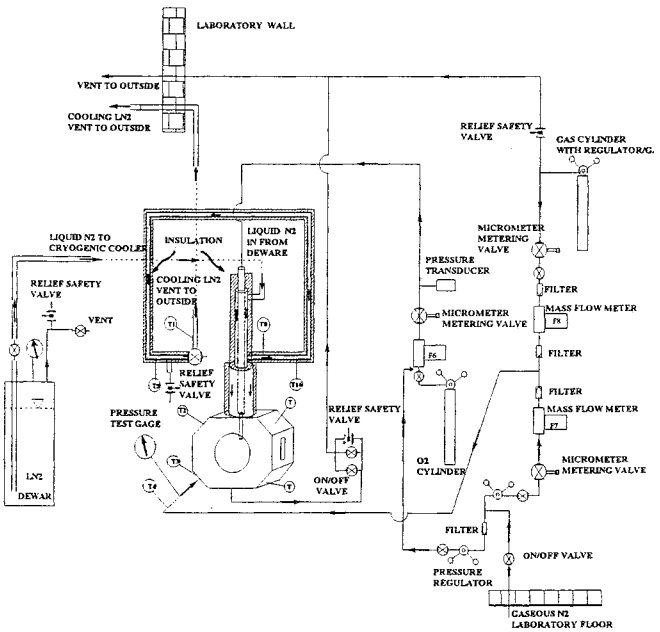

Figure 1. Schematic diagram of experimental setup for sub- to supercritical jet injection

An entrance length of 50 to 100 injector hole diameter is typically needed to achieve a fully-developed turbulent flow for the range of the Reynolds numbers used in this study (25,000 to 70,000), see *Schlichting [14]*. The injection in this work is through a sharp-edged 50 mm long stainless steel tube with a 1.59 mm (1/16") diameter and a 508 micron (0.020") inner hole (length-to-diameter ratio of 100). The length of the hole is therefore long enough to ensure a fully-developed turbulent pipe flow at the exit of the injector. The rig is fully instrumented with thermocouples, pressure gages, transducers, and mass flowmeters at the locations indicated in Fig. 1.

Optical Setup

A Powerlite 8010 frequency-doubled Nd:Yag pulsed laser by Continuum Corporation was used at 532 nm and 330 mJ/pulse as a source to induce the Raman effect. The repetition rate for this laser was 10 Hz with a pulse width of 10 ns. Data was only collected using every 10^{th} pulse due to limitations of the camera used in this study. As justified in the Appendix, a passive pulse stretcher was designed to reduce the possibility of plasma formation as shown in Fig. 2. The laser beam passed through three

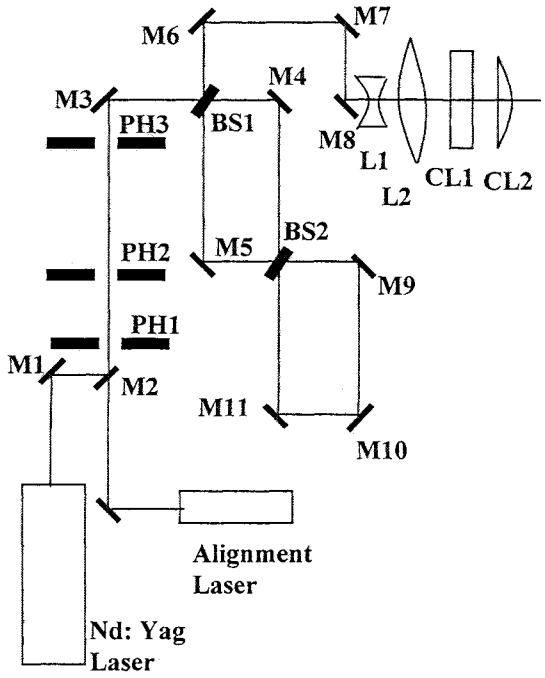

Figure 2. Schematic diagram of the laser beam/sheet path showing the delay loops and the alignment laser. BS (beam Splitter), PH (pinhole), M (mirror), L (spherical lens), and CL (cylindrical lens).

adjustable pinholes (PH1, PH2, and PH3) positioned at sufficiently far distances to allow periodic inspection of the incident beam alignment. Because the laser cavity was located on a separate optical table, this arrangement was found to be a very effective method for realignment. Also, this was used to direct a He-Ne alignment laser beam collinear with the Nd:Yag beam for the initial phase of the alignment procedure. Although the wavelengths of the two beams were not the same, this initial alignment was nearly identical to the final one which is ultimately determined using the Nd:Yag laser. This was found to be a safer and more efficient approach.

In Fig. 2, the laser beam meets the first beam splitter at BS1 and about 35% of its intensity is split towards the M6 mirror. The remaining goes through the first loop (BS1-M4-BS2-M5-BS1) in about 8 ns of time. Note that only about 35% of this remaining energy is reflected by the mirror M5, the rest goes through the loop (BS2-M11-M10-M9-BS2) in an additional 8 ns. Therefore, the original pulse is extended in time by dividing the original pulse into three major pulses, each being 10 ns in duration, but delayed in time by 8 ns and 16 ns. The final pulse duration is about 26 ns. Precision laser mirrors with a damage threshold of 10 J/cm2 (10ns pulse) and VIS coating from Edmond Scientific are used. The laser beam is shaped by passing through a Galilean beam expander (L1 & L2) before forming a thin sheet via two cylindrical lenses CL1 and CL2, see Fig. 2. The laser sheet thickness is measured using an attenuator attached to a CCD camera and found to be about 100 micron. The entire assembly, consisting of the mirror M8 and all lenses, are on a separate optical bench, which could be traversed as a unit vertically (into the plane of Fig. 2) as well as in one horizontal direction. This gave sufficient flexibility to adjust both the thickness of the sheet as well as its vertical and horizontal locations. The vertical and horizontal traverse directions provide axial and radial traverse capabilities, respectively.

The scattered Raman signal at 607 nm is detected by a cooled 576x384 pixel ICCD camera from Princeton Instruments. A set of three filters is also used to separate the Raman signal from the 532 nm incident beam. A high-pass OG570 filter is used to reduce the light at 532nm by more than 10^5 and at 607 nm by not more than 10%. A holographic supernotch plus filter attenuates the light at 532nm by better than 10^6 while less than 20% at 607nm. Finally, a 10 nm bandwidth interference filter centered at 610 nm reduces the scattered light at 532nm by better than 10^4 while attenuating by about 0.5 at 607nm. Therefore, an optical density of better than 15 is achieved at 532nm laser wavelength with the Raman signal transmittance of 0.36. This arrangement was found to be adequate to ensure removal of stray light while passing sufficient Raman for detection at 607nm. The lens package consists of a Nikon PK-12/14 extension ring connected to one end of a Noct-Nikkor 58mm F/# (1.2 to 16) lens with a NIK-2734 close-up lens located in its front.

A Summary of Previous Results

During the past two years, results from the injection of several fluids into an ambient under both sub- and supercritical pressures at sufficiently high Reynolds numbers to be considered as fully-turbulent flow have been reported for the same test facility shown in Fig.1, see *Chehroudi et al. [8,9]*. A variety of ambient fluids was used into which pure N_2 , He, and O_2 fluids were injected. The effects of chamber pressure (density) ranging from the thermodynamic subcritical to supercritical values at a supercritical chamber temperature (based on the critical pressure and temperature, Pc, Tc, of the injectant) were observed by the acquisition of shadowgraph images from the injector exit region using a CCD camera illuminated by short-duration light pulses.

At sufficiently low subcritical chamber pressures, the disturbances on the jet interface amplified downstream and eventually broke up into irregularly-shaped small entities. A further increase of chamber pressure initiated the formation of many small ligaments and droplets at the interface of the jet only within a narrow regime below the thermodynamic critical pressure of the injected pure fluid, resembling a second wind-induced liquid jet breakup. At even higher chamber pressures, near but below the critical pressure of the injectant, the expected transition into a full atomization regime to produce a liquid spray was inhib-

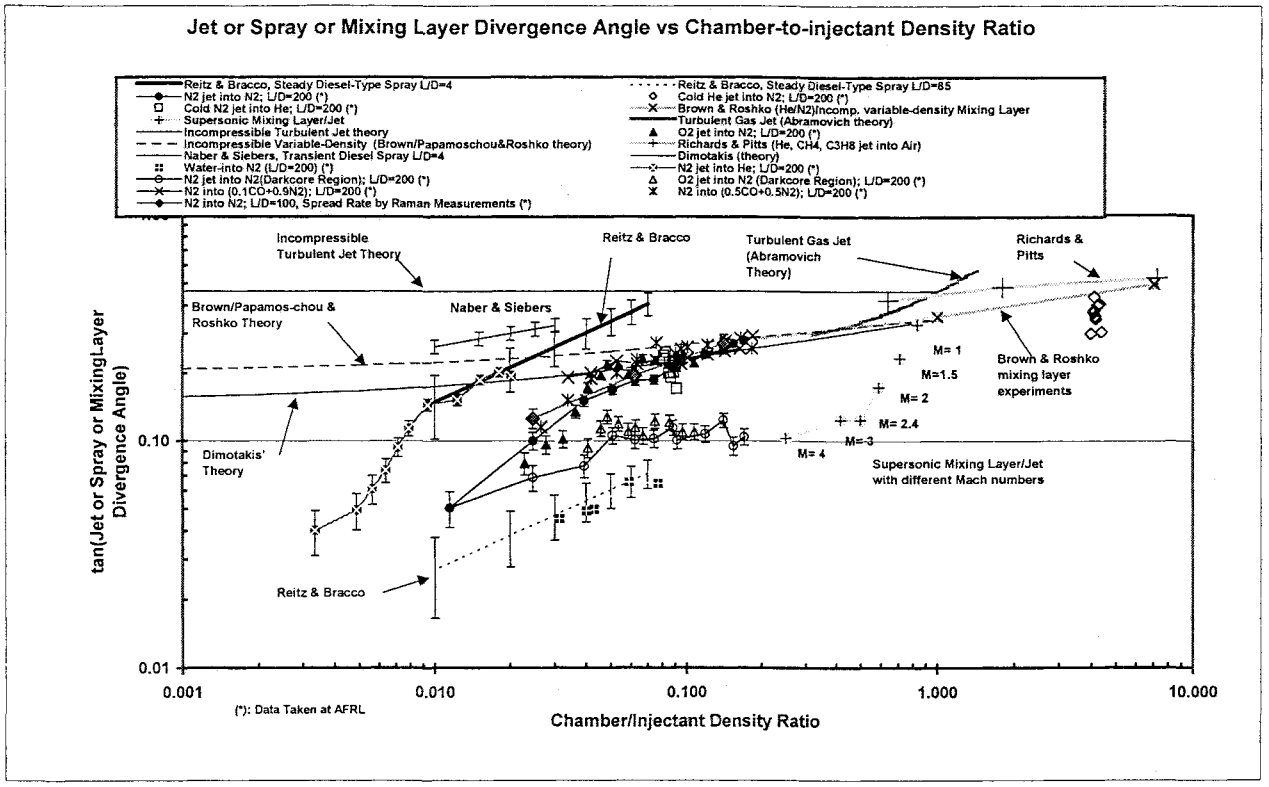

Figure 3. Initial growth rate of fluid jets as a function of the chamber-to-injectant density ratio for a variety of cases.

ited due to reduction of both the surface tension and the heat of vaporization. The jet appearance changed abruptly at this pressure and resembled that of a turbulent gas jet for all higher chamber pressures. The initial growth rate of the jet was plotted together with available data on liquid fuel injection in diesel engine environments, and turbulent incompressible, supersonic, and variable-density jets and mixing layers. The resulting plot is unique in its own right, covering as it does four order of magnitude in density ratio, see Fig. 3. At near- and super-critical pressures, these measurements agreed well with the theoretical growth rate equations proposed *by Brown [15], Papamoschou and Roshko [16],* and *Dimotakis [17]* for incompressible but variable-density turbulent mixing layers. This constitutes the first quantitative evidence in support of the past qualitative observations that the jet appeared to evolve into a gas-like behavior under supercritical condition. The geometry of the jet interface was also examined for the first time by fractal analysis. The results clearly indicated a transition from a Euclidean to a fractal interface, with a fractal dimension close to values measured for gaseous turbulent jets. This provided an additional quantitative evidence for the hypothesis that the jet evolved into a gas-like behavior. Finally, an equation was proposed based on a physical model proposing that at the point of transition from liquid-like to gas-like appearances and growth rates, the characteristic time of the vaporization process is of the same order as that of the interfacial "bulge" formation/separation events. The model equation agreed well with the experimental growth rate data.

Experimental Results and Discussion

Before any image of the jets was obtained, the basic operation of the entire system was verified. For this purpose, measurements were made of the Raman intensity from pure gaseous nitrogen inside the high-pressure chamber at different chamber pressures. The ratios of the measured Raman intensities (corrected for the dark count) should be proportional to the density ratios calculated through an equation of state or thermodynamic tables. Figure 4 shows results from such a test.

In each column of this figure, the grayscale (or false color, if seen in color) representation of the scattered Raman intensity from the laser sheet is shown along with an averaged intensity profile averaged across 5 rows. The averaging was done within the two thick horizontal lines (covering 5 rows of pixels) shown in the images. The lower edge of the laser sheet is clearly seen in each image, and is located where the dark black zone meets the brighter color code. After removal of the dark-count from the images, the measured intensity ratios were compared with those calculated using the ideal gas law for nitrogen. The agreement was found to be within 2 percent, and considered to be satisfactory.

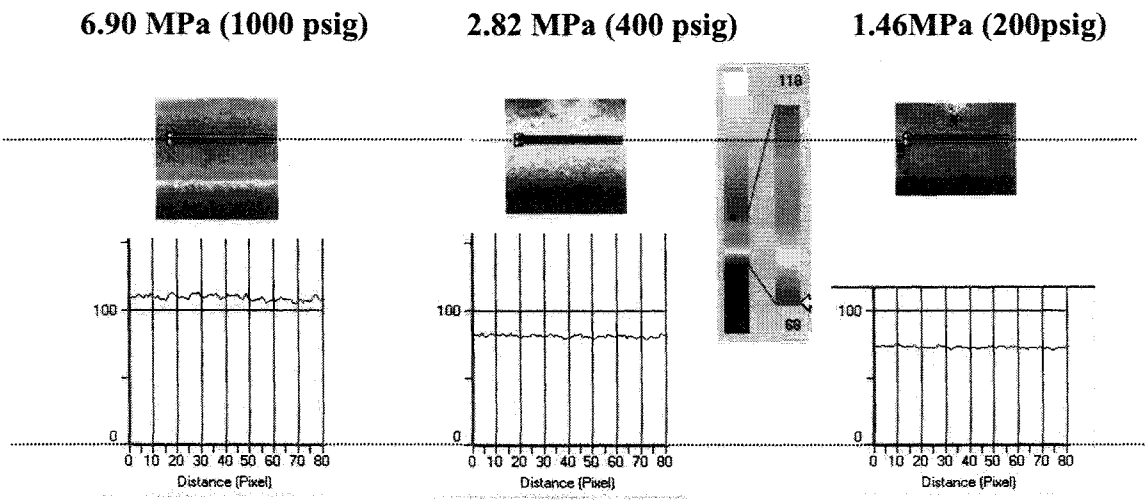

Figure 4. Raman intensity measured by passing the laser sheet into the chamber filled with N_2 at three different pressures.

The image acquisition procedure was performed in two steps. The first step consisted of acquiring an initial dark count image, followed by images at three different chamber pressures (6.9, 2.82, and 1.46 MPa), similar to Fig. 4. This information was needed to remove the dark count level and establish reference intensity levels at the aforementioned chamber pressures. These images also served as a check for the proper operation of the entire system setup. The second step was the Raman image acquisition from the LN_2 jet at these same chamber pressures. Forty frames were acquired and averaged at each condition in order to improve the signal to noise ratio. The number of images was limited to 40 by the memory available in the image acquisition system and the practical operating time of the facility. This was found to be adequate for the reported experiments. It should be noted that it was possible to gain some instantaneous information from the data. However the data has not yet been processed to gain this additional information.

Typical averaged raw images of the LN_2 jet at subcritical

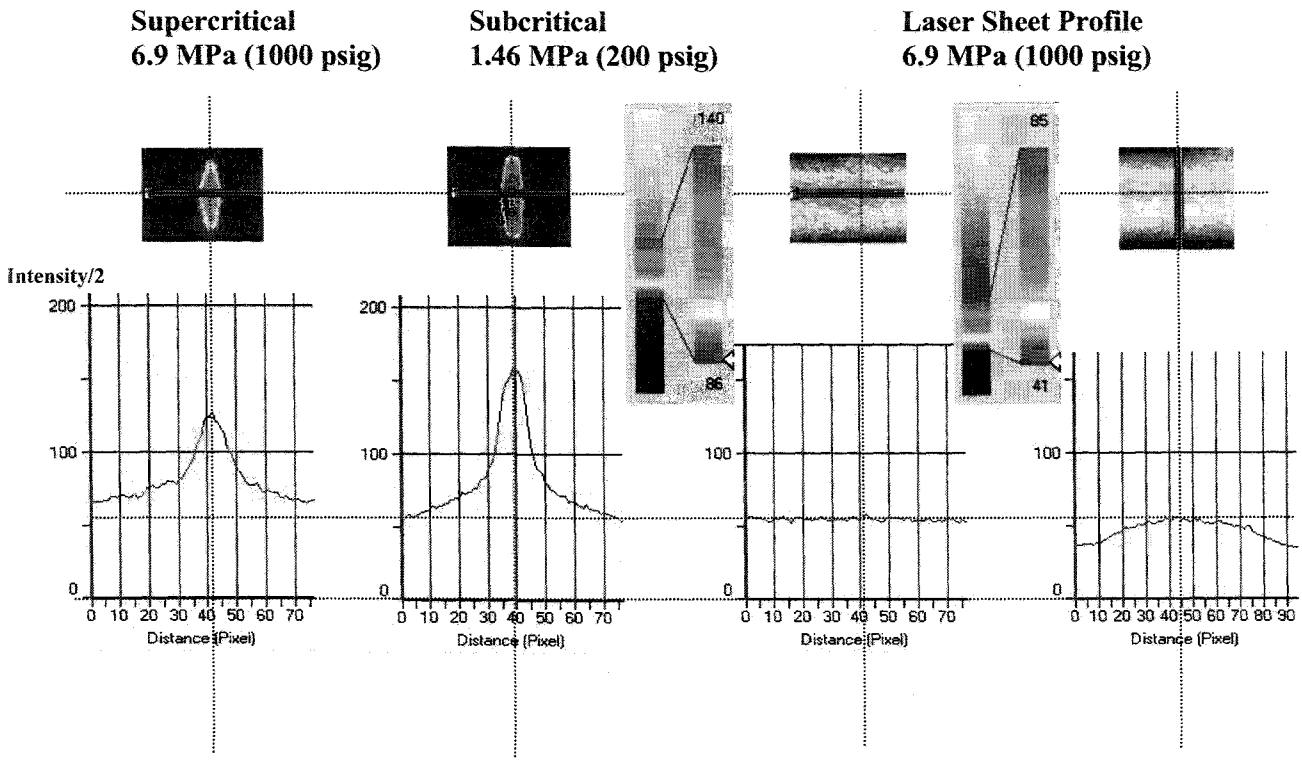

Figure 5. Typical 40-frame-averaged false-color images of the jet at sub-and supercritical chamber conditions. The laser sheet profile is also shown to be reasonably fat within the measurement region. Measured intensities are shown in each case.

and supercritical chamber conditions along with images characterizing the sheet profile at this measurement location are shown in Fig. 5. Note that the Raman intensity profile for the subcritical case is higher in magnitude at the center of the jet and appears narrower in shape. With LN_2 injection, it was observed that the measured intensity well outside the jet area (representing the chamber density) was higher than when injection was turned off. This was due to the interaction of the laser and the jet and was particularly severe for the subcritical case where a clear sharp interface can be defined. This interface caused reflection of a fraction of the laser energy contributing to higher measured Raman intensity values and noise levels. As an example, on the 40-frame-averaged images, when jet flow was off, the pixel-averaged measured Raman signals within a fixed rectangular region where laser entered the chamber were 101.4 and 70.6 units for the 6.9 MPa and 1.46 MPa cases, respectively; whereas the corresponding values for when the LN_2 jet was flowing were 116.4 and 98.0 units. Therefore, this suggested a methodology for a first order correction to the raw data as follows. For each set of data at a given condition, Raman images were collected with no injection followed by the Raman images from the jets as described earlier. Using the example above, all pixel values for images at chamber pressure of 6.9MPa were then reduced by (116.4 - 101.4 = 15) and those for the 1.46 MPa by (98.0 – 70.6= 27.4). It is seen that the contribution of this laser/jet interaction to the measured raw intensity is almost twice as much for the subcritical case, indicating difficulty in complete removal of this side effect for this case.

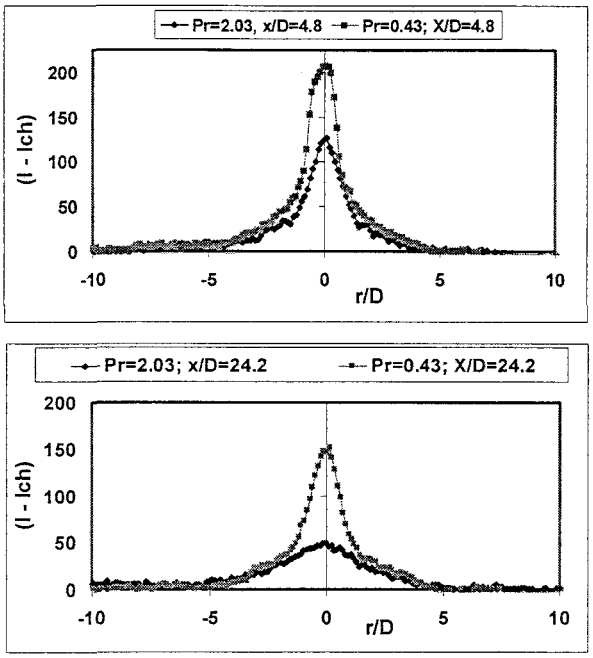

Figure 6. 40-frame-averaged Raman relative intensity radial profiles at two different distances from the injector and at sub- and supercritical chamber conditions. D is injector hole diameter.

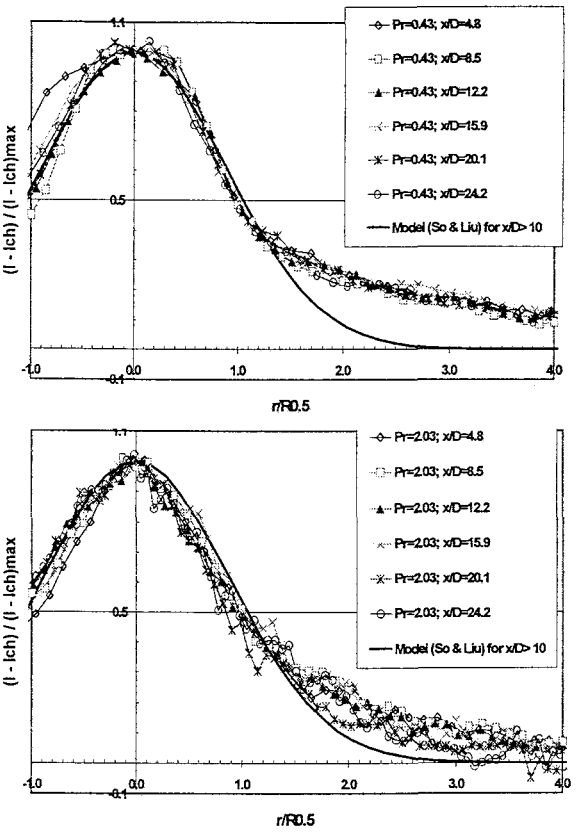

Figure 7. Similarity-type plot for the measured Raman intensity surplus (I – Ich) at subcritical (top) and supercritical (bottom) chamber pressures. The R0.5 is the radius at which (I – Ich) drops to half of its maximum.

The test conditions for the Raman imaging were selected to correspond and complement our previously-reported shadowgraphy studies. Figure 6 shows typical radial profiles of the 40-frame-averaged Raman intensities (I) as measured with reference to the far field chamber intensity (Ich) values at two distances from the injector exit plan and at sub- and supercritical chamber pressures. The laser sheet propagation direction is from right to left in this figure. It is seen that the centerline intensity surplus (I-Ich) declines with distance from the injector as well as

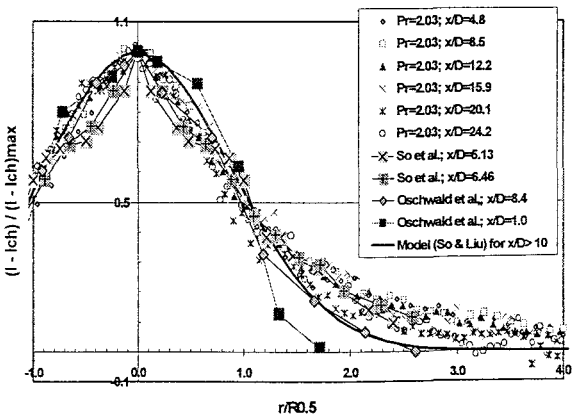

Figure 8. Similar to Fig. 7 but additional results by other investigators are also shown.

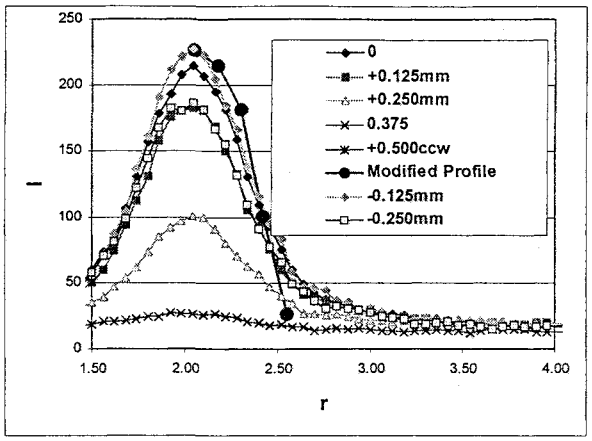

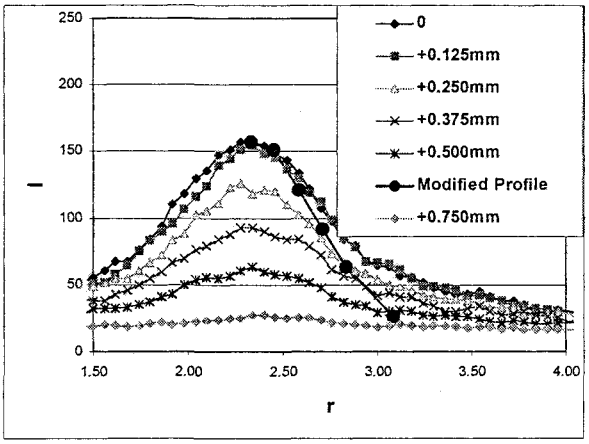

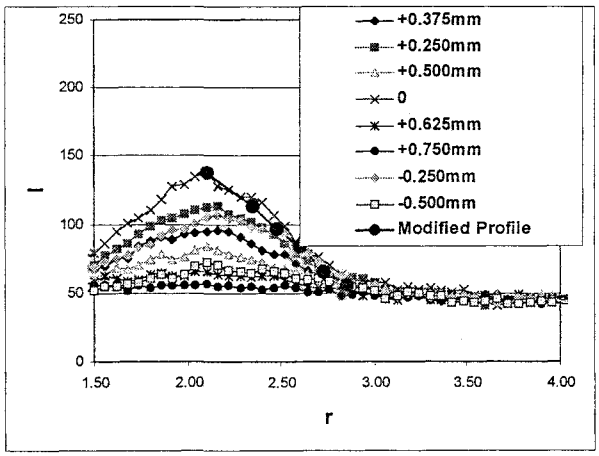

Figure 9. Dark-count-corrected Raman intensity (I) profiles at several different horizontally-traverse locations but at a fixed distance from the injector exit plane (x/D=12.2). The Laser sheet is parallel to the axis of the jet and is traversed horizontally towards (positive idntifier) or away (negative identifier) from the camera. Positive number identifiers for each curve is a traverse distance towards the camera measured with respect to the reference curve (i.e. "0"). Pr= 0.43(top), 0.83(middle), and 2.03(bottom).

when chamber pressure is raised to a supercritical value. Hence, reasonable trends are observed. One point of concern, however, is the existence of an unusually wide tail in these profiles particularly for the subcritical case. This issue will be discussed later.

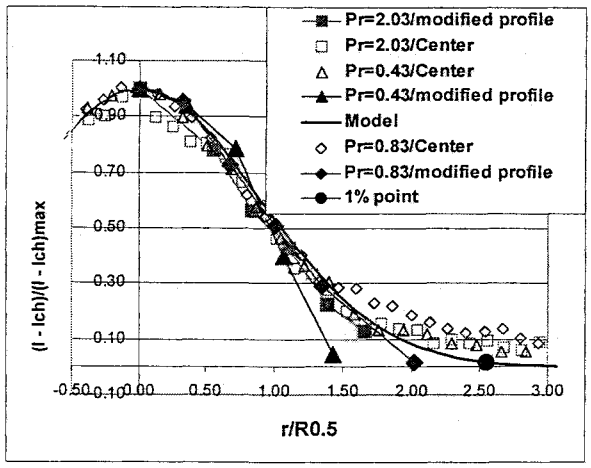

Figure 10. Normalized plot of the Modified and center (i.e. "0") profiles at x/D=12.2 shown in Fig. 8.

Figure 7 shows a similarity-type plot of the intensity surplus at different axial distances and at sub- and supercritical pressures along with a proposed model for turbulent jets. Note that, according to *Wygnanski and Fiedler [18],* a fully self-preserved velocity field of a turbulent air jet should be observed at an x/D of greater than 40 when Re is near 100,000. *So et al. [19]* reported self-preservation for x/D larger than about 20 for a binary gas jet at Re of 4,300. Although there appears to be some inconsistencies in these criteria, one expects to achieve a self-similarity profile at the last few axial distances measured here. Within experimental accuracy, Fig. 7 suggests reasonable self-similarity for both cases. It is worthwhile to indicate that *Richards and Pitts [20]* stated that self-similarity is not possible for flows in which the density varies appreciably across the flow; that is, a self-similar solution does not exist for the governing equations. In view of the results presented here, this statement should be reevaluated for near- and super- critical conditions.

What emerges as immediately obvious in Fig. 7 is the wide tail in the profiles particularly for the subcritical case. Also, the profiles appear to be flatter near the center for the subcritical case exhibiting a tendency for a near top-hat shape in this region. In Fig. 8, results *by So et al. [19]* (gaseous jets) and *Oschwald et al. [13]* (supercritical cryogenic jets) are also shown. They clearly point to difficulties in obtaining both high spatial resolution and high fidelity information at these distances from the injector exit plane. Note that the outer part of the *So et al.* profiles agree with our data whereas those by *Oschwald et al.* follow the model at x/D of 8.4. Although only two profiles are shown, data by *Oschwald et al. [13]* appears to be more intuitive as it suggests a gradual change of the shape with distance towards the far field model.

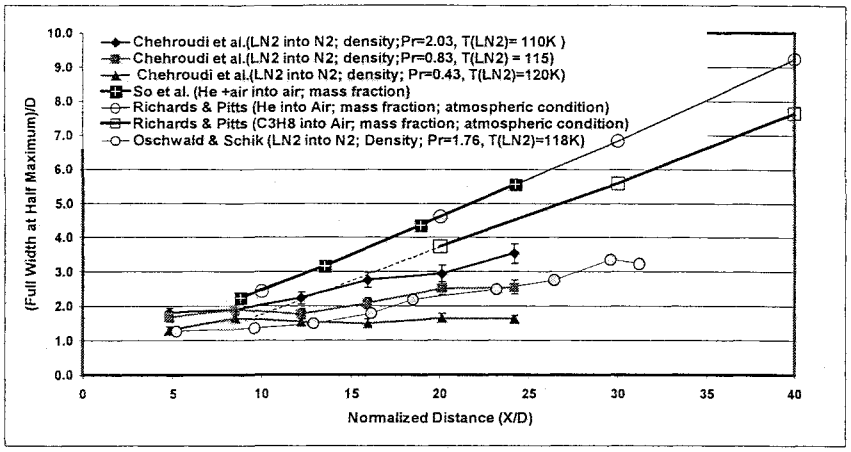

Figure 11. Normalized FWHM of the density surplus radial profiles as a function of the normalized distance from the injector.

	Fluid Inj/Cham	Tinj K	Pch MPa	Tch K	Reduced Pressure Pr	Inj/Chamb Density Ratio	Diameter D mm	L/D	x/D	Raynolds number Re	Profile used to measure FWHM	
Oschwald et al	N2/N2	118	4	298	1.17	3.34	1.9	11.5	8.42	1.2E+05	Density	in Figs. 7, 8
Oschwald et al	N2/N2	140	4	298	1.17	12.5	1.9	11.5	1.05	1.3E+05	Density	in Figs. 8
Chehroudi et al	N2/N2	95	6.9	295	2.03	7.1	0.505	100	4.8 to 24.4	3.5E+04	Density	in Figs. 8,10,11
Chehroudi et al	N2/N2	110	1.5	295	0.43	40.6	0.505	100	4.8 to 24.5	1.2E+04	Density	in Figs.10,11
So et. al.	(He+Air)/Air	275	0.1	275	0.08	0.64	9.5		5.1	5.0E+03	Concentration&Density	in Figs. 8, 11
So et. al.	(He+Air)/Air	275	0.1	275	0.08	0.64	9.5		6.4	5.0E+03	Concentration&Density	in Figs. 8, 11
Richards & Pitts	He into Air	275	0.1	275	0.44	0.138	6.35	~50	20-80	4.0E+03	Mass fraction	in Fig. 11
Richards & Pitts	C3H8 into Air	275	0.1	275	0.02	1.56	6.35	~50	40-120	2.5E+04	Mass fraction	in Fig. 11

Table 1. Some information extracted from works by other investigators reported here. Tinj and Tch are injection and chamber temperatures. Pch is chamber pressure.

To investigate the causes for the aforementioned profile broadening, the vertical laser sheet was traversed horizontally towards and away from the camera and results were analyzed at several selected axial positions. Results from such tests are shown in Fig. 9. A "modified" profile is then constructed using the maximum values of the Raman intensity profiles at each horizontally-traversed position, as indicated in Fig. 9. It is seen that this modified profile is narrower than the profile taken when the laser sheet slices the jet containing the centerline. This effect is particularly strong at subcritical pressures, and almost negligible at supercritical pressures. This suggests that reflections from the jet boundary may induce an additional Raman effect in this zone, causing broadening of the intensity surplus profiles indicated earlier. Considering the injector hole diameter used in this study, such a broadening is to be expected.

The above conclusions from the modified radial profiles suggest that these profiles exhibit self-similarity for near critical and supercritical pressures. Self-similarity may also hold at subcritical pressures, although, strictly speaking, it cannot be stated unless data at other axial positions are analyzed. Figure 10 shows similarity-type plots for the modified and their corresponding "center" profiles. A center profile is that with the highest peak intensity. The $R_{0.5}$ point (i.e. the radius at the half maximum) is determined for each profile independently. The single solid circle shows the end of the 1% point to be about 2.5 times the full width at the half maximum (FWHM) value (i.e. 2.5* $R_{0.5}$). These modified profiles suggest a self-similarity profile equation different that that seen in gaseous turbulent jets (solid black model curve in Fig. 10) at the lowest subcritical condition (i.e. Pr=0.43). In contrast, a tendency towards such a similarity equation is observed at Pr of 0.83 and 2.03. Admittedly, the agreement is not perfect.

Comparing the modified profiles with those taken at the center location from a single averaged image, one can deduce that the error in the FWHM values from these center profiles is less than 5%, despite the existence of the broadening effect. When available, the best value for the FWHM were considered. The observed broadening in this work prevents us from using the jet thickness definition used by *Brown and Roshko [21]* based on the 1% free stream density point on the radial profiles. Instead, the FWHM appears to be a safer parameter to determine in this work for comparison with other results. Also, there is doubt if density values can be measured to within 1% accuracy. Nevertheless, *Brown and Roshko [21]* reported that their 1% thickness definition corresponded fairly well with the

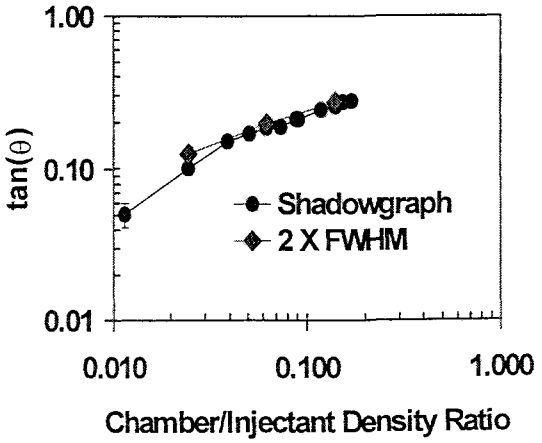

Figure 12. Comparison of the spreading angle measured using shadowgraph and Raman techniques using twice the FWHM values..

extent of the mixing visible on the shadowgraph images. However, the spread angle based on the density profile was always larger than that on the velocity profile.

The FWHM at each axial position was determined and the results, along with data by other investigators, are shown in Fig. 11. More information on the experimental conditions is given in Table 1. Note that except for *Chehroudi et al. [8, 9]* and *Oschwald_et al. [13],* all others performed injection of gaseous fluids into an ambient gas at subcritical pressures (based on the injectant critical pressure). Also, note that the FWHM was determined using the mass fraction profiles in both *So et al. [19]* and *Richards and Pitts [21].* However, reported FWHM values by *So et al. [19]* using both density and mass fraction profiles were comparable. The results of the present work in Fig. 11 show an increasingly larger spreading rate as chamber pressure is raised. The data at the supercritical condition (P_r = 2.03) approaches that of *Richards and Pitts [20]* acquired at a density ratio of 1.56 even though it is substantially smaller than ours. Data at larger distances are not currently available for our jet to develop a more comprehensive comparison between the cases.

Richards and Pitts [20] concluded that if care is exercised to ensure that the flow is free of buoyancy and coflow effects, the spreading rate in variable-density jets is independent of the initial density ratio, velocity profile, and turbulence level, and conforms with the constant-density results of others. In addition, they propose a slope in the range between 0.212 to 0.220 for the linear jet growth rate equation, see Fig. 11. However, a linear least-square fit to our data at Pr=2.03 gives a slope of 0.102, almost half of that *by Richards and Pitts [20].* One possible explanation for this difference is that our data covers a range much closer to the injector exit plane than that of *Richards and Pitts [20],* causing lowered growth rate. A tendency towards higher growth rate can be seen if only the farthest two data points are considered in our data. However, a solid conclusion cannot be drawn at this time based on these two points. It is also possible that at some high enough injectant-to-chamber density ratio, the spread rate universality indicated by *Richards and Pitts* breaks down and one observes a somewhat retarded growth rate for variable-density turbulent jets. Evidence for this can also be seen in Fig. 3 as *Richards and Pitts* data is higher than almost all other cases.

The measured spreading rate using Raman scattering was compared with the spreading rate we reported in the past from the shadowgraph visualizations. The results are plotted in Fig. 12. It can be seen that the spreading rate at twice the FWHM values agrees well with the shadowgraph measurements. Note that the finding that twice the FWHM matches our previous shadowgraph results is not related to the factor of ½ mentioned earlier regarding the growth rates. At subcritical pressures, a factor slightly less than 2 would give a better agreement as implied from Figs. 10 and 12. Thus the correspondence of the two different techniques for measuring the width of the jet has been established.

Summary and Conclusions

Two-dimensional Raman-shifted scattered light from a cryogenic LN_2 jet was acquired at several distances from the injector both at subcritical and supercritical pressures. Difficulties arose with optical breakdown of the N_2 molecules in drops and ligaments caused by the local focusing of the laser beam dominating the Raman signal, particularly at sub- and near- critical regions. The severity of this problem was reduced by temporally stretching the laser pulse width using a double-loop passive pulse stretcher design. Careful and painstaking alignment was required to take advantage of this design.

Reflection of the laser from the jet boundary produced additional effects in this zone such as causing profile broadening, particularly at subcritical pressures. This effect was demonstrated through systematic horizontal traverses of the laser sheet towards and away from the camera.

In general, the profiles exhibited self-similarity at all conditions tested here. Within experimental accuracy, the "modified" intensity surplus profiles indicate a tendency towards the self-similarity equation observed for classical constant and variable-density gaseous/liquid jets only at near- and super-critical conditions. It is believed that a self-similar condition also exists at subcritical conditions. However, more data must be analyzed to make this conclusion. Because of this broadening effect, twice the FWHM of the radial profile is a better estimator to use for the jet thickness and growth rate than the 1% criterion. The growth rate of the LN_2 jet increases monotonically as chamber pressure increases. At supercritical pressures, the growth rates approach those reported for conventional gaseous jets. It is also shown that a plot of twice the FWHM versus density ratio agrees with the jet thickness measured through our shadowgraphy studies. This establishes an equivalency between these two different jet thickness determination methods.

Acknowledgement

Mr. Mike Griggs and Mr. Earl Thomas are thanked for their valuable support. We also appreciate Mr. Mike Mckee's contribution in part of the data acquisition. This work is sponsored by the Air Force Office of Scientific Research under Mr. Mitant Birkan, program manager.

References

1. Mayer, et al. "Injection and mixing processes in high pressure LOX/GH2 rocket combustors," AIAA Paper no. 96-2620, Lake Buena Vista, Florida, 1996.
2. Mayer, et al. "Propellant atomization in LOX/GH2 rocket combustors," AIAA Paper no. 98-3685, 1998.

3. Chen, L.-D. and Sui, P.-C. "Atomization during the injection of supercritical fluid into high pressure environment," in *Mechanics and Combustion of Droplets in Sprays* by Chiu and Chigier.
4. Woodward , R. D. and Talley, D. G. "Raman imaging of transcritical cryogenic propellants," AIAA Paper 96-0468, Reno, Nevada, January 1996.
5. Harstad, K and Bellan, J. "Isolated fluid oxygen drop behavior in fluid hydrogen at rocket chamber pressures," International Journal of Heat and Mass transfer 41, pp. 3537-3550, 1998.
6. Delplanque J. P. and Sirignano W. A. Atomization and Sprays, 4:325-349, 1994.
7. Oefelein, J. C. and Yang V. "Modeling High-pressure Mixing and combustion Processes in Liquid Rocket Engines," J. Propulsion & power, Vol. 14, no. 5, September-October, 1998.
8. Chehroudi, B., Talley, D.G., and Coy, E.B., "Initial Growth Rate and Visual Characteristics of a Round Jet into a Sub- to Supercritical Environment of Relevance to Rocket, Gas Turbine, and Diesel Engines," AIAA paper 99-0206, Reno, Nevada, 1999.
9. Chehroudi, B., Talley, D., and Coy, E. "Fractal geometry and growth rate of cryogenic jets near critical point," AIAA Paper 99-2489, 35th AIAA/ASME/SAE/ASEE Joint Propulsion Conference, Los Angeles, CA, June 20-24, 1999.
10. Anderson, T.J., Woodward, R.D., and Winter, M. "Oxygen Concentration Measurements in a High Pressure Environment Using Raman Imaging," AIAA Paper 95-0140, 33rd Aerospace Sciences Meeting and Exhibit, January 9-12, Reno, NV, 1995.
11. Decker, M C, Schik, A, Meier, U E, Stricker R W. "Quantitative Raman Imaging Investigations of Mixing Phenomena in High Pressure Cryogenic Jets," *Appl Opt* 37:5620-5627, 1998.
12. Oschwald, M. and Schik, A. "Supercritical Nitrogen Free Jet Investigated by Spontaneous Raman Scattering," *Experiments in Fluids*, 27, 497-506, 1999.
13. Oschwald, M, Schik, A, Klar, M, Mayer, W, "Investigation of Coaxial LN2/GH2-Injection at Supercritical Pressure by Spontaneous Raman Scattering," 35th AIAA/ASME/SAE/ASEE Joint Propulsion Conference and Exhibit, Los Angeles, CA, 20-24 June, 1999.
14. Schlichting, H. *Boundary Layer Theory*, MacGraw-Hill Book Company, seventh edition, 1979.
15. Brown G., "The entrainment and large structure in turbulent mixing layers," 5th Australasian Conf. on Hydraulics and Fluid Mech., 1974, pp. 352-359.
16. Papamoschou, D. and Roshko, A. "The compressible turbulent shear layer: an experimental study," J. Fluid Mech., vol. 197, 1988, pp. 453-477.
17. Dimotakis, P. E. "Two-dimensional shear-layer entrainment," AIAA Journal, 21, No. 11, 1986, pp. 1791-1796.
18. Wygnanski, I and Fiedler, H. E. "The two-dimensional Mixing region," J. Fluid Mech., 41, 327, 1970.
19. So, R M C, Zhu, J Y, Otugen, M V, and Hwang, B C, "Some Measurements in a Binary Gas Jet," *Experiments in Fluids*, 9, 273-284, 1990.
20. Richards, C. D. and Pitts, W. M. "Global density effects on the self-preservation behavior of turbulent free jets," J. Fluid Mech., vol. 254, 1993, pp. 417-435.
21. Brown, G. and Roshko, A. "On density effects and large structure in turbulent mixing layers," *J. Fluid Mech.*, vol. 64, 1974, part 4, pp. 775-816.

APPENDIX

Synopsis on Raman Effect:

To make the paper reasonably self-sufficient and useful to a more broader readers, this synopsis on Raman effect is included. When a transparent medium is irradiated, some fraction of the beam is scattered in all directions. If the medium contains particles of molecular dimension, a weak scattered radiation having the same wavelength is observed (Rayleigh scattering). When aggregates of particles have sizes approximating that of the wavelength of the radiation, however, scattering becomes evident as the Tyndall effects or as a turbidity. Raman, in 1928, discovered that the wavelength of a very small fraction of the scattered radiation by certain molecules shifted in an amount dependent upon the chemical structure of the molecules responsible for the scattering. The theory of Raman scattering shows that the phenomenon results from the same type of quantized vibrational changes that are associated with infrared absorption. Therefore, the observed *difference* in wavelength corresponds to wavelength in mid-infrared regions. However, an important advantage of Raman over infrared spectra is that water does not cause interference. In addition, glass or quartz windows can be used instead of the inconvenient sodium chloride or other atmospherically unstable windows.

The Raman spectra are obtained by irradiating a sample with a powerful visible monchromatic source. The scattered signal is usually observed at 90 degrees to the incident beam with a suitable visible-region detector or spectrometer. The scattered radiation does not exceed 0.001 % of the source, as a result detection and measurement is difficult except for the resonant Raman which is explained below. The scattered light is of three types, Stokes, anti-Stokes, and Rayleigh. Rayleigh, which has exactly the same frequency as the excitation source, is substantially more intense than either two. Stokes peak lines are found at wavelengths larger (lower energies) than the Rayleigh peak while anti-Stokes are at smaller (higher energies) than the wavelength of the source. It is critical to realize that the magnitude of the Raman shifts are independent of the wavelength of excitation source. Although, superficially, the appearance of the Stokes shifts are similar to the Stokes shifts observed in fluorescence, they arise from fundamentally different processes. Generally, the Stokes lines are more intense than the anti-Stokes and for this reason usually only this part of the spectrum is observed. It is also important to

indicate that fluorescence can interfere with detection of the Stokes shifts but not with anti-Stoke shifts.

The wave theory of Raman relates this effect to the change in polrizability of the molecule which may occur during its vibration. That is, the ease with which the electrons of the bonds can be distorted from their normal position by the excitation source. The wave theory cannot predict the fact that the Stokes lines are stronger than the anti-Stokes lines. Quantum mechanics, considers elastic (no net exchange of energy, like Rayliegh) and inelastic collisions (like Raman effect) between photons and molecules. In the latter, the vibrational energy of the bond is subtracted and added to the energy of the photon thus shifting its frequency, see Fig. 13. It is important to indicate that the normal Raman (or spontaneous Raman) process is not quantized and depending on the frequency of the excitation, the molecule can assume any number of infinite virtual states as shown in Fig. 13. The relative populations of the states in this figure are such that Stokes emission is much favored over the anti-Stokes. Also, the ratio of anti-Stokes to Stokes intensities increases with temperature as larger fraction of the molecules make transition and stay in the first vibrational excited state under such higher temperature conditions. The intensity of the normal Raman depends on the polarizability of the molecules, the source intensity, concentration of the scatterers, and other factors. In the absence of absorption, the intensity of Raman emission increases with fourth power of the source frequency (or ~ $1/\lambda^4$). However, care must be exercised at shorter source wavelengths (ultraviolet) as likelihood of the photodecomposition will increase particularly if sample is not flowing past the interrogation zone. Source frequencies must be chosen so it is not absorbed by the sample unless resonant Raman is considered. Normal Raman intensities usually are linearly dependent on the concentration of the molecule (similar to Fluorescence) unlike logarithmic behavior for the absorption. Raman signal is found to be polarized to a various degree depending on the type of vibration responsible for the scattering. Generally, the scattered Raman is more polarized when excited mode of vibration is symmetric when a plane-polarized radiation source is used (such as a laser). Depolarization ratio, defined as the ratio of the perpendicularly-polarized by the parallel polarized scattered Raman, is 0.022 for N_2 molecule. Theoretically, it can be shown that depolarization ratio is ¾ for nonsymmetric vibration while always less than this value for the symmetric case.

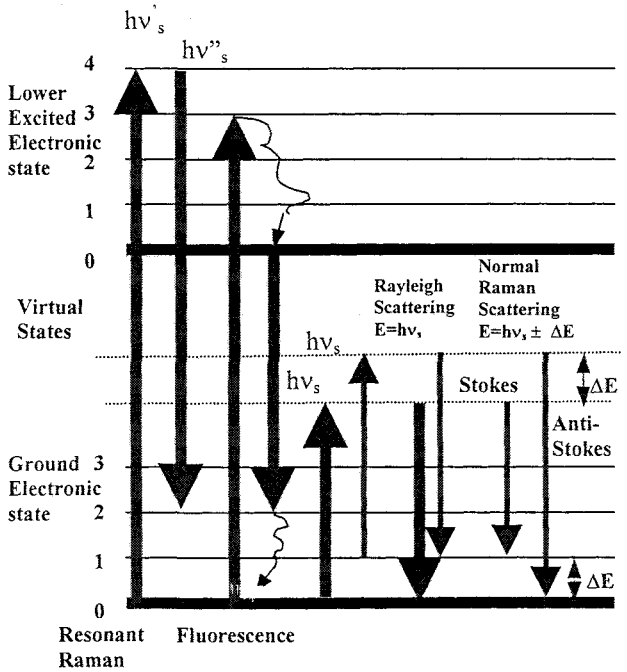

Figure 13. Quantum mechanical description of the Rayleigh, Raman, resonant Raman, and Fluorescence effects

When the excitation frequency falls within a frequency range of a molecule's (vibrational or electronic) absorption band in the visible or UV spectrum, the radiation is scattered by either resonance Raman or resonance fluorescence, see Fig. 13. Both produce much more intense radiation than normal Raman. Resonance Raman intensities can be higher that normal Raman by up to 2 orders of magnitude. In resonance fluorescence, the absolute frequencies of the fluorescence do not shift when the source frequency is changed as long as it stays within the absorption band. However, the absolute frequency of the Raman (both normal and resonant) shifts with exactly the same amount as the changes in source frequency. Finally, in situations where the intensity of the source exceeds certain threshold power, coherent pumping of the molecules of the sample into an excited vibrational state occurs. This coherent frequency is equal to that of the laser minus the vibrational frequency. The power in the scattered radiation may itself cause further stimulated Raman emission by a repetition of the original process, producing a frequency equal to the laser minus twice the frequency of the vibrational mode that is involved in the scattering. Also, an unusual observation in stimulated Raman is the excitation of an intense anti-Stoke radiation which may even be stronger than the Stokes in some cases. It occurs as a result of the pumping of the molecules from ground vibrational state into upper excited states by the initial laser power. These excited molecules can then be pumped by further radiation into ground state through simultaneous stimulated emission of coherent radiation at a frequency equals to laser plus the molecular vibrational frequency, see Fig. 13.

This Page Intentionally Left Blank

APPENDIX K

"The Fractal Geometry of Round Turbulent Cryogenic Nitrogen Jets at Subcritical and Supercritical Pressures"

The Fractal Geometry of Round Turbulent Cryogenic Nitrogen Jets at Subcritical and Supercritical Pressures

B. Chehroudi [*] ***and D. Talley*** [+]

[*] ***Engineering research Corporation***
Principal Scientist
(Corresponding Author)

+Air Force Research Laboratory
AFRL/PRSA Propulsion Directorate
Edwards AFB, CA 93524-7680

Submitted to

Atomization & Sprays

Dept. Mechanical Engineering
Carnegie Mellon University
Pittsburgh, PA 15213-3890

(March, 2002)

Abstract

Box-counting and EDM methods were used to measure the fractal dimension of round turbulent cryogenic nitrogen jets at pressures ranging from subcritical to supercritical pressures. Both method produced similar trends, with close quantitative agreement for a suitably small box-counting scale. At subcritical pressures, the fractal dimension was found to be consistent with the fractal dimension of a spray in the 2nd wind-induced atomization regime. The fractal dimension tended to increase as pressure increased, until at supercritical pressures the fractal dimension was found to be consistent with that of gas jets and mixing layers. The results constitute additional quantitative evidence for the hypothesis that subcritical jets exhibit mainly spray-like behavior, while supercritical jets exhibit mainly gas-like behavior. This appears to have been the first time pressure effects on the fractal dimension of turbulent jets has been measured.

Introduction

As combustion chamber pressures become increasingly higher in order to realize performance and/or efficiency benefits in a wide range of propulsion and energy conversion applications, the injected fluid(s) may experience ambient pressures exceeding the critical pressure(s) of the propellants. For example, in the cryogenic liquid hydrogen/liquid oxygen Space Shuttle Main Engine, the thrust chamber pressure is about 22.3 MPa, and thrust chamber pressures for the oxygen/hydrogen Vulcain engine used to launch the Ariane 5 vehicle have been recorded to reach up to 10 MPa. Both of these pressures exceed the critical pressure of 5.043 MPa for liquid oxygen. In many applications, including liquid rockets, the initial temperature of the propellant is often below the critical temperature, and later heats up to a supercritical temperature as it is mixed and burned in the combustion chamber.

As chamber pressures approach and exceed the critical pressure, combustion mechanisms can be expected to become distinctly different than conventional spray combustion processes at low pressures. For example, for single component fluids, the distinct difference between the gas and liquid phases disappears when the pressure exceeds the critical pressure or the temperature exceeds the critical temperature. Surface tension and the enthalpy of vaporization vanish, and large variations in the density, thermal conductivity, and mass diffusivity occur near the critical point. For multicomponent fluids, the solubility of the gas phase in the liquid phase increases as pressure approaches the critical pressure, and mixture effects need to be taken into account in calculating the critical properties. When mixture effects are considered, the critical pressure of a mixture can be found to be several times the critical pressure of the propellant of interest. Understanding and modeling the effect of these differences on the shear layer of the injected propellant are vital to understanding the mixing and performance characteristics of these high performance engines.

Until recently, understanding of the injection process under these conditions has been limited. However, recent experimental and theoretical work, motivated to a large extent by liquid rocket combustion applications, has begun to allow a picture of the shear layer dynamics to emerge. See for example, *Mayer et al. [1,2], Chen and Sui [3], Woodward and Talley [4], Harstad and Bellan [5], Delplanque and Sirignano [6], Oefelein and Yang [7],* and *Chehroudi et al. [8, 9]*. One of the important experimental findings was the transition in the morphology of the injected jet boundary as chamber pressure increases from a subcritical to supercritical pressure. *Chehroudi et al. [8,9]* studied cryogenic liquid nitrogen jets (simulating liquid oxygen in liquid rocket engines) injected into room temperature nitrogen at various subcritical and supercritical pressures. The initial

temperature of the jet was between 90 and 110 K, which is below the critical temperature of 126.2 K for nitrogen. Back-illuminated visualizations of the results are shown in Fig. 1. It was found that at subcritical chamber pressures, the jet appears to be liquid-like with instabilities that grow downstream of the injector. In the shear region, very fine drops are found to be ejected from the jet. Major structural changes occur as the pressure is increased to near the critical pressure. Drops are no longer detected in the shear region. These drops are replaced by small comb-like ligaments which "dissolve" into the surrounding media due to the combined effects of the reduction in surface tension and negligible latent heat of vaporization. As chamber pressure is increased further beyond the critical pressure, the jet begins to take on the appearance of a turbulent gas jet injected into a gaseous environment. A quantitative examination of the shear layer growth rate, using both high-speed back-lit images and Raman scattering data, also indicates that the growth rate of the jet was consistent with that of round sprays at subcritical pressures, and consistent with that of shear layers surrounding gas jets at supercritical pressures. See *Chehroudi et al. [10]* for more details.

This metamorphic change of the cryogenic jet or shear layer boundary was the motivation for investigating the change in the fractal dimension of the boundary in the present study. The objective was to further quantify the extent to which the jets may behave like conventional sprays at subcritical pressures, but like gas jets at supercritical pressures. The present study appears to be the first time the fractal dimension of jets has been investigated over a range of subcritical to supercritical pressures.

The Fractal Dimension

The notion of a fractal has been given a strong foundation and application by its founder *Mandelbrot [11]*, and is intimately connected to the concept of scaling and self-similarity. *Peitgen, et. al. [12]* pointed out that in examining the structure of a cauliflower, the head may be found to be composed of several branches or parts, which when removed and compared with the whole are very much similar in shape to the whole, only smaller. The parts can in turn be decomposed into even smaller parts, which again are very much similar in shape to the whole as well as to the first generation of parts. This self-similarity as a function of scale only carries through for about three to four stages, after which the cauliflower is no longer self similar. The scales over which self similarity applies is said to range from an inner, or smallest, scale, to an outer, or largest, scale.

The concept of dimension in mathematics has a historical evolution. In Euclidean geometry, a line, a plane, and a surface in space have dimensions of one, two, and three respectively. In topology, things are slightly different. For example, a straight line and any non-self-intersecting curve are equivalent and have the same "topological dimension." Finally, these concepts were shaken by the introduction of the so-called "space-filling" curves. Given some patch of a plane, there exists a "space-filling" curve which meets every point in that patch. Thus, a curve, which by nature is something one-dimensional, can fill something two-dimensional. This questions the intuitive perception of curves as one-dimensional objects, because they fill the plane, an object which is intuitively perceived as two-dimensional. Looking at a self-similar curve with the notion defined in relation to the cauliflower, there is a power law relation between the number of pieces, N, and the reduction factor, ε, as: $N = (1/\varepsilon)^{D_S}$. In other words, this power-law relationship states that if a self-similar curve is reduced by, say, ε =1/2, the number of similar pieces increases by 2^{D_S} . The quantity D_S is defined as the "self-similarity dimension" of the curve. Obviously, for a line, a square, and a cube, we have D_S=1, 2, 3, respectively, which happen to be the topological dimensions. For self-similar curves this dimension is determined through an exercise to measure the total length of the curve using rulers with

different compass settings (or yardstick lengths). The reciprocal compass setting can be considered to be the precision of the length measurement. Mechanistically, one selects a fixed compass setting and attempts to find the number of compass settings needed to cover the entire curve. In other words, one measures the total length of the curve using a fixed setting of the compass. This is repeated for different compass settings. Plotting the number of compass lengths required to cover the curve at a given compass setting as a function of the reciprocal compass setting itself traces a line in a log-log plot for a self-similar curve. The slope of this line, d, and the self-similarity dimension, D_S, can be shown related by: $D_S = 1 + d$, where d is positive in magnitude. Usually, however, the number of compass lengths at a given fixed setting is plotted against the compass setting itself (which in this case, $D_S = 1 - d$ as d is negative in magnitude). Motivated by this result for self-similar curves, the fractal (compass) dimension for shapes that are not strictly self-similar curves such as the jet boundary we would like to analyze are defined as: $D_C = 1 + d$. With this, the fractal dimension of the coast of the England that has many wrinkles is 1.36 whereas the that of the state border of Utah having smooth straight lines is equal to 1. Note that a non-integer number is attributed to the dimension (fractal). The fractal dimension of any curve is between 1 and 2 and the more wrinkled and "space-filling" it looks the larger the dimension value becomes. Natural curves, similar to a cauliflower, are self-similar only to within a narrow range of scales. Our objective here is to measure the fractal dimension of the interface of the jets injected into the chamber to examine if any pattern is uncovered. To our knowledge, this is the first application of the fractal approach to the liquid jet interface under high pressures up to supercritical conditions.

Practical Measurement of the Fractal Dimension

In the literature there are several methods to determine the fractal dimension of a boundary. For example the above-mentioned ruler method is also called the caliper method or the arc-swinging method. This method is difficult to implement for computer analysis, so more computer-compatible and faster algorithms have been devised. One popular method for evaluating the fractal dimension is referred to as box-counting, or the Kolmogrov dimension (see *Russ [13], [14], and Kaye [15]*). One overlays the curve on a square grid with mesh size ε and counts the number of grid boxes which contain any part of the curve. This gives a number $N(\varepsilon)$ which depends on the mesh size ε. The negative of the slope of the line fitted to the linear section of the plot of $\log[N(\varepsilon)]$ *vs.* $\log(\varepsilon)$ is the box-counting dimension. Another approach leads to what is referred to as Minkowski dimension, see *Russ [13]*. In this method, the center of a circle with radius ε is swept continuously along the curve. This creates what is known as a Minkowski sausage around the curve. The area of the sausage as a function of the radius of the circle is drawn on a log-log plot. The Minkowski dimension is equal to (2 – the slope of the linear region). In this paper both box-counting and Minkowski methods are used to calculate the fractal dimension. For the latter method, the Euclidean Distance Mapping (EDM) algorithm of *Russ [13]* is implemented. Consider a black object in a white background where the fractal dimension of the boundary between the two is desired. EDM is an image processing operation that is applied to a black and white image to produce a gray-scale image in which each black pixel is given a brightness value equal to its distance from the nearest white background point. Therefore, the larger the distance of a pixel from the nearest border the higher its assigned gray-scale intensity value, being linearly proportional to the distance. The same procedure can assign values to the white background pixels based on their distance from the nearest point on the object. Thresholding the distance map for either the object or the background produces uniform erosion and dilation of the boundary to any desired distance from the original boundary, without iteration. The EDM method is superior to the classical erosion/dilation method, see *Russ [14]*. It is really not necessary to perform the thresholding operations. Counting the pixels as a function of their brightness (distance) values produces a plot that directly

provides the Minkowski dimension. Both Box-counting and Minkowski methods are shown to provide reliable results, see *Hall et al [16]*. However, the EDM algorithm in determining the fractal dimension is more isotropic, more efficient, and generally more precise than the box-counting method, and easy to implement on a computer, see *Russ and Russ [17]*. Both techniques are limited to only self-similar and not self-affine boundaries.

Fractal Analysis of Cryogenic Jets

Before running the fractal analysis program for the computation of fractal dimensions, the images need to be conditioned. In particular, corrections to images are applied to account for the reference background condition. Then smoothing and twice-sharpening filters are applied. Also, an appropriate pixel intensity threshold level (described later) is selected to identify the boundary of the jet injected into the chamber. A 200X200 pixel image of a square boundary within our 432 x 477 full frame size is used as a test image to evaluate the fractal analysis program. Theoretically, the fractal dimension of the smooth boundary of this square must be equal to one. The analysis, however, gives a fractal dimension higher than one by at most 3% for the box-counting and EDM methods. For the box-counting dimension, two different methods are used to change the mesh size. In one case, the mesh size is increased by the following sequence, 1x1, 2x2, 3x3,…, 32x32 pixels, and in the other by 2x2, 4x4, 6x6, 8x8, …, 64x64 pixels. In this paper they are referred to as BOX32 and BOX64 respectively.

In order to define a closed-loop jet boundary for fractal analysis of the jet images in Fig. 1, one needs to manually select a section of the jet image that excludes regions covering the image of injector tip and the part of the image near the lower edge of the frames. This creates two smooth straight lines joining the left and the right boundaries of the jet at the top and the bottom. The effect of adding these two smooth sections on the fractal dimension value is analyzed by several different methods. First, the left and the right boundaries are manually moved close to each other so the length of the upper smooth line is minimized. The minimization is done on the upper section because the jet diverges downward in the images. Second, the upper and lower smooth lines are replaced by pieces of the right and/or left boundaries of the jet. The fractal dimension increased by 2 to 3 % applying such corrections on the jet images for various chamber pressures. For ease of analysis, however, we determine the fractal dimension of jet images with the two upper and lower smooth lines and uniformly apply a 2.5% increase to all final values as a first-degree correction. The selection of the pixel intensity threshold for jet boundary determination is an important factor. For this reason, at each tested chamber pressure the fractal dimensions of the jets are calculated for a wide range of threshold levels and the results are plotted. A maximum excursion of up to 10% is observed at high pressures as the threshold is varied. In most cases, one can detect a plateau region in which a threshold value can be selected. If not, a value at the center of the explored threshold range is chosen. As a cross check, the boundary generated at the chosen threshold is visually overlaid and inspected to follow the original gray scale image as close as is discernable. Figure 2 shows a log-log plot of the number of boxes counted versus the box size for a selected jet at high pressure and for five different threshold levels. On the thresholded images one observes many vein-like structures that are not part of the closed-loop jet boundary but attached to it. These are removed by an appropriately selected sequence of erosion/dilation image processing cycles. Special treatment is also required for images at low pressures (i.e. the subcritical regime). The boundary of the jet is determined such that all isolated and single-pixel touching ligaments and drops are excluded. This is achieved by application of series of erosion and dilation steps as described in *Russ[13]*.

In the past ten years a number of applications of fractal analysis have been demonstrated in different disciplines. For example, *Sreenivasan and Meneveau [18]* computed the box-counting and Minkowski fractal dimension of the turbulent boundary of a smoke-tagged turbulent gas jet visualized across its diameter using a laser sheet, where the laser sheet thickness was smaller or comparable to Kolmogorov scale to minimize "fuzzing" due to the finite thickness of the sheet. *Sreenivasan [19]* summarized the results and reported fractal dimensions of 1.35, 1.34, and 1.38 for a round gaseous jet, a plane gaseous mixing layer, and a boundary layer flow, respectively, using two-dimensional digital imaging from LIF visualizations. At atmospheric pressure, *Shavit and Chigier [20]* established a relationship between the peak of the fractal dimension calculated at different streamwise directions and the breakup point as well as the intact length of a jet (or spray) produced by a coaxial air-assist injector. They report the peak-value dimension to range from 1.12 to 1.32 as the air speed is increased from 30 to 90 m/s. It is also interesting to mention that *Mantzaras et al [21],* who measured the Minkowski dimension of flames in spark-ignited engines, and *North and Santavicca [22],* who measured the Minkowski dimension of atmospheric pressure premixed flames, both report a progressive increase in the fractal dimension from 1.05 to 1.36 as the turbulence level is increased. This indicates a progressive wrinkling and space-filling of the flame front by turbulence. Finally, modeling turbulent flames using fractal concepts is discussed in *Gouldin [23]* and *Gouldin et al. [24]*.

Fractal dimension measurements of the nitrogen jet images are plotted as a function of the reduced pressure (chamber pressure divided by the critical pressure of nitrogen) in Fig. 3. Separate curves are shown for the BOX32, BOX64, and EDM methods, and a fourth curve plots the average of all three. The value of the fractal dimension at each pressure is the average of 18 to 20 images. The BOX64 method produces systematically higher measurements than the other two, which is believed to be due to contributions beyond the 32x32 grid size. Considering the better accuracy of the EDM method and its closeness to the BOX32 results, the latter two methods are considered to produce more representative measurements of the fractal dimension. Also plotted in Fig. 3 are fractal dimensions measured by other researchers of liquid sprays and gaseous jets, mixing layers, and boundary layers. The measurements reported for *Dimotakis et al. [25]* and *Taylor and Hoyt [27]* are our measurements made from scanned images of pictures contained in those references.

The general trend of all the curves in Fig. 3 is that the fractal dimension increases as the chamber pressure increases. At low pressures, the trend of the curves is towards the Euclidian value of 1 for a smooth circular cylinder with no surface irregularities. The magnitude of the measurements at the lowest pressures where the jets are subcritical is consistent with the fractal dimension of a 2nd wind-induced spray measured from the scanned images of *Taylor and Hoyt [27]*. As pressure increases, a dip in the curves occurs at a reduced pressure of about 0.9, due to a transition out of the 2nd wind-induced atomization regime. At the highest pressures where the jets are supercritical, the magnitude of the fractal dimension becomes consistent with the fractal dimensions of gaseous jets and layers.

These results support the hypothesis that subcritical jets exhibit mainly spray-like behavior, while supercritical jets exhibit mainly gas-like behavior. Earlier support for this hypothesis included qualitative observations of the jet appearance and the quantitative spreading rate measurements of *Chehroudi, et. al. [8]*. The present fractal dimension measurements constitute the second quantitative respect and the third overall respect in which the hypothesis is true.

Summary and Conclusions

The fractal dimensions of round turbulent cryogenic nitrogen jets have for the first time been measured at various pressures ranging from subcritical to supercritical. The jets were injected at an initially subcritical temperature into room temperature gaseous nitrogen. A comparison of the box-counting and EDM methods of measuring the fractal dimension revealed the same trends as a function of pressure in all cases, and close quantitative agreement when the box-counting scale is suitably small. At subcritical pressures, the fractal dimension is consistent with a conventional spray in the 2nd wind-induced atomization regime. The fractal dimension tends to increase as pressure increases, until at supercritical pressures the fractal dimension is consistent with those of gaseous jets and layers. These results constitute further quantitative evidence that subcritical jets exhibit mainly spray-like behavior, and supercritical jets exhibit mainly gas-like behavior.

REFERENCES

1. Mayer, W., Schik, A., Schwitzer, C., and Schaffler, M. "Injection and mixing processes in high pressure LOX/GH2 rocket combustors," AIAA Paper no. 96-2620, Lake Buena Vista, Florida, 1996.
2. Mayer, W., Ivancic, A., Schik, A., and Hornung, U. "Propellant atomization in LOX/GH2 rocket combustors," AIAA Paper no. 98-3685, Cleveland, Ohio, 1998.
3. Chen, L.-D. and Sui, P.-C. "Atomization during the injection of supercritical fluid into high pressure environment," in *Mechanics and Combustion of Droplets in Sprays* by Chiu and Chigier.
4. Woodward , R. D. and Talley, D. G. "Raman imaging of transcritical cryogenic propellants," AIAA Paper 96-0468, Reno, Nevada, January 1996.
5. Harstad, K and Bellan, J. "Isolated fluid oxygen drop behavior in fluid hydrogen at rocket chamber pressures," International Journal of Heat and Mass transfer 41, pp. 3537-3550, 1998.
6. Delplanque J. P. and Sirignano W. A. "Boundary layer stripping effects on droplet transcritical convective vaporization," Atomization and Sprays, 4:325-349, 1994.
7. Oefelein, J. C. and Yang V. "Modeling high-pressure mixing and combustion processes in liquid rocket engines," J. Propulsion & Power, Vol. 14, no. 5, September-October, 1998.
8. Chehroudi, B., Talley, D., and Coy, E. "Visual characteristics and initial growth rates of round cryogenic jets at subcritical and supercritical pressures," Physics of Fluids, Vol. 14, No. 2, February, 2002.
9. Chehroudi, B., Talley, D., and Coy, E. "Fractal geometry and growth rate of cryogenic jets near critical point," AIAA Paper 99-2489, 35th AIAA/ASME/SAE/ASEE Joint Propulsion Conference, Los Angeles, CA, June 20-24, 1999.
10. Chehroudi, B., Cohn, R., Talley, D. and A. Badakhshan. "Raman scattering measurements in the initial region of sub- and supercritical jets," AIAA Paper 99-2489, 36th AIAA/ASME/SAE/ASEE Joint Propulsion Conference, Huntsville, AL, July 17-19, 2000.
11. Mandelbrot, B. B. "The Fractal Geometry of Nature," W. H. Freeman and Company, San Francisco, 1983.
12. Peitgen, H-O, Hartmut, J., Dietmar, S. "Fractals for the Classroom, Part one Introduction to Fractals and Chaos," Springer-Verlag New York Inc., New York, 1992.
13. Russ, J. C. "The image processing handbook: 2nd edition," Boca Raton, FL, CRC Press, Inc. ,P. 674, 1995.
14. Russ, J. C. "Fractal Surfaces," New York: Plenum Press, 1998.

15. Kaye, B H. "Image analysis techniques characterizing fractal structures from the fractal approach to heterogeneous chemistry," (D. Avnir, editor). John Wiley & Sons , 1989.
16. Hall, M. J., Dai, W., and Matthews, R. D. "Fractal analysis of turbulent premixed flame images from SI engines," International Fuel and Lubricants Meeting and Exposition, San Francisco, California, SAE Technical paper 922242, October 19-22, 1992.
17. Russ J. C. and Russ, J. C. "Uses of Euclidean Distance Map for the measurement of features in images," Journal of computer assisted microscopy, Vol.1, no. 4, pp. 343-375, 1989.
18. Sreenivasan, K. R. and Meneveau, C. "The fractal facets of turbulence," J. Fluid Mech. Vol. 173, pp. 357-386, 1986.
19. Sreenivasan, K. R. "Fractals and multifractals in fluid turbulence," Annu. Rev. Fluid Mech, Vol. 23 pp. 539-600, 1991.
20. Shavit, U. and Chigier, N. "Fractal dimensions of liquid jet interface under breakup," Atomization and Sprays, vol. 5, pp. 525-543, 1995.
21. Mantzaras, J., Felton, P. G., and Bracco, F. V. "Fractals and turbulent premixed engine flames," Combustion and Flames, vol. 77, pp. 295-310, 1989.
22. North, G. L. and Santavicca, D. A. "The fractal nature of premixed turbulent flames," Combust. Sci. and Tech., vol. 72, pp. 215-232, 1990.
23. Gouldin, F. C. "An application of fractals to modeling premixed turbulent flames," Combustion and Flames, vol. 68, pp. 249-266, 1987.
24. Gouldin F. C., Hilton, S. M., and Lamb, T. "Experimental evaluation of the fractal geometry of flamelets," Twenty-second Symposium (International) on Combustion/ The combustion Institute, pp. 541-550, 1988.
25. Dimotakis, P. E., Miake-Lye, W. G., and Papantoniou, D. A. "Structure and dynamics of round turbulent jets," Physics of Fluids, 26, no. 11, p. 3185-92.
26. Chehroudi, B., Talley, D., and Coy, E. "Behavior of a round cryogenic jet at below and above the critical pressure." The Tenth Annual Propulsion Symposium, Propulsion Engineering Research Center (PERC) at Penn State, NASA Marshall Space Flight Center, Huntsville, Alabama, October 26-27, 1999.
27. Taylor, J. J. and Hoyt, J. W. "Water jet photography-techniques and methods," Exp. Fluids, Vol. 1, pp. 113-120, 1983.

ACKNOWLEDGEMENT

The authors would like to thank and appreciate the assistance of Mr. Paul Loftsgard in running the fractal analysis program on the jet images.

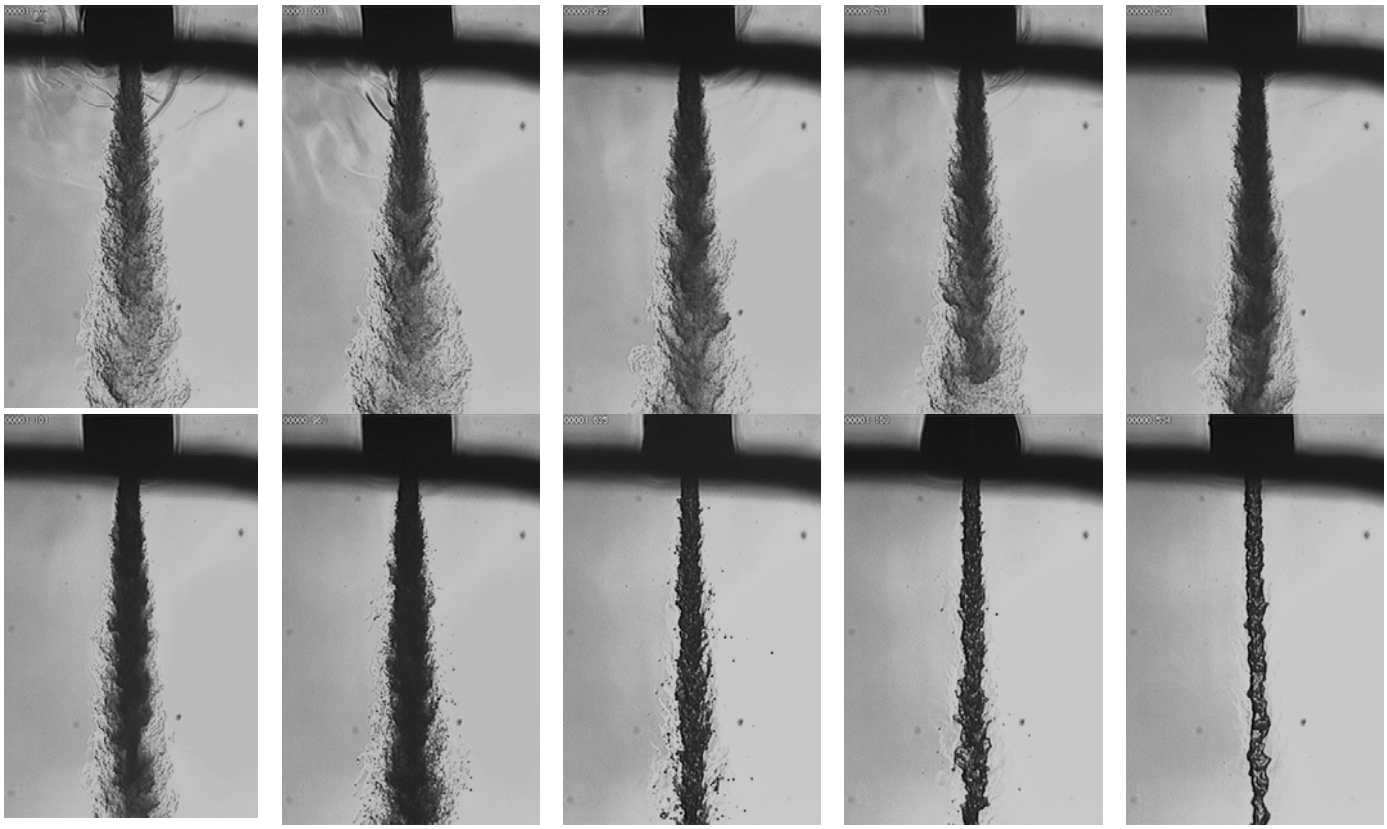

Figure 1. Back-illuminated images of cryogenic nitrogen injected into ambient nitrogen at a fixed supercritical temperature of 300 K but varying sub- to supercritical pressures ($P_{critical}$ = 3.39 MPa; T_c = 126.2 K). Reduced pressure, P_r = $P_{ch}/P_{critical}$= 0.23, 0.43, 0.83, 1.03, 1.22, 1.62, 2.03, 2.44, 2.74; from lower right to upper left. Reynolds number= 25,000 to 75,000. Injection velocity: 10-15 m/s. Froud number: 40,000 to 110,000. Injectant temperature: 99 to 120 K.

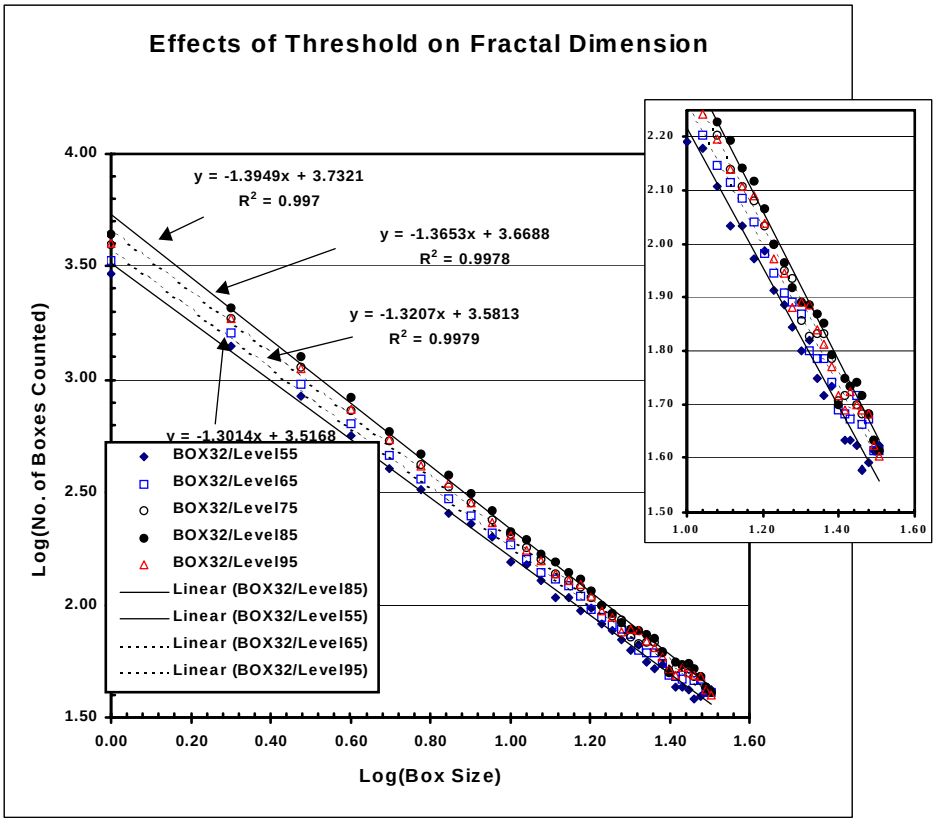

Figure 2. Log-log plot of the number of boxes counted as a function of the box size for four different thresholded binary images of the same original high-chamber-pressure gray-scale jet image indicating effects of the threshold level on the fractal dimension. The slope of the least square fit line is the negative of the box-counting dimension. R^2 is the correlation coefficient of the linear fits.

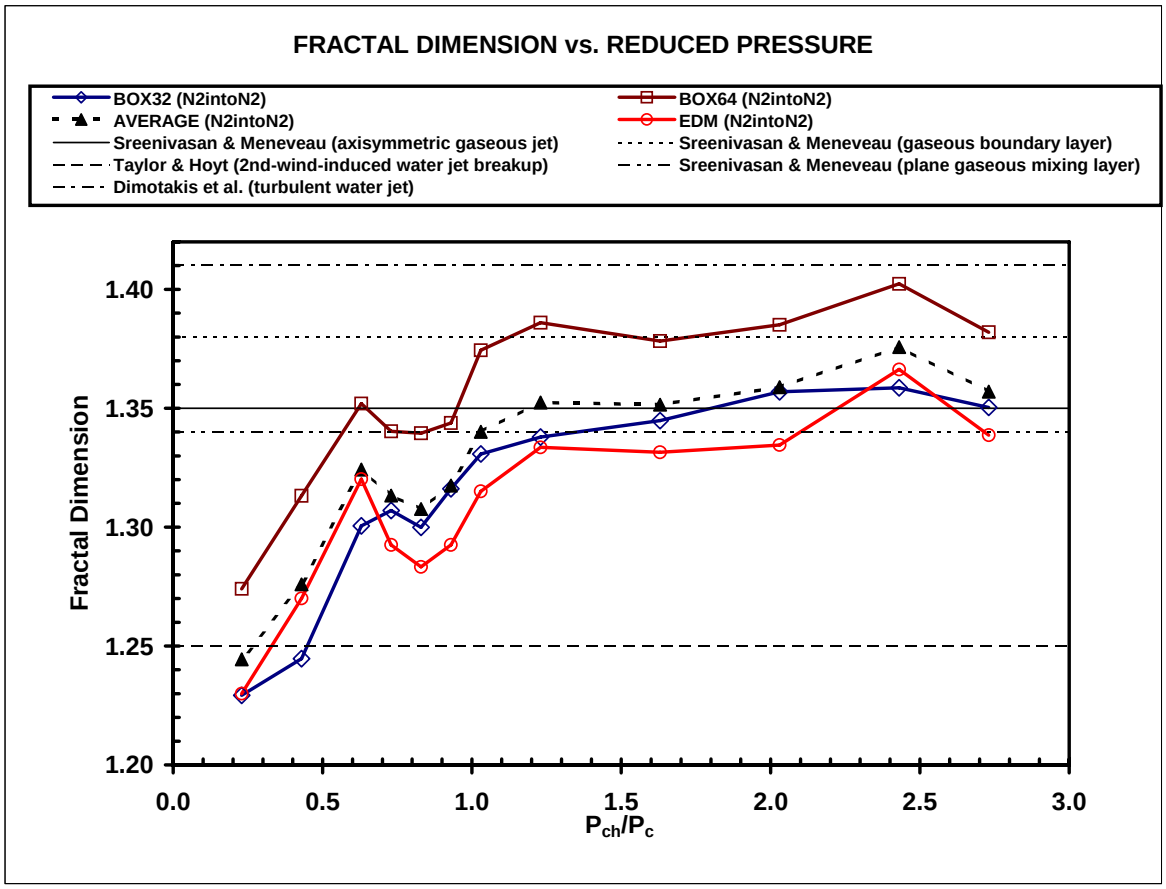

Figure 3. Box-counting and Minkowski (EDM algorithm) fractal dimensions of the visual boundary of the jet as a function of the reduced chamber pressure for N_2-into-N_2 injection. AVERAGE (N2 into N2) is the average of the three shown fractal dimension measurements.

APPENDIX L

"Visual Characteristics and Initial Growth Rates of Round Cryogenic Jets at Subcritical and Supercritical Pressures"

Visual Characteristics and Initial Growth Rates of Round Cryogenic Jets at Subcritical and Supercritical Pressures

***B. Chehroudi*[*], *D. Talley*[†], *and E. Coy*[†]**

*Engineering Research Corporation
AFRL/PRSA
10 E. Saturn Boulevard
Edwards AFB, CA 93524-7680
(corresponding author)

[†]Air Force Research Laboratory
AFRL/PRSA
10 E. Saturn Boulevard
Edwards AFB, CA 93524-7680
661-275-6175

Submitted to

Physics of Fluids
Editorial Office
Department of Chemical Engineering
University of California
Santa Barbara, CA 93106
805-893-3200
pof@engineering.ecsb.edu

Short Abstract

The visual characteristics and initial growth rates of round cryogenic jets injected into subcritical and supercritical pressures were studied. It is found that the jet exhibits liquid-like and gas-like characteristics at subcritical and supercritical pressures, respectively. Explanations are offered. The jet spreading angle at supercritical pressures has been demonstrated to agree quantitatively with the theoretical spreading angle derived for incompressible but variable density turbulent gas jets, the first time more than a qualitative visual similarity with gas jets has ever been demonstrated. In addition, the present measurements of spreading rates have been plotted along with other measurements for subsonic incompressible constant density and variable density jets, liquid sprays, supersonic jets, and other mixing layers in a plot spanning four orders of magnitude in gas-to-liquid density ratio. This is the first time these results have been consolidated in a single plot over such a large range of density ratio.

Abstract

Cryogenic liquids initially at a subcritical temperature were injected through a round tube into an environment at a supercritical temperature, at various pressures ranging from subcritical to supercritical pressures. Pure N_2 and O_2 were injected into environments composed of N_2, He, Ar, and various mixtures of $CO+N_2$. The results were photographically observed and documented near the exit region using a CCD camera illuminated by a short duration back-lit strobe light. At low subcritical chamber pressures, the jets showed surface irregularities that amplified downstream, exhibiting intact, shiny, but wavy (sinuous) surface features which eventually broke up into irregularly-shaped small entities. A further increase of chamber pressure at constant jet initial and ambient temperatures caused the formation of many small droplets to be ejected from the surface of the jet, similar to what is observed in the second wind-induced jet breakup regime. As the chamber pressure was further increased, the transition to a full atomization regime was inhibited near but slightly below the critical pressure. The jet structure at this point changed and began to resemble a turbulent gas jet with no detectable droplets. The reason was attributed to the reduction of the surface tension and enthalpy of vaporization as the critical pressure is approached. The initial divergence angle of the jet was measured at the jet exit and compared with the divergence angle of a large number of other mixing layer flows, including atomizing sprays, turbulent incompressible jets, supersonic jets, and incompressible but variable density jets. The divergence angle for all these cases was plotted over four orders of magnitude in the gas-to-liquid density ratio, the first time such a plot has been reported over this large a range of density ratios. At and above the critical pressure, the jet growth rate measurements agreed quantitatively with theory for incompressible but variable density gas mixing layers. This is the first time a quantitative parameter has been used to demonstrate that the similarity between the two flows extends beyond mere qualitative physical appearance. Finally, as the pressure is reduced to progressively more subcritical values, the spreading rate approaches that measured by others for liquid sprays.

Introduction

In rockets, gas turbines, and diesel engines, liquids are injected into a high temperature and pressure combustion chamber to react. In chemical rocket engines, either the fuel or oxidizer or both may initially be liquids, while for gas turbines and diesel engines, typically only the fuel is initially liquid. Simple thermodynamic analysis of the rocket thrust chamber (combustion chamber plus the expansion nozzle) shows that higher chamber pressures lead to a higher specific impulse for the engine, motivating a trend towards higher chamber pressures. A similar trend is also true for diesel and gas turbine engines to increase power and efficiency. At high enough pressures, the injected liquid may find itself near or above the thermodynamic critical pressure. For example, the liquid H_2/liquid O_2 Space Shuttle Main Engine combustion chamber pressure is about 22.3 MPa, while the combustion chamber pressure for the Vulcain engine (used on the Ariane 5) with the same propellants can reach up to a record value of 28.2 MPa. In comparison, the critical pressure and temperature pairs for N_2, O_2, and H_2 in (K, MPa) units

are (126.2, 3.4), (154.6, 5.04), and (32.94, 1.28), respectively. Very little information is available in the fluid physics literature on liquid jets injected into a supercritical environment, especially when the jets are cryogenic liquids. This motivated initiating an organized and systematic experimental investigation of initially liquid jets injected at sub- and supercritical pressures.

There are drastic changes in some important equilibrium properties of a pure substance as it approaches the thermodynamic critical point (CP). For example, under thermodynamic equilibrium condition, the sharp distinction between liquid and gas phases disappears at and above the critical pressure, and the substance is more properly considered to be a fluid whose density can vary widely but continuously as temperature is changed at fixed pressure. Density changes can become particularly large near the critical point. Other properties that vary widely near the critical point are the thermal conductivity and mass diffusivity. In addition, the constant-pressure specific heat becomes very large and surface tension vanishes. Finally, the solubility of gases into the liquid phase becomes significant as the ambient pressure is raised, making it necessary to consider multicomponent phase equilibrium or nonequilibrium.[1] For mixtures, the determination of critical conditions, called the "critical mixing temperature or pressure" (critical lines for a two-component mixture as opposed to a critical point for a pure substance), can be complex.[2] For example, for a pure hydrocarbon drop in a nitrogen environment, the amount of nitrogen dissolved on the surface of the liquid drop increases with pressure. [3] As a result, the critical mixing temperature of the layer decreases.[4] This forms a layer which is a mixture of nitrogen and fuel that spreads spatially in time. In what follows, unless otherwise made clear, the terms subcritical and supercritical, and the reduced pressure and temperature, will refer to the critical condition of the pure substance used in the drops or jets and not that of the mixture.

There are only a few studies of liquid injection into supercritical conditions.[5-9] *Newman and Brzustowski*[5] studied steady CO_2 jets injected into a chamber of pure N_2 and also mixtures of CO_2+N_2 at both sub- and supercritical pressures and temperatures. They explained the effects of increased chamber temperature on the jet appearance to be due to the progressive reduction in ambient gas density, the reduction in surface tension to zero at the critical temperature, and the increase in liquid CO_2 evaporation. Based on coarse photographs, they proposed the possibility of jet gasification, namely that at supercritical temperatures and pressures the jet could be treated as a variable density single phase turbulent submerged gas jet. *Mayer, et al.*,[6] studied liquid cryogenic N_2 (LN_2) jets at a fixed temperature of 105 K injected into a N_2 environment at 300 K, but at varying ambient sub- to supercritical pressures, and observed drastic changes in the jet structure near and above the critical pressure. They attributed this behavior to a continual decline of surface tension until it vanished at and above the critical pressure. They also studied the coaxial injection of LN_2 (at 97 K) inside gaseous He (at 280 K), as simulant fluids for H_2 and O_2, the coaxial configuration being similar to ones used in cryogenic rocket engines. As before, changes in the jet structure as pressure increases were clearly observed, and attributed to increases in the solubility of He into N_2 and reductions in the surface tension. Finally, they studied H_2 / O_2 combustion in a windowed model rocket combustion chamber, and again observed structural changes in the jet with pressure in both the ignition and steady state combustion phases. No evidence of droplets was observed at supercritical conditions. *Woodward and Talley*[9] studied the injection of LN_2 jets into gaseous N_2 and gaseous mixtures of N_2 and He at much lower Reynolds numbers than the above studies. For N_2/N_2 systems, observation of the resulting fluid structures at and above the critical pressure showed strong evidence that surface tension becomes negligibly small either at the instant of mass injection or very rapidly thereafter. Adding gaseous He (~20 wt%), however, was found to produce structures which again showed strong evidence of having surface tension at pressures up to twice the critical pressure of pure N_2, demonstrating the strong effect of composition on the critical mixing properties.

While previous studies have provided valuable insight into the structural changes of jets as a function of sub- to supercritical ambient pressures, the observations have to date been largely qualitative. The objective of the present study was to characterize the fluid mechanical changes qualitatively and offer a more quantitative approach than before. The quantitative parameter chosen was the spreading rate of the mixing layer in the near field region. This is believed to be the first time the effect of the critical condition on this parameter has been systematically studied. The paper continues with a description of the experimental arrangement, presentation of the results and their discussions, and ends with a summary and conclusion.

Experimental setup

Experiments were conducted in the stainless steel chamber shown in Fig. 1. The chamber can withstand pressures to 137 atm (2000 psi) and temperatures to 473 K. The front and back of the chamber contain 133.4 mm (5.25") diameter circular sapphire windows oriented parallel to each other. The size of the windows and their proximity to the injection axis were chosen so that the system f/# was limited by the size of the collection optics rather than the size of the windows, even when the collection optics are traversed across the entire field of flow. Each side of the vessel contains 120.7 mm x 12.7 mm (4.75" x 0.50") oblong UV-grade quartz windows. These windows were designed to admit laser sheets for laser diagnostics of the flow. However, these windows were not used in the present study.

Injectants were supplied initially in the gas phase and regulated by a conventional mass flow meter and precision micrometer valve. Prior to injection, the injectants were cooled and/or liquified by a cryogenic cooler which is integral to the pressure vessel. Liquid N_2 from a dewar was used as the coolant. Gaseous N_2 was designed to be the primary ambient chamber medium. However, other gases or mixtures of gases can be introduced through a branch line. For more details, refer to *Woodward and Talley*[9] and *Chehroudi, et al.* [10] The injection in this study was through a sharp-edged 50 mm long stainless steel tube with a 1.59 mm (1/16") outer diameter and a 254 micron (0.010") inner diameter (inner length-to-diameter ratio of 200). With Reynolds numbers ranging from 25,000 to 70,000, an entrance length of 50 to 100 diameter was needed to produce fully developed turbulent pipe flow at the exit.[11] The rig was fully instrumented with thermocouples, pressure gages and transducers, and mass flowmeters at the locations indicated in Fig. 1. Back-illumination with diffuse light flashes (0.8 micro-second duration) and a model K2 Infinity long distance microscope was used with a TM-745E high resolution (768(H) x 493(V) pixels in 8.8(H)x6.6(V) mm actual sensing area) interlaced CCD camera by PULNix to form images of the injected jets. With this setup, objects of 30 +/- 7 microns and larger can be resolved. The exit LN_2 temperature at the tip of the small injector for this study was measured to vary from 90 to 110 K. This was due to changes in injected N_2 specific heat and density as chamber pressure was varied. In this work, the tip temperature is used for calculations of the other jet property values. For more details, refer to *Chehroudi, et al.*[10]

Results and Discussion

Jet visual structure

Froude number values were calculated at each chamber pressure to examine the importance of buoyancy forces within the distances investigated in this study. This number ranges from 42,000 to 110,000. The length scale of *Chen and Rodi*[12] is given by $x_b = Fr^{-1/2}(\rho/\rho_\infty)^{-1/4}(x/d)$, where x is the axial distance, d is the initial jet diameter, ρ and ρ_∞ are the jet

and ambient densities, respectively, $Fr \equiv \rho U^2 / gd\left|\rho_\infty - \rho\right|$ is the Froude number, where U is the velocity difference and g is the gravitational acceleration, and where x_b is a constant. *Chen and Rodi*[12] suggested that the flow is momentum dominated for $x_b < 0.53$, while *Papanicolaou and List*[13] suggested $x_b < 1$. Considering the more conservative estimate by *Chen and Rodi*[12], the jet used here is momentum dominated for distances less than 30 to 40 mm from the injector exit. Pictures presented here cover up to about 5.5 mm (axial distance/diameter ratio of 21.6) from the injector and hence buoyancy effects can be ignored in favor of the inertial forces.

Figure 2 shows images of a cold (90–110 K) N_2 jet injected into warm N_2 at a fixed supercritical chamber temperature (300 K) but at various pressures ranging above and below the critical pressure. Objects of 30 +/- 7 microns and larger can be resolved in these images. The reduced pressures $P_r = P_{chamber} / P_{critical}$ shown are given with respect to the critical pressure of pure nitrogen. The images show a demarcation of regions where changes in index of refraction occur due to density variations. At the lowest subcritical chamber pressure in Fig. 2, P_r=0.23, the jet is liquid-like with surface instabilities that grow downstream, where it has twisted appearance. At P_r=0.43, all instabilities are further amplified, until at P_r=0.63, many surface ligaments and drops are seen to be ejected from the jet. At P_r=0.83, very fine drops are seen surrounding the jet and its spanwise dimension noticeably grows away from the injector exit plane (*i.e.*, the jet diverges). At P_r=1.03 the N_2 jet enters into a supercritical temperature and pressure environment. There are drastic changes in the details of the interface. There are no detectable drops under this condition with the highest software magnification used to view these high resolution images. There are thread- or finger-like entities which emerge from the jet but are not broken up into droplets as before. They seemingly are dissolved at a spectrum of distances from the dark core. This, in a sense, forms a mixing layer in which phase transition and/or large local density nonuniformities occur. Any further increase of the chamber pressure decreases the length and the thickness of the internal dark core, and images progressively resemble the injection of a gaseous turbulent jet into a gaseous environment.

Figure 3 shows selected images from Fig. 2 under additional magnification. The images are chosen to represent typical mixing layer regimes at subcritical, transitional, and supercritical pressures. At subcritical pressures, the gas-to-liquid density ratio is reasonably low, and jet behavior corresponds more or less to classical liquid atomization theory. The left hand picture in Fig. 3 corresponds roughly to the second wind-induced jet breakup regime (see further discussion below). At higher pressures, near the critical pressure, the jet enters into a transitional regime where coherent comb-like dense structures are dissipated into the surroundings about as fast as they can be ejected by turbulence from the jet. Droplets are no longer observed to form and these comb-like structures remain at the interface. As the pressure increases further above the critical pressure, the density ratio becomes increasingly larger, causing the aforementioned dense structures to disappear. The mixing layer increasingly resembles that of a classical gas/gas turbulent mixing layer. An examination of a large number of images at high magnification revealed no evidence of any droplet formation in this gas/gas regime. These observations are consistent with the observations of *Mayer, et al.*[6] and *Newman and Brzustowski.*[5]

It is worthwhile to compare the images in Figs. 2 and 3 to the classical liquid jet breakup regimes. Classical liquid jet breakup refers here to the condition at fixed gas-to-liquid density ratios having a fairly small magnitude (~0.002). For a narrow range of density ratio, atomization and breakup regimes of liquid jets can be mapped onto plots of Ohnesorge number $Oh = \mu_l/(\rho_l \sigma d)^{1/2}$ versus Reynolds number $Re = \rho_l U d/\mu_l$, where U is liquid exit velocity , d is the nozzle diameter, and ρ_l, σ, and μ_l are the liquid density, surface tension, and viscosity, respectively. On a Oh-versus-Re plot and at both fixed fluid properties and exit nozzle

diameter (i.e. fixed Ohnesorge number), increasing the exit velocity causes a horizontal path to be traced from left to right of this plot as the Reynolds number increases. According to *Reitz and Bracco*,[14] at small gas-to-liquid density ratios, different liquid jet breakup regimes are observed along this horizontal path as the Reynolds number increases. One moves from the Rayleigh liquid jet breakup regime, to the first and second wind-induced breakup, and finally to the full liquid atomization or simply atomization regime. Rayleigh breakup is characterized by the growth of axisymmetric oscillations of the jet interface, induced by the surface tension. Drops with diameters larger than the jet diameter are produced in this regime. In the second wind-induced regime, drops are generated by the growth of short-wavelength surface waves on the jet surface due to the relative motion of the jet with respect to the environment. This unstable growth is opposed by the surface tension. Breakup happens at a distance of multiple diameters, and drops with average diameters less than the jet diameter are produced. In the atomization regime, the jet is completely broken up at the nozzle exit and average drop diameters of much less than jet diameter are observed. For the range of Reynolds number applicable here (25,000 to 75,000), calculations show that the jet in Fig. 2 should start in the first and/or second wind-induced zone and quickly pass the atomization regime as chamber pressure is raised from the lowest value shown in Fig. 2. In Fig. 2, first or second wind-induced tendencies can be observed at the lowest two chamber pressures, and second wind-induced features are clearly observed at the next two higher pressures. However, it seems that before assuming a full atomization character, the jet begins to take on the appearance of a gas jet. This departure from the classical behavior can be attributed to two factors. First, as the chamber pressure increases and approaches the critical pressure, surface tension is reduced to a near-zero value, and the Ohnesorge number sharply swings from a low (estimated to be $2.8\text{x}10^{-3}$) to a very large (infinity when surface tension is zero) value. The large Ohnesorge number regime and its importance are discussed by *Faeth*[15] and *Tseng, et al.*,[16] who find that even for small density ratios, Ohnesorge numbers larger than about 2 or 3 have a stabilizing influence. However, the other factor is that the gas-to-liquid density ratio also increases as pressure is raised in Fig. 2. Thus the classical liquid breakup regime plots which are for a narrow range of density ratios has limitations. The density ratio in Fig. 2 eventually exceeds 0.1, a value approaching what might be expected in gas/gas jets. This, coupled with the reduction in surface tension, provides an intuitively appealing explanation for why the liquid atomization regime is suppressed in favor of a more gas/gas jet-like appearance.

The possible transition to atomization regime is also tested by another criterion of *Reitz and Bracco*[14] in which chamber-to-injectant density ratio, nozzle geometrical factor, and Weber and Reynolds numbers are all included. For a class of single-hole atomizers with a wide range of length-to-diameter ratios the atomization criteria are as follows. $\text{Criterion (a), if } (\rho_l/\rho_g)(\text{Re}/\text{We})^2 \geq 1 \text{ then } (\rho_l/\rho_g)^{0.5} \leq k, \text{ where } k = 18.3/\sqrt{A} \text{ and } A = 3.0 + (L/d)/3.6.$ And, criterion $\text{(b), if } (\rho_l/\rho_g)(\text{Re}/\text{We})^2 \to 0 \text{ then } ((\rho_l/\rho_g)(\text{We}/\text{Re}))^{0.33} \leq k.$ Here, We $=\rho_l U^2 d/\sigma$ is Weber number with σ representing the surface tension and the parameter k shows effects of nozzle geometry in terms of different hole length-to-diameter (L/d) ratios. The condition $(\rho_l/\rho_g)(\text{Re}/\text{We})^2 \geq 1$ is valid from the lowest chamber pressure tested here to just below the critical pressure. Increasing the chamber pressure, the $(\rho_l/\rho_g)(\text{Re}/\text{We})^2$ parameter changes from about 2180 to 3.35 just below the critical pressure. In our application, k is calculated to be 2.39 and $(\rho_l/\rho_g)^{0.5}$ ranges from 9.33 at the lowest chamber pressure to 3.67 just below the critical point. Therefore, it is clear that the atomization criterion (a), that is $(\rho_l/\rho_g)^{0.5} \leq k$, is not satisfied. Approaching the critical pressure, and as the surface tension diminishes, one calculates a sharp drop in the $(\rho_l/\rho_g)(\text{Re}/\text{We})^2$ parameter to very low values (~ $6.32\text{x}10^{-11}$). Hence one should

consider the (b) criterion instead. The $((\rho_l/\rho_g)(We/Re))^{0.33}$ parameter approaches large values ($\sim 1.66 \times 10^2$) and with k parameter remaining unchanged the atomization criterion (b) also fails. Therefore, within the limitations of these criteria discussed by *Reitz and Bracco*[14], no full atomization is allowed and agreeably not visually observed.

The suppression of the full atomization regime can also be physically understood by means of approximate characteristic time estimates. *Tseng, et al.*[16] describe the initial turbulent breakup scenario of an intact liquid jet by the formation of a drop from a turbulent eddy with a characteristic dimension of L and a cross-stream velocity and v_l, respectively, in the form of a bulge from the surface of the jet. A characteristic time for the separation of this bulge from the jet to form a drop is proposed to be proportional to $(\rho_l L^3/\sigma)^{1/2}$. On the other hand, the characteristic vaporization time of an isolated liquid drop can be crudely estimated by assuming that drops obey the "D-square" law. This characteristic time is proportional to D^2/K, where D is the initial diameter, and K is the vaporization constant $K=(8k_g/(\rho_l C_{pg}))\ln(B+1)$, where $B=C_{pg}(T_{oo} - T_{boil})/h_{fg}$. Here, T_{oo} and T_{boil} are the chamber gas temperature at a large distance from the drop and the boiling temperature of the liquid, k_g and C_{pg} are the thermal conductivity and constant-pressure specific heat of the environment, and ρ_l and h_{fg} are the density of the liquid drop and latent heat of vaporization. The value of these crude estimates is revealing the trends as σ and h_{fg} approach zero when the chamber pressure reaches the critical point. The trends are that the characteristic drop formation time becomes very large, whereas the characteristic evaporation time becomes very small. Therefore, it takes a progressively longer time for the bulges on the jet boundary to turn into isolated drops as pressure increases, and when/if they do, they are gasified increasingly faster as the critical pressure is approached. In the limit, although irregularly-shaped bulges are formed on the jet, they dissipate before having a chance to separate into isolated entities.

In summary, for the N_2 into N_2 injection at a supercritical ambient temperature but sub- to supercritical pressures, there appears to be two structural transitions. One is when the intact jet with irregularly-looking surface waves (which exhibits features similar to the first wind-induced atomization) transforms into a diverging jet with ligaments and many small droplets, indicative of the second wind-induced atomization regime. The other is when the latter structure changes, not into the full atomization, but into a gas/gas jet appearance slightly below the critical pressure. The reason for the latter is due to the progressive reduction of surface tension and the enthalpy of vaporization approaching zero.

Similar observations were made for cryogenic O_2 injected into warm gaseous N_2. It was observed that similar transition characteristics occurred, but at a pressure closer to the critical pressure of oxygen.

Jet growth rate

The nature of the growth rate of jets and mixing layers is usually assessed through measurements of the visual spreading angle. Because our angle measurements are very close to the injector exit plane (distance-to-diameter of up to 21.6), attempt is made to only examine those for gaseous and liquid jets/mixing layers that are within a comparable zone. Comparison with mixing layer data is justified because our measurements are within the initial mixing layer of the jet and do not extend far beyond the length of the potential core (for single-phase gaseous or liquid jets) and the intact core (for two-phase liquid sprays). To substantiate this, we note that according to *Abramovich*[17] the length of the potential core in isothermal uniform-density axisymmetric two-dimensional jets are about 6 to 10 injector diameters, whereas for nonisothermal cold jets injected into hot

environments, it can reach up to about 25 injector diameters, depending on the jet temperature. Comparison with liquid spray's intact core is also justified because, first, the state of the injectant at the exit is liquid, and second, as seen earlier the jet appears to undergo pre-atomization stages such as first- and second- wind-induced breakup regimes. According to *Chehroudi, et al.*,[18] the intact core of liquid sprays, similar to the ones used in diesel engines, is given by $Cd(\rho_l/\rho_g)^{1/2}$, in which ρ_l and ρ_g are liquid injectant and chamber gas densities, respectively, d is the effective jet exit diameter, and C is a constant between 3.3 to 11. This implies an intact core length of between 33 to 110 injector diameters for a chamber-to-injectant density ratio of 0.01, and 16.5 to 55 diameters for a density ratio of 0.04. As will be discussed further below, the density ratio range of 0.01 to 0.04 corresponds to the observed spray-like behavior of the jet. Thus our spreading rate data measured to within a 5.5 mm distance from the injector exit face (length-to-diameter of 21.6) corresponds to the mixing layer region surrounding the potential core or intact core of the single- and two-phase jets.

The "initial" spread angle was measured using Image-ProPlus, the image processing program by Media Cybernetics. After enhancing the images, lines anchored at the injector exit are drawn to go through the averaged outer boundary of the jet, one on each side, and the angle is then calculated by the program. For each condition, 20 images are used to form an averaged image from which angle measurements are made. Two angles are measured. The angle determined by the outermost observable extent of the jet, commonly used for growth rate determination, and the angle determined by the extent of the spreading of the dark-looking internal core referred to as dark-core angle. The dark-core angle data is not discussed here and shown only for completeness. The maximum overall uncertainty band on the angle measurements is shown for the O_2 and N_2 data in Fig. 4 as two short dashes above and below each symbol. They are visible only if the uncertainty band height is larger than the size of the symbol itself. The inverse of the above angle measurement procedure is also investigated. The angle for each image within a set of 20 (per condition) are measured individually and then averaged. No appreciable differences were observed between the two procedures (not more than 4.5% percent difference).

In the following, first, experimental measurements and theoretical treatment of the single-phase gaseous jet and mixing layer growth rate are presented. Next, similar information for the two-phase liquid sprays are reviewed. In particular, our focus is to consider cases where dissimilar fluids and/or large density differences are used. Our measured sub- and supercritical data as well as its discussion are presented lastly. In the process, a unique and comprehensive growth rate plot of all the relevant results is developed. This plot not only serves to show our conclusions regarding the supercritical jets but is also believed to provide a unique and useful template for other researchers.

(a) Single-phase gaseous experimental data

The experimental results of *Brown and Roshko*[19] in which helium and nitrogen were used in a subsonic two-dimensional incompressible turbulent gaseous mixing layer studies are of particular importance here. They measured mixing layer spreading in a two-dimensional arrangement by both shadowgraphy (called the visible jet thickness), as well as through velocity profiles extracted from the combined results of a concentration probe (*Brown and Rebollo*[20]) and a Pitot tube dynamic pressure measurements within the layer (called the vorticity thickness, as described in the Appendix). They made a distinction between mixing layers in which density changes are caused by temperature changes, by high-speed compressible (high Mach number and supersonic) flows, and by differences in molecular weights (i.e. different gases). Using forms of the turbulent continuity and momentum equations that are applicable for both the supersonic and incompressible but variable-density cases,

they show that at low Mach number squared values, there is no distinction between mixing layers made of two streams having differences in molecular weights, differences in temperature, and high speed compressibility effects. For comparison purposes, the two-dimensional turbulent "gaseous" mixing layer experimental data of *Brown and Roshko*[19] was used to infer the "initial" spreading rate for the axisymmetric jets. The results are plotted in Fig. 4. Plotting the results from this two-dimensional mixing layer study on the same plot as the axisymmetric results reported here is justified because, according to both *Brown and Roshko*[19] and *Abramovich, et al.*[21], two-dimensional mixing layers are found to be fairly well approximated by the initial mixing region of axisymmetric jets. This is why all the angle measurements in present study are made using only the information within the first 5.5 mm distance from the injector exit plane. The ambient velocity is zero in the present study (quiescent chamber), and for this case, there are only two measured visual growth rates with corresponding vorticity growth rates reported by *Brown and Roshko*[19]. All other data, including the supersonic mixing layer measurements by other researchers (but used by *Brown and Roshko* for comparison) are given as vorticity growth rates. Based on these two data points a conversion factor is calculated between the visual and vorticity growth rates. This factor is also applied to the vorticity growth rate values of other researchers collected by and reported in *Brown and Roshko*[19] for the supersonic jets.

Richards and Pitts[22] used a long sharp-edged-entrance round tube to inject momentum dominated helium, propane, and methane turbulent round jets into air. Rayleigh scattering was used to measure concentrations. Through concentration plots they define and report the half-radius jet thickness (the radius at which the concentration drops by fifty percent of its maximum centerline value). Their first two reported measurement locations, where all the gas data was taken, are at distance/diameter ratios of 20 and 30 from the injector, and are used to calculate the jet spreading angle. In comparison, the images in Fig. 2 correspond to distance/diameter ratios of up to about 21.6. Thus results from *Richards and Pitts*[22] taken at larger distances/diameter ratios can not be compared with the present results and are therefore not plotted in Fig. 4. Considering the similarity of their injector geometry to ours, the data is close enough to be considered for comparison. Based on their mass fraction plots, the full thickness of the jet is judged to be about 4 times the half-radius jet thickness value. This full thickness is taken to be the equivalent of the jet visual thickness.

*I*n a series of experiments on sub- to supersonic two-dimensional turbulent mixing layers, *Papamoschou and Roshko*[23] use Schlieren photography and Pitot probe (dynamic pressure) measurements to document the mixing layer spreading characteristics. They observe, as have others in the past, that at supersonic velocities the spreading angle decreases compared to classical turbulent incompressible mixing layers. Although compressibility definitely has an influence, the spreading angle also depends on other important parameters such as the velocity and density ratios of the two streams forming the mixing layer. Their spreading rate is determined by a linear least square fit to the "Pitot tube thickness" data at distances above 75 mm from a centerbody divider installed in their flow facility. In this work, they also discuss the relationship between the three mixing layer thicknesses, namely, δ_{vis} (visual thickness), δ_{pit} (Pitot tube thickness), and δ_{ω} (vorticity thickness). These are defined in the Appendix. They propose the following relationships between them: $\delta_{\omega} = 0.5\delta_{vis}$ and $\delta_{pit} = 1.44\delta_{\omega}$, leading to $\delta_{pit} = 0.72\delta_{vis}$. However, based on the data from *Brown and Roshko,* $\delta_{pit} = 0.90\delta_{vis}$ although $\delta_{pit} = 0.80\delta_{vis}$ was finally used, following *Konrad*[24]. Here the relationship $\delta_{\omega} = 0.5\delta_{vis}$ was used to convert the supersonic mixing layer results to visual thickness values for presentation in Fig. 4.

(b) Single-phase theoretical treatment

To separate effects of compressibility, *Papamoschou and Roshko*[23], following *Bogdanoff*[25], define a convective velocity U_c and a convective Mach number $M_c = (U-U_c)/a$, where a is the speed of sound, and $U_c = (U_1\sqrt{\rho_1} + U_2\sqrt{\rho_2})/(\sqrt{\rho_1} + \sqrt{\rho_2})$, where (ρ_1,U_1) and (ρ_2,U_2) are the density and velocity of the two streams forming the mixing layer. They find this definition of the Mach number to be more appropriate than the individual streams' Mach numbers in the mixing layer, see also *Brown and Roshko*[19]. Note the difference between this equation and the characteristic velocity of equation 5 in the Appendix. For an incompressible variable-density mixing layer, *Papamoschou and Roshko*[23] assume that the main effect of the density ratio is to determine the convective velocity of the structure. In a reference frame moving with the convection velocity, they conjecture that the growth rate is proportional to $\Delta U = U_1 - U_2$. Hence, the density ratio is not in the equation in this moving reference frame, leading to $\delta_{vis} \sim \Delta U/U_c$. From this, an equation is proposed for δ'_{vis}, the rate of change of visual thickness in streamwise direction, for incompressible variable-density mixing layers:

$$\delta'_{vis} = 0.17(\Delta U/U_c) = 0.17(1 - U_2/U_1)[1 + (\rho_2/\rho_1)^{1/2}]/[1 + (U_2/U_1)(\rho_2/\rho_1)^{1/2}]$$

The constant 0.17 was obtained experimentally from *Brown and Roshko*[19]. This equation has also been derived for a temporily growing mixing layer by *Brown*[26]. This equation agrees well with experimental data part of which is shown in Fig. 4. Therefore, this equation is used to compare with our sub- and supercritical jet growth rate results and is plotted in Fig. 4 for $U_2/U_1 = 0$. Results for different Mach numbers are shown for comparison and completeness only and are not further discussed here. Interested readers should refer to *Papamoschou and Roshko*[23].

In a different treatment, *Dimotakis*[27] uses an observation that the entrainment into the mixing layer from each stream is not the same and offers a geometrical argument to derive an equation. This equation is valid for two-dimensional incompressible variable-density vorticity thickness growth in a system moving with the aforementioned convection velocity. The equation is of the following form.

$$\delta'_{\omega} = \varepsilon\{(1 - U_2/U_1)/[1 + (\rho_2/\rho_1)^{1/2}(U_2/U_1)]\}\{1 + (\rho_2/\rho_1)^{1/2} - [1 - (\rho_2/\rho_1)^{1/2}]/[1 + 2.9(1 + U_2/U_1)/(1 - U_2/U_1)]\}$$

As indicated before, this growth rate can be multiplied by a factor of 2 to convert to the visual mixing layer thickness growth rate, and is plotted in Fig. 4 for $\varepsilon = 0.17/2$ to account for its adaptation to the axisymmeteric jets.

(c) Two-phase experimental/theoretical work

Because the images in Fig. 2 exhibit both liquid-like and gas-like visual jet appearances, it is appropriate to also plot spreading angles for liquid sprays produced from single hole nozzles. The atomization of liquids through round single hole injectors is a complex phenomenon that depends on many parameters, including injector geometry, ambient density, viscosity and surface tension of the liquid, initial turbulence, cavitation, and liquid supply pressure oscillations. According to *Reitz and Bracco*[14], in the "full atomization" or simply "atomization" regime the liquid jet visually diverges immediately at the exit of the injector hole. Also, for an aerodynamic surface-wave growth mechanism of liquid atomization, they show that the theoretical spray angle for a steady liquid jet can be determined by combining the radial velocity of the fastest growing unstable surface waves

with the axial injection velocity. A form of an equation is then derived for the spray spreading angle that reproduces the experimental density ratio and viscosity dependency trends. They indicate that the incompressible variable-density equation proposed in *Abramovich*[17] significantly overpredicts the spray spreading angle for all nozzles at low chamber gas densities (this equation is derived by setting the U_r to zero in equation 6 of the Appendix). This can be seen in Fig. 4. *Reitz and Bracco*[14] measured the spray angle in the atomization regime within the first 5 mm from the nozzle exit plane (distance-to-diameter ratios ranging from 20 to 40). Therefore, their measurements are within the comparable spatial region as the present measurements. For the two cases shown in Fig. 4, the Reynolds numbers ranged between 25,000 to 40,000. Both *Reitz and Bracco*[14] and *Hiroyasu and Arai*[28] show profound effects of the nozzle design on the spray angle. Therefore, theoretical equations derived by *Reitz and Bracco*[17] for two different length-to-diameter ratios are shown in Fig. 4 with vertical error bands indicating experimental data scatter around them. The experimental data was for the isothermal sprays. As a cross check, a recent curve-fitted equation to experimental data proposed by *Naber and Siebers*[29] is also shown. They measured a transient liquid fuel jet injected into a high pressure chamber for both vaporizing and non-vaporizing sprays. The transitory effects is shown to rapidly die and jet angle reaches those measured under steady state condition. The zone over which they measured spray angles extends slightly beyond our initial region as well as those by *Reitz and Bracco*[14]. This to some extent contributes to disagreement seen between the two sets of data shown for liquid sprays even though the same injector length-to-diameter ratio of about 4 was used in both cases. Their vaporizing liquid spray data show a 15% reduction in spreading angle at a density ratio of 0.01, decreasing to no noticeable reduction at a density ratio of 0.04. This reduction is explained to be due to the contraction of the jet caused by the entrained ambient gas cooled by the vaporizing liquid, as well as the vaporization of the drops at the outer boundary of the spray. This is important and suggests that the spreading rate of the vaporizing sprays is not much different from the isothermal ones shown in Fig. 4.

Other treatments worth considering as points of reference are given here. The simplest result is perhaps the prediction of the linear jet growth or constant spreading angle for a turbulent incompressible submerged jet. This is derived using the mixing length concept as detailed in the Appendix. Here, the parameter "2b", the jet thickness from the velocity profiles, is apparently measured at the 95% roll-off point. Next, following *Abramovich*[17], is the semi-empirical equation that attempts to incorporate the effects of density variations by introduction of a characteristic velocity as shown in the Appendix. These two cases are plotted in Fig. 4. Note that aforementioned growth rates are based on velocity profiles, however all others discussed here are determined using scalar field. In cases when scalar field growth rate is not reported a proposed conversion factor is used as described earlier.

(d) Current results and discussion

Our experimental results are presented next. For the N_2-into-N_2 case, beginning somewhere near a density ratio of 0.075 and higher, an average curve through the data points in Fig. 4 reaches very close to the theoretical curve of *Dimotakis*[27]. This density ratio is for when the chamber pressure is very near but below the critical point of N_2. Below this density ratio, the difference between the experimental data and this theory increases as the chamber pressure becomes increasingly subcritical and the jet enters the classical breakup regime. Note that the present data tends to approach and assume the trend of the results by *Reitz and Bracco*[14] for liquid sprays generated by a comparable sufficiently-large length-to-diameter ratio nozzle (i.e. 85). Data for the O_2-into-N_2 case shows a steeper drop in angle near but below the critical pressure of O_2 as the injectant. A similar trend can also be seen for the case in which N_2 is injected into He gas. To build confidence and also generate gaseous jet data

from our injector, the identical arrangement employed to acquire the sub- to supercritical jet images was considered to inject cooled He gas into warm N_2 and vice versa. The results are shown in Fig. 4 for chamber pressures ranging from 0.77 to 4.19 MPa. Although there is scatter in the data at various chamber pressures, it is interesting to note that injecting N_2 into He produces a narrower angle than injecting He into N_2, consistent with the results of *Brown and Roshko.*

Injection of N_2 into other gases and gaseous mixtures were also considered and some results are presented in Fig. 4. In general, effects of these other mixtures are through the changes they cause in the density ratio, surface tension, and diffusion of N_2 into the ambient. Nevertheless, their measured growth rates closely follow the theoretical predictions of *Dimotakis*[27], *Brown*[26], and *Papamoschou and Roshko*[23] .

It is clear that for a range of density ratios in which our images show gas-jet-like appearance, the experimental data agrees well with the proposed theoretical equation by *Dimotakis*[27], and closely follows the trend of that of *Brown*[26] and *Papamoschou and Roshko*[23]. Thus not only do the jets have the same appearance as gas jets when the ambient is at a supercritical temperature and pressure, the spreading rates of the two flows are quantitatively the same. This is the first time a quantitative parameter has been used to demonstrate that the similarity between the two flows extends beyond that of mere qualitative physical appearance. It is interesting that results for the liquid sprays at high density ratios for the short length-to-diameter nozzle tend to converge to incompressible jet value and not the proposed *Dimotakis* [27] or *Brown* [26]*/Papamoschou and Roshko*[23] equations. Even though the jet investigated here appears to go through the initial phases of the liquid breakup process, there is marked disagreement in both magnitude and slope between liquid sprays (at a comparable length-to-diameter ratio of 85) and our data when the chamber pressure reaches critical point of the injectant and beyond (at and above density ratio of about 0.04), see Fig. 4. Considering that the injected fluid is thermodynamically in liquid phase at the exit, one expects that our jet should follow the liquid spray results, but it does not. Disagreement increases as chamber pressure is increased at supercritical condition. Moreover, pure evaporation of the liquid sprays should narrow the spreading angle as shown by *Naber and Siebers*[29] making this disagreement even stronger. The reason is that although the jet studied here shows second wind-induced breakup features similar to liquid jets, it fails to reach full atomization because the thermodynamic state approaches the critical point and consequently both surface tension and heat of vaporization are reduced to a near zero value. Transition into the full atomization region is therefore inhibited.

In plotting the spreading rates of both liquid sprays and gas/gas turbulent mixing layers, Fig. 4 spans density ratios ranging from 0.001 to 10.0. To our knowledge, this is the first time spreading rate results have been consolidated into a single plot covering four orders of magnitude in density ratio, making this a unique and useful plot on its own right. Unfortunately, the data points in this figure do not cluster to form a universal curve. This implies that all the relevant parameters are not considered in defining its axes. Clearly, within the range plotted, the constant spreading angle results for an incompressible turbulent jet overpredicts nearly all the others in Fig. 4. There is also increasing disagreement between the turbulent gas jet of *Abramovich*[17] and the incompressible variable-density model of *Papamoschou and Roshko*[23] as the density ratio increases. Within the range shown, the axisymmetric jet spreading angle by *Richards and Pitts* [22] is higher in value than all the others. The supersonic jet angle narrows as density ratio is decreased (or Mach number increased). Disagreements in the measurements shown in this Fig. 4 can to some extent be attributed to differences in definition of the mixing layer thicknesses, their measurement methods, and the correction factors used to convert them into equivalent visual thicknesses. This is despite the fact that the best possible estimates for the conversion factors have been used. Even for those cases when the visual

thicknesses were measured directly, different photographic techniques caused differences in results by different researchers, the degree of which is yet to be assessed.

Summary and conclusions

Structural transitions and the initial growth rate of jets injected into an environment at a fixed supercritical temperature but varying pressures from subcritical to supercritical values are described and analyzed. All evidences support the hypothesis that as far as the growth rate is concerned, the jets investigated here behave similar to an incompressible variable-density gas jet when the ambient pressure reaches and exceeds the critical pressure of the injectant. The evidences are summarized in the following sentences. First, the lack of any visual detection of drops in the acquired images and the visual impression of a gaseous jet. Second, the inhibition of transition into the full atomization regime when the pressure approaches and exceeds the critical pressure as tested by the available atomization criteria. Third, quantitative agreement of the jet growth rate measurements with those predicted by the theoretical equations for incompressible variable-density gaseous jets. This quantitative evidence was presented here for the first time. Fourth, disagreement of the growth rate data under supercritical environment with those obtained in liquid sprays produced by a comparable nozzle geometry to ours. As mentioned before, although strictly speaking droplets less than about 30 microns cannot be definitively resolved by the imaging system employed here, all the aforementioned evidences, in particular the newly-demonstrated quantitative agreement between our measured growth rate and the previously established gaseous mixing layer theories, strengthen the hypothesis that the growth rate of the supercritical jets should be treated as incompressible but variable-density jets. Finally, for the first time, a unique plot has been generated through conversion of all growth rate types to the "visual" growth rate using the most relevant works reported by other researchers on variable-density incompressible mixing layers, axisymmetric incompressible and compressible gas jets, supersonic jets/mixing layers, and liquid sprays. The resulting plot of spreading angle as a function of density ratio spans four orders of magnitude in density ratio.

Acknowledgement

The authors would like to thank Mr. Mike Griggs for machining work and assisting in setup modifications, and Mr. Mike McKee for Labview data acquisition programming. We appreciate Mr. Theodore Miles's effort in searching copies of many requested publications. Also, Mr. Paul Loftsgard is thanked for his assistance in part of the data acquisition and processing. This work is sponsored by the Air Force Office of Scientific Research under Dr. Mitant Birkan, program Manager.

References

1. Harstad, K and Bellan, J. "Isolated fluid oxygen drop behavior in fluid hydrogen at rocket chamber pressures," International Jpournal of Heat and Mass transfer 41, 1998, pp. 3537-3550.

2. Bruno, T. J. and Ely, J. F. *Supercritical fluid technology: review in modern theory and applications*, CRC Press, 1991.

3. Umemura, A. "Supercritical droplet gasification combustion," IUTAM Symposium on theories ? combustion on droplets and sprays, December 1994, Taiwan.

4. Lazar R. S. and Faeth, G. M. "Bipropellant droplet combustion in the vicinity of the critical point", Thirteen Symposium (International) on Combustion, The Combustion Institute, P.801, 1971.

5. Newman, J. A. and Brzustowski. "Behavior of a liquid jet near the thermodynamic critical region," AIAA Journal, vol. 9, 1971, no. 8, pp. 1595-1602.

6. Mayer, W., Schik, A., Schweitzer, C., and Schaffler, M. "Injection and mixing processes in high pressure LOX/GH2 rocket combustors," AIAA Paper no. 96-2620, 32nd AIAA/ASME/SAE/ASEE Joint Propulsion Conference & Exhibit, Lake Buena Vista, Florida, 1996.

7. Mayer, W., Ivancic, A., Schik, A., and Hornung, U. "Propellant atomization in LOX/GH2 rocket combustors," AIAA Paper no. 98-3685, 34 the AIAA/ASME/SAE/ASEE Joint Propulsion Conference & Exhibit, Cleveland, Ohio, , July 13-15, 1998.

8. Chen, L.-D. and Sui, P.-C. *"Atomization during the injection of supercritical fluid into high pressure environment,"* in Mechanics and Combustion of Droplets in Sprays by Chiu and Chigier.

9. Woodward , R. D. and Talley, D. G. "Raman imaging of transcritical cryogenic propellants," AIAA Paper 96-0468, 34 the AIAA Aerospace Sciences Meeting and Exhibit, Reno, Nevada, January 1996.

10. Chehroudi, B., Talley, D., and Coy, E., 1999. "Initial Growth Rate and Visual Characteristics of a Round Jet into a Sub- to Supercritical Environment of Relevance to Rocket, Gas turbine, and Diesel Engines," 37th AIAA Aerospace Science Meeting and Exhibit, AIAA 99-0206, Reno, NV, January 11-14.

11. Schlichting, H. *Boundary Layer Theory*, MacGraw-Hill Book Company, seventh edition, 1979.

12. Chen, C. J. and Rodi, W. "Vertical Turbulent Buoyant Jets- A Review of Experimental Data. 1980, Pergamon.

13. Papanicolaou, P. N. and List, E. J. "Investigations of round vertical turbulent buoyant jets," J. Fluid Mech., 195, 1988, pp. 341-391.

14. Reitz, R. D. and Bracco, F. V. "On the dependence of spray angle and other spray parameters on nozzle design and operating condition," SAE international Congress and Exposition, SAE Paper no. 790494, Detroit, Michigan, February 26-March 2, 1979.

15. Faeth, G. M., "Structure and atomization properties of dense turbulent sprays," Twenty-third Symposium (International) on Combustion, The Combustion Institute, P.1345, 1990.

16. Tseng, L.,-K., Ruff, G. A., P.-K., Wu, Faeth, G. M., "Continuous- and dispursed-phase structure of pressure-atomized sprays," Progress in Astronautics and Aeronatics: Recent Advances in Spray Combustion, February, 1995.

17. Abramovich, G. N. *The theory of turbulent jets*, M.I.T. Press, 1963.

18. Chehroudi, B., Chen, S. H., Bracco, F. V., and Onuma, Y. "On the Intact Core of Full-Cone Sprays," Society of Automotive Engineers, 1985 Congress and Exposition, SAE Transaction Paper 850126, February 25-March 1, 1995.

19. Brown, G. and Roshko, A. "On density effects and large structure in turbulent mixing layers," J. Fluid Mech., vol. 64, 1974, part 4, pp. 775-816.

20. Brown G L, and Rebollo, M R, “A small fast-response probe to measure composition of a binary gas mixture,” AIAA Journal, 10, 1972, 649.

21. Abramovich, G. N., Yakovlevsky, O. V., Smirnova, I. P., Secundov, A. N., and Krasheninnkov, S., Yu. “An Investigation of turbulent jets of different gases in a general stream,” Astronautica Acta, 14, 1969, 229.

22. Richards, C. D. and Pitts, W. M. “Global density effects on the self-preservation behavior of turbulent free jets,” J. Fluid Mech., vol. 254, 1993, pp. 417-435.

23. Papamoschou, D. and Roshko, A.. “The compressible turbulent shear layer: an experimental study,” J. Fluid Mech., vol. 197, 1988, pp. 453-477.

24. Konard, J. H. “An experimental investigation of mixing in two-dimensional turbulent shear flows with applications to diffusion-limited chemical reactions,” PhD thesis, California Institute of Technology, 1976.

25. Bogdanoff, D. W. “Compressibility effects in turbulent shear layers,” AIAA Journal, 21, 1983, pp. 926-927.

26. Brown, G. “The Entrainment and Large Structure in Turbulent Mixing Layers,” 5th Australian Conf. on Hydraulics and Fluid Mech., 1974, pp. 352-359.

27. Dimotakis, P. E. “Two-dimensional shear-layer entrainment,” AIAA Journal, 21, No. 11, 1986, pp. 1791-1796.

28. Hiroyasu, H. and Arai, M. “Fuel spray penetration and spray angle in diesel engines,” Trans. JSAE, Vol. 21, 1980, pp. 5-11.

29. Naber, J. D. and Siebers, D. L. “Effects of gas density and vaporization on penetration and dispersion of diesel sprays,” SAE international Congress and Exposition, SAE Paper no. 960034, Detroit, Michigan, February 26-29, 1996.

Appendix

(a) Growth rate for incompressible and compressible jets, as documented in *Abramovich* [17]:

For an incompressible turbulent submerged jet, three special regions are defined, namely, the initial, transitional, and main regions. The initial region roughly extends just beyond the end of the potential core and the main region is where a self-similarity solution becomes applicable. Using Prandtl's mixing length theory, assuming the mixing length is only a function of streamwise distance, *Abramovich*[17] indicates that the jet growth rate is controlled by the transverse velocity fluctuations, v':

$$\frac{Db}{Dt} \propto v' \propto -\ell \frac{\partial \overline{U}}{\partial y} \propto -\ell \frac{U_{cl}}{b} \propto U_{cl} \qquad (1)$$

and since

$$\frac{Db}{Dt} = \frac{db}{dx}\frac{dx}{dt} \propto U_{cl}\frac{db}{dx} \qquad (2)$$

from the above two:

$$\frac{db}{dx} = \text{constant} \Rightarrow b = (\text{constant})x \Rightarrow$$

$$\ell = (\text{constant})\, x \qquad (3)$$

2b is defined as the thickness of the velocity profile, Db/Dt is the total derivative, ℓ is mixing length, v' is the transverse velocity fluctuations, and U_{cl} is the centerline maximum value of the time - averaged streamwise velocity profile.

For a compressible jet, *Abramovich* [17] proposes a semi-empirical theory for the jet spreading as follows:

$$\frac{db}{dx} \propto \frac{U_1 - U_2}{U_{char}}$$; where U_1 and U_2 are streamwise velocities at the boundaries of the mixing zone, U_{char} a characteristic velocity in the zone, and x is in streamwise direction.

$$\text{For incompressible flow}: U_{char} = \frac{U_1 + U_2}{2} \qquad (4)$$

$$\text{For compressible flow}: U_{char} = \frac{\rho_1 U_1 + \rho_2 U_2}{\rho_1 + \rho_2} \qquad (5)$$

From above equations for compressible flow :

$$\frac{db}{dx} = C\frac{1+\rho_r}{2}\frac{1-U_r}{1+\rho_r U_r}; \text{ where}$$

$$U_r = \frac{U_2}{U_1} \text{ and } \rho_r = \frac{\rho_2}{\rho_1}.$$

In the main region of the jet :

$$U_r = \frac{U_{ambient}}{U_{cl}};$$

$$\rho_r = \frac{\rho_{ambient}}{\rho_{cl}}; U_{cl} = U_{cl}(x); \rho_{cl} = \rho_{cl}(x)$$

If U_r and ρ_r do not depend on x (i.e. initial region) then from above :

$$\frac{b}{x} = C\frac{1+\rho_r}{2}\frac{1-U_r}{1+\rho_r U_r} \qquad (6).$$

From experiments in the initial region of the submerged jet (i.e. $U_r = 0$) of an incompressible fluid ($\rho_r = 1$) $C = 0.27$ is proposed. However, various experiments in hot jets, high - velocity jets, and supersonic jets under off - design discharge suggest a value of $C = 0.22$.

(b) Definition of different mixing layer thicknesses:

The vorticity thickness δ_ω is defined through measurements of the streamwise time-averaged ($\overline{U}$) velocity profile in the mixing layer. It is equal to $(U_1 - U_2)/ (d\overline{U}/dy)_{max}$ where the derivative is taken across the mixing layer and U_1 and U_2 are the free stream velocities for each stream forming the mixing layer. *Brown and Roshko*[19] state that this definition, in addition to being convenient, is also appropriate, because the problem of the growth of the turbulent mixing layer is basically the kinematic problem of the unstable motion induced by the vorticity.

The Pitot thickness δ_{pit} is the width of the pressure profile measured with at Pitot tube from 5% to 95% of the difference of the two free-stream values, (see *Papamoschou and Roshko*[23]).

The visual thickness δ_{vis} is the thickness determined via a photographic technique. It is measured by the shadowgraphy and schlieren approaches in *Brown and Roshko* [19] and *Papamoschou and Roshko*[23], respectively.

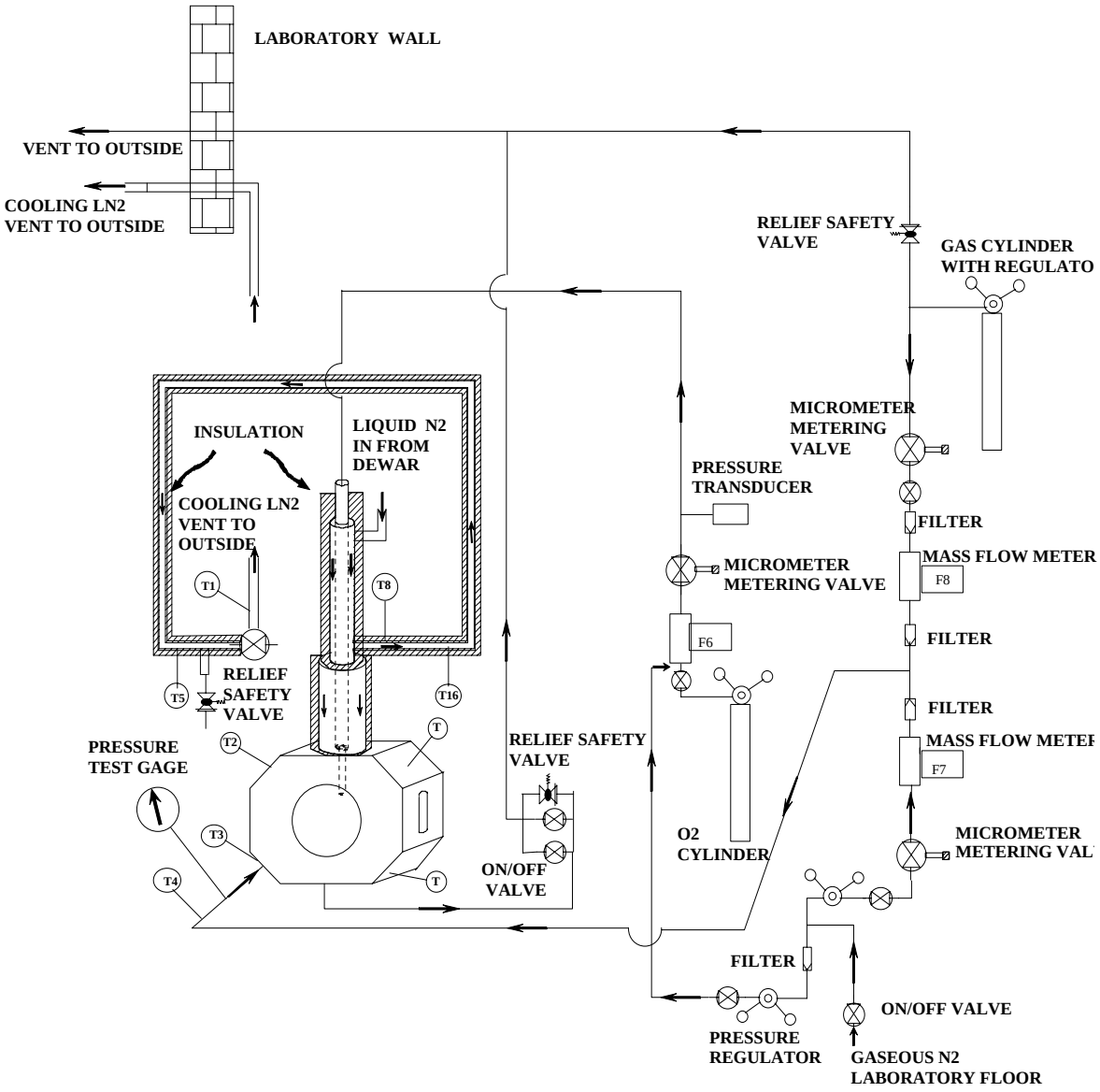

Figure 1. Schematic diagram of experimental setup for sub- to supercritical jet injecti

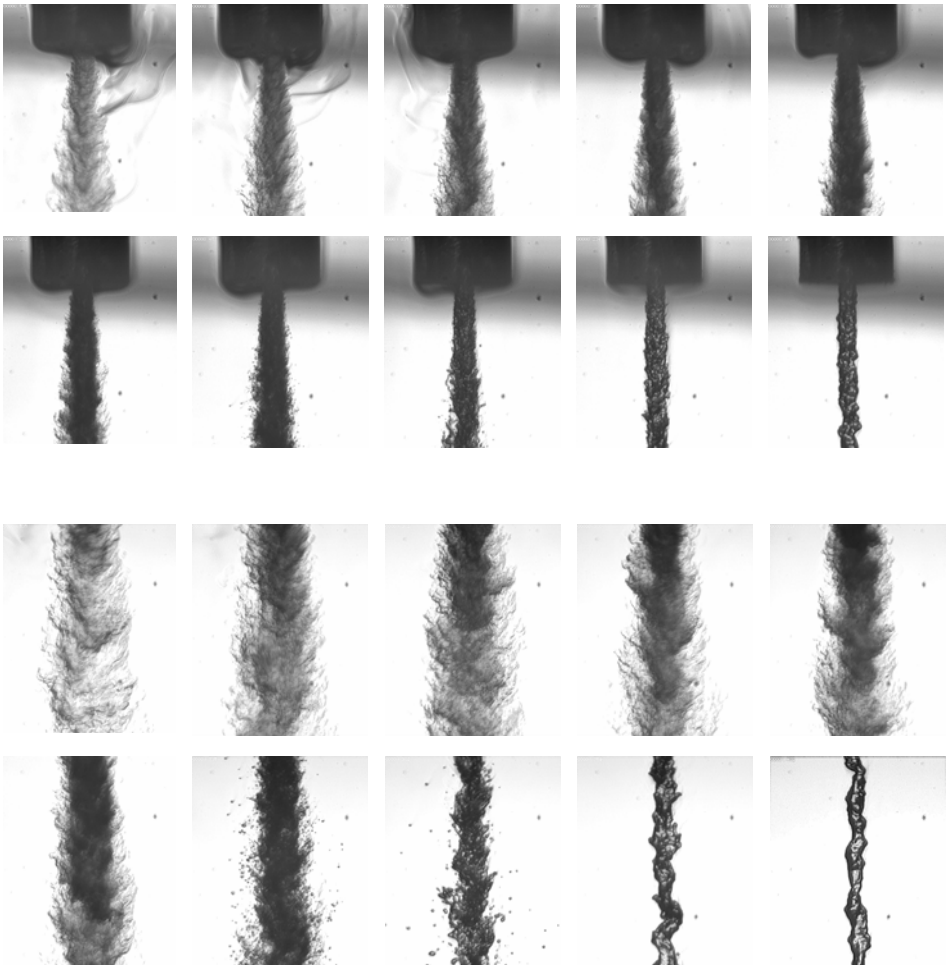

Figure 2. Back-illuminated images of the nitrogen injected into a chamber of nitrogen at a fixed supercritical temperature of 300 K but varying sub- to supercritical pressure. For the first two rows, chamber pressure decreases left to right from upper-left to lower-right corner: P_{ch}/P_c= 2.74, 2.44, 2.03, 1.64, 1.23, 1.03, 0.83, 0.63, 0.43, and 0.23. Lower two row images are corresponding images for the upper ones but further downstream. The axial distance at the bottom of the upper two row images is the same as the top of the ones in the two lower rows. The magnification can be inferred knowing the injector outer diameter of 1.59 mm (1/16"). Re # range: 25,000 to 75,000; injection velocity range: 10 to 15 m/s; Froude # range: 40,000 to 110,000. P_c and T_c are critical pressure and temperature of the injectant and P_{ch} and T_{ch} are chamber pressure and temperature. For N_2: P_c=3.4 MPa, T_c=126.2 K.

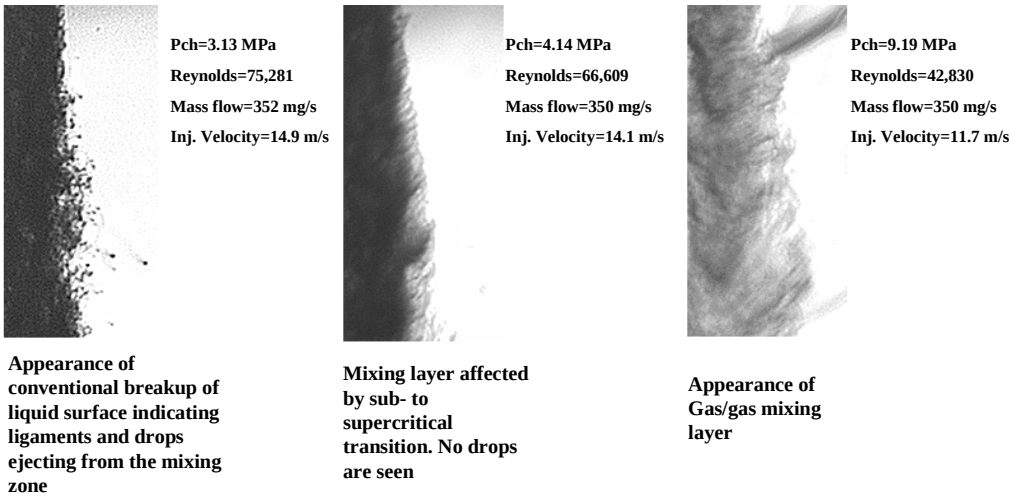

Figure 3. Software magnified images of the jet at its outer boundary showing transition to the gas-jet like appearance starting at just below the critical pressure of the injectant. Images are at fixed supercritical chamber temperature of 300 K.

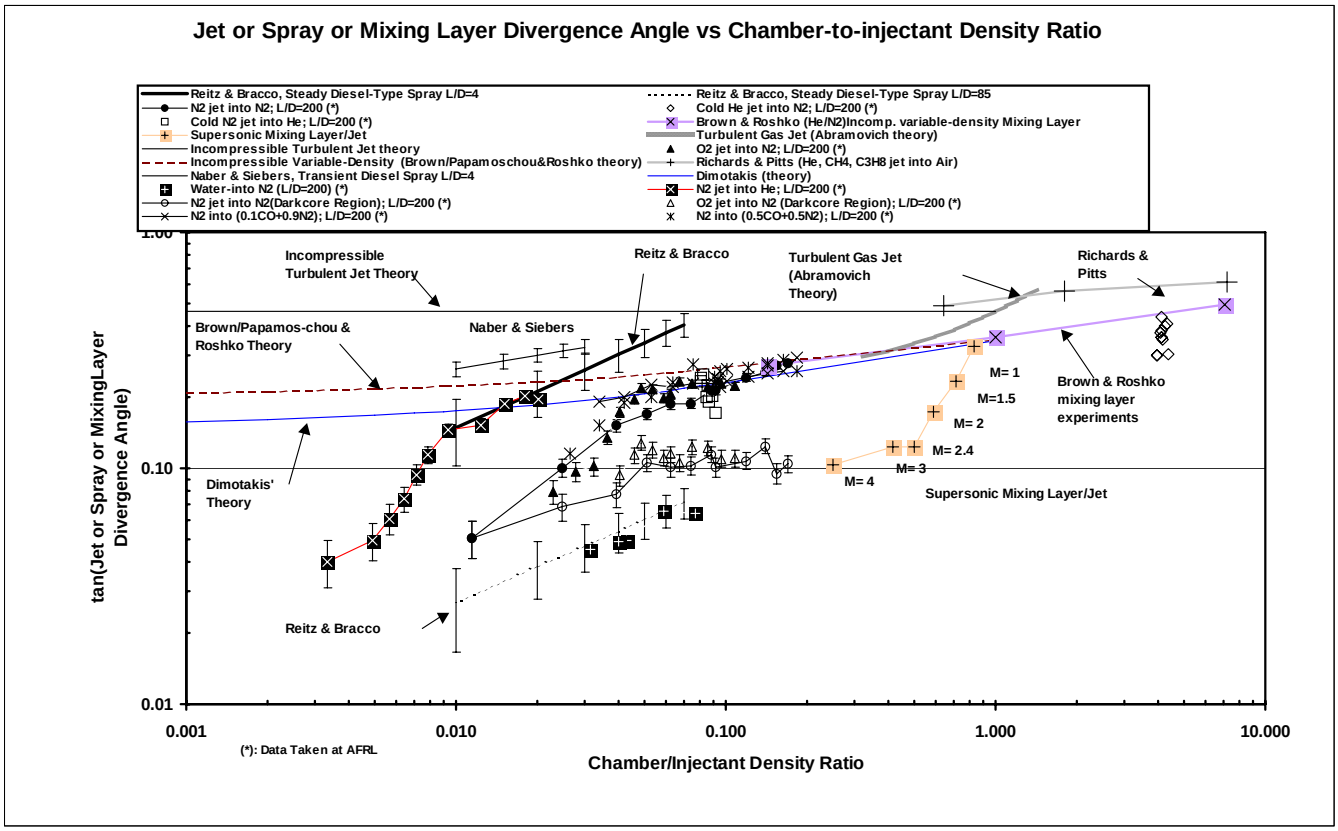

Figure 4. Shows spreading or growth rate as tangent of the visual spreading angle versus the chamber-to-injectant density ratio. (*) refers to data taken at AFRL.

This Page Intentionally Left Blank

APPENDIX M

"Cryogenic Shear Layers: Experiments and Phenomenological Modeling of the Initial Growth Rate Under Subcritical and Supercritical Conditions"

This Page Intentionally Left Blank

ELSEVIER

International Journal of Heat and Fluid Flow 23 (2002) 554–563

International Journal of HEAT AND FLUID FLOW

www.elsevier.com/locate/ijhff

Cryogenic shear layers: experiments and phenomenological modeling of the initial growth rate under subcritical and supercritical conditions

B. Chehroudi [a,*], R. Cohn [b], D. Talley [b]

[a] *Engineering Research Consultants Inc., 10 E. Saturn Blvd., Edwards AFB, CA 93524-7680, USA*
[b] *Air Force Research Laboratory (AFRL), Space and Missile Propulsion Division, AFRL/PRSA, 10 E. Saturn Blvd, Edwards AFB, CA 93524-7680, USA*

Abstract

A jet of a cryogenic fluid, typically liquid N_2, is injected into a chamber whose ambient pressure is varied to values exceeding the critical pressure of the injectant. The structure of the jet and the shear layer between the jet and the ambient have been examined. Results from visualization, jet initial growth rate, fractal analysis, and Raman scattering measurements indicate that the behavior of the injected fluid changes from liquid spray-like to gaseous jet-like behavior as pressure increased. This is attributed to the reduction of the surface tension and enthalpy of vaporization as the critical pressure of the injectant is approached. The initial divergence angle indicating the growth rate of the jet is measured at the jet exit. These values are then compared with those measured from a large number of other mixing layer flows, including atomized liquid sprays, turbulent incompressible gaseous jets, supersonic jets, and incompressible but variable density jets covering over four orders of magnitude in the gas-to-liquid density ratio, the first time such a plot has been reported over this large a range of density ratios. At and above the critical pressure of the injected fluid, the jet initial growth rate measurements agrees well with the theory and measurements of incompressible, variable density, gaseous mixing layers. This is the first time a quantitative parameter has been used to demonstrate that the similarity between the two flows extends beyond mere qualitative physical appearance. The initial growth rate using Raman scattering is also in reasonably good agreement with our measurements using shadowgraphy if twice the FWHM of the normalized intensity radial profiles are used. Finally, an equation based on a proposed physical mechanism combined with the characteristic gasification time (τ_g) and interfacial bulge formation/separation time (τ_b) is proposed, $\theta = 0.27[\tau_b/(\tau_b + \tau_g) + (\rho_g/\rho_l)^{0.5}]$, that shows good agreement with the measured initial growth rate data. It is found that the transition point from sub- (liquid-jet like) to supercritical (gas-jet like) behavior occurs when the time scale ratio ($\tau_b/(\tau_b + \tau_g)$) is approximately equal to 0.5. © 2002 Published by Elsevier Science Inc.

1. Introduction

In recent years, combustion chamber operating pressures have been increased in order to realize performance and/or efficiency benefits in a wide range of propulsion and energy conversion applications. In some cases, this has resulted in the injected fluid(s) experiencing ambient pressures exceeding their thermodynamic critical pressure(s). An example of particular interest in rocket applications is the cryogenic liquid hydrogen/liquid oxygen Space Shuttle Main Engine in which the combustion or thrust chamber pressure is about 22.3 MPa. Thrust chamber pressures for the Vulcain (Ariane 5) engine have been recorded to reach up to 10 MPa. Both of these pressures exceed the critical pressure of oxygen ($P_{cr} = 5.043$ MPa). In these applications, the initial temperature of the oxygen is below its critical temperature ($T_{cr} = 154.58$ K), and then undergoes a transition to a supercritical temperature as the oxygen is mixed and burned in the combustion chamber.

For single component fluids, the distinct difference between the gas and liquid phases disappears when either the pressure exceeds the critical pressure or the temperature exceeds the critical temperature. Near the critical point, the surface tension and enthalpy of vaporization vanish. Large variations in the density, thermal conductivity, and mass diffusivity also occur. For multicomponent fluids, the solubility of the gas phase in the liquid phase increases as pressure approaches the critical pressure, and mixture effects need to be taken into account in calculating the critical properties. The critical

* Corresponding author.
E-mail address: bruce.chehroudi@edwards.af.mil (B. Chehroudi).

0142-727X/02/$ - see front matter © 2002 Published by Elsevier Science Inc.
PII: S0142-727X(02)00151-0

properties of mixtures are referred to as the "critical mixing temperature" and the "critical mixing pressure" (Bruno and Ely, 1991). The critical mixing pressure can be many times the critical pressure of the individual components as seen in Woodward and Talley (1996).

Previous efforts, (for example, Newman and Brzustowski, 1971; Mayer et al., 1996), have reported a gas-like jet visual appearance at a supercritical chamber temperature and pressure with no evidence of droplets. Newman and Brzustowski (1971) studied steady CO_2 jets injected into a chamber of pure N_2 and also mixtures of $CO_2 + N_2$ at both sub- and supercritical pressures and temperatures. They explained the effects of increased chamber temperature on the jet appearance to be due to the progressive reduction in ambient gas density, the reduction in surface tension to zero at the critical temperature, and the increase in liquid CO_2 evaporation. Based on coarse photographs, they proposed the possibility of jet gasification, namely that at supercritical temperatures and pressures the jet could be treated as a variable-density single-phase turbulent submerged gas jet. Mayer et al. (1998) studied liquid cryogenic N_2 (LN_2) jets at a fixed temperature of 105 K injected into a N_2 environment at 300 K, but at varying ambient sub- to supercritical pressures, and observed drastic changes in the jet structure near and above the critical pressure. They attributed this behavior to a continual decline of surface tension until it vanished at and above the critical pressure. They also studied the coaxial injection, similar to the injection scheme used in cryogenic rocket engines, of LN_2 (at 97 K) inside gaseous He (at 280 K), as simulant fluids for H_2 and O_2. As before, changes in the jet structure were clearly observed as pressure increases were clearly observed. Again, these changes were attributed to increases in the solubility of He into N_2 and reductions in the surface tension. Finally, they studied H_2/O_2 combustion in a windowed model rocket combustion chamber, and again observed structural changes in the jet with pressure in both the ignition and steady state combustion phases. No evidence of droplets was observed at supercritical conditions.

Woodward and Talley (1996) studied the injection of LN_2 jets into gaseous N_2 and gaseous mixtures of N_2 and He at much lower Reynolds numbers than the above studies. For N_2/N_2 systems, observation of the resulting fluid structures at and above the critical pressure showed strong evidence that surface tension becomes negligibly small either at the instant of mass injection or very rapidly thereafter. Adding gaseous He ($\sim$20 wt.%), however, was found to produce structures which again showed strong evidence of having surface tension at pressures up to twice the critical pressure of pure N_2, demonstrating the strong effect of composition on the critical mixing properties.

Anderson et al. (1995), Decker et al. (1998), Oschwald and Schik (1999), Oschwald et al. (1999), and Chehroudi et al. (2000) used Raman scattering to investigate the structure of a cryogenic nitrogen jet under supercritical conditions. Decker et al. (1998) observed a smooth transition from the high-density core of a cryogenic, N_2 jet to the more rarefied, warmer N_2 in the ambient outer region. There was no distinct phase interface. The density radial profile was never observed to have a top hat profile, even as close as 2.5 injector diameters from the outlet. Based on limited tests, they concluded that the thermodynamic state of an injected supercritical fluid was of prime importance in determining the jet growth, and not the injection velocity or momentum.

The objective of this paper is to concisely present the experimental and modeling experiences gained thus far at AFRL on the injection of cryogenic fluids under subcritical to supercritical pressures. The structural features of the jet and the shear layer between the jet and the ambient will be described. An initial attempt to model the measured growth rates of the jet shear layer is also presented.

2. Experimental apparatus

Fig. 1 shows a schematic diagram of the experimental rig. The stainless steel chamber can withstand pressures and temperatures of up to 20 MPa and 473 K, respectively. It has two facing circular sapphire windows with two UV-grade side-mounted slot-shaped quartz windows for optical diagnostics and laser illumination of the chamber. Liquid N_2 is used to cool and/or liquefy the injectant passing through the cryogenic cooler prior to injection. The mass flow rate of the injectant is measured and regulated via a mass flowmeter, and a precision micrometer valve. Back-illumination of the jet is accomplished with diffuse light flashes (0.8 μs duration). A model K2 Infinity long distance microscope is used with a TM-745E high resolution ($768(H) \times 493(V)$ pixels in $8.8(H) \times 6.6(V)$ mm actual sensing area) interlaced CCD camera by PULNix to form images of the injected jets. The resolution of this setup is 30 ± 7 μm. For the results reported, the cryogenic jet is injected through a sharp-edged stainless steel tube with a length, $l = 50$ mm, and inner and outer diameters measuring $d_e = 0.254$ mm and $d_o = 1.59$ mm respectively. This results in $l/d_e = 200$, which is sufficient to ensure fully developed turbulent pipe flow at the exit plane. The Reynolds number in these studies ranges from 25,000 to 70,000. The rig is fully instrumented to measure pressure, temperature, and mass flow rate of the injected fluid.

For the Raman scattering experiments, a Contunuum Powerlite 8010 frequency-doubled Nd:Yag pulsed laser (532 nm output wavelength) with a pulse energy of

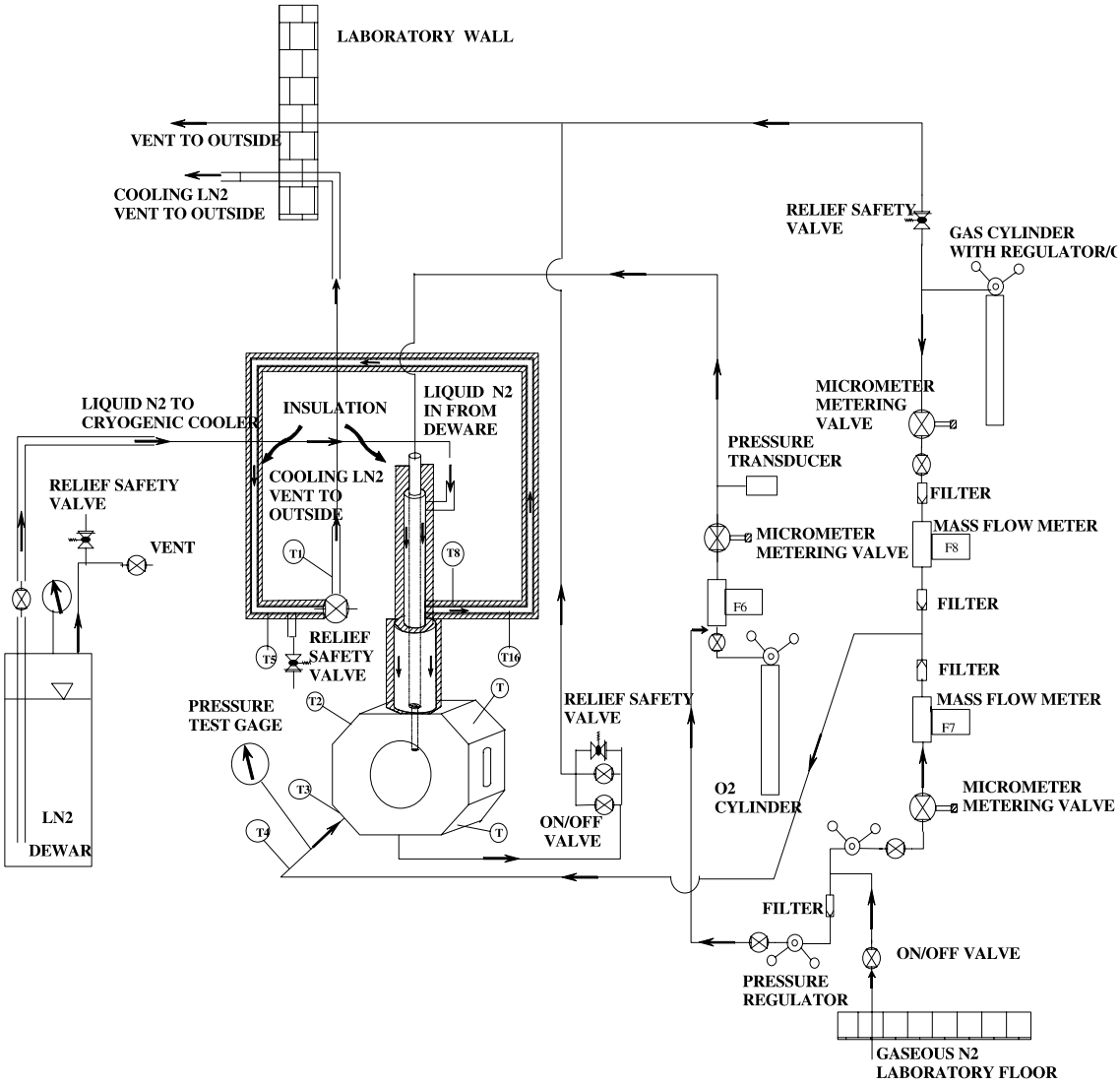

Fig. 1. Schematic diagram of experimental setup for sub- to supercritical jet injection.

330 mJ/pulse as a source to induce the Raman effect. The pulse repetition rate for this laser is 10 Hz with a pulse width of 10 ns. A passive pulse stretcher is designed to reduce the possibility of plasma formation. The original pulse is extended in time by dividing it into three major pulses, each being 10 ns in duration, but delayed in time by 8 and 16 ns. This results in a final pulse duration of about 26 ns. The laser beam is shaped by passing through a Galilean beam expander before forming a thin sheet via two cylindrical lenses. The laser sheet thickness was measured using an attenuator attached to a CCD camera and found to be about 100 μm. The entire assembly is on a separate optical bench which can be traversed in both vertical and horizontal directions.

The scattered Raman signal at 607 nm is detected by a cooled 576 × 384 pixel ICCD camera from Princeton Instruments. A set of three filters is also used to separate the Raman signal from the 532 nm incident beam. A high-pass OG570 filter is used to reduce the light at 532 nm by more than 10^5 and at 607 nm by not more than 10%. A holographic supernotch plus filter attenuates the light at 532 nm by better than 10^6 while less than 20% at 607 nm. Finally, a 10 nm bandwidth interference filter centered at 610 nm reduces the scattered light at 532 nm by better than 10^4 while attenuating by about 0.5 at 607 nm. Therefore, an optical density of better than 15 is achieved at the 532 nm laser wavelength while the transmittance of the Raman signal is 0.36. This arrangement was found to be adequate to ensure the removal of stray light while passing sufficient Raman signal for detection. The lens package consists of a Nikon PK-12/14 extension ring connected to one end of a Noct-Nikkor 58 mm F/# (1.2–16) lens with a NIK-2734 close-up lens located in its front. For more detailed on experimental setup see Chehroudi et al. (2002, 1999, 2000).

3. Visual appearance changes in cryogenic jets and shear layers

Fig. 2 (top row) shows representative images of a jet of liquid nitrogen (LN_2) ($P_{cr} = 3.39$ MPa, $T_{cr} = 126.2$ K) injected at an initial temperature of 99–110 K into room temperature (300 K) gaseous nitrogen (GN_2). For the results presented here, the chamber pressure is normalized (or reduced) by the critical pressure of the pure fluid in the jet; P_r (i.e. reduced pressure) $= P_{chamber}/P_{cr}$. Froude number values were calculated at each chamber pressure to examine the importance of buoyancy forces within the distances investigated in this study. This number ranges from 42,000 to 110,000. Chen and Rodi (1980) suggested that the flow is momentum dominated when a defined length scale $x_b < 0.53$, while Papanicolaou and List (1988) suggested $x_b < 1$. Considering the more conservative estimate by Chen and Rodi (1980), the jet used here is momentum dominated for distances less than 30 to 40 mm from the injector exit. Pictures presented here cover up to about 5.5 mm (axial distance/diameter ratio of 21.6) from the injector and hence buoyancy effects can be ignored in favor of the inertial forces.

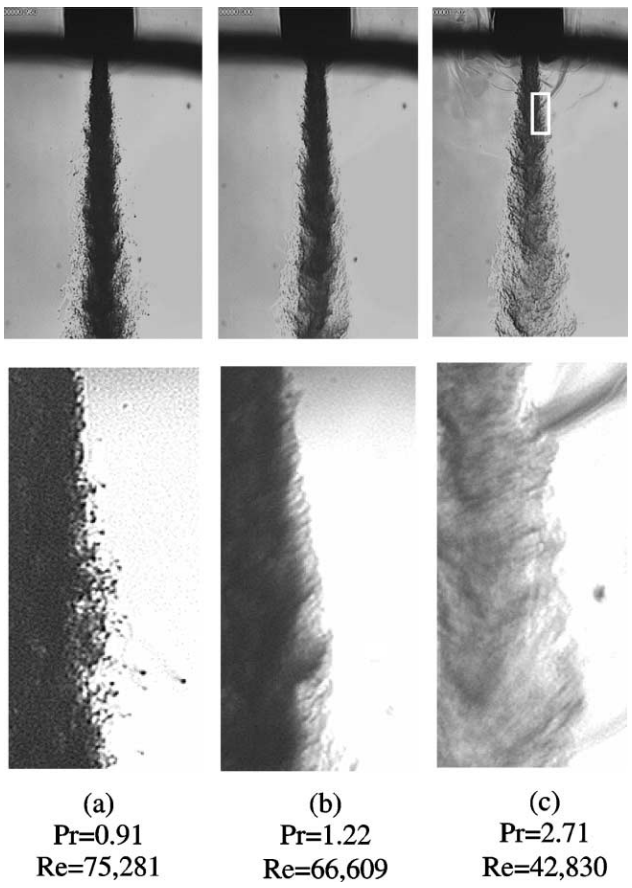

Fig. 2. LN_2 injected into room temperature nitrogen at different pressures. The bottom row contains magnified images of the top row in order to examine the shear layer.

The bottom row of Fig. 2 shows the jet shear layer. Generally, it is apparent that as pressure is increased, the jet width increases and the structure of the shear region changes from being dominated by ligaments and droplets to being dominated by finger-like structures. The results presented here are not unique to the injection of liquid nitrogen. Similar results have been found injecting liquid oxygen into gaseous nitrogen. In column (a), where the chamber pressure is subcritical, the jet has a classic liquid-like appearance. Consistent with the classical liquid jet breakup regimes described by Reitz and Bracco (1979), surface instabilities grow downstream from the injector and very fine ligaments and drops are ejected from the jet. This has been confirmed to correspond to the second wind-induced liquid jet breakup regime in Reitz and Bracco (1979).

Major structural and interfacial changes occurred at $P_r = 1.03$. Above this P_r, drops are no longer detected and regular finger-like entities are observed at the interface. Rather than breaking up into droplets, the interface dissolves at different distances from the dense core. These structures are illustrated at a $P_r = 1.22$ in column (b) of Fig. 2. This change in the morphology of the mixing layer is evidently due to the combined effects of reductions in the surface tension as the critical pressure is exceeded and enthalpy of vaporization because of this transition.

As chamber pressure is further increased, the length and thickness of the dense core decreased, and the jet begins to appear similar to a turbulent gaseous jet injected into a gaseous environment. This is illustrated in column (c). Any further droplet production, and consequently any additional classical liquid atomization, are completely suppressed.

4. Jet and shear layer growth rates

In order to compare with classical mixing layer theory, the initial growth rate of the jets was measured at distances less than 28 jet diameters from the exit. As discussed by Chehroudi et al. (2002), this distance was well within the mixing layer region. The results were then plotted in Fig. 3 as the tangent of the spreading angle versus the chamber-to-injectant density ratio. Overlaid on top of the present data are the results of other researchers. Note that the jet studied here exhibits a dual character personality, liquid-like and gas-like. When liquid-like, it atomizes and produces a fine liquid droplet spray. However, consistent with other researchers, such a behavior is not detected and the jet resembles a gaseous jet injected into a gaseous environment under supercritical ambient pressure. Observing these two completely different characters motivated

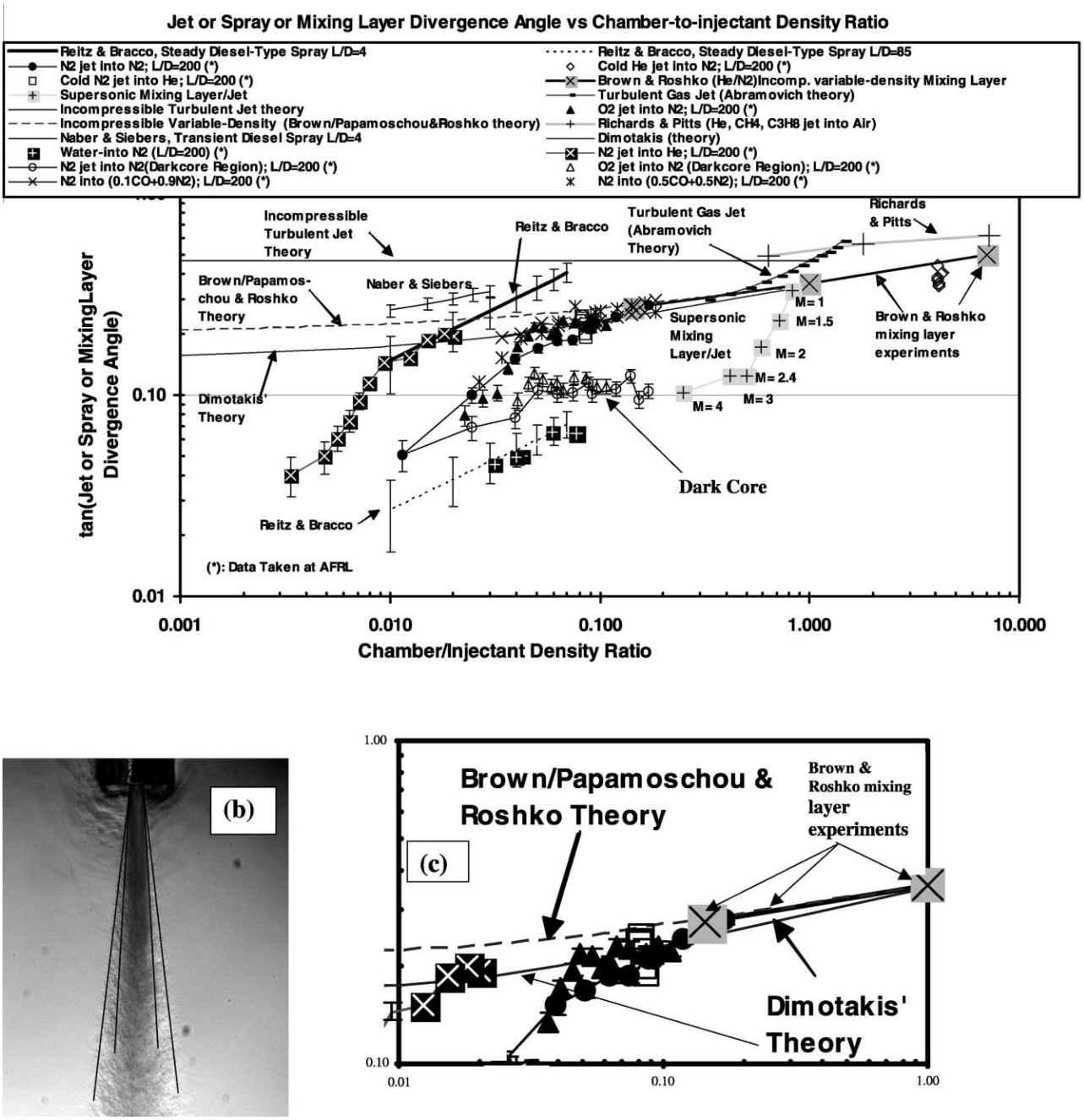

Fig. 3. (a) Spreading or growth rate as tangent of the visual spreading angle versus the chamber-to-injectant density ratio. (*) refers to data taken at AFRL. (b) An image of the jet depicting spread angle and dark-core angle measurements under high ambient pressure. (c) Plot is similar to (a) showing magnified data near the critical point.

us to simultaneously present ''visual'' spread rate for both liquid sprays (two-phase flow) and gaseous jets/mixing layers (single-phase flow). With the exception of the supersonic jet (shown for completeness) and incompressible gas jet theories (used as a reference), we selected those information found in the literature that are closest and of immediate relevance to the present case. All the data presented in this plot share the following attributes: straight-hole injectors, sufficiently-long nozzle hole length-to-diameter ratio (to ensure fully-developed flow before the injector exit plane), Reynolds number range, momentum-dominated jets in the initial measurement zone, turbulent jet, comparable measurement zone for the growth rate, and consideration of the ''visual'' growth rate (all other growth rates were converted to ''visual'' rates). This resulted in a plot that is unique in that it spans nearly four orders of magnitude in density ratio and compares growth rates for both two-phase liquid sprays and single-phase turbulent jets.

We will first examine the subcritical region of Fig. 3. A more complete description can be found in Chehroudi et al. (2002). In this region, the LN_2 jet appears visually to have spray-like characteristics, as seen in Fig. 2a. The growth rate of this jet approaches the trend of that seen in liquid spray measurements such as Reitz and Bracco (1979), shown in Fig. 3. Their results represent the predictions of the linear stability atomization theory, while the error bars represent the extent of experimental scatter around the theoretical predictions. Results by Naber and Siebers (1996) are also shown for comparison purposes. Reitz and Bracco's data show the well-known result that the initial spreading rates of sprays from plain round orifices are sensitive to the injector internal geometry and, in particular, to the injector hole parameter, L/d_e. However, in comparing the shape of the curves, their data for $L/d_e = 85$ closely correspond to the LN_2 jet data at $L/d_e = 200$. In both of these cases, the flow is fully developed. As the density ratio is increased into the transition region (as seen in Fig. 2b), the jet and shear layer growth rate also increases. Near the critical pressure, the rate of increase becomes much steeper. Note that the abrupt change occurs at different density ratios for the different data sets in Fig. 3 because the data sets correspond to different mixtures with different critical properties.

At supercritical chamber pressures, where the LN_2 jet visually resembles a turbulent gas jet, the growth rate closely follows both the theoretical equation proposed by Dimotakis (1986) and the independently-derived equation by Papamoschou and Roshko (1988) for incompressible variable-density mixing layers. The spreading angle of the jet shear layer also agrees with Brown and Roshko's (1974) spreading angle measurements of an incompressible variable-density turbulent mixing layer between helium and nitrogen gases. Comparison with mixing layer data is justified because our measurements are within the initial mixing layer of the jet and do not extend far beyond the length of the potential core (for single-phase gaseous or liquid jets) and the intact core (for two-phase liquid sprays), see Chehroudi et al. (2002, 1999).

These growth rate measurements complement and extend the visualization results of the previous section. At supercritical pressures, not only do the jets have the visual appearance of a turbulent gas jet, but also the growth rates measurements are consistent with incompressible variable-density turbulent jets. This quantitative agreement was first shown in Chehroudi et al. (1999). At subcritical pressures, the jets have the same appearance and growth rate trend as liquid sprays. The transition between the two regimes occurs near the critical pressure. The above conclusions have been demonstrated for the case of a fully-developed flow at the jet exit. Other initial conditions have not yet been examined.

5. Fractal analysis

The notion of a fractal has been given a strong foundation and application by its father Mandelbrot (1983). Fractals are intimately connected to the concept of self-similarity. In essence, a similarity transformation involves one or combination of multiplication by a scale factor, pure translation, and pure rotation. Under such a transformation a geometrical object stays similar to the original or to a preceding stage if repetitively applied. Self-similarity, however, in a strict sense means that if one chooses any point of a geometrical object and locally magnifies, it will look similar to the "whole" object. In a sense infinite number of the scaled-down version of the "whole" are embedded in the "whole." In nature such idealized mathematical objects do not exit. For example, Peitgen et al. (1992) explain that a cauliflower head contains branches or parts, which when removed and compared with the whole are very much the same, only smaller. Applying the proper scale factor, the head and the branches are identical. These can again be decomposed into smaller ones, which again look very similar to the whole as well as to the first generation branches. This self-similarity carries through for about three to four stages, unlike the mathematical fractals which can be decomposed an infinite number of times. After that the structures are too small for a further dissection. Hence, in natural geometrical constructs self-similarity is confined between two sizes (or scales) referred to as inner (the smallest size) and outer cut-offs (the largest size).

The fractal dimension of any curve is between 1 and 2. The more wrinkled and space-filling the curve, the larger the value of the fractal dimension. Natural curves, similar to a cauliflower, are self-similar only to within a narrow range of scales. Our objective here is to measure the fractal dimension of the interface of the jets injected into the chamber to see if any pattern is uncovered. To our knowledge, this is the first application of the fractal approach to the liquid jet interface under sub- and supercritical conditions.

The fractal dimension of jets at various pressures ranging from subcritical to supercritical was calculated and compared to results of other researchers. Reference results were taken from Sreenivasan and Meneveau (1986) who measured the fractal dimensions of a variety of turbulent gaseous jets, mixing layers and boundary layers. These results indicate a fractal dimension between 1.33 and 1.38. In addition, the fractal dimensions of a turbulent water jet (Dimotakis et al., 1983) and of a liquid jet in the second wind-induced atomization regime (Taylor and Hoyte, 1983) were computed from high-resolution scanned images.

The fractal dimensions from the above reference cases are shown as horizontal lines in Fig. 4. Overlaid on top of these lines are discrete points indicating the fractal

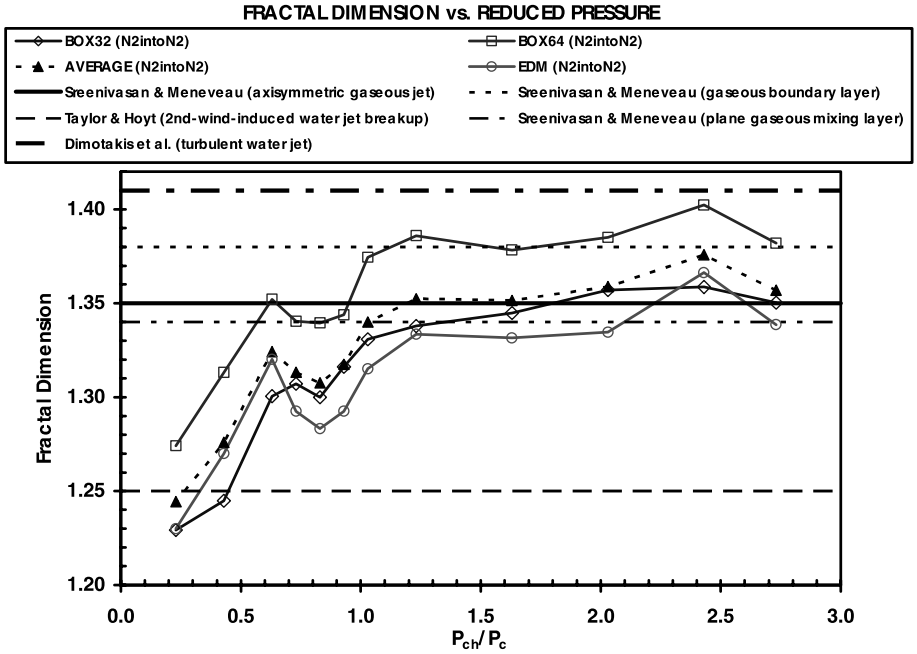

Fig. 4. Fractal dimensions of the boundaries of various jets as a function of reduced pressure (chamber pressure divided by the critical pressure of the jet material). Discrete points are data from the present study. Box32, Box64, and EDM are different methods of calculating the fractal dimension, giving an impression of the extent of variability, for details see Chehroudi et al. (1999).

dimension of LN_2 jets injected into GN_2 at various chamber pressures. At supercritical chamber pressures, the fractal dimension approaches a value similar to gaseous turbulent jets and mixing layers. As the chamber pressure is decreased, the fractal dimension also decreases. Below $P_r = 0.8$, the fractal dimension rapidly reduces to a value approximately equal to that of a liquid spray in the second wind-induced liquid jet breakup regime.

A more thorough discussion of the above results is found in Chehroudi et al. (1999). The key observation to be taken is that the results from the fractal analysis complement and extend the previous results. At supercritical pressures, jets have a fractal dimension similar to turbulent gas jets, and at subcritical pressures, cryogenic jets have a fractal dimension similar to liquid sprays. The transition occurs at about the same pressure as the transition in visual appearance and growth rate.

6. Modeling the growth rate

Using the data collected on the growth of the cryogenic jet, a phenomenological model for the growth rate has been developed. Complete details about the development of this equation are given in Chehroudi et al. (1999). The physical reasoning motivating the equation is outlined below.It was noticed that previous expressions for the growth rate of liquid sprays and of turbulent jets have a remarkably similar form. Reitz and Bracco (1979) proposed that the growth rate of an isothermal steady liquid spray could be expressed as

$$\theta \approx 0.27[0 + (\rho_g/\rho_l)^{0.5}].$$

The first term in the bracket is the number zero to contrast with other equations discussed next. Similarly, Papamoschou and Roshko (1988) suggested the following form for incompressible, but variable-density, turbulent gaseous jets:

$$\theta = 0.212[1 + (\rho_g/\rho_l)^{0.5}].$$

The similarity in the form of these equations suggests the potential for a link between the two. Imagine a jet that is being injected into a subcritical pressure environment similar to the ones shown in Fig. 2. Clearly there are drops and ligaments, testifying the existence of a surface tension. Also evidence of a phase change is seen. Hence, one appropriate characteristic time of the problem (at subcritical, $P_r < 1$) is the "bulge" formation/separation time (τ_b) on the interface of the turbulent liquid jet. This time characterizes the formation and separation event of bulges from the liquid jet producing isolated ligaments and drops. Tseng et al. (1995) suggest that this time is equal to $(\rho_l L^3/\sigma)^{1/2}$ for the primary breakup of turbulent liquid jets where ρ_l, L, and σ are liquid density, characteristic dimension of turbulent eddy, and surface tension, respectively. The second relevant characteristic time (at subcritical) is the gasification time (τ_g). Here, an estimate of this time is calculated through the so-called D-square law for drops to be equal

to D^2/K where D and K are drop diameter and vaporization constant, respectively. In addition, we also propose the following hypothesis. If the aforementioned characteristic times (calculated for appropriate length scales) are nearly equal in magnitude then the interface bulges are not able to separate as unattached entities from the jet interface to form ligaments and drops because they are gasified as fast as they desire to be detached. Here, this is defined as the onset of the gas-jet like behavior. Therefore, the transition between liquid-like and gas-like behavior would be governed by finding the point at which these time scales are approximately equal. This is suggested by the comb-like structures seen in Fig 2(b).

Using the above physical models, an equation was proposed for the N_2/N_2 system as

$$\theta = 0.27[\tau_b/(\tau_b + \tau_g) + (\rho_g/\rho_l)^{0.5}].$$

In the limit, when $\tau_g \gg \tau_b$ and $\tau_g \to \infty$, this equation collapses to the isothermal liquid spray case. This equation agrees well with the current data at subcritical pressures for $\tau_b/(\tau_b + \tau_g) < 0.5$. A constant value of 0.5 was used to predict the spreading rate for higher pressures, including supercritical pressures.

For injection of N_2 into N_2, the characteristic time ratio, $\tau_b/(\tau_b + \tau_g)$, was calculated from experimental measurements of bulge and droplet sizes and calculations of the relevant properties. For N_2 injection into other gases, however, reliable information about the mixture properties at the interface, particularly the surface tension, prevents such a calculation from being performed. To model these cases, it is hypothesized that the characteristic time ratio is a dominant function of the density ratio, i.e. $\tau_b/(\tau_b + \tau_g) = F(\rho_g/\rho_l)$. Brown and Roshko (1974), indicate that this hypothesis is reasonable because at low Mach numbers there is no distinction between mixing layers where the two streams have different molecular weights, temperatures, or compressibility effects. Measurements and calculations of $\tau_b/(\tau_b + \tau_g)$ provides the shape of the function F for the N_2/N_2 system and is provided as a plot in Chehroudi et al. (1999). A curve fit of that plot gives

$$F(\rho_g/\rho_l) = 5.325(\rho_g/\rho_l) + 0.0288 \quad \rho_g/\rho_l < 0.0885$$
$$= 0.5 \quad \rho_g/\rho_l \geqslant 0.0885$$

It was found that the same function, F, calculated from measurements of the N_2/N_2 system could be made to work for other cases, provided that a case-dependant transformation was made to the density ratio at which F is evaluated. The final form of the equation thus arrived at is

$$\theta = 0.27[F(x(\rho_g/\rho_l)) + (\rho_g/\rho_l)^{0.5}],$$

where, $x = 1.0$ for N_2-into-N_2, $x = 0.2$ for N_2-into-He, and $x = 1.2$ for N_2-into-Ar.

In other words, the same functional form of the characteristic time ratio, $\tau_b/(\tau_b + \tau_g) = F(\rho_g/\rho_l)$, for the N_2 -into-N_2 case is used but with a density-ratio coordinate transformation. The quality of the agreement with experimental data is demonstrated in Fig. 5. Hence there are no major changes in the form of the proposed

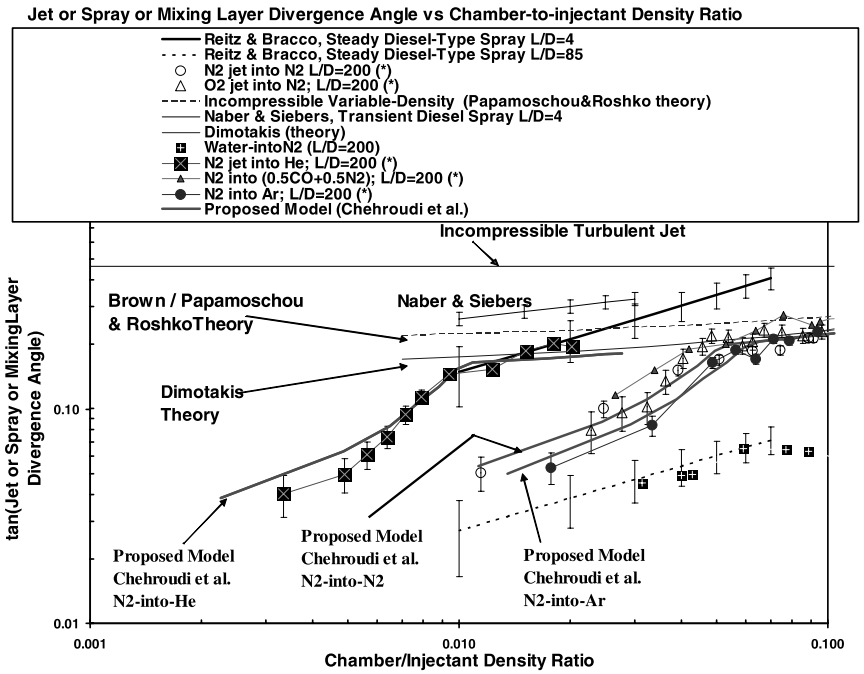

Fig. 5. Comparison of the proposed growth rate model by Chehroudi et al. (1999) with experimental data.

model equation even for as extreme of an arrangement as injection of N_2 into He. However, an observation is made here. The factor $x = 0.2$ in the N_2-into-He case is comparable to the molecular weight ratio of He to N_2 of 0.14, while the factor $x = 1.2$ in the N_2-into-Ar case is comparable to the molecular weight ratio of 1.42. This also suggests the dominant effect of the density ratio parameter between the cases.

7. Raman scattering measurements

In addition to the line-of-sight shadowgraph images from which the preceeding results have been acquired, spontanenous Raman scattering has also been used to obtain spatially-resolved measurements of the density distribution within the cryogenic jet. Raman scattered light results from an inelastic collision between light photons and molecules. Since the process is inelastic, the incident beam will be shifted a fixed amount dependent upon the structure of the molecule. Generally, the intensity of the Raman scattered signal yields information on the number density of the gas being examined. The Raman spectra are obtained by irradiating a sample with a powerful visible monchromatic source. The scattered signal is usually observed at 90° to the incident beam with a suitable visible-region detector or spectrometer. The scattered radiation does not exceed 0.001% of the source, as a result detection and measurement is difficult except for the resonant Raman. The scattered light is of three types, Stokes, anti-Stokes, and Rayleigh. Rayleigh, which has exactly the same frequency as the excitation source, is substantially more intense than either two. Stokes peak lines are found at wavelengths larger (lower energies) than the Rayleigh peak while anti-Stokes are at smaller (higher energies) than the wavelength of the source. It is critical to realize that the magnitude of the Raman shifts are independent of the wavelength of excitation source. A more detailed description of these experiments and Raman effect can be found in Chehroudi et al. (2000).

Fig. 6 shows typical averaged raw images of the LN_2 jet at sub- and supercritical conditions. The Raman intensity profile for the subcritical case is larger in magnitude at the center of the jet and is narrower in shape than the corresponding image of the supercritical jet. The observed Raman intensity radial profile broadening prevented us from using the jet thickness definition proposed by Brown and Roshko (1974) based on the 1% free stream density point on the radial profiles. Instead, the full-width of the radial profiles measured where the intensity increment was half the maximum (Full-Width-Half-Maximum, FWHM) appeared a safer parameter for comparison with other results. Also, it is not known if density values can be measured to within 1% accuracy. Nevertheless, Brown and Roshko (1974) reported that

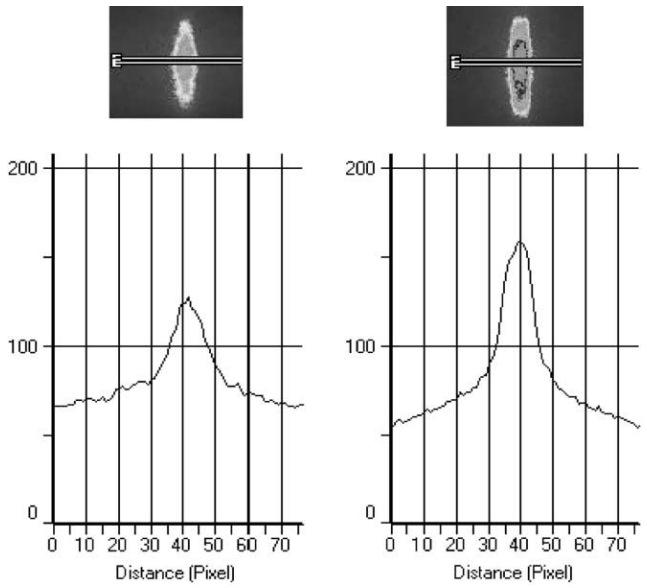

Fig. 6. Averaged Raman images of LN_2 jet (flowing downward) at sub- and super-critical chamber conditions. Raman intensity radial profiles (radial direction is quantified by pixels) are also shown. Left: Chamber pressure of 6.9 MPa (supercritical); right: chamber pressure of 1.46 MPa (subcritical).

their 1% thickness definition corresponded fairly well with the extent of the mixing visible on the shadowgraph pictures. The FWHM was extracted from the measured Raman data, and the spreading rate thus measured was compared with the spreading rate measured from the shadowgraph visualizations. The results are plotted in Fig. 7. It was found that the spreading rate measured at twice the FWHM values of the Raman data agreed well with the shadowgraph measurements. Thus the correspondence of the two different techniques of measuring the width of the jet was established.

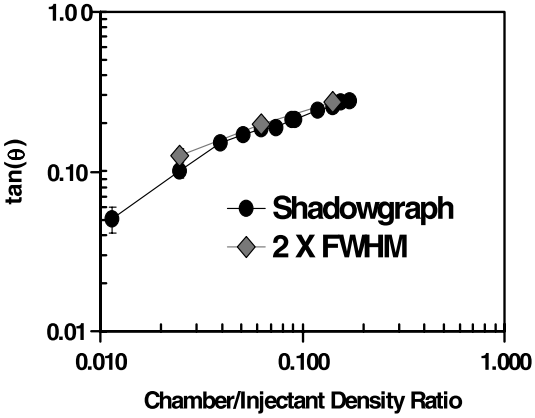

Fig. 7. Comparison of the tangent of the spreading angle measured using shadowgraph and Raman techniques using twice the FWHM values.

8. Summary and conclusions

The structure and initial growth rate of cryogenic jets injected into an ambient with a pressure which ranged from subcritical to supercritical have been studied at AFRL. At subcritical pressures, comparison of shadowgraph measurements show that the jets have the appearance of a conventional liquid spray. As pressure is increased beyond the injected fluid critical pressure, the structure of the jet changes. Under these conditions, the cryogenic jets have the appearance of turbulent gaseous jets. Quantitative agreement of the jet initial growth rate measurements with those predicted by the theoretical equations and measurements for incompressible variable-density gaseous jets has been shown for the first time. Also, for the first time, a unique plot has been generated through conversion of all growth rate types to the "visual" growth rate using the most relevant works reported by other researchers on variable-density incompressible mixing layers, axisymmetric incompressible and compressible gas jets, supersonic jets/mixing layers, and liquid sprays. The resulting plot of spreading angle as a function of density ratio spans four orders of magnitude in density ratio.

A physically-based phenomenological model was developed which proposes a mechanism governed by the characteristic gasification times and interfacial turbulent bulge formation times to predict the measured growth rate behavior. Spontaneous Raman scattering measurements of the density have been used to confirm the earlier shadowgraph measurements. Growth rate measurements derived from the Raman measurements at twice the FWHM distance correspond very closely to the growth rate derived from the shadowgraph measurements.

Acknowledgements

Mr. Mike Griggs and Mr. Earl Thomas are thanked for their valuable support. Mr. Paul Loftsgard is thanked for his assistance in part of the data acquisition/processing and fractal analysis work. This work is sponsored by the Air Force Office of Scientific Research under Dr. Mitat Birkan, program manager.

References

Anderson, T.J., Woodward, R.D., Winter, M. 1995. Oxygen Concentration Measurements in a High Pressure Environment Using Raman Imaging, AIAA Paper 95-0140, 33rd Aerospace Sciences Meeting and Exhibit, January 9–12, Reno, NV, 1995.

Brown, G., Roshko, A., 1974. On density effects and large structure in turbulent mixing layers. J. Fluid Mech. 64 (4), 775–816.

Bruno, T.J., Ely, J.F., 1991. Supercritical fluid technology: review in modern theory and applications. CRC Press, Boca Raton.

Chehroudi, B.R., Cohn, R., Talley, D., Badakhshan, A. 2000. Raman scattering measurements in the initial region of sub- and supercritical jets. AIAA Paper 2000-3392.

Chehroudi, B., Talley, D.G., Coy, E.B., 2002. Visual characteristics and initial growth rates of round cryogenic jets at subcritical and supercritical pressures. Phys. Fluids 14 (2), 850–861.

Chehroudi, B., Talley, D.G., Coy, E.B. 1999. Fractal geometry and growth rate of cryogenic jets near critical point. AIAA paper 99-2489.

Chen, C.J., Rodi, W., 1980. Vertical turbulent buoyant jets—a review of experimental data. Pergamon, New York.

Decker, M.C., Schik, A., Meier, U.E., Stricker, R.W., 1998. Quantitative raman imaging investigations of mixing phenomena in high pressure cryogenic jets. Appl. Opt. 37, 5620–5627.

Dimotakis, P.E., 1986. Two-dimensional shear-layer entrainment. AIAA J. 21 (11), 1791–1796.

Dimotakis, P.E., Miake-Lye, W.G., Papantoniou, D.A., 1983. Phys. Fluids 26, 3185.

Mandelbrot, B.B., 1983. The Fractal Geometry of Nature. W.H. Freeman and Company, San Francisco.

Mayer, W., Schik, A., Schweitzer, C., Schaffler, M. 1996. Injection and mixing processes in high pressure LOX/GH2 rocket combustors, AIAA Paper no. 96-2620, 32nd AIAA/ASME/SAE/ASEE Joint Propulsion Conference & Exhibit, Lake Buena Vista, Florida.

Mayer, W., Ivancic, A., Schik, A., Hornung, U. 1998. Propellant atomization in LOX/GH2 rocket combustors, AIAA Paper no. 98-3685, 34 the AIAA/ASME/SAE/ASEE Joint Propulsion Conference & Exhibit, Cleveland, Ohio, July 13–15.

Naber, J.D., Siebers, D.L. 1996. Effects of gas density and vaporization on penetration and dispersion of diesel sprays, SAE Paper no. 960034.

Newman, J.A., Brzustowski, 1971. Behavior of a liquid jet near the thermodynamic critical region. AIAA J. 9 (8), 1595–1602.

Oschwald, M., Schik, A., 1999. Supercritical nitrogen free jet investigated by spontaneous Raman scattering. Exp. Fluids 27, 497–506.

Oschwald, M., Schik, A., Klar, M., Mayer, W. 1999. Investigation of Coaxial LN2/GH2-Injection at Supercritical Pressure by Spontaneous Raman Scattering, 35th AIAA/ASME/SAE/ASEE Joint Propulsion Conference and Exhibit, Los Angeles, CA, 20–24 June.

Papamoschou, D., Roshko, A., 1988. The compressible turbulent shear layer: an experimental study. J. Fluid Mech. 197, 453–477.

Papanicolaou, P.N., List, E.J., 1988. Investigations of round vertical turbulent buoyant jets. J. Fluid Mech. 195, 341–391.

Peitgen, H.-O., Hartmut, J., Dietmar, S., 1992. Fractals for the Classroom, Part one Introduction to Fractals and Chaos. Springer-Verlag New York Inc, New York.

Reitz, R.D., Bracco, F.V. 1979. On the dependence of spray angle and other spray parameters on nozzle design and operating condition, SAE Paper no. 790494.

Sreenivasan, K.R., Meneveau, C., 1986. The fractal facets of turbulence. J. Fluid Mech. 173, 357–386.

Taylor, J.J., Hoyte, J.W., 1983. Water jet photography-technique and methods. Exp. Fluids 1, 113–120.

Tseng, L.-K., Ruff, G.A., Wu, P.-K., Faeth, G.M. 1995. Continuous- and dispersed-phase structure of pressure-atomized sprays. Progress in Astronautics and Aeronautics: Recent Advances in Spray Combustion, February, 1995.

Woodward, R.D., Talley, D.G. 1996. Raman imaging of transcritical cryogenic propellants, AIAA paper 96-0468.

APPENDIX N

“Injection of Fluids into Supercritical Environments”

This Page Intentionally Left Blank

Combust. Sci. and Tech., 178: 49–100, 2006

ISSN: 0010-2202 print/1563-521X online
DOI: 10.1080/00102200500292464

Taylor & Francis
Taylor & Francis Group

INJECTION OF FLUIDS INTO SUPERCRITICAL ENVIRONMENTS

M. OSCHWALD*
J. J. SMITH
R. BRANAM
J. HUSSONG
A. SCHIK

German Aerospace Center (DLR), Institute of Space Propulsion, Lampoldshausen, Germany

B. CHEHROUDI

Engineering Research Consultants, Lancaster, Pennsylvania, USA

D. TALLEY

U.S. Air Force Research Laboratory (AFRL), Propulsion Directorate, Edwards Air Force Base, California, USA

This paper summarizes and compares the results of systematic research programs at two independent laboratories regarding the injection of cryogenic liquids at subcritical and supercritical pressures, with application to liquid rocket engines. Both single

Received 27 July 2004; accepted 17 April 2005.

The DLR would like to acknowledge all those who have been involved in the research programs. These people include colleagues at the test bench and technicians who have helped make these studies possible. The last two authors would like to thank Mr. Mike Griggs and Mr. Earl Thomas, and Mr. Mark Wilson for their assistance in machining, setup, and operation of the AFRL facility. Ms. Jennie Paton is also thanked for making literature available in a timely manner. The AFRL part of the work is sponsored by the Air Force Office of Scientific Research under Dr. Mitat Birkan, program Manager.

*Address correspondence to michael.oschwald.dlr.de

jets and coaxial jets have been studied. Cold flow studies provided valuable information without introducing the complexities of combustion. Initial studies utilized a single jet of cryogenic nitrogen injected into a quiescent room temperature nitrogen environment with pressures below and above the thermodynamic critical pressure of the nitrogen. Later, the work was extended to investigate the effects of a co-flowing gas. Parallel to this work, combustion studies with cryogenic propellants were introduced to understand high pressure coaxial injection phenomena with the influence of chemical reaction. Shadowgraphy and spontaneous Raman scattering were used to measure quantities such as growth rates, core lengths, turbulent length scales, fractal dimensions, and jet breakup regimes. It is found that jets injected at supercritical pressures do not atomize as they do at subcritical pressures. Rather, they behave in many respects like variable density turbulent gas jets.

Keywords: propellant injection, sprays, supercritical pressure

INTRODUCTION

In recent years, laboratories at the German Aerospace Center (DLR) and the Air Force Research Laboratory (AFRL) have both conducted independent studies of the injection of cryogenic liquids at subcritical and supercritical pressures, with application to liquid rocket engines. In some instances, the studies involved were similar, allowing conclusions to be drawn regarding the degree to which the results at each laboratory corroborate each other. In other instances, studies at one laboratory extended beyond what was done at the other, allowing a breadth of scope which would not have been possible at either laboratory by itself. The purpose of this joint paper is to consolidate and compare the findings of both laboratories to date in a single place.

In what follows, background material regarding high pressure combustion in liquid rocket engines and thermophysical properties is provided in order to be better able to interpret the results to be presented subsequently. Following that, descriptions of the test benches and optical diagnostics are given, again in sufficient detail to be able to interpret the results to be presented subsequently. Next, results pertaining simple round jets are systematically presented, followed by a systematic extension to more complex coaxial jets more representative of liquid rocket engine injectors. Emphasis is placed throughout on the change in phenomenology of the jets as pressure is increased from subcritical to supercritical values. A summary and conclusions section completes the paper.

Table 1. Combustion chamber pressure of LOX/H_2 engines in units of the critical pressure of oxygen

Combustor	SSME	LE-7A	Vulcain	Vinci
P/Pc	4.4	2.40	2.28	1.19

High-Pressure Combustion in Liquid Rocket Engines

By a simple thermodynamic analysis of a liquid rocket engine thrust chamber, it can be shown that higher chamber pressures allow a higher specific impulse for the engine to be produced. Higher chamber pressures similarly increase the power output and efficiency of gas turbines and diesel engines. This has motivated a general trend towards increasingly higher chamber pressures in propulsion applications. However, at higher pressures, the injected propellant can and often does find itself near or above the thermodynamic critical pressure. Table 1 shows the chamber pressures of several current liquid rocket engines which use liquid oxygen (LOX) and hydrogen as propellants, including the Space Shuttle Main Engine (SSME) and the Vulcain engine which powers the Ariane 5 launch vehicle. The chamber pressures are shown relative to the critical pressure of oxygen. It can be seen that all of the chamber pressures are supercritical relative to oxygen. Table 2 gives the critical properties of several relevant fluids.

In rocket applications, fluids injected into a supercritical ambient pressure often possess a subcritical initial temperature. The jet is then heated up beyond its critical temperature as it mixes and burns in the combustion chamber, a process which has sometimes been called ''transcritical'' injection. Prior to the systematic investigations started by the DLR and AFRL laboratories, little reliable information existed on how jet behavior may change as the pressure is increased from a subcritical to a supercritical value. The main objective of these investigations was to provide a better understanding of atomization, mixing, flow dynamics,

Table 2. Critical properties of relevant fluids

Critical properties	N_2	He	O_2	H_2
Critical pressure P_{crit} (MPa)	3.4	0.23	5.04	1.28
Critical temperature T_{crit} (K)	126.2	5.2	154.6	32.94

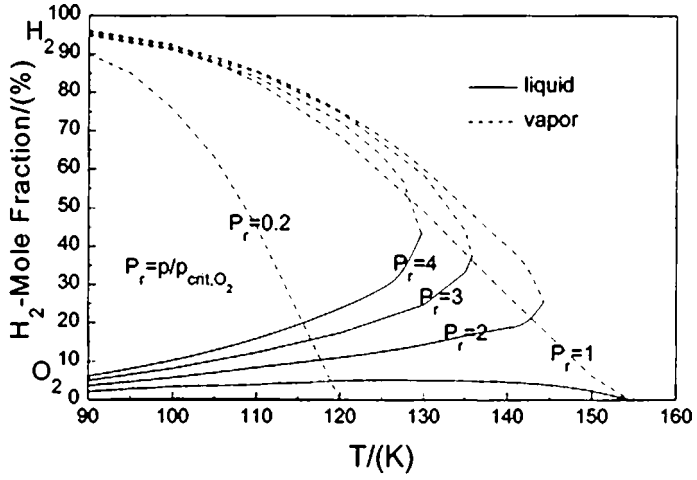

Figure 1. Phase equilibrium of the binary O_2/H_2 system. The concentration of the H_2/O_2 species is also displayed.

and flame stabilization for high pressure subcritical and supercritical jets. It is expected that these will lead to enhanced physical models for an improved design methodology.

Thermophysical Properties and Issues Specific to Transcritical Injection

In this section, the behavior of relevant thermophysical properties is discussed. For coaxial injection of O_2 and H_2 in a liquid rocket engine, the oxygen is typically injected at a cold, subcritical temperature, with a liquid-like density through the center post, while the hydrogen, which is typically used to first cool the engine nozzle, is injected at a warm, supercritical temperature with a gas-like density in the annular passage. The propellants then mix and burn in the resulting shear layer. Under these conditions, caution must be used when referring to the thermodynamic state of the fluids. At elevated pressures, the solubility of the gas in the liquid can be substantially increased, and it becomes necessary to consider the critical properties of a mixture. A single critical "point" then no longer exists; instead, critical mixing lines define the thermodynamic state. In general, the critical properties of a mixture shift relative to the critical properties of any of its constituents.

The phase diagram for the binary H_2/O_2-system is shown in Figure 1. For a given reduced pressure $P_r = P_{ch}/P_{crit_{O_2}}$, there is a critical mixing temperature above which the mixture is in a supercritical state. Below the critical mixing temperature, a binary system separates into liquid and gaseous phases. At a given temperature, the two phases are identified by the dashed and solid lines for the gaseous and liquid components, respectively. As seen in Figure 1, the solubility of H_2 in the liquid O_2 increases with an increase in temperature, whereas the amount of the hydrogen in the gaseous phase mixture decreases (see the dashed curve). At the critical mixing temperature, the mole fractions of each species in the gaseous and liquid phases are identical, the phase boundary disappears, and a supercritical condition exists.

Figure 2 shows the critical mixing temperature as a function of pressure for the various binary systems of interest. Below the critical mixing temperature, phase equilibrium between the liquid and gas exists. Above this temperature, the mixture exhibits supercritical behavior. The general trend is that the critical mixing temperature decreases with increasing pressure.

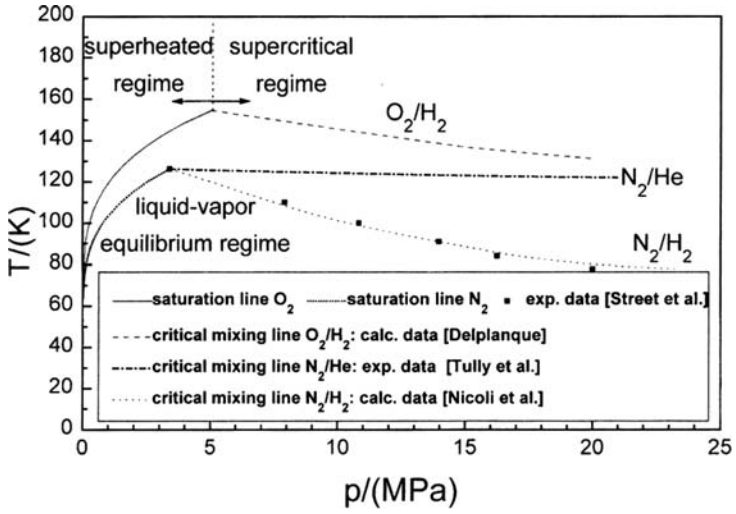

Figure 2. Critical mixing lines for binary O_2/H_2, N_2/He, and N_2/H_2-systems. Data are from Delplanque and Sirignano (1993), Nicoli et al. (1996), Street and Calado (1978), and Tully et al. (1970).

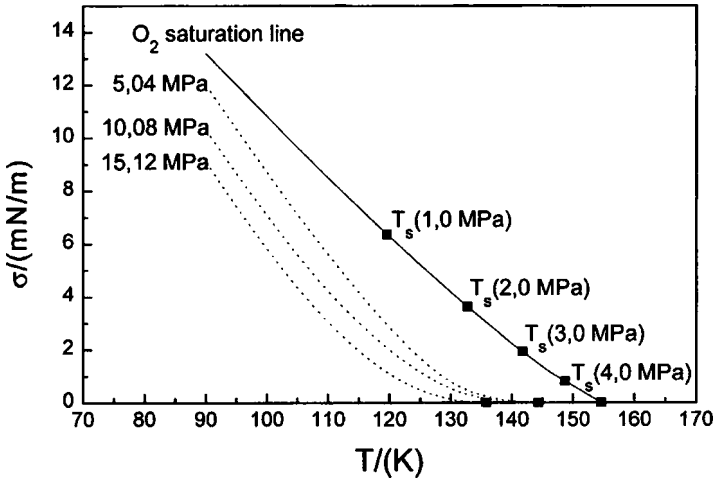

Figure 3. Phase equilibrium of the O_2/H_2 binary system. The solid line is for pure oxygen and the dashed lines are for binary mixtures.

The surface tension of a binary H_2/O_2 mixture has been computed using the Macleod-Sugdon correlation (see Tully et al., 1970 and Macleod, 1923), and is shown in Figure 3. The results indicate that at pressures above the critical pressure of pure O_2, surface tension may still be present in the binary H_2/O_2 system, as long as the temperature remains below the critical mixing temperature. This is of course consistent with the fact that the phase diagram in Figure 1 predicts two phases for these conditions.

At pressures near the critical pressure, fluid properties become very sensitive to changes in temperature. The variation of density as a function of temperature is shown in Figure 4 for pure nitrogen at a pressure of 4 MPa, which is a little greater than the critical pressure (3.4 MPa) of nitrogen. At a temperature of 129 K, the density of the nitrogen varies by up to 21% per degree Kelvin. The specific heat is also shown in Figure 4 to increase precipitously by nearly an order of magnitude as temperature increases, reaching a distinct maximum at a temperature of 129.5 K in this example, and then it decreases again equally as precipitously. The temperature at which the specific heat reaches a maximum will be designated her as T^*. When the pressure is equal to the critical pressure, the temperature T^* is equal to the critical temperature, and the specific heat becomes infinite. At pressures greater than the critical pressure, the

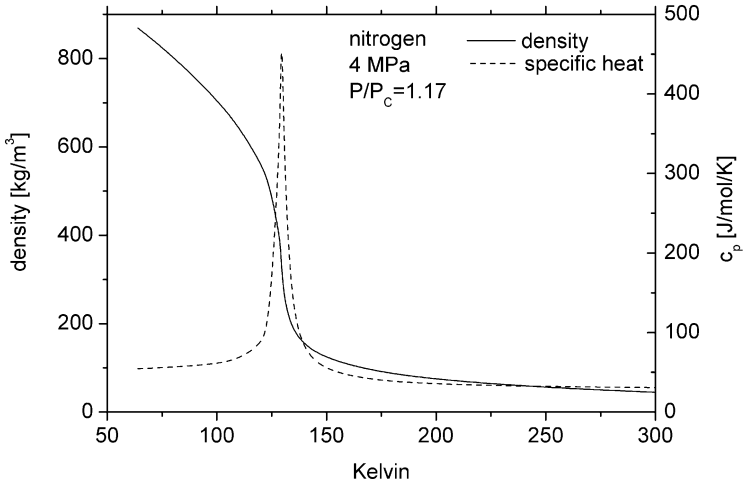

Figure 4. Density and specific heat of N_2 in the region near the critical point. The specific heat reaches a maximum at $T^* = 129.5\,K$.

specific heat can no longer become infinite, but a maximum is still reached. Near the critical pressure, the maximum can be quite pronounced, as it is in Figure 4, but reduces in significance as pressure increases. A plot of T^* as a function of pressure is shown as the dashed line in Figure 5. Also plotted as a solid line in Figure 5 is the two-phase coexistence line at lower pressures. The dashed (T^*, P) curve is seen to form a continuation of the solid two phase coexistence line; for this and other reasons to be discussed later it is called here the "pseudo-boiling" line. Also shown in Figure 5 is a contour plot of the thermal diffusivity. It can be seen that when the temperature is equal to T^*, where the specific heat is at its maximum, the thermal diffusivity reaches a distinct minimum. Variations such as these have distinct consequences for the transport of species and energy, as results will illustrate further later.

TEST BENCHES AND EXPERIMENTAL SETUPS

Both laboratories utilized specially designed, high pressure facilities for their studies, sharing a common goal. Studies at AFRL have focused mainly on nonreacting flows, at a physical scale much smaller than the DLR nonreacting flow studies. Studies at DLR have also included reacting flows. Details of each facility can be found in the respective authors' previous publications, many of which are listed in the extensive

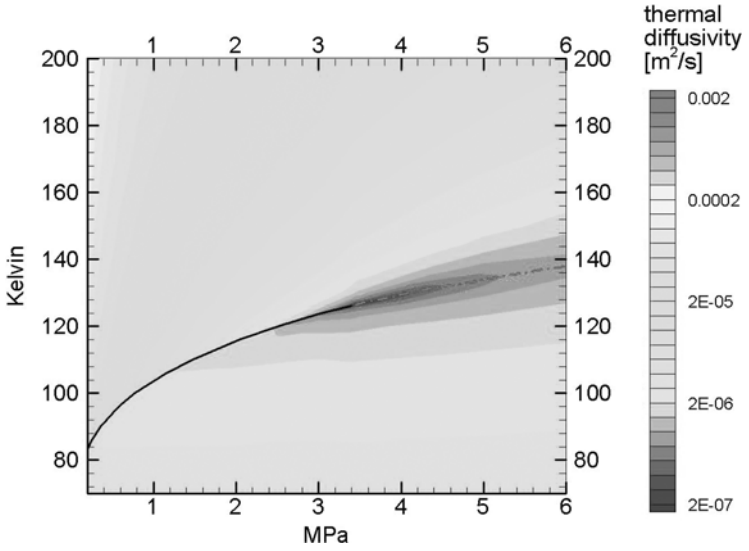

Figure 5. Thermal diffusivity of N_2 in the region near the critical point. The solid line is the two-phase coexistence line. The dashed line is the pseudo-boiling line, or T^* as a function of pressure (See Color Plate 1 at the end of this issue).

references provided at the end of this paper (Branam and Mayer, 2003; Chehroudi et al. 1999a, 1999b, 2000, 2002a, 2002b, 2003; Chehroudi and Talley, 2004); Davis and Chehroudi (2004); Decker et al. (1998); Mayer et al. (Mayer and Tamura, 1996; Mayer et al., 1996, 1998a, 1998b, 2001, 2003); Oschwald et al. (1999, 1999; Oschwald and Micci, 2002). However, adequate information regarding the facility, injector geometries, and diagnostics used is necessary in order to better understand the results presented here and to make this paper reasonably self-sufficient and complete. Therefore a brief description of the facilities is given next.

AFRL Test Bench

Figure 6 shows a schematic diagram of the test bench at AFRL. The stainless steel chamber can withstand pressures and temperatures of up to 20 MPa and 473 K, respectively. It has two facing circular sapphire windows for optical diagnostics. Liquid N_2 is used to cool and/or liquefy the injectant passing through a cryogenic cooler (heat exchanger) prior to injection. The mass flow rate of the injectant is measured and regulated

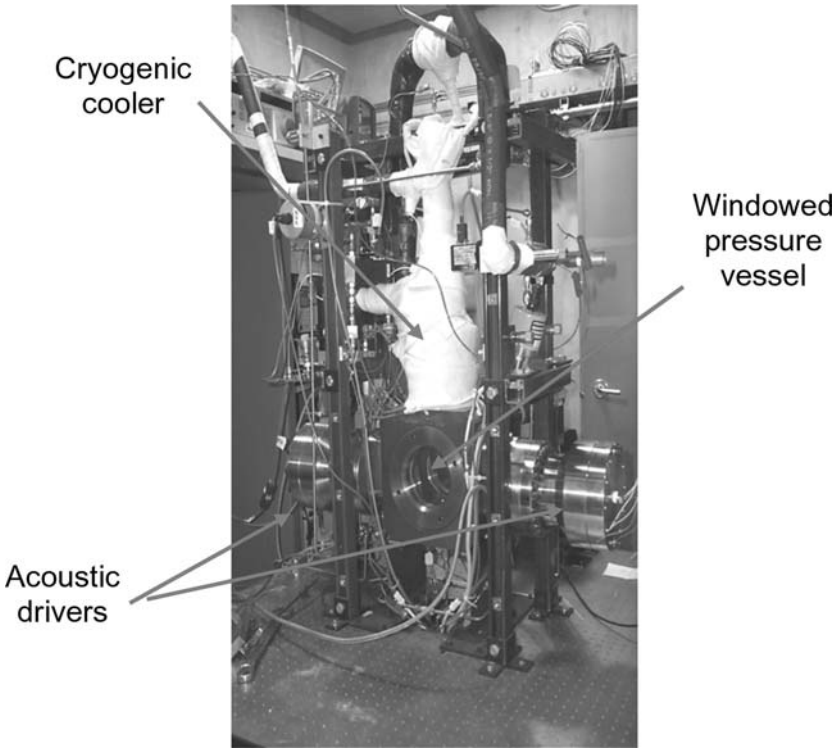

Figure 6. Test bench at AFRL.

via a mass flowmeter and a precision micrometer valve. Back-illumination of the jet is accomplished with diffuse light flashes (0.8 μs duration). A model K2 Infinity long distance microscope is used with a high resolution (1280(H) × 1024(V) pixels in an 8.6(H) × 6.9(V) mm actual sensing area with a pixel size of 6.7 μm × 6.7μm) CCD camera by the Cooke Corporation to form images of the injected jets. The injection for the single jet studies was through a sharp-edged 50 mm long stainless steel tube with a 1.59 mm ($1/16''$) outer diameter and a 254 micron ($0.010''$) inner diameter, resulting in a length-to-diameter ratio of 200. With the Reynolds number ranging from 25,000 to 70,000, the entrance length of 50 to 100 is needed for fully-developed turbulent flow (see Schlichting, 1979). The length is therefore long enough to ensure fully-developed turbulent pipe flow at the exit. For the coaxial injector, the cryogenic jet is injected through a sharp-edged stainless steel tube having a length L of 50 mm,

and inner and outer diameters measuring $d_i = 0.508$ mm and $d_o = 1.59$ mm, respectively. The resulting L/d_i was 100, which is also sufficient to ensure fully-developed turbulent pipe flow at the exit plane. The Reynolds number in these studies ranged from 6,000 to 30,000. The outer tube had an inner diameter of 2.286 mm, forming a gaseous fluid annular passage of 0.348 mm in the radial direction. The bench is fully instrumented to measure pressure, temperature, and mass flow rate of the injected fluid. A specially designed piezo-siren by Hersh Acoustical Engineering, Inc., capable of producing sound pressure levels (SPL) of up to 180 dB in an impedance tube at its resonant frequencies (lying between 1000 to 8000 Hz) and at pressures up to 13 MPa was used with a circular-to-rectangular transition coupling to bring the acoustic waves into the interaction zone inside the chamber. A model 601B1 Kistler piezoelectric-type pressure transducer was used to measure the acoustic pressure variations inside the chamber at various pressures very near the jet location. The piezo-siren acoustic driver was able to generate between 161 to 171 db when coupled with the high-pressure chamber.

DLR Cryo-Injector Test Bench

The cryo-injector test bench at DLR is designed for experimental investigations of both single and coaxial jets at background pressures up to 6 MPa. With N_2 as a model fluid, this pressure corresponds to a reduced pressure of 1.76. Quartz windows allow the application of qualitative visualization as well as quantitative optical diagnostic techniques (Mayer et al., 2003; Oschwald and Schik, 1999). Two different injectors have been used. In early studies, the diameter of the LN_2 tube was $D = 1.9$ mm, with an L/D of 11.6. Later, in order to ensure fully developed pipe turbulence could be assumed as an initial condition, a new injector was designed with $D = 2.2$ mm diameter and $L/D = 40$. In coaxial injection experiments He as well as H_2 has been used as a annular gaseous co-flow. H_2 is Raman active, and thus the gaseous component of choice for quantitative density measurements based on Raman scattering (Oschwald et al., 1999).

DLR High-Pressure Combustion Test Bench P8

The European test bench P8 is a French/German high-pressure test facility for research and technology investigations at combustion chamber

conditions representative of modern cryogenic rocket engines. See Figure 7. Propellant supply systems (LOX, LH_2 and GH_2) can provide pressures up to 360 bar at the test bench interface to the test specimen. Mass flow rates can be controlled between 200 g/s and 8 kg/s for LOX, 50 g/s and 1.5 kg/s for GH_2, and 200 g/s and 3 kg/s for LH_2, respectively. Further details regarding the test facility P8 can be found in the article of Haberzettl et al. (2000).

The model combustor "C" has been used in the hot fire tests and under supercritical pressures. The modular combustor is equipped with a single coaxial injector head. A module with optical access enables the application of non-intrusive optical diagnostic techniques at pressures as high as 9 MPa. The windows are protected from the thermal loads by hydrogen film cooling at ambient temperature. The H_2 film cooling does not influence the flow or combustion processes at the near injector region, which is the primary area of interest for the studies presented here. As demonstrated during the latest tests, the combustion chamber can be operated with LOX and GH_2 propellants for up to 300 continuously.

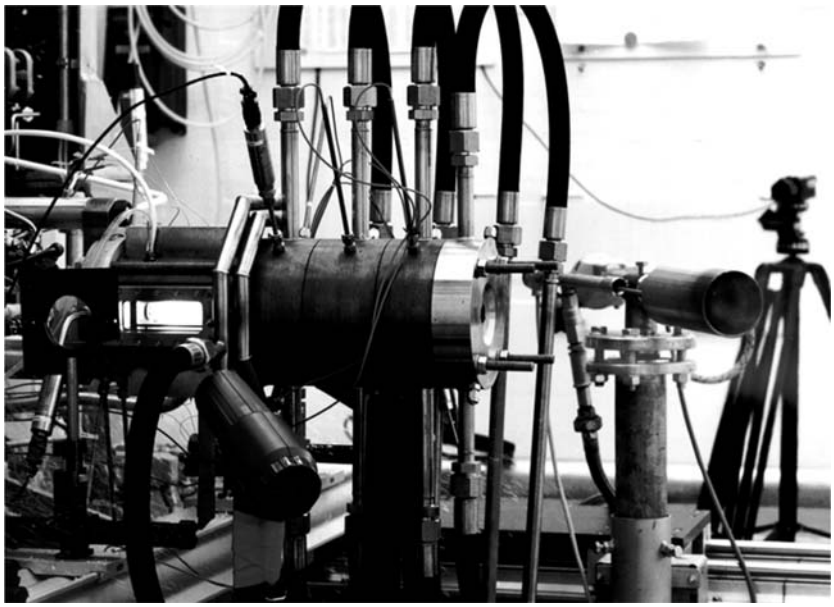

Figure 7. Windowed combustion chamber "C" with module for optical access at test bench P8.

Diagnostic Methods

The large density gradients associated with the cryogenic high pressure flows create a challenging environment for any quantitative optical diagnostics, as they result in large refractive index gradients. Even at supercritical pressures, when surface tension vanishes, the variation of the density field on small length scales is strong enough to cause reflection and refraction of the light beams. An initial evaluation of the effects of the distortion on imaging caused by the refraction showed that it can be neglected for the conditions discussed in this paper (see Oschwald and Schik, 1999). Both laboratories have found shadowgraphy and spontaneous Raman scattering to be the methods of choice for visualization and quantitative measurements.

Shadowgraphy. Although a qualitative, line-of-sight method, shadowgraphy has been shown to be an effective diagnostic tool to investigate single and coaxial jet injection. Due to the huge density gradients of the cryogenic supercritical fluids relative to the background gas, geometrical properties such as the spreading angle and the intact core length are accessible by this method regardless of whether the jet is subcritical or supercritical. Using a short time-exposure light source, more detailed information on features reflecting the interaction of the jet with its environment can be obtained. For instance, geometric properties of the jet surface area and characteristic length scales of the density variations in the mixing layer of the supercritical jet can be revealed.

When applying the shadowgraphy method in high pressure combustion, it is essential to gate the background light originating from the flame emission by short-exposure times. In the tests at the P8 bench at DLR, this has been accomplished by mechanical shutters.

Spontaneous Raman Scattering. When a medium is irradiated, some fraction of the beam is scattered in all directions. If the medium contains particles of molecular dimension, a weak scattered radiation having the same wavelength is observed, called Rayleigh scattering. Raman, in 1928, discovered that the wavelength of a very small fraction of the scattered radiation by certain molecules shifted by an amount dependent upon the chemical structure of the molecules responsible for the scattering. The Raman spectra are obtained by irradiating a sample with a powerful visible monchromatic source. The scattered signal is usually

observed at 90 degrees to the incident beam with a suitable visible-region detector or spectrometer, see Eckbreth (1996).

The scattered radiation is a very small percentage of the source, as a result detection and measurement is difficult except for the resonant Raman that is explained later. The scattered light is of three types, Stokes, anti-Stokes, and Rayleigh. The Rayleigh component has exactly the same frequency as the excitation source and is substantially more intense than either two. Stokes peak lines are found at wavelengths larger (lower energies) than the Rayleigh peak while anti-Stokes are at smaller (higher energies) than the wavelength of the source. It is critical to realize that the magnitude of the Raman shifts are independent of the wavelength of excitation source. Generally, the Stokes lines are more intense than the anti-Stokes and for this reason usually only this part of the spectrum is observed. It is also important to indicate that fluorescence can interfere with detection of the Stokes shifts but not with anti-Stoke shifts. This shift of the lines are specific to the scattering molecule and hence, in multicomponent systems, Raman scattering allows the detection of each individual component. This property of the Raman diagnostics is an important advantage when compared to the visualization techniques such as shadowgraphy when analyzing mixing processes during a two-component coaxial injection.

The Raman signal strength at ambient conditions is proportional to the molecular number density. It is well known that at high densities, the Raman scattering cross-section becomes density dependent due to internal field effects. No reliable quantitative data are yet available for densities of cryogenic N_2 in the critical pressure region. In the experiments presented in this paper, densities have been calculated assuming a pressure independent cross section (Decker et al., 1998; Oschwald and Schik, 1999). In the near injector region, the density gradients are extremely high for most of the injection conditions discussed here. When the excitation laser beam passes through this region, beam steering occurs, which leads to a blurred image in the Raman detection channel.

Two different optical setups were used by the DLR for Raman measurements. A continuous wave (CW) Ar-Ion laser operating at 488 nm has been used by Oschwald and Schik (1999). A data acquisition time of 1 s was necessary to achieve a sufficient signal-to-noise ratio. The use of a CW-laser practically prevents the formation of signal due to stimulated Raman scattering that may interfere with the spontaneous Raman signal.

Using a pulsed XeF excimer laser at 351 nm allows time-resolved single-pulse measurements to be performed (Decker et al., 1998; Mayer et al., 2003). The laser was operated with two independent laser tubes in a double oscillator configuration. The two laser tubes fired with a short delay to reduce the peak intensity of the laser and to increase the total pulse length to about 40 ns in order to avoid gas optical breakdown.

At AFRL, Chehroudi et al. (2000) used a frequency-doubled Nd:Yag pulsed laser (532 nm output wavelength) with a passive pulse stretcher designed to reduce the possibility of plasma formation. The original pulse was extended in time by dividing it into three major pulses, each being 10 ns in duration, but delayed in time by 8 ns and 16 ns. This resulted in a final pulse duration of about 26 ns. The scattered Raman signal was collected at 607 nm.

SINGLE-JET INVESTIGATIONS

In a quest to understand liquid breakup mechanisms for injection at subcritical and supercritical pressures, researchers at DLR and AFRL began working with the simplest and perhaps the most popular and fundamental of all cases, that is, the injection of a single nonreacting round jet into a quiescent environment. The injection of the single jet was studied at various chamber pressures ranging from subcritical to supercritical, and included chamber pressures representative of those experienced in a typical cryogenic liquid rocket engine. For safety reasons it was preferred to simulate liquid oxygen with liquid nitrogen; early studies had confirmed that the injection behavior of these two fluids was similar as long as chemical reactions did not take place. To avoid complications introduced by mixture effects as discussed in section 1.2, many of these studies involved injecting cryogenic liquid nitrogen into room temperature gaseous nitrogen. However, injection into other ambient gases was also investigated.

The results acquired by the groups were interpreted and analyzed both qualitatively and quantitatively. The purpose of this section of the paper is to present key findings by the groups and to highlight the conclusions confirmed independently by each laboratory regarding single jet injection.

Jet Surface

Phenomenology at Subcritical and Supercritical Pressures. Figure 8 shows representative images of cryogenic LN_2 jets injected into ambient

temperature gaseous nitrogen at 300 K. The initial temperature of the jets was measured in separate experiments under identical flow conditions with a small thermocouple. Depending on the flow condition, the measured initial temperature varied from 99 K to 110 K. The bottom row of Figure 8 shows a magnification of the image in the same column on the top row, to more clearly show the shear layer structure. Pressures in the figure are reported as reduced pressures, defined to be the chamber pressure divided by the critical pressure of nitrogen.

In column (a), where the chamber pressure is subcritical, the jet has a classical spray appearance. Consistent with the classical liquid jet breakup regimes described by Reitz and Bracco (1979), surface instabilities grow downstream from the injector, and very fine ligaments and drops are ejected from the jet. This has been confirmed to correspond

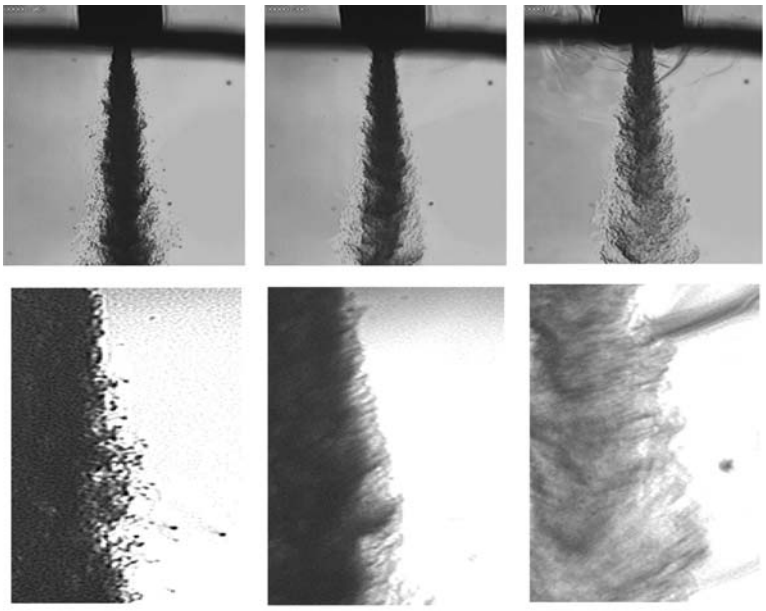

Figure 8. LN_2 injected into ambient temperature nitrogen at three reduced pressures ranging from subcritical to supercritical. The bottom row contains magnified images of the top row.

to the second wind-induced liquid jet breakup regime described by Reitz and Bracco (1979).

Major structural and interfacial changes occur at about $P_r = 1.03$. Above this pressure, drops are no longer detected, and regular finger-like entities are observed at the interface. Rather than breaking up into droplets, the interface dissolves at different distances from the dense core. These structures are illustrated at $P_r = 1.22$ in column (b) of Figure 8. This change in the morphology of the mixing layer is evidently due to the combined effects of the reduction in the surface tension as the critical pressure is exceeded and disappearance of the enthalpy of vaporization because of this transition.

As chamber pressure is further increased, the length and thickness of the dense core decreases, and the jet begins to appear to be similar to a turbulent gaseous jet injected into a gaseous environment. This is illustrated in Figure 8, column (c). Any further droplet production, and consequently, any additional classical liquid atomization, are completely suppressed. These observations were confirmed both at AFRL and DLR; for example, see Mayer et al. (1996, 1998a) and Chehroudi et al. (2002a). As mentioned before, similar results were found when injecting liquid oxygen.

Because of the large density variations in the chamber, it was of interest to establish whether the evolution of the jet within the region of measurement is affected by the buoyancy forces. Therefore, Froude number values were calculated for the AFRL facility at each condition. As an example, Chehroudi et al. (1999a, 2002a) showed that for their experiments the Froude number ranges from 42,000 to 110,000. Chen and Rodi (1980) suggested that the flow is momentum dominated when a defined length scale x_b is less than 0.53, while Papanicolaou and List (1988) suggested $x_b < 1$. The length scale is given by $x_b = Fr^{-1/2}(\rho/\rho_\infty)^{-1/4}\ (x/d)$, where x is the axial distance, d is the initial jet diameter, ρ and ρ_∞ are the jet and ambient densities, respectively. The Froude number is defined as $Fr \equiv \rho U^2/gd|\rho_\infty - \rho|$ where U is the velocity difference, and g is the gravitational acceleration. Considering the more conservative estimate by Chen and Rodi (1980), the jet used by them is momentum dominated for distances less than 30 to 40 mm from the injector exit. Pictures presented in Figure 8 cover up to about 5.5 mm (axial distance/diameter ratio of 21.6) from the injector, and hence buoyancy effects can be ignored in favor of inertial forces. This conclusion applies to all of the quantitative measurements performed at AFRL.

Length Scale Analysis. Disintegration of a single LN_2 jet without an annular co-flow gas has been investigated at DLR at ambient pressures of 4 MPa and 6 MPa, corresponding to a reduced pressure of 1.17 and 1.76, respectively. The initial injection temperature of the nitrogen was near the critical temperature and it was injected into an N_2 environment at a temperature of 298 K. Branam and Mayer (2003) provided a measure of the length scales by analyzing the images taken through the shadowgraphy method and named it the "visible length scale." They isolated the intensity values of any two arbitrarily selected pixels located at a certain distance for 30 to 60 images and then formed the two-point correlation coefficient of these two sets of intensity information. Then, by changing the distance of one of these pixels with respect to the other fixed pixel, they were able to construct a correlation coefficient plot from which a "visible" length scale is calculated. The length scale can be determined through an integration operation, similar to the integral length scale, or by selecting the pixel-to-pixel separation at the 50% correlation value. The latter approach was selected for this particular analysis due to speed and ease of implementation, accepting a certain level of inaccuracy.

Both axial and radial length scales were determined in this manner. Figure 9 shows a typical result of the geometrically-averaged length scale (average of radial and axial length scales) measured at an x/D of 10 as a function of the radial position. Results from a k-ε computational method are also shown (see section 3.3.2). This suggests that the visible length

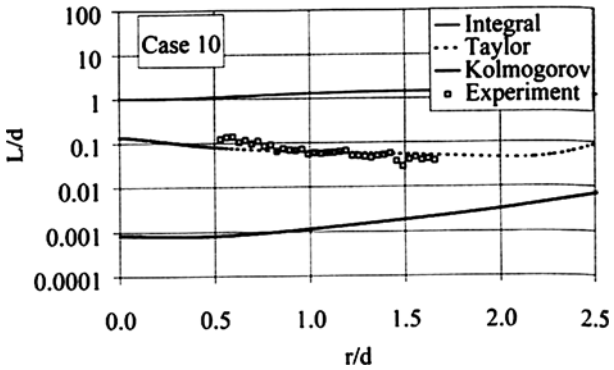

Figure 9. Comparison between calculated and experimental length scales L_{int}, L_{Kol}, L_{Tay} at $x/d = 10$, 6 MPa, 1.9 m/s, T = 132 K.

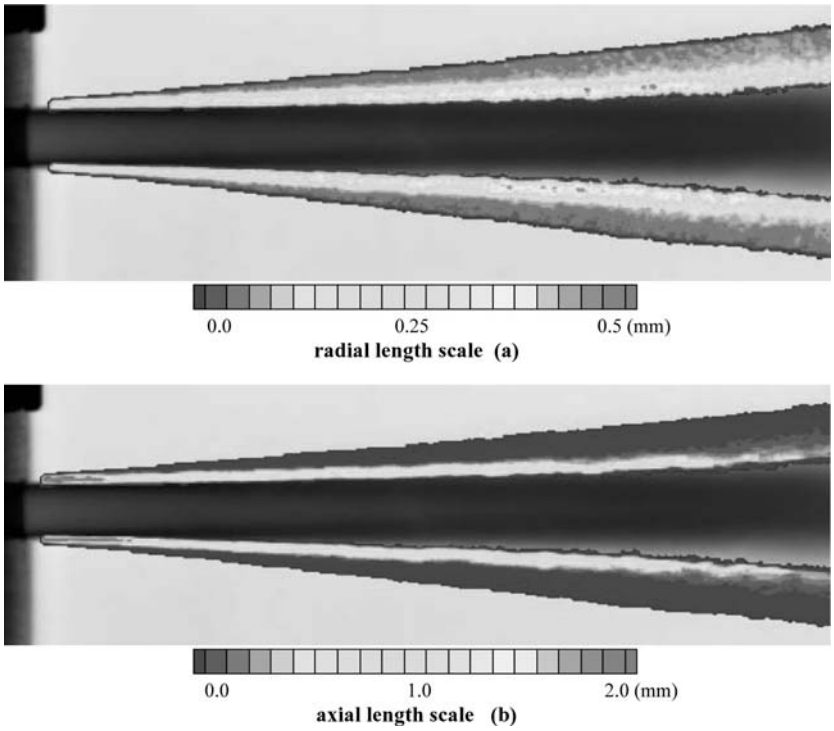

Figure 10. Experimental length scales for LN_2 into GN_2, 4 MPa, 123 K (See Color Plate 2 at the end of this issue).

scale is comparable in magnitude to the Taylor length scale as determined by the computational method.

The ratio of the axial to the radial length scales expresses whether the visible structures are spherical or more ellipsoidal. Both length scales are shown in Figure 10 for an injection temperature of 123 K; i.e., injection of N_2 at a high density. In the near injector region, the axial length scales are much larger than the radial ones. Further downstream the visible structures become more circular in shape. At a higher injection temperature (132 K), the asymmetry between the L_{rad} and L_{ax} is not as pronounced as that seen under lower temperature conditions (123 K).

Fractal Analysis

Fractals are intimately connected to the concept of self-similarity (see Mandelbrot, 1983). In essence, a similarity transformation involves

one or a combination of multiplication by a scale factor, pure translation, and pure rotation. Under such a transformation a geometrical object stays similar to the original or to a preceding stage if repetitively applied. Self-similarity, however, in a strict sense means that if one chooses any point of a geometrical object and locally magnifies, it will look similar to the "whole" object. In nature, however, self-similarity is confined between two sizes (or scales) referred to as inner (the smallest size) and outer cutoffs (the largest size).

The fractal dimension of any curve is between 1 and 2. The more wrinkled and space-filling the curve, the larger the value of the fractal dimension. Natural curves, such as the outline of a cauliflower, are self-similar only to within a narrow range of scales. The objective here is to measure the fractal dimension of the interface of the jets injected into the chamber to see if any pattern is uncovered.

The fractal dimension of jets at various pressures ranging from subcritical to supercritical was calculated and compared to results of other researchers. Reference results were taken from Sreenivasan and Meneveau (1986) who measured the fractal dimensions of a variety of turbulent gaseous jets, mixing layers and boundary layers. These results indicate a fractal dimension between 1.33 and 1.38. In addition, the fractal dimensions of a turbulent water jet (Dimotakis et al., 1986) and of a liquid jet in the second wind-induced atomization regime (Taylor and Hoyt, 1983) were computed from high-resolution scanned images.

The fractal dimensions from the above reference cases are shown as horizontal lines in Figure 11. Overlaid on top of these lines are discrete points indicating the fractal dimension of LN2 jets injected into GN_2 at various chamber pressures. At supercritical chamber pressures, the fractal dimension approaches a value similar to gaseous turbulent jets and mixing layers. As the chamber pressure is decreased, the fractal dimension also decreases. Below $P_r = 0.8$, the fractal dimension rapidly reduces to a value approximately equal to that of a liquid spray in the second wind-induced liquid jet breakup regime.

A more thorough discussion of the above results is found in Chehroudi and Talley (2004). The key conclusion here is that the results from fractal analysis complement and extend the imaging data. At supercritical pressures, jets have a fractal dimension similar to turbulent gas jets, and at subcritical pressures, cryogenic jets have a fractal dimension similar to liquid sprays. The transition occurs at about the same pressure as the transition in visual appearance and growth rate.

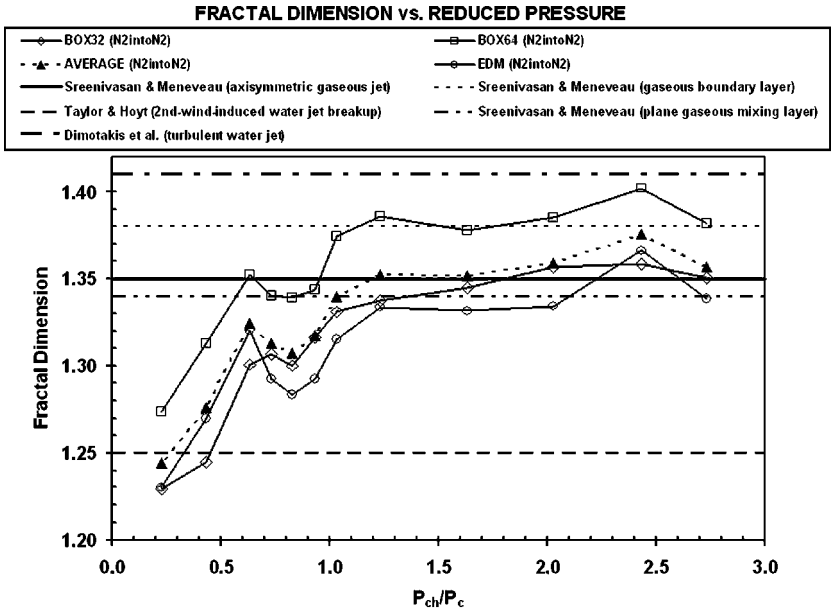

Figure 11. Fractal dimensions of the boundaries of various jets as a function of reduced pressure (chamber pressure divided by the critical pressure of the jet material). Discrete points are data from Chehroudi et al. (1999b). Box32, Box64, and EDM are different methods of calculating the fractal dimension, giving an impression of the extent of variability; for details, see Chehroudi et al. (1999b).

Jet Decay

Visualization of Jet Core Length. According to Abramovich (1963), the length of the potential core in isothermal uniform density axisymmetric and two-dimensional jets is estimated to be about 6 to 10 injector diameters; whereas for non-isothermal cold jets injected into hot environments, it can reach up to about 25 injector diameters depending on jet temperature.

Also, according to Chehroudi et al. (1985) the intact core length of the liquid sprays similar to the ones used in diesel engines is given by $Cd_j(\rho_l/\rho_g)^{1/2}$ where ρ_l and ρ_g are liquid injectant and chamber gas densities respectively, "d_j" is an effective jet exit diameter and C is a constant between 3.3 to 11. This translates to an intact core length between 33 to 110 injector diameters for the chamber-to-injectant density ratio of 0.01 and between 16.5 to 55 diameters for the

chamber-to-injectant density ratio of 0.04. These results are presented in Figures 12 (a) and (b) for better comparison with our current data.

Note that the classical two-stream mixing layer starts from the injector exit to approximately the end of the potential core (or intact core) of the jet. Assuming that the jet dark-core seen in images plays the same role as the intact core or potential core, Figure 12(a) indicates that growth rate data (presented next) taken by Chehroudi et al. (2002a) is from the corresponding and appropriate initial region to ensure existence of a classical mixing layer. It is only then that a valid comparison can be made between these results and the two-stream mixing layers available in the literature.

A complementary result by the DLR researchers is shown in Figure 12 (b). These results were determined through a log-log plot of the centerline intensity measured by Raman scattering to distinguish different flow regions. Note that the horizontal axis for Figures 12(a) and (b) are the inverse of each other. The DLR data are at or below the lower bound of the Chehroudi et al. (1985) model (i.e., solid curves in Figure 12(b)) which was proposed based on the liquid spray data in various atomization regimes. For chamber-to-injectant density ratios of less than 0.1 in Figure 12 (a) (or injectant-to-chamber ratio of greater than 10 in Figure 12 (b)) it appears that the Chehroudi et al. experimental data shown in Figure 12 (a) is larger by about a factor of 1.5 to 2 compared with the ''correlation'' data of Branam and Mayer (2003) in Figure 12(b).

The core length measurements above are currently a point of disagreement between the two laboratories which needs to be investigated further. Considering that the raw data used by the two groups are from two different measurement methodologies (Raman versus shadowgraphy), however, such a result is perhaps not unexpected. In fact, Chehroudi et al. (2000) have also shown such differences when Raman and shadowgraphs were used in the context of growth rate measurements. However, improved techniques with more precise measurements are necessary in order to accurately assess this quantity. This is currently being investigated at AFRL.

Mapping of the Density and Temperature Fields. The main purpose of using Raman scattering measurements was to provide quantitative information and to map out the jet density field. Using this information, temperatures can also be calculated assuming application of a suitable equation of state. Typically, results such as radial density profiles are

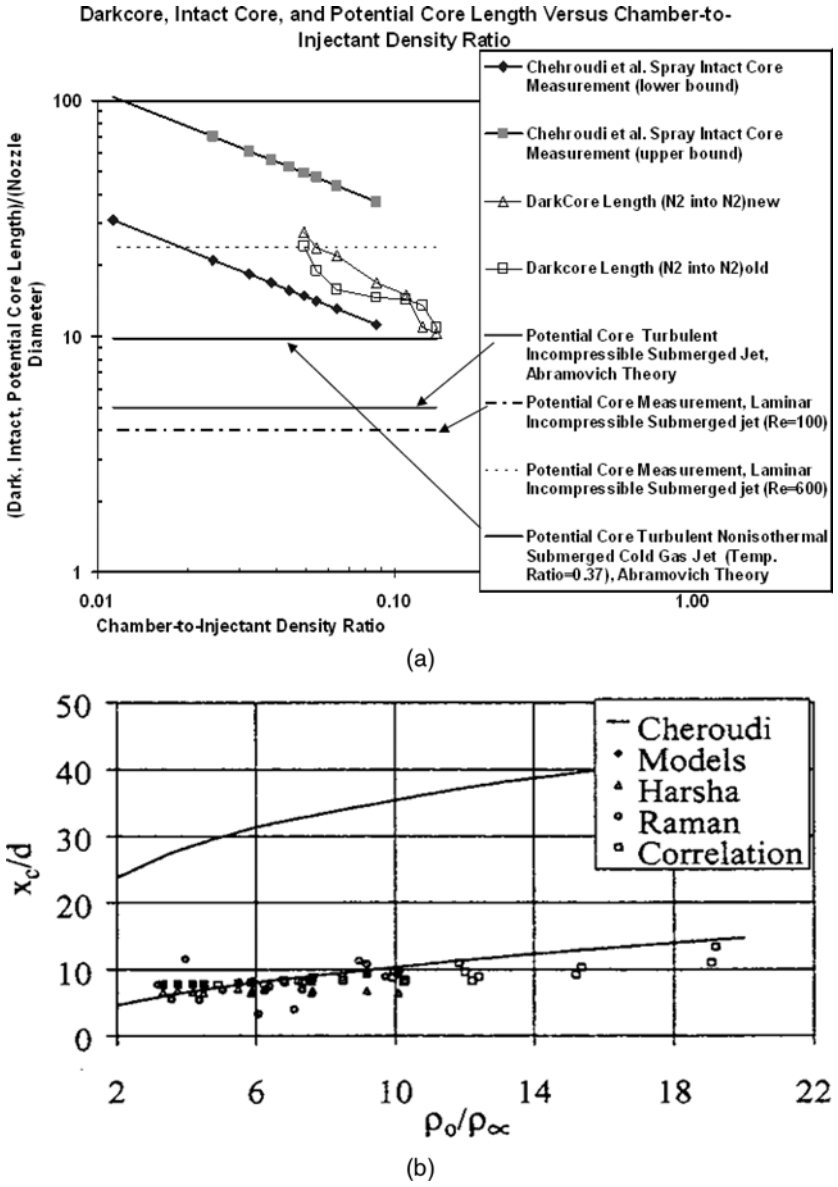

Figure 12. Ratio of either the Dark-core, intact-core, or potential-core length, depending on the case, divided by the density ratio. Case a: Chehroudi et al. (2002a), determined by analysis of shadowgraphs, for an injector $L/D = 200$. Case b: Branam and Mayer (2003), determined via Raman data, injector $L/D = 40$. Models: determined by computer simulation. Correlation: a correlation using a set of Raman data by Branam and Mayer.

presented in an appropriately normalized fashion. In addition to these density profiles, it should be apparent that the growth rate (or spreading angle) of the jet can also be extracted from these data. Growth rate data from these measurements are discussed in the next section. Here the centerline density/temperature profiles as a function of the axial distance from the injector exit plane and the self-similarity assessment are discussed.

The test conditions were chosen in order to assess the influence of the thermodynamic state of the injected cryogenic N_2 on the jet disintegration process. A well known anomaly at the critical point is the singularity of the specific heat at the critical point, as mentioned earlier. Above the critical pressure, the specific heat is finite but exhibits a maximum at a particular temperature (see Figure 4). At this same point, the thermal diffusivity exhibits a minimum. Three test cases were investigated as shown in Figure 13 (a). In test case A, the initial injection temperature is both above the critical temperature and above the temperature where the specific heat is a maximum, whereas for test cases B and C the initial injection temperatures are both below the critical temperature and the temperature where the specific heat is a maximum.

Figures 13 (b) and (c) show normalized centerline profiles of the density and temperature acquired by Oschwald and Schik (1999) at a chamber pressure of 4 MPa (near the critical pressure of nitrogen). Note that the density decay becomes slower as the initial injection temperature is decreased. The temperature profile, however, stays flat for up to a normalized distance (x/D) of about 25 to 30. As pointed out by Oschwald and Micci (2002), the development of the centerline temperature reflects the thermophysical properties of the nitrogen, specific to the region where the specific heat reaches a maximum. For initial injection temperatures below the temperature where the specific heat reaches a maximum, as the jet heats up, the fluid has to pass a state with a maximum specific heat. It can reach a value where a large amount of heat can be stored without any noticeable increase in temperature. It appears that the maximum specific heat line in a supercritical fluid results a behavior similar to a liquid at its boiling point. That is, heat transfer to the nitrogen does not increase its temperature but merely expands the fluid (i.e., increases its specific volume). It is also for this reason that the dashed curves in Figures 5 and 13 (a) are referred to as ''pseudo-boiling lines.'' Note that the density of the fluid varies strongly with temperature in this zone. At 6MPa ($P_r = 1.76$, data not shown), the maximum of the

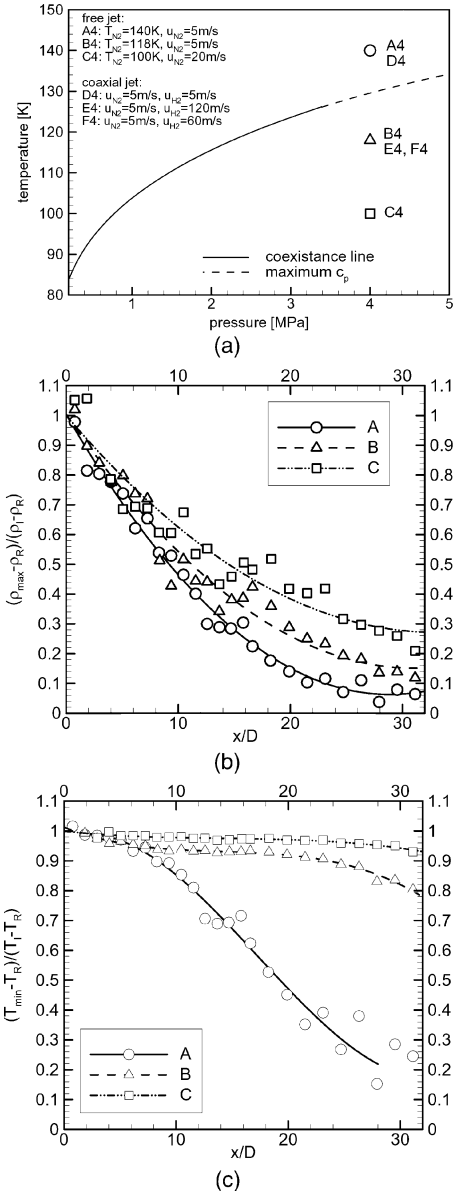

Figure 13. Normalized centerline density (b) and temperature (c) axial profiles of LN_2 injected into GN_2 at three different injection temperatures and a chamber pressure of 4 MPa (i.e., near critical pressure). The plot (a) shows the thermodynamic conditions under which test cases A, B, and C are conducted. The dashed line is the pseudo-boiling line. Note, A4, B4, and C4 symbols represent A, B, and C cases, respectively.

specific heat is much less pronounced and the effects of the pseudo-boiling line is not as distinct as those seen under chamber pressure of 4 MPa. As shown by Oschwald and Schik (1999) however, far downstream, it was observed that the temperature of the disintegrating and mixing supercritical fluid jet approaches a value representative of a fully-mixed jet, but at a slower pace than that for the jet density.

The self-similarity of the density field has also been investigated and the results are presented in Figure 14. According to Wygnanski and Fiedler (1970), a fully self-preserved velocity field of a turbulent air jet should be observed at an x/D of greater than 40 when the Reynolds number is near 100,000. So et al. (1990) reported self-preservation for x/D values larger than about 20 in a binary gas jet at $Re = 4300$. Although it appears that some inconsistencies exist in these criteria, one can see that for the near critical and supercritical pressures, the density radial profile approaches the similarity model curve in Figure 14(a), with the disagreement being the largest at subcritical pressures where the model is the least applicable. Results published by Oschwald and Schik (1999) also indicate similarity-type profiles for x/D values greater than about 10. See examples of the two radial profiles of density from their work shown in Figure 14(b).

Jet Spreading Angles. Measurements and estimations of the growth rate of a jet has been a subject of intense research because it provides a primary measure of mixing and development of the jet. Chehroudi et al. (1999a) were the first to extract quantitative measurements of this physical parameter from the images taken of a cryogenic N_2 jet injected into GN_2 under both subcritical and supercritical pressures. These measurements led to important conclusions regarding the character of the growth rate and the behavior of the jet under such conditions.

The spreading angle or growth rate is measured from a field of view within 5.5 mm from the injector exit plane (distance-to-diameter ratio of up to 21.6) and are inertially dominated as discussed previously. Results presented in Figure 15 were also taken from the corresponding and appropriate initial region to ensure existence of a classical mixing layer. The initial jet spreading angle or its growth rate is measured for all the acquired images, and results along with those of others are presented in Figure 15. Of importance in this figure is the justification for the selection of the data sets and the nature of their measurements by other researchers. They are elaborated in sufficient detail in earlier papers;

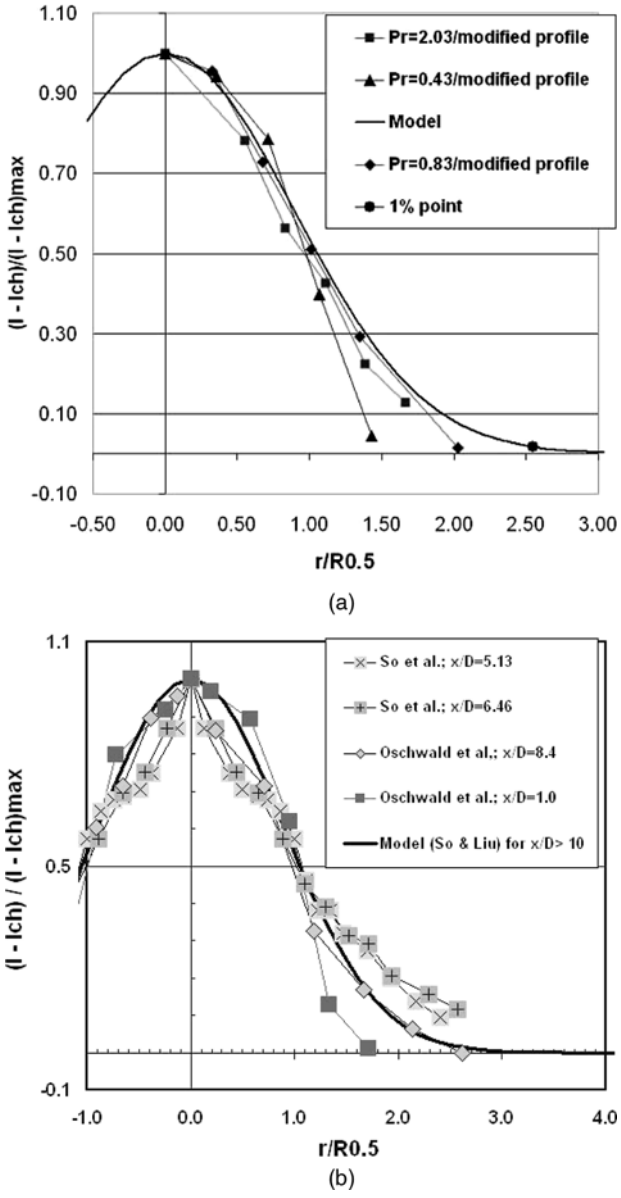

Figure 14. (a) Plots of normalized intensity vs. normalized radius for LN_2 injected into GN_2, at $x/D = 12.2$, at subcritical, near-critical, and supercritical pressures (Chehroudi et al. (2000)). (b) Similar results by Oschwald and Schik (1999), and gaseous jet experimental data by So et al. (1990). The solid curve is the self-similar model that represents data from a gaseous jet injected into a gaseous environment. I and Ich are measured intensities in the jet and in the chamber far away from the jet.

in order to gain a deeper appreciation of these selections see particularly Chehroudi et al. (2002a). Therefore, they are only mentioned here in brief as needed.

Since the jets investigated here exhibit both liquid-like and gas-like appearances, depending on pressure, appropriate comparisons for both liquid sprays and gas jets are presented in Figure 15. The simplest is the prediction of the linear growth or constant spreading angle for the turbulent incompressible submerged jet using the mixing length concept. Following Abramovich (1963), a semi-empirical equation is used that attempts to incorporate the effects of density variations by an introduction of a characteristic velocity (see Chehroudi et al., 2002a).

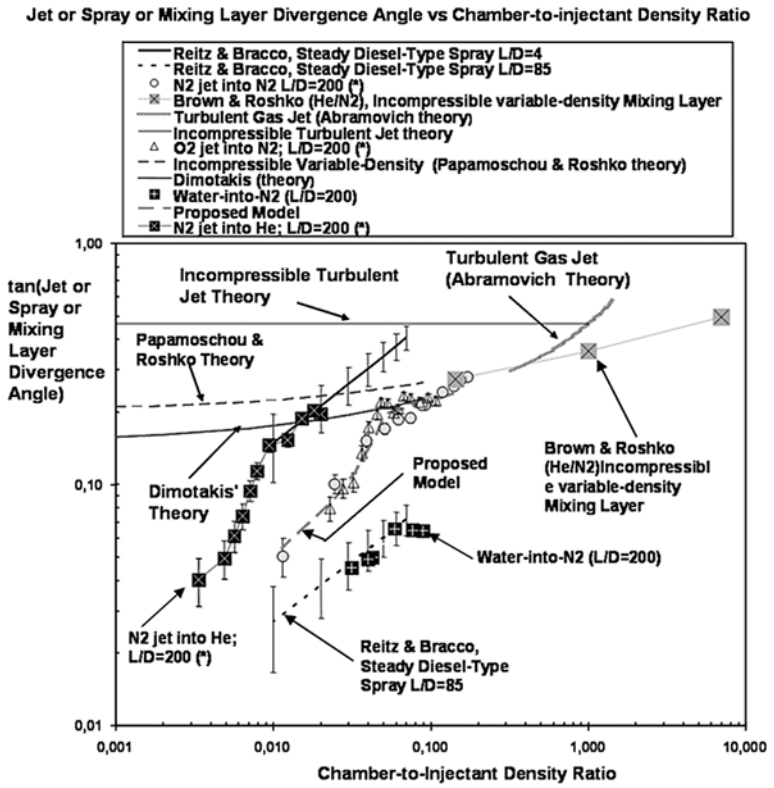

Figure 15. Spreading or growth rate as a tangent of the visual spreading angle versus the chamber-to-injectant density ratio. Data taken at AFRL are indicated by an asterisk (*) in the legend.

Brown and Roshko (1974) measured spreading angles for a subsonic, two-dimensional, incompressible, turbulent mixing layer in which helium and nitrogen were used. Brown (1974) (for temporally growing mixing layer) and Papamoschou and Roshko (1988) proposed a theoretical equation for incompressible variable-density mixing layers. Finally, Dimotakis (1986) used the observation that, in general, the entrainment into the mixing layer from each stream is not the same and, in a system moving with a convection velocity, offered a geometrical argument to derive an equation for two-dimensional incompressible variable-density mixing layers. Predictions from all of these models are plotted in Figure 15. Results by Richards and Pitts (1993) for variable-density jets are also noteworthy and have been taken into consideration by both groups.

Conversion of the two-dimensional mixing layer data for comparison with our data is justified because, according to both Brown and Roshko (1974) and Abramovich (1963), two-dimensional mixing layers are found to be fairly well approximated by the initial mixing region of axisymmetric jets. For this reason all angle measurements by Chehroudi et al. (2002a) were made using only the information within the first 5.5 mm from the injector exit plane. Because both liquid-like and gas-like visual jet behaviors are observed, the growth rate for the liquid sprays produced from single-hole nozzles, typical of the ones used in diesel engines, are also shown in this figure. Figure 15 covers a density ratio of four orders of magnitude, a unique and new plot in its own right. To some extent, and for comparable cases, disagreements in this figure can be attributed to differences in the definition of the mixing layer thicknesses and the adopted measurement methods. For detailed discussion of this figure, see Chehroudi et al. (1999a, 2002a).

The important point shown in Chehroudi et al. (2002a) is that for a range of density ratios in which images show gas-jet like appearance, the experimental data agrees well with the proposed theoretical equation by Dimotakis (1986) and closely follows the trend of the Brown/Papamoschou and Roshko equation as shown in Figure 15. This can be taken as an important quantitative evidence that at supercritical pressures, the injected jets visually behave like a gas. Chehroudi's work was the first time such quantitative evidence had been developed. The fractal results discussed earlier added additional evidence later for this hypothesis.

It is worth mentioning that above the critical point, there is a marked disagreement in both magnitude and slope between the liquid sprays (at a comparable length-to-diameter ratio of 85) and Chehroudi et al. data

(see Figure 15). Approaching the critical point, the jet appears to go through initial phases of the liquid atomization process, as shown in Figure 8; however, the cascade of events typical of the liquid jet atomization and break-up does not take place once the critical point is passed. The reason is that, although the jet shows the second wind-induced breakup features similar to liquid jets, it fails to reach a full atomization state as chamber pressure (actually, density) is raised. This is because the pressure approaches the critical pressure, and consequently both surface tension and heat of vaporization are reduced to near-zero values. Transition into the full liquid atomization regime is therefore inhibited and hence no agreement is seen between the liquid sprays and our jet beyond such point.

Initially, the growth rate measurements by Chehroudi et al. using results acquired during the Raman scattering work did not provide the same jet thickness values as those determined by the shadowgraphy. Apparently, as discussed by Brown and Roshko (1974), different thickness definitions exist, and one can explore their relationship. Similar attempts showed that within the distances investigated, twice the full width half maximum (FWHM) of the Raman intensity radial profiles was equivalent to the thickness values measured through photography. Realization of this relationship was very critical to combine the results

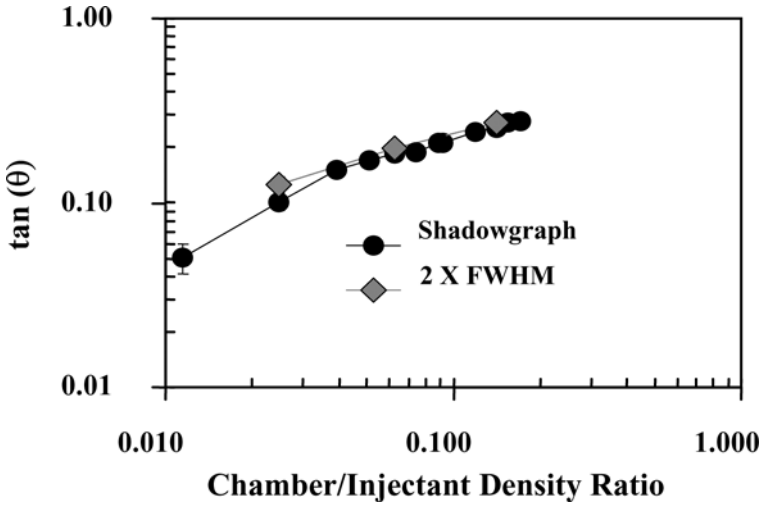

Figure 16. Comparison of the tangent of the spreading angle measured using shadowgraph and Raman techniques using twice the FWHM values.

from two different methodologies. Figure 16 shows the growth rate measured using the Raman data in contrast to those determined by shadowgraph images.

These results were subsequently confirmed and extended by DLR researchers through a similar measurement technique. For example, Oschwald and Micci (2002) showed that when twice the FWHM of the Raman radial intensity profiles are used for x/D values within 15 and 32, a good agreement exists between the results from the two laboratories (see the case designated as "p = 0.36" in Figure 17, where "p" is the exponent of the curve fitted through the data). However, the twice FWHM criterion did not agree with shadowgraphs as well for $x/D < 15$ in the study of Oschwald and Micci (2002) (see the case identified as "p = 1.0" in Figure 17).

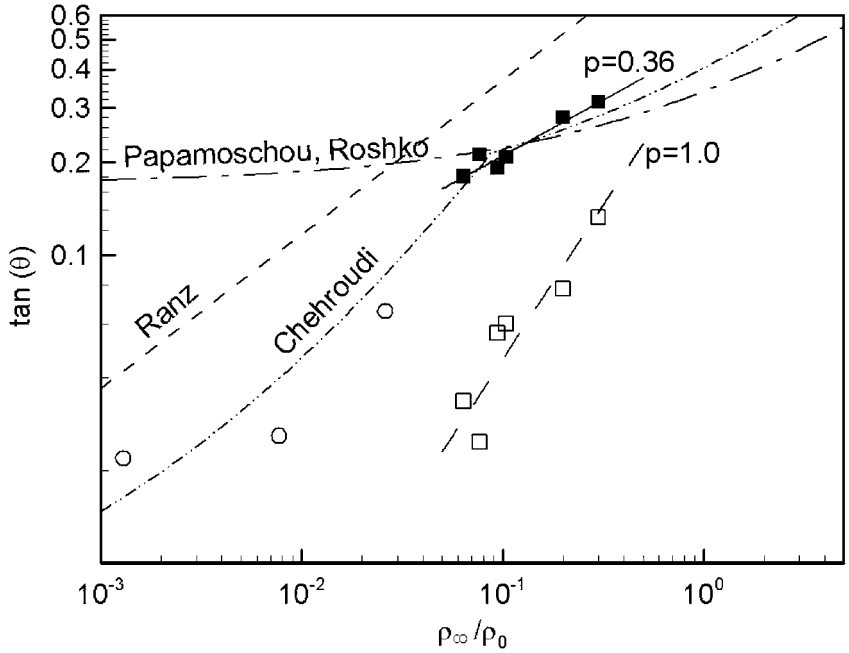

Figure 17. Comparison of the tangent of the spreading angle by Raman techniques using twice the FWHM values (DLR data). Solid squares are for data from x/D of 15 to 32 whereas hollow squares are from x/D of 0.5 to 14. Chehroudi's model is also shown as dash-dot-dot curve. LN_2 into GN_2 with injector L/D = 11.6. Data from Oschwald and Micci (2002). Open circles are data points from Reitz and Bracco (1979).

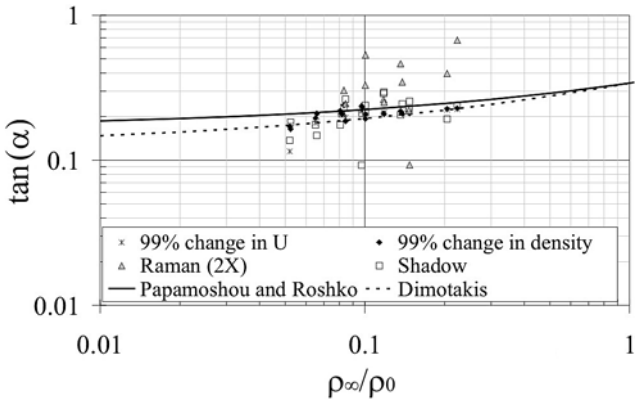

Figure 18. Comparison of the tangent of the spreading angle measured using shadowgraph and Raman techniques using twice the FWHM values and computer simulation (DLR data). LN_2 into GN_2 with injector $L/D = 40$. Data by DLR and Branam and Mayer (2003).

Results from Oschwald and Micci (2002) are plotted in a different form in Figure 18, as tangent of the spreading angle as a function of density ratio. Again it is shown that the twice FWHM criterion sometimes does and sometimes does not predict the shadowgraph data.

Within the x/D values which both laboratories studied in common, both laboratories confirmed the twice FWHM criterion for those values. DLR measured a larger range of axial distances, and found that the criterion was not universal at extended ranges. AFRL has not yet attempted to duplicate these extended measurements, but care in interpreting the results would in any case be warranted. Even if a different trend were to be observed, it is possible that the results of the two laboratories would still be fully consistent with each other. There are several reasons why different trends might be observed. It has to be noted that shadowgraphy and Raman scattering measure different physical properties. The Raman signal is taken to be proportional to density whereas shadowgraphy is sensitive to the gradients of the density distribution. Thus a unique relationship between the results measured by the two methods may only be valid for specific configurations. Recall that the data discussed above were obtained from injectors with different L/D ratios. Another potential cause of problems is errors in attempting to perform Raman measurements close to the injector inlet where density variations and thus index of refraction variations can be very large.

Jet Disintegration under the Influence of an External Acoustic Field. Overwhelming evidence gathered by investigations in the past have attributed combustion instability to a complex interaction of the external acoustic field with the fuel injection processes, thereby leading to incidences of instability in rocket engines. Also, Oefelein and Yang (1993) indicated that the near-injector processes in the thrust chamber are generally more sensitive to velocity fluctuations parallel to the injector face than normal to it. For this and other reasons, controlled studies have been conducted in the past probing into the effects of acoustic waves on the gaseous and liquid jets from a variety of injector designs.

Chehroudi and Talley (2002b) used a unique piezo-siren design capable of generating sound waves with a sound power level (SPL) of up to 180 dB. This was used at three chamber pressure conditions of 1.46, 2.48, and 4.86 MPa (reduced pressures of 0.43, 0.73, and 1.43, respectively). The assembly, consisting of an acoustic driver and a high-pressure chamber, forms a cavity that resonates at several frequencies, the strongest being at 2700 and 4800 Hz. They injected LN_2 into GN_2 at room temperature under sub- and supercritical pressures. Three different flow rates were considered, and the nature of the aforementioned interaction was documented via a high-speed imaging system using a CCD camera.

Figure 19 shows some sample results from this study. It appears that the acoustic field constricts the jet in the wave propagation direction and stretches the jet in the direction perpendicular to the propagation. Chehroudi and Talley (2002a) found that the impact of the acoustic waves on the jet structure is strong at subcritical pressures, strongest at near-critical pressures, and weakest at supercritical pressures. They also observed that the interaction was the strongest at low injectant flow rates. The weak effect at supercritical pressures suggests that the mechanisms governing the coupling between acoustic waves and jets may be significantly different for supercritical jets than for subcritical jets.

Modeling and Simulation of Single-Jet Injection at High Pressure

Phenomenological Model of the Jet Growth Rate. Using the experimental data collected on the growth of a cryogenic jet, a phenomenological model for the growth rate has been developed. Complete details on the development of this equation are to be found in Chehroudi et al. (1999b).

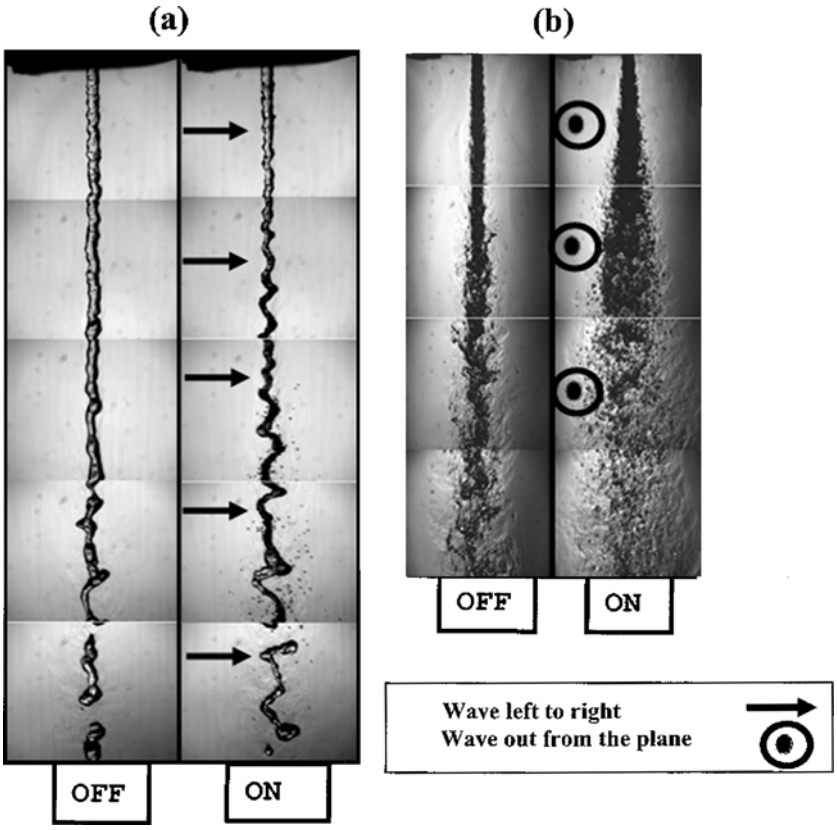

Figure 19. Interaction of acoustic waves with a single LN_2 jet injected into GN_2 at subcritical pressure. "ON" and "OFF" indicate the state of the acoustic driver; (a) front view and (b) side view.

The physical reasoning motivating the proposed model equation is outlined below.

It was noticed that previous expressions for the growth rate of liquid sprays and of turbulent jets have a remarkably similar form. Reitz and Bracco (1979) proposed that the growth rate of an isothermal steady liquid spray could be expressed as,

$$\theta \approx 0.27[0 + (\rho_g/\rho_l)^{0.5}].$$

The first term in the bracket is the number zero to contrast with other equations discussed next. Similarly, Papamoschou and Roshko (1988)

suggested the following form for incompressible, but variable-density, turbulent gaseous jets:

$$\theta = 0.212[1 + (\rho_g/\rho_l)^{0.5}].$$

The similarity in the form of these equations suggests a potential for a linkage between the two cases. Imagine a jet that is being injected into a subcritical pressure environment similar to the ones shown in Figure 8. Clearly there are drops and ligaments, testifying to the existence of a surface tension. Also, evidence of a phase change is seen. Hence, one appropriate characteristic time of the problem (at subcritical, $P_r < 1$) is the "bulge" formation/separation time (τ_b) on the interface of the turbulent liquid jet. This time characterizes the formation and separation event of bulges from the liquid jet producing isolated ligaments and drops. Tseng et al. (1995) suggests that this time is equal to $(\rho_l L^3/\sigma)^{1/2}$ for the primary breakup in turbulent liquid jets, where ρ_l, L, and σ are liquid density, characteristic dimensions of turbulent eddies, and surface tension, respectively. The second relevant characteristic time (for subcritical jets) is the gasification time (τ_g). Here, an estimate of this time is calculated through the so-called D-squared law for drops to be equal to D^2/K where D and K are drop diameter and vaporization constant, respectively. In addition, we also propose the following hypothesis. If the aforementioned characteristic times (calculated for appropriate length scales) are nearly equal in magnitude, then the interface bulges are not able to separate as unattached entities from the jet interface to form ligaments and drops, because they are gasified as fast as they desire to be detached. Here, this is defined as the onset of the gas-jet-like behavior. Therefore, the transition between liquid-like and gas-like behavior would be governed by finding the point at which these time scales are approximately equal. This picture is also suggested by the comb-like structures seen in Figure 8(b).

Using the above physical models, an equation was proposed for the N_2/N_2 system as

$$\theta = 0.27[(\tau_b/(\tau_b + \tau_g) + (\rho_g/\rho_l)^{0.5}].$$

In the limit, when $\tau_g \gg \tau_b$ and $\tau_g \to \infty$, this equation collapses to the isothermal liquid spray case. This equation agrees well with the current data at subcritical pressures for $\tau_b/(\tau_b + \tau_g) < 0.5$. A constant value of 0.5 was used to predict the spreading rate for higher pressures, including supercritical pressures.

For injection of N_2 into N_2, the characteristic time ratio, $\tau_b/(\tau_b + \tau_g)$, was calculated from the experimental measurements of bulge and droplet sizes and calculations of the relevant properties. For N_2 injection into other gases, however, reliable information about the mixture properties at the interface, particularly the surface tension, prevents such a calculation from being performed. To model these cases, it is hypothesized that the characteristic time ratio is a dominant function of the density ratio; i.e., $\tau_b/(\tau_b + \tau_g) = F(\rho_g/\rho_l)$. Brown and Roshko (1974) indicate that this hypothesis is reasonable, because at low Mach numbers there is no distinction between mixing layers where the two streams have different molecular weights, temperatures, or compressibility effects. Measurements and calculations of $\tau_b/(\tau_b + \tau_g)$ provides the shape of the function F for the N_2/N_2 system and is provided as a plot in Chehroudi et al. (1999b). A curve fit of that plot gives

$$\begin{aligned} F(\rho_g/\rho_l) &= 5.325(\rho_g/\rho_l) + 0.288 \qquad \text{when} \quad \rho_g/\rho_l < 0.0885 \\ &= 0.5 \qquad\qquad\qquad\qquad\quad \text{when} \quad \rho_g/\rho_l \geq 0.0885 \end{aligned}$$

It was found that the same function, F, calculated from measurements of the N_2/N_2 system could be made to work for other cases, provided that a case-dependant transformation was made to the density ratio at which F is evaluated. The final form of the equation thus arrived at is

$$\theta = 0.27[F(\mathrm{x}(\rho_g/\rho_l)) + (\rho_g/\rho_l)^{0.5}],$$

where, $x = 1.0$ for N_2-into-N_2, $x = 0.2$ for N_2-into-He, and $x = 1.2$ for N_2-into-Ar.

In other words, the same functional form of the characteristic time ratio, $\tau_b/(\tau_b + \tau_g) = F(\rho_g/\rho_l)$, for the N_2-into-N_2case is used but with a density-ratio coordinate transformation. The quality of the agreement with experimental data is demonstrated in Figure 20. Hence here are no major changes in the form of the proposed model equation, even for an extreme arrangement such as injection of N_2 into He. However, an observation is made here. The factor $x = 0.2$ in the N_2-into-He case is comparable to the molecular weight ratio of He to N_2 of 0.14, while the factor $x = 1.2$ in the N_2-into-Ar case is comparable to the molecular weight ratio of 1.42. This also suggests the dominant effect of the density ratio parameter between the cases.

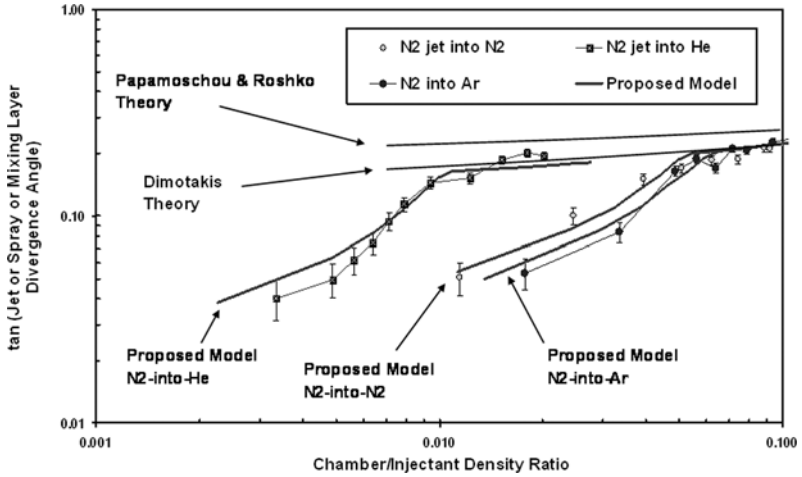

Figure 20. Comparison of the proposed growth rate model with experimental data.

Numerical Simulation of Injection under Supercritical Pressures (LN_2 into GN_2). Supercritical injection has been simulated using a commercial CFD program. The intention was to use the simulations as an engineering design tool. However, the reliability of the results produced by the program needs to be evaluated by a comparison with the experimental data. Using the CFD-ACE software package, simulation of this multiphysical problem appeared as a straightforward computational approach. Details of the simulation technique are given by Mayer et al. (2001). Real gas nitrogen properties have been used and the computational model can capture the weakly compressible effects.

The software package takes into account turbulent heat transfer by use of a turbulent Prandtl number. The effective coefficient of thermal conductivity K_{eff} is modeled according to

$$K_{eff} = k + \frac{\nu_T \rho c_p}{\mathrm{Pr}_T}$$

where $\mathrm{Pr}_T = \nu_T/(\kappa/\rho c_p)$ is the turbulent Prandtl number. A constant value of $\mathrm{Pr}_T = 1.0$ proved to be consistent with the experimental findings.

The boundary conditions for this model are very important and extremely sensitive to the values of temperature. Measured mass flow, temperature, and pressure determine the injector exit conditions. From measurements of these quantities, initial inlet velocity, turbulent kinetic

energy (k) and rate of dissipation (ε) are calculated and considered as the inputs to the model.

The simulation predicts a transition from a top-hat (liquid-like jet) shape to a fully developed (gas-like jet) behavior as shown in Figure 21. The normalized density $\rho^* \equiv (\rho_{\text{jet}} - \rho_{\text{ambient}})/(\rho_{\text{jet}} - \rho_{\text{ambient}})_{\text{max}}$ is plotted as a function of the radial distance, normalized by $r_{1/2}$, the value at which $\rho^* = 1/2$. Note that for $x/D > 10$, all simulated density fields $\rho^*(r/r_{1/2})$ fall relatively close together, indicating a nearly self-similar behavior. The experimental data appears to confirm this, but the uncertainty in the Raman data is not sufficiently resolved to confirm it. For the axial velocity $u^* \equiv (u_{\text{jet}} - u_{\text{ambient}})/(u_{\text{jet}} - u_{\text{ambient}})_{\text{max}}$ profiles, the transition to the self-similarity behavior is seen to occur at a similar normalized distances as the density profiles, see Figure 22. Note that, all radial profiles of $u^*(r/r_{1/2})$ are rather identical for $x/D > 10$.

For all the test cases, the simulation results predicted the existence of a potential core. Figure 23 shows the normalized centerline density as a function of axial distance from the injector for an initial injection temperature of 133 K, which is above the pseudo-boiling line. The simulation indicates a potential core length of about $x/D = 7.6$. The potential core length increased as the initial injection temperature decreased. For example, in Figure 24, a cryogenic nitrogen jet with an injection temperature of 120 K, falling below the pseudo-boiling line, shows a simulated potential core length of about $x/D = 9$. The experimental results derived from the Raman data show this effect more dramatically.

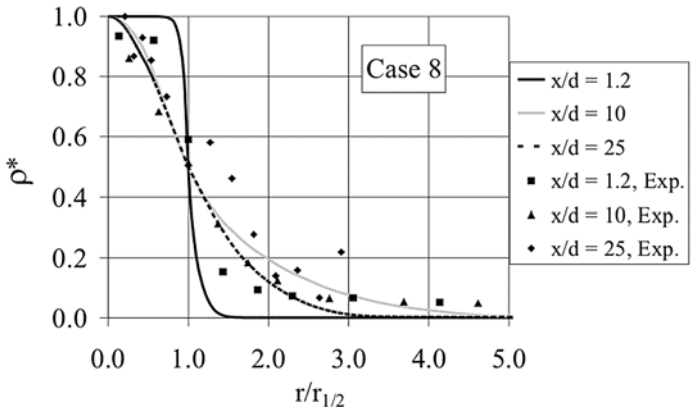

Figure 21. Density; 5.0 MPa, 123 K, 2.0 m/s.

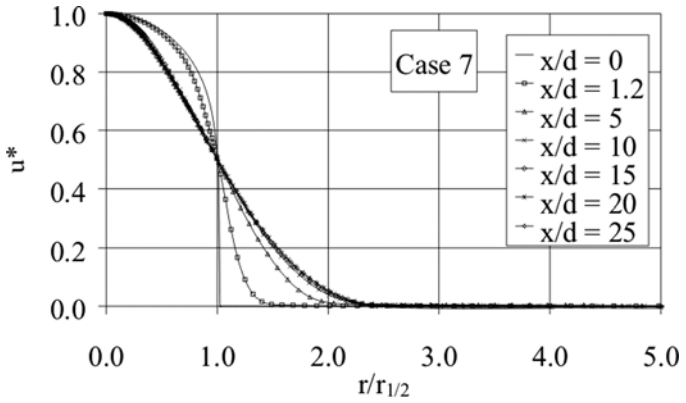

Figure 22. Velocity; 4.9 MPa, 104 K, 1.8 m/s.

For the 133 K injection temperature, the normalized potential core length is shorter than about x/D = 5. For the 120 K injection temperature case, the measured centerline densities match the computer simulation data quite well, see Figure 24.

At a distant of x/D = 150, the density falls off quickly toward the chamber value, suggesting that the jet has almost completely dissipated. The calculations showed that this location in the chamber was at the far edge of a recirculation zone established to transfer mass back toward the

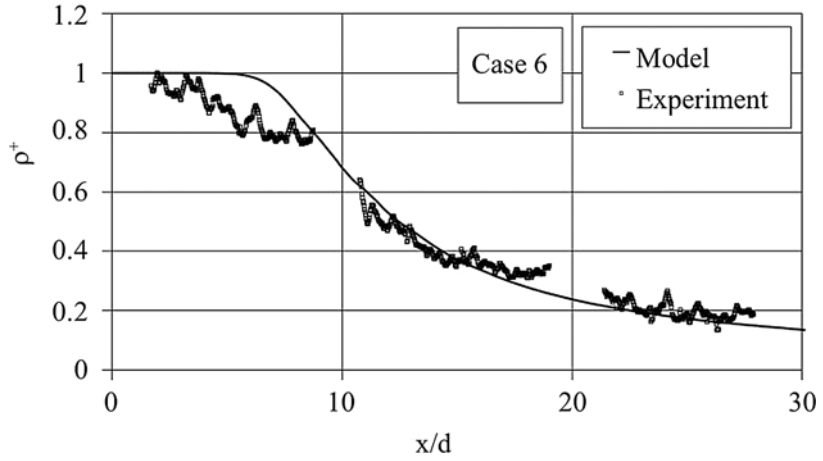

Figure 23. Centerline density; 3.9 MPa, 133 K (above the pseudo-boiling line), 5.4 m/s.

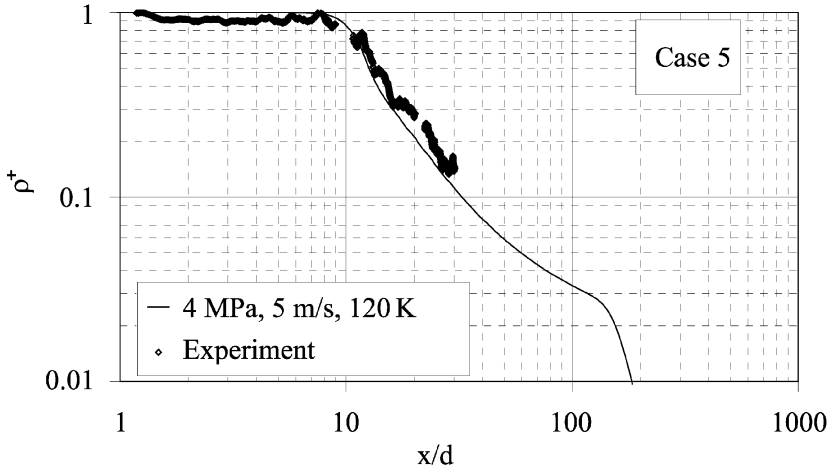

Figure 24. Centerline density; 4.0 MPa, 123 K (below the pseudo-boiling line), 4.9 m/s.

injector exit area. This is the mass entrained in the jet flow from the chamber environment.

COAXIAL JET INVESTIGATIONS

Nonreactive Coaxial Jet Atomization

Visualization of Coaxial LN_2/He-Injection. The influence of the ambient pressure on the atomization phenomena from subcritical to supercritical pressures has been experimentally studied for coaxial LN_2/He injection. Telaar et al. (2000) used a coaxial injector with an inner diameter of $d_{LN_2} = 1.9$ mm for the cryogenic nitrogen flow and an annular slit width of 0.2 mm with an outer diameter of 2.8 mm for helium. Two examples of the flow visualization by shadowgraphy near the injector region are shown in Figure 25. The changes in the atomization mechanism at a reduced surface tension is quite evident. At the low chamber pressure of 1 MPa in Figure 25A, a liquid spray is formed, whereas at the supercritical pressure of 6 MPa in Figure 25B, a gas-like turbulent mixing of he dense and light fluids is seen. At 6 MPa in Figure 25B, the initial temperature of the center LN_2 jet was 97 K, whereas the critical mixing temperature of He/N_2 mixtures at this pressure is 125.7 K. Thus, in the mixing layer between the LN_2 and He, transcritical zones may exist. The visual boundary of the LN_2 jet as shown in Figure 25 is assumed

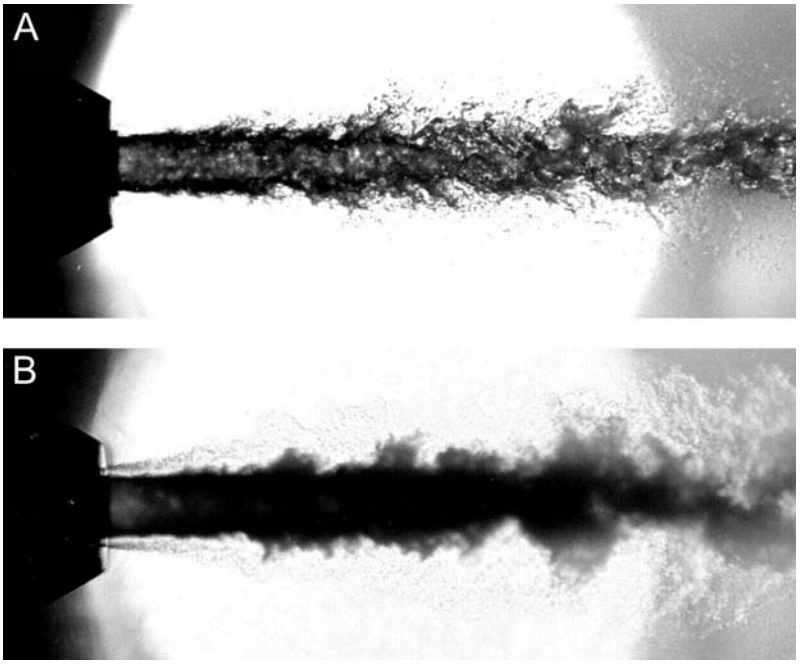

Figure 25. Binary liquid N_2/GHe system at A: 1.0 MPa, B: 6.0 MPa. $d_{LN_2} = 1.9$ mm, $v_{LN_2} = 5$ m/s, $v_{He} = 100$ m/s, $T_{LN_2} = 97$ K, $T_{He} = 280$ K (from Mayer and Smith, 2004).

to be the layer at which the temperature reaches the critical mixing temperature. The influence of the surface tension forces as compared to the shear forces appears to be negligible.

Density Measurements in a Coaxial LN_2/GH_2-Jet. In previous sections, the potential of the spontaneous Raman scattering as a diagnostic tool for quantitative density measurements was demonstrated in the context of injecting a single LN_2 jet into the nitrogen gas. In a mixture of N_2 and H_2, however, the Raman signals of the N_2 and H_2 are generated at two different wavelengths. Thus, using an appropriate filtering technique, the signals from both species can be analyzed independently and the partial densities of each species can be determined.

This diagnostic method has been used to investigate the atomization and mixing of coaxial LN_2/H_2 injection at pressures which are supercritical with respect to critical pressure of pure nitrogen (Oschwald et al., 1999). The test matrix is listed in Table 3 and in Figure 13a. During

Table 3. Injection conditions for Raman scattering tests

	Test case	v_{N_2} [m/s]	T_{N_2} [K]	v_{H_2} [m/s]	T_{H_2} [K]
Single N_2-jet	A4	5	140	–	–
	B4	5	118	–	–
Coaxial N_2/H_2-jet	D4	5	140	60	270
	E4	5	118	120	270
	F4	5	118	60	270

all the tests, the fluids were injected into a flow channel filled with N_2 at near atmospheric temperature at a pressure of 4MPa ($P/P_{crit} = 1.17$). Plots for coaxial LN_2/H_2 injection are shown in Figure 26(b), as contrasted with a single jet case shown in Figure 26(a). The decrease of the measured densities at large positive r/D values is due to the refraction of the laser beam experienced as a result of the density gradients existing at the H_2/LN_2 interface. Similar radial profiles have been obtained for a range of axial distances from the injector. From these data, the two-dimensional species distribution can be reconstructed. For the test case designated by the symbol D4, such a distribution for the H_2 is shown in Figure 27.

The maximum of the radial density distribution at each axial distance has been plotted as functions of the normalized distance (x/D) from the injector in Figures 28, 29, and 30. This is used as a measure of the evolution of the injection process for the LN_2 jet downstream of the injector, as well as the mixing between the H_2 and N_2 species. Compared to the test case without the co-flow (Figure 13b), it appears that the existence of the H_2 co-flow lowers the measured nitrogen density much faster from its initial injection value of (ρ_{INJ}) to a plateau (ρ_∞). The x/D value at which this plateau occurs represents a complete mixing of the jet with its background gas. The axial distance ($x_{1/2}$) at which the nitrogen density falls by 50% ($\rho(x_{1/2}) = \rho_\infty + 0.5(\rho_{INJ} - \rho_\infty)$) is determined and listed in Table 4. In comparing test case A4 (no co-flow, Figure 13b) with test case D4 (with co-flow, Figure 28), it can be seen that the co-flow of H_2 increases the mixing efficiency of the injector. Also, in comparing test case D4 ($T_{N_2} = 140$ K, Figure 28), where the initial temperature is above the pseudo-boiling temperature, with test cases E4 ($T_{N_2} = 118$ K; Figure 29) and F4 ($T_{N_2} = 118$ K; Figure 29), it can be seen a jet initially above the pseudo-boiling temperature has a shorter decay length than a jet with an injection temperature initially below it. In both

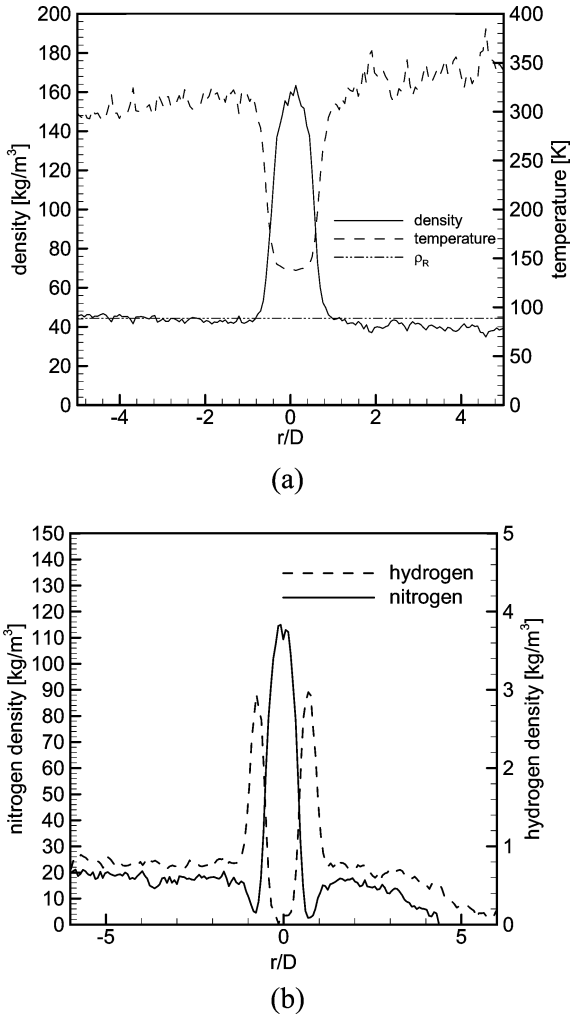

Figure 26. (a) Radial N_2 density profile for test case A4 (single jet), 2 mm ($x/D = 1.05$) downstream of the injector exit. (b) Radial N_2 and H_2 density profiles for coaxial LN_2/H_2 injection for test case D4, 2 mm ($x/D = 1.05$) downstream the injector exit. Laser beam direction is from left to right.

cases, the injected N_2 is at a supercritical pressure. However, nitrogen above the pseudo-boiling temperature has a gas-like density, whereas N_2 below this temperature has a much higher, liquid-like density. Thus the jet has more inertia to resist the shear forces from the annular H_2

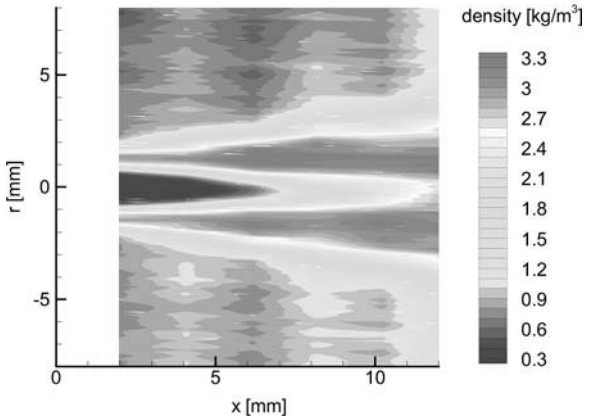

Figure 27. H_2 density for coaxial LN_2/H_2 injection for test case D4 ($T_{N_2} = 140\,K$, $T_{H_2} = 270\,K$) (See Color Plate 3 at the end of this issue).

jet. The effect of higher H_2 velocity was found not to be as pronounced as this effect of the initial N_2 density. This is seen when comparing the decay-lengths of the test cases E4 ($v_{H_2} = 120\,m/s$) and F4 ($v_{H_2} = 60\,m/s$) in Figures 29 and 30, respectively.

Although a decrease in the density of H_2 with axial distance might reasonably have been expected, the Raman measurements in Figures 28

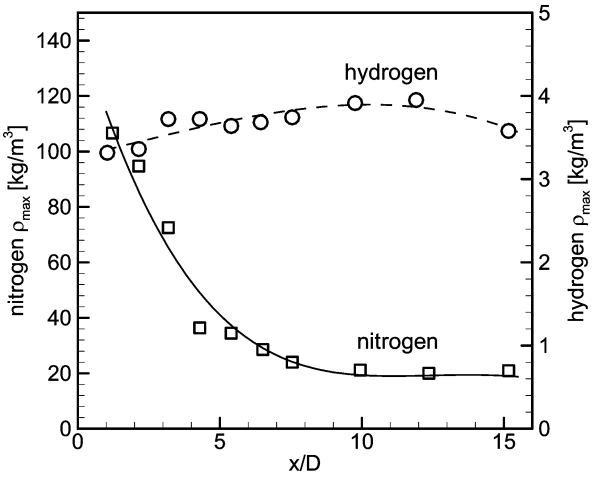

Figure 28. Evolution of the maximum nitrogen and hydrogen density downstream of the injector for test case D4.

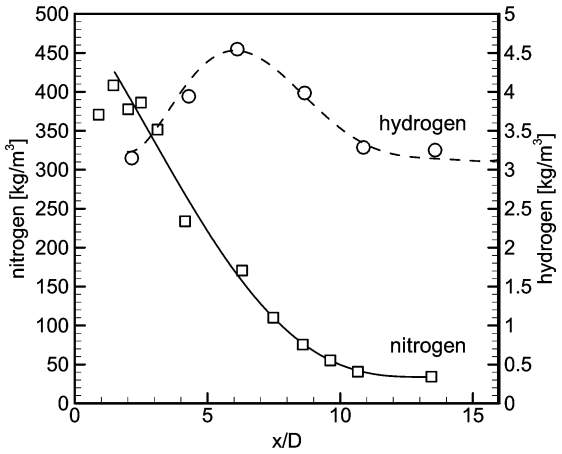

Figure 29. Evolution of the maximum nitrogen and hydrogen density downstream of the injector for test case E4.

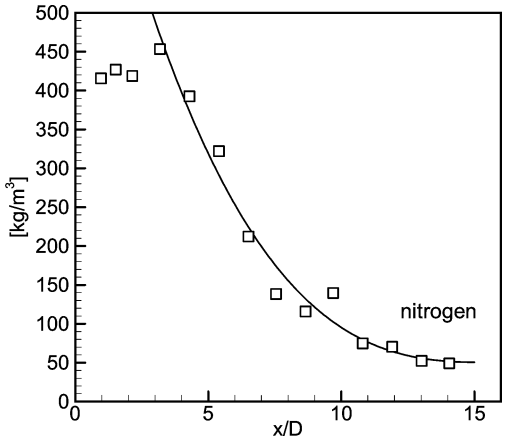

Figure 30. Evolution of the maximum nitrogen density downstream of the injector for test case F4.

Table 4. Distance where nitrogen density has decayed to 50% of its injection value

Test case	A4	B4	D4	E4	F4
$x_{1/2}/D$	9	11	3	5.5	6

and 20 show that the opposite trend can occur. This effect is significantly more pronounced for the test case of E4 ($T_{N_2} = 118$ K) in Figure 29 than that of D4 ($T_{N_2} = 140$ K) in Figure 28. The increase of the hydrogen density is therefore attributed to the net result of two effects: heat transfer from the hydrogen to the cryogenic nitrogen (cooling it down) and diffusion of the hydrogen into the dense nitrogen areas. In the near injector zone, the net effect is dominated by the heat transfer to the cryogenic N_2, resulting in a decrease of the hydrogen temperature and consequently an increase in its density.

Coaxial LN_2/GN_2-Injection under the Influence of an External Acoustic Field. Cold flow studies of the interaction of acoustic waves with single jets have recently been extended to include coaxial injectors, and initial attempts made to understand how the results may relate to historical liquid rocket engine instability data. Preliminary results were reported by Chehroudi et al. (2003) and Davis and Chehroudi (2004). The observation that the interaction with acoustic waves tends to be stronger at subcritical pressures than at supercritical pressures appears to remain generally true, although an influence of the mass flow ratio and initial temperature was also observed. Efforts continue to be underway to better understand how the various parameters control coupling mechanisms.

Hot Fire Tests: LOX/GH_2-Injection (DLR)

Thus far, injection and mixing have been demonstrated to be very different even in cold flow, depending on whether the pressure is subcritical or supercritical. However, heat release due to chemical reactions may also be expected to have a first-order effect. Accordingly, combustion studies have been performed at DLR.

Shadowgraphs of the combustion a LOX/H_2 coaxial jet at subcritical and supercritical pressures is shown in Figure 31, from Mayer and Tamura (1996). The chamber pressure in Figure 31a was 1.5 MPa, well below the critical pressure of pure oxygen (5.04 MPa). The chamber pressure in Figure 31b was 10 MPa, well above the critical pressure. In Figure 31a, the shadowgraph shows that the LOX jet undergoes atomization with evidence of surface tension. A spray is formed having flow patterns similar to those visualized in cold flow studies. Ligaments are detached from the LOX jet surface, which then forms droplets

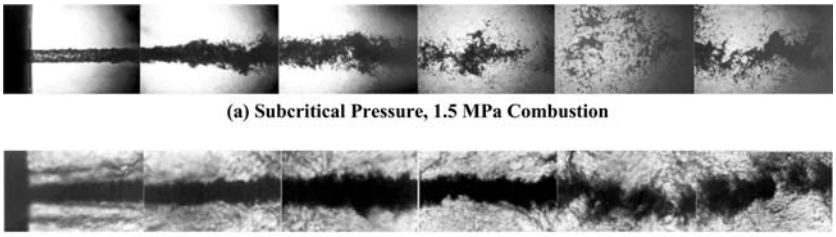

Figure 31. Combustion of the LOX jet at subcritical (a) and supercritical (b) pressures, from Mayer and Tamura (1996).

which finally go through the evaporation process. The droplet number density was found to be much lower than the cold flow conditions, a fact that is due to the rapid vaporization of the small droplets in the burning spray.

At 10 MPa, the mixture may initially be below the critical mixing temperature. However, due to the convective transport of hot gases from the reaction zone to the O_2 jet surface, the local temperature will increase and the jet reaches a supercritical temperature. A shadowgraph of the O_2 jet at 10 MPa is shown in Figure 31b. Droplets are no longer visible, and stringy or thread-like structures are seen attached to the O_2-jet, which typically develop, grow, and dissolve rapidly without separation from the main jet. There is no evidence of surface tension. At this pressure, the flow is dominated by the turbulent gas-like mixing processes. The boundary between the dense, cryogenic O_2 core and the gaseous co-flow appears fuzzy with a smooth transition from the center of the jet to far radial distances, a contrast to the well-defined boundary between the liquid O_2 jet and the co-flow gas at 1.5 MPa seen in Figure 31a.

Further downstream in Figure 31b at 10 MPa, the visualization showed an oscillating but compact jet core, whereas at 1.5 MPa in Figure 31a, the jet has already disintegrated into ligaments and droplets. Magnified images of the region between 60–72 mm downstream of the injector are shown in Figure 32 for three chamber pressures. These demonstrate a remarkable difference in injection processes as a function of pressure. At 1.5 MPa (subcritical relative to pure oxygen), a spray of LOX droplets and ligaments can be seen. At 6 MPa and 10 MPa (supercritical relative to pure oxygen), the jet disintegrates into O_2 clumps of a size much larger than a typical liquid entity observed in the subcritical case.

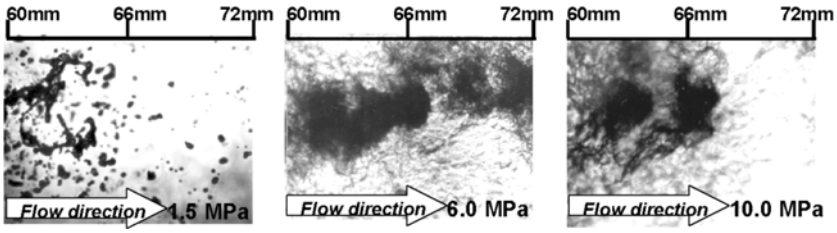

Figure 32. Visualization of O_2-jet disintegration with varying chamber pressure (Mayer and Smith, 2004).

SUMMARY AND CONCLUSIONS

Two independent laboratories have conducted studies of the injection of cryogenic liquids at subcritical and supercritical pressures, with application to liquid rocket engines. The results have been reviewed and compared here. In some cases, the findings of each laboratory corroborate each other, in other cases there are differences which need to be addressed, and in other cases, results have been obtained which the other laboratory has not attempted to verify. The conclusions to date can be summarized as follows.

For single round jets of cryogenic nitrogen injected into room temperature gaseous nitrogen, both laboratories have confirmed that the visual appearance of the jet undergoes a drastic change as the pressure is increased from a subcritical to a supercritical value. The subcritical jet has the appearance of a conventional spray, but the supercritical jet has a more gas-like appearance. Both laboratories have confirmed that the spreading rate of supercritical jets based on shadowgraph measurements is quantitatively the same as that predicted by theory for variable density gas mixing layers. Both laboratories have also compared shadowgraph measurements with density profiles obtained from spontaneous Raman scattering. The Raman measurements were found to be most useful in supercritical jets, due to issues with stimulated and plasma emission in subcritical jets. Both laboratories have confirmed that the density profiles of supercritical jets approach self-similar shapes at about 10 diameters downstream. At axial distances which both laboratories have studied, both laboratories have confirmed that the spreading angles of supercritical jets measured using shadowgraphy correspond to the spreading angles measured using Raman scattering when the jet width using the latter is defined to be twice the full width half maximum

(FWHM) distance of the measured density profiles. However, DLR explored a larger range of axial distances than AFRL, and found that the twice FWHM rule may not apply universally at all axial distances. AFRL has not yet attempted to independently confirm this finding. Both laboratories have also attempted to measure the length of the potential core, but with different diagnostic methods. The AFRL measurements were performed using shadowgraphy, and were found to be larger by a factor of 1.5 to 2 than the DLR measurements, which were performed using Raman scattering. The reason for the discrepancy needs to be further explored, but could be due to the different physical quantities measured by the two diagnostic methods.

DLR demonstrated a significant effect of the initial jet temperature, depending on whether this temperature is above or below the pseudo-boiling temperature, defined to be the temperature at a supercritical pressure where the specific heat reaches a maximum. Jets having an initial temperature below the pseudo-boiling temperature have to pass through this maximum in specific heat, where heat addition can result mostly in expansion with little increase in temperature, i.e., a pseudo-boiling process. The initial temperature of the jet can be preserved a considerable distance downstream. On the other hand, the temperature of jets having an initial temperature initially above the pseudo-boiling temperature decays monotonically from the injection point. DLR also measured length scales from shadowgraph images, and found that these visible scales correspond most closely to Taylor length scales. For initial temperatures close to the pseudo-boiling temperature, the axial length scales near the jet exit can be much longer than the radial scales. At higher initial temperatures, the disparity between the axial and radial length scales decreases. The disparity between the axial and radial length scales for all jets also decreases as a axial distance increases.

AFRL measured the fractal dimension of the jets, and found that the fractal dimension of subcritical jets approaches that of conventional sprays, while the fractal dimension of supercritical jets approaches that of gas jets. AFRL also studied cryogenic nitrogen jets injected into various gases other than nitrogen, and developed a semi-empirical model for their spreading rates. Finally, AFRL studied the effect of transverse acoustic waves on the jets, and found that the waves have a significant effect on subcritical jets, but significantly less effect on supercritical jets. Preliminary results for coaxial jets suggest that this general trend may

continue to be true, although additional effects of mass flow ratio also seem to be evident.

For coaxial jets, AFRL has focused mainly on acoustic effects as described above. On the other hand, DLR has performed broader non-acoustic studies. In general, whether in cold flow or hot fire, these studies continue to confirm spray-like behaviour at subcritical pressures and gas-like behaviour at supercritical pressures. Raman studies were performed on N_2/H_2 jets, where N_2 and H_2 densities could be measured separately by detecting different wavelengths. It was found that the H_2 co-flow produced more efficient mixing than without co-flow. Initial temperatures above the pseudo-boiling temperature also produced more efficient mixing than initial temperatures below it. It was also found that the H_2 density can increase with downstream distance, due to cooling by the cold central jet.

In hot fire, the combustion of LOX/H_2 coaxial jets showed that the subcritical LOX breaks up into small ligaments and drops far downstream. In contrast, supercritical O_2 was found to break up into large clumps having typical dimensions much larger than corresponding subcritical entities.

REFERENCES

Abramovich, G.N. (1963) The Theory of Turbulent Jets, MIT Press, Cambridge.

Branam, R. and Mayer, W. (2003) Characterization of cryogenic injection at supercritical pressure. *J. Propul. Power*, **19**(3), 342–355.

Brown, G. (1974) The entrainment and large structure in turbulent mixing layers. *5th Australasian Conference on Hydraulics and Fluid Mechanics*, Sydney, Australia, pp. 352–359.

Brown, G. and Roshko, A. (1974) On density effects and large structure in turbulent mixing layers. *J. Fluid Mech.*, **64**(4), 775–816.

Chehroudi, B., Chen, S.-H., Bracco, F.V., and Onuma, Y. (1985) On the intact core of full-cone sprays. *SAE Transaction Paper* 850126, Warrendale, Pennsylvania.

Chehroudi, B., Cohn, R., Talley, D., and Badakhshan, A. (2000) Raman scattering measurements in the initial region of sub- and supercritical jets, *AIAA* 2000-3392. 36th Joint Propulsion Conference, Huntsville, AL.

Chehroudi, B., Davis, D., and Talley, D. (2003) *Initial Results from a Cryogenic Coaxial Injector in an Acoustic Field*. *AIAA* 2003-1339, 41st Aerospace Sciences Meeting and Exhibit, Reno, NV.

Chehroudi, B., Talley, D., and Coy, E. (1999a) Initial growth rate and visual characteristics of a round jet into a sub- to supercritical environment of relevance

to rocket, gas turbine, and diesel engines. *AIAA* 99-0206. 37th AIAA Aerospace Science Meeting and Exhibit, Reno, NV, 11–14 January.

Chehroudi, B., Talley, D., and Coy, E. (1999b) Fractal geometry and growth rate changes of cryogenic jets near the critical point. *AIAA* 99-2489, 35th Joint Propulsion Conference, Los Angeles, CA.

Chehroudi, B., Talley, D., and Coy, E. (2002a) Visual characteristics and initial growth rates of round cryogenic jets at supercritical and supercritical pressures. *Physics of Fluids*, **14**, 2, 850–861.

Chehroudi, B. and Talley, D. (2002b) Interaction of acoustic waves with a cryogenic nitrogen jet at sub- and supercritical pressures. *AIAA* 2002-0342, 40th Aerospace Sciences Meeting and Exhibit, Reno, NV.

Chehroudi, B. and Talley, D. (2004) Fractal geometry of a cryogenic nitrogen round jet injected into sub- and super-critical conditions. *Atomization Sprays*, **14**, 81–91.

Chen, C.J. and Rodi, W. (1980) Vertical Turbulent Buoyant Jets: A Review of Experimental Data, HMT The Science & Applications of Heat Transfer, Pergamon Press, Oxford and New York, **4**, 94.

Davis, D. and Chehroudi, B. (2004) The Effects of Pressure and Acoustic Field on a Cryogenic Coaxial Jet. 42nd AIAA Aerospace Sciences Meeting and Exhibit, Paper No. AIAA-2004-1330, Reno, Nevada, January 5–8, 2004.

Decker, M., Schik, A., Meier, U.E., and Stricker, W. (1998) Quantitative Raman imaging investigations of mixing phenomena in high-pressure cryogenic jets. *Appl. Optics*, **37**(24), 5620–5627.

Delplanque, J.-P. and Sirignano, W.A. (1993) Numerical study of the transient vaporization of an oxygen droplet at sub- and supercritical conditions. *Int. J. Heat Mass Trans.*, **36**, 303–314.

Dimotakis, P.E. (1986) Two-dimensional shear-layer entrainment. *AIAA J.*, **21**(11), 1791–1796.

Eckbreth, A. (1996). Laser Diagnostics for Combustion, Temperature, and Species, 2nd Edition, Combustion Science and Technology Book series, Vol. 3, Gordon and Breach, New York.

Haberzettl, A., Gundel, D., Bahlmann, K., Oschwald, M., Thomas, J.L., and Vuillermoz, P. (2000) European research and technology test bench P8 for high pressure liquid rocket propellants, *AIAA* 2000-3307, 36th Joint Propulsion Conference.

Macleod, D.B. (1923) Relation between surface tension and density. *Trans. Far. Soc.*, **19**, 38–41.

Mandelbrot, B.B. (1983) The Fractal Geometry of Nature, W. H. Freeman and Company, San Francisco.

Mayer, W., Ivancic, A., Schik, A., and Hornung, U. (1998b) Propellant atomization in LOX/GH_2 rocket combustors, *AIAA Paper* No. 98-3685, 34th

AIAA/ ASME/SAE/ASEE Joint Propulsion Conference & Exhibit, Cleveland, Ohio, 13–15 July.

Mayer, W., Schik, A., Schweitzer, C., and Schaffler, M. (1996) Injection and mixing processes in high pressure LOX/GH_2 rocket combustors. *AIAA paper* No. 96-2620, 32nd AIAA/ASME/SAE/ASEE Joint Propulsion Conference & Exhibit, Lake Buena Vista, Florida.

Mayer, W., Schik, A., Vielle, B., Chaveau, C., Gökalp. I., and Talley, D. (1998a) Atomization and Breakup of cryogenic propellants under high pressure subcritical and supercritical conditions. *J. Propul. Power*, **14**(5), 835–842.

Mayer, W. and Tamura, H. (1996) Propellant injection in a liquid oxygen/gaseous hydrogen rocket engine. *J. Propul. Power*, **12**(6), 1137–1147.

Mayer, W., Telaar, J., Branam, R., Schneider, G., and Hussong, J. (2001) Characterization of Cryogenic Injection at Supercritical Pressure, *AIAA 2001-3275*, 37th Joint Propulsion Conference, Salt Lake City, Utah.

Mayer, W., Telaar, J., Branam, R., Schneider, G., and Hussong, J. (2003) Raman measurements of cryogenic injection at supercritical pressure. *Heat Mass Trans.*, **39**, 709–719.

Mayer, W.O.H. and Smith, J.J. (2004) Fundamentals of supercritical mixing and combustion of cryogenic propellants, Chapter 9. In Yang, V., et al. (Eds.) *Liquid Rocket Engine Thrust Chambers*, Progress in Aeronautics and Astronautics, Vol. 200, AIAA: Virginia, pp. 339–367.

Nicoli, C., Haldenwang, P., and Daou, J. (1996) Substitute mixtures for LOX droplet vaporization study. *Combust. Sci. Technol.*, **12**, 55–74.

Oefelein J.C. and Yang, V. (1993) Comprehensive review of liquid propellant combustion instabilities in F-1 engines. *J. Propul. Power*, **9**(5), 657–677.

Oschwald, M. and Micci, M. (2002) Spreading angle and centerline variation of density of supercritical nitrogen jets. *Atomizations Sprays*, **11**, 91–106.

Oschwald, M. and Schik, A. (1999) Supercritical nitrogen free jet investigated by spontaneous Raman scattering. *Exper. Fluids*, **27**, 497–506.

Oschwald, M., Schik, A., Klar, M., and Mayer, W. (1999) Investigation of coaxial LN2-GH2-injection at supercritical pressure by spontaneous Raman scattering. *AIAA* 99-2887, 35th Joint Propulsion Conference, Los Angeles, CA.

Papamoschou, D. and Roshko, A. (1988) The compressible turbulent shear layer: an experimental study. *J. Fluid Mech.*, **197**, 453–477.

Papanicolaou, P.N. and List, E.J. (1988) Investigations of round vertical turbulent buoyant jets. *J. Fluid Mech.*, **195**, 341–391.

Reitz, R.D. and Bracco, F.V. (1979) On the dependence of spray angle and other spray parameters on nozzle design and operating condition. *SAE Paper* no. 790494, Warrendale, Pennsylvania.

Richards, C.D. and Pitts, W.M. (1993) Global density effects on the self-preservation behavior of turbulent free jets. *J. Fluid Mech.*, **254**, 417–435.

Schlichting, H. (1979) Boundary Layer Theory 7th ed., McGraw-Hill, New York.

So, R.M.C., Zhu, J.Y., Otugen, M.V., and Hwang, B.C. (1990) Some measurements in a binary gas jet. *Exper. Fluids*, **9**, 273–284.

Sreenivasan, K.R. and Meneveau, C. (1986) The fractal facets of turbulence. *J. Fluid Mech.*, **173**, 357–386.

Street, W.B. and Calado, J.C.G. (1978) Liquid-vapor equilibrium for hydrogen and nitrogen at temperatures from 63 to 100 K and pressures to 57 MPa. *J. Chem. Therm.*, **10**, 1089–1100.

Taylor, J.J. and Hoyte, J.W. (1983) Water jet photography-technique and methods. *Exp. Fluids*, **1**, 113–120.

Telaar, J., Schneider, G., and Mayer, W. (2000) Experimental Investigation of Breakup of Turbulent Liquid Jets, ILASS-Europe 2000, Darmstadt, Germany.

Tseng, L.-K., Ruff, G.A., Wu, P.-K., and Faeth, G.M. (1995) Continuous- and dispersed-phase structure of pressure-atomized sprays. In Kuo, K.K. (Ed.) *Recent Advances in Spray Combustion: Spray Combustion Measurements and Model Simulation*, Progress in Astronautics and Aeronomics Series, AIAA: New York, **171**, 3–30.

Tully, P.C., DeVaney, and Rhodes (1970) Phase equilibria of the Helium-Nitrogen system from 122 to 126 K. *Advanced Cryogenic Engineering*, U.S. Bureau of Mines, **16**, pp. 88–95, Helium Research Center, Amarillo, Texas.

Wygnanski, I. and Fiedler, H.E. (1970) The two-dimensional mixing region. *J. Fluid Mech.*, **41**, 327–361.

APPENDIX O

“Interaction of Acoustic Waves with a Cryogenic Nitrogen Jet at Sub- and Supercritical Pressures”

AIAA 2002-0342

Interaction of Acoustic Waves with a Cryogenic Nitrogen Jet at Sub- and Supercritical Pressures

B. Chehroudi* and D. Talley#

***Engineering Research Corporation Inc**
10 E. Saturn Boulevard
Edwards AFB, CA 93524-7680

#Air Force Research Laboratory
Propulsion Directorate
10 E. Saturn Boulevard
Edwards AFB, CA 93524-7680

40th AIAA
Aerospace Sciences Meeting & Exhibit
14-17 January, 2002
Reno, Nevada

Interaction of Acoustic Waves with a Cryogenic Nitrogen Jet at Sub- and Supercritical Pressures

B. Chehroudi[*] *and D. Talley*[#]

[*]Engineering Research Corporation Inc.
10 E. Saturn Boulevard
Edwards AFB, CA 93524-7680
(Corresponding author)

[#]Air Force Research laboratory
10 E. Saturn Boulevard
Edwards AFB, CA 93524-7680

Abstract

To better understand the nature of the interaction between acoustic waves and liquid fuel jets in rocket engines, cryogenic liquid nitrogen is injected into a room temperature high-pressure chamber having optical access on its sides. A piezo-siren capable of generating sound waves with an SPL of up to 180 dB is used under three chamber pressures of 1.46, 2.48, and 4.86 MPa. The reduced pressures for these pressures are 0.43 (subcritical), 0.73 (near-critical), and 1.43 (supercritical), respectively. The assembly consisting of the acoustic driver and the high-pressure chamber form a cavity that resonates at several frequencies, the strongest being at 2700 and 4800 Hz. Three different flow rates are considered and the nature of the aforementioned interaction has been documented via a high-speed imaging system using a CCD camera. It is found that the impact of the acoustic waves on the jet structure is strongest from low to near-critical chamber pressures and at low injectant flow rates. No significant effects of the acoustic waves are detected at the supercritical chamber pressure examined. It suggests that engine operation either near the critical point or in transition passing through the critical point could be troublesome and may lead to or feed combustion instabilities in liquid rocket engines. Further work is needed to directly relate these effects to the observed instabilities.

Introduction

Combustion instability has always been one of the most complex phenomena in liquid rocket engines, and therefore difficult to fully control particularly in the design of large output rockets. These difficulties stem from the emergence of oscillatory combustion with large pressure amplitudes. In one classification, high-amplitude, low-frequency (less than several hundred Hertz) pressure variations (or chugging) due to combustion is understood to be coupled with the feed line and structural modes of oscillations. Chugging is responsive to system-type analysis. Another instability is characterized by high amplitudes and high frequencies (screaming), and can lead to local burnout of the combustion chamber walls and injector plates (acoustic instability). This is caused by extreme heat-transfer rates brought about by high-frequency pressure and gas velocity fluctuations, see *Harrje and Reardon [1]*.

Two types of instabilities have been recognized in the past: linear instability, also called spontaneous or self-triggered, and nonlinear instability (or dynamic instability). Dynamic instability refers to a linearly stable system that becomes nonlinearly unstable in response to a sufficiently large disturbance. The underlying mechanism is the widely cited general principle by *Lord Rayleigh [2]*. In essence, he stated that the interaction between the combustion heat release and the acoustic field is the strongest if heat is added in a region of space and at the time when the acoustic amplitude is the highest. Although this view has been useful, overwhelming evidence gathered by past investigations attributed combustion instability to a complex interaction of the external acoustic field with the fuel injection processes, thereby leading to incidences of instability in rocket engines. For this and other reasons, controlled studies have been conducted probing into the effects of acoustic waves on gaseous and liquid jets from a variety of injector hole designs. A series of investigations concentrated on disturbances induced from within the injection system. They considered the effects of acoustic fields on many phenomena such as flow structure, vortex pairing, and shear layer growth rate in the initial region of the jet (for example, see a short review article by *Kiwata, et al. [3]*). More relevant to the work reported here, are a few reports and articles on gaseous or (in particular) liquid jets under the influence of external (transverse and longitudinal) acoustic fields. Although both longitudinal and transverse acoustic mode instabilities exist in rocket engines, for at least two reasons longitudinal modes are more stable. First, the exhaust nozzle provides heavier damping for the longitudinal modes than the tangential modes. Second, near-injector processes in the thrust chamber are generally more sensitive to velocity fluctuations parallel to the injector face than normal to it, see *Oefelein and Yang [4]*. Those investigations using external acoustic disturbances can be divided into two subgroups based on the state of the injected fluid, i.e., gaseous or liquid. In the following, selected works of immediate relevance to ours will be briefly described with more focus on those employing transverse acoustic waves

with a particular attention to liquid phase injection systems.

To provide maximum effects, *Miesse [5]* used two opposing localized acoustic drivers 180 degrees out of phase to investigate the impact of a transverse acoustic field on a low velocity liquid jet ($10 < L/d < 40$) at atmospheric chamber pressure. Images showed that the amplitude of the jet dispersion decreased with an increase in both the frequency (less than 200 Hz was used) of the driver and pressure drop across the injector (i.e. flow rate). It was also noted that the sound field considerably reduced the length of the solid stream. Maximum dispersion was observed at the natural frequency of the jet defined as approximately 0.029U/d, where U and d are mean jet velocity and diameter respectively.

Buffum and Williams [6] considered the interaction of external transverse acoustic waves at frequencies ranging from 100 to 500 Hz on a liquid turbulent jet at atmospheric pressure. The main physical quantity measured was the oscillatory displacement of the liquid jet as it passed through an acoustic standing wave field in a resonant tube. Using a closed tube and driving it at its fundamental resonant frequency, sinusoidal acoustic intensities up to about 160 dB were obtained. Resonance effects at different frequencies were achieved through variations of the tube length in this study. It was found that the peak-to-peak jet deflection decreased when jet diameter or velocity was increased due to increased fluid mass in the acoustic field. The jet deflection was unobservable below 130 dB and ummeasurable below 140 dB. Shearing atomization began at about 161 dB and was proposed to cause sizable periodic reactant sources to sustain or amplify combustion instabilities. Also, they measured higher drag coefficients for turbulent liquid jets in transverse acoustic fields and found them to be an order of magnitude larger than that of a solid cylinder having a diameter the same as that of the injector orifice. This caused enhanced jet deflections in the acoustic field and may be one source for sustaining the instability in liquid rocket engines.

Heidmann and Groeneweg [7] considered the effects of transverse traveling and standing acoustic waves (5 to 20 % of the mean chamber value) on both a single round jet (liquid oxygen burning with gaseous hydrogen) and an impinging jet. The time varying jet length was observed to be coupled with the acoustic field which raised the suspicion that unstable combustion was directly related to the dynamic behavior of the liquid jet. From the observations in the impinging jets (nitrogen oxides and hydrazine), they stated that nonlinear instability occurred when the acoustic oscillations were of sufficient magnitude to cause jet breakup before the impingement point. The severity of this nonlinear instability was reduced by protecting the jets with thin walled tubing and thus maintaining impingement.

A work in which transverse disturbances generated by an oscillating plate at a fixed amplitude but different frequencies (1000 to 10000 Hz) is also of interest here. A relatively large planar nozzle was used by *Rockwell [8]* to inject water and investigate the details of vortex formation and their interactions near the exit area. The effects of the frequency of oscillations on the natural vortex coalescence was classified based on a Strouhal number ($St=fd/U$, where f, d, and U are the excitation frequency, jet diameter, and mean jet velocity) versus Reynolds number ($Re=\rho Ud/\mu$, where ρ and μ are the injectant density and viscosity) plot. For the range of Re investigated (1860 to 10800), natural breakdown of the jet (with no external disturbance) was observed to within a few nozzle widths. The dimensionless frequency (St_N) was found to change with Re as $St_N = 0.012\ (Re)^{0.5}$. *Becker and Massaro [9]* also found the same value for axisymmetric air jets for Reynolds number ranging from 1,000 to 10,000. Four regimes were distinguished based on the observed effects of the external disturbance on the nature of the vortex interaction. The reference regime was that corresponding to the natural breakdown of the jet. The four regimes were named, in order of decreasing St number, "upper zone," "preservation," "matched excitation," and "forced fusion" regimes. A plot of these regimes will be given later and compared with the values estimated in our study, see Fig. 11. In the upper zone regime where the excitation frequencies were higher than about 3 to 4 times the natural breakdown frequency ($St > 3\ St_N$) no effects were observed. In the preservation regime, the core flow of the jet tended to be preserved followed by the induction of smaller vortices, the time-averaged velocity profile was narrowed, and the longitudinal turbulence was decreased (relative to undisturbed case). When the excitation frequency was matched with the natural breakdown frequency (matched regime), the effect was to accelerate the process of vortex formation and growth relative to the undisturbed case. Also, transverse distortion of the jet core was seen due to the vortex growth and coalescence. For the symmetrical jet work of *Becker and Massaro [9]*, symmetrical ring vortices were produced and highest time-averaged widening of the jet occurred. This was in contrast to the planar jet case in which vortices on the two sides of the jet were 180 degrees out of phase with each other. This regime merges to the preservation regime at higher Re number (~ 10,000). In the forced fusion regime (frequencies ~1/3 of natural jet breakdown), the natural breakdown vortices were forced to fuse early as a result of the formation of large-diameter applied disturbance vortices. *Vaslov and Ginevskiy [10]* found that in this regime the time-averaged velocity profile of the jet was broadened. Finally, in the lower zone regime, (frequencies < 1/10 of natural jet breakdown) the vortex growth was unaffected in their formation region. In the limit, however, as St approaches zero, the jet experienced a quasi-steady deflection process. *Rockwell [8]* stated that a fallacious averaged jet widening is detected if a time-averaged measurement technique is used downstream the injector, when in reality the jet is being deflected by the applied transverse disturbance.

We therefore have a preponderance of evidence pointing at the important role played by the near injector phenomena and their interaction with the acoustic waves in combustion instabilities observed in rocket engines. Considering the forgoing, it is clear that although useful information has been collected in the past, there is a large gap in information regarding the effects of the acoustic waves on turbulent jets under more realistic conditions relative to liquid rocket engines. Knowledge on the effects of acoustic waves under high ambient pressure and in particular under near- and super-critical pressures is lacking. To this end, experimental research has been undertaken at the Air Force Research Laboratory (AFRL) to investigate the impact of acoustic waves under high pressures ranging from subcritical to supercritical pressures. To our knowledge, this is the first time such an interaction has been studied. This work extends the previous activities of the group on supercritical jet breakup phenomena of relevance to cryogenic liquid rocket engines, see *Chehroudi et al. [11,12,13]*.

Experimental Setup

To better understand the nature of the interaction between acoustic waves and injected liquid fuels in rocket engines, cryogenic liquid nitrogen is injected into a room temperature high-pressure chamber with full optical access on its four sides. Figure 1 shows a schematic diagram of the experimental rig. The stainless steel chamber can withstand pressures and temperatures of up to 20 MPa and 473 K, respectively. It has two facing circular sapphire windows for optical diagnostics. Liquid N_2 is used to cool and/or liquefy the injectant passing through the cryogenic cooler prior to injection. The mass flow rate of the injectant is measured and regulated via a mass flowmeter, and a precision micrometer valve. Back-illumination of the jet

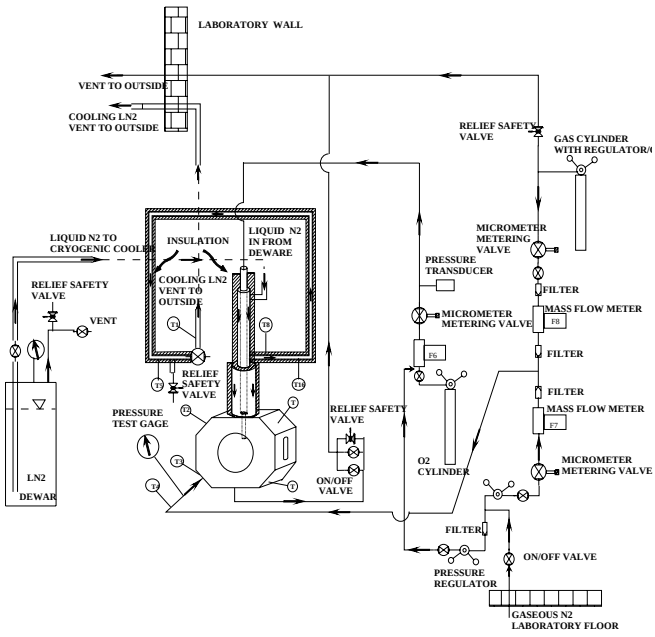

Figure 1. Schematic diagram of experimental setup for sub- to supercritical jet injection

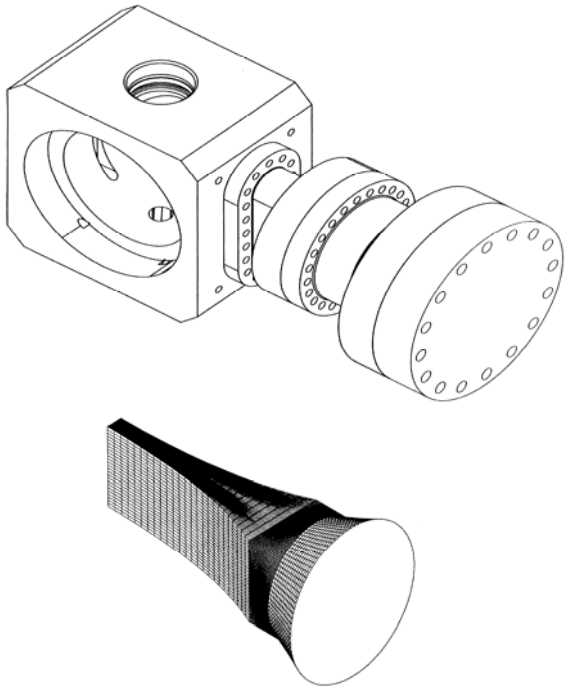

Figure 2. Top: coupling of the acoustic driver (piezo-siren) with the high-pressure chamber. Bottom: the design of the circular-to-rectangular channel to guide the waves into the chamber.

is accomplished with diffuse light flashes (0.8 μs duration). A model K2 Infinity long distance microscope is used with a high resolution (1280(H) x 1024(V) pixels in an 8.6(H)x6.9(V) mm actual sensing area with a pixel size of 6.7μm x 6.7 μm) CCD camera by the Cooke Corporation to form images of the injected jets. For the results reported, the cryogenic jet is injected through a sharp-edged stainless steel tube having a length, L of 50 mm, and inner and outer diameters measuring d_i = 0.254 mm and d_o = 1.59 mm, respectively. The resulting L/d_i was 200, which is sufficient to ensure fully developed turbulent pipe flow at the exit plane. The Reynolds number in these studies ranges from 14,000 to 80,000. The rig is fully instrumented to measure pressure, temperature, and mass flow rate of the injected fluid. A specially designed piezo-siren by Hersh Acoustical Engineering, Inc., capable of producing sound pressure levels (SPL) of up to 180 dB (in an impedance tube) at its resonant frequencies (lying between 1000 to 8000 Hz) and at pressures up to 2000 psi is used with a circular-to-rectangular transition coupling to bring the acoustic waves into the interaction zone inside the chamber. The SPL is defined as $20\log(P_e/P_{e,\,ref})$ where P_e is the RMS of the pressure oscillations and the reference pressure is 20.4 μPa. For example, a 1 psi amplitude of the sinusoidal fluctuations is equivalent to 167.4 dB. A model 601B1 Kistler piezoelectric-type pressure transducer is used to measure the acoustic pressure variations inside the chamber at various pressures very near the jet location. The piezo-siren acoustic driver is

able to generate between 161 to 171 db when coupled with the high-pressure chamber.

A Summary of Previous Results on Supercritical Jets at AFRL

During the past three years, results from the injection of several fluids into an ambient under both sub- and supercritical pressures at sufficiently high Reynolds numbers to be considered as fully-turbulent flow have been reported for the same test facility shown in Fig.1, see *Chehroudi et al. [11]*. A variety of ambient fluids was used into which pure N_2, He, and O_2 fluids were injected. The effects of chamber pressure (density) ranging from thermodynamic subcritical to supercritical pressures at a supercritical chamber temperature (based on the critical pressure and temperature, P_c, T_c, of the injectant) were observed by the acquisition of shadowgraph images from the injector exit region using a CCD camera illuminated by short-duration light pulses.

At sufficiently low subcritical chamber pressures, the disturbances on the jet interface amplified downstream and eventually broke up into irregularly-shaped small entities. A further increase of chamber pressure initiated the formation of many small ligaments and droplets at the interface of the jet only within a narrow regime below the thermodynamic critical pressure of the injected pure fluid, resembling a second wind-induced liquid jet breakup. At even higher chamber pressures, near but below the critical pressure of the injectant, the expected transition into a full atomization regime to produce a liquid spray was inhibited due to reduction of both the surface tension and the heat of vaporization. The jet appearance changed abruptly at this pressure and resembled that of a turbulent gas jet for all higher chamber pressures. The initial growth rate of the jet was plotted together with available data on liquid fuel injection in diesel engine environments, and turbulent incompressible, supersonic, and variable-density jets and mixing layers. The resulting plot is unique in its own right, covering four order of magnitude in density ratio. At near- and super-critical pressures, these measurements agreed well with the theoretical growth rate equations proposed *by Brown [14], Papamoschou and Roshko [15],* and *Dimotakis [16]* for incompressible but variable-density turbulent mixing layers. This constituted the first quantitative evidence in support of the past qualitative observations that the jet appeared to evolve into a gas-like behavior under supercritical condition. The geometry of the jet interface was also examined for the first time by fractal analysis. The results clearly indicated a transition from a Euclidean to a fractal interface, with a fractal dimension close to values measured for gaseous turbulent jets. This provided an additional quantitative evidence for the hypothesis that the jet evolved into a gas-like behavior. An equation was proposed based on a physical model proposing that at the point of transition from liquid-like to gas-like appearances and growth rates, the characteristic time of the vaporization process is of the same order as that of the interfacial "bulge" formation/separation events. The model equation agreed well with the experimental growth rate data. Finally, The initial growth rate of the jet as judged by the Raman signature was in reasonably good agreement with our earlier measurements using shadowgraphy if twice the full width half maximum (FWHM) of the normalized intensity plots was used, *see Chehroudi et al. [17]*.

Experimental Results

It is found that a certain minimum oscillation amplitude is needed to bring about a detectable interaction. When a rapid transition is made from below to above this minimum value, a strong and transitory effect is observed, characterized by eruption of many drops and ligaments from the surface of the jet combined with amplification of the surface wave instabilities. When set at its highest achievable acoustic wave amplitude, the oscillation augmented the unstable surface waves and imposed a zigzag-shaped contour to the jet. Preliminary results under subcritical condition indicates constriction of the jet in the acoustic propagation direction (perpendicular to the jet axis) near the injector exit followed by the acceleration of the atomization process further downstream. Figures 3, 4, and 5 shows effects of acoustic waves (traveling from left to right in these figures) on the liquid nitrogen jet at three different flow rates and at subcritical, near-critical, and supercritical pressures, respectively. Each composite jet image consists of a mosaic of several images taken from the same test run but at different times and jet axial locations. At each axial position up to 10 images were taken. These images were not taken at any specific phase with respect to the acoustic driver. The acoustic coupling guide and the high-pressure chamber form a cavity that resonates at certain distinct frequencies. Under the current setup, the highest amplitude of pressure oscillations can be detected at only two frequencies (~ 2700 and ~ 4800 Hz). Considering a speed of the sound of about 357 m/s, the acoustic wavelength is 13.1 and 7.4 cm/s when the driver oscillates at 2700 and 4800 Hz, respectively. This value is much larger than the jet diameter investigated here. Figures 3, 4, 5 are taken when the acoustic piezo-siren was driven at about 4800 Hz. Similar images were collected at 2700 Hz but are not shown here. However, the general wave/jet interaction effects are the same at these two frequencies.

Reduced Pressure Pch/Pc , Pc is critical Pressure	**Chamber Pressure Pch, MPa**	**LN2 FLOW RATE, mg/s**		
		150	**300**	**500**
		REYNOLDS # ESTIMATE		
0.43	**1.46**	**14323**	**33674**	**47742**
0.73	**2.48**	**20489**	**48172**	**68296**
1.43	**4.86**	**24816**	**59771**	**82721**

Table1. Estimates of the Reynolds numbers at different injectant flow rates.

Dramatic effects of the acoustic field on the jet structure, particularly at low flow rates and near-critical conditions can easily be seen at a first glance. Also, the narrowing of the jet is apparent near the injector exit region, as though it is pinched in the acoustic wave direction. The jet intact length is shortened and consequently a larger amount of mass is evaporated as compared to the unexcited jet (see the case for the lowest flow rate in Figs. 3 and 4). At the lowest flow rate the jet is seen to have been deflected in the mean sense in the direction of acoustic wave propagation, see Fig. 3. However, these effects are hardly detectable at supercritical pressures, see Fig. 5. Inspection of Figs. 6, 7, and 8, taken perpendicular to the direction shown in Figs. 3, 4, and 5, clearly indicates strong effects of the acoustic waves on spreading the liquid nitrogen mass in the direction perpendicular to the acoustic wave propagation. These images were taken on a different test run than those shown in Figs. 3, 4, and 5. However, the operating conditions were as close as possible to those in the previous figures. Although not shown here, the general behavior is similar when the acoustic driver was driven at 2700 Hz.

The impact of the acoustic waves on the jet is reduced as inertia forces increase through an increase of flow rate. This is similar to the observation of Buffum and Williams [6]. To extract some quantitative information from these images, a distance from the injector exit plane is selected within the first frame of the composite images shown in Figs. 3 to 8. This axial distance was at about 5 injector diameters in order to be representative of the effects in the initial region of the jet. Horizontal-row pixel information for a region of one injector diameter in the axial direction is averaged to extract a jet thickness value. Also, the information for up to 10 injector diameters is used to measure the initial jet spreading angle. For each case the average of 10 images was used for these calculations. Results from these measurements are shown in Figs. 9 and 10. A thickness of about 90 pixels in these figures represents one injector hole diameter. This can be seen for data taken at the lowest chamber pressure. The data with and without acoustic waves were taken back-to-back and from the same run. The contraction of the jet in the acoustic direction can be seen in Figs. 9(a) and (b) particularly at 2700 Hz. The strongest expansion of the jet is measured at low flow rates and low to near-critical chamber pressures, being highest at near-critical pressures. This observation is also supported by inspection of the data in Fig. 10. As proposed by others, this enlarged impact of the acoustic waves near the critical point of the injectant can be one important underlying reason for combustion instability in liquid rocket engines.

The situation for supercritical jets is quite different. Minimal effects of the acoustic waves on jet structure or its spread rate is seen. To search for some plausible reason, we use the information that at supercritical pressures, the unperturbed jet spreading rate is the same as an incompressible variable-density gaseous jet, see *Chehroudi et al. [11]*. For this reason, one expects existence of vortices similar to what has been described, for example, by *Rockwell [8]*. To investigate this matter further, our supercritical data is superimposed on a plot by him indicating different regimes discussed in the introduction section. Figure 11 shows a plot of the Strouhal number as a function of the Reynolds number. The curve marked "matched excitation" is the same equation proposed by *Becker and Massaro [9]* for the natural breakdown of the jet. Results from current study is beyond the regions studied before and one should beware of the dangers of extrapolation. Fortunately, the extrapolation is not too far from those reported in Fig. 11. Figure 11 suggests that the frequencies used here are not expected to bring about noticeably large effects of the acoustic waves because they lie in the region identified by *Rockwell [8]* as the "lower zone." No effects of the transverse disturbance on the jet were observed in the studies conducted by *Rockwell [8]* in this regime as described in the introduction section. Note that the lowest flow rate case tends to enter into the "forced fusion" regime where stronger interaction is expected, see Fig. 11.

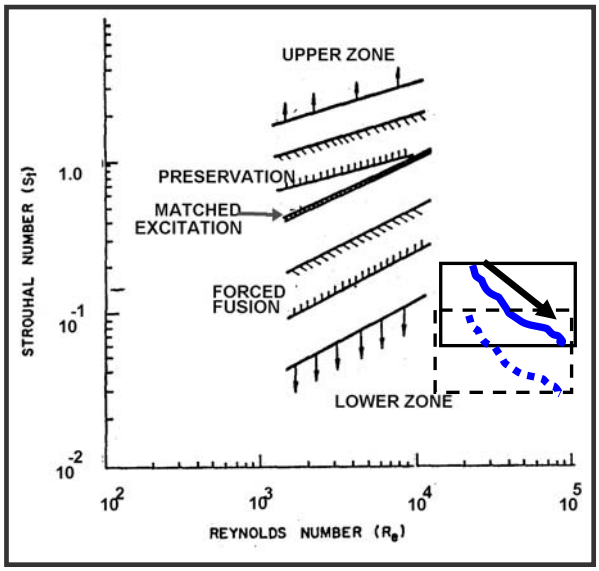

Figure 11. Regimes discussed by *Rockwell [8]* shown on an excitation Strouhal number versus the jet Reynolds number plot. The small solid rectangle to the right indicates the approximate region in which the current study lies when excitation is at 4800 Hz. The curve in this rectangle shows the approximate path as flow is increased from the lowest to the highest . Similar region for the 2700 Hz excitation is shown as a dashed rectangle.

Summary and Conclusions

Cryogenic nitrogen is injected into a chamber filled with gaseous nitrogen at room temperature which can support controlled acoustic waves. These waves are generated via mechanical vibration of a plate by a piezoelectric material. The chamber resonates at certain distinct frequencies found to be suitable for this study due to its high amplitude oscillations. At the lowest chamber pressure tested here (subcritical), the jet is strongly affected by the

waves. As the flow rate is increased, the inertia forces become very large and the observed interaction is substantially weakened. Operation of the chamber at near the critical pressure profoundly affected the jet structure, bringing early breakup and dispersion of the jet. Again, this effect is subdued at higher flow rates. At a supercritical chamber pressure, the effects of the acoustic field on the jet becomes unnoticeable. Due to its gas-jet like behavior, the supercritical jet is assumed to posses similar vortex formation and coalescence observed in turbulent jets, as reported by *Rockwell [8]*. Comparison to his results showed that the excitation St number used in the current work is too low to bring about any noticeable effects in the initial region of the jet.

Acknowledgement

Mr. Mike Griggs, Mr. Earl Thomas, and Mr. Randy Harvey are thanked for their valuable support. Ms. Jennie Paton and Ms. Tony Collett are to be especially thanked for making the requested literature available in a timely manner. We also appreciate Mr. Kevin Bradley's contribution in part of the data acquisition and processing. Dr. Rich Cohn is thanked for kindly offering his expertise in image acquisition area. This work is sponsored by the Air Force Office of Scientific Research, Dr. Mitat Birkan, program manager.

References

1. Harrje, T. D. and Reardon, H. F., Liquid Propellant Rocket Combustion Instability, NASA report number NASA SP-194, 1972.

2. Rayleigh, Lord, "The Explanation of Certain Acoustical Phenomena," *Royal Institution Proceedings*, vol. VIII, London, 1878, pp. 536-542.

3. Kiwata, T., Okajima, A., and Ueno, H., "Effects of excitation on plane and coaxial jets," Proceedings of the 3rd Joint ASME/JSME Fluid Engineering Conference, July 18-22, San Francisco, California, 1999.

4. Oefelein J. C. and Yang, V., "Comprehensive Review of Liquid Propellant Combustion Instabilities in F-1 Engines, *Journal of Propulsion and Power*, Vol. 9, No. 5, 1993, pp.657-677.

5. Miesse, C. C., The Effect of Ambient Pressure Oscillations on the Disintegration and Dispersion of a Liquid Jet," *Jet Propulsion*, 25, pp. 525-530, 534, 1955.

6. Buffum, F. G., and Williams, F. A., "Response of Turbulent Liquid Jets to Transverse Acoustic Fields," Proceedings of the 1967 Heat Transfer and Fluid Mechanics Institute, Edited by P. A. Libby, D. B. Olfe, and C. W. Van Atta, 1967, pp. 247-276, 1967.

7. Heidmann, M. F. and Groeneweg, J. F., "Analysis of the Dynamic Response of Liquid Jet Atomization to Acoustic Oscillations," NASA Technical Note, NASA TN D-5339, July, 1969.

8. Rockwell, D. O.," External Excitation of Planar Jets," *Journal of Applied Mechanics*, pp. 883-891, December 1972.

9. Becker, H. A. and Massaro, T. A., "Vortex Evolution in a Round Jet," *Journal of Fluid Mechanics*, Vol. 31, Part 3, pp.435-448, 1968.

10. Vaslov, Ye. V. and Ginevskiy, A. S., "Acoustic Effects on Aerodynamic Characteristics of a Turbulent Jet," Foreign Technology Division, Air Force Systems Command, No. FTD-MT-24-232-68, Aug., 1968.

11. Chehroudi, B., Talley, D.G., and Coy, E., "Fractal Geometry and Growth Rate Changes of Cryogenic Jets Near the Critical Point," 35th AIAA/ASME/SAE/ASEE Joint Propulsion Conference and Exhibit, paper AIAA 99-2489, 20-24 June, Los Angeles, CA, 1999.

12. Chehroudi, B., Cohn, R., and Talley, D.G., "Cryogenic Shear Layers: Experiments and Phenomenological Modeling of the Initial Growth Rate Under Subcritical and Supercritical Conditions," *International Journal of Heat and Fluid Flow*, to appear (2002).

13. Chehroudi, B., Cohn, R., and Talley, D.G., "Visual Characteristics and Initial Growth Rates of Round Cryogenic Jets at Subcritical and Supercritical Pressures," *Physics of Fluids*, vol. 14, no. 2, February, 2002.

14. Brown G., "The Entrainment and Large Structure in Turbulent Mixing Layers," 5th Australasian Conf. on Hydraulics and Fluid Mech., 1974, pp. 352-359.

15. Papamoschou, D. and Roshko, A. "The Compressible Turbulent Shear Layer: an Experimental Study," *Journal of Fluid Mechanics*, vol. 197, 1988, pp. 453-477.

16. Dimotakis, P. E. "Two-Dimensional Shear-Layer Entrainment," *AIAA Journal*, 21, No. 11, 1986, pp. 1791-1796.

17. Chehroudi, B., Cohn, R., Talley, D., and Bakakhshan, A., "Raman Scattering Measurements in the Initial Region of Sub- and Supercritical Jets," 36th AIAA/ASME/SAE/ASEE Joint Propulsion Conference, paper AIAA-2000-3392, 17-19 July, 2000.

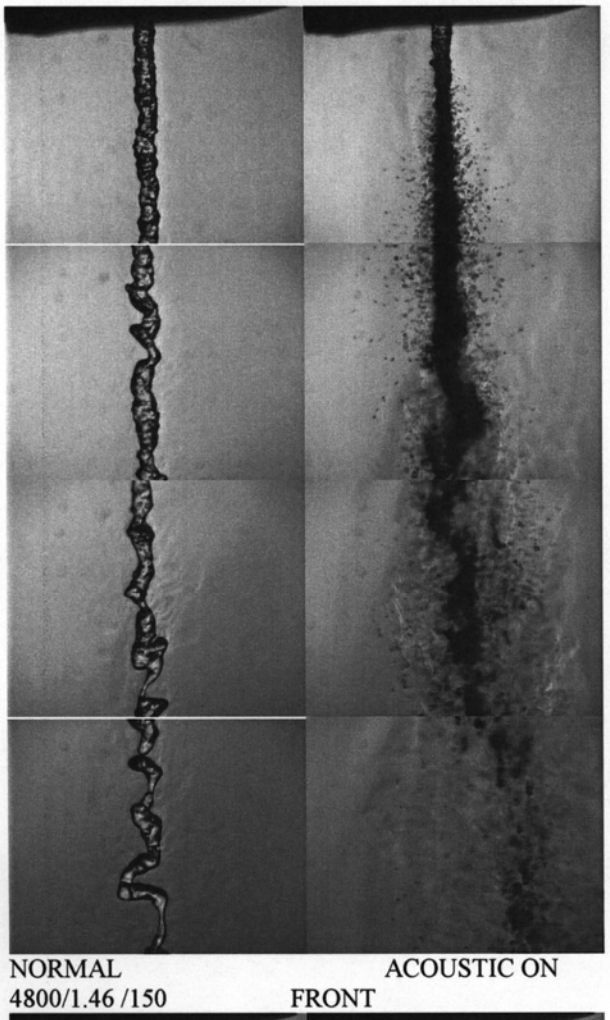

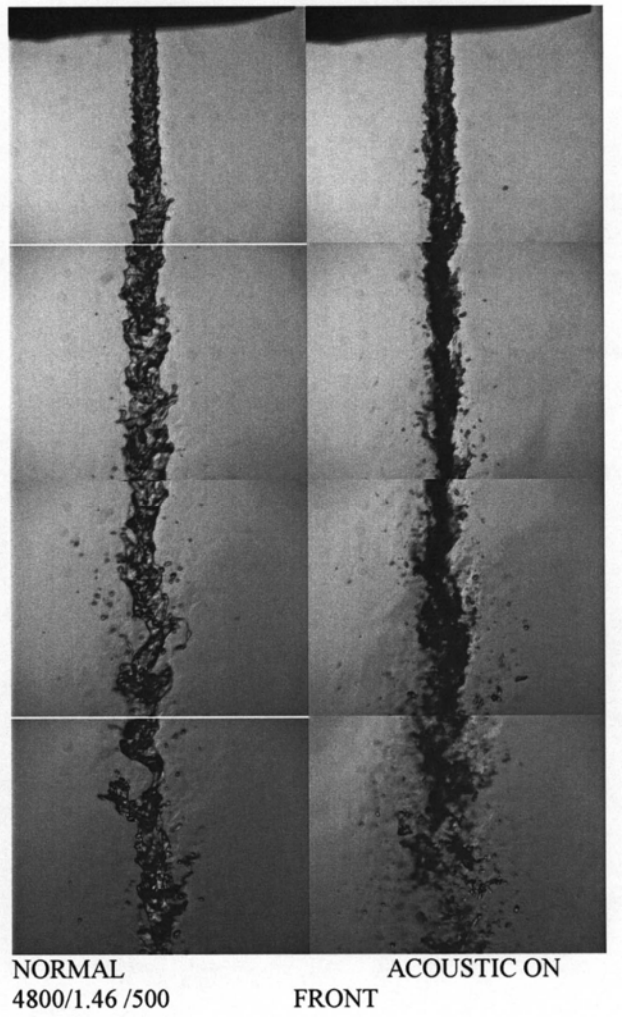

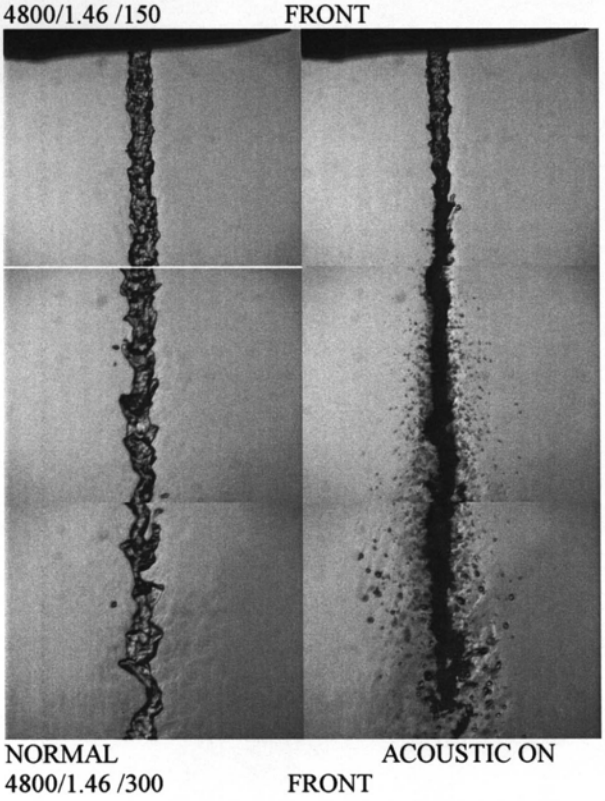

Figure 3. Images of the liquid nitrogen jet injected into the gaseous nitrogen chamber at a subcritical chamber pressure of 1.46 MPa and three different injected flow rates of 150, 300, and 500 mg/s. Acoustic waves are traveling from left to right in these images. The acoustic wave frequency was set at 4800 Hz. Each composite jet image consists of a mosaic of several images taken from the same run but at different times and jet axial locations.

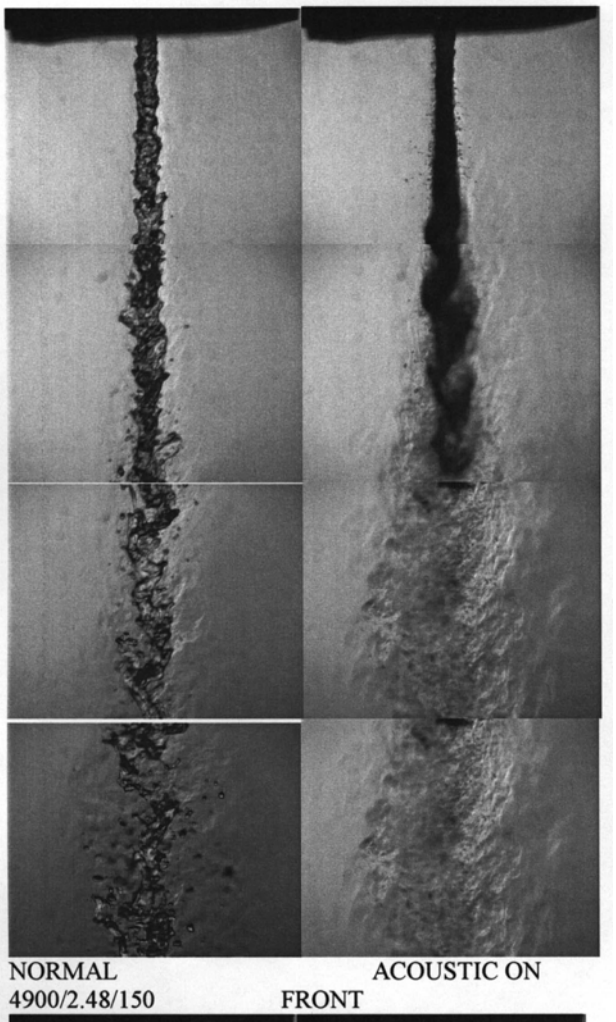

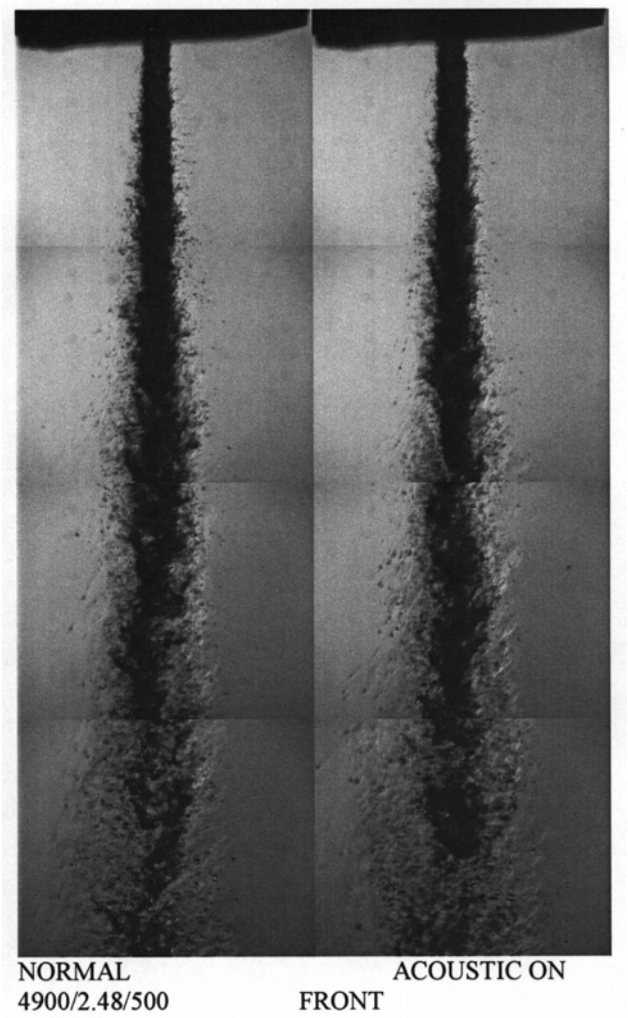

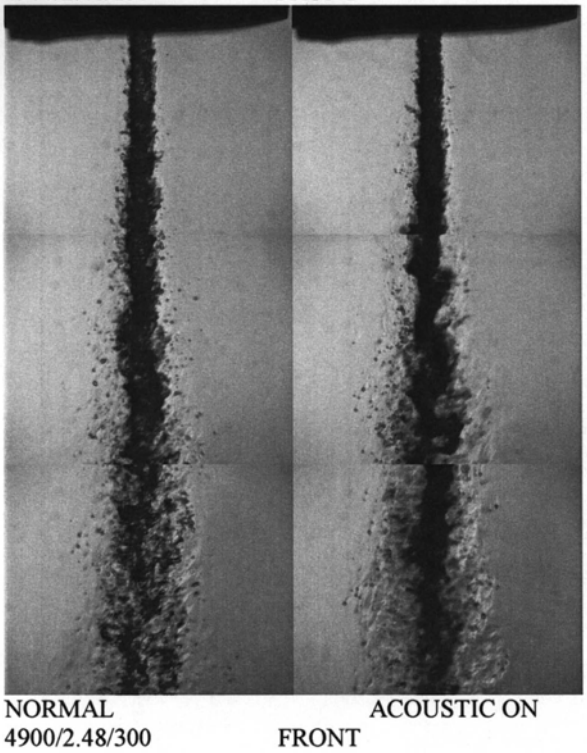

Figure 4. Images of the liquid nitrogen jet injected into the gaseous nitrogen chamber at a near-critical chamber pressure of 2.48 MPa and three different injected flow rates of 150, 300, and 500 mg/s. Acoustic waves are traveling from left to right in these images. The acoustic wave frequency was set at 4900 Hz. Each composite jet image consists of a mosaic of several images taken from the same run but at different times and jet axial locations.

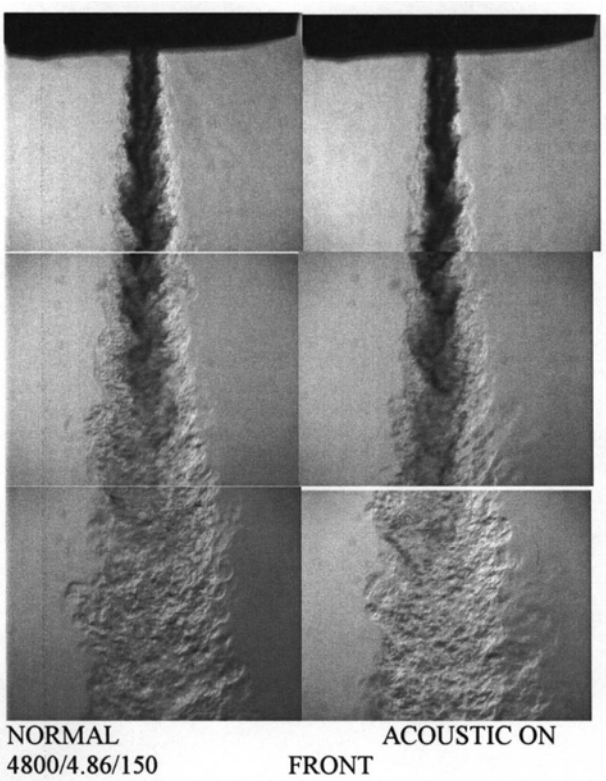

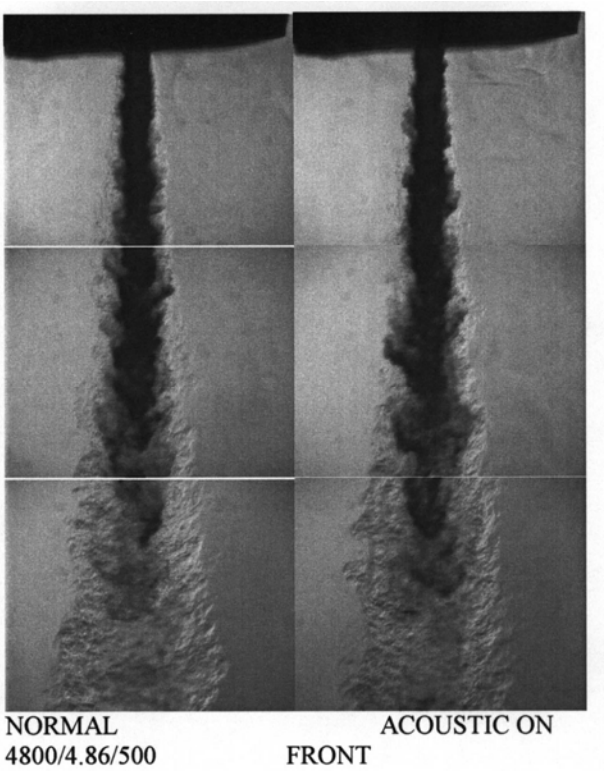

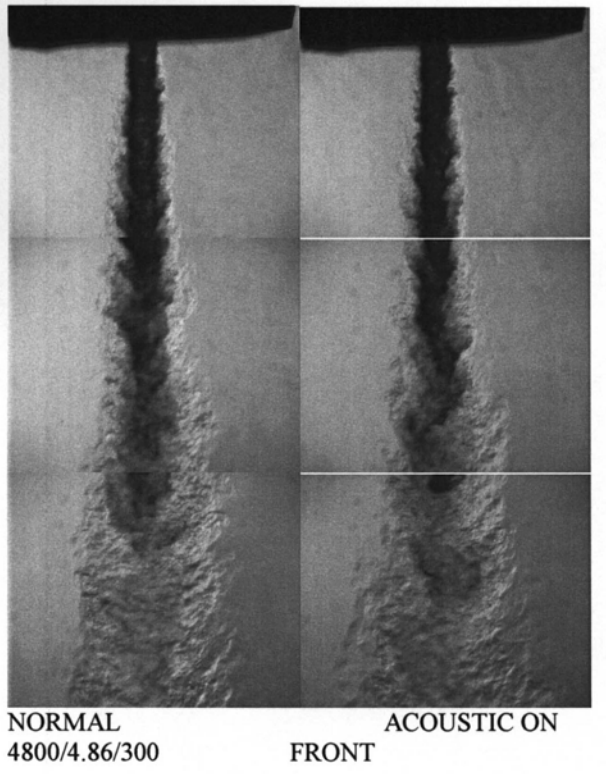

Figure 5. Images of the liquid nitrogen jet injected into the gaseous nitrogen chamber at a supercritical chamber pressure of 4.86 MPa and three different injected flow rates of 150, 300, and 500 mg/s. Acoustic waves are traveling from left to right in these images. The acoustic wave frequency was set at 4800 Hz. Each composite jet image consists of a mosaic of several images taken from the same run but at different times and jet axial locations.

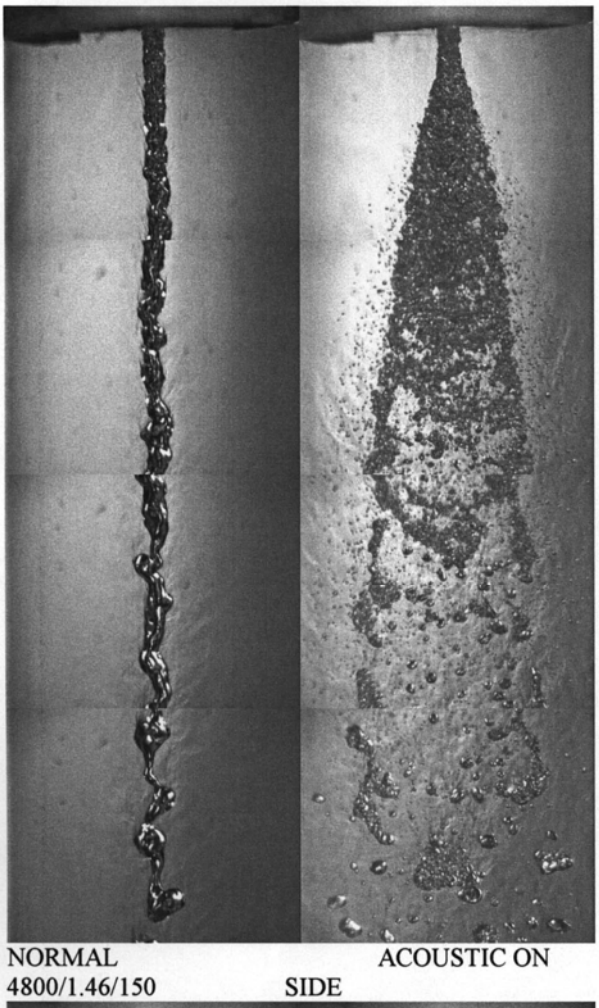

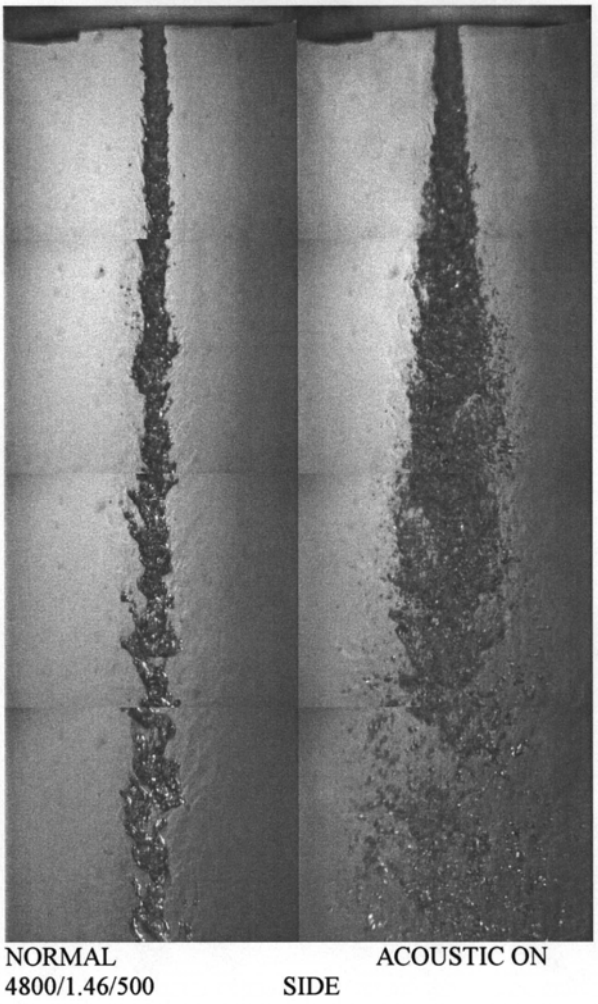

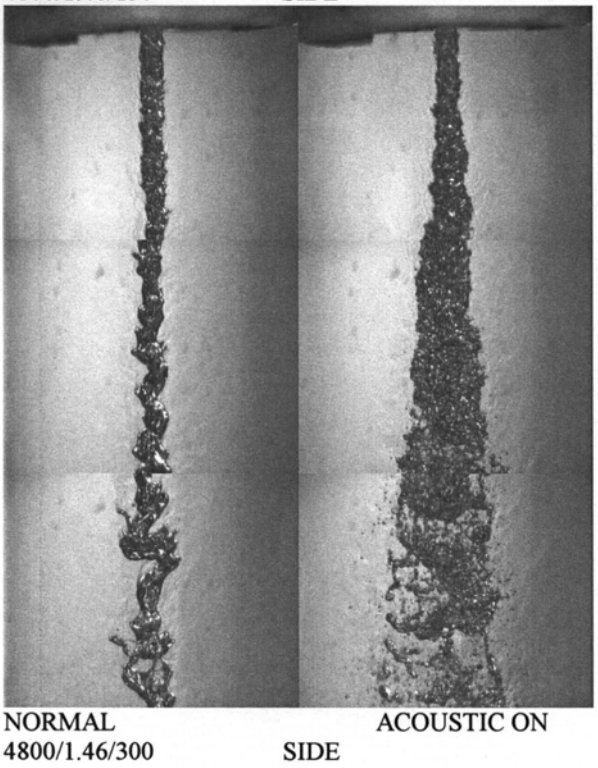

Figure 6. Images of the liquid nitrogen jet injected into the gaseous nitrogen chamber at a subcritical chamber pressure of 1.46 MPa and three different injected flow rates of 150, 300, and 500 mg/s. Acoustic waves are traveling perpendicular and out from the page in these images. The acoustic wave frequency was set at 4800 Hz. Each composite jet image consists of a mosaic of several images taken from the same run but at different times and jet axial locations.

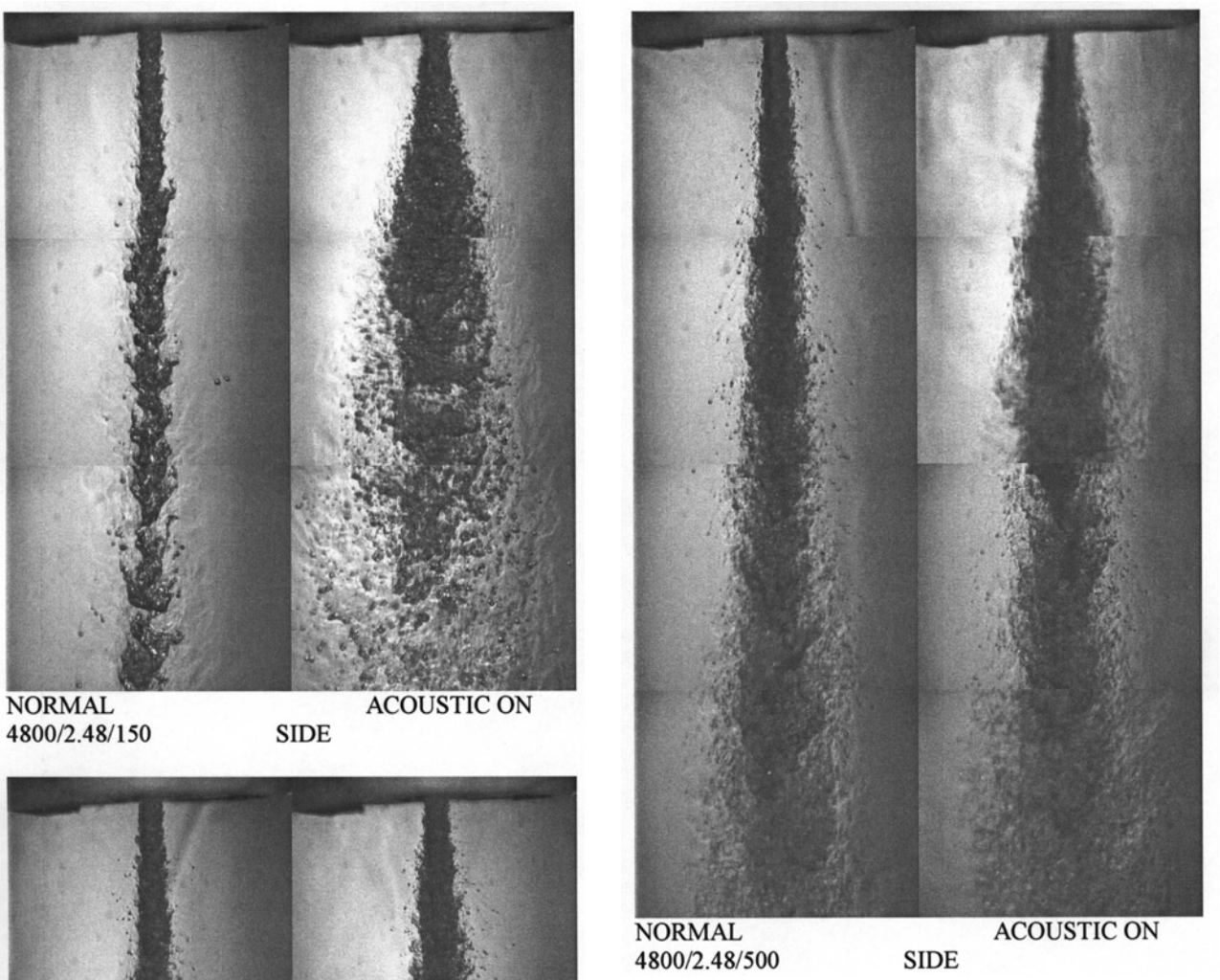

Figure 7. Images of the liquid nitrogen jet injected into the gaseous nitrogen chamber at a near-critical chamber pressure of 2.48 MPa and three different injected flow rates of 150, 300, and 500 mg/s. Acoustic waves are traveling perpendicular and out from the page in these images. The acoustic wave frequency was set at 4800 Hz. Each composite jet image consists of a mosaic of several images taken from the same run but at different times and jet axial locations.

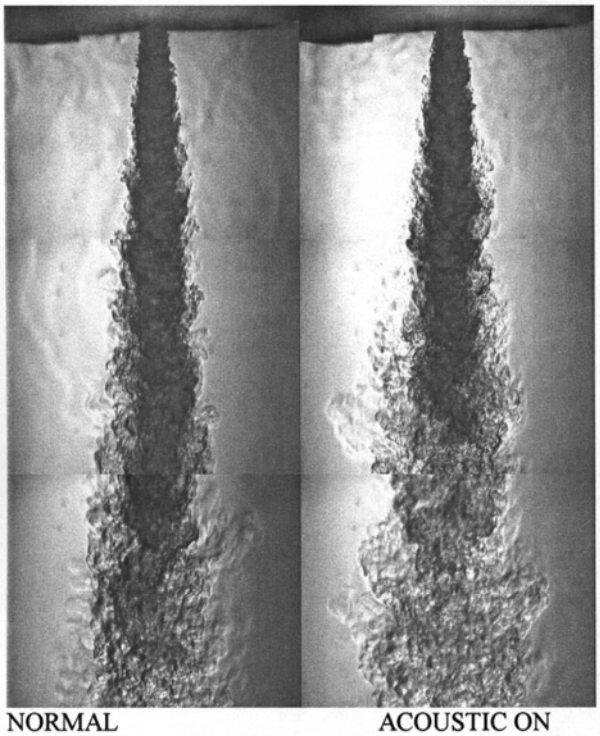

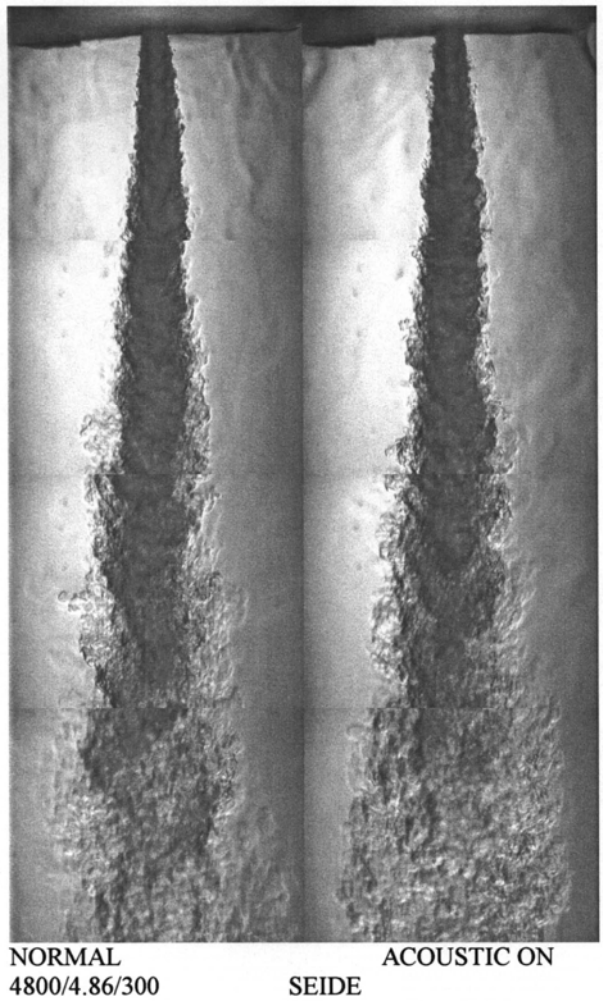

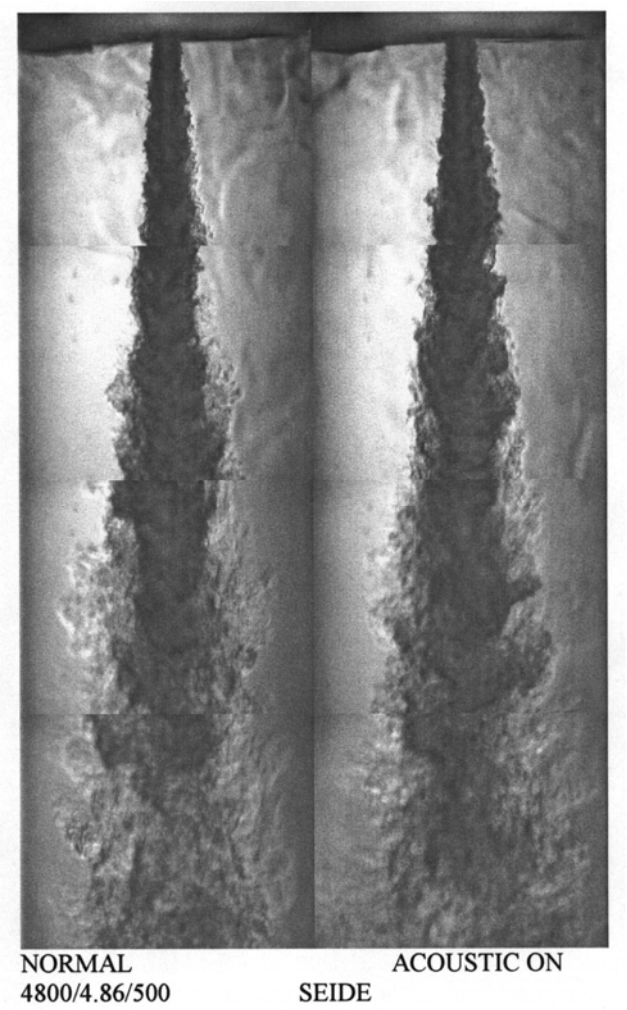

Figure 8. Images of the liquid nitrogen jet injected into the gaseous nitrogen chamber at a supercritical chamber pressure of 4.86 MPa and three different injected flow rates of 150, 300, and 500 mg/s. Acoustic waves are traveling perpendicular and out from the page in these images. The acoustic wave frequency was set at 4800 Hz. Each composite jet image consists of a mosaic of several images taken from the same run but at different times and jet axial locations.

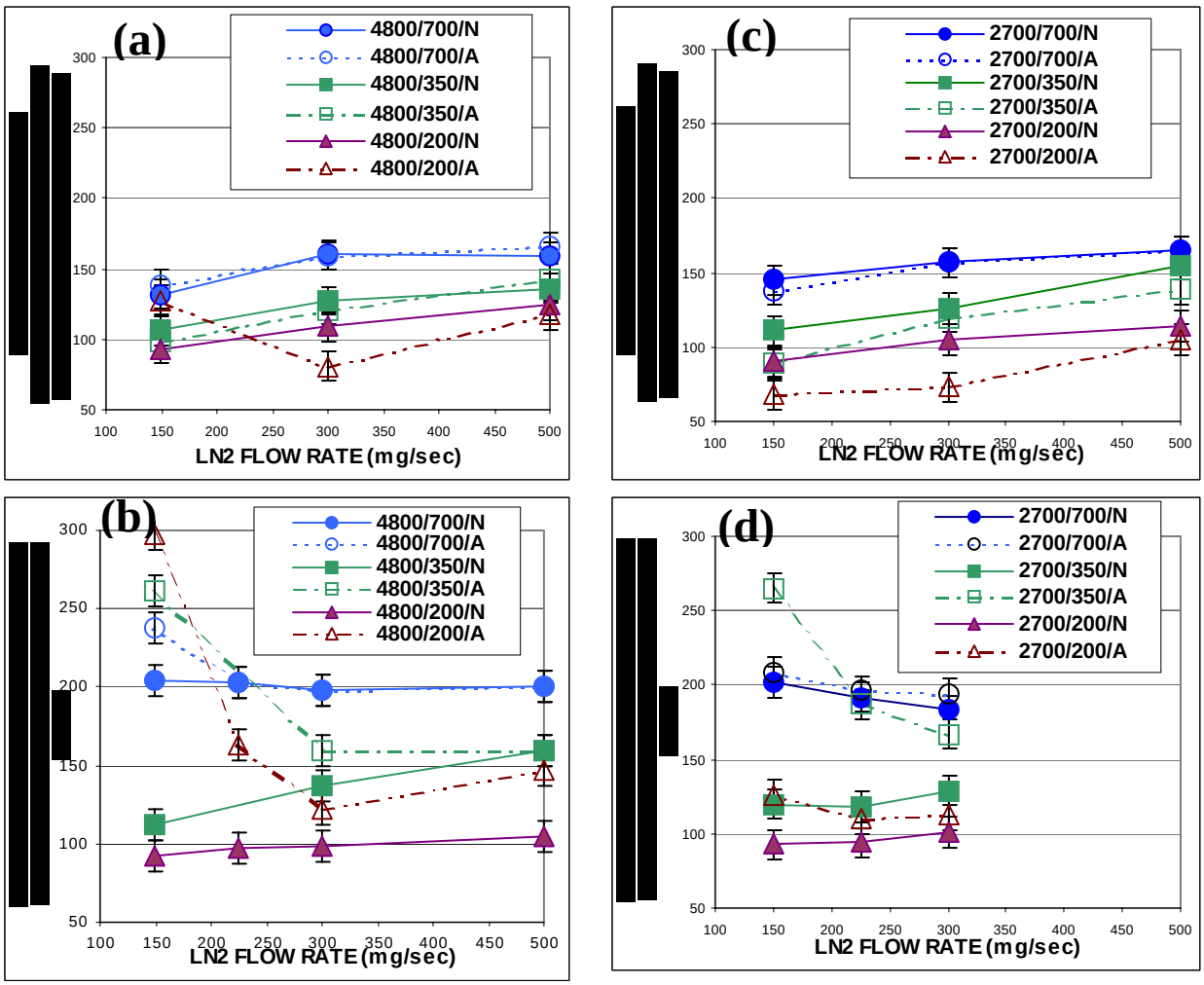

Figure 9. Jet thickness values measured at a distance of 5 injector diameters from the exit and three different flow rates, three chamber pressures, and at two different excitation frequencies of ~2700 and ~4800 Hz. Dashed and solid lines are for with and without presence of acoustic waves respectively. The vertical bar on each symbol indicates the uncertainty of the presented data. The numbers 200, 350, and 700 correspond to chamber pressures of 1.46, 2.48, and 4.86 MPa. The letters N and A refer to the case with and without acoustic waves. LN2 refers to liquid nitrogen. Each image pixel represents approximately 2.82 micron in physical world.

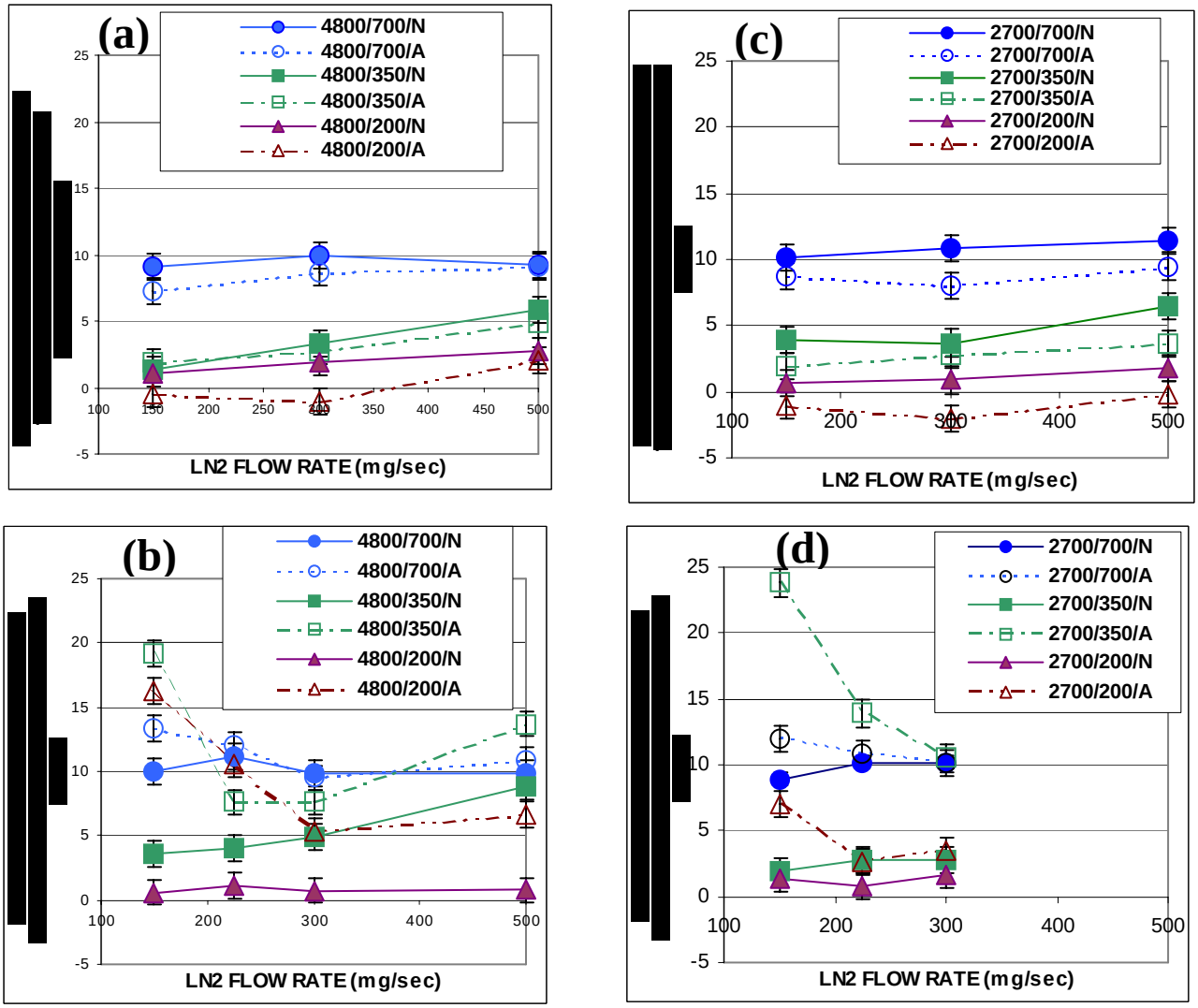

Figure 10. Initial jet angle values measured from information to within about 10 injector diameters from the exit at three different flow rates, three chamber pressures, and at two different excitation frequencies of ~2700 and ~4800 Hz. Dashed and solid lines are for with and without presence of acoustic waves respectively. The vertical bar on each symbol indicates the uncertainty of the presented data. The numbers 200, 350, and 700 psig correspond to chamber pressures of 1.46, 2.48, and 4.86 MPa. The letters N and A refer to the case with and without acoustic waves. LN2 refers to liquid nitrogen. Each image pixel represents approximately 2.82 micron in physical world.

APPENDIX P

"Initial Results From A Cryogenic Coaxial Injector in an Acoustic Field"

AIAA 2003-1339

Initial Results From A Cryogenic Coaxial Injector In An Acoustic Field

B. Chehroudi*, D. Davis*, and D. Talley#

***Engineering Research Corporation Inc**
10 E. Saturn Boulevard
Edwards AFB, CA 93524-7680

#Air Force Research Laboratory
Propulsion Directorate
10 E. Saturn Boulevard
Edwards AFB, CA 93524-7680

41st AIAA
Aerospace Sciences Meeting & Exhibit
6-9 January, 2003
Reno, Nevada

Initial Results From A Cryogenic Coaxial Injector In An Acoustic Field

B. Chehroudi[*] , D. Davis, and D. Talley[#]*

[*]Engineering Research Corporation Inc.
10 E. Saturn Boulevard
Edwards AFB, CA 93524-7680
ChehroudiB@aol.com
(Corresponding author)

[#]Air Force Research laboratory
10 E. Saturn Boulevard
Edwards AFB, CA 93524-7680

Abstract

A coaxial injector was made to inject liquid nitrogen (LN2) with a coflow of gaseous nitrogen (GN2) in its annular region as part of a program to better understand the nature of the interaction between acoustic waves and liquid fuel jets in cryogenic rocket engines. The LN2 was injected into a room temperature high-pressure chamber having optical access on its sides. A piezo-siren capable of generating sound waves with an SPL of up to 180 dB was employed under two chamber pressures of 2.14 and 4.86 MPa. The reduced pressures for these pressures are 0.63 (subcritical), and 1.43 (supercritical), respectively. The assembly consisting of the acoustic driver and the high-pressure chamber form a cavity that resonates at several frequencies, the strongest being at 2700 and 4800 Hz. Initial results for only one LN2 flow rate but at three co-flow rates and at 2700 Hz are reported here. The nature of the aforementioned interactions has been captured via a CCD camera high-speed imaging system. These evidences indicate that the warmer co-flow GN2 affects the thermodynamic condition of the LN2 jet near the inner wall surface, reducing the jet initial visual diameter, particularly at higher co-flow rates. Dramatic effects of the periodic transverse acoustic waves can be seen to impose a sinusoidal shape to the jet appearance. The wavelength of this wavy shaped structure is established by the acoustic-induced transverse deflection of the jet considering the fact that the jet exists in the velocity antinode of the acoustic field. Injector modifications to provide a more realistic flow conditions and collection of more data are needed to fully map and explain these initially-observed interesting interactions.

Introduction

In evaluating injector performance, it is customary to conduct reasonably simple and cost-effective non-fired studies at elevated ambient pressures. Water and nitrogen are often used as simulants under non-fired conditions for reasons of safety and convenience. The question often arises as to what extent the information gained in such cold tests is of value. Normally, the tests are designed to match certain non-dimensional parameters to those of actual combustors, for example, liquid-to-gas mass, momentum, density, and velocity ratios, and Weber, Reynolds, Ohnesorge, etc. numbers. Matching all parameters is not always possible. Therefore, it is highly desirable to follow a systematic approach whereby links are established between non-fired and fired tests. These established links make the non-fired studies a valuable exercise for design engineers. Non-fired studies can yield valuable insight into the atomization efficiency and performance of different designs of injectors, for instance. The non-fired studies reported in this paper were performed under a similar logic whereby the results will eventually be linked to fired conditions inside cryogenic liquid rocket engines.

In this preliminary work, we report some initial results obtained on a coaxial injector. The key idea is to systematically extend extensive results obtained on single-jet injectors obtained by *Chehroudi et al [1,2,3]* by adding an annular co-flow. In the preliminary results reported here, the center jet is liquid nitrogen and the co-flow is gaseous nitrogen, and the co-flow velocity is small in order to relate the results to previous non-coflowing results. Results are reported at a subcritical pressure and a supercritical pressure. Future efforts will include subcritical and supercritical results at higher co-flow velocities and using helium as the co-flow gas, as well as fired results using liquid oxygen and gaseous hydrogen. In addition, the test facility has a unique high-pressure acoustic driver, also used in a single-jet study of *Chehroudi et al. [4]*, where the effects of acoustic perturbation can be studied under both subcritical and supercritical conditions. This should create a unique set of features to approach the problem of combustion instability in cryogenic liquid rocket engines systematically and in a stepwise manner.

Experimental Setup

Cryogenic liquid nitrogen is injected into a room temperature high-pressure chamber with full optical access on its four sides. Figure 1 shows a schematic diagram of the experimental rig. The stainless steel chamber can withstand pressures and temperatures of up to 20 MPa and 473 K, respectively. It has two facing circular sapphire windows for optical diagnostics. Liquid N_2 is used to cool and/or liquefy the injectant passing through the cryogenic cooler prior to injection. The mass flow rate of the injectant is measured and regulated via a mass flow meter and a precision micrometer valve. Back-illumination of the jet is accomplished with diffuse light flashes (0.8 μs duration). A model K2 Infinity long distance microscope is

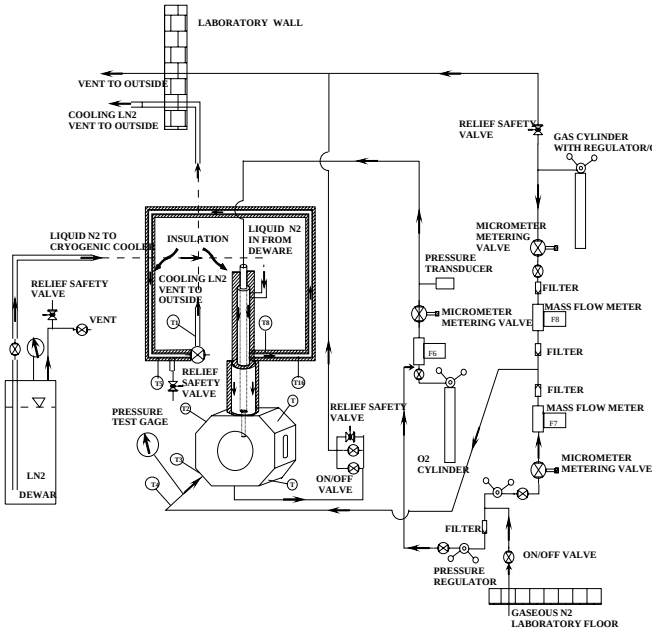

Figure 1. Schematic diagram of experimental setup for sub- to supercritical jet injection

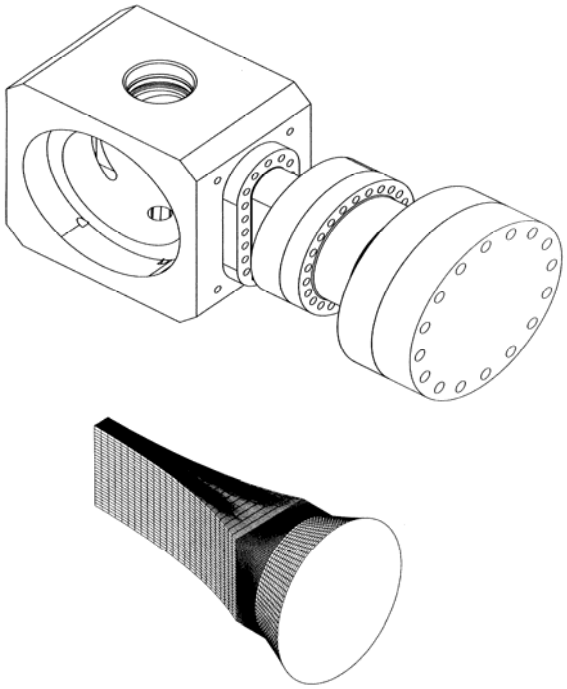

Figure 2. Top: coupling of the acoustic driver (piezo-siren) with the high-pressure chamber. Bottom: the design of the circular-to-rectangular channel to guide the waves into the chamber.

used with a high resolution (1280(H) x 1024(V) pixels in an 8.6(H)x6.9(V) mm actual sensing area with a pixel size of 6.7μm x 6.7 μm) CCD camera by the Cooke Corporation to form images of the injected jets. For the results reported, the cryogenic jet is injected through a sharp-edged stainless steel tube having a length L of 50 mm, and inner and outer diameters measuring d_i = 0.508 mm and d_o = 1.59 mm, respectively. The resulting L/d_i was 100, which is sufficient to ensure fully developed turbulent pipe flow at the exit plane. The Reynolds number in these studies ranges from 6,000 to 30,000. The outer annular tube has the inner diameter of 2.286 mm, forming a gaseous fluid annular passage of 0.348 mm in the radial direction. This was the first of a series of designs with different aforementioned dimensions that was tested and initial results are presented here. Figure 3 shows a picture of the assembled coaxial injector used in this study. The gas first goes into a ring manifold to be equally distributed later through four 90-degree spaced holes into the annular region well upstream of the injector exit plane. The rig is fully instrumented to measure pressure, temperature, and mass flow rate of the injected fluid. A specially designed piezo-siren by Hersh Acoustical Engineering, Inc., capable of producing sound pressure levels (SPL) of up to 180 dB (in an impedance tube) at its resonant frequencies (lying between 1000 to 8000 Hz) and at pressures up to 2000 psi is used with a circular-to-rectangular transition coupling to bring the acoustic waves into the interaction zone inside the chamber. A model 601B1 Kistler piezoelectric-type pressure transducer is used to measure the acoustic pressure variations inside the chamber at various pressures very near the jet location. The piezo-siren acoustic driver is able to generate between 161 to 171 db when coupled with the high-pressure chamber. The siren hardware is illustrated in Figure 2.

Figure 3. A picture of the assembled coaxial injector.

Previous Results at AFRL on Supercritical Jets

During the past three years, results from the injection of several fluids into an ambient under both sub- and supercritical pressures at sufficiently high Reynolds numbers to be considered as fully-turbulent flow have been reported for the same test facility shown in Fig.1, see *Chehroudi et al. [1,2,3]*. A variety of ambient fluids was used into which pure N_2 , He, and O_2 fluids were injected. The ef-

fects of chamber pressure (density) ranging from the thermodynamic subcritical to supercritical values at a supercritical chamber temperature (based on the critical pressure and temperature, Pc, Tc, of the injectant) were observed by the acquisition of shadowgraph images from the injector exit region using a CCD camera illuminated by short-duration light pulses.

At sufficiently low subcritical chamber pressures, the disturbances on the jet interface amplified downstream and eventually broke up into irregularly-shaped small entities. A further increase of chamber pressure initiated the formation of many small ligaments and droplets at the interface of the jet only within a narrow regime below the thermodynamic critical pressure of the injected pure fluid, resembling a second wind-induced liquid jet breakup. At even higher chamber pressures, near but below the critical pressure of the injectant, the expected transition into a full atomization regime to produce a liquid spray was inhibited due to reduction of both the surface tension and the heat of vaporization. The jet appearance changed abruptly at this pressure and resembled that of a turbulent gas jet for all higher chamber pressures. The initial growth rate of the jet was plotted together with available data on liquid fuel injection in diesel engine environments, and turbulent incompressible, supersonic, and variable-density jets and mixing layers. The resulting plot is unique in its own right, covering four order of magnitude in density ratio. At near- and super-critical pressures, these measurements agreed well with the theoretical growth rate equations proposed *by Brown [5], Papamoschou and Roshko [6],* and *Dimotakis [7]* for incompressible but variable-density turbulent mixing layers. This constituted the first quantitative evidence in support of the past qualitative observations that the jet appeared to evolve into a gas-like behavior under supercritical condition. The geometry of the jet interface was also examined for the first time by fractal analysis. The results clearly indicated a transition from a Euclidean to a fractal interface, with a fractal dimension close to values measured for gaseous turbulent jets. This provided an additional quantitative evidence for the hypothesis that the jet evolved into a gas-like behavior. An equation was proposed based on a physical model proposing that at the point of transition from liquid-like to gas-like appearances and growth rates, the characteristic time of the vaporization process is of the same order as that of the interfacial "bulge" formation/separation events. The model equation agreed well with the experimental growth rate data. The initial growth rate of the jet as judged by the Raman signature was in reasonably good agreement with our earlier measurements using shadowgraphy if twice the FWHM of the normalized intensity plots were used, *see Chehroudi et al. [8]*. The interaction of the acoustic waves with the same jet studied earlier was considered in *Chehroudi et al. [4]*. It was found that the impact of the acoustic waves on the jet structure was strongest from low to particularly near-critical chamber pressures and at low injectant flow rates. No significant effects of the acoustic waves were detected at the supercritical chamber pressure examined under the range of the excitation Strouhal (St) number studied (0.03 to 2).

Experimental Results

In this paper, only preliminary results from a newly designed coaxial injector are shown. Currently, the system is not fully optimized and the work is in progress. Hence, the purpose here is to demonstrate opportunities for systematic acoustic-coaxial jet interaction studies with the intention to elucidate some features of combustion instabilities in cryogenic liquid rocket engines.

Figure 4 shows images taken at a subcritical chamber pressure of 2.14 MPa (a reduced pressure of .63) at three different coflow mass flow rates, exposed to no acoustic field (off) and to a high acoustic field (on) at a frequency of 2700 Hz. Figure 4 (a) is the base or reference image with the lowest value of the co-flow (nearly zero) and for when the acoustic excitation is turned off. First, the effects of the co-flow can be observed by inspection of Figs. 4 (a), (c), and (e). Although the velocity of the co-flow is not as high as it is desired to enable sufficiently strong aerodynamic interaction, one can observe a reduction of the jet diameter even at the injector exit plane. Also, one sees a simultaneous fuzziness of the jet boundary covered with a cushion layer of vaporized (lower density) and cold nitrogen. This cushion feature can be better seen in high resolution images. The aforementioned co-flow velocity limitation is being relaxed by modifications of the injector outer tube dimensions and will be examined in the near future. Currently, co-flow/jet velocity ratios in the range of about 1 to 3 are achievable. The nitrogen co-flow gas temperature (~ 250 K) is not low enough to be detected in our images but is sufficiently warm to affect the near-wall liquid nitrogen thermodynamic states inside the inner tube which guides the LN2 jet. The reduction of the visual jet diameter at the exit plane as the co-flow is raised from 5 mg/s to 188 mg/s is thought to be due to this effect. No substantial further differences are seen when the co-flow rate is further raised to 350 mg/s in Fig. 4 (e).

The effects of the transverse external acoustic waves at 2700 Hz at a subcritical chamber pressure and at three different co-flow rates can be seen by examining the following image pairs: Figs. 4 [(a) and (b)], [(c) and (d)], and [(e) and (f)]. The acoustic waves oscillate between left and right in these figures as well as in Fig. 5. Earlier pressure field mapping using a pressure transducer showed that the jet is located at a velocity antinode at this frequency. A velocity antinode means large transverse velocity oscillations The impact of the acoustic waves is seen to accelerate the jet instability and breakup processes. A distinct sinusoidal spatial wave has been imposed on the jet in Figs. 4 (d) and 4 (f). It is possible that the sinusoidal appearance is actually the result of a helical structure, but this has not yet been confirmed. From estimates of the co-flow gas velocity, the wavelengths seen in the figures are consistent with the driving frequency of 2700 Hz.

At a supercritical chamber pressure of 4.86 MPa (a reduced pressure of 1.42), an increase in the co-flow rate alone tends to slightly narrow the jet with no other distinct visual effects. This unexpected result is due to the limitation of the co-flow velocity mentioned earlier. However, the effects of the acoustic waves are not only to increase the initial jet angle, but to again impose a sinusoidal shape to the jet, see Figs. 5 (b), (d), and (f). The wavelength is noticeably and consistently smaller than what is seen under the subcritical chamber pressure, see Figs. 4 (d) and (f). One would then expect that as the penetration rate of the newly injected fluid is reduced, for example under higher chamber pressures (supercritical), the wavelength should decrease. This is indeed what one sees examining Figs 4 and 5. Rough calculation of the jet velocity from the acoustic frequency and this spatial wavelength gives velocities near the jet velocity estimated form the knowledge of mass flow rates. Depending on the relative magnitude of the jet exit momentum to that imposed by the acoustic waves and frequencies, one may or may not expect to see these spatial waves. Also, note that the onset of this wavy feature moves closer to the injector at the supercritical condition. In summary, the effects seen in Figs. 4 and 5 are the combined effects of the coflow and acoustic perturbations. More data is needed to fully map these interactions.

Summary and Conclusions

Initial results from a coaxial injector, injecting liquid nitrogen surrounded by a gaseous nitrogen co-flow into a subcritical and supercritical ambient with and without acoustic excitation showed a large impact of the acoustic waves on the jet structure. In essence, the acoustic waves tend to impose a sinusoidal shape on the jet with a wavelength that can be explained through periodic transverse variations of the chamber gas velocities at the velocity antinode of the acoustic field. Evidence indicates that there is strong heat transfer interaction inside the injector between the co-flow gaseous nitrogen and the liquid nitrogen jet. Due to the low GN2 coflow velocities achieved thus far, dominant aerodynamic interaction was not observed. Injector modifications are underway to provide a more realistic flow conditions and more data is needed to fully map the aforementioned interactions.

Acknowledgement

Mr. Mike Griggs, Mr. Earl Thomas, and Mr. Randy Harvy are thanked for their valuable support in the design and retrofitting of the current injector to high-pressure chamber. Ms. Jennie Paton, librarian and Ms. Tony Collett are specially thanked to make requested literature available in a timely manner. This work is sponsored by the Air Force Office of Scientific Research under Mr. Mitat Birkan, program manager.

References

1. Chehroudi, B., Talley, D., and Coy, E. Initial Growth Rate and Visual Characteristics of a Round Jet into a Sub- to Supercritical Environment of Relevance to Rocket, Gas turbine, and Diesel Engines, 37th AIAA Aerospace Science Meeting and Exhibit, AIAA 99-0206, Reno, NV, January 11-14, 1999.
2. Chehroudi, B., Talley, D., and Coy, E. Visual Characteristics and Initial Growth Rates of Round cryogenic Jets at Subcritical and Supercritical Pressures, *Physics of Fluids*, Vol. 14, No. 2, February, 2002.
3. Chehroudi, B., Cohn, R., and Talley, D. Cryogenic Shear Layers: Experiments and Phenomenological Modeling of the Initial Growth Rate Under Subcritical and Supercritical Conditions, *Invited Paper, International Journal of Heat and Fluid Flow*, 23, pp. 554-563, 2002.
4. Chehroudi, B. and Talley, D. Interaction of Acoustic Waves with a Cryogenic Nitrogen Jet at Sub- and Supercritical Pressures, 40th AIAA Aerospace Sciences Meeting & Exhibit, AIAA Paper 2002-0342, Reno, Nevada, 14-17 January, 2002.
5. Brown G., "The entrainment and large structure in turbulent mixing layers," 5th Australasian Conf. on Hydraulics and Fluid Mech., 1974, pp. 352-359.
6. Papamoschou, D. and Roshko, A. "The compressible turbulent shear layer: an experimental study," *J. Fluid Mech*., vol. 197, 1988, pp. 453-477.
7. Dimotakis, P. E. "Two-dimensional shear-layer entrainment," *AIAA Journal*, 21, No. 11, 1986, pp. 1791-1796.
8. Chehroudi, B., Cohn, R., Talley, D., and A. Badakhshan. Raman Scattering Measurements in the Initial Region of Sub- and Supercritical Jets, AIAA/SAE/ASME/ASEE Joint Propulsion Meeting, AIAA 2000-3392, Huntsville, AL, 17-19 July, 2000.

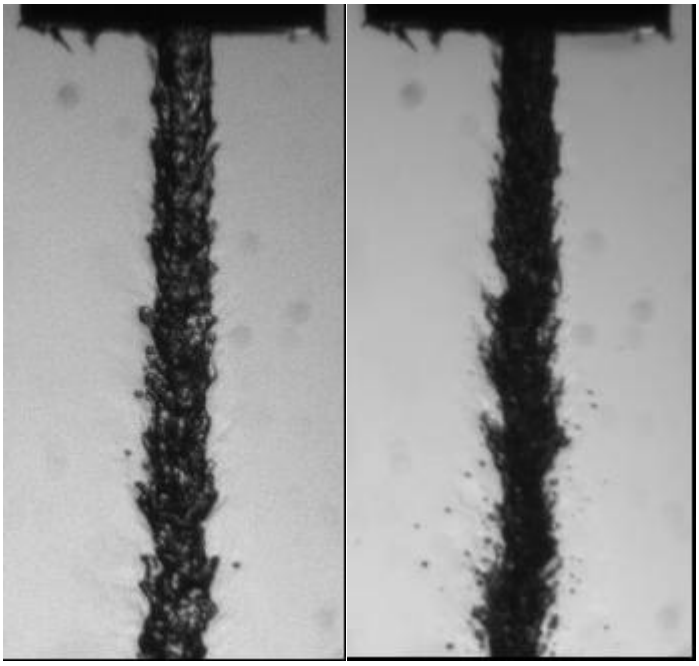

(a) 300-305-5-off (b) 300-305-5-on

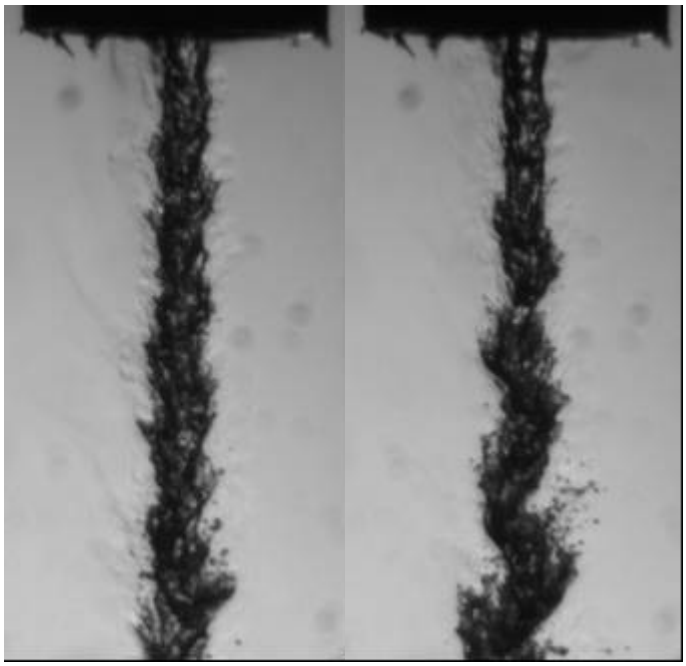

(c) 300-305-188-off (d) 300-305-188-on

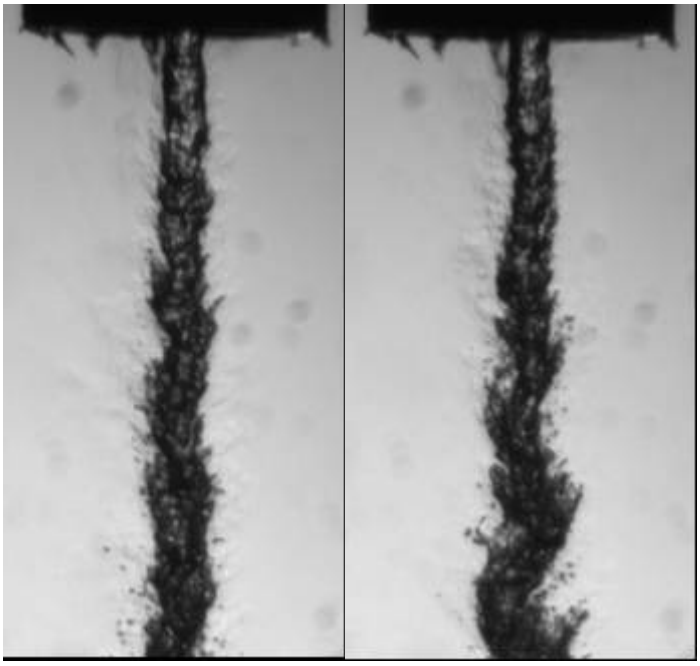

(e) 300-305-350-off (f) 300-305-350-on

Figure 4. Shows effects of acoustic waves on a co-axial injector at a subcritical pressure and at three different co-flow mass flow rates of 5, 188, 350 mg/s. The code, 300-305-5-off means a chamber pressure of 2.14 MPa (300 psig), a jet flow rate of 305 mg/s, and a co-flow rate of 5 mg/s, with acoustic excitation turned off. Acoustic field frequency is 2700 Hz when on.

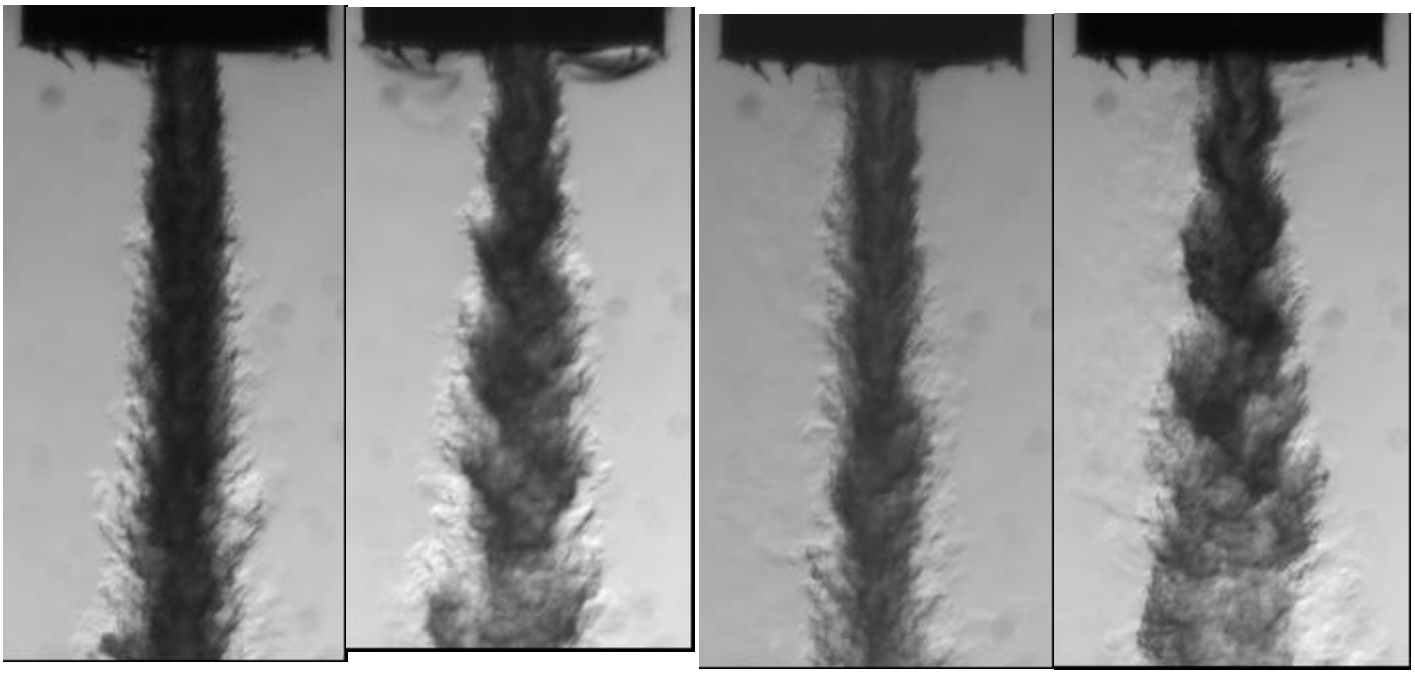

(a) 700-305-5-off (b) 700-305-5-on (c) 700-305-188-off (d) 700-305-188-on

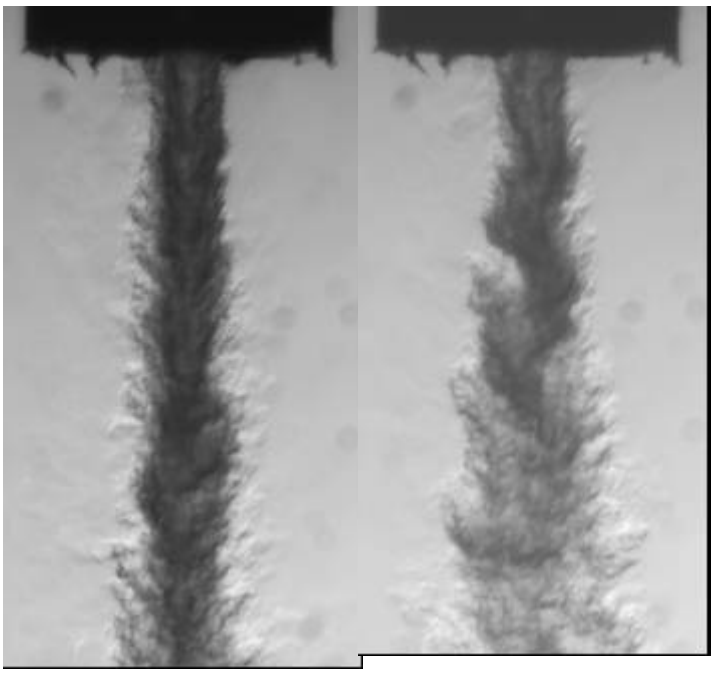

(e) 700-305-350-off (f) 700-305-350-on

Figure 5. Shows effects of acoustic waves on a co-axial injector at a supercritical pressure and at three different coflow mass flow rates of 5, 188, 350 mg/s. The code, 700-305-5-off means a chamber pressure of 4.86 MPa (700 psig), a jet flow rate of 305 mg/s, and a co-flow rate of 5 mg/s, with acoustic excitation turned off. Acoustic field frequency is 2700 Hz when on.

APPENDIX Q

“The Effects of Pressure and Acoustic Field on a Cryogenic Coaxial Jet”

42nd Aerospace Sciences
Meeting and Exhibit
Reno, NV
5-8 Jan 2004

AIAA 2004-1330

THE EFFECTS OF PRESSURE AND ACOUSTIC FIELD ON A CRYOGENIC COAXIAL JET

D. Davis and B. Chehroudi*

Engineering Research Corporation, Inc.
10 E. Saturn Boulevard
Edwards AFB, CA 93524-7680
*ChehroudiB@aol.com(Corresponding author)

ABSTRACT

A coaxial injector was designed to inject liquid nitrogen (LN2) with a coflow of gaseous nitrogen (GN2) in its annular region as part of a program to better understand the nature of the interaction between acoustic waves and liquid fuel jets in cryogenic rocket engines. Backlit images were taken from the jets at various flow rates and at sub-, near-, and super-critical chamber pressures with and without the presence of a 2700 Hz standing wave acoustic field. Injector exit plane temperature measurements were made in both the center jet and annular regions. Results indicate that when the jet core appeared short and "thin", mostly under supercritical chamber pressures, the jet became insensitive to the external acoustic field. The strongest interaction was observed when the jet core looked long and "thick". To explore their implications, the characteristic acoustic impedance of the central jet and fuel/oxidizer momentum ratios are considered to play a role in the observed interactions. It is feasible that they play a similar role in cryogenic rocket engine combustion instability of the coaxial jet.

INTRODUCTION

Coaxial type injectors have been used in liquid rocket engines since the 1940's and are found in the present day hardware such as the Space Shuttle Main Engine (SSME), see Hulka and Hutt[1]. Rocket engines such as the SSME use liquid oxygen (LOX) and hydrogen (H_2) as propellants with the LOX flowing through an inner tube (or the center post) of a coaxial injector design, and H_2 through the outer annular region. The two streams undergo jet breakup and mixing processes in the shear layer between the two streams after they exit the injector. Subsequently, combustion and heat release occurs to produce the desired engine thrust.

Often the combustion processes are controlled by, or at least intimately related to, the jet breakup and mixing of the oxidizer and fuel streams. These processes can safely and inexpensively be studied using chemically-inert fuel and oxidizer simulants. Often, parameters such as velocity ratio, mass ratio, density ratio, Reynolds number (Re), Weber number (We), Ohnesorge number (Oh), etc., are scaled to those of the real engine. The scaling allows reasonable comparisons and evaluation of different injector designs before ever being tested under hot fire conditions.

Studies using water (H_2O) as the LOX simulant and nitrogen (N_2) as the fuel simulant have been conducted at both ambient and elevated chamber pressures, for example *Strakey et. al* [2, 3] These studies can often yield a great deal of information about the atomization and mixing characteristics of a particular type of injector. As combustion chamber pressures increase, one disadvantage of studies with H_2O and N_2 is the effect of the multi-species mixtures on the thermodynamic critical properties of system. The critical properties of a mixture vary with the composition, see *Davis*[4], and then consequently vary both spatially and temporally in the flow field. For example, water has critical pressure of 22.06 MPa, and mixtures of N_2 with H_2O may have mixture critical pressures many times higher than this value, according to the equation of state calculations made with a modified form of Redlich – Kwong – Soave.[5] Also, H_2O – N_2 studies lack simulating the heat transfer processes which occur both inside and outside the injectors in a real cryogenic rocket engine. Additionally, many systems do not possess the capabilities to acoustically excite the injector flow externally. Acoustical excitations are typically observed under hot-fire conditions and can be amplified and lead into combustion instabilities and eventual loss of engine.

Investigations targeted at fundamentally understanding the injection processes and combustion stability, although ideally desirable to perform in a full-scale engine, are practically problematic and costly for many reasons, including the need for an optically-accessible full scale liquid rocket engine, special material choices, and optical diagnostic limitations. A single-element non-combusting test rig having as much of the key features of a real cryogenic rocket engine as possible, such as, cryogenic temperatures, transcritical temperature ranges, supercritical pressures, realistic

velocity ratios, and activation of an acoustical field inside its test chamber, is as close as one can get to the actual engine, yet avoiding indicated complications associated with the combustion in a full-scale setup. Think the test rig used in this study has such desirable characteristics. Combination of the cryogenic liquid N_2 and gaseous N_2 (to eliminate mixture critical phenomena), and N_2 – helium (He) system, to better simulate the LOX – H_2 injection issues, are available.

EXPERIMENTAL SETUP

The experimental facility, as described in detail by *Chehroudi et al.*[6,7], cools and liquefies (if at subcritical pressures) high pressure gaseous nitrogen (GN_2) via a heat exchanger utilizing a relatively low pressure (~0.15 MPa) liquid nitrogen (LN_2) as the cooling fluid. The liquefied nitrogen is then fed to the inner central tube of the coaxial injector (see Figure 1). A close up view of the injector tip is shown in Figure 2. For the results reported here, the cryogenic jet is injected through a sharp-edged stainless steel inner tube having a length (L) of 50 mm and inner and outer diameters measuring $d_i = 0.508$ mm and $d_o = 1.59$ mm, respectively. The resulting L/d_i is 100, considered sufficient to ensure a fully-developed turbulent pipe flow at the exit plane. The gap width (d_g) between the inner and outer tubes, defining the annular region, was 0.415 mm. The injector had an 8% bias of the mean gap width. The inner tube was slightly recessed (about one d_i). For reference, the SSME injector has a d_i of 4.77mm and a d_g of 2.24 mm.[3] The GN_2 for the annular flow is passed through a heat exchanger (different than the one mentioned above) to lower its exit temperature from the ambient to a range of 142 K – 193 K, depending on the chamber pressure and mass flow rate of the GN_2. Then, the cooled GN_2 is split and flows into two equally-spaced inlets of the ring manifold to be equally distributed later through four 90-degree-spaced tubes into the annular region well upstream of the injector exit plane. The injector is then wrapped by an insulating PTFE (Teflon) tape to minimize heat flow into the cryogenic injector from the warm chamber environment (260 K to 280 K).

The information presented here is the continuation of our work published earlier on the coaxial injection phenomena under cryogenic conditions with and without acoustic field interaction, see *Chehroudi et al.*[6,7]

The test rig is fully instrumented to measure pressure, temperature, and mass flow rates of the injected fluids. The maximum mass flow rate for the inner liquid-like flow is about 700 mg/s. The GN_2 flow fed to the ring manifold which defines the annular flow is measured using a series of three mass flow meters with a total maximum mass flow rate of 3 g/s. A specially-designed piezo-siren by Hersh Acoustical Engineering, Inc., capable of producing sound pressure levels (SPL) of up to 180 dB (in an impedance tube) at its resonant frequencies (lying between 1000 to 8000 Hz) and at pressures up to 2000 psi is used with a circular-to-rectangular transition coupling to bring the acoustic waves into the interaction zone inside the chamber. A model 601B1 Kistler piezoelectric-type pressure transducer is used to measure the acoustic pressure variations inside the chamber at various pressures very near the jet location. The jet is located at a pressure node or velocity antinode, of a standing wave, as indicated by the measurements with the transducer. The piezo-siren acoustic driver is able to generate between 161 to 171 db when coupled with the high-pressure chamber. Back-illumination of the jet is accomplished with diffuse light flashes (0.8 μs duration). A Nikon 50 mm to 105 mm lens is used with a high resolution (1280(H) x 1024(V) pixels in an 8.6(H)x6.9(V) mm actual sensing area with a pixel size of 6.7μm x 6.7 μm) CCD camera by the Cooke Corporation to form images of the injected jets.

EXPERIMENTAL RESULTS

To help aid in discussion and be easily able to relate them to actual injectors used in cryogenic liquid rockets, the cryogenic liquid or liquid-like flow of N_2 issuing from the inner tube will be referred to as "oxidizer" and the gas or gas-like flow of N_2 issuing from the annulus between the inner and outer tubes will be called as "fuel", even though both are N_2 and neither is a fuel nor an oxidizer. However, when referring to coaxial injectors for combustion, such as Space Shuttle Main Engine (SSME), typically the oxidizer is the liquid phase oxygen and flows from the inner tube (center post) and the fuel (H2) flows from the annulus. For reference, the critical temperatures of H_2, N_2, and O_2, are 33.2, 126.2, and 154.6K, respectively; the critical pressures of H_2, N_2, and O_2, are 1.32, 3.40, and 5.04 MPa, , respectively.

Temperature Measurements

In order to estimate the physical properties and flow velocities, exit plane temperatures are needed. Many temperature measurements at various chamber pressures, "fuel" mass flow rates, and "oxidizer" mass flow rates, were made. This was accomplished by inserting a type E exposed junction thermocouple with a bead diameter (d_{tc}) of approximately 0.4 mm into the flow in both the "oxidizer" and the "fuel" at the exit plane of the injector. The temperature measurements were performed in test runs separate from those when images were collected .

Accurate temperature measurements are very challenging here due to the small sizes of the d_i and d_g which are of the same order as that of d_{tc}. If d_{tc} is smaller than d_i, then a better measurement of the injector exit temperature can be made, but the momentum of the fluid can break the bead or the lead wires. Considering that the thermocouple bead diameter is about the same size as the center tube inner diameter, one expects that the thermocouple bead may be touching the walls of the tube and/or locally disturbing the flow field. This will raise a question as to what temperature the thermocouple is measuring. However, attempts in correcting the thermocouple measurements by using a commercial computational fluid dynamic code (CFD++ from Metacomp, Inc.) were unsuccessful mainly because of the limitations in the equation of states utilized in the CFD++ program. Hence, we were unable to accurately predict the physical and thermodynamic properties of the nitrogen at conditions of interest in this work. However, work is underway to incorporate such features and attempt a reasonable approach in correcting the data. Nonetheless, temperature measurements were fairly repeatable and, unless otherwise indicated, uncorrected measurements were used to analyze the data presented here. Even though the absolute magnitudes of the temperature measurements are in question here, the relative trends can be regarded as reliable because of the repeatability of the test results.

Figures 3 to 5 show the center jet (oxidizer) reduced temperature measurements (T/T_C) as a function of the normalized annular fuel mass flow rate at four different pressures and for central jet mass flow rates of about 275, 450, and 625 mg/s, respectively. The annular fuel flow rate was normalized by its maximum mass flow rate at each pressure and oxidizer mass flow rate. The curves in Figures 3 to 5 are least squares fits of Equation 1 to the raw data. Equation 1 was selected because it best fits the trends of the data in Figures 3 to 5.

$$T_r = \frac{A}{\left(\frac{\dot{m}_{fuel}}{\max\left(\dot{m}_{fuel}\right)} + B \right)^6} + C\,\frac{\dot{m}_{fuel}}{\max\left(\dot{m}_{fuel}\right)} + D$$

Equation (1)

Where,

$T_r = T/T_c$ the reduced temperature of the "oxidizer",

$\dot{m}_{fuel}$ is the mass flow rate of the "fuel",

$\max\left(\dot{m}_{fuel}\right)$ is the maximum "fuel" mass flow rate at a given pressure and "oxidizer" mass flow rate, and

A, B, C, and *D* are regression constants.

At a pressure of 1.4 MPa and at all three "oxidizer" mass flow rates, the exit temperature measurements are relatively constant. Although at chamber pressure of 1.4 MPa the "oxidizer" exit temperature is within a few Kelvins of each other, there is a slight decline in the temperature as the "fuel" mass flow rate increases from a zero value. This drop in temperature is present at all pressures and "oxidizer" mass flow rates, but becomes more pronounced at higher pressures than those seen at the 1.4 MPa chamber pressure. At the zero "fuel" flow rate, warmer chamber gases are present in the annular region of the injector causing high heat transfer to the "oxidizer" through the tube walls and hence a warmer exit temperature is measured. Note that in our setup, the "fuel" flow is passed through a heat exchanger prior to introduction to the injector manifold, lowering the "fuel" temperatures well below that of the warm chamber environment. As the "fuel" flow rate is slightly increased from the zero level, it lowers the outer wall temperature of the central tube, reducing the rate of the heat losses from the inner-tube LN2, explaining the drop in its measured temperatures.

However, as the "fuel" flow rate is increased further, the "oxidizer" exit temperature increases monotonically particularly at higher chamber pressures. For all practical purposes, we can regard the inner oxidizer temperature insensitive to changes in fuel flow rate at the lowest subcritical pressure. Also, noticeable here is the less sensitive nature of the oxidizer temperature as its flow rate is increased. This is seen in Figures 3 to 5 as the fitted curves approach one another.

Figures 6, 7, and 8 show the plots of the fuel annular-flow reduced temperature measurements versus the normalized "fuel" mass flow rate at four different chamber pressures and for "oxidizer" mass flow rates of about 275, 450, and 625 mg/s, respectively. The normalization of the "fuel" mass flow rate was done the same manner as that of the "oxidizer" temperature plots presented earlier. The data were curve-fitted to a third order polynomial at each pressure and "oxidizer" mass flow rate. Exceptions to this rule are the data for the oxidizer mass flow rate of 450 mg/s (at 2.4 and 3.5 MPa) and 625 mg/s (at 2.4 and 3.5 MPa). The data for these cases were combined for curve-fitting purposes. The lumping of the data was done because of the limited amount of data at these conditions and the realization of the fact that they are very close to each other with no identifiable trend.

As shown in Figures 6 to 8, the measured "fuel" exit temperature never goes below the critical temperature. There is a general trend for all the cases in these figures characterized by a decline of the temperature to a minimum and a gradual rise as the fuel flow rate is increased. This appears to be a manifestation of the improved GN2 heat exchanger performance at low end and decreased residence time at the high end of the flow range investigated here. At supercritical chamber pressures, the "fuel" temperatures are generally higher than those at the subcritical and near –critical chamber pressures. However, this difference is largely reduced at the higher mass flow rates. In the middle of the "fuel" mass flow rate range, the "fuel" temperatures approaches to within 10% above the critical temperature of the nitrogen used in this study.

The temperature curve fits developed so far are convenient tools to compute differential fuel and oxidizer temperatures ("fuel" – "oxidizer"). Results are shown in Figures 9 to 11. Due to a much stronger variations of the fuel temperature with fuel mass flow rate as compared to similar changes in oxidizer temperature, the shape of the differential temperature is dictated by the annular-flow fuel temperature variations.

Using the equations of the curves fitted to the raw data, the chamber pressure measurements, and mass flow rates, densities and speed of sound of the fluids exiting the injector were computed using NIST 12 equations of state.[8] Viscosity and the thermal conductivity were calculated using the methods described in *Reid et al*.[9]

The computed fuel-to-oxidizer velocity ratios, used by some authors for assessment of possible combustion instabilities, are plotted versus chamber pressure in Figure 12. The diamond symbols in Figure 12 are the uncorrected raw data from the curve fits. The square symbols in Figure 12, are corrected "oxidizer" temperatures based on the assumption that the thermocouple measures the bulk mix mean temperature of a turbulent pipe flow, the corrected "oxidizer" temperature is what the centerline temperature would be based the turbulent pipe flow. The average correction was about 7 K. The lowering of the "oxidizer" temperature by about 7 K also agreed physically with the images taken at subcritical chamber pressures, in which the core of the jet appeared to be liquid. The uncorrected "oxidizer" temperature measurements produced densities that were on the vapor side of the saturation curve, this because at the slightly higher, uncorrected, "oxidizer" temperatures the vapor pressure is greater than the chamber pressure. At supercritical chamber pressures very little difference in uncorrected and corrected velocity ratio is evident.

Operating Conditions

The experimental matrix for the image data consisted of four different chamber pressures (~1.4, 2.4, 3.5, and 4.8 MPa), three "oxidizer" mass flow rates (~275, 450, and 625 mg/s), and five "fuel" flow rates (~0, 450, 1300, 2200, and 2800 mg/s), with the acoustic field on (at 2700 Hz) and off at each condition. Several conditions were repeated to build confidence and check the repeatability, and ten images were taken at each condition bringing the total number of images to greater than about 1400. In these tests, the "oxidizer" Reynolds numbers (Re), based on the d_i, were in the range of 1.43×10^4 to 1.88×10^5, and the "fuel" Re, based on the hydraulic diameter, d_g, reached up to 8.40×10^4. Injector exit velocity ratios ("fuel"/"oxidizer") from 0 to 35 were produced. The velocity ratios at the lowest chamber pressure reached up to about 42, whereas it approached a value near 5 at the highest pressure, see Figure 12. Note that Hulka and Hutt[1] suggested a value higher than 13 to ensure stable operation in engines utilizing coaxial injectors. However, the temperature measurements for most of the works cited therein were made well upstream of the injector exit plane and, as such, a fair comparison between the two sets of velocity ratios is not available at this time. This subject will be further investigated in our future works. There are also several factors involved in estimating velocity ratios. Our search for a better technique to make temperature measurements and/or correction logic continues to the future to provide a better estimate of this and other parameters. Also, even though the mass flow rates and the injector inner cross-section areas remained the same, the injection temperature of the "oxidizer" increased as the chamber pressure was increased (see Figures 3 to 5). Finally, the "oxidizer" temperature level in our tests are near the critical region and thus small changes in temperature (5 to 10 K) can produce large variations in the value of density, hence changing the "oxidizer" exit velocity greatly. This difficulty has also been reported by Hulka and Hutt.[1]

Image Data

A sample of the images is shown in Figure 13, and the operating conditions of the images are shown in Table 1. Images 1 to 10 are at approximately the same subcritical chamber pressure (~ 1.41 MPa), images 11 to 20 are at the same near critical pressure (~ 3.46 MPa), and images 21 to 30 are at about the same supercritical pressure (~ 4.77 MPa). The acoustic driver is off in the odd-numbered images, and on in the even-numbered images (every other row). The mass flow rate of the "oxidizer" through the inner tube is approximately the same for all the images (~ 275 mg/s) shown in Figure 13. Each column is at about a constant "fuel" mass flow rate, but increases from the left

column to the right. The mass flow rates of "fuel" from left to right in

Inspection of these images reveals some key features. For example, when the acoustic driver is off, the "dark core" of the jet is decreased as atomizing fuel flow rate is increased from the second column (i.e., the first non-zero fuel flow rate case) to the far right column of the images in Figure 13. The fuel flow rate plays two key roles in this injector design. First, it assists the inner jet breakup for the subcritical condition and enhances mixing for the supercritical case. Second, because of the temperature differences between the fuel and the oxidizer, there is a heat exchange between the two both inside and outside the injector. Clues for the heat transfer behavior can be taken by examination of the injector temperature measurements. For instance, as mentioned earlier it appears that at the lowest subcritical chamber pressure, the inner oxidizer jet temperature is fairly insensitive to the annular fuel flow rate. However, at all other elevated pressures, particularly at the supercritical one, a gradual increase in the oxidizer exit temperature can be detected.

The case for the zero fuel flow rate is interesting. Under this condition, the annular passage of the injector is filled with the warm chamber nitrogen, strongly affecting the heat transfer not only inside but also outside the injector. Clear evidences for the high heat transfer rate inside the injector come from the exit temperature measurements under this condition, see Figures 3 to 8. Here, the observed elevated temperature is believed to be the effects of the warm chamber gases present inside the annular space of the injector. Hence, even though no atomizing flow is at work here, one sees a shorter dark core than those seen in other images presented in the second column from the left (i.e. the lowest atomizing fuel flow rate), see Figure 13. A small flow of the colder-than-chamber fuel in the annular passage, although assists the jet breakup, lowers the oxidizer exit temperature. The two phenomena work in such a way that the net effect is an apparent longer dark core in most cases, compare the images in column one and two from the left of Figure 13. Effects of the acoustic field are discussed in the next section.

Effects of the Acoustic Field

Looking at images in Figure 13, one trend that stands out is that the coaxial jet appears to be more sensitive to the existence of the acoustic field under subcritical chamber pressure. Although the images shown in this figure are typical, we thought to devise an approach to be able to systematically assess the interaction of the jet and the acoustic field.

In order to assess the global effects of the acoustic field, each data condition was assigned an acoustic effect of 0, 1, or 2, based upon the qualitative behavior of the jet. An acoustic effect of "0" corresponds to no distinguishable effect from all the images at a given condition. For example, images 15 and 16 in Figure 13. An acoustic effect of "2" corresponds to a strong effect, such as the large-amplitude spatially-superimposed sinusoidal wave seen in images 6 and 8 as compared to images 5 and 7, respectively, or the interaction shown in images 1 and 2 in Figure 13. An acoustic effect of "1" corresponds to a weaker effect than that of a "2", but definitely present, unlike an acoustic effect of "0". An example of an acoustic effect of "1" is the small amplitude sinusoidal wave of image 12 as compared to image 11 and the contraction of the length of the dark core in image 24 compared to image 23 in Figure 13. For the images shown in Figure 13 the rating of the acoustic field effect is listed in Table 1.

In order to determine the effect of the flow rates (fuel/oxidizer ratio) and chamber pressure, rating of the acoustic field effects is plotted in Figure 14. It is now clear that the strongest effect of the acoustic field occurs at the lowest chamber pressure and as pressure increases towards the supercritical conditions, the observable acoustic effect diminishes. However, there are still cases that even under supercritical chamber pressures one can isolate observable effects of the acoustic field. Interestingly, there is a zone in mass flow rate ratios space, located nearly in the middle of the investigated range, in which one sees no acoustic effects even under subcritical condition, see Figure 13. For further processing of the acoustic effects, an average of all the ratings was computed at each chamber pressure, regardless of "fuel" or "oxidizer" mass flow rates, and results are plotted versus chamber pressure in Figure 15. The plot shows that, on the average as the chamber pressure increases to the critical pressure value, the effect of the acoustic field decreases. Interestingly, near the critical pressure and beyond into the supercritical regime, the acoustic field has minimal effect on the coaxial injector flow dynamics.

Obviously, the jet behaves differently at different "fuel" mass flow rates. Recall that the fuel mass flow rate acts as the atomizing gas, accelerating the breakup mechanism. At the lowest subcritical chamber pressure, for the case of a single inner-tube jet (i.e., zero "fuel" mass flow rate), comparing images 1 and 2 (Figure 13) the acoustic field shatters the jet into many droplets and ligaments, causing accelerated jet breakup. As the mass flow rate of the "fuel" increases slightly (~ 487 mg/s), such as images 3 and 4 (Figure 13), the "oxidizer" begins to break up into relatively large droplets and ligaments as a result of the atomizing "fuel" flow. The droplets and ligaments, which have a slightly higher

density at these conditions, see exit temperature measurements at the lowest subcritical pressure, consequently have a higher momentum, and thus acoustic field has somewhat of a lesser effect. Note that from our previous measurements, the jet is located at the pressure node or velocity antinode. As the "fuel" flow rate increases even more, finer droplets and ligaments are formed from the "oxidizer", and more of its mass from the intact core is converted into droplets and ligaments. This consequently produces a shorter and less dark core for the oxidizer jet. Additionally, as the "fuel" flow rate increases, the heat transfer from the "fuel" to the "oxidizer" increases outside the injector, lowering the average density of the oxidizer core in the injector near field area. Under the subcritical condition, this combined annular fuel-flow-enhanced atomization and heat transfer creates a dark core region more susceptible to the acoustic field, see Figures 6 to 8.

As the pressure increases to a near-critical value (images 11 to 20, Figure 13) droplets are no longer evident as the surface tension approaches zero. Examination of many images including those shown in Figure 13 indicates that the acoustic effects are substantially reduced and hardly noticeable. A weak sinusoidal wave is visible superimposed on the jet when the acoustic driver is turned on under the zero "fuel" mass flow rate condition and at near-critical chamber pressure (see images 11 and 12 in Figure 13). However, at the higher atomizing "fuel" mass flow rates, no distinguishable effect of the acoustic field is observed (see images 15 through 20 in Figure 13). Similarly, at supercritical chamber pressures (images 21 through 30, Figure 13), only minor effects of the acoustic field are observed at the lowest nonzero "fuel" flow rate conditions. This, although unclear in images 23 and 24 of Figure 13, but was evident when all the 20 images at these two particular conditions were studied. Acoustic field effects are even weaker at higher atomizing "fuel" flow rates, see image pairs (25, 26), (27, 28), and (29, 30).

It is thought that acoustic impedance of the jet core may play a role in what is observed here. Hence, a phase diagram was created to map the characteristic acoustic impedance, i.e., product of the density and speed of sound (ρc) at the injector exit plane conditions, and is shown in Figure 16. The data conditions in this figure are corrected based upon the assumption that the flow approaching the thermocouple beads has a turbulent profile and that the thermocouple measures a mixed-mean temperature. The correction methodology attempts to estimate the value of temperature at the center of the profile. This correction logic was applied only for the subcritical pressures for the following reason. At first attempt the uncorrected raw data was plotted and we found that at subcritical chamber pressures, the raw data fell on the vapor side of the saturation curve. After this correction was applied only one point remained on the vapor side of the saturation curve. This was due to the fact that the chamber pressure was lower than the saturation pressure at the measured inner tube "oxidizer" temperature values, thus suggesting a vapor state from the equilibrium thermodynamics considerations. However, the magnified images at these subcritical conditions strongly suggested that the center jet ("oxidizer") goes through the classical liquid-phase breakup processes at these conditions. Therefore, it was deemed necessary to provide the best temperature correction available at present time (described earlier) to preserve a physically consistent picture between evidences from the acquired images and temperature measurements. We continue exploring better measurement techniques and correction methodologies for a more accurate determination of the injector exit plane temperature. The characteristic acoustic impedance of the "oxidizer" is the highest at subcritical pressures.

One may theorize that the larger the differences between the acoustic impedance (ρc) for the "oxidizer" with respect to the warm chamber environment gases (particularly for the dark core zone) the greater the effects of the acoustic field would be on the jet. Figure 16 shows that amongst the cases where strong acoustic effects were observed (i.e. diamond symbol), a large majority (10 out of 12, not counting the subcritical pressure point on the vapor side of the saturation curve) of them have high acoustic impedance and exist under subcritical chamber pressure. Conversely, good majorities (21 out of 32) of those that exhibit no acoustic effect (i.e. square symbol) have low acoustic impedance and exist under supercritical chamber pressure. However, there are still some cases where despite their high impedances, are apparently insensitive to the acoustic field, (see all the square symbols at and below 2.5 MPa in Figure 16).

Figure 17 shows coaxial instability data for actual engines reported in Hulka and Hutt.[1] Superimposed on these results are velocity ratios from our injector. Based on a large set of data from both stable and unstable engine operation, they offered a triangular zone beyond which most engines were stable. In fact, they suggested that as long as the injector velocity ratio is above a number of 13, the engine would highly likely be stable. It was unclear, however, what the underlying physical reasons were. Looking at our data in Figure 17, it is apparent that it tells a different story. That is, whenever we rate the injector to be minimally sensitive to the acoustic field, such as supercritical condition, the velocity ratio is low and buried into the triangular zone

Hulka and Hutt[1] consider as unstable engine operation. The temperature measurements made in our work were made at the injector exit plane. It is unclear where the temperature measurements were made in the real rocket engine conditions (probably upstream of the injector exit plane) presented by Hulka and Hutt.[1] This matter becomes even more important near the critical point as small changes in temperature leads to large variations in density and velocity ratio calculations. Therefore, some caution must be used at this point before making one to one comparisons. However, we feel that these initial data have a good degree of relevancy to actual engines. Primarily, we have some initial clues because of our unique setup, being able to span subcritical to supercritical chamber pressures, cryogenic fluid simulant, and coaxial injector bearing major features of the production ones.

To offer a perspective, although not complete and evolving, we would like to propose a hypothesis based on our evidences here and other researchers, Oefelien and Yang[10], who reported that an acoustically-established crossflow interaction with the jet is one important parameter playing a role in engine stability. We have two choices to formulate this hypothesis and to connect what is observed here to the actual engine combustion instability. Intuitively, one can assume that the coaxial jet we observe and rate here as sensitive to the acoustic field leads to an engine instability when carried into an actual engine. In other words, the assumption is that the jet characteristics (visual and nonvisual) which make our coaxial injector highly sensitive to the acoustic field also are responsible for the observed engine instability. The reason this is a possibility comes from the fact that engines become stable when hydrogen fuel temperature is raised beyond a threshold value. One would expect that the heat transfer at higher temperatures tends to "shorten and thin" the jet core region, similar to what is observed here, particularly at supercritical pressures when the jet in our facility becomes insensitive to the external acoustic field. On the other hand, factors responsible for a most sensitive injector in our rig may actually be stabilizing agents in actual engines. The argument in favor of this case comes from the fact that in an actual engine the existence of the mixing critical temperature and pressure in the mixing layer can create a jet core similar to what is observed in our most sensitive cases (such as those under subcritical condition). Although this latter hypothesis is aligned with the Hulka and Hutt[1] data in Figure 17, the former appears more intuitive. Certainly, more work is needed to establish this important connection between our measurements and the engine combustion instability

A comment regarding Figure 17 is necessary here. Note that although Hulka and Hutt[1] present their stability data in a form of the velocity ratio, what usually used for stability rating is the so-called "temperature ramping". This means that there is a threshold minimum fuel (hydrogen) temperature above which engine has shown stable operation. It appears that one important phenomenon at play with the coaxial injectors is the heat transfer, both inside the injector element and in the mixing layer between the central "oxidizer" jet and the annular "fuel" flow in the chamber. This phenomenon is fairly complex especially under supercritical chamber conditions. What we think acting here is the combination of the characteristic acoustic impedance and the momentum of the jets. Obviously, it is the temperature of the fuel and, in effect, the nature of the heat transfer (both inside and immediately outside of the injector) that affects both factors particularly at near- and supercritical conditions. Note that our temperature measurements in Figures 3 to 5 show that at subcritical temperatures the oxygen exit temperature is unaffected by the nature of the heat transfer inside the injector. However, this is not the case for the supercritical condition.

Figure 18 shows a plot of the fuel/oxidizer momentum ratio as a function of the fuel/ambient characteristic acoustic impedance ratio. Note that how our data at different chamber pressures are separated in this diagram. If one defines a region where most of the cases with acoustic interaction rating of 2 lie, and likewise the same for those with rating of zero, one will see two separated zones with some overlap region. Although data is scarce, it suggests that when both momentum ratio and the acoustic impedance of the jet are high, one should expect maximum interaction between the jet and the acoustic field and vice versa.

Although we do not yet have a fully coherent picture, we feel that both the acoustic impedance (see Figures 16 and 18) and the momentum of the jet create a condition under which the coaxial jet becomes highly sensitive to the acoustic field disturbances. In fact, at first glance, it is possible that as temperature is ramped up in a production engine for stability analysis, strong heat transfer, both inside and immediately outside the injector, "shortens" and "thins" the oxidizer core in a manner similar to what is observed in image pairs of (7 and 27) or (9 and 29) to make it insensitive to the acoustic field that is established inside the combustion chamber.

SUMMARY AND CONCLUSIONS

Temperature measurements were made at the exit plane of a model of the coaxial injectors used in cryogenic rocket engines. The trends should be viewed specific to our facility unless it is verified for practical engines. Everything else being the same, the results of the

temperature measurements showed that as the chamber pressure increases the center jet ("oxidizer") temperature increases. The mass flow rate of the "fuel" in the annular passage of the injector has a stronger effect on both the "fuel" and the "oxidizer" exit temperatures than the "oxidizer" mass flow rate. As the "fuel" mass flow rate increases from zero, both the "fuel" and "oxidizer" temperatures first decrease, reach a minimum, but at different flow rates, somewhere in the middle of the "fuel" mass flow range, and then increase again. Due to measurement difficulties in very small passages, the magnitudes of the actual temperatures are not yet known with great accuracies. However, their trends with pressure and mass flow rate can be regarded as valid.

Back-lit images of the coaxial jet were taken at four chamber pressures, three "oxidizer" mass flow rates, and five "fuel" flow rates with a 2700 Hz external acoustic field turned either on or off. Preliminary analysis of the data shows that the effects of the acoustic field was more noticeable at subcritical chamber pressures where the jet behaved liquid-like and had high characteristic acoustic impedance. For the most part, the coaxial jet became insensitive to the external acoustic field under supercritical conditions where the dark central core of the jet became short and "thin". Under this condition, the characteristic acoustic impedances are generally lower than those under subcritical conditions.

We postulated that the sensitivity characteristics of the coaxial jet to the external acoustic field in our setup may correspond to that causing combustion instability in engines. However, exact nature of this connection is to be further investigated. Stronger effects of the acoustic field on the coaxial jet were evident at higher velocity ratios (> 10) whereas weaker interactions were seen at lower velocity ratios (< 10). Although Fuel/oxidizer velocity ratio is used as one parameter for characterization of the engine instability, we felt to search for a different set of parameters to physically represent our data. It is proposed that fuel/oxidizer momentum ratio and an acoustic parameter, such as characteristic acoustic impedance, be used. That the characteristic acoustic impedance of the central "oxidizer" jet plays a role and ultimately a parameter to be considered in engine stability studies remain to be further studied through more data and analysis. Preliminary evidences from the data presented here are pointing in that direction.

ACKNOWLEDGEMENT

The authors would like to acknowledge Dr. Douglas Talley for his interest, support, and contributions with this ongoing project. Also, the authors would like to acknowledge Mr. Mike Griggs for his valuable contributions. Mr. Randy Harvey, Mr. Earl Thomas and Mr. Mark Wilson are thanked for their efforts. Additionally, Ms. Jennie Paton is thanked for making literature available in a timely manner. This work is sponsored by the Air Force Office of Scientific Research under Mr. Mitant Birkan, program manager.

REFERENCES

1. Hulka, J. and Hutt, J.J. *Instability Phenomena in Liquid Oxygen/Hydrogen Propellant Rocket Engines*, in *Liquid Rocket Engine Combustion Stability*, V. Yang and W. Anderson, Editors. 1994, AIAA: Washington. p. 39-71.
2. Strakey, P.A., Talley, D.G., and Hutt, J.J. *Mixing Characteristics of Coaxial Injectors at High Gas/Liquid Momentum Ratios.* Journal of Propulsion and Power, 2001. 17(2): p. 402-410.
3. Strakey, P.A., et al. *Effects of Liquid-Oxygen Post Biasing on SSME Injector Wall Compatibility.* Journal of Propulsion and Power, 2002. 18(2): p. 240-246.
4. Davis, D. *Supercritical Fuel Injection Studies for Advanced Gas Turbine Engines*, M.S. Thesis, *Mechanical Engineering*. 2001, The Pennsylvania State University: University Park. p. 103.
5. API, *Technical Data Book - Petroleum Refining*. Sixth Ed., Thirteenth Revision Package ed, ed. T.E. Daubert and R.P. Danner. 1999, Washington: American Petroleum Institute.
6. Chehroudi, B. and Talley, D. *Interaction of Acoustic Waves with a Cryogenic Nitrogen Jet at Sub- and Supercritical Pressures*. in *40th AIAA Aerospace Sciences Meeting and Exhibit*. 2002. Reno, NV.
7. Chehroudi, B., Davis, D., and Talley, D. *Initial Results From A Cryogenic Coaxial Injector In An Acoustic Field*. in *41th AIAA Aerospace Sciences Meeting & Exhibit*. 2003. Reno, Nevada.
8. Lemmon, E.W., et al. *NIST 12 Thermodynamic and Transport properties of Pure Fluids*. 2000, U. S. Secretary of Commerce.
9. Reid, R.C., Prausnitz, J.M., and Poling, B.E. *The Properties of Gases and Liquids*. 4th ed. 1987, New York: McGraw-Hill. 741.
10. Oefelien, J.C. and Yang, V. *Comprehensive Review of Liquid Propellant Combustion Instabilities in F-1 Engines.* Journal of Propulsion and Power, 1993. 9(5): p. 657-677.

FIGURES

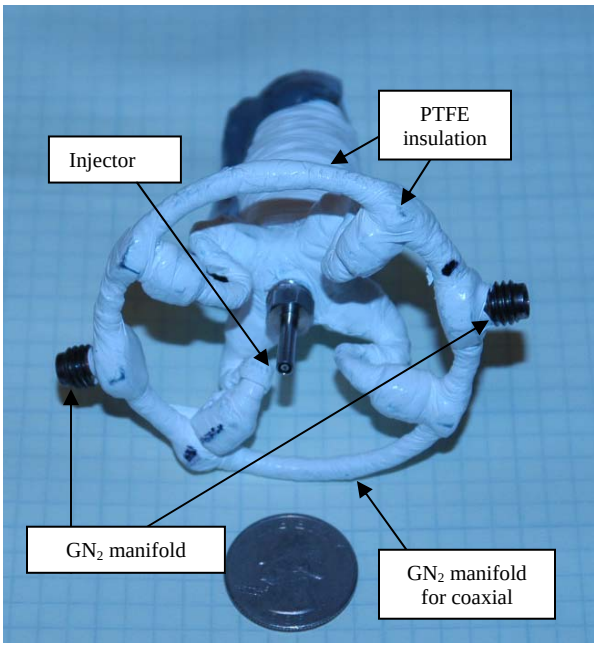

Figure 1 Picture of the coaxial injector.

Figure 2 Close up view of the coaxial injector tip.

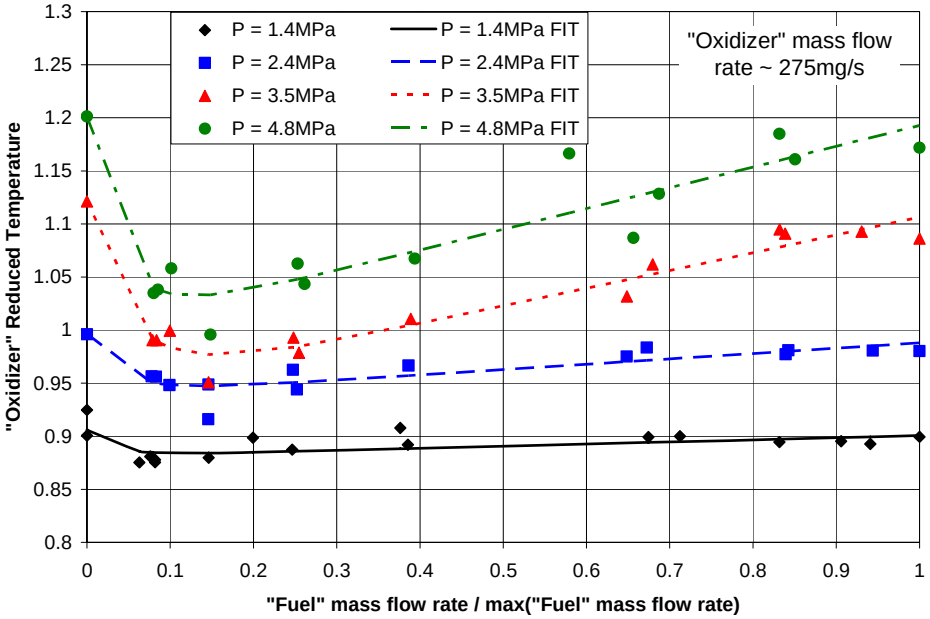

Figure 3 The center jet ("oxidizer") reduced temperature versus the annular flow ("fuel") mass flow rate normalized by the maximum "fuel" mass flow rate at four different chamber pressures. Oxidizer mass flow rate is fixed at about 275 mg/s. The lines, called “FIT” on the inset, are curve fits to the raw data. The maximum “fuel” mass flow rates for 1.4, 2.4, 3.5, and 4.8 MPa are 2995, 2985, 2974, 2918 mg/s, respectively.

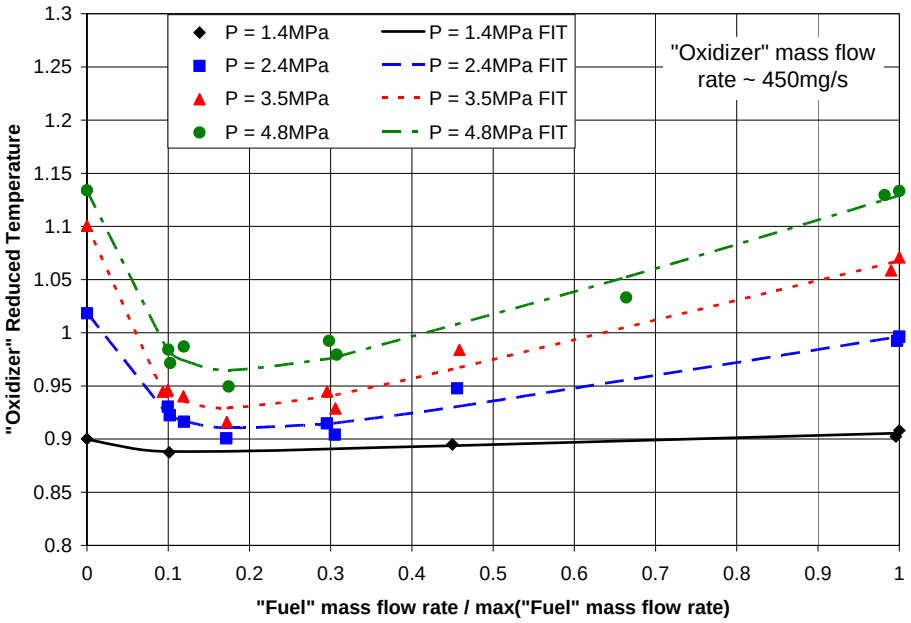

Figure 4 The center jet ("oxidizer") reduced temperature versus the annular flow ("fuel") mass flow rate normalized by the maximum "fuel" mass flow rate at four different chamber pressures. Oxidizer mass flow rate is fixed at about 450 mg/s. The lines, called “FIT” on the inset, are curve fits to the raw data. The maximum “fuel” mass flow rates for 1.4, 2.4, 3.5, and 4.8 MPa are 2535, 2513, 2511, 2485 mg/s, respectively.

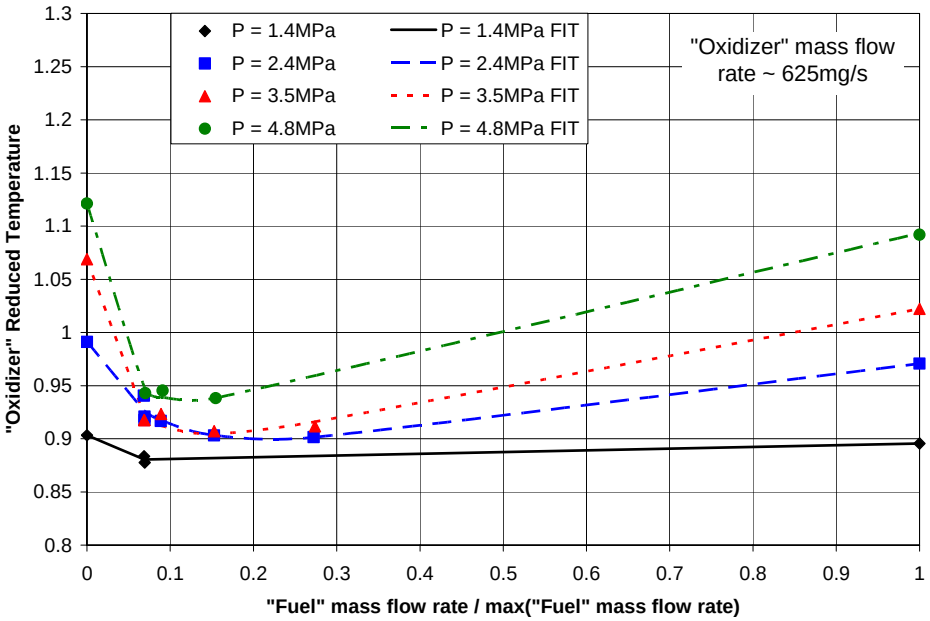

Figure 5 The center jet ("oxidizer") reduced temperature versus the annular flow ("fuel") mass flow rate normalized by the maximum "fuel" mass flow rate at four different chamber pressures. Oxidizer mass flow rate is fixed at about 635 mg/s. The lines, called “FIT” on the inset, are curve fits to the raw data. The maximum “fuel” mass flow rates for 1.4, 2.4, 3.5, and 4.8 MPa are 2814, 2821, 2805, 2757 mg/s, respectively.

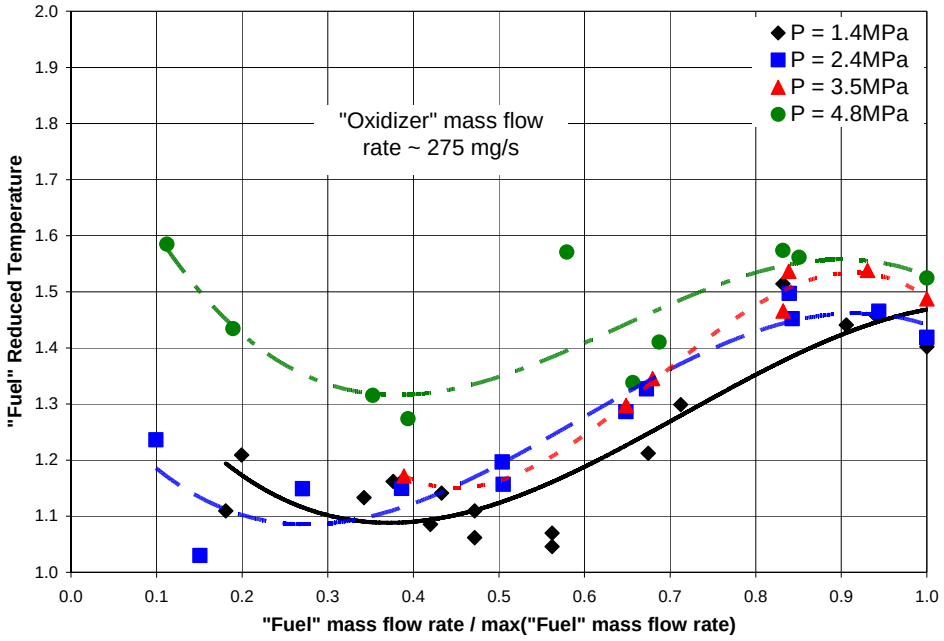

Figure 6 The annular flow ("fuel") reduced temperature versus the normalized "fuel" mass flow rate at four different chamber pressures. Oxidizer mass flow rate is fixed at about 275 mg/s. The lines are curve fits to the raw data. The maximum "fuel" mass flow rates for 1.4, 2.4, 3.5, and 4.8 MPa are 2995, 2985, 2974, 2918 mg/s, respectively.

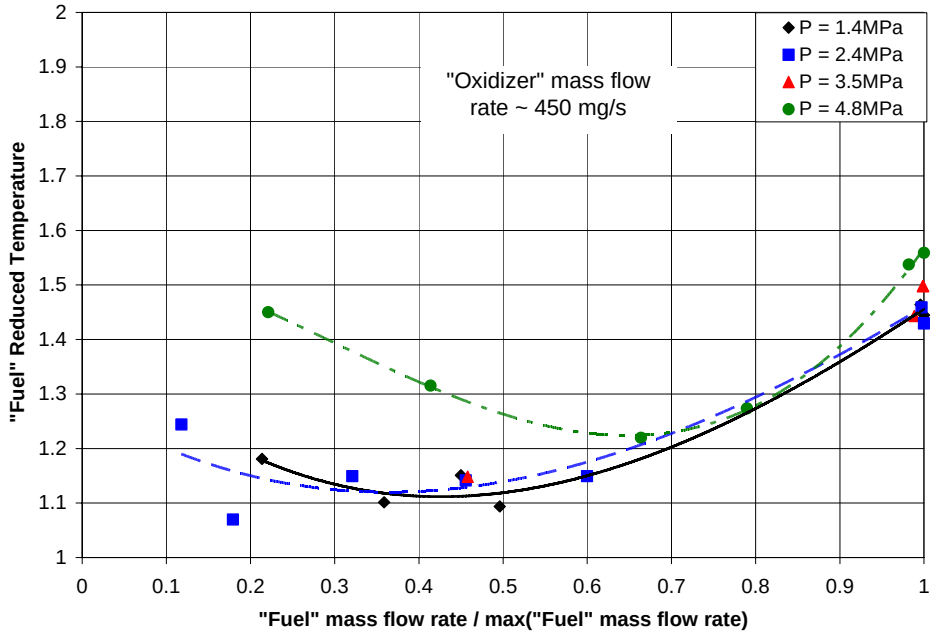

Figure 7 The annular flow ("fuel") reduced temperature versus the normalized "fuel" mass flow rate at four different chamber pressures. Oxidizer mass flow rate is fixed at about 450 mg/s. The lines are curve fits to the raw data. Data for the chamber pressures of 2.4 and 3.5 MPa are combined for curve fitting. The maximum "fuel" mass flow rates for 1.4, 2.4, 3.5, and 4.8 MPa are 2535, 2513, 2513, 2485 mg/s, respectively.

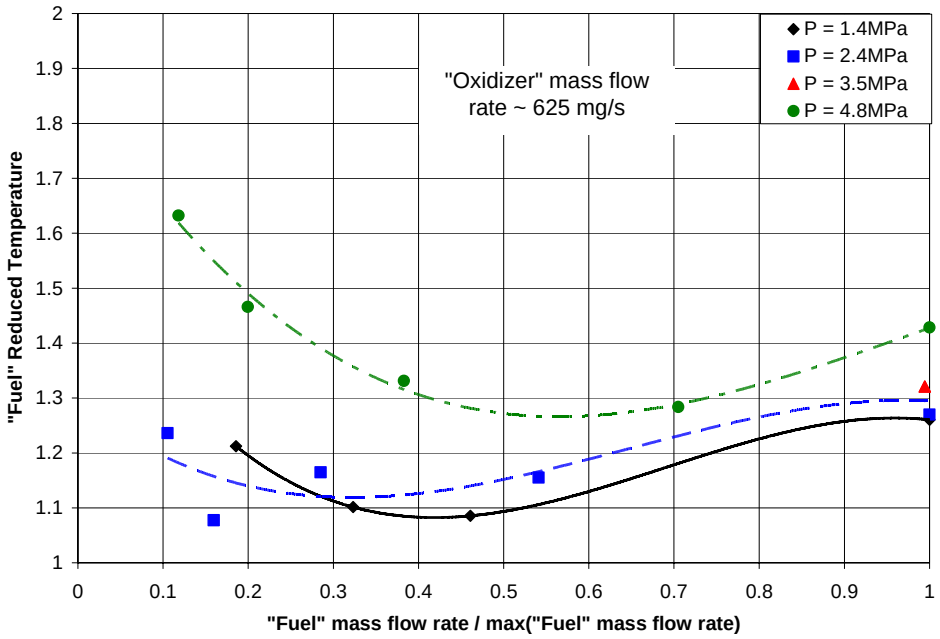

Figure 8 The annular flow ("fuel") reduced temperature versus the normalized "fuel" mass flow rate at four different chamber pressures. Oxidizer mass flow rate is fixed at about 625 mg/s. The lines are curve fits to the raw data. Data for the chamber pressures of 2.4 and 3.5 MPa are combined for curve fitting. The maximum "fuel" mass flow rates for 1.4, 2.4, 3.5, and 4.8 MPa are 2814, 2821, 2821, 2757 mg/s, respectively.

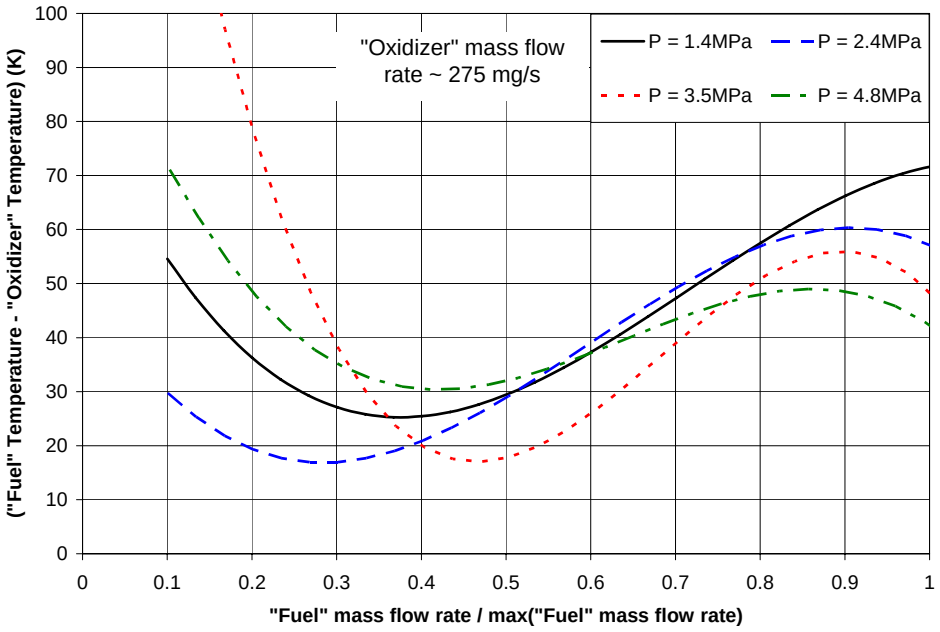

Figure 9 Differential temperature ("fuel" –"oxidizer") for four different chamber pressures, at an "oxidizer" mass flow rate of about 275 mg/s.

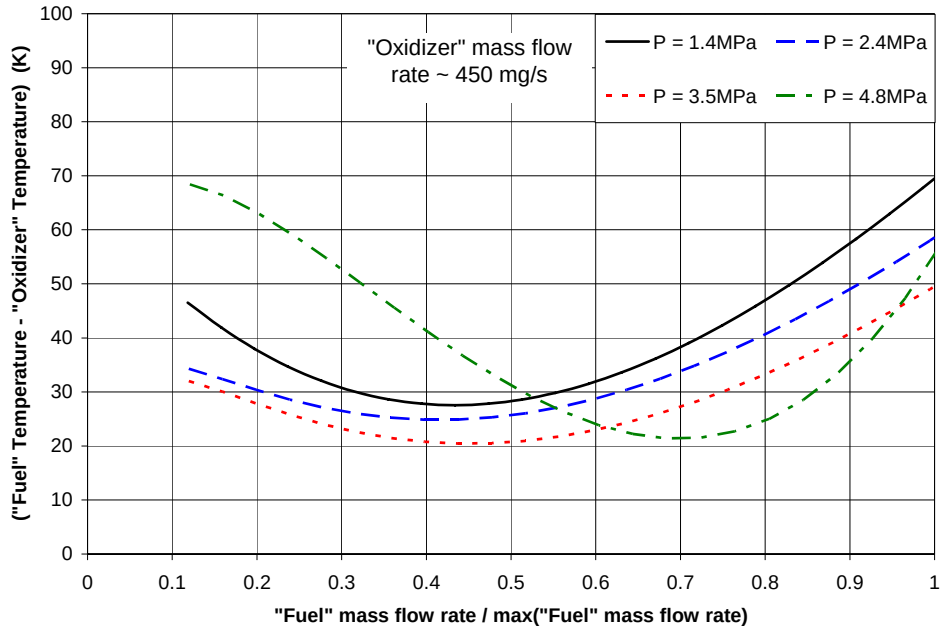

Figure 10. Differential temperature ("fuel" –"oxidizer") for four different chamber pressures, at an "oxidizer" mass flow rate of about 450 mg/s.

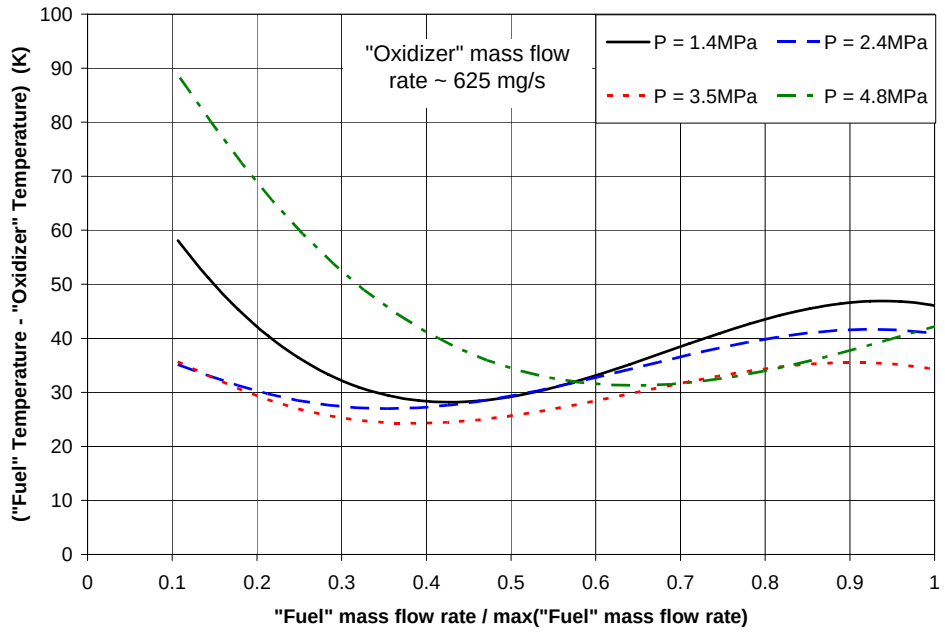

Figure 11 Differential temperature ("fuel" –"oxidizer") for four different chamber pressures, at an "oxidizer" mass flow rate of about 625 mg/s.

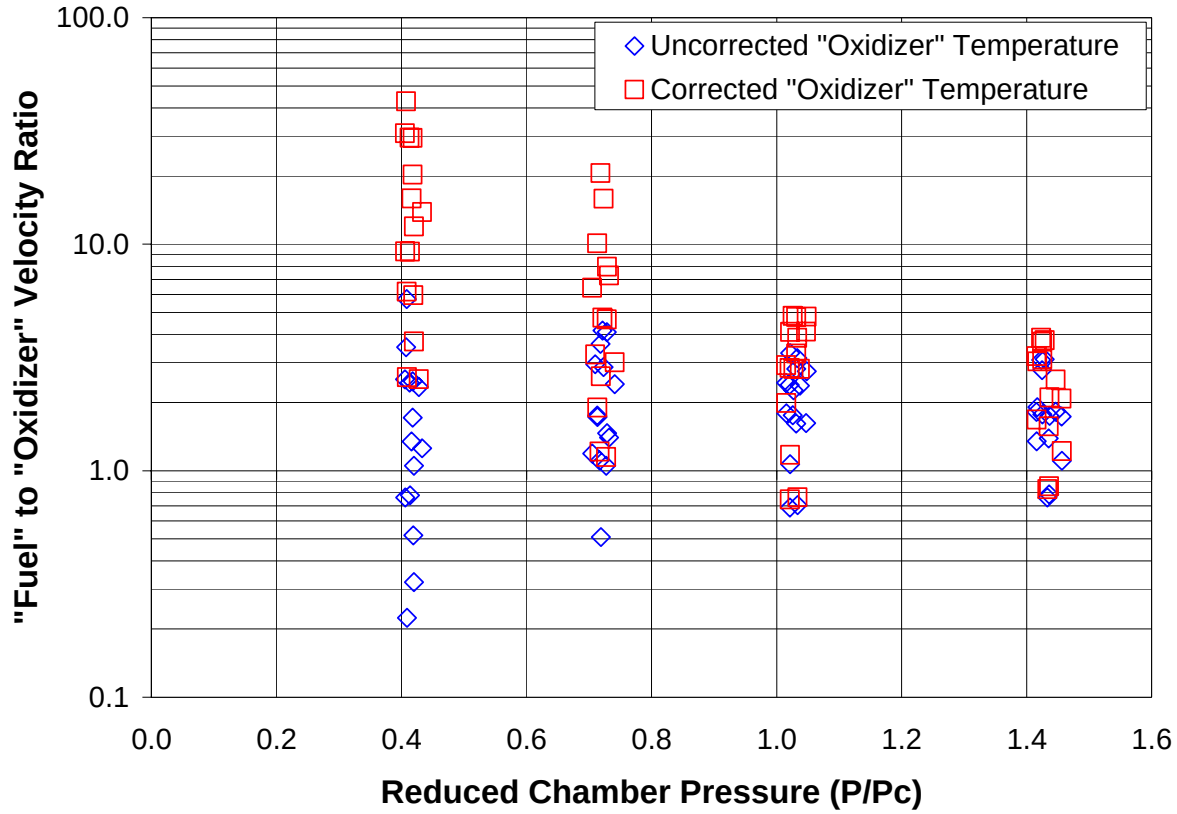

Figure 12 "Fuel" / "Oxidizer" Injection velocity ratio variation over the pressure range of the tested conditions. Corected “oxidizer” temperature was lower by about 7K. Critical pressure of nitrogen is 3.4 MPa.

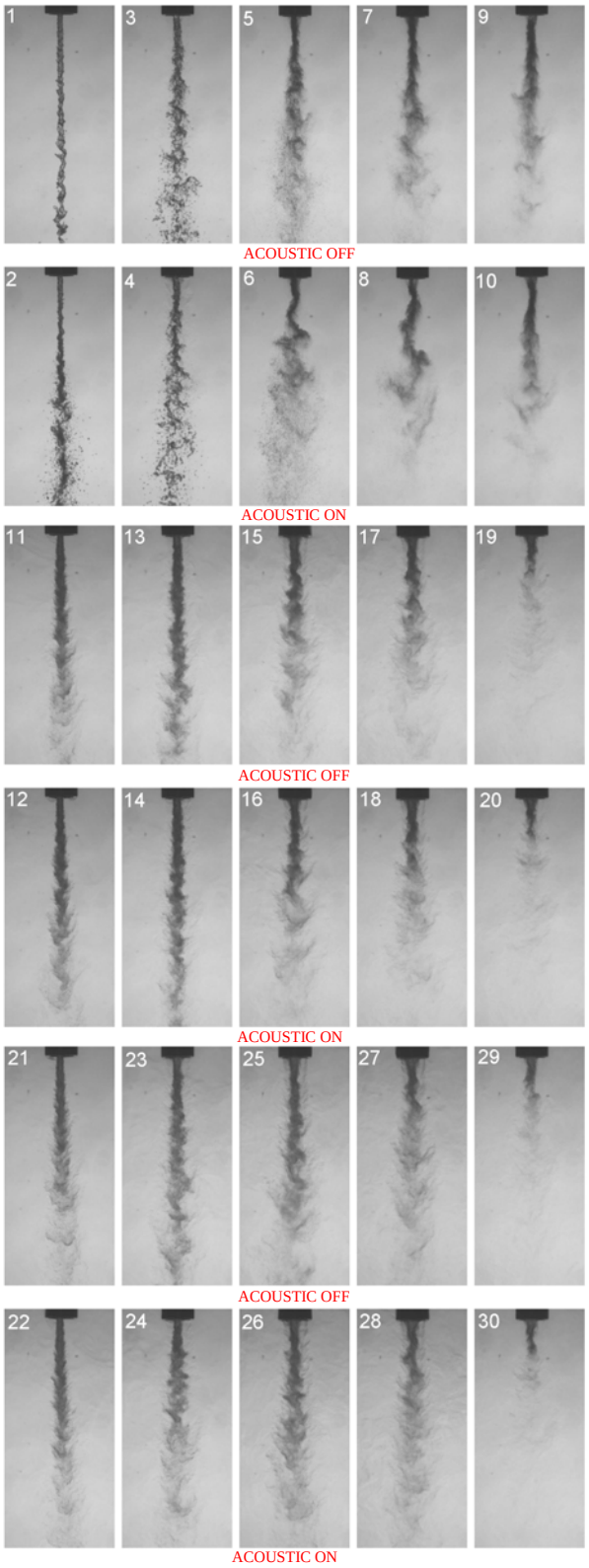

Figure 13. Images of the coaxial jet at approximately the same "oxidizer" mass flow rates through the inner tube (~ 275 mg/s). Columns are at about the same "fuel" mass flow rates passing through the annulus. For each row, the "fuel" mass flow rate starts at a zero value and increases from the left column to the right. The acoustic driver is off/on for the odd/even numbered jet images, respectively. The chamber pressure levels for images 1-10 are subcritical, for 11-20 are near-critical, and for 21-30 are supercritical. The data conditions are shown in Table 1 of the Appendix.

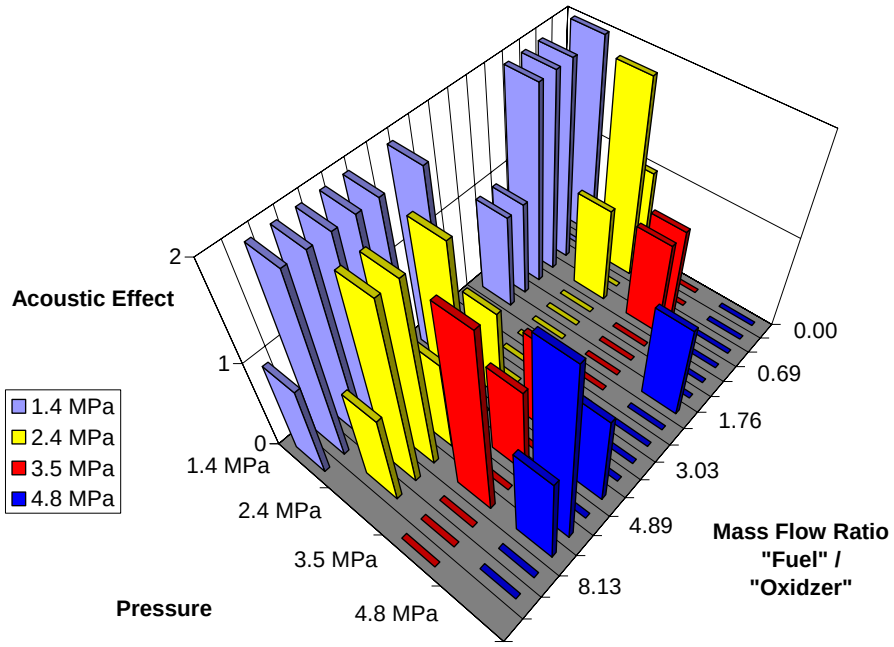

Figure 14 Changes in the rating of the acoustic field effects with variations of the chamber pressure and "fuel" / "oxidizer" mass flow rate ratio. Critical pressure of nitrogen is 3.4 MPa.

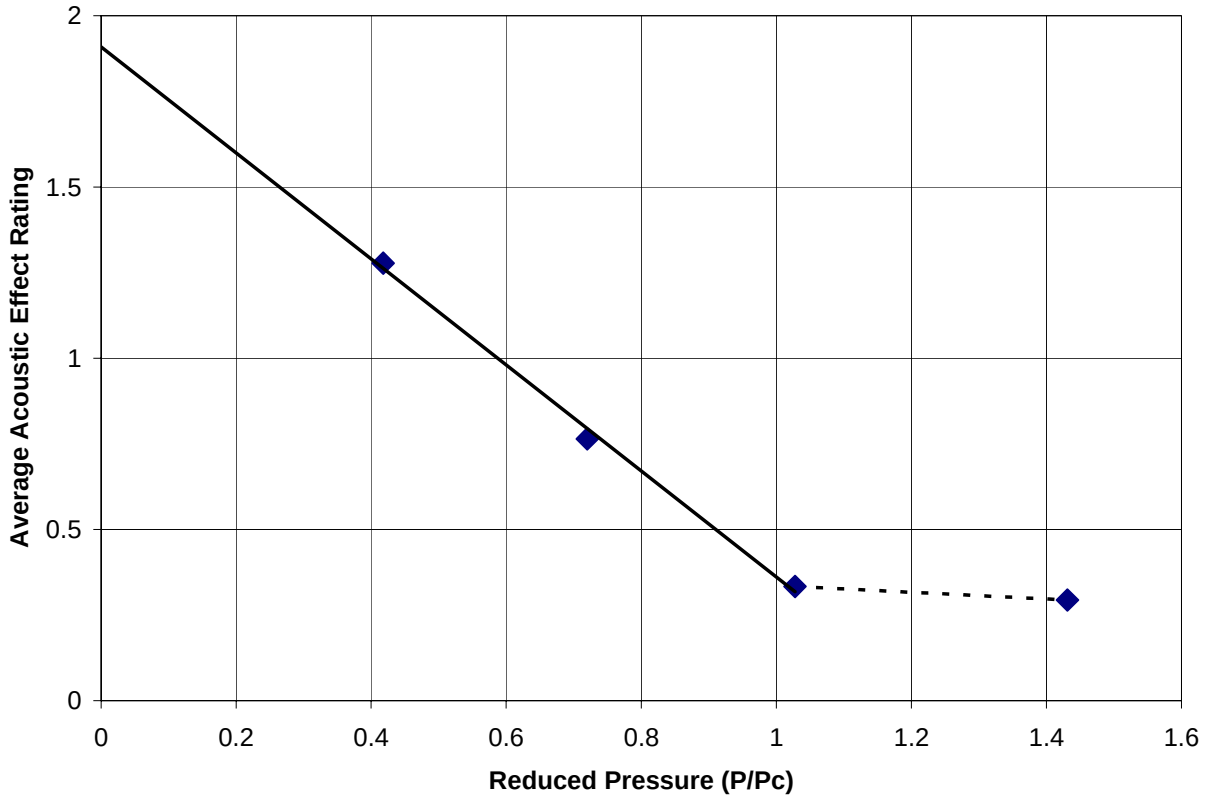

Figure 15 Averaged acoustic effect rating as a function of the reduced chamber pressure. At each pressure, averaging is done over all the fuel/oxidizer mass ratios shown in Figure 14.

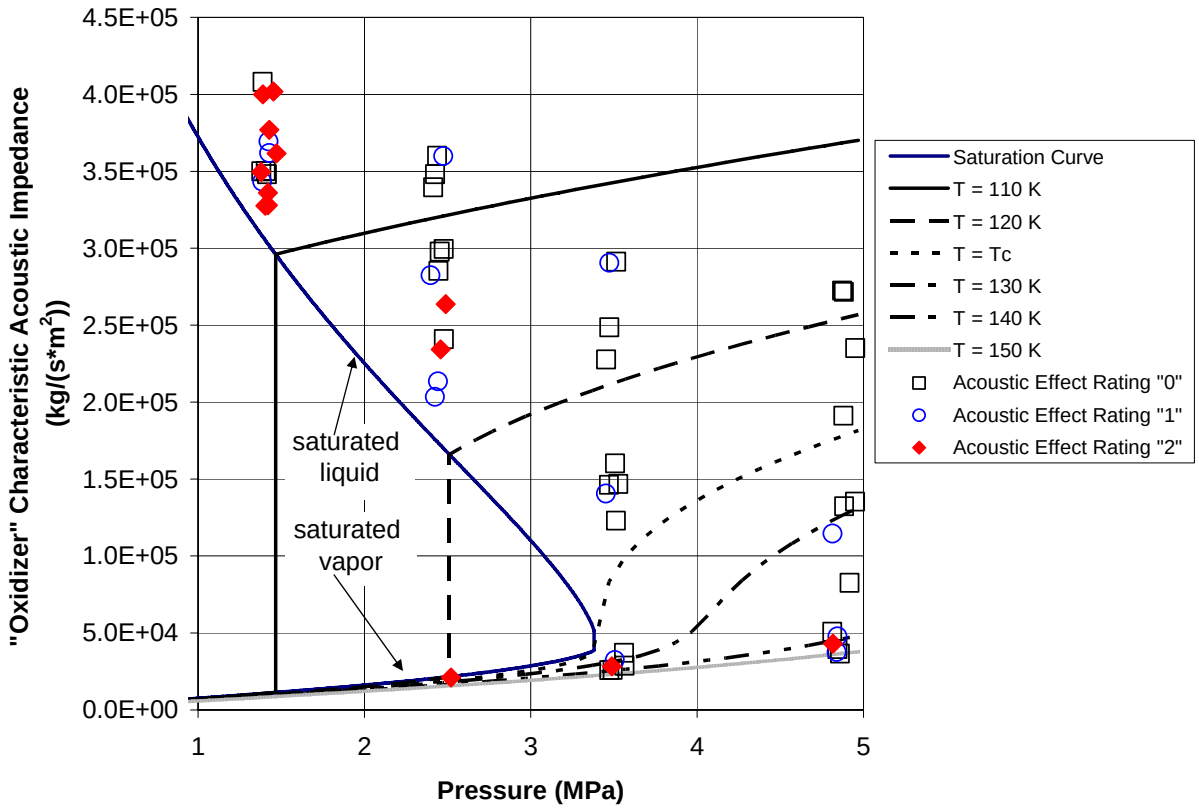

Figure 16 Phase diagram of the calculated characteristic acoustic impedance at the injector exit plane for the "oxidizer". Note that the present data was corrected at subcritical chamber pressures.

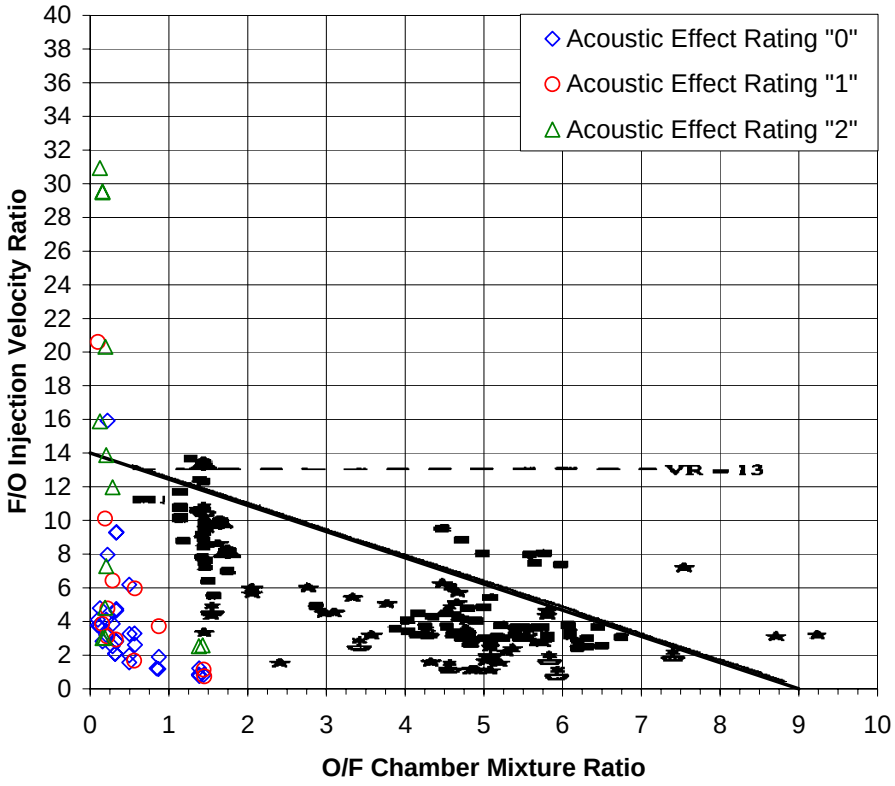

Figure 17. Coaxial injector instability zone by Hulka and Hutt[1], indicting a triangular zone in which most of the unstable engine operation was observed. The hollow diamond, hollow up-triangle, and hollow circle show results from the injector used in this study, the solid points are from Hulka and Hutt.[1]

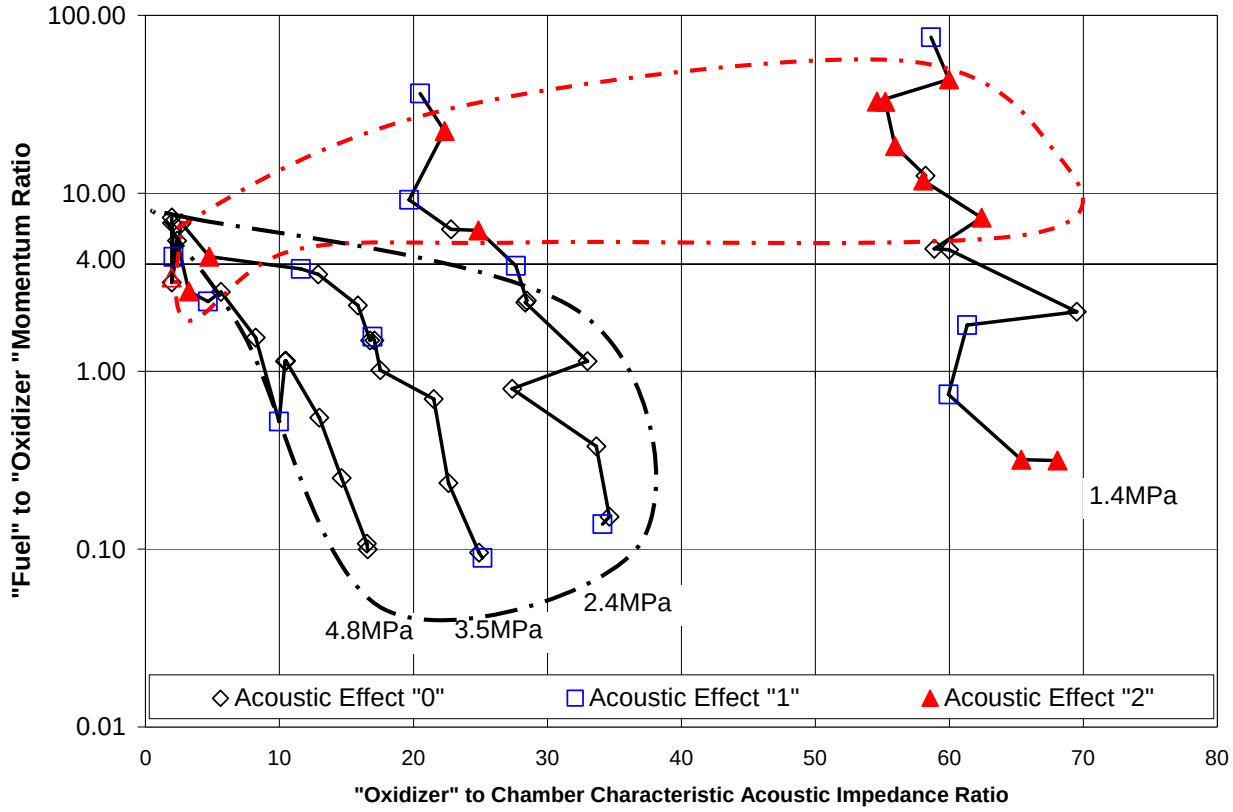

Figure 18 Shows the fuel/oxidizer momentum ratio as a function of the acoustic impedance ratio for all the conditions tested. Different symbols indicate our acoustic-jet interaction ratings. The dashed curve attempts to enclose most of the up-triangle symbol and dash-dot curve does the same for the diamond. The single hollow up-triangle is at 2.4 MPa and is on the vapor side of saturation curve at the predicted temperature.

TABLE

Table 1. Conditions at which the jet images shown in Figure 13 are taken.

Jet Number -	Acoustic Field -	Chamber Pressure MPa	Exit Temperature "Fuel" K	Exit Temperature "Oxidizer" K	Mass Flow Rate "Fuel" mg/s	Mass Flow Rate "Oxidizer" mg/s	Re "Fuel" -	Re "Oxidizer" -	Acoustic Effect -
1	off	1.36	179	114	0	276	0.00E+00	8.09E+04	2
2	on	1.36	179	114	0	276	0.00E+00	8.10E+04	2
3	off	1.44	146	112	488	276	1.67E+04	8.14E+04	1
4	on	1.40	146	112	486	276	1.67E+04	8.18E+04	1
5	off	1.47	144	112	1360	276	4.69E+04	8.08E+04	2
6	on	1.45	144	112	1354	277	4.68E+04	8.12E+04	2
7	off	1.49	173	113	2255	277	6.71E+04	8.06E+04	2
8	on	1.35	173	113	2255	277	6.74E+04	8.17E+04	2
9	off	1.38	182	114	2812	278	8.08E+04	8.15E+04	1
10	on	1.36	182	114	2820	278	8.10E+04	8.16E+04	1
11	off	3.47	179	138	0	275	0.00E+00	5.83E+04	1
12	on	3.52	179	138	0	275	0.00E+00	5.79E+04	1
13	off	3.47	146	119	488	275	1.47E+04	1.49E+04	0
14	on	3.44	146	119	489	275	1.48E+04	1.49E+04	0
15	off	3.45	144	126	1362	275	4.12E+04	1.97E+04	0
16	on	3.50	144	126	1355	276	4.08E+04	1.95E+04	0
17	off	3.51	173	133	2255	276	6.29E+04	5.59E+04	0
18	on	3.50	173	133	2254	276	6.29E+04	5.61E+04	0
19	off	3.37	182	137	2836	277	7.73E+04	5.95E+04	0
20	on	3.41	182	137	2835	276	7.71E+04	5.89E+04	0
21	off	4.74	245	144	0	271	0.00E+00	4.81E+04	0
22	on	4.90	245	144	0	268	0.00E+00	4.62E+04	0
23	off	4.78	189	126	486	270	1.23E+04	1.56E+04	1
24	on	4.73	189	126	486	272	1.23E+04	1.58E+04	1
25	off	4.78	163	134	1363	272	3.62E+04	3.27E+04	0
26	on	4.73	163	134	1363	272	3.64E+04	3.34E+04	0
27	off	4.78	185	142	2262	270	5.78E+04	4.61E+04	0
28	on	4.76	185	142	2275	270	5.82E+04	4.65E+04	0
29	off	4.74	193	148	2835	273	7.11E+04	4.98E+04	0
30	on	4.77	193	148	2838	272	7.11E+04	4.95E+04	0

APPENDIX R

"The Constant Volume Limit of Pulsed Propulsion for a Constant γ Ideal Gas"

The Constant Volume Limit of Pulsed Propulsion for a Constant γ Ideal Gas
(Formerly presented as paper AIAA-2000-3216)

Doug Talley and Ed Coy
Air Force Research Laboratory[1]

Abstract

The constant volume (CV) limit of pulsed propulsion is explored theoretically, where the combustion chamber is approximated as being time-varying but spatially uniform, and the nozzle flow is approximated as being one dimensional but quasi-steady. Isentropic blow down of a constant γ ideal gas is assumed. Notably, all the fixed expansion ratio results can be expressed as analytical solutions. Using an appropriately selected fixed expansion ratio nozzle was found not to result in more than a 3% performance penalty over using a variable expansion ratio nozzle optimized at all times for the instantaneous ratio of chamber to ambient pressure. It was also found that an optimized CV device produces more impulse than an optimized constant pressure (CP) device operating at the fill pressure of the CV device, for all ambient pressures except in a vacuum. However, the latter conclusion applies to optimum expansion ratios which are infinite in a vacuum. Caution is required in applying the latter conclusion to the finite expansion ratios of real devices.

[1]AFRL/PRSA, 10 E. Saturn Blvd., Edwards AFB, CA 93524-7660

Nomenclature

A - area

c - speed of sound

c_F - thrust coefficient

c_p - specific heat at constant pressure

F - thrust

$g(\gamma)$ - eq. (4)

I - impulse

$\dot{m}$ - rate of mass flow

M - Mach number

v - velocity

P - pressure

r - ρ / ρ_0

R - gas constant

t - time

T - temperature

V - volume

Greek

ε - expansion ratio

ϕ - P / P_∞

γ - ratio of specific heats

ι - $I / \rho_0 c_0 V$; dimensionless impulse

ρ - density

Ω, Φ -eq. (23)

τ - $t / c_0 A^* V$; dimensionless time

Subscripts

cp - pertaining to a constant pressure cycle

e - nozzle exit

f - fill condition

lc - pertaining to limit cycle operation

0 - initial condition before start of blow down

∞ - ambient condition

Superscripts

* - throat condition

Introduction

Recent interest in pulsed detonation propulsion has spawned a number of attempts to model the system performance, the specific impulse predictions from which have tended to vary widely[1]. One limiting case from which system performance estimates can be made is the so-called constant volume (CV) limit. Pulsed detonation devices approach the CV limit because large detonation wave speeds allow combustion to be complete before the gases in the combustion chamber have time to expand appreciably beyond the original volume of the chamber, resulting in a nearly constant volume combustion process. The CV limit is approached more exactly in real devices in the limit of large combustion chambers and small nozzles, where there is ample time for transient waves to decay in the combustion chamber before an appreciable amount of mass can exit the nozzle. In this latter limit, *i.e.*, where characteristic wave

transit times are much shorter than characteristic blowdown times, the CV limit can be approached even when the mechanism of combustion is not detonations, and is therefore useful to consider as a reference case. Hence the CV limit is referred to here simply as the CV limit of pulsed propulsion, regardless of the mechanism of combustion. By neglecting heat losses and assuming isentropic expansions following heat addition, an upper bound for the impulse produced by a CV limit device can be calculated. In what follows, the isentropic blowdown of a constant γ ideal gas in a CV limit device is explored, where the combustion chamber is approximated as being spatially uniform but time-varying, while the flow in the nozzle is approximated as being quasi-steady and one-dimensional. The results are compared to the performance of conventional constant pressure (CP) devices.

The constant volume (CV) limit as envisioned herein corresponds to the conceptual device illustrated in Fig. 1. An instantaneously actuated propellant valve controls the introduction of fresh reactants, while an instantaneously actuated valve in the nozzle controls the exhaust of combustion products. Time $t = 0^-$ corresponds to an initial condition with both valves closed, where the combustion chamber is initially filled with fresh reactants at some uniform fill pressure P_f, uniform fill temperature T_f, and uniform fill density ρ_f. Heat is then added, and both valves remain closed until all transients decay, at which time the chamber will have relaxed to some initial uniform combustion pressure P_0, initial uniform combustion temperature T_0, and initial combustion density $\rho_0 = \rho_f$. The pressure rise P_0 / P_f is not specified and is left as a free parameter. For reactants initially in the gaseous state, the pressure rise P_0 / P_f may be on the order of 10. For reactants initially in a liquid state, the pressure rise may be more on the order of 1,000. Heat addition and the decay of transients is assumed to take zero time, and to be complete by time $t = 0$. The nozzle valve then opens instantaneously at time $t = 0$, constant volume

blowdown begins, impulse begins to be produced, and the pressure, temperature, and density become functions of time, although they remain spatially uniform. The combustion products are assumed to be calorically perfect, with constant specific heats and molecular weight throughout the blow down. Heat losses from the chamber are neglected, and the blowdown is considered to be isentropic throughout the chamber and nozzle. The flow in the nozzle is assumed to vary one dimensionally, but is quasi-steady at any instant of time. Blowdown occurs at least until the chamber pressure reaches the fill pressure P_f. The propellant valve is then instantaneously opened, introducing fresh reactants which push the remaining products out. The blowdown changes at this point from having a constant volume and varying pressure in the chamber, to having a constant pressure and varying volume (of the products) in the chamber. The fill of fresh reactants continues until the chamber is full, at which time both valves close instantaneously, and the system is returned to its initial state.

A mathematical model of the CV limit under these assumptions is formulated next.

Formulation

General

The impulse produced by the unsteady blow down of the combustion gases in the CV limit is the integral of the thrust $F = \dot{m}v_e + (P_e - P_\infty)A_e$ over time, where $\dot{m}$ is the mass flow rate, P_∞ is the ambient pressure, and v_e, P_e, and A_e are the velocity, pressure, and area, respectively, at the nozzle exit plane. Under the transformation $dt = (dt/d\rho)d\rho = -(V/\dot{m})d\rho$ and the further transformation $r \equiv \rho/\rho_0$, where V is the combustion chamber volume and ρ_0 is the initial chamber density after combustion but before blow down at time $t = 0$, the total impulse I and blow down time t may be expressed as

$$I(t) = \int_0^t F(t)dt = \rho_0 V \int_r^1 (v_e + (P_e - P_\infty)A_e / \dot{m})dr \ , \tag{1}$$

$$t = \int_0^t dt = \rho_0 V \int_r^1 dr / \dot{m} \tag{2}$$

Fixed Nozzles

For quasi-steady isentropic flow, the instantaneous exit velocity is $v_e = \sqrt{2c_p(T - T_e)}$, where T and T_e are the instantaneous chamber and exit temperatures, respectively. Pressures and densities will be related in a simple fashion to temperatures according to $T/T_0 = (\rho/\rho_0)^{\gamma-1} = (P/P_0)^{(\gamma-1)/\gamma}$, where γ is the ratio of specific heats and where the subscript "0" denotes conditions in the chamber at time $t = 0$. With $c_0 = \sqrt{\gamma R T_0}$ and $c_p = \gamma R/(\gamma - 1)$, the exit velocity can be expressed as

$$v_e = c_0 r^{(\gamma-1)/2} \left(\frac{2}{\gamma - 1} \right)^{1/2} \sqrt{1 - r_e^{\gamma-1}} \ , \tag{3}$$

where $r_e \equiv \rho_e / \rho$ is the ratio of the density at the exit plane to the density in the chamber. For isentropic nozzle flow, the exit density ratio is related to the expansion ratio $\varepsilon \equiv A_e / A^*$, where A^* is the throat area, by (*see* eq. 5.3 in ref. 2):

$$\varepsilon = \frac{g(\gamma)}{r_e \sqrt{1 - r_e^{\gamma-1}}} \ ; \tag{4}$$

$$g(\gamma) \equiv \left(\frac{\gamma - 1}{2} \right)^{1/2} \left(\frac{2}{\gamma + 1} \right)^{(1/2)(\gamma+1)/(\gamma-1)}$$

Equation (4) has two solutions for r_e corresponding to subsonic and supersonic flow at the exit plane. These solutions will depend only on ε and γ. For supersonic flow, the density ratio r_e will therefore remain constant during blow down as long as compression waves do not enter the

nozzle, and eq. (3) will be analytically integrable when inserted into eq. (1). Compression/expansion waves will remain external to the nozzle for all *r* such that

$$r > \frac{1}{r_e}\left(\frac{\phi_e'}{\phi_0}\right)^{1/\gamma}, \tag{5}$$

where $\phi_0 \equiv P_0 / P_\infty$ and $\phi_e \equiv P_e / P_\infty$ are the ratios of the initial chamber and nozzle exit pressures, respectively, to the ambient pressure, and where ϕ_e' is the critical value of ϕ_e below which a compression wave enters the nozzle. The critical value of ϕ_e is given by (*see* eqs. 2.48a and 5.2 of ref. 2)

$$\phi_e' = \left[1 + \frac{2\gamma}{\gamma+1}(M_e^2 - 1)\right]^{-1}, \tag{6}$$

where

$$M_e^2 = \frac{2}{\gamma - 1}\left[\left(\frac{1}{r_e}\right)^{\gamma-1} - 1\right]. \tag{7}$$

While eq. (5) holds, the flow will be choked, and the throat conditions will be functions only of γ. For a throat density and velocity given by (*see* eq. 2.35a of ref. 2) $\rho^* = r\rho_0[2/(\gamma+1)]^{1/(\gamma-1)}$ and $v^* = \sqrt{\gamma R T^*} = c_0(2/(\gamma+1))^{1/2} r^{\gamma-1}$, and with $P_e = P_0 r_e^\gamma r^\gamma$, the instantaneous mass flow and thrust become

$$\dot{m}(r) = \rho^* A^* v^* = \rho_0 c_0 A^* g(\gamma)\left(\frac{2}{\gamma-1}\right)^{1/2} r^{(\gamma+1)/2} \tag{8}$$

$$F(r)/P_0 A^* g(\gamma) = r^\gamma \gamma \frac{2}{\gamma-1}\sqrt{1 - r_e^{\gamma-1}} + \frac{1}{r_e\sqrt{1 - r_e^{\gamma-1}}}\left(r_e^\gamma r^\gamma - \frac{P_\infty}{P_0}\right) \tag{9}$$

where eq. (4) has also been used. Thus all terms in eq. (1) will integrable analytically.

Define $\iota \equiv I/\rho_0 c_0 V$ and $\tau \equiv t c_0 A^*/V$ to be a dimensionless impulse and a dimensionless time, respectively. Then integrating eqs. (1) and (2) gives

$$\iota(r) = \sqrt{1-r_e^{\gamma-1}}\left(\frac{2}{\gamma-1}\right)^{1/2}\left(\frac{2}{\gamma+1}\right)a(r) + \frac{1}{\gamma r_e\sqrt{1-r_e^{\gamma-1}}}\left(\frac{\gamma-1}{2}\right)^{1/2}\left[r_e^{\gamma}\,\frac{2}{\gamma+1}\,a(r) - \frac{1}{\phi_0}\left(\frac{2}{\gamma-1}\right)b(r)\right] \quad (10)$$

$$\tau(r) = \frac{1}{g(\gamma)}\left(\frac{2}{\gamma-1}\right)^{1/2} b(r), \quad (11)$$

where

$$a(r) \equiv 1 - r^{(\gamma+1)/2} \qquad b(r) \equiv (1/r)^{(\gamma-1)/2} - 1. \quad (12)$$

The quantity ι/τ will be related to the average thrust $\overline{F} = I/t$. Noting that $c_0^2 = \gamma R T_0$ and $P_0 = \rho_0 R T_0$, then combining constants after dividing leads to

$$\gamma\iota/\tau = \overline{F}/P_0 A^* \equiv \overline{c}_F, \quad (13)$$

where $\overline{c}_F$ is the average thrust coefficient for the blow down.

Variable Nozzles

Fixed expansion ratio nozzles will be optimized for at most only a single value of *r* during the blow down; losses will occur at all other values. To assess what the performance would be if these losses were not present, a variable nozzle can be envisioned where the expansion ratio is continuously adjusted to maintain the optimum expansion ratio for the given ratio of chamber to ambient pressure at all times. The variable nozzle limit produces the maximum possible impulse, and is therefore useful as a reference case.

With the exit pressure always matched to the ambient pressure, only the exit velocity term $v_e = \sqrt{2c_p(T - T_e)}$ in eq. (1) will be of concern. For fixed nozzles, it was found that the term $T_e/T = r_e^{\gamma-1}$ was a constant, but here the exit temperature is fixed by the exit conditions $P_e = P_\infty$,

$\rho_e = \rho_0 (1/\phi_0)^{1/\gamma}$, and $T_e = T_0 (1/\phi_0)^{(\gamma-1)/\gamma}$. Therefore T_e / T will not be constant in this case. The dimensionless impulse in this case becomes

$$\imath(r) = \left(\frac{2}{\gamma - 1} \right)^{1/2} \int_r^1 \sqrt{r^{\gamma-1} - (1/\phi_0)^{(\gamma-1)/\gamma}}\, dr \,. \tag{14}$$

Eq. (14) cannot be integrated analytically but may easily be integrated numerically.

The blow down time for the variable nozzle limit will depend on the mass flow, and calculation of the mass flow will depend on whether the exit area or the throat area is varied to optimize the expansion ratio. The mass flow is best calculated using whichever area which is being held constant. If the exit area is assumed to be varied, as might approximately be the case with an automatically compensating nozzle such as a plug nozzle, the mass flow and blow down time based on a constant throat area are still given by eqs. (8) and (11), respectively. If the throat area is varied, then the mass flow and blow down time for a fixed exit area are

$$\dot{m} = \rho_e A_e v_e = \rho_0 c_0 A_e \left(\frac{2}{\gamma - 1} \right)^{1/2} \left(\frac{1}{\phi_0} \right)^{1/\gamma} \sqrt{r^{\gamma-1} - (1/\phi_0)^{(\gamma-1)/\gamma}} \tag{15}$$

$$\tau_e(r) = \phi_0^{1/\gamma} \left(\frac{\gamma - 1}{2} \right)^{1/2} \int_r^1 dr \Big/ \sqrt{r^{\gamma-1} - (1/\phi_0)^{(\gamma-1)/\gamma}} \tag{16}$$

where $\tau_e = t c_0 A_e / V$ is defined this time in terms of the exit area. Eq. (16) also cannot be integrated analytically but may easily be integrated numerically. Inasmuch as shocks and expansion waves will not occur when the expansion ratio is always matched to the instantaneous pressure ratio, eqs. (14)-(16) above for the variable nozzle case will apply until the expansion ratio reduces to unity and the flow becomes unchoked, *i.e.*, for all *r* such that

$$r > \left(\frac{\gamma + 1}{2} \right)^{1/(\gamma-1)} \left(\frac{1}{\phi_0} \right)^{1/\gamma} \tag{17}$$

Limit Cycle Operation

In repetitive operation, intake valves are opened at some point during the blow down in order to introduce fresh propellants for the next cycle, as illustrated in Fig. 1. Any remaining combustion products not yet expelled would be pushed out, or purged, by the incoming fresh propellants. If the purge of the remaining combustion products can be approximated as a constant pressure process, and the value of *r* is large enough to prevent shocks from entering the nozzle, then the above equations can be used to calculate the time to purge the remaining mass and the additional impulse produced. Specifically, the time required to purge the remaining mass is $t_{cp}(r) = \rho V / \dot{m} = \rho_0 V r / \dot{m}(r)$, and the additional impulse produced is $I_{cp}(r) = F(r) t_{cp}(r)$, where $F(r)$ and $\dot{m}(r)$ are given by eqs. (8) and (9) at a constant value of *r* during the purge. The additional dimensionless impulse and blow down times can still be expressed in the forms of eqs. (10) and (11), but with the functions *a*(*r*) and *b*(*r*) given instead by

$$a_{cp}(r) = \frac{\gamma+1}{2} r^{(\gamma+1)/2} \qquad b_{cp}(r) = \frac{\gamma-1}{2} r^{(\gamma-1)/2} \tag{18}$$

where the subscript "*cp*" stands for the these constant pressure additions. The total impulse for the entire cycle can then be expressed, again in the forms of eqs. (10) and (11), but this time with the functions *a*(*r*) and *b*(*r*) given by

$$a_{lc}(r) = a(r) + a_{cp}(r) = 1 + \frac{\gamma-1}{2} r^{(\gamma+1)/2} \qquad b_{lc}(r) = b(r) + b_{cp}(r) = \frac{\gamma+1}{2}\left(\frac{1}{r}\right)^{(\gamma-1)/2} - 1 \tag{19}$$

where the subscript "*lc*" stands for "limit cycle." For limit cycle operation with variable nozzles, the total cycle impulse is given instead by the sum of the constant pressure impulse with the impulse calculated by eq. (14), and the total cycle blow down time is the sum of the constant pressure time plus the blow down time calculated by eq. (11) or eq. (16). The expansion ratio always

matches the pressure ratio in the variable nozzle case, so the exit density ratio must be set to $r_e = (1/r)(1/\phi_0)^{1/\gamma}$.

The density ratio *r* cannot be specified arbitrarily if limit cycle operation is to be achieved. Limit cycle operation requires the blow down to proceed at least until the chamber pressure reaches the fill pressure at which fresh propellants are introduced. This gives $r \le (P_f / P_0)^{1/\gamma}$, where P_f is the fill pressure. The inequality sign indicates that the blow down can proceed to a pressure lower than the fill pressure if the fresh reactants undergo compression during the fill. Given that $\rho_0 = \rho_f$ for CV heat addition, the ratio P_f / P_0 could be on the order of 1,000 times smaller for propellants in an initial liquid state compared to an initial gaseous state.

For a given density ratio *r*, the blow down of the remaining combustion products in a CP mode produces a greater impulse than if the blow down had been permitted to proceed to a lower density ratio. Therefore, given a choice, the density ratio *r* should be selected to be the maximum value possible consistent with limit cycle operation and available injection pressure, namely $r = (P_f / P_0)^{1/\gamma}$.

Comparisons with Constant Pressure Devices

Comparisons of the dimensionless impulse or the thrust coefficient with corresponding quantities for constant pressure (CP) processes can be performed if the normalization constants are the same in both cases. Here the normalization constants are chosen to be those of the CV process, leading to the correction factors Ω and Φ in the resulting expressions below. Assuming the expansion ratio for the CP process is the optimum expansion ratio, the resulting dimensionless impulse, blow down time, and average thrust coefficient become

$$\iota_{cp} = \frac{1}{\Omega}\left(\frac{2}{\gamma-1}\right)^{1/2}\sqrt{1-(\Phi/\phi_0)^{(\gamma-1)/\gamma}} \tag{20}$$

$$\tau_{cp} = \frac{\Phi}{\Omega}\frac{1}{g(\gamma)}\left(\frac{\gamma-1}{2}\right)^{1/2} \tag{21}$$

$$\bar{c}_{F,cp} = \gamma g(\gamma)\frac{2}{\gamma-1}\frac{1}{\Phi}\sqrt{1-(\Phi/\phi_0)^{(\gamma-1)/\gamma}}\ , \tag{22}$$

where

$$\Omega \equiv c_0 / c_{cp} \qquad\qquad \Phi \equiv P_0 / P_{cp} \tag{23}$$

and where $\iota_{cp} \equiv I_{cp} / \rho_0 c_0 V$, $\tau_{cp} \equiv t_{cp} c_0 A^* / V$, $\bar{c}_{F,cp} \equiv \bar{F} / P_0 A^*$, and the values of ρ_0, c_0, P_0, and V are those of the constant volume process. The quantity τ_{cp} in this context can be interpreted to be the dimensionless time required by the constant pressure process to expel the same mass as the initial mass of the constant volume process.

Results and Discussion

Effect of Thermochemistry

The dimensionless impulse and blow down time, eqs. (10)-(12), depend explicitly on r and implicitly only on γ, r_e (or ε), and ϕ_0. Of these, only γ depends on the thermochemistry, but this dependency is weak. The major influence of thermochemistry comes through the initial speed of sound c_0 used to normalize the impulse. Thus the specific impulse $I_s = \iota c_0$ is maximized when c_0 is maximized. This in turn implies that the optimum thermochemistry is that which maximizes the initial combustion temperature T_0 and minimizes the molecular weight. The same general guidance is known to also apply to constant pressure devices. *Thus constant volume devices should optimize at approximately the same mixture ratios as constant pressure*

devices. Also, like constant pressure devices, the thrust is maximized by maximizing the initial chamber pressure and the throat area, as implied by eq. (9).

Fixed Nozzles

Much can be understood about the blow down of fixed nozzles by examining conventional steady state thrust coefficient curves such as can be found in standard texts.[3] The thrust coefficient is defined in eq. (13), where P_0 in the steady state case is interpreted to be the steady chamber pressure of a constant pressure device. A set of these curves for the steady state case is given in Fig. 2 for $\gamma = 1.2$. These curves were generated by setting $r = 1$ in eq. (18), substituting into eqs. (10) and (11), and then calculating $\bar{c}_F$ per eq. (13). The curves reproduce those given in ref. 3. Dimensionless isobars (curves of constant ϕ_0) initially increase with ε, reach a maximum, then decrease to a minimum where a shock enters the nozzle and the above formulation is no longer valid. The curve for $\phi_0 = \infty$ reaches a maximum only at $\varepsilon = \infty$. A curve connecting the maxima indicates the expansion ratio producing the maximum thrust for a given isobar.

The blow down of a fixed nozzle CV device proceeds along a vertical path of constant ε between two isobars. The thrust produced will be some average between the two isobars. Picking any two isobars in Fig. 2, say between $\phi_0 = 50$ and $\phi_0 = 20$, and following the vertical line between them for various ε, it can be envisioned that the average thrust will reach a maximum neither at large ε nor at $\varepsilon = 1$, but at some optimum ε in between. However, the average thrust cannot be calculated directly from Fig. 2, because the thrust coefficient is proportional to the thrust divided by the chamber pressure, not the thrust alone. A blow down from $\phi_0 = 50$ to $\phi_0 = 20$ is replotted in Fig. 3 where the curve for $\phi_0 = 20$ is normalized by the same pressure as for $\phi_0 = 50$, making all curves proportional to the thrust. This is accomplished by multiplying the

thrust coefficient of Fig 2. by 0.4 for $\phi_0 = 20$. The curve labeled "b.d." gives the average thrust coefficient for the blow down and is seen to be an average of the curves for $\phi_0 = 50$ and $\phi_0 = 20$, as expected. The variable nozzle case shown in Fig. 3 will be discussed later.

Average thrust coefficients are plotted as functions of ϕ_0 and ε for blow downs to $r = 0.75$, 0.5, and 0.25 in Figs. 4, 5, and 6, respectively. Dimensionless blow down times are plotted as a function of r for two values of γ in Fig. 7. As can be seen from eq. (11) and Fig. 7, blow down times are independent of ϕ_0, and depend only weakly on γ. Because τ is fixed and independent of ϕ_0 for a fixed r, the curves in Figs. 4, 5, and 6 will also be proportional to the dimensionless impulse $\imath$, as can be shown from eq. (13). However, the constant of proportionality will be different for each r, increasing as r decreases, because τ increases as r decreases. The constant of proportionality is given in the figures. The overall trend in these figures is that the average thrust coefficient decreases as r decreases. This is due to τ increasing more rapidly than $\imath$ as r decreases, because $\imath$ also increases as r decreases.

The expansion ratio which produces the maximum impulse can in principle be found by taking the first derivative of eq. (10) with respect to r_e and setting it equal to zero. The resulting expression cannot be solved analytically, however, so the optimum expansion ratio is computed here by finding the maximum impulse using a numerical search. The optimum expansion ratio is plotted as a function of ϕ_0 and r in Fig. 8, and the dimensionless impulse produced at the optimum expansion ratio is plotted in Fig. 9. Because r is variable, τ is also, so the dimensionless impulse and the average thrust coefficient curves are no longer directly proportional as they were in earlier figures, where r was fixed. The optimum thrust coefficient is plotted in Fig. 10.

Variable Nozzles

Because the expansion ratio is always optimized for variable nozzles, the blow down of variable nozzles proceeds along the curve of maximum thrust in Fig. 2. The dimensionless impulse produced can be computed as a function of ϕ_0 and r by integrating eq. (14), and compared with the performance of fixed nozzles operating at the optimum expansion ratio. The results are not easily viewed in the form of Fig. 9, however, so they are plotted instead here in Fig. 11 as the impulse penalty in using optimized fixed nozzles compared to the variable nozzle case, based on the percentage of the variable nozzle impulse. The penalty is shown not to exceed about 3% for all cases calculated. The reason the penalty is not more severe can be traced to the flatness of the curves in Fig. 2 near the points of maximum thrust. This is illustrated more clearly in Fig. 3, where the difference between the variable and optimized fixed nozzle blow down paths is shown. As can be seen, the maximum instantaneous thrust coefficient is not that much higher for the variable nozzle case than for optimized fixed nozzles, leading to calculated average thrust coefficients which are very close.

Comparison with Constant Pressure Devices

By normalizing with the same constants as used for the CV device, the correction factors Ω and Φ as defined in eq. (23) and used in eqs. (20)-(22) allow the normalized quantities for CP devices to be directly compared with CV devices at any arbitrary CP chamber pressure and speed of sound (temperature). However, only certain cases will be of interest here. It is presumed that the two cycles are to be compared for the same propellant combination and at the optimum mixture ratio for each cycle, the latter of which as discussed above should be approximately the same in both cases. If T_f is the initial fill temperature before combustion, and q is the heat of reaction per unit mass for a given propellant combination and mixture ratio, then the initial CP

temperature after combustion will be approximately $T_{cp} = T_f + q/c_p$. Neglecting for the moment small possible differences in *q* between CV and CP combustion, then the initial CV temperature after combustion will be approximately $T_0 = T_f + \gamma q/c_p$. Thus Ω will vary only over a very narrow range near unity, namely from $\Omega = 1$ for $q = 0$ to $\Omega = \gamma^{1/2}$ for $q/c_p >> T_f$. For $\gamma = 1.2$, this corresponds to $1 \le \Omega \le 1.095$. The conclusion that Ω will vary only over a very narrow range near unity remains unchanged even when small possible differences in *q* between CV and CP combustion are considered.

The question now arises as to which of the various pressures encountered over the CV blow down, or not encountered, should a CP device be operated at in order to compare with a CV device. Only two possibilities will be considered here. The first is the case where the pressure of the CP device is the same as the fill pressure of the CV device, namely $\Phi = P_0/P_f$. This would allow a comparison of two devices having equivalent feed systems. Assuming the purge pressure is the same as the feed pressure, limit cycle operation gives $r = (P_f/P_0)^{1/\gamma}$. Given further that $P_0 = \rho_0 R T_0$ and that $\rho_0 = \rho_f$ for a CV device, where ρ_f is the density after propellant fill but before combustion, then $P_0/P_f = 10$ would be representative of propellants in an initial gaseous state, while $P_0/P_f = 1000$ would approach propellants in an initial liquid state. A CP device operating at the same pressure as the fill pressure of the CV device will be referred to here as a "CP$_f$" device for brevity.

The second possibility will be to compare the performance of combustion chambers experiencing the same material stresses. A very rough approximation of this would be a CP device operating at the same pressure as the peak pressure of a CV device, namely $\Phi = 1$. A CP device

operating at the same pressure as the peak pressure of the CV device will be referred to here as a "CP_p" device, again for brevity.

The ratio of the dimensionless impulse produced by a CP_f device to the dimensionless impulse of a CV device is presented in Fig. 12, and the ratio of the dimensionless impulse produced by the CP_p device to the dimensionless impulse of a CV device is presented in Fig. 13. Because the same quantities are used to non-dimensionalize the impulse in all cases, these plots also give the ratio of the total impulses and the ratio of the specific impulses. The expansion ratios used for the CP and CV devices are those which produce the maximum possible impulse in each case, namely a fixed expansion ratio which is optimized for the fixed ratio of the chamber to ambient pressures for the CP device, and a variable expansion ratio which changes with the variable ratio of chamber to ambient pressure for the CV device. The CV device is operated in limit cycle mode where the blow down is performed to the maximum value of *r* consistent with limit cycle operation, $r = (P_f / P_0)^{1/\gamma}$. It is assumed that $q / c_p >> T_f$ in all cases, giving $\Omega = \gamma^{1/2}$.

Curves are drawn in Figs. 12 and 13 for different ratios of the peak pressure to the fill pressure, P_0 / P_f. Increases in this ratio indicate either more energetic chemistry (greater temperature/pressure rise), or the presence of condensed phases in the initial fill. Increases over two orders of magnitude as shown in the figures would be largely the result of the presence of condensed phases. Increases in P_0 / P_f always increase the difference between the CP and CV performance. The right hand extent of all the curves is dictated by the shock limit, beyond which a shock enters the nozzle and the present formulation no longer applies. The left hand extent of the curves as drawn in the figures is limited solely for reasons of graphical clarity; the curves in both figures actually all extend to $1/\phi_0 = 0$. The limiting values of the curves at $1/\phi_0 = 0$ are given in

the figures. These limiting values are exactly the same for both the CP_f and CP_p cases. The reason for this is that eq. (20) becomes independent of the chamber pressure when $1/\phi_0 = 0$.

Away from $1/\phi_0 = 0$, the impulse of a CP_f device is shown in Fig. 12 to be inferior to that of the CV device, and the impulse of a CP_p device is shown in Fig. 13 to be superior to that of the CV device. The relative differences diminish as $1/\phi_0$ approaches zero. At large enough $1/\phi_0$, the relative differences are significantly larger than the 3% maximum performance penalty shown in Fig. 11 attributed to using an optimized fixed nozzle instead of a variable nozzle. This implies that, at large enough $1/\phi_0$, the performance penalty associated with the practical simplicity of using an optimized fixed nozzle might be tolerable compared with the complications of developing a variable nozzle. To assess whether a practically attainable device could fall within a regime where such losses might be tolerable, a reference case consisting of the approximate operating point of a stoichiometric kerosine/air (jet fuel/air) system operating at 1 atm ambient pressure and a 3 atm fill pressure is plotted as a black dot in Fig. 12. The operating point is shown to be well within a regime where such performance losses might be tolerable. Whether such losses would in fact be tolerable in a practical system would of course depend on all the other system losses.

The case $1/\phi_0 \to 0$ is an important limit in that it represents operation where the ambient pressure approaches a vacuum, *i.e.*, in space. The trends of the curves in Figs. 12 and 13 as $1/\phi_0 \to 0$ are discussed below. It is to be emphasized, however, that the comparisons in Figs. 12 and 13 are for optimized expansion ratios. As $1/\phi_0 \to 0$, this means expansion ratios that approach infinity. Clearly no real device in space would operate with an infinite expansion ratio. Therefore the curves in Figs. 12 and 13 are to be interpreted cautiously in drawing conclusions

about real devices as $1/\phi_0 \to 0$. A treatment more applicable to real devices would need to account for practical considerations which constrain the finite sizes of nozzles on spacecraft. Such a treatment is beyond the scope of the present work.

For optimized expansion ratios, the difference between a CP_f device and a CP_p device vanishes as $1/\phi_0$ approaches zero, and the impulse of the CP device can become either slightly higher or slightly lower than the impulse of the CV device, depending on the magnitude of P_0/P_f. The reason for this may be found in deriving the following analytical expression for $\imath/\imath_{cp}$, which is possible when $1/\phi_0 = 0$. For limit cycle operation, integrate eq. (14) from $r = (P_f/P_0)^{1/\gamma}$ to $r = 1$, which now can be done analytically, and add the impulse from the constant pressure part of the cycle by using the functions from eq. (18) in eq. (10). Note that $r_e = 0$ ($\varepsilon = \infty$) when $1/\phi_0 = 0$. Divide the result into eq. (20). The result is

$$\frac{\imath_{cp}}{\imath} = \frac{1}{\Omega}\left(\frac{\gamma+1}{2}\right)\left[1+\frac{\gamma-1}{2}\left(\frac{P_f}{P_0}\right)^{(\gamma+1)/2\gamma}\right]^{-1}. \qquad (24)$$

The maximum value of the expression occurs as $P_0/P_f \to \infty$, which for $\Omega = \gamma^{1/2}$ and $\gamma = 1.2$ is $\imath/\imath_{cp} = 1.004$. As P_0/P_f becomes smaller, the magnitude of the impulse ratio also becomes smaller, until eventually it is reduced to a value less than unity. For $P_0/P_f = 10$, this value becomes $\imath/\imath_{cp} = 0.992$. Limit values of $\imath/\imath_{cp}$ at $1/\phi_0 = 0$ shown in Figs. 12 and 13 were calculated using eq. (24).

Conclusions

Analytical solutions of the constant volume (CV) limit of pulsed propulsion for fixed expansion ratios have been explored and compared with the case where a variable nozzle is used to

match the pressure ratio at all times during the blow down. The solutions apply for all supersonic flows where compression waves remain exterior to the nozzle. The solutions were also compared with constant pressure (CP) devices. It was found that:

1. CV devices should optimize at approximately the same mixture ratio as CP devices, namely the mixture ratio which maximizes the initial temperature and minimizes the molecular weight.
2. The thrust of CV devices is maximized in the same way as for CP devices, namely by maximizing the initial pressure and the throat area.
3. The blow down time depends on $r = \rho / \rho_0$, only weakly on γ, and is independent of the initial pressure ratio $\phi_0 = P_0 / P_\infty$.
4. In general an optimum expansion ratio exists which maximizes the impulse produced by the blow down of a CV device at a fixed expansion ratio.
5. Using an optimized fixed expansion ratio nozzle results in an impulse penalty that does not exceed 3% (for the cases considered) of the impulse that would be produced using the more complicated variable expansion ratio nozzle.
6. A comparison between a CP device operating at its optimum expansion ratio and a CV device in limit cycle operation with a variable expansion ratio leads to the following additional conclusions:
    a. Except near $1/\phi_0 = P_\infty / P_0 = 0$, the impulse produced by a CV device is superior to that of a CP device operating at the same pressure as the fill pressure of the CV device, but inferior to the impulse produced by a CP device operating at the same pressure as the peak pressure of the CV device.

b. The magnitude of the difference between a CV device and the two CP devices considered increases as $1/\phi_0$ increases.

c. At large enough $1/\phi_0$, the relative difference between a CV device and the two CP devices considered is significantly larger than the impulse penalty associated with using an optimized fixed expansion ratio instead of a variable nozzle on the CV device.

d. The regime where the relative difference between a CV device and a CP device is significantly larger than the impulse penalty associated with using an optimized fixed expansion ratio on the CV device appears to be practically achievable for at least the one reference case considered, which involved kerosine/air operation at 1 atm ambient pressure.

e. For infinite expansion ratios at $1/\phi_0 = P_\infty / P_0 = 0$, the difference between the two CP devices considered vanishes, and the impulse of the CP device can become either slightly higher or slightly lower than the impulse of the CV device, depending on the magnitude of P_0 / P_f. However, these conclusions may not apply to real devices operating in space, which have finite expansion ratios.

This work was supported by the Propulsion Directorate of the Air Force Research Laboratory. Many valuable discussions with Dr. Phil Kessel concerning this work are gratefully acknowledged.

References

[1]Kailasanath, K., Patnaik, G., and Li, C., "Computational Studies of Pulse Detonation Engines: A Status Report," 35th AIAA/ASME/SAE/ASEE Joint Propulsion Conference and Exhibit, paper AIAA 99-2634, 20-24 June 1999, Los Angeles, CA.

[2]Leipman, H.W., and Roshko, A., Elements of Gasdynamics, John Wylie & Sons, 1957.

[3]Sutton, G.P., Rocket Propulsion Elements, 6th ed., John Wiley & Sons, 1992.

List of Figures

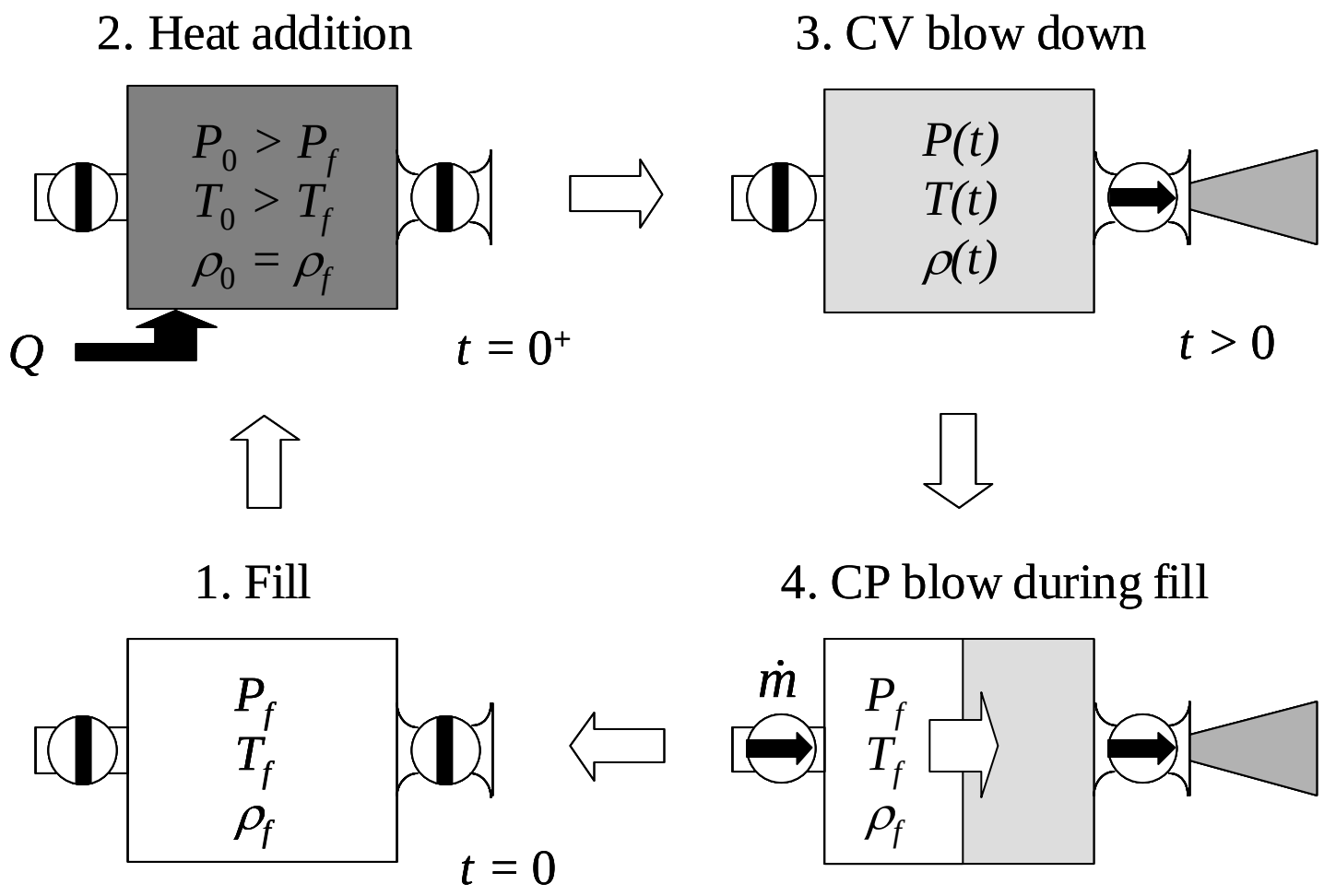
2. Heat addition
3. CV blow down
$P_0 > P_f$
$T_0 > T_f$
$\rho_0 = \rho_f$
$P(t)$
$T(t)$
$\rho(t)$
Q
$t = 0^+$
$t > 0$
1. Fill
4. CP blow during fill
P_f
T_f
ρ_f
$\dot{m}$
$t = 0$

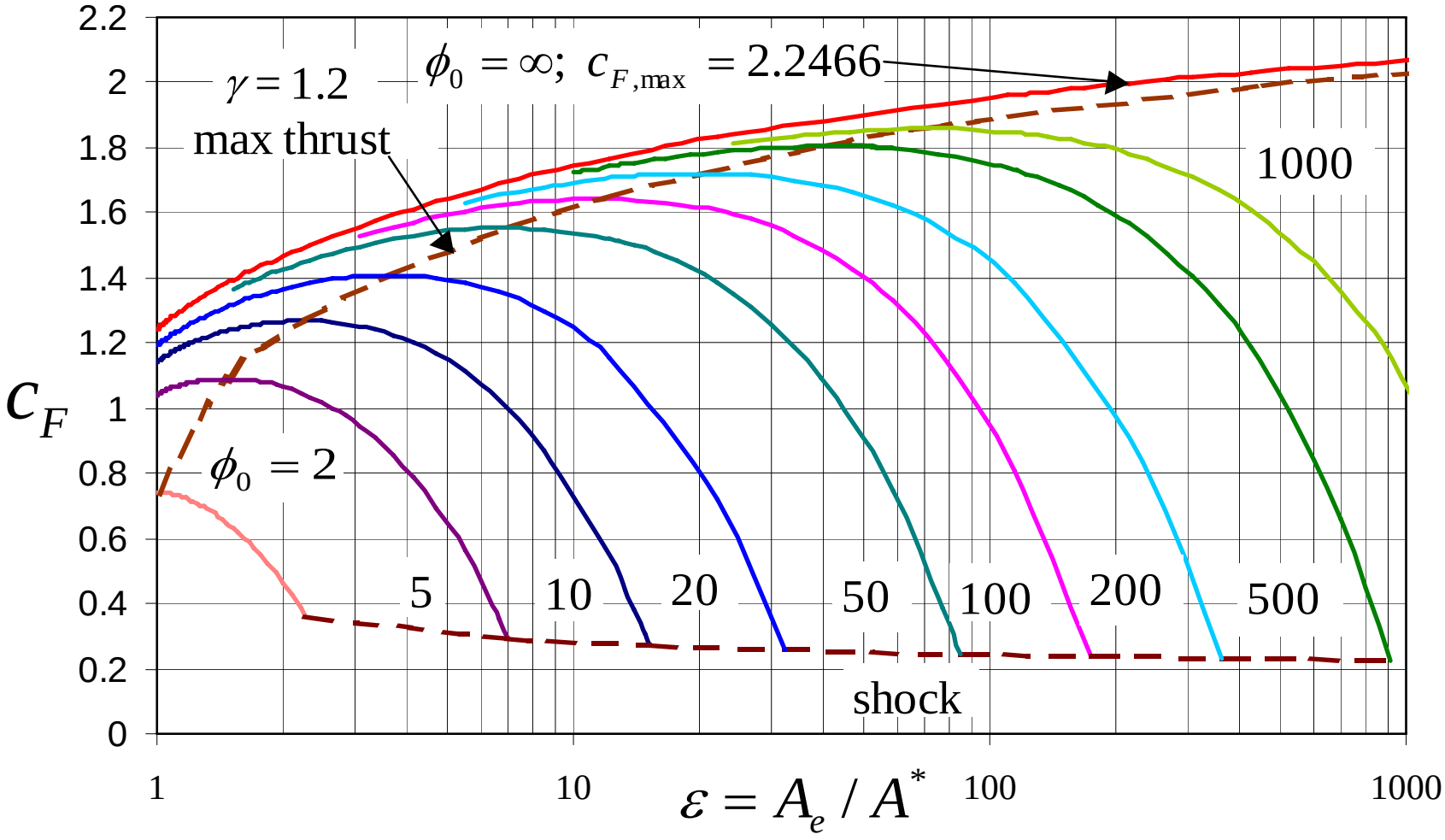
$\gamma = 1.2$
max thrust
$\phi_0 = \infty;\ c_{F,\max} = 2.2466$
1000
$\phi_0 = 2$
5
10
20
50
100
200
500
shock
c_F
$\varepsilon = A_e / A^*$
2.2
2
1.8
1.6
1.4
1.2
1
0.8
0.6
0.4
0.2
0
1
10
100
1000

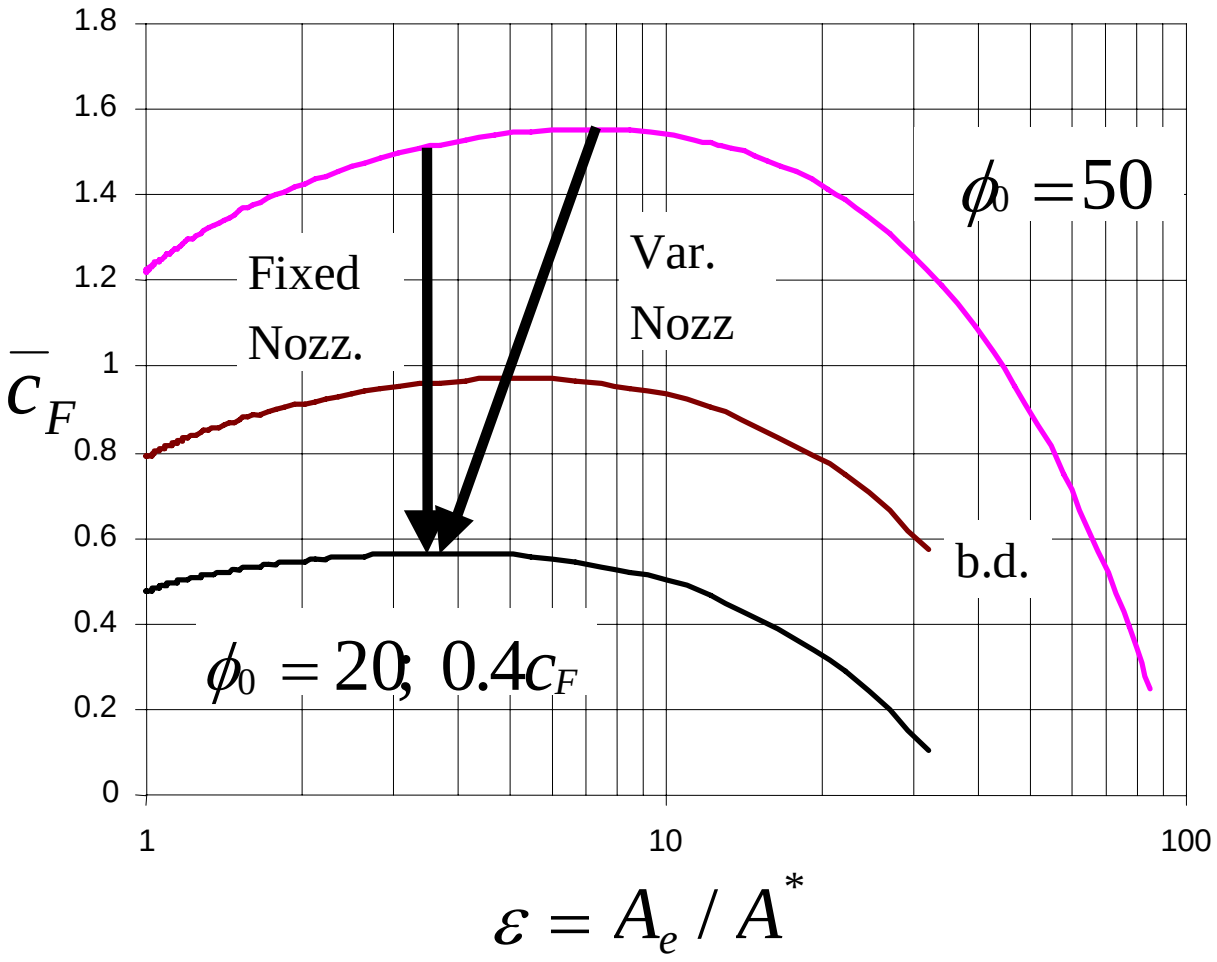
1.8
1.6
1.4
1.2
1
0.8
0.6
0.4
0.2
0
1
10
100
$\overline{C}_F$
$\varepsilon = A_e / A^*$
$\phi_0 = 50$
Fixed
Nozz.
Var.
Nozz
b.d.
$\phi_0 = 20;\ 0.4c_F$

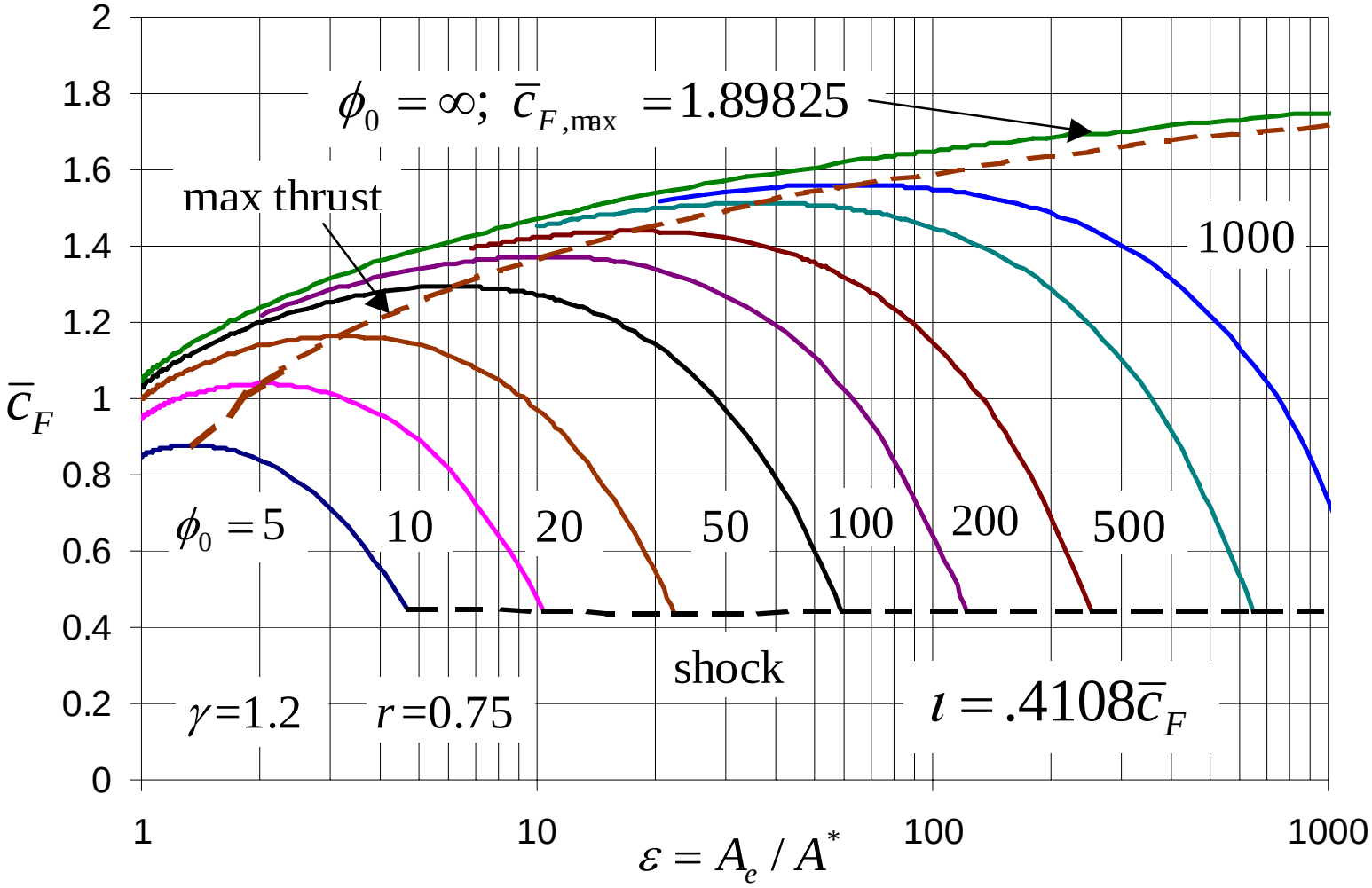
$\phi_0 = \infty;\ \bar{c}_{F,\max} = 1.89825$
max thrust
1000
$\phi_0 = 5$
10
20
50
100
200
500
shock
γ=1.2
r=0.75
$\iota = .4108\bar{c}_F$
$\bar{c}_F$
$\varepsilon = A_e / A^*$
2
1.8
1.6
1.4
1.2
1
0.8
0.6
0.4
0.2
0
1
10
100
1000

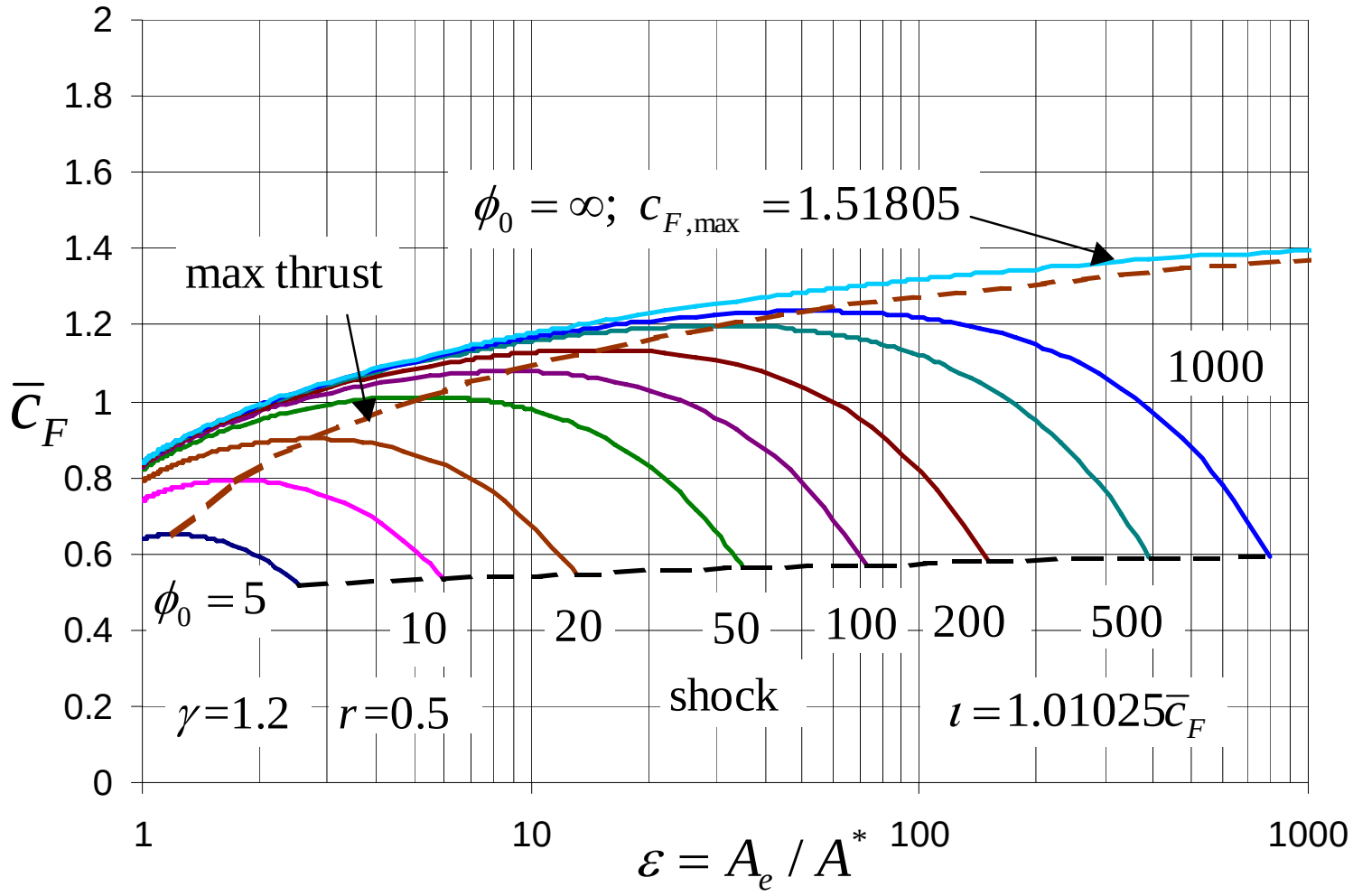
$\phi_0 = \infty;\ c_{F,\max} = 1.51805$
max thrust
1000
$\phi_0 = 5$
10
20
50
100
200
500
γ=1.2
r=0.5
shock
$\iota = 1.01025\bar{c}_F$
$\bar{C}_F$
$\varepsilon = A_e / A^*$
2
1.8
1.6
1.4
1.2
1
0.8
0.6
0.4
0.2
0
1
10
100
1000

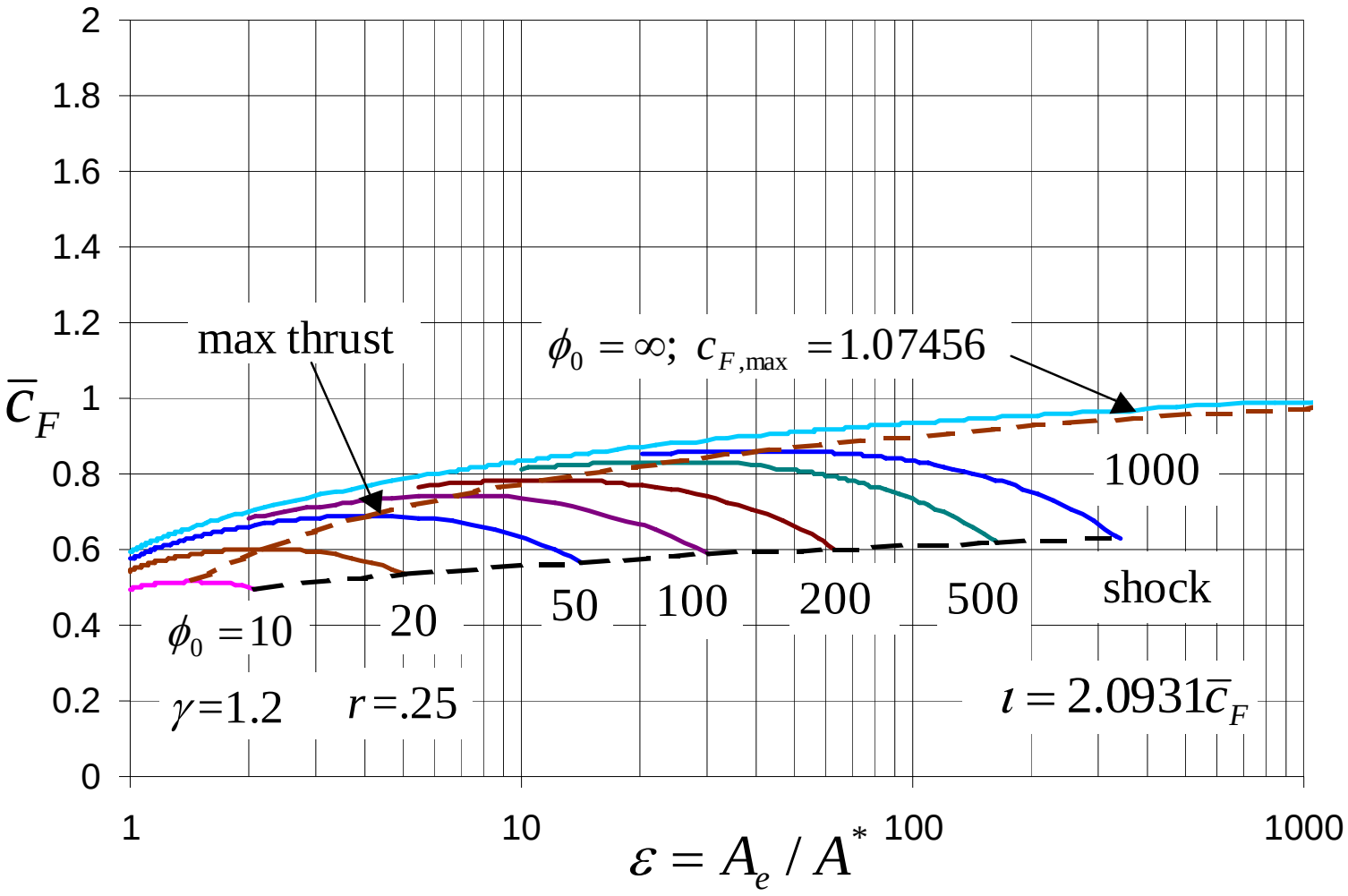
2
1.8
1.6
1.4
1.2
1
0.8
0.6
0.4
0.2
0
$\overline{C}_F$
max thrust
$\phi_0 = \infty;\ c_{F,\max} = 1.07456$
1000
shock
500
200
100
50
20
$\phi_0 = 10$
γ=1.2
r=.25
$\iota = 2.0931\overline{c}_F$
1
10
100
1000
$\varepsilon = A_e / A^*$

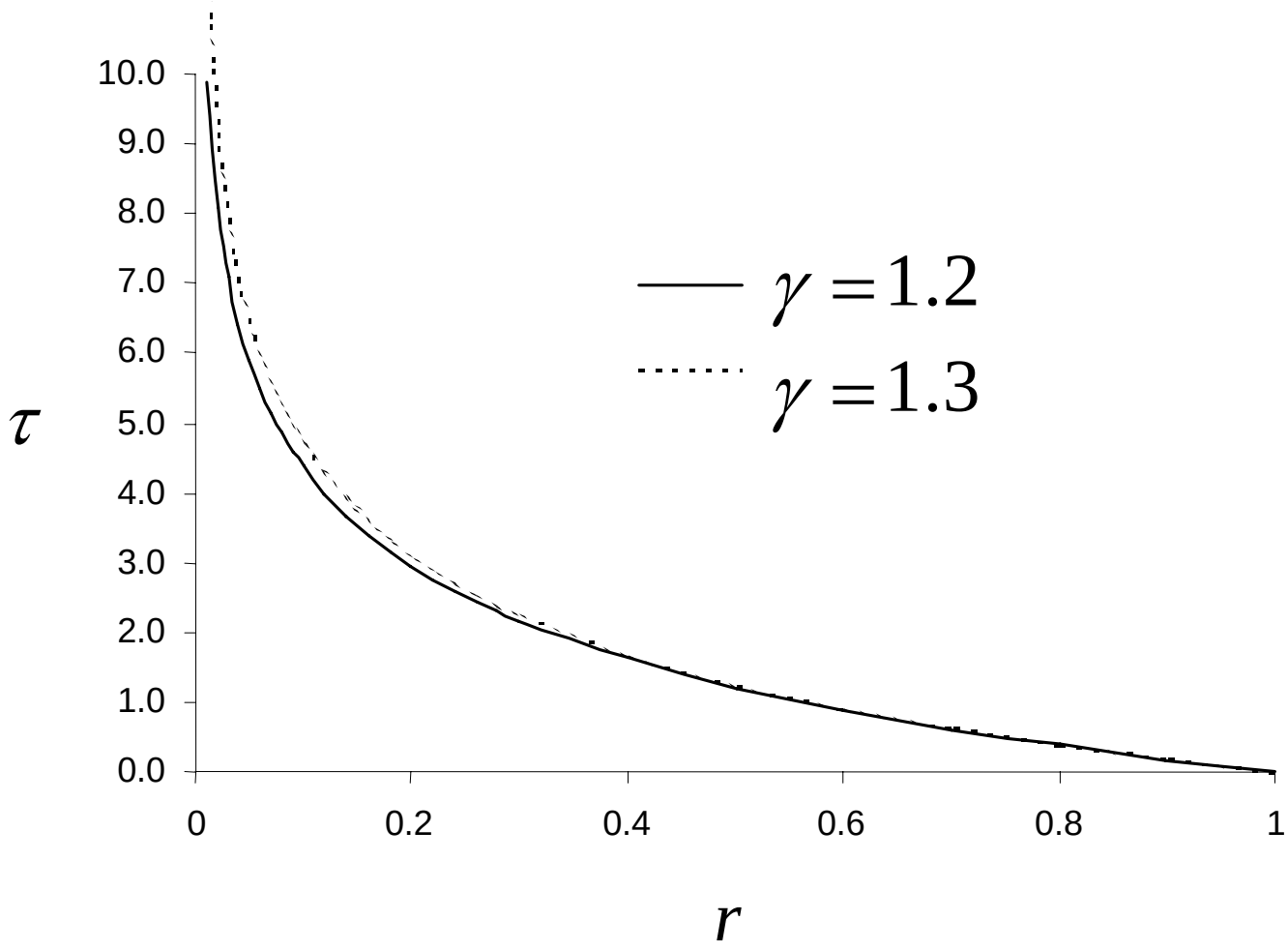
10.0
9.0
8.0
7.0
6.0
5.0
4.0
3.0
2.0
1.0
0.0
τ
0
0.2
0.4
0.6
0.8
1
r
γ =1.2
γ =1.3

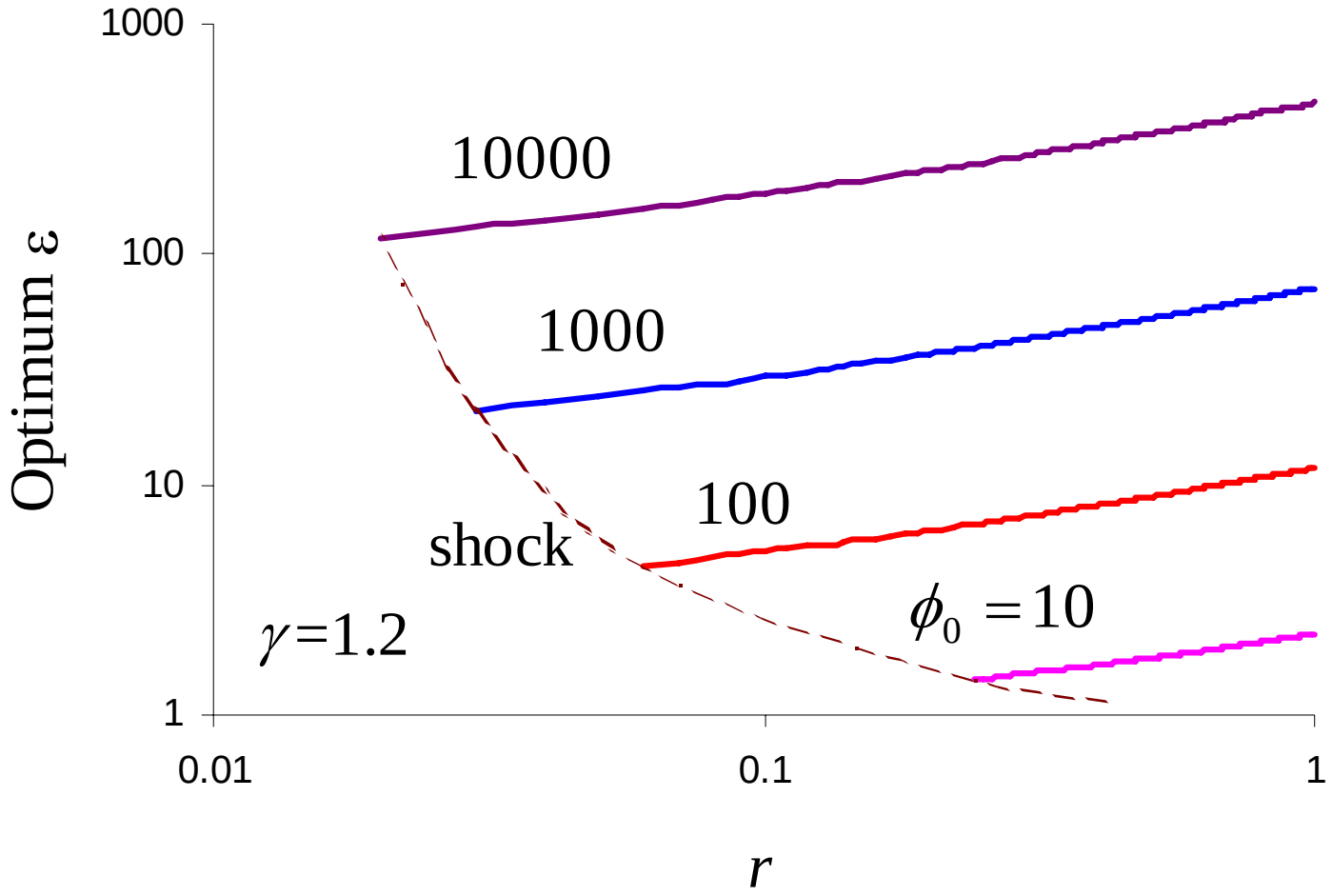
1000
100
10
1
Optimum ε
10000
1000
100
shock
γ=1.2
$\phi_0 = 10$
0.01
0.1
1
r

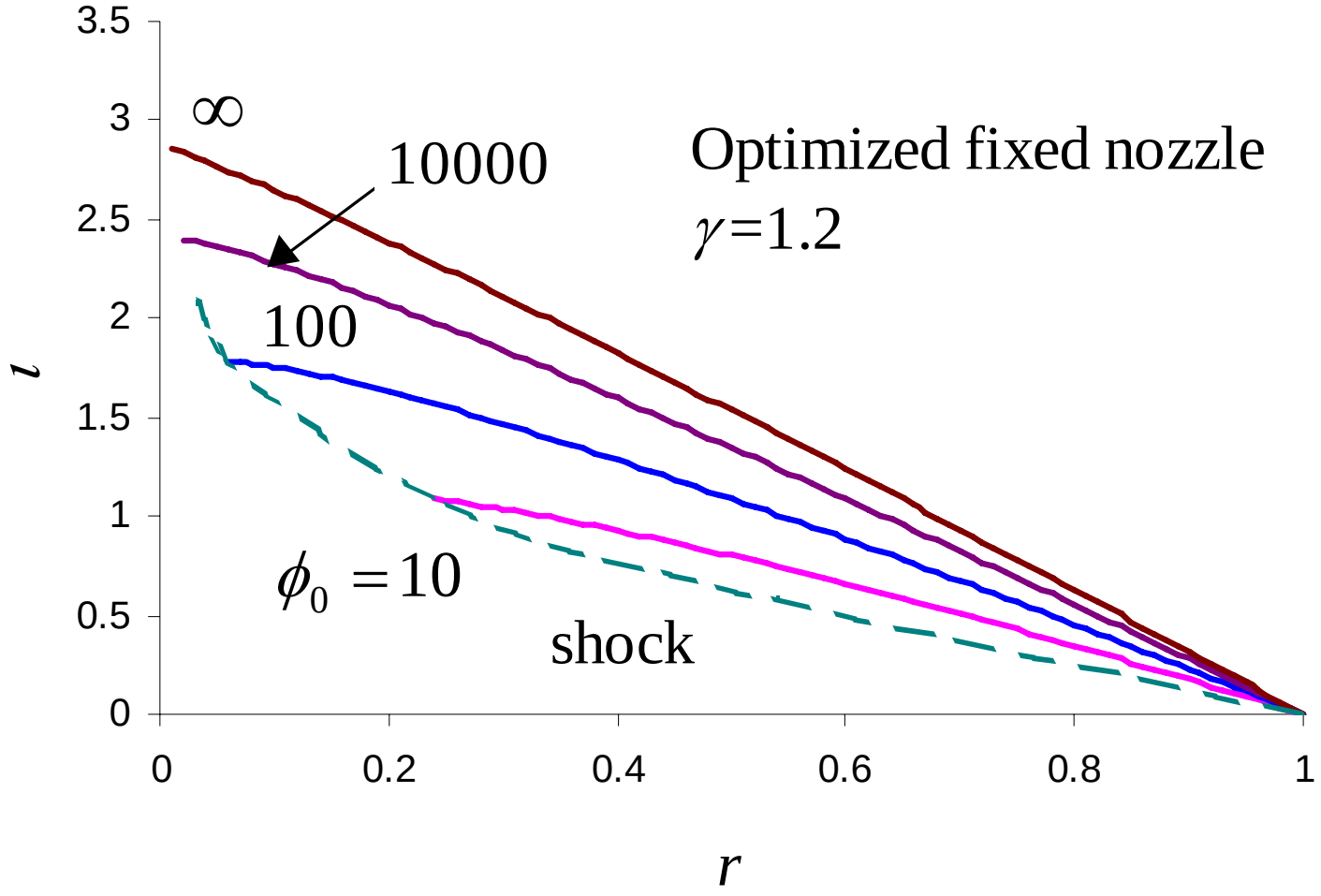
3.5
3
2.5
2
1.5
1
0.5
0
0
0.2
0.4
0.6
0.8
1
∞
10000
100
$\phi_0 = 10$
shock
Optimized fixed nozzle
γ=1.2
t
r

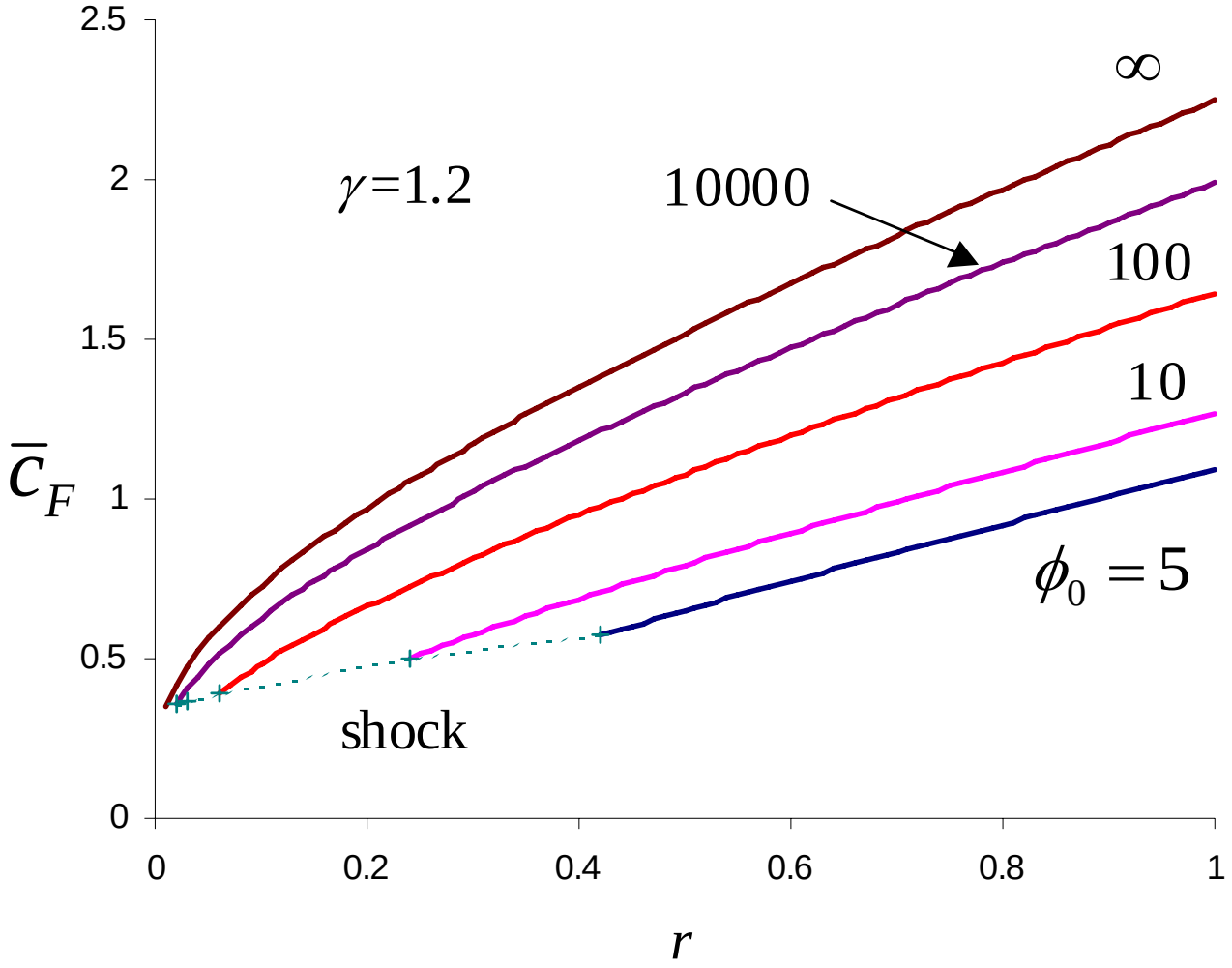
2.5
2
1.5
1
0.5
0
0
0.2
0.4
0.6
0.8
1
$\overline{C}_F$
r
γ=1.2
∞
10000
100
10
$\phi_0 = 5$
shock

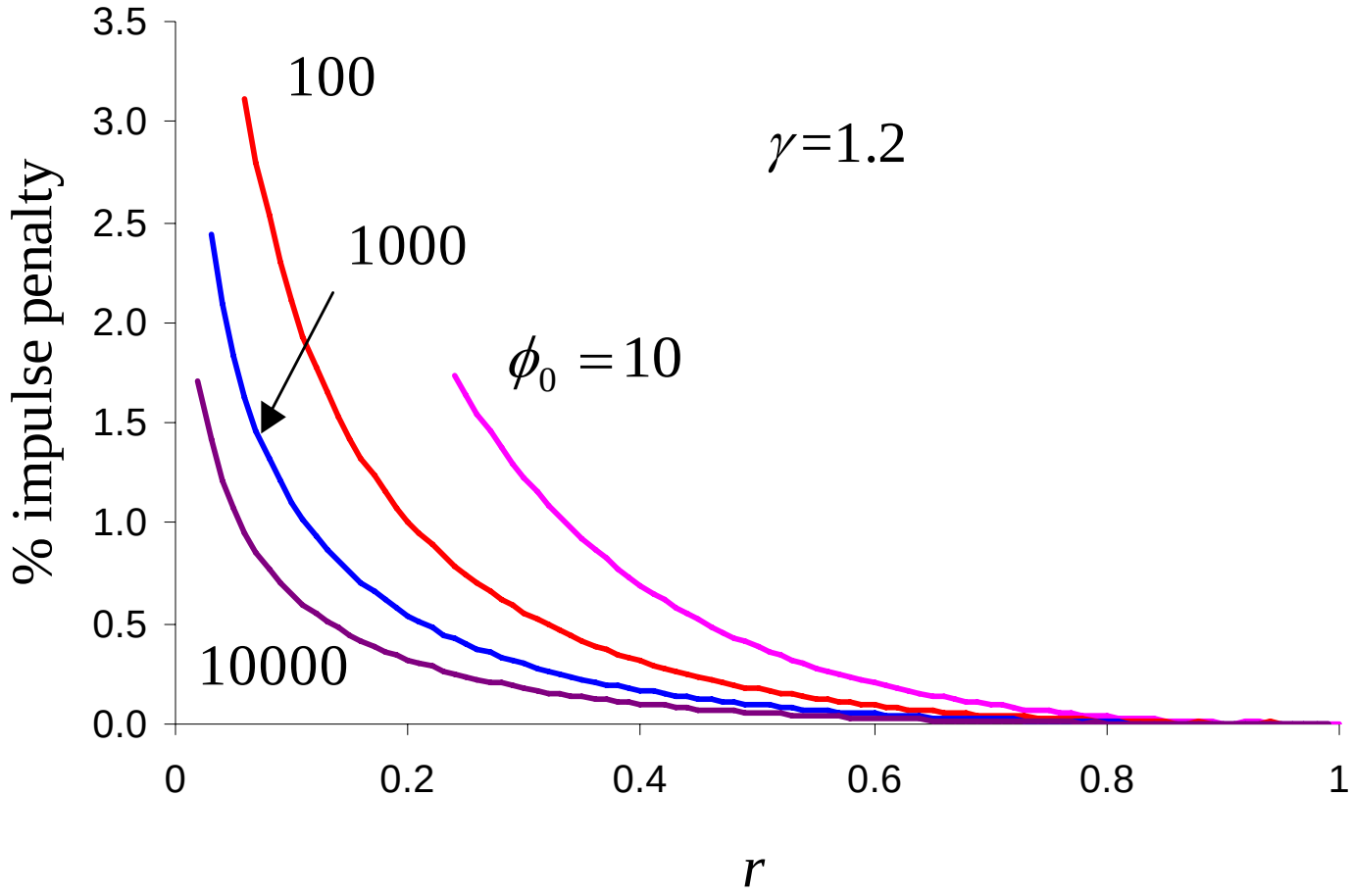
% impulse penalty
3.5
3.0
2.5
2.0
1.5
1.0
0.5
0.0
0
0.2
0.4
0.6
0.8
1
r
100
1000
10000
γ=1.2
φ0 =10

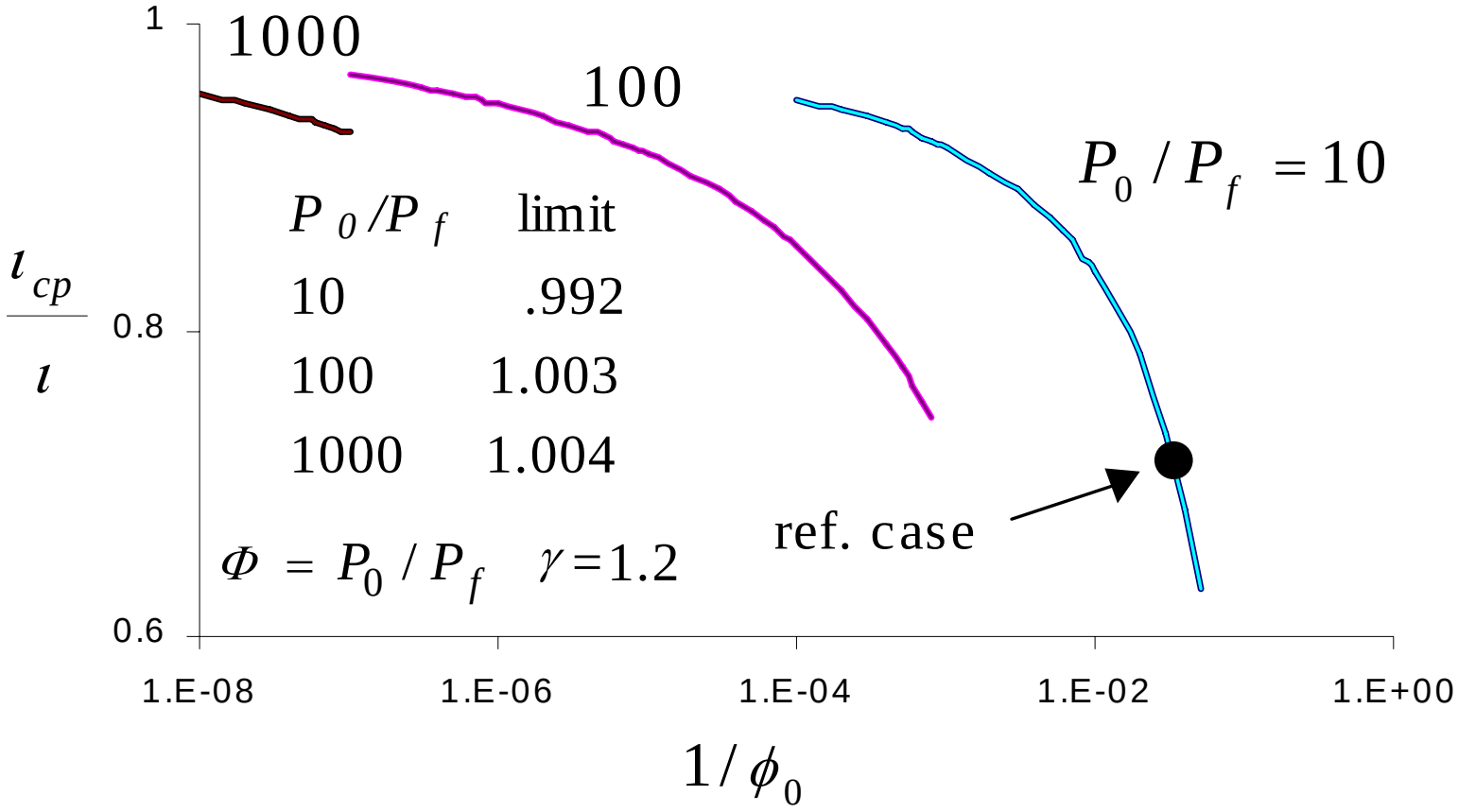
1
0.8
0.6
1000
100
$P_0 / P_f = 10$
P_0/P_f limit
10 .992
100 1.003
1000 1.004
$\Phi = P_0 / P_f \quad \gamma = 1.2$
ref. case
ι_{cp} / ι
1.E-08
1.E-06
1.E-04
1.E-02
1.E+00
$1/\phi_0$

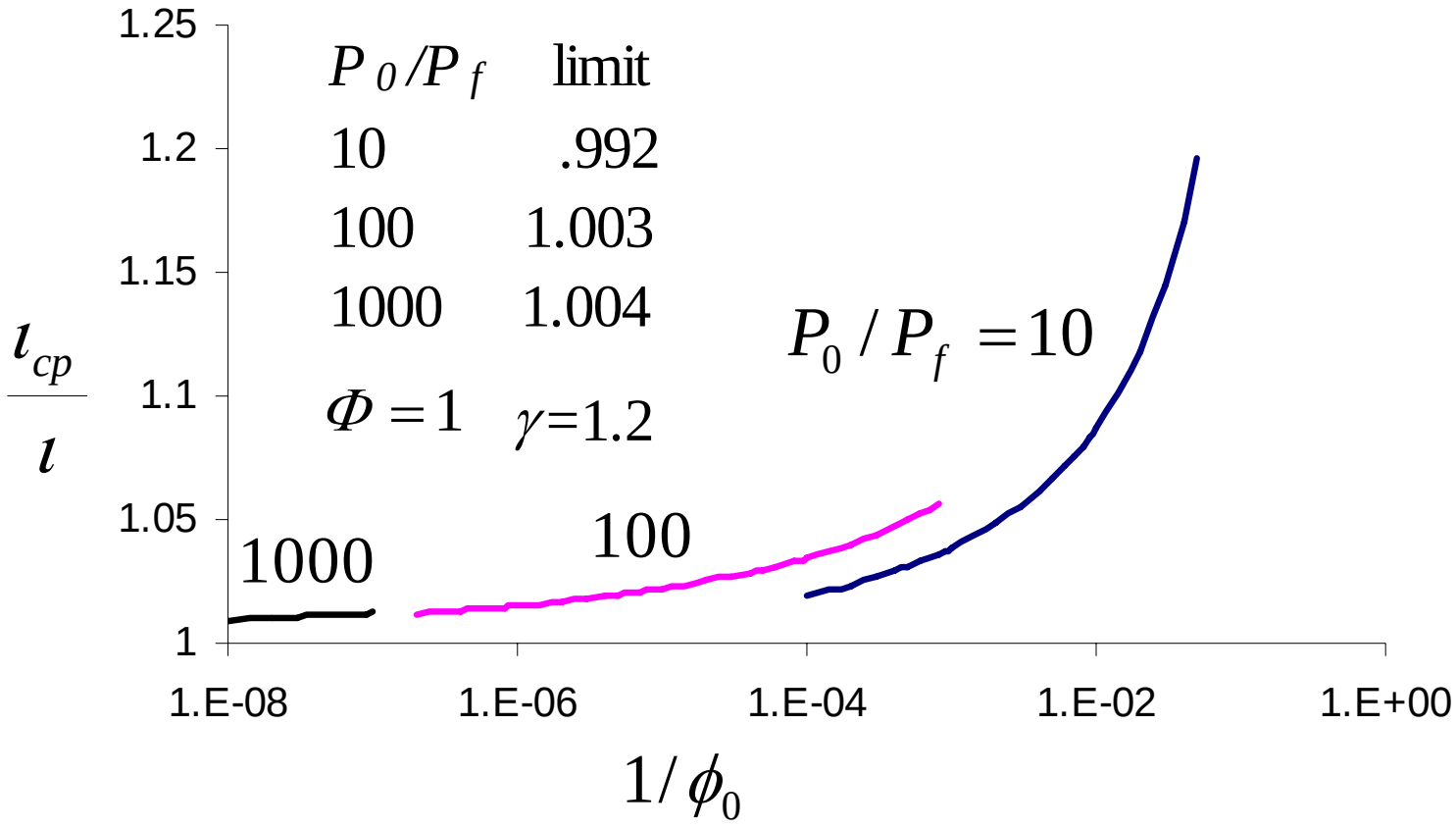
1.25
1.2
1.15
1.1
1.05
1
$\frac{l_{cp}}{l}$
P_0/P_f limit
10 .992
100 1.003
1000 1.004
$\Phi = 1$ γ=1.2
$P_0 / P_f = 10$
100
1000
1.E-08
1.E-06
1.E-04
1.E-02
1.E+00
$1/\phi_0$

APPENDIX S

"Cryogenic, Multiphase, Hydrogen-Oxygen Detonations"
(AIAA Paper 2005-1462)

43rd AIAA Aerospace Sciences Meeting and Exhibit
10 - 13 January 2005, Reno, Nevada

AIAA 2005-1462

Cryogenic, Multiphase, Hydrogen-Oxygen Detonations

Edward B. Coy* and Jonathan M. Watts†
Air Force Research Laboratory, Edwards AFB, CA 93524

Sampath Palaniswamy‡
Metacomp Technologies, Agoura Hills, CA

Detonations of flowing mixtures of hydrogen and oxygen at temperatures between 90 and 110 K, pressures from 3 to 5 bar, and mixture densities of 3-6 kg/m^3 have been studied. The effect of liquid oxygen on wave speeds and peak wall pressures are reported. Data taken at cryogenic conditions are compared with ambient temperature data taken at similar initial densities and equivalence ratios, as well as with equilibrium, Chapman-Jouget theory calculations. For the conditions studied, liquid oxygen was found to result in increased wave speeds and peak wall pressures. These observations are shown to be consistent with a highly stratified mixture with high concentrations of oxygen in a layer adjacent to the wall and low concentrations along the axis of the tube.

I. Introduction

THIS paper presents results from an investigation of detonations of flowing mixtures of cryogenic gaseous hydrogen and liquid oxygen. This work was undertaken to support development of pulse detonation rocket engines (PDRE). Cryogenic propellants will be desirable for PDRE applications for many of the same reasons that they are used for conventional rocket engines: the density is increased, which reduces tank volume, and cooling of the combustion chamber is facilitated. There is an additional advantage for PDREs insofar as a major advantage of the cycle is the reduced pumping requirements associated with the low injection pressures. High density enables a larger mass to be charged into the chamber for a given supply pressure. Hydrogen and oxygen were chosen for this study due to their high specific impulse, ease of detonability, and the existing experience with handling and design.

There is an extensive list of phenomena which could be significant in detonations of liquid oxygen and hydrogen. There are phenomena that affect the initial state of the mixture which include atomization, turbulent dispersion, vaporization, turbulent mixing, wall-wetting, and heat-transfer. Other phenomena affect the propagation of the detonation through the mixture which include droplet shattering, vaporization, chemical induction time, wall friction and heat transfer within the reaction zone, and longitudinal and axial variations in the mixture composition. There have not been any previous studies which characterized the propagation of detonations under all of these complex conditions. Studies which examined subsets of the problem are briefly reviewed here.

Previous studies of detonations of cryogenic, quiescent, gaseous mixtures of hydrogen and oxygen have found that measured wave velocities and pressures agree well with ideal-gas equilibrium Chapman-Jouget calculations up to initial pressures of approximately 5 atm and densities of 5 kg/m^3. [1,2,3] At higher pressures and densities the ideal-gas calculations under-predict wave speed and pressure, and a real-gas equation of state produces better agreement. This result was also obtained in a study of ambient temperature, high-pressure (up to 40 atm) quiescent, hydrogen-oxygen detonations.[4]

There are an extensive number of references on detonations in sprays. The vapor pressure of the fuel has a large influence on the propagation mechanisms of the detonation. For high vapor pressure liquids, a detonation can be supported in the gas-phase, and the liquid fraction is consumed in the products and does not contribute to the processes which drive the leading shock. For low vapor pressure liquids, the successful propagation of a detonation has been shown to depend on the rate at which droplets are decomposed into a "micromist" by the high velocity

* Propulsion Research Engineer, Aerophysics Branch, 10 East Saturn Blvd., Member AIAA
† Propulsion Research Engineer, Aerophysics Branch, 10 East Saturn Blvd.
‡ Senior Scientist, Metacomp Technologies, Member AIAA

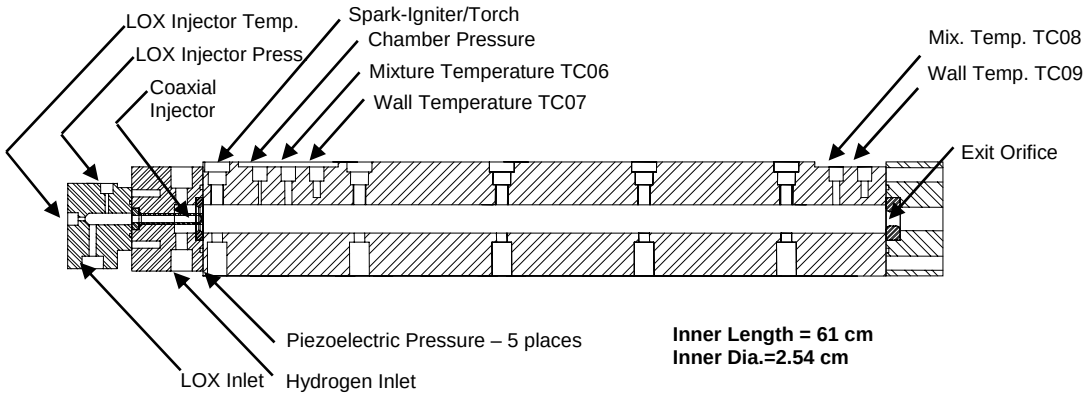

Figure 1. Cross-section view of test article showing locations of instrumentation. Orientation was vertical during tests.

flow following the leading shock wave[5]. Studies using 400-2600 micron droplets have shown that following a chemical induction time delay, the micromist explodes, sending shock waves forward to reinforce the leading shock, and rearward, as a retonation. The droplet shattering and evaporation processes are much slower than the gas-phase kinetics of the combustion reactions and result in much longer reaction zones than are typical of gas phase detonations. It has also been observed that a thin film of a low vapor-pressure liquid hydrocarbon deposited on the wall of a tube can support a combustion wave that propagates at nearly the CJ velocity[6]. In this case the high-velocity gas behind the leading shock creates a shear flow over the liquid that strips away small droplets. The droplets rapidly react, and the heat release sustains the process.

Due to their fundamentally different mode of propagation, low vapor pressure spray and film detonations do not in general match propagation velocities and pressures obtained from CJ thermodynamic equilibrium calculations. Wave velocities and pressures are typically reduced. For detonations in tubes the discrepancy has been attributed to heat transfer and wall friction in the extended reaction zone[5]. For detonations initiated directly by high explosive charges, the discrepancy has been attributed to the simultaneous decay of the initiating blast wave and increasing length of the reaction zone, implying that the reduced velocity is a transient phenomena and that the theoretical value would be reached in a sufficiently long apparatus.[7]

The purpose of this work was to experimentally investigate the behavior of detonating mixtures of liquid oxygen and cryogenic gaseous hydrogen under conditions expected to be relevant to pulse detonation rocket engines. The results are applicable to the development of the next generation of repetitively pulsed, multi-tube test articles and also are intended to be used to qualify computational models under development for use in system application studies.

II. Experimental Setup

The test article was a vertically oriented, 304 stainless steel tube, with 61 cm inner length and a 2.54 cm inner diameter and a design pressure of 70 MPa. The injector was a swirled co-axial design. Angular momentum was imparted to the liquid oxygen through an off-axis inlet port. Oxygen exited through the center post and hydrogen through the surrounding annulus. Visualization of the injector flow was performed using air and water as simulants in the AFRL/PRSA Flow Laboratory. Water matched the density and volumetric flow rate of liquid oxygen to within 5%. Atmospheric pressure air matched the density of hydrogen at the test conditions to within 10% and the volumetric flow rate within 5%. The liquid was well atomized with a maximum droplet size of approximately 100 micrometers. The injector produced a hollow-cone spray with a divergence angle of 30^0 resulting in the majority of the liquid being deposited on the walls of the tube during the experiments.

The fuel for the detonation tests was industrial grade hydrogen, 99.9% pure with methane as the principal impurity. The hydrogen was supplied from high-pressure cylinders and chilled to cryogenic temperatures in a shell-and-tube heat exchanger with saturated, 2.6 atm liquid nitrogen on the shell side. The hydrogen mass flow rate was measured using a sonic nozzle. The mass flow rate was calculated using an in-house developed program that solves the 1-D Euler equations for sonic orifice flow using real-gas properties. The discharge coefficient for the nozzle was provided by the manufacturer and was certified to be accurate within +/- 2%.

Industrial grade liquid oxygen, 99.5 % with nitrogen as the principal impurity, was supplied from a 200 liter dewar pressurized with helium. Volumetric flow rate was measured using a turbine meter, and the inlet state was measured with a thermocouple and pressure transducer to determine the density. The dewar was located on an electronic scale to enable the flow rate of liquid oxygen to be independently determined from the rate of change of mass of the dewar. This arrangement enabled the turbine meter to be calibrated in-situ with an accuracy of +/- 0.5%.

The extent of vaporization of liquid oxygen varied along the length of the test article due to heat transfer to the oxygen from the hydrogen and the tube wall. Two methods were used to estimate the extent of vaporization. The first assumed adiabatic mixing of the streams of hydrogen and oxygen at the inlet enthalpies and is listed in the data tables below as the initial gaseous oxygen fraction. The second assumed that liquid and gas phases reached thermal equilibrium at the measured exit temperature. This assumption was supported by typical data for mixture temperature as shown in figure 2. Prior to 115 seconds both thermocouples were exposed to saturated oxygen at a pressure of 1.5 atm. At 115 seconds the hydrogen flow was initiated and a two-phase mixture of hydrogen and liquid oxygen began impinging on TC06 causing large fluctuations in temperature. The temperature trended downward as the flow from the heat exchanger cooled the system components and the hydrogen inlet temperature decreased. Near the exit at TC08 the hydrogen and oxygen had reached thermal equilibrium as evidenced by the lack of fluctuations. Based on the measured temperature at TC08 the vapor pressure of gaseous oxygen was determined from the saturation curve and this was used to determine the mass fraction of oxygen in the gas phase. For the case shown, the mass fraction of oxygen in the gas phase was 0.76 +/- .08. In several cases the temperature fluctuations at TC08 indicated that thermal equilibrium had not been reached. For those cases the reported value of oxygen mass fraction was based on the average temperature, and the uncertainty was based on the magnitude of the temperature fluctuations. To complete the discussion of the figure, at 120 seconds the mixture was ignited and both thermocouples went off-scale.

All thermocouples were checked for accuracy in a liquid nitrogen bath prior to installation. In addition, during each test the interval when saturated oxygen was present enabled routine checks to be performed. To prevent the thermocouples exposed to the detonation products from melting, the beads were blanketed with a flow of nitrogen that was initiated coincident with the ignition.

Five piezoelectric transducers (Kistler 603B1) were mounted flush with the inner surface of the tube at 12.7 cm intervals. The signals were recorded at 1 MHz and 12 bit resolution for a precision of 24 KPa. Each transducer, associated range capacitor (Kistler 571A3), impedance-converter (Kistler 558), and cables were calibrated as a set by the manufacturer and certified to be linear to less than +/- 1% of full scale. The calibrations were performed at 295 K over the range 0-69 MPa. The manufacturer's literature listed a nominal value for the temperature coefficient of sensitivity of -0.027 %/K. For the cryogenic tests this amounted to -5.5%; however, because a calibration was not performed at the operating temperature, we have estimated the uncertainty at +/- 10%. The response of the piezoelectric transducers was checked in our laboratory under shock tube and gaseous detonation conditions. For the shock tests, a driver tube and burst disc were installed in place of the injector, and the exit orifice was replaced with a blank. The measured wave speed was used to predict pressure behind the incident and reflected shocks using a thermodynamic equilibrium model. The predicted values agreed within 10% with the measurements. The gaseous detonation tests were performed with flowing mixtures. The flow rates were set to produce an initial density and equivalence ratio representative of the target conditions for the cryogenic tests. The measured peak pressures and wave speeds are shown in figures 3 and 4 for a test with an initial mixture density of 3.6 +/- .1 Kg/m^3 and an equivalence ratio of 1.5 +/- .1. The pressure signals were not filtered. The trends in pressure and velocity are consistent with an initially over-driven detonation relaxing to a steady state. Also given are equilibrium Chapman-Jouget calculations obtained using the Cheetah code[8] with 10 product species. The calculations were performed using ideal-gas and JCZ3 equations of state. The results differed by about 1% in both pressure and velocity with slightly better agreement obtained with JCZ3. These results are

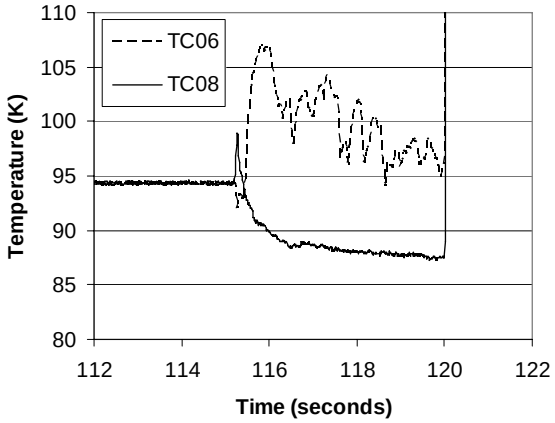

Figure 2. Mixture temperatures at inlet (TC06) and exit (TC08). Prior to 115 s saturated oxygen is flowing. At 115 s hydrogen flow is started. At 120 s ignition occurs. Liquid and gas have reached thermal

included here to indicate the level of agreement with CJ theory that was obtained for ambient-temperature, gaseous detonations and will be compared with results presented below for cryogenic, liquid-gas detonations.

The spark ignition system was a conventional automotive system, and produced approximately 110 millijoules per spark. The spark plug was a surface gap, Champion G52V. When the spark plug was cooled below approximately 100 K it would not discharge, so it could not be located in the wall of the test article. An ignition chamber with a volume of approximately 15 cm^3 was added that could be maintained above 100 K with heating tape. Prior to ignition the chamber was charged from the hydrogen-oxygen mixture flowing in the test article, and at ignition it injected a flame jet into the test article through a 5 mm orifice. The ignition chamber could be located near the injector at the position shown in figure 1 or in the exhaust tube downstream of the exit orifice. The detonation velocities given in the figures are averages over the 12.7 cm intervals between transducers and were based on the time the pressure signals had risen to at least half of their peak value. The manufacturer's literature specifies that the Kistler 603B1 transducers have a rise time from 10-90% of 1 μs. The signals were also digitized at 1 μs intervals. Assuming the timing of the wave arrival could be in error by one microsecond, the uncertainty of wave speed ranged from +/- 65-110 m/s.

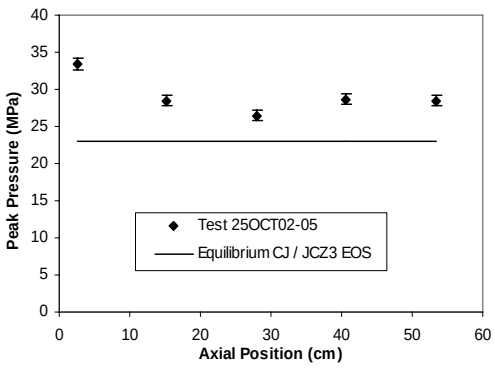

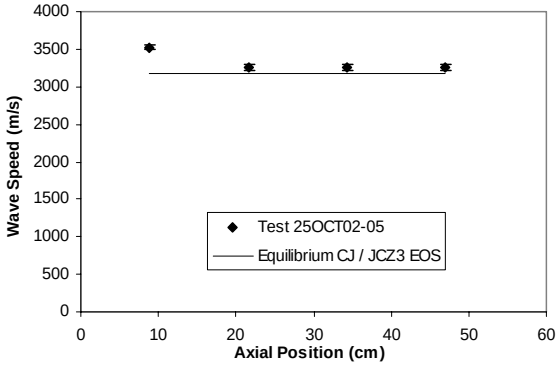

Figures 3 and 4. Peak wall pressures and wave velocities from an ambient temperature detonation of a flowing mixture of hydrogen and oxygen. Equilibrium CJ calculations were performed using the Cheetah code and the JCZ3, real-gas, equation of state. Level of agreement between measurements and theory can be compared with results for cryogenic mixtures.

A. Experimental Methodology

Prior to a firing, the liquid oxygen dewar was vented to atmosphere and the oxygen was allowed to boil until it reached a saturated state. The propellant systems and test article were cooled with liquid nitrogen. When temperatures reached 100 K, the liquid oxygen dewar was pressurized with helium, and the systems were flushed and filled with propellants. The automated firing sequence began by flowing liquid oxygen until the fluid was sub-cooled by approximately 20 K at the injector. This typically required 60-120 seconds. The hydrogen flow began approximately 5 seconds before ignition. At 100 milliseconds prior to ignition, the test article and injector pressure transducers were isolated to prevent over-ranging. At the time of ignition, liquid oxygen temperatures at the injector were in the range of 95-115 K, hydrogen inlet temperatures were 100-120 K and wall temperatures were 110-120 K. Pressure in the test article was 2.7-4.4 atm. The spark system was fired, and a warm nitrogen purge flow was initiated to flush combustion products and minimize ice formation in the tube. Several series of tests were performed at fixed flow rates of hydrogen and varying flow rates of oxygen. At low oxygen flow rates the liquid was entirely vaporized, and at higher flow rates an increasing fraction remained a liquid.

III. Results

The initial conditions for two representative tests at high equivalence ratio are given in table 1. Both tests had liquid oxygen present at the injector and were fully vaporized at the exit condition. In test 12FEB04-17 the mixture was ignited in the exhaust tube and the detonation propagated towards the injector. In test 18FEB04-03 the ignition was at the injector and the detonation propagated towards the exit orifice. Wave speeds and peak wall pressures are shown in figures 5 and 6. The arrows indicate the direction of propagation. The measured wave speeds agree

within 5% with the equilibrium code predictions except near the injector, where the measured velocity is significantly lower. The level of agreement away from the injector is similar to that obtained in the ambient temperature detonations at similar densities. The measured peak pressures are a factor of two or more higher than the equilibrium code predictions. This is a larger deviation than was observed in the ambient temperature detonations and is believed to be significant. The changes in pressure along the tube do not appear to be correlated with changes in wave speed. There also is no observable effect on pressures or wave speeds due to the ignition location.

Table 2 gives the initial conditions for two representative tests at near-stoichiometric equivalence ratio. The initial gaseous oxygen fractions are significantly lower than those in the high equivalence ratio tests due to the higher flow rate of liquid oxygen. The exit flow is predicted to be fully vaporized in both cases; however, inspection of the exit temperature time traces showed there were fluctuations indicating full thermal equilibrium had not been reached. Both tests exhibit wave speeds approximately 20% greater than the equilibrium code predictions, however, there were also cases where the wave speed nearly matched the equilibrium value or fell a few percent below. The high velocity cases are particularly noteworthy, because deviations of this magnitude have not been reported previously for cryogenic or spray detonations. The peak pressures are approximately a factor of two greater than the equilibrium code, and the fluctuations in pressure do not appear to be correlated to changes in wave speed. The ignition location did not have an observable effect.

A summary of the wave speed results plotted as a function of equivalence ratio is given in figure 13. The average velocity over the 50.8 cm interval between the first and last transducers is shown. The equilibrium CJ calculations were performed assuming a nominal initial density of 4 kg/m^3 as wave speed is a weak function of the initial density. The CJ calculation stands as a lower bound on the data. This is a noteworthy result, as other studies of detonations in sprays have found that the equilibrium CJ velocity is an upper bound and only reached in the limit of very small droplets or high vapor pressure fuels. The data were examined to determine if wave speed was correlated with any other parameter such as the extent of vaporization of the oxygen, the density of the mixture, the direction of propagation, the peak pressure of the wave, the initial wall temperature, and the date of the test. The wave speed did not correlate with any of these variables.

A summary of the peak pressure data is given in figure 14. Pressure is a strong function of the initial density as well as the equivalence ratio, so the measured pressures were normalized by the equilibrium CJ values calculated for each test condition. The average value and the standard deviation for each measurement location are shown. The deviations of the averages from the CJ values are statistically significant for all except the first transducer and are greater than the +/- 10 % uncertainty that was assigned to the pressure measurement. The high peak wall pressures must therefore be a feature of the test conditions.

In addition to the average deviations from the CJ values, peak pressures also exhibited large changes within a given test. The average value of the coefficient of variation for the five measurements of peak pressure within each test was 29%. The COV for the variation from test to test ranged from 57% for the first transducer to 20% for the fourth. These measures are comparable in magnitude and greater than the uncertainty in the pressure measurement; therefore, large fluctuations in peak wall pressures as well as random deviations from the CJ value are features of the test conditions.

IV. Discussion

Detonations of cryogenic mixtures of gaseous-hydrogen and liquid-oxygen were found to be characterized by higher than CJ propagation velocities as well as high average and fluctuating wall pressures. These results differ from those obtained by other researchers for cryogenic gaseous-hydrogen gaseous-oxygen mixtures and ambient temperature spray detonations as discussed previously. Explanations for the new findings were sought in the fact that the apparatus used in this study was designed to represent conditions that are expected to be significant to the design of a PDRE; i.e., relative to previous studies, the tube was short and the mixtures were flowing and non-uniform.

B. Transient Effects

Scientific detonation studies are usually performed in tubes several meters long to ensure that steady state conditions have been reached at the measurement location. The distance required depends on the method of initiation and the initial density, but generally a detonation passes through an over-driven condition before relaxing to a steady velocity[4]. While in the over-driven state the detonation propagates at a higher velocity and has higher peak pressure than CJ values. Thus a transient effect appears to be a plausible explanation for the observations.

Table 1. Initial conditions for two tests with cryogenic mixtures at high equivalence ratio. Tests represent injector-end and exit-end ignition locations. The liquid oxygen was vaporized at the exit of the tube.

	12FEB04-17	+/-	18FEB04-03	+/-
Equivalence ratio, Φ	2.44	0.15	2.07	0.13
LOX injector temp. TC04 (K)	120.9	0.6	119.8	0.6
Hydrogen inlet temp. TC10 (K)	122.9	0.6	106.6	0.6
Upper wall temp. TC07 (K)	112.9	1.1	107.4	1.1
Lower wall temp. TC09 (K)	118.6	1.1	107.8	1.1
Exit mixture temp. TC08 (K)	105.3	0.56	90.7	0.56
Initial tube press. PT06 (Pa)	430711	8623	360576	8623
Mixture density (Kg/m3)	3.52	0.28	3.77	0.32
Initial gaseous O2 fraction	0.88	0.04	0.60	0.02
Exit gaseous O2 fraction	1.00	0.00	1.00	0.00
Mixture average velocity (m/s)	33.7	3.1	30.1	3.0
Ignition location	Exit		Injector	
Theoretical CJ velocity (m/s)	3727		3619	
Theoretical CJ pressure (MPa)	22.3		19.91	

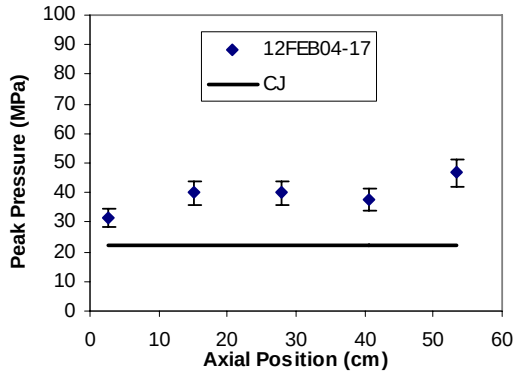

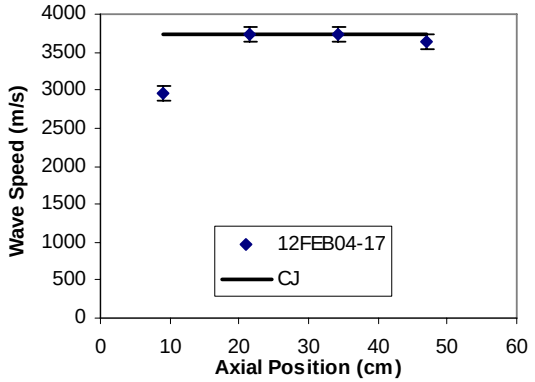

Figures 5 and 6. Data for high equivalence ratio cryogenic detonation ignited at exit of tube. Oxygen was partially vaporized near injector and fully vaporized at exit. Detonation propagates at near CJ velocity and with wall pressures relative to CJ similar to those obtained in ambient temperature test.

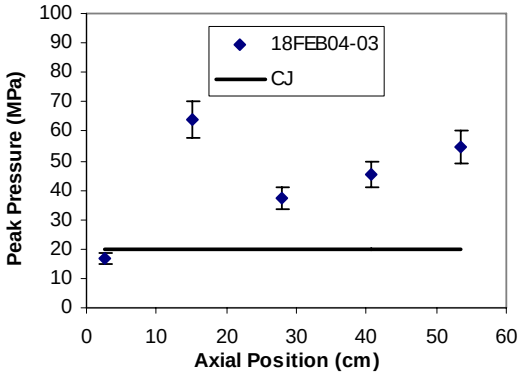

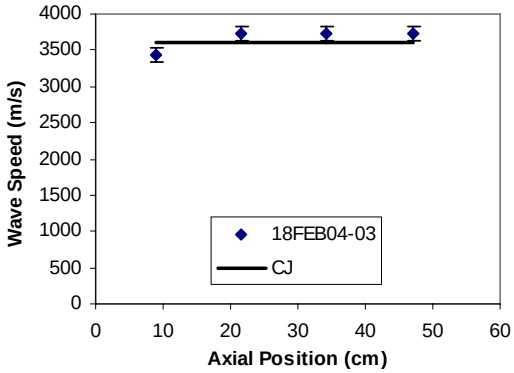

Figures 7 and 8. Data for high equivalence ratio cryogenic detonation ignited near injector. A higher fraction of oxygen was in a liquid state than the previous test (12FEB04-17). The oxygen was fully vaporized at the exit. Wall pressures are significantly higher than CJ and wave velocities slightly higher relative to results obtained for ambient temperature test.

Table 2. Initial conditions for two tests with cryogenic mixtures at near-unity equivalence ratio. Tests represent injector-end and exit-end ignition locations.

	12FEB04-09	+/-	20FEB04-09	+/-
Equivalence ratio, Φ	1.15	0.05	1.18	0.05
LOX injector temp. TC04 (K)	105.6	0.6	101.7	0.6
Hydrogen inlet temp. TC10 (K)	117.9	0.6	111.3	0.6
Upper wall temp. TC07 (K)	112.4	1.1	106.0	1.1
Lower wall temp. TC09 (K)	113.6	1.1	105.6	1.1
Exit mixture temp. TC08 (K)	107.4	0.6	102.3	0.6
Initial tube press. PT06 (Pa)	409959	8623	430200	3446
Mixture density (Kg/m3)	5.12	0.31	5.56	0.30
Initial gaseous O2 fraction	0.40	0.01	0.34	0.01
Exit gaseous O2 fraction	1.00	0.00	1.00	0.00
Mixture average velocity (m/s)	33.5	2.4	34.0	2.1
Ignition location	Exit		Injector	
Theoretical CJ velocity (m/s)	3152		3208	
Theoretical CJ pressure (MPa)	23.7		27.08	

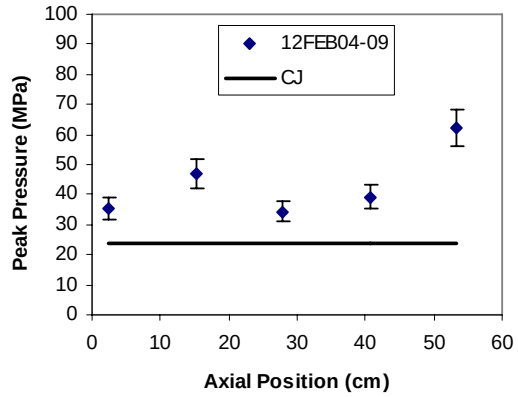

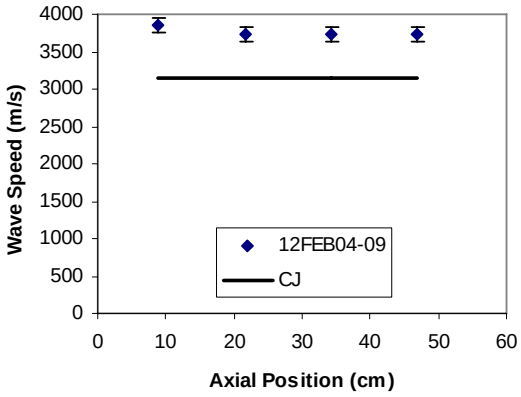

Figures 9 and 10. Data for low equivalence ratio cryogenic detonation ignited at the exit. Oxygen was estimated to be 66% liquid after injection and nearly vaporized at the exit. Both wall pressures and wave speeds are significantly greater relative to CJ than results obtained in ambient temperature test.

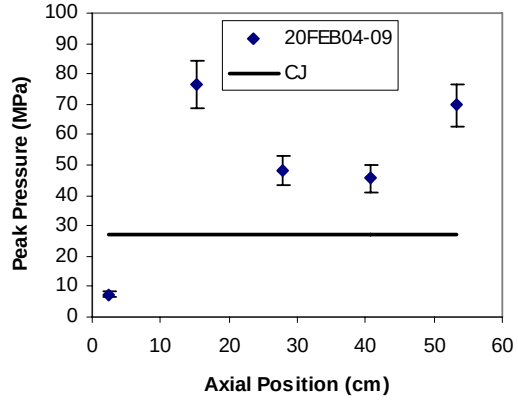

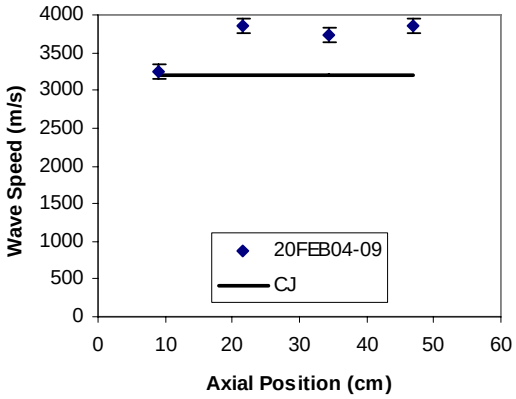

Figures 11 and 12. Data for low equivalence ratio cryogenic detonation ignited near the injector. Oxygen was estimated to be 66% liquid after injection and nearly vaporized at the exit. Both wall pressures and wave speeds are significantly greater relative to CJ than results obtained in ambient temperature test. Wall pressures exhibit large fluctuations.

Previous studies of cryogenic and high pressure hydrogen-oxygen detonations did not report the minimum distance required to reach steady conditions; however in one study[3], reasonably good agreement with the CJ state was obtained in less than 10 cm. In addition, data obtained in this study includes instances where the detonation accelerated after the wave was fully formed. There were also instances where the wall pressure decreased at the same time the velocity increased. These observations were not consistent with the hypothesis that the detonations were over-driven due to an initiation transient.

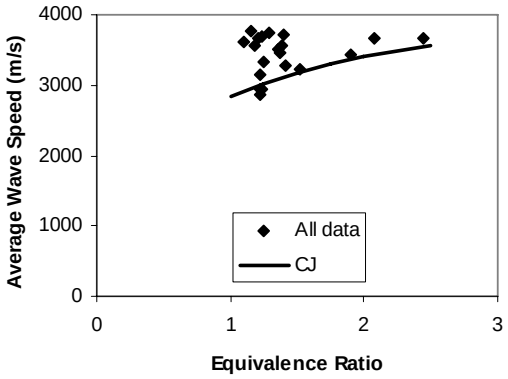

Figure 13. All wave speed results plotted as a function of equivalence ratio. CJ theory represents a lower bound on the data.

C. Non-uniform Mixtures

The mixtures in the tube were non-uniform in the axial direction due to vaporization and heat addition from the tube, and also in the radial direction because the hollow-cone spray directed liquid oxygen onto the wall. Due to the large density difference between the oxygen-rich wall layer and the hydrogen, the radial stratification likely persisted for many diameters downstream of the injector. This may have created a situation similar to that reported for solid explosives with gas-filled longitudinal channels[9]. In those systems, the explosion products act as a piston on the gas, driving a powerful shock down the channel, which in turn initiates or accelerates the reaction in the solid. Detonations have been observed to propagate at 1.5-2 times the velocity of the solid charge alone. There has been some previous work on layered detonations in gaseous systems; however, high-speed detonations have not been reported. Dabora[10] et al. found that surrounding a gaseous detonation with a layer of inert gas in fact causes a velocity decrement that depends on the density ratio of the reactive gas to the inert, and the width of the reactive layer. When hydrogen or helium was used in the inert layer, the reaction zone was observed to propagate at 50% of the CJ velocity. The studies of layered mixtures of Liu[11] and Jones[12] also did not report higher than CJ velocities and pressures, apparently because these studies focused on diffraction phenomena during the initial formation of the detonation in the surrounding layer.

D. Numerical Simulations

Numerical simulations were performed to test the layered detonation hypothesis using CFD++, a commercially available code from Metacomp Technologies for compressible reacting flows. Only the overall features of the flow were of interest, so the simulations were performed with a mesh size set at approximately 10 times the estimated detonation cell size, or 0.41 mm in the axial direction and 0.67 mm in the radial. Hydrogen-oxygen chemistry was modeled using a 9 species, 18 reactions mechanism. An inviscid Euler equation set was solved using a scheme second order accurate in global time step.

For the layered detonation simulation, half of the cross-sectional area adjacent to the wall was filled with a stoichiometric mixture of hydrogen and oxygen, and the other half along the centerline was filled with hydrogen. A second simulation was performed as a control where the same amounts of reactants were distributed uniformly across the tube for an equivalence ratio of 2.5. In both cases the initial pressure was 1 atmosphere and the temperature was 100 K. The detonations were initiated by a 2.5 cm

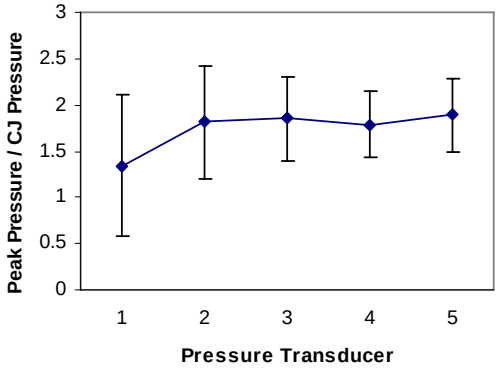

Figure 14. Peak wall pressures average nearly a factor of two greater than CJ theory. Large fluctuations are typical.

layer adjacent to the closed end of the tube that was initialized at 10 atm and 1800 K.

Results for wave speed and peak wall pressure as a function of axial distance along the tube are given in figure 15. The detonation in the layered mixture initially propagates at the CJ velocity of the stoichiometric layer but then accelerates from 2800 m/s to 5300 m/s, while the detonation in the uniform mixture propagates at a steady velocity of 3500 m/s. The peak wall pressure of the layered detonation is initially at the CJ detonation pressure of the stoichiometric layer but then increases to a maximum of three times that of the homogeneous mixture and then decreases to a steady value approximately 2.5 times the homogeneous. In summary, the calculations exhibit the same qualitative characteristics observed in the experiments: high velocities and peak wall pressures and large changes in velocities and pressures.

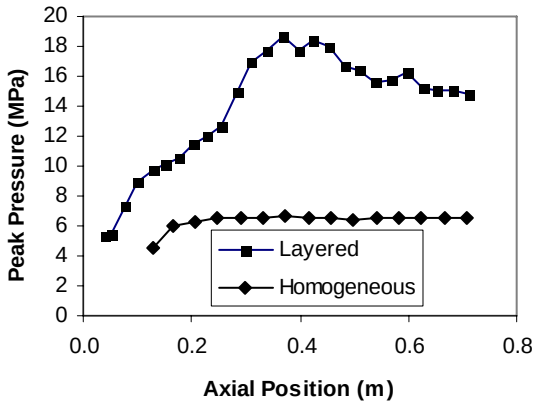

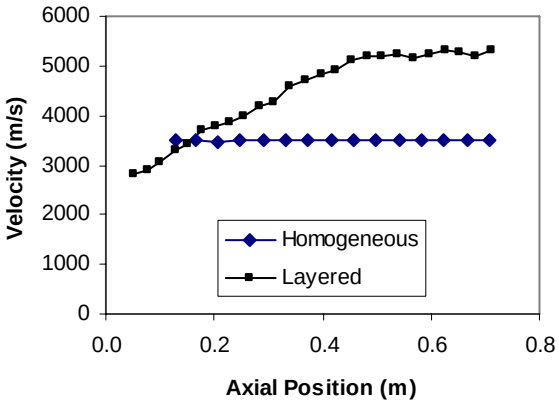

Figures 15 and 16. Results of CFD simulations of detonation in a layered mixture of stoichiometric hydrogen and oxygen in wall layer and hydrogen on centerline. Wave velocities and wall pressures exceed the values obtained for a homogeneous mixture of the same components.

E. Layered Detonation Flow Features

Figure 16 shows some of the key features of the layered detonations. The leading shock in the hydrogen layer along the centerline is curved. There is a break in the curve at the boundary between hydrogen and hydrogen/oxygen wall layer. In the wall layer the shock is highly oblique (approximately 20^0 angle to the direction of incoming flow). The shock strength is insufficient to initiate prompt reactions and propagate as an oblique detonation; instead the reaction zone is concentrated at the point where the oblique shock reflects from the wall. Due to the compression by the incident and reflected shocks, peak pressure in this zone is 15 MPa or 2.5 times the CJ detonation pressure of a homogeneous mixture.

Expansion waves emanating from the reaction zone compress the core hydrogen and create a high pressure region on the axis about 1 tube diameter behind the shock front. The pressure drives a flow of hydrogen along the axis at 7600 m/s in the direction of travel of the detonation. This flow recompresses and drives the leading shock front.

The reaction zone sets up transverse waves that couple with the tube and persist for many tube diameters behind the front. These waves are unrelated to any detonation cell structure which would exist at length scales an order of magnitude below the resolution of the simulation; in fact, due to the fundamentally different mode of propagation, detonation cell structure as it is commonly understood may not exist for this mode of propagation. Since the reaction zone is concentrated at the point the oblique shock reflects from the wall, there may not be any propagating Mach-stems traversing the wave front.

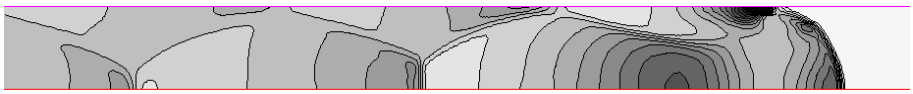

Pressure: 0 to15 MPa

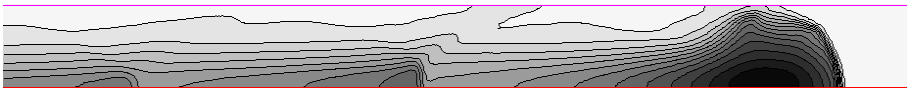

Axial Velocity: -300 to 7600 m/s

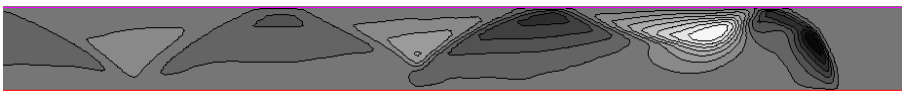

Radial Velocity: -2400 to 2000 m/s

Figure 16. Pressure (top), axial-velocity (middle), radial-velocity (bottom) for layered detonation of stoichiometric gaseous hydrogen and oxygen in wall layer and hydrogen along centerline. Magnitude increases as grey scale darkens. Wave is moving left to right. Wall is at top and centerline at bottom. Initial state is 1 atm and 100 K.

F. Specific Impulse

An interesting question relevant to pulse detonation rocket engines is whether the high propagation velocity and wall pressure of a detonation in a layered mixture of hydrogen and oxygen could result in an increase in specific impulse relative to a homogeneous mixture. Included in the simulations was a calculation of the impulse produced from the time of ignition until the tube pressure equaled the ambient pressure. The exit flow was modeled by including the region 1 meter axially and 0.75 meter radially from the exit. This region was initialized with 100 Pa of hydrogen. The exit boundary condition for the tube was initially specified to be a one-way flow blockage boundary. When the detonation front reached the exit, the boundary condition was changed to an exit flow boundary condition.

The layered detonation produced an impulse of 0.870 N-s and the homogeneous 0.907 N-s. We attribute the lower impulse of the layered detonation to higher dissociation in the stoichiometric layer and the divergence angle of the exit flow.

V. Conclusion

Detonations in cryogenic gaseous-hydrogen/liquid-oxygen mixtures were observed to propagate at velocities up to 20% higher and produce wall pressures up to a factor of 3 higher than Chapman-Jouget equilibrium code calculations. This behavior differed significantly from previous studies of cryogenic gaseous-hydrogen, gaseous-oxygen detonations which exhibited close agreement with CJ calculations, and also differed from previous studies of detonations in sprays which exhibited lower than CJ velocities and pressures. Consideration of the data in several cases leads us to believe that this was not a transient phenomena associated with an initially overdriven detonation relaxing to a steady state.

In this study the liquid oxygen was sprayed into the chamber in a hollow-cone pattern that directed the liquid onto the wall of the tube. This created a layered mixture that had a high concentration of oxygen on the periphery and a low concentration on the centerline. CFD calculations showed that detonations in mixtures configured in this way can propagate at velocities a factor of 2 higher, and produce peak wall pressures up to a factor of 3 higher than the CJ values of homogeneous mixtures.

The layered detonation phenomena does not appear to have any advantages for pulse detonation rocket engines as the theoretical impulse was 96% of that of a homogeneous mixture at the same initial state.

Acknowledgments

This work was supported in part by the Air Force Office of Scientific Research under Mitat Birkan, Program Manager. Appreciation is extended to Mike Griggs, Randy Harvey and Tom Werner for their technical contributions to this work.

---

[1] Ragland, K.W., Cosens, G.L., Cullen, R.E., "Detonation of Hydrogen-Oxygen at Low Temperature and High Pressure", *AIAA Journal*, Vol. 2, No. 1, 1964, pp. 142-144

[2] Plaster, M., McClenagan, R.D., Benz, F.J., Shepherd, J.E. Lee, J.H.S., "Detonation of Cryogenic Gaseous Hydrogen-Oxygen Mixtures," *Dynamics of Detonations and Explosions; International Colloquium on Dynamics and Explosions of Reactive Systems*, 12th, 1989, pp. 37-55

[3] Zitoun, R., Desbordes, D., Guerraud, C., Deshaies, B., "Direct initiation of detonation in cryogenic gaseous H_2-O_2 mixtures", *Shock Waves*, V. 4, 1995, pp. 331-337

[4] Strauss, W.A., Scott, J.N., "Experimental Investigation of the Detonation Properties of Hydrogen-Oxygen and Hydrogen-Nitric Oxide Mixtures at Initial Pressures up to 40 atm", *Combustion and Flame*, Vol. 19, 1972, pp. 141-143

[5] Ragland, K.W., Dabora, E.K., Nicholls, J.A., "Observed Structure of Spray Detonations", Physics of Fluids, Vol.11, No.11, pp. 2377-2388, 1968

[6] Bowen, J.R., Ragland, K.W., Steffes,F.J., Loflin, T.G., "Heterogeneous Detonation Supported by Fuel Fogs or Films," 13th Symposium (International) on Combustion, The Combustion Institute, pp.1131-1140, 1971

[7] Bar-Or, R., Sichel, M., Nicholls, J.A., "The Propagation of Cylindrical Detonations in Monodisperse Sprays," Eighteenth Symposium (International) on Combustion, The Combustion Institute, 1981, pp. 1599-1606

[8] Fried, L.E., Howard, W.M., Souers, P.C., *Cheetah 2.0 User's Manual*, Lawrence Livermore National Laboratory, UCRL-MA-117541, 1998

[9] Mitrofanov, V.V., "Ultrahigh-speed Detonation in Charges with Longitudinal Channels," Fizika Goreniya Vzryva, Vol. 11, No. 1, pp.73-81, 1974

[10] Dabora, E.K., Nicholls, J.A., Morrison, R.B., "The Influence of a Compressible Boundary on the Propagation of Gaseous Detonations," Tenth Symposium (International) on Combustion, pp. 817-830, 1965

[11] Liu, J.C. Liou, J.J., Sichel, M., Kauffman, C.W., Nicholls, J.A., "Diffraction and Transmission of a Detonation into a Bounding Explosive Layer," Twenty First Symposium (International) on Combustion/The Combustion Institute, pp, 1639-1647, 1986

[12] Jones, D.A., Sichel, M., Oran, E.S., Guirguis, R., "Detonation Transmission in Layered Explosives," Twenty Third Symposium (International) on Combustion/The Combustion Institute, pp.1805-1811, 1990

APPENDIX T

"Cryogenic, Multiphase, Hydrogen-Oxygen Detonations"
(Journal of Propulsion and Power)

This Page Intentionally Left Blank

Cryogenic, Multiphase, Hydrogen-Oxygen Detonations

Edward B. Coy* and Jonathan M. Watts†

Air Force Research Laboratory, Edwards AFB, CA 93524

Sampath Palaniswamy‡

Metacomp Technologies, Agoura Hills, CA

Detonations of flowing mixtures of hydrogen and oxygen at temperatures between 90 and 110 K, pressures from 3 to 5 bar, and mixture densities of 3-6 kg/m^3 have been studied. The effect of liquid oxygen on wave speeds and peak wall pressures are reported. Data taken at cryogenic conditions are compared with ambient temperature data taken at similar initial densities and equivalence ratios, as well as with equilibrium, Chapman-Jouget theory calculations. For the conditions studied, liquid oxygen was found to result in increased wave speeds and peak wall pressures. These observations are shown to be consistent with a highly stratified mixture with high concentrations of oxygen in a layer adjacent to the wall and low concentrations along the axis of the tube.

I. Introduction

THIS paper presents results from an investigation of detonations of flowing mixtures of cryogenic gaseous hydrogen and liquid oxygen. This work was undertaken to support development of pulse detonation rocket engines (PDRE). Cryogenic propellants will be desirable for PDRE applications for many of the same reasons that they are used for conventional rocket engines: the density is increased, which reduces tank volume, and cooling of the

---

* Propulsion Research Engineer, Aerophysics Branch, 10 East Saturn Blvd., Member AIAA

† Propulsion Research Engineer, Aerophysics Branch, 10 East Saturn Blvd.

‡ Senior Scientist, Metacomp Technologies, Member AIAA

combustion chamber is facilitated. There is an additional advantage for PDREs insofar as a major advantage of the cycle is the reduced pumping requirements associated with the low injection pressures. High density enables a larger mass to be charged into the chamber for a given supply pressure. Hydrogen and oxygen were chosen for this study due to their high specific impulse, ease of detonability, and the existing experience with handling and design.

There is an extensive list of phenomena which could be significant in detonations of liquid oxygen and hydrogen in PDREs[1]. There are phenomena that affect the initial state of the mixture which include atomization, turbulent dispersion, vaporization, turbulent mixing, wall-wetting, and heat-transfer. Other phenomena affect the propagation of the detonation through the mixture which include droplet shattering, vaporization, chemical induction time, wall friction and heat transfer within the reaction zone, and longitudinal and axial variations in the mixture composition. There have not been any previous studies which characterized the propagation of detonations under all of these complex conditions. Studies which examined subsets of the problem are briefly reviewed here.

Previous studies of detonations of cryogenic, quiescent, gaseous mixtures of hydrogen and oxygen have found that measured wave velocities and pressures agree well with ideal-gas equilibrium Chapman-Jouget calculations up to initial pressures of approximately 5 atm and densities of 5 kg/m^3. [2,3,4] At higher pressures and densities the ideal-gas calculations under-predict wave speed and pressure, and a real-gas equation of state produces better agreement. This result was also obtained in a study of ambient temperature, high-density (up to 15 Kg/m^3) quiescent, hydrogen-oxygen detonations.[5]

There are an extensive number of references on detonations in sprays. The vapor pressure of the fuel has a large influence on the propagation mechanisms of the detonation. For high vapor pressure liquids, a detonation can be supported in the gas-phase, and the liquid fraction is consumed in the products and does not contribute to the processes which drive the leading shock. For low vapor pressure liquids, the successful propagation of a detonation has been shown to depend on the rate at which droplets are decomposed into a “micromist” by the high velocity flow following the leading shock wave[6]. Studies using 400-2600 micron droplets have shown that following a chemical induction time delay, the micromist explodes, sending shock waves forward to reinforce the leading shock, and rearward, as a retonation. The droplet shattering and evaporation processes are much slower than the gas-phase kinetics of the combustion reactions and result in much longer reaction zones than are typical of gas phase detonations. It has also been observed that a thin film of a low vapor-pressure liquid hydrocarbon deposited on the

wall of a tube can support a combustion wave that propagates at nearly the CJ velocity[7]. In this case the high-velocity gas behind the leading shock creates a shear flow over the liquid that strips away small droplets. The droplets rapidly react, and the heat release sustains the process.

Due to their fundamentally different mode of propagation, low vapor pressure spray and film detonations do not in general match propagation velocities and pressures obtained from CJ thermodynamic equilibrium calculations. Wave velocities and pressures are typically reduced. For detonations in tubes the discrepancy has been attributed to heat transfer and wall friction in the extended reaction zone[5]. For detonations initiated directly by high explosive charges, the discrepancy has been attributed to the simultaneous decay of the initiating blast wave and increasing length of the reaction zone, implying that the reduced velocity is a transient phenomena and that the theoretical value would be reached in a sufficiently long apparatus.[8]

The purpose of this work was to experimentally investigate the behavior of detonating mixtures of liquid oxygen and cryogenic gaseous hydrogen under conditions expected to be relevant to pulse detonation rocket engines. The results are applicable to the development of the next generation of repetitively pulsed, multi-tube test articles and also are intended to be used to qualify computational models under development for use in system application studies.

II. Experimental Setup

Fig. 1 shows the major features and instrumentation locations on the test article. The tube was vertically oriented, with 61 cm inner length and a 2.54 cm inner diameter and a design pressure of 70 MPa. The injector was a swirled co-axial design. Angular momentum was imparted to the liquid oxygen through an off-axis inlet port. Oxygen exited through the center post and hydrogen through the surrounding annulus. Visualization of the injector flow was performed using air and water as simulants in the AFRL/PRSA Flow Laboratory. Water matched the density and volumetric flow rate of liquid oxygen to within 5%. Atmospheric pressure air matched the density of hydrogen at the test conditions to within 10% and the volumetric flow rate within 5%. The liquid was well atomized with a maximum droplet size of approximately 100 micrometers. The injector produced a hollow-cone spray with a divergence angle of 30^0 resulting in the majority of the liquid being deposited on the walls of the tube during the experiments.

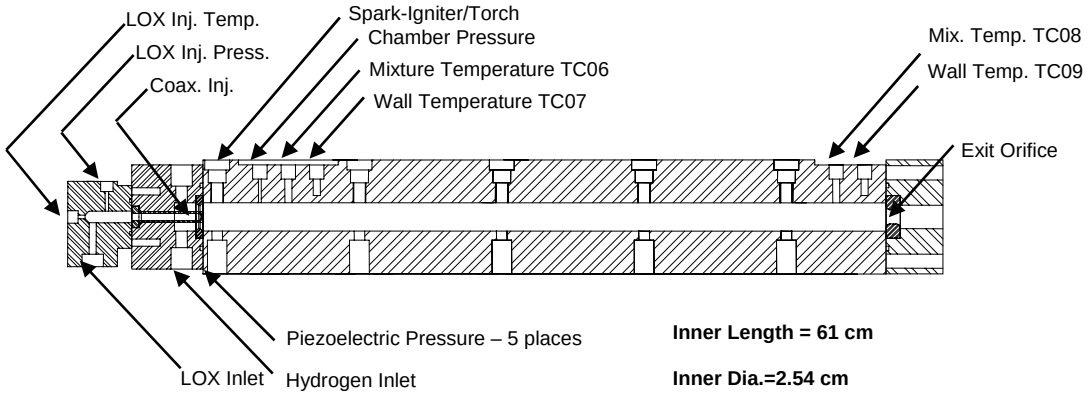

Fig. 1 Cross-section view of test article showing locations of instrumentation. Orientation was vertical during tests.

The fuel for the detonation tests was industrial grade hydrogen, 99.9% pure with methane as the principal impurity. The hydrogen was supplied from high-pressure cylinders and chilled to cryogenic temperatures in a shell-and-tube heat exchanger with saturated, 2.6 atm liquid nitrogen on the shell side. The hydrogen mass flow rate was measured using a sonic nozzle. The mass flow rate was calculated using an in-house developed program that solves the 1-D Euler equations for sonic orifice flow using real-gas properties[9]. The discharge coefficient for the nozzle was provided by the manufacturer and was certified to be accurate within +/- 1%.

Industrial grade liquid oxygen, 99.5 % with nitrogen as the principal impurity, was supplied from a 200 liter dewar pressurized with helium. Volumetric flow rate was measured using a turbine meter, and the inlet state was measured with a thermocouple and pressure transducer to determine the density. The dewar was located on an electronic scale to enable the flow rate of liquid oxygen to be independently determined from the rate of change of mass of the dewar. This arrangement enabled the turbine meter to be calibrated in-situ with an accuracy of +/- 0.5%.

The extent of vaporization of liquid oxygen varied along the length of the test article due to heat transfer to the oxygen from the hydrogen and the tube wall. Two methods were used to estimate the extent of vaporization. The first assumed adiabatic mixing of the streams of hydrogen and oxygen at the inlet enthalpies and is listed in the data tables below as the initial gaseous oxygen fraction. The second assumed that liquid and gas phases reached thermal equilibrium at the measured exit temperature. This assumption was supported by typical data for mixture temperature as shown in Fig. 2. Prior to 115 seconds both thermocouples were exposed to saturated oxygen at a pressure of 1.5 atm. At 115 seconds the hydrogen flow was initiated and a two-phase mixture of hydrogen and

liquid oxygen began impinging on TC06 (located 5 cm downstream of the injector) causing large fluctuations in temperature. The temperature trended downward as the flow from the heat exchanger cooled the system components and the hydrogen inlet temperature decreased. Near the exit at TC08 the hydrogen and oxygen had reached thermal equilibrium as evidenced by the lack of fluctuations. Based on the measured temperature at TC08 the vapor pressure of gaseous oxygen was determined from the saturation curve and this was used to determine the mass fraction of oxygen in the gas phase. In several cases the temperature fluctuations at TC08 indicated that thermal equilibrium had not been reached. For those cases the reported value of oxygen mass fraction was based on the average temperature, and the uncertainty was based on the magnitude of the temperature fluctuations. To complete the discussion of the Fig. 2, at 120 seconds the mixture was ignited and both thermocouples went off-scale.

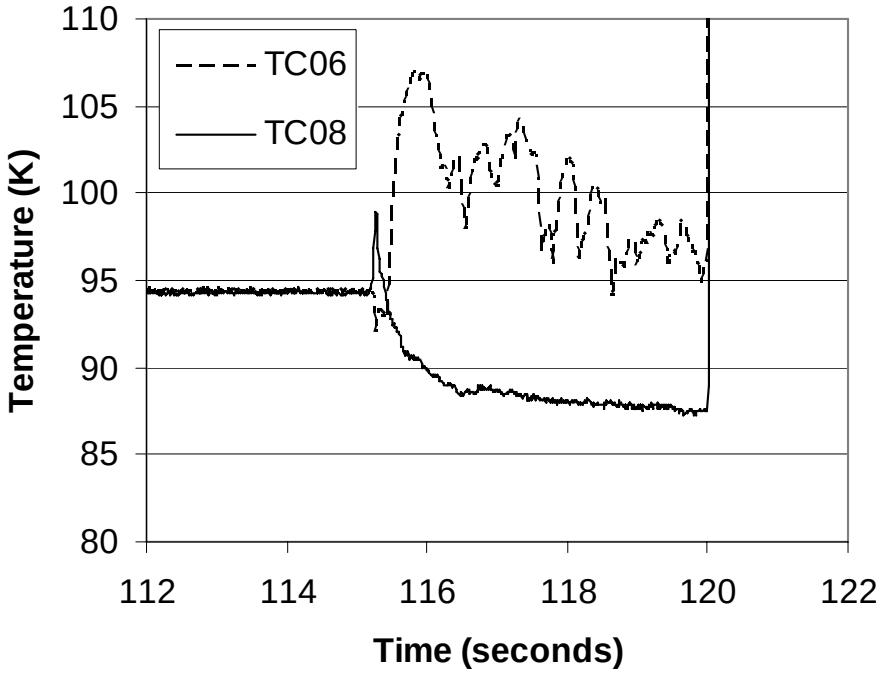

Fig. 2 Temperatures of flowing mixtures prior to ignition at inlet (TC06) and exit (TC08).

All thermocouples were checked for accuracy in a liquid nitrogen bath prior to installation. In addition, during each test there was an interval when saturated oxygen was present and this enabled routine checks to be performed. To prevent the thermocouples exposed to the detonation from melting, the beads were blanketed with a flow of nitrogen that was initiated coincident with the ignition.

Five piezoelectric transducers (Kistler 603B1) were mounted flush with the inner surface of the tube at 12.7 cm intervals. The signals were recorded at 1 MHz and 12 bit resolution for a precision of 24 KPa. Each transducer, associated range capacitor (Kistler 571A3), impedance-converter (Kistler 558), and cables were calibrated as a set by the manufacturer and certified to be linear to less than +/- 1% of full scale. The calibrations were performed at 295 K over the range 0-69 MPa. The manufacturer's literature listed a nominal value for the temperature coefficient of sensitivity of -0.027 %/K. For the cryogenic tests this amounted to -5.5%; however, because a calibration was not performed at the operating temperature, we have estimated the uncertainty at +/- 10%. The response of the piezoelectric transducers was checked in our laboratory under shock tube and gaseous detonation conditions. For the shock tests, a driver tube and burst disc were installed in place of the injector, and the exit orifice was replaced with a blank. The measured wave speed was used to predict pressure behind the incident and reflected shocks using a thermodynamic equilibrium model. The predicted values agreed within 10% with the measurements. The gaseous detonation tests were performed with flowing mixtures. The flow rates were set to produce an initial density and equivalence ratio representative of the target conditions for the cryogenic tests. Peak pressures and wave speeds are shown in Fig. 3 for a test with an initial mixture density of 3.6 +/- .1 kg/m^3 and an equivalence ratio of 1.5 +/- .1. The trends in pressure and velocity are consistent with an initially over-driven detonation relaxing to a steady state. Also given are equilibrium Chapman-Jouget calculations obtained using the Cheetah code[10] with 10 product species. The calculations were performed using ideal-gas and JCZ3 equations of state. The results differed by about 1% in both pressure and velocity with slightly better agreement obtained with JCZ3. These results are included here to indicate the level of agreement with CJ theory that was obtained for ambient-temperature, gaseous detonations and will be compared with results presented below for cryogenic, liquid-gas detonations.

The detonation velocities given in the figures are averages over the 12.7 cm intervals between transducers and were based on the time the pressure signals had risen to at least half of their peak value. The manufacturer's literature specifies that the Kistler 603B1 transducers have a rise time from 10-90% of 1 μs. The signals were

digitized at 1 μs intervals. Assuming the timing of the wave arrival could be in error by one microsecond, the uncertainty of wave speed ranged from +/- 65-110 m/s.

The spark ignition system was a conventional automotive system, and produced approximately 110 millijoules per spark. The spark plug was a surface gap, Champion G52V. When the spark plug was cooled below approximately 100 K it would not discharge, so it could not be located in the wall of the test article. An ignition chamber with a volume of approximately 15 cm^3 was added that could be maintained above 100 K with heating tape. Prior to ignition the chamber was charged from the hydrogen-oxygen mixture flowing in the test article, and at ignition it injected a flame jet into the test article through a 5 mm orifice. The ignition chamber could be located near the injector at the position shown in Fig. 1 or in the exhaust tube downstream of the exit orifice.

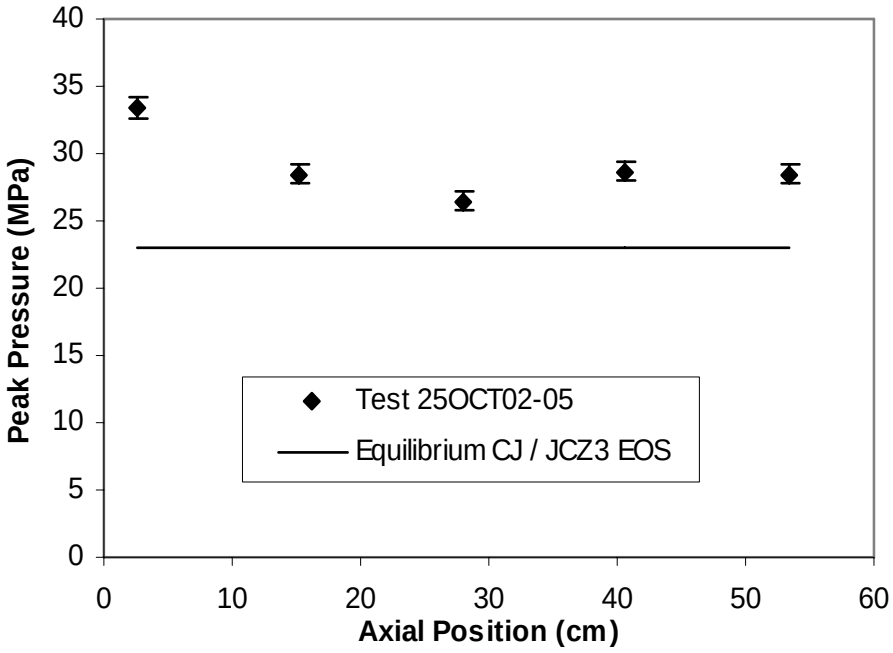

a)

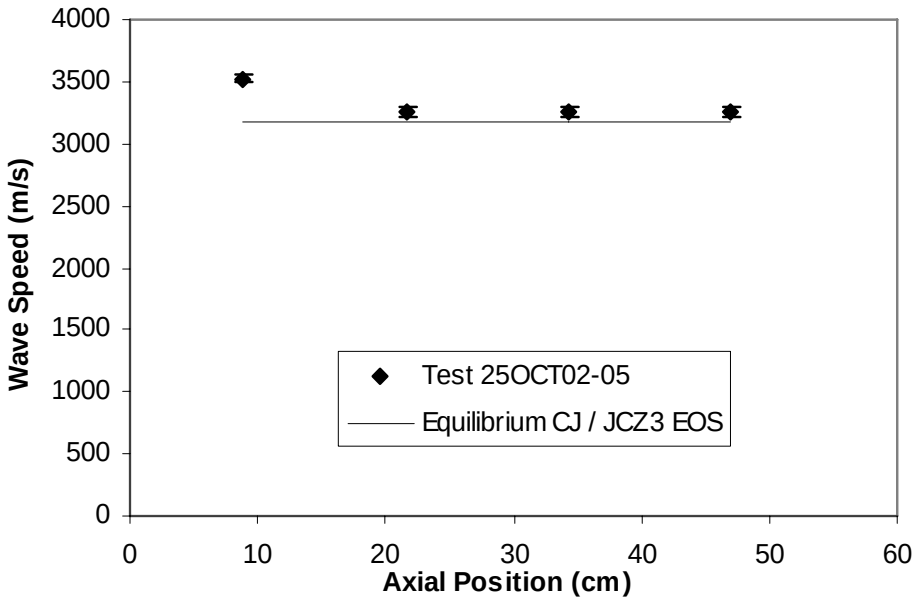

b)

Fig. 3 Detonation of a flowing, ambient temperature mixture of hydrogen and oxygen. a) Peak wall pressures and b) wave velocities.

A. Experimental Methodology

Prior to a firing, the liquid oxygen dewar was vented to atmosphere and the oxygen was allowed to boil until it reached a saturated state. The propellant systems and test article were cooled with liquid nitrogen. When temperatures reached 100 K, the liquid oxygen dewar was pressurized with helium, and the systems were flushed and filled with propellants. The automated firing sequence began by flowing liquid oxygen until the fluid was sub-cooled by approximately 20 K at the injector. This typically required 60-120 seconds. The hydrogen flow began approximately 5 seconds before ignition. At 100 milliseconds prior to ignition, the test article and injector pressure transducers were isolated to prevent over-ranging. At the time of ignition, liquid oxygen temperatures at the injector were in the range of 95-120 K, hydrogen inlet temperatures were 100-120 K and wall temperatures were 110-120 K.

Pressure in the test article was 2.5-5.0 atm. The spark system was fired, and a warm nitrogen purge flow was initiated to flush combustion products and minimize ice formation in the tube. Several series of tests were performed at fixed flow rates of hydrogen and varying flow rates of oxygen. At low oxygen flow rates the liquid was entirely vaporized, and at higher flow rates an increasing fraction remained a liquid.

III. Results

The initial conditions for two representative tests at high equivalence ratio are given in Table 1. Both tests had liquid oxygen present at the injector and were fully vaporized at the exit condition. In test 12FEB04-17 the mixture was ignited in the exhaust tube and the detonation propagated towards the injector and in test 18FEB04-03 the reverse occurred. Wave speeds and peak wall pressures are shown in Figs. 4 and 5. The measured wave speeds agree within 5% with the equilibrium code predictions except near the injector, where the measured velocity is significantly lower. The level of agreement away from the injector is similar to that obtained in the ambient temperature detonations at similar densities. The measured peak pressures are a factor of two or more higher than the equilibrium code predictions. This is a larger deviation than was observed in the ambient temperature detonations and is believed to be significant. The changes in pressure along the tube do not appear to be correlated with changes in wave speed. There is no observable effect on pressures or wave speeds due to the ignition location.

Table 2 gives the initial conditions for two representative tests at near-stoichiometric equivalence ratio and the peak wall pressures and wave speeds are plotted in Figs. 6 and 7. The initial gaseous oxygen fractions are significantly lower than those in the high equivalence ratio tests due to the higher flow rate of liquid oxygen. The exit flow is predicted to be fully vaporized in both cases; however, inspection of the exit temperature time traces showed there were fluctuations indicating full thermal equilibrium had not been reached. Both tests exhibit wave speeds approximately 20% greater than the equilibrium code predictions. The high velocity cases are noteworthy because deviations of this magnitude have not been reported previously for cryogenic or spray detonations. The peak pressures are approximately a factor of two greater than the equilibrium code, and the fluctuations in pressure do not appear to be correlated to changes in wave speed. The ignition location did not have an observable effect.

A summary of the wave speed results plotted as a function of equivalence ratio is given in Fig. 8. The average velocity over the 50.8 cm interval between the first and last transducers is shown. All of the equilibrium CJ

calculations were performed assuming a nominal initial density of 4 kg/m^3 as wave speed is a weak function of the initial density. The CJ calculation stands as a lower bound on the data. This is a noteworthy result, as other studies of detonations in sprays have found that the equilibrium CJ velocity is an upper bound and only reached in the limit of very small droplets or high vapor pressure fuels. The data were examined to determine if wave speed was correlated with any other parameter such as the extent of vaporization of the oxygen, the density of the mixture, the direction of propagation, the peak pressure of the wave, the initial wall temperature, and the date of the test. The wave speed did not correlate with any of these variables.

A summary of the peak pressure data is given in Fig. 10. Pressure is a strong function of the initial density as well as the equivalence ratio, so the measured pressures were normalized by the equilibrium CJ values calculated for each test condition. The average value and the standard deviation for each measurement location are shown. The deviations of the averages from the CJ values are statistically significant for all except the first transducer and are greater than the +/- 10 % uncertainty that was assigned to the pressure measurement.

In addition to the average deviations from the CJ values, peak pressures also exhibited large changes within a given test. The average value of the coefficient of variation for the five measurements of peak pressure within each test was 29%. The COV for the variation from test to test ranged from 57% for the first transducer to 20% for the fourth. These measures are comparable in magnitude and greater than the uncertainty in the pressure measurement; therefore, large fluctuations in peak wall pressures as well as random deviations from the CJ value are features of the test conditions.

IV. Discussion

Detonations of cryogenic mixtures of gaseous-hydrogen and liquid-oxygen were found to be characterized by higher than CJ propagation velocities as well as high average and fluctuating wall pressures. These results differ from those obtained by other researchers for cryogenic gaseous-hydrogen gaseous-oxygen mixtures and ambient temperature spray detonations as discussed previously. Explanations for the new findings were sought in the fact that the apparatus used in this study was designed to represent conditions that are expected to be significant to the design of a PDRE; i.e., relative to previous studies, the tube was short and the mixtures were flowing and non-uniform.

B. Transient Effects

Scientific detonation studies are usually performed in tubes several meters long to ensure that steady state conditions have been reached at the measurement location. The distance required depends on the method of initiation and the initial density, but generally a detonation passes through an over-driven condition before relaxing to a steady velocity[4]. While in the over-driven state the detonation propagates at a higher velocity and has higher peak pressure than CJ values. Thus a transient effect appears to be a plausible explanation for the observations.

Table 1. Initial conditions for two tests with cryogenic mixtures at high equivalence ratio.

	12FEB04-17	+/-	18FEB04-03	+/-
Equivalence ratio, Φ	2.44	0.15	2.07	0.13
LOX injector temp. TC04 (K)	120.9	0.6	119.8	0.6
Hydrogen inlet temp. TC10 (K)	122.9	0.6	106.6	0.6
Upper wall temp. TC07 (K)	112.9	1.1	107.4	1.1
Lower wall temp. TC09 (K)	118.6	1.1	107.8	1.1
Exit mixture temp. TC08 (K)	105.3	0.56	90.7	0.56
Initial tube press. PT06 (Pa)	430711	8623	360576	8623
Mixture density (Kg/m3)	3.52	0.28	3.77	0.32
Initial gaseous O2 fraction	0.88	0.04	0.60	0.02
Exit gaseous O2 fraction	1.00	0.00	1.00	0.00
Mixture average velocity (m/s)	33.7	3.1	30.1	3.0
Ignition location	Exit		Injector	
Theoretical CJ velocity (m/s)	3727		3619	
Theoretical CJ pressure (MPa)	22.3		19.91	

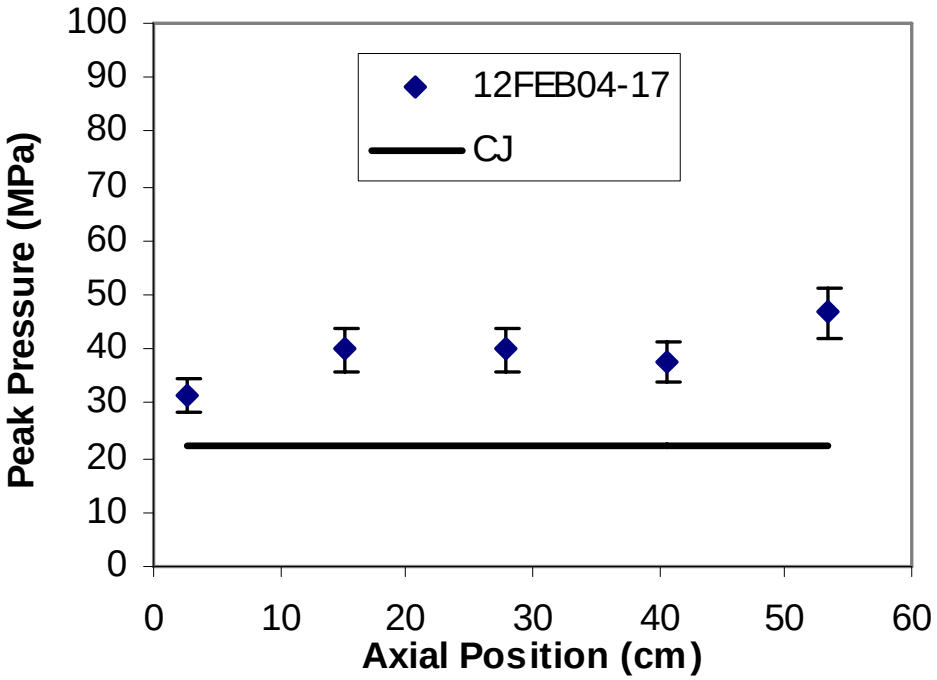
100
90
80
70
60
50
40
30
20
10
0
Peak Pressure (MPa)
12FEB04-17
CJ
0
10
20
30
40
50
60
Axial Position (cm)

a)

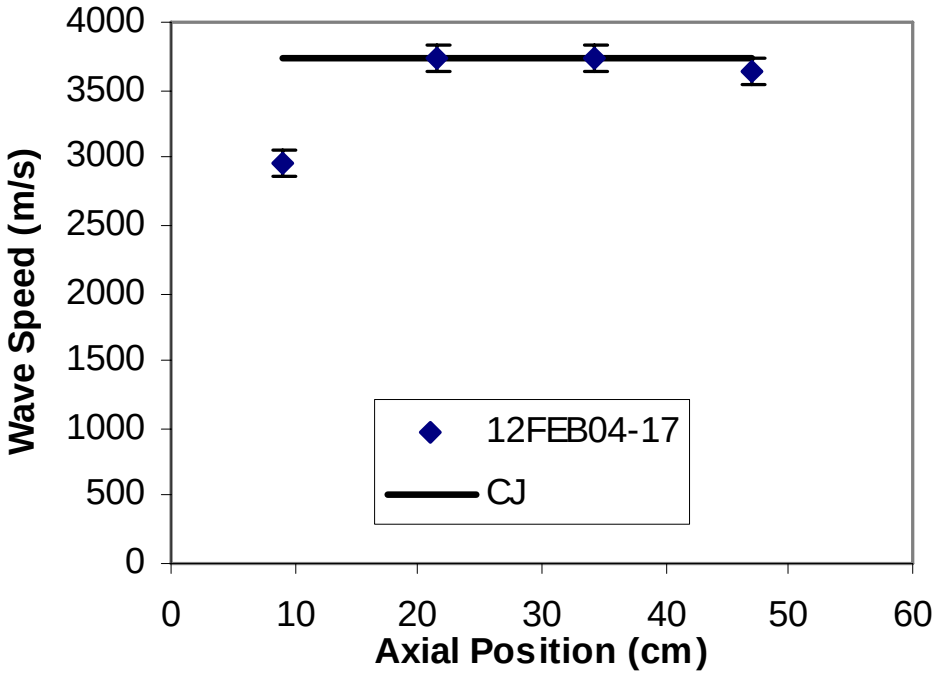

b)

Fig. 4 a) Peak wall pressures and b) wave speeds for test conditions 12FEB04-17 given in Table 1.

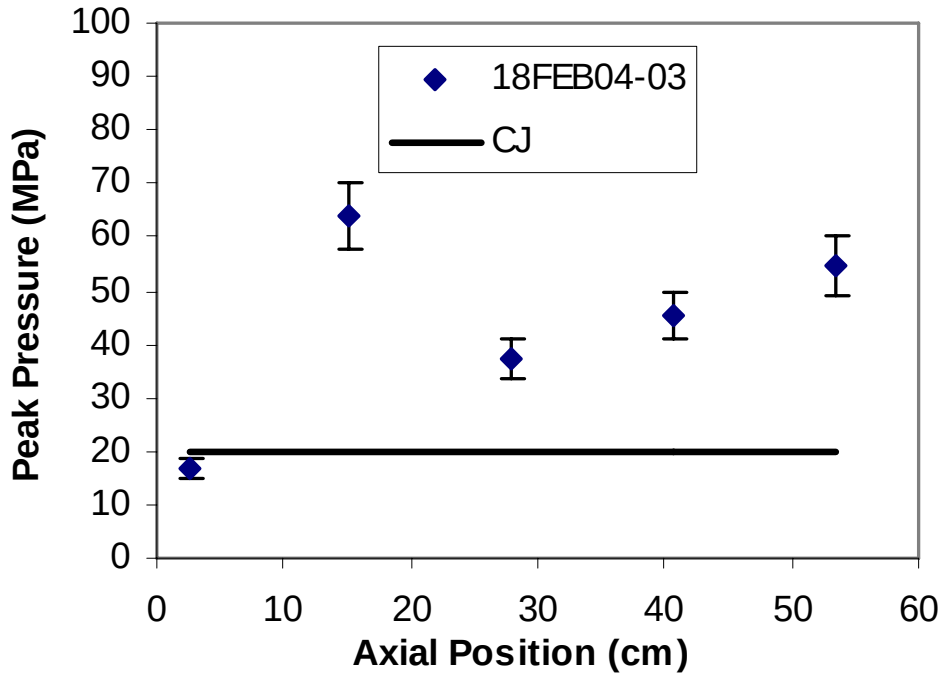
Peak Pressure (MPa)
Axial Position (cm)
18FEB04-03
CJ
0
10
20
30
40
50
60
70
80
90
100
0
10
20
30
40
50
60

a)

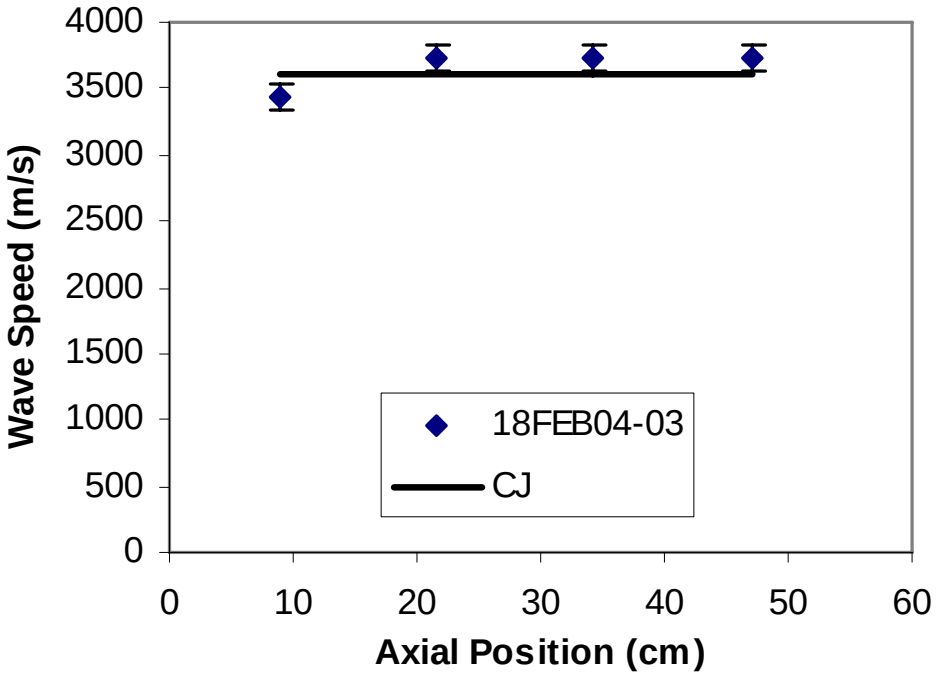

b)

Fig. 5 a) Peak wall pressures and b) wave speeds for test conditions 18FEB04-03 given in Table 1.

Table 2. Initial conditions for two tests with cryogenic mixtures at near-unity equivalence ratio.

	12FEB04-09	+/-	20FEB04-09	+/-
Equivalence ratio, Φ	1.15	0.05	1.18	0.05
LOX injector temp. TC04 (K)	105.6	0.6	101.7	0.6
Hydrogen inlet temp. TC10 (K)	117.9	0.6	111.3	0.6
Upper wall temp. TC07 (K)	112.4	1.1	106.0	1.1
Lower wall temp. TC09 (K)	113.6	1.1	105.6	1.1
Exit mixture temp. TC08 (K)	107.4	0.6	102.3	0.6
Initial tube press. PT06 (Pa)	409959	8623	430200	3446
Mixture density (Kg/m3)	5.12	0.31	5.56	0.30
Initial gaseous O2 fraction	0.40	0.01	0.34	0.01
Exit gaseous O2 fraction	1.00	0.00	1.00	0.00
Mixture average velocity (m/s)	33.5	2.4	34.0	2.1
Ignition location	Exit		Injector	
Theoretical CJ velocity (m/s)	3152		3208	
Theoretical CJ pressure (MPa)	23.7		27.08	

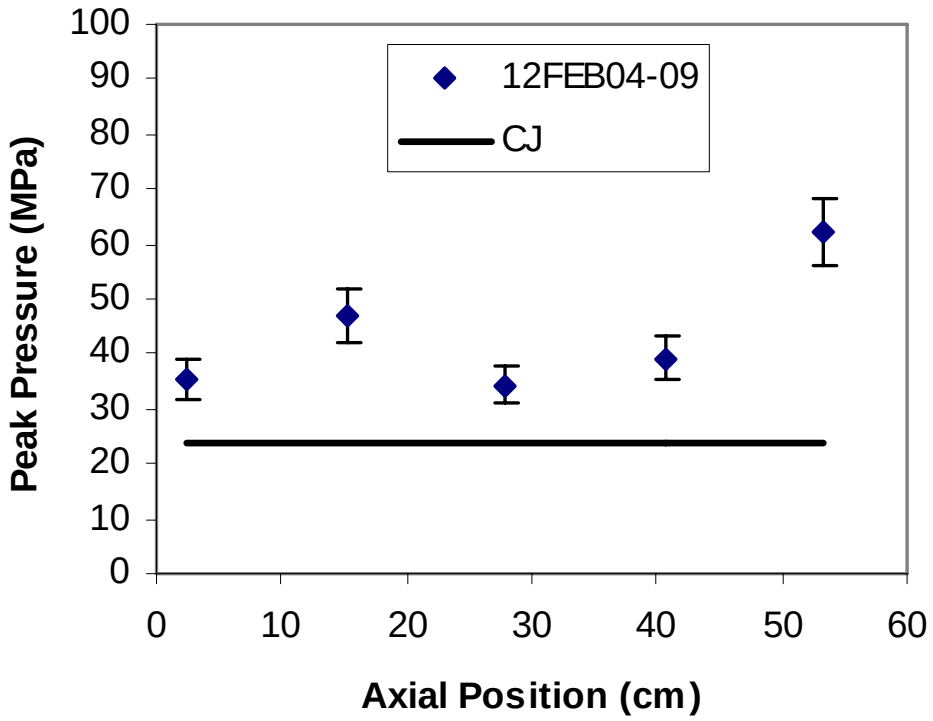

a)

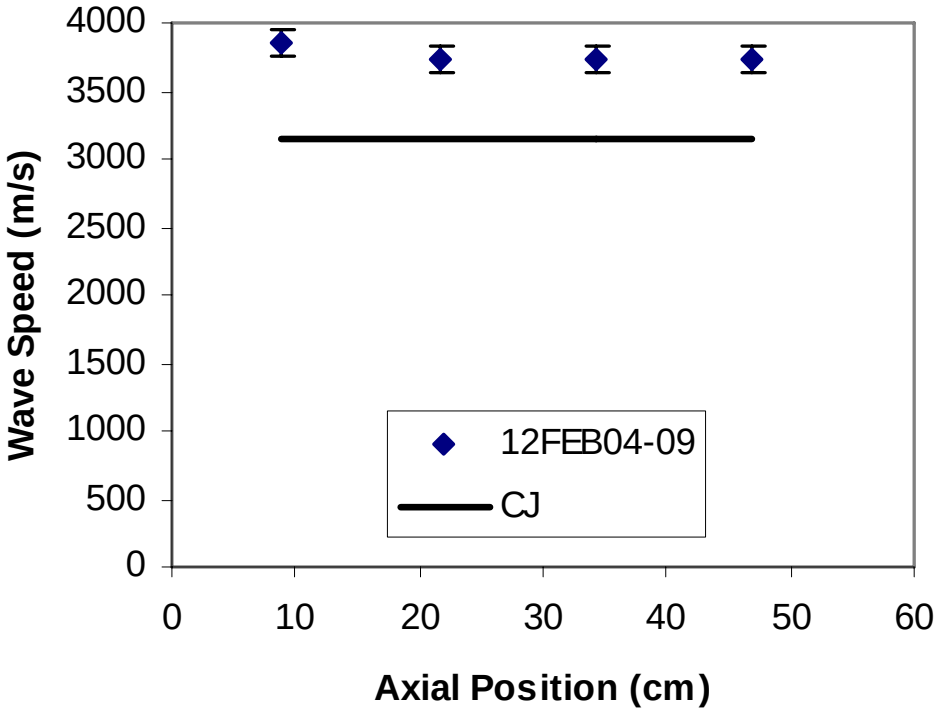

b)

Fig. 6 a) Peak wall pressures and b) wave speeds for test conditions 12FEB04-09 given in Table 2.

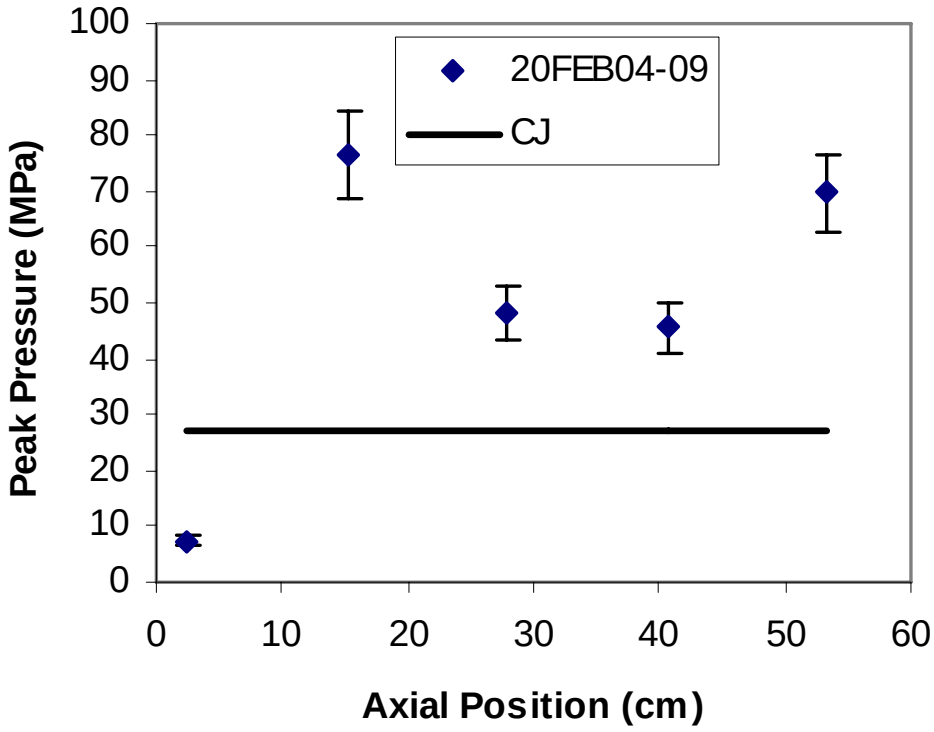
100
90
80
70
60
50
40
30
20
10
0
Peak Pressure (MPa)
0
10
20
30
40
50
60
Axial Position (cm)
20FEB04-09
CJ

a)

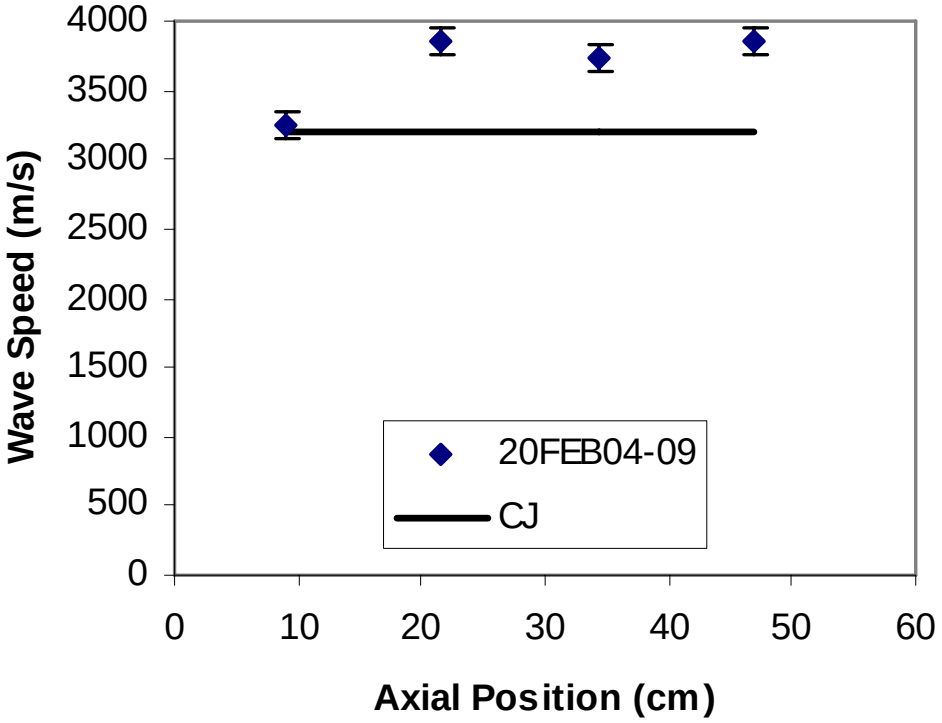

b)

Fig. 7 a) Peak wall pressure and b) wave speeds for test conditions 20FEB04-09 given in Table 2.

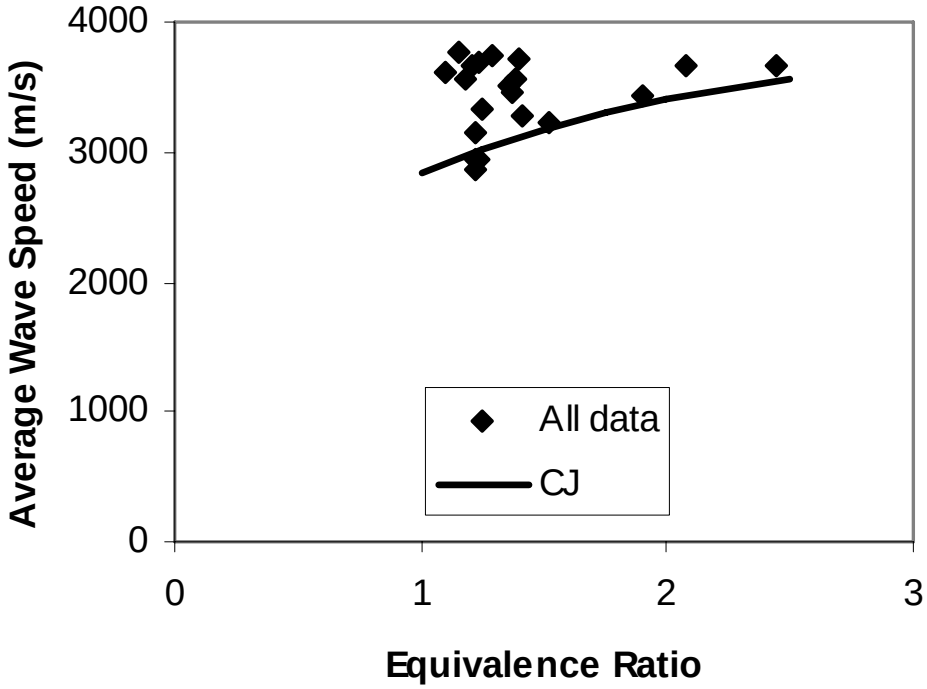

Fig. 8 All wave speed results as a function of equivalence ratio.

Previous studies of cryogenic and high pressure hydrogen-oxygen detonations did not specifically report the minimum distance required to reach steady conditions; however in one study, a distance less than 10 cm was required to achieve agreement with the CJ state[3].

Data obtained in this study included instances where the detonation accelerated after the wave was fully formed. There were also instances where the wall pressure decreased at the same time the velocity increased. These observations were not consistent with the hypothesis that the detonations were over-driven due to an initiation transient.

C. Non-uniform Mixtures

The mixtures in the tube were non-uniform in the axial direction due to vaporization and heat addition from the tube, and also in the radial direction because the hollow-cone spray directed liquid oxygen onto the wall. Due to the

large density difference between the oxygen-rich wall layer and the hydrogen, radial stratification likely persisted for many diameters downstream of the injector. This may have created a situation similar to that reported for solid explosives with gas-filled longitudinal channels[11]. In those systems, the explosion products act as a piston on the gas, driving a powerful shock down the channel, which in turn initiates or accelerates the reaction in the solid. Detonations have been observed to propagate at 1.5-2 times the velocity of the solid charge alone. There has been some previous work on layered detonations in gaseous systems; however, high-speed detonations have not been reported. Dabora[12] et al. found that surrounding a gaseous detonation with a layer of inert gas in fact causes a velocity decrement that depends on the density ratio of the reactive gas to the inert, and the width of the reactive layer. When hydrogen or helium was used in the inert layer, the reaction zone was observed to propagate at 50% of the CJ velocity. The studies of layered mixtures of Liu[13] and Jones[14] also did not report higher than CJ velocities and pressures, apparently because these studies focused on diffraction phenomena during the initial formation of the detonation in the surrounding layer.

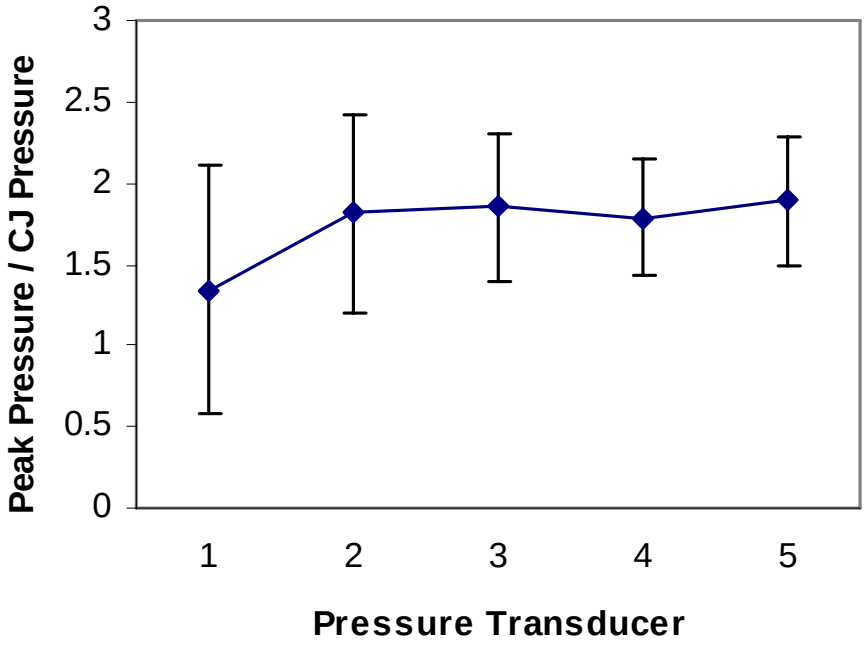

Fig. 9 Peak wall pressure data for all tests showing average and 95% error bars.

D. Numerical Simulations

Numerical simulations were performed to test the layered detonation hypothesis using CFD++, a commercially available code from Metacomp Technologies for compressible reacting flows. Only the overall features of the flow were of interest, so the simulations were performed with a mesh size set at approximately 10 times the estimated detonation cell size, or 0.41 mm in the axial direction and 0.67 mm in the radial. Hydrogen-oxygen chemistry was modeled using a 9 species, 18 reactions mechanism. An inviscid Euler equation set was solved using a scheme second order accurate in global time step.

For the layered detonation simulation, half of the cross-sectional area adjacent to the wall was filled with a stoichiometric mixture of hydrogen and oxygen, and the other half along the centerline was filled with hydrogen. A second simulation was performed as a control where the same amounts of reactants were distributed uniformly

across the tube for an equivalence ratio of 2.5. In both cases the initial pressure was 1 atmosphere and the temperature was 100 K. The detonations were initiated by a 2.5 cm layer adjacent to the closed end of the tube that was initialized at 10 atm and 1800 K.

Results for wave speed and peak wall pressure as a function of axial distance along the tube are given in Fig. 10. The detonation in the layered mixture initially propagates at the CJ velocity of the stoichiometric layer but then accelerates from 2800 m/s to 5300 m/s, while the detonation in the uniform mixture propagates at a steady velocity of 3500 m/s. The peak wall pressure of the layered detonation is initially at the CJ detonation pressure of the stoichiometric layer but then increases to a maximum of three times that of the homogeneous mixture and then decreases to a steady value approximately 2.5 times the homogeneous. In summary, the calculations exhibit the same qualitative characteristics observed in the experiments: high velocities and peak wall pressures and large changes in velocities and pressures.

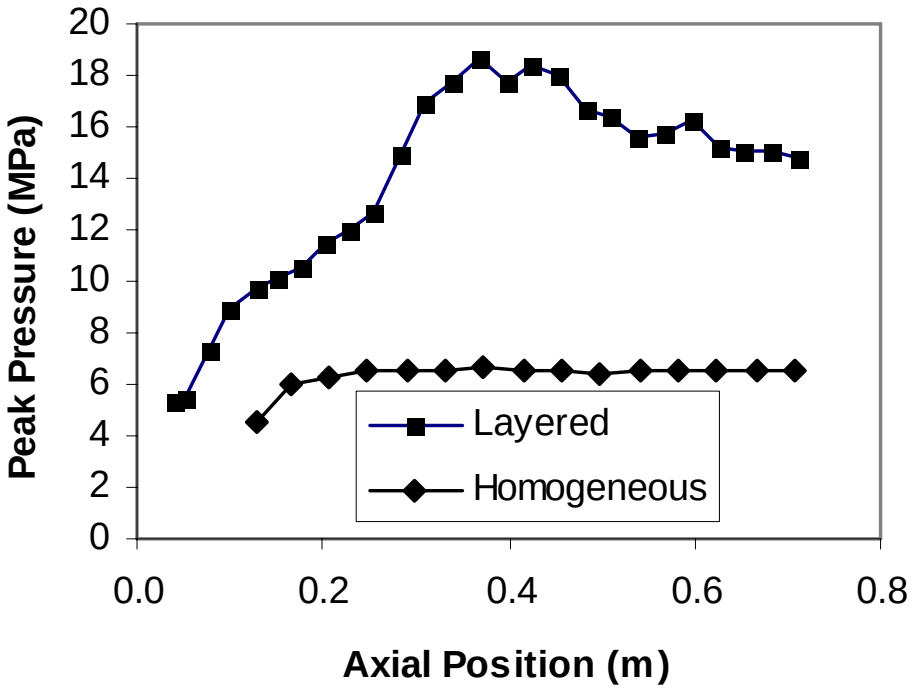

a)

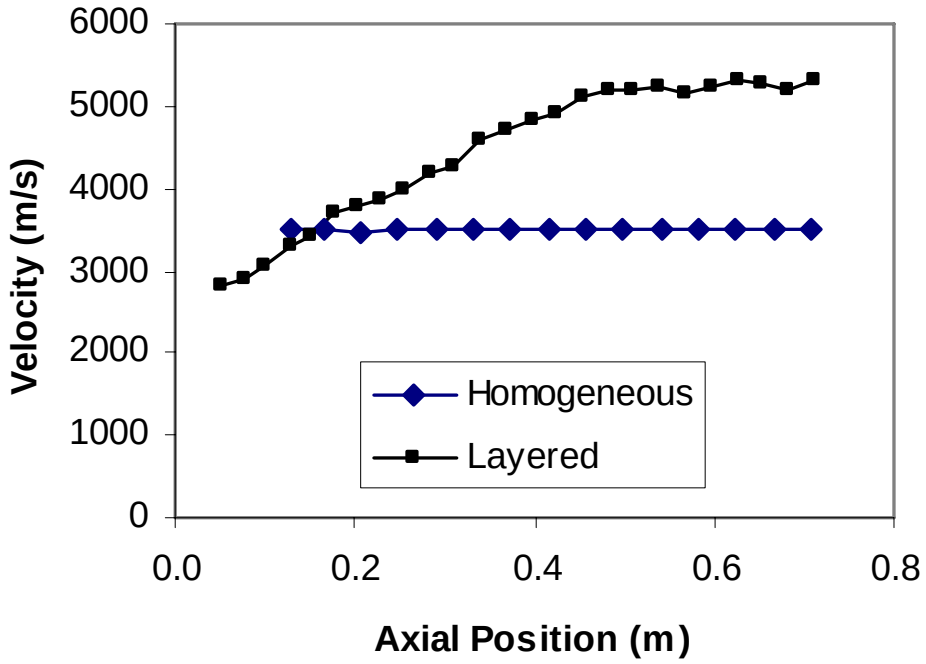

b)

Fig. 10 a) Peak wall pressure and b) wave speed from CFD simulation of detonation of a layered mixture.

E. Layered Detonation Flow Features

Fig. 11 shows the major features of the layered detonations. The leading shock in the hydrogen layer along the centerline is curved. There is a break in the curve at the boundary between hydrogen and hydrogen/oxygen wall layer. In the wall layer the shock is highly oblique (approximately 20^0 angle to the direction of incoming flow). The shock strength is insufficient to initiate prompt reactions and propagate as an oblique detonation; instead the reaction zone is concentrated at the point where the oblique shock reflects from the wall. Due to the compression by the incident and reflected shocks, peak pressure in this zone is 15 MPa or 2.5 times the CJ detonation pressure of a homogeneous mixture.

Expansion waves emanating from the reaction zone compress the core hydrogen and create a high pressure region on the axis about 1 tube diameter behind the shock front. The pressure drives a flow of hydrogen along the axis at 7600 m/s in the direction of travel of the detonation. This flow recompresses and drives the leading shock front.

The reaction zone sets up transverse waves that couple with the tube and persist for many tube diameters behind the front. These waves are unrelated to any detonation cell structure which would exist at length scales an order of magnitude below the resolution of the simulation; in fact, due to the fundamentally different mode of propagation, detonation cell structure as it is commonly understood may not exist for this mode of propagation. Since the reaction zone is concentrated at the point the oblique shock reflects from the wall, there may not be any propagating Mach-stems traversing the wave front.

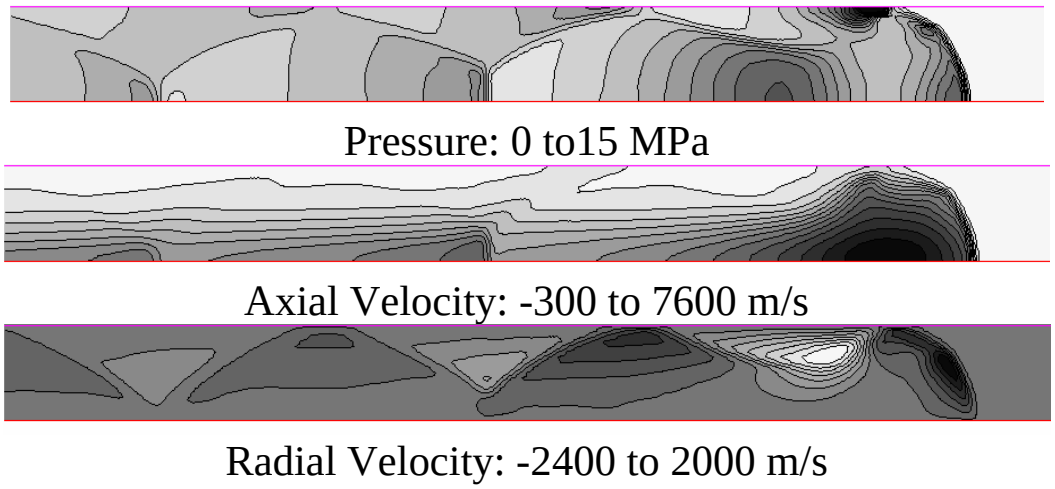

Fig. 11 Pressure (top), axial-velocity (middle), radial-velocity (bottom) for layered detonation of stoichiometric gaseous hydrogen and oxygen in wall layer and hydrogen along centerline. Magnitude increases as grey scale darkens. Wave is moving left to right. Wall is at top and centerline at bottom.

F. Specific Impulse

An interesting question relevant to pulse detonation rocket engines is whether the high propagation velocity and wall pressure of a detonation in a layered mixture of hydrogen and oxygen could result in an increase in specific impulse relative to a homogeneous mixture. Included in the simulations was a calculation of the impulse produced

from the time of ignition until the tube pressure equaled the ambient pressure. The exit flow was modeled by including the region 1 meter axially and 0.75 meter radially from the exit. This region was initialized with 100 Pa of hydrogen. The exit boundary condition for the tube was initially specified to be a one-way flow blockage boundary. When the detonation front reached the exit, the boundary condition was changed to an exit flow boundary condition.

The layered detonation produced an impulse of 0.870 N-s and the homogeneous 0.907 N-s. We attribute the lower impulse of the layered detonation to higher dissociation in the stoichiometric layer and the divergence angle of the exit flow.

V. Conclusion

Detonations in cryogenic gaseous-hydrogen/liquid-oxygen mixtures were observed to propagate at velocities up to 20% higher and produce wall pressures up to a factor of 3 higher than Chapman-Jouget equilibrium code calculations. This behavior differed significantly from previous studies of cryogenic gaseous-hydrogen, gaseous-oxygen detonations which exhibited close agreement with CJ calculations, and also differed from previous studies of detonations in sprays which exhibited lower than CJ velocities and pressures. Consideration of the data in several cases leads us to believe that this was not a transient phenomena associated with an initially overdriven detonation relaxing to a steady state.

In this study the liquid oxygen was sprayed into the chamber in a hollow-cone pattern that directed the liquid onto the wall of the tube. This created a layered mixture that had a high concentration of oxygen on the periphery and a low concentration on the centerline. CFD calculations showed that detonations in mixtures configured in this way can propagate at velocities a factor of 2 higher, and produce peak wall pressures up to a factor of 3 higher than the CJ values of homogeneous mixtures.

The layered detonation phenomena does not appear to have any advantages for pulse detonation rocket engines as the theoretical impulse was 96% of that of a homogeneous mixture at the same initial state.

Acknowledgments

This work was supported in part by the Air Force Office of Scientific Research under Mitat Birkan, Program Manager.

[1] Kailasanath, K., "Recent Developments in the Research on Pulse Detonation Engines," *AIAA Journal*, Vol. 41,No. 2, February 2003, pp. 145-159

[2] Ragland, K.W., Cosens, G.L., Cullen, R.E., "Detonation of Hydrogen-Oxygen at Low Temperature and High Pressure", *AIAA Journal*, Vol. 2, No. 1, 1964, pp. 142-144

[3] Plaster, M., McClenagan, R.D., Benz, F.J., Shepherd, J.E. Lee, J.H.S., "Detonation of Cryogenic Gaseous Hydrogen-Oxygen Mixtures," *Dynamics of Detonations and Explosions; International Colloquium on Dynamics and Explosions of Reactive Systems*, 12th, 1989, pp. 37-55

[4] Zitoun, R., Desbordes, D., Guerraud, C., Deshaies, B., "Direct initiation of detonation in cryogenic gaseous H_2-O_2 mixtures", *Shock Waves*, V. 4, 1995, pp. 331-337

[5] Strauss, W.A., Scott, J.N., "Experimental Investigation of the Detonation Properties of Hydrogen-Oxygen and Hydrogen-Nitric Oxide Mixtures at Initial Pressures up to 40 atm", *Combustion and Flame*, Vol. 19, 1972, pp. 141-143

[6] Ragland, K.W., Dabora, E.K., Nicholls, J.A., "Observed Structure of Spray Detonations", Physics of Fluids, Vol.11, No.11, pp. 2377-2388, 1968

[7] Bowen, J.R., Ragland, K.W., Steffes,F.J., Loflin, T.G., "Heterogeneous Detonation Supported by Fuel Fogs or Films," 13th Symposium (International) on Combustion, The Combustion Institute, pp.1131-1140, 1971

[8] Bar-Or, R., Sichel, M., Nicholls, J.A., "The Propagation of Cylindrical Detonations in Monodisperse Sprays," Eighteenth Symposium (International) on Combustion, The Combustion Institute, 1981, pp. 1599-1606

[9] Younglove, B.A., "Thermophysical Properties of Fluids. I. Argon, Ethylene, Parahydrogen, Nitrogen, Nitrogen Trifluoride, and Oxygen," J. Phys. Chem. Ref. Data, Vol. 11, Suppl. 1, pp. 1-11, 1982.

[10] Fried, L.E., Howard, W.M., Souers, P.C., *Cheetah 2.0 User's Manual*, Lawrence Livermore National Laboratory, UCRL-MA-117541, 1998

[11] Mitrofanov, V.V., "Ultrahigh-speed Detonation in Charges with Longitudinal Channels," Fizika Goreniya Vzryva, Vol. 11, No. 1, pp.73-81, 1974

[12] Dabora, E.K., Nicholls, J.A., Morrison, R.B., "The Influence of a Compressible Boundary on the Propagation of Gaseous Detonations," Tenth Symposium (International) on Combustion, pp. 817-830, 1965

[13] Liu, J.C. Liou, J.J., Sichel, M., Kauffman, C.W., Nicholls, J.A., "Diffraction and Transmission of a Detonation into a Bounding Explosive Layer," Twenty First Symposium (International) on Combustion/The Combustion Institute, pp, 1639-1647, 1986

[14] Jones, D.A., Sichel, M., Oran, E.S., Guirguis, R., "Detonation Transmission in Layered Explosives," Twenty Third Symposium (International) on Combustion/The Combustion Institute, pp.1805-1811, 1990

AFRL-PR-ED-TR-2005-0023 (Revised)
Primary Distribution of this Report:

AFRL/PRSA (3 CD + 2 HC)
Dr. Doug Talley
10 E. Saturn Blvd.
Edwards AFB CA 93524-7680

ERC, Inc. (1 CD + 1 HC)
Dr. Bruce Chehroudi
10 E. Saturn Blvd.
Edwards AFB CA 93524-7680

ERC, Inc. (1 CD + 1 HC)
Mr. Dustin Davis
10 E. Saturn Blvd.
Edwards AFB CA 93524-7680

AFRL/PRSA (1 CD +1 HC)
Dr. Richard Cohn
10 E. Saturn Blvd.
Edwards AFB CA 93524-7680

AFRL/PRSA (1 CD +1 HC)
Dr. Edward B. Coy
10 E. Saturn Blvd.
Edwards AFB CA 93524-7680

AFRL/PROI (1 CD + 1 HC)
Mr. Ranney Adams
2 Draco Drive
Edwards AFB CA 93524-7808

AFRL/PR Technical Library (2 CD + 1 HC)
6 Draco Drive
Edwards AFB CA 93524-7130

Chemical Propulsion Information Agency (1 CD)
Attn: Tech Lib
10630 Little Patuxent Parkway, Suite 202
Columbia MD 21044-3200

Defense Technical Information Center
(1 Electronic Submission via STINT)
Attn: DTIC-ACQS
8725 John J. Kingman Road, Suite 94
Ft. Belvoir VA 22060-6218